

Technical Report

TR-23-09

March 2023



Post-closure safety for SFR, the final repository
for short-lived radioactive waste at Forsmark

Radionuclide transport and dose calculations, PSAR version

SVENSK KÄRNBRÄNSLEHANTERING AB

SWEDISH NUCLEAR FUEL
AND WASTE MANAGEMENT CO

Box 3091, SE-169 03 Solna
Phone +46 8 459 84 00
skb.se

SVENSK KÄRNBRÄNSLEHANTERING

ISSN 1404-0344

SKB TR-23-09

ID 1979491

March 2023

**Post-closure safety for SFR, the final repository
for short-lived radioactive waste at Forsmark**

**Radionuclide transport and dose
calculations, PSAR version**

Svensk Kärnbränslehantering AB

Keywords: Post-closure safety, SFR, Final repository, Low- and intermediate-level radioactive waste, Forsmark, Safety assessment, Radionuclide transport.

This report is published on www.skb.se

© 2023 Svensk Kärnbränslehantering AB

Summary

The final repository for short-lived radioactive waste (SFR) at Forsmark, Sweden is used for the final disposal of low- and intermediate-level operational waste from Swedish nuclear facilities. The PSAR assessment of post-closure safety is an important part of the construction licence application for the extension of SFR. This report constitutes one of the main references supporting the **Post-closure safety report** and describes the radionuclide transport modelling and dose calculations, essential for the assessment of the repository's radiological consequences and compliance with the regulatory requirements on the capability to protect human health and the environment (calculations of dose rates to non-human biota is described in the **Biosphere synthesis report**).

The assessment of the protective capability is based on a set of scenarios that together illustrate the most important courses of development of the repository and its environs (**Post-closure safety report**). In the current report, the radiological consequences of the different scenarios have been estimated.

The report describes the models developed to calculate radionuclide transport from the repository (near-field) through the bedrock (geosphere) to the surface system (biosphere) (Chapter 4), including the repository layout and radionuclides considered in the calculations (Chapter 3). For each calculation case, radionuclide transport is quantified and the resulting doses that humans can incur from exposure to repository derived radionuclides are evaluated (Chapters 5–8). Finally, this report also documents the calculations of collective dose (Chapter 9).

In the calculation cases adopted for analysing the main scenario, the maximum annual dose throughout the assessment period is less than 6 μSv , i.e. well below the dose corresponding to the regulatory risk criterion that is approximately 14 μSv . For calculation cases evaluating less probable scenarios, which have a lower probability than the calculation cases in the main scenario, the maximum doses are within the range 5–50 μSv .

Sammanfattning

Slutförvaret för kortlivat radioaktivt avfall (SFR) i Forsmark, Sverige används för slutförvaring av låg- och medelaktivt driftavfall från svenska kärntekniska anläggningar. Analysen av säkerhet efter förslutning i PSAR är en viktig del av ansökan om medgivande för utbyggnaden av SFR. Denna rapport utgör en av huvudreferenserna till **Huvudrapporten säkerhet efter förslutning**. Här beskrivs radionuklidtransport-modellering och dosberäkningar, som är avgörande för utvärderingen av uppfyllnad av myndighetskrav avseende förmågan att skydda människors hälsa och miljön.

Utvärderingen av skyddsförmågan baseras på en uppsättning scenarier som tillsammans illustrerar de viktigaste förloppen av betydelse för utvecklingen av slutförvaret och dess omgivning. De radiologiska konsekvenserna av de olika scenarierna har uppskattats i denna rapport.

Rapporten beskriver de modeller som utvecklats för att beräkna radionuklidtransport från förvaret genom berggrunden till ytsystemet (kapitel 4), inklusive förvarslayout och radionuklider som beaktats i beräkningarna (kapitel 3). För varje beräkningsfall beräknas radionuklidtransport och de resulterande doser som människor kan utsättas för vid exponering för radionuklider från förvaret utvärderas (kapitel 5–8). Slutligen presenteras i denna rapport även beräkningar av kollektivdos (kapitel 9).

I de beräkningsfall som antagits för att analysera huvudscenariot är den maximala årsdosen under hela den beräknade tidsperioden lägre än $6 \mu\text{Sv}$, det vill säga långt under den dos som motsvarar riskkriteriet, som är cirka $14 \mu\text{Sv}$. För beräkningsfall som utvärderar mindre sannolika scenarier, som har lägre sannolikhet än beräkningsfallen i huvudscenariot, ligger de maximala doserna inom intervallet $5\text{--}50 \mu\text{Sv}$.

Contents

1	Introduction	9
1.1	Background	9
1.2	Post-closure safety assessment	10
1.2.1	Overview	10
1.2.2	Report hierarchy	11
1.3	This report	12
1.3.1	Purpose	12
1.3.2	Main developments since the SR-PSU	13
1.3.3	Contributing experts	13
1.4	Structure of this report	14
1.5	Terms and abbreviations	15
2	Assessment methodology and modelling approach	19
2.1	Introduction	19
2.2	Overview of the methodology	19
2.3	Calculation cases	21
2.4	Modelling approach	23
2.4.1	Modelling chain and general methodology	23
2.4.2	Overview of input data	24
2.4.3	Assessment endpoints	27
2.4.4	Simplifying assumptions	28
2.5	Management of uncertainties	29
2.5.1	Scenario uncertainties	29
2.5.2	System uncertainties	30
2.5.3	Modelling uncertainties	30
2.5.4	Data uncertainty	30
3	Repository and radionuclide inventory	31
3.1	Repository layout	31
3.1.1	Silo, vault for intermediate-level waste	32
3.1.2	1–2BMA vaults for intermediate-level waste	34
3.1.3	1BRT, vault for segmented reactor pressure vessels	37
3.1.4	1–2BTF, vaults for concrete tanks	39
3.1.5	1–5BLA, vaults for low-level waste	41
3.1.6	Plugs and other closure components	43
3.2	Initial radionuclide inventory	43
3.3	Selection of radionuclides	45
3.3.1	Safety-relevant initial inventory radionuclides	45
3.3.2	Safety-relevant decay products	46
3.3.3	Selected radionuclides	48
3.3.4	Other exposure pathways	50
3.3.5	Handling of uncertainties in the radionuclide reference inventory	50
3.3.6	Comparison with previous assessments of SFR	50
3.4	Inventory and radiotoxicity over time	53
4	Model description	57
4.1	Introduction	57
4.1.1	The compartment modelling approach	57
4.2	Near-field transport models	57
4.2.1	Control volumes and compartments	58
4.2.2	Processes handled in the near-field model	59
4.2.3	Modelling of transport through cracked concrete	60
4.2.4	Mathematical model description	60
4.2.5	Analytical estimates of the residence time based on flow and vault capacity	64

4.3	Geosphere transport model	65
4.3.1	Processes handled in the geosphere model	66
4.3.2	Conceptual model and mathematical model description	66
4.4	Biosphere transport and exposure model	69
4.4.1	Biosphere objects	69
4.4.2	Radionuclide transport model	71
4.4.3	Assessment endpoints for humans	74
5	Calculation cases in main scenario – <i>base case</i> and supporting calculation cases	77
5.1	General description	77
5.2	External conditions	77
5.3	Near-field	78
5.3.1	General handling and conditions	78
5.3.2	Silo calculations and results	83
5.3.3	1BMA calculations and results	88
5.3.4	2BMA calculations and results	93
5.3.5	1BRT calculations and results	96
5.3.6	1–2BTF calculations and results	101
5.3.7	1–5BLA calculations and results	108
5.3.8	Vault comparison for key radionuclides	111
5.3.9	Summary of the near-field radionuclide transport	120
5.4	Near-field – geosphere interface	121
5.4.1	The interface between the silo and the geosphere	121
5.5	Geosphere	122
5.5.1	Handling in the geosphere model	122
5.5.2	Releases from the geosphere	128
5.5.3	Additional analysis	129
5.5.4	Summary geosphere	135
5.6	Geosphere – biosphere interface	136
5.7	Biosphere	137
5.7.1	Handling in the biosphere models	137
5.7.2	Annual doses	140
5.7.3	Summary biosphere	145
5.8	Supporting calculation cases	145
5.8.1	Introduction	145
5.8.2	Timing of shoreline regression	145
5.8.3	Delayed release from repository	149
5.9	Summary and conclusions	154
5.9.1	Introduction	154
5.9.2	Retention in the waste vaults	154
5.9.3	Radionuclide contributions to dose	157
5.9.4	Uncertainties	165
5.9.5	Conclusions	165
6	Calculation cases in main scenario – climate evolution	167
6.1	Introduction	167
6.2	Warm climate	167
6.2.1	General description	167
6.2.2	External conditions	168
6.2.3	Handling in the near-field and geosphere models	169
6.2.4	Handling in the biosphere model	169
6.2.5	Annual release from the near-field and the geosphere	171
6.2.6	Annual doses	171
6.2.7	Summary and conclusions	174
6.3	Cold climate	174
6.3.1	General description	174
6.3.2	External conditions	175
6.3.3	Handling in the near-field and geosphere models	176

6.3.4	Handling in the biosphere model	176
6.3.5	Releases from the near-field and the geosphere	177
6.3.6	Annual doses	178
6.3.7	Summary and conclusions	180
7	Calculation cases in the less probable scenarios	181
7.1	Introduction	181
7.2	Glaciation calculation case	181
7.2.1	General description	181
7.2.2	External conditions	181
7.2.3	Handling in the near-field model	184
7.2.4	Handling in the geosphere model	187
7.2.5	Handling in the biosphere model	188
7.2.6	Annual release from the near-field	189
7.2.7	Annual release from the geosphere	191
7.2.8	Annual doses	191
7.2.9	Summary and conclusions	193
7.3	High concentrations of complexing agents calculation case	194
7.3.1	General description	194
7.3.2	Handling in the near-field models	195
7.3.3	Annual release from the near-field	196
7.3.4	Handling in the geosphere model	200
7.3.5	Handling in the biosphere model	201
7.3.6	Annual doses	201
7.3.7	Summary and conclusions	202
7.4	Alternative concrete evolution calculation case	203
7.4.1	General description	203
7.4.2	Silo calculations and results	203
7.4.3	1BMA calculations and results	206
7.4.4	2BMA calculations and results	208
7.4.5	1BRT calculations and results	210
7.4.6	1-2BTF calculations and results	212
7.4.8	Handling in the geosphere model	216
7.4.9	Handling in the biosphere model	216
7.4.10	Annual doses	216
7.4.11	Summary and conclusions	218
7.5	Earthquake calculation case	220
7.5.1	General description	220
7.5.2	Handling in the transport models	220
7.5.3	Annual doses	221
7.5.4	Summary and conclusions	222
8	Calculation cases in the residual scenarios	223
8.1	Introduction	223
8.2	Hypothetical early permafrost	224
8.2.1	General description and external conditions	224
8.2.2	Description of the calculation cases	225
8.2.3	Results	226
8.2.4	Summary and conclusions	228
8.3	Loss of engineered barrier function	228
8.3.1	General description	228
8.3.2	No sorption in the repository calculation case	229
8.3.3	No hydraulic barriers in the repository	232
8.3.4	Summary and conclusions	235
8.4	Loss of geosphere barrier function	237
8.4.1	General description	237
8.4.2	Description of the calculation cases	238
8.4.3	Results	238
8.4.4	Summary and conclusions	239

8.5	Alternative radionuclide inventory	241
8.5.1	General description	241
8.5.2	Extended operation of reactors	241
8.5.3	Increased fuel damage frequency	243
8.5.4	Extended use of molybdenum alloy fuel spacers	244
8.5.5	Summary and conclusions	246
8.6	Oxidising conditions	247
8.6.1	General description	247
8.6.2	Description of the calculation case	247
8.6.3	Results	248
8.6.4	Summary and conclusions	252
8.7	Initial concrete cracks	252
8.7.1	General description	252
8.7.2	Description of the calculation case	252
8.7.3	Results	252
8.7.4	Summary and conclusions	254
8.8	Unrepaired 1BMA	256
8.8.1	General description	256
8.8.2	Description of the calculation case	256
8.8.3	Results	258
8.8.4	Summary and conclusions	260
8.9	Unsealed repository	261
8.9.1	General description	261
8.9.2	Description of the calculation case	261
8.9.3	Results	261
8.9.4	Summary and conclusions	262
9	Collective doses	263
9.1	Introduction	263
9.2	Estimating collective doses	263
9.2.1	Collective dose to the global population	263
9.2.2	Collective dose to the regional population	264
9.3	Results	264
10	Summary and conclusions	265
10.1	Introduction	265
10.2	Summary of calculation cases	266
10.2.1	Main scenario	269
10.2.2	Supporting calculation cases	269
10.2.3	Less probable scenarios	270
10.2.4	Residual scenarios	271
10.3	Management of uncertainties	273
10.4	Conclusions	274
	References	277
	Appendix A Input data and quality assurance	283
	Appendix B Modelling of radionuclide transport through cracks in the concrete structures	299
	Appendix C Comparison with SR-PSU	305
	Appendix D Sensitivity analysis	317
	Appendix E Analytical expressions for the near-field	327

1 Introduction

This document is one of the main references to the **Post-closure safety report** that contributes to the preliminary safety analysis report (PSAR) for SFR, the repository for short-lived radioactive waste at Forsmark in Östhammar municipality, Sweden.

This chapter gives the background and a short overview of the PSAR post-closure safety assessment undertaken as part of the construction license application for the extension of SFR. Moreover, the purpose and content of this report are described.

1.1 Background

SFR is operated by the Swedish Nuclear Fuel and Waste Management Company, SKB, and is part of the Swedish system for management of waste from nuclear power plants, other nuclear activities, industry, research and medical care. In addition to SFR, the Swedish nuclear waste system also includes the repository for spent nuclear fuel and the repository for long-lived radioactive waste (SFL).

SFR consists of the existing part, SFR1 (Figure 1-1, grey part), and the extension, SFR3 (Figure 1-1, blue part). SFR1 is designed for disposal of short-lived low- and intermediate-level waste produced during operation of the Swedish nuclear power reactors, as well as waste generated during the application of radioisotopes in medicine, industry, and research. This part became operational in 1988. SFR3 is designed primarily for disposal of short-lived low- and intermediate-level waste from decommissioning of nuclear facilities in Sweden. The extension is called SFR3 since the name SFR2 was used in a previous plan to build vaults adjacent to SFR1. The repository is currently estimated to be closed by year 2075.

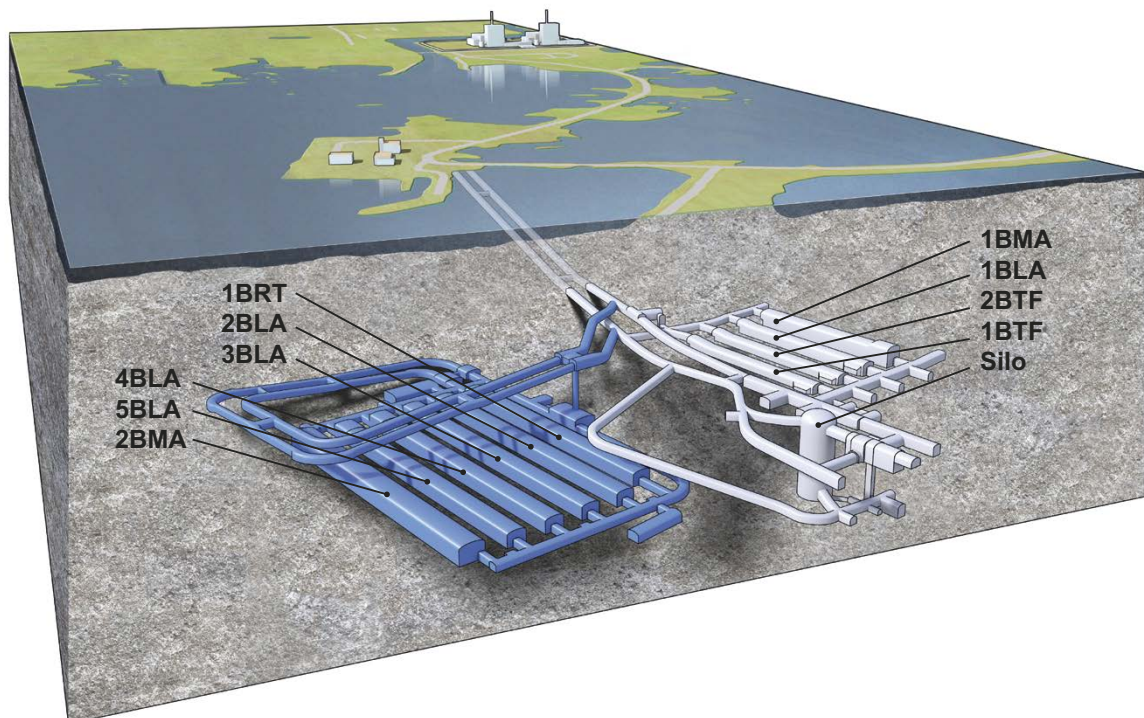


Figure 1-1. Schematic illustration of SFR. The grey part is the existing repository (SFR1) and the blue part is the extension (SFR3). The waste vaults in the figure are the silo for intermediate-level waste, 1–2BMA vaults for intermediate-level waste, 1BRT vault for reactor pressure vessels, 1–2BTF vaults for concrete tanks and 1–5BLA vaults for low-level waste.

The SFR waste vaults are located below the Baltic Sea and are connected to the ground surface via two access tunnels. SFR1 consists of one 70-metre-high waste vault (silo) and four 160-metre-long waste vaults (1BMA, 1–2BTF and 1BLA), covered by about 60 metres of bedrock. SFR3 consists of six waste vaults (2BMA, 1BRT and 2–5BLA), varying in length from 255 to 275 m, covered by about 120 metres of bedrock.

A prerequisite for the extension of SFR is the licensing of the extended facility. The licensing follows a stepwise procedure. In December 2014, SKB submitted two licence applications to extend and continue the operation of SFR, one to the Swedish Radiation Safety Authority (SSM) for permission under the Act on Nuclear Activities (SFS 1984:3) and one to the Land and Environment Court for permissibility under the Environmental Code (SFS 1998:808). In October 2019 SSM submitted their pronouncement to the Swedish Government and recommended approval of the permission sought by SKB. In November 2019 the Court submitted its statement to the Swedish Government and recommended approval of the licence application. The Swedish Government granted permit and permissibility in December 2021.

The current step in the licensing of the extended SFR is the processing of the construction license application, submitted by SKB to SSM for review under the Act on Nuclear Activities. The licence documentation consists of an application document and a set of supporting documents. A central supporting document is the preliminary safety analysis report (PSAR), with a general part consisting of ten chapters¹. Chapter 9 of the general part of that report addresses post-closure safety. The **Post-closure safety report** is the main reference to Chapter 9, and this report is a main reference to the **Post-closure safety report**.

1.2 Post-closure safety assessment

1.2.1 Overview

The main role of the post-closure safety assessment is to demonstrate that SFR is radiologically safe for humans and the environment after closure. This is done by evaluating compliance with respect to the Swedish Radiation Safety Authority's regulations concerning post-closure safety and the protection of human health and the environment. Furthermore, the post-closure safety assessment is being successively developed in the stepwise licensing process for the extended SFR, and thus the results from the PSAR assessment² provide input to the forthcoming updated assessment to be carried out before trial operation of the facility.

The overall aim in developing a geological repository for nuclear waste is to ensure that the amounts of radionuclides reaching the accessible biosphere are such that possible radiological consequences are acceptably low at all times. Important aspects of the regulations are that post-closure safety shall be maintained through a system of passive barriers. The barrier system of SFR comprises engineered and natural barriers and the function of each barrier is to, in one or several ways, contribute to the containment and prevention or retention of dispersion of radioactive substances, either directly or indirectly by protecting other barriers in the barrier system. To achieve post-closure safety, two safety principles have been defined. *Limitation of the activity of long-lived radionuclides* is achieved by only accepting waste for disposal that conforms with the waste acceptance criteria for SFR. *Retention of radionuclides* is achieved by the function of the engineered and natural barriers. The two safety principles are interlinked and applied in parallel. The engineered barrier system is designed for an inventory that contains a limited amount of long-lived radionuclides, given the conditions at the selected site and the natural barriers.

¹ SKB, 2022. PSAR SFR – Allmän del kapitel 1 – Introduktion. SKBdoc 1702853 ver 3.0, Svensk Kärnbränslehantering AB. (In Swedish.) (Internal document.)

² For brevity, the PSAR post-closure safety assessment for SFR is also referred to as “the PSAR assessment” or “the PSAR” in the present report.

The basis for evaluating compliance is a safety assessment methodology that conforms to the regulatory requirements regarding methodology, and that supports the demonstration of regulatory compliance regarding post-closure safety and the protection of human health and the environment. The overall safety assessment methodology applied is described in the **Post-closure safety report**, Chapter 2. The methodology was developed in SR-PSU (SKB TR-14-01³) based on SKB's previous safety assessment for SFR1 (SAR-08, SKB R-08-130). Further, it is consistent with the methodology used for the post-closure safety assessment for the final repository for spent nuclear fuel to the extent appropriate given the different nature of the two repositories.

1.2.2 Report hierarchy

The **Post-closure safety report** and main references for the post-closure safety assessment are listed and briefly described in Table 1-1, also including the abbreviated titles (in bold) by which they are identified in the text. Furthermore, there are numerous additional references that include documents compiled either by SKB or other organisations, or that are available in the scientific literature, as indicated in Figure 1-2.

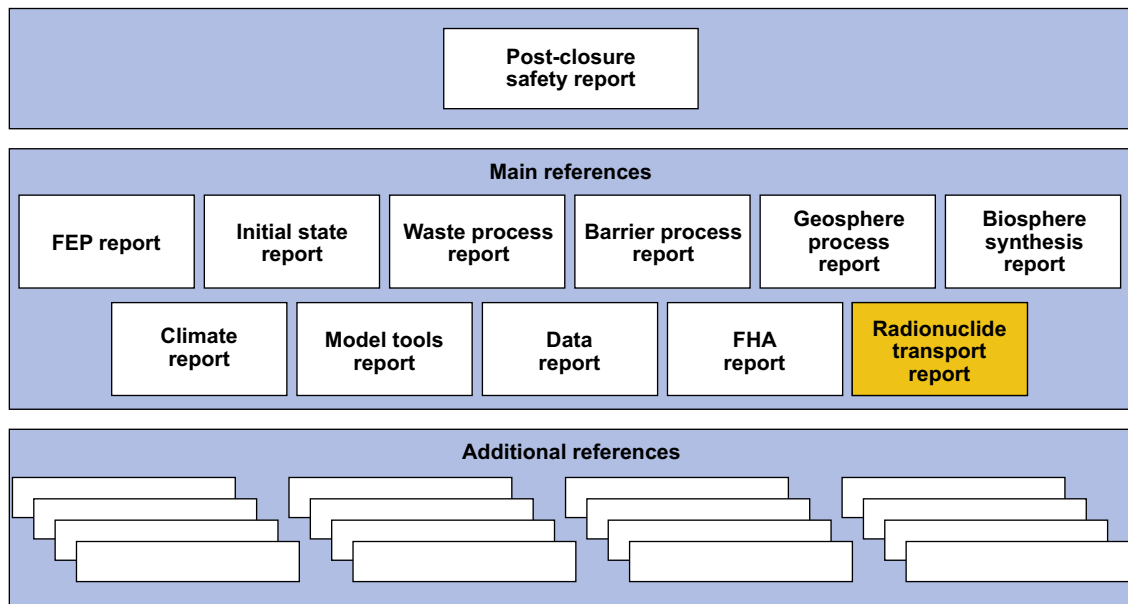


Figure 1-2. The hierarchy of the Post-closure safety report, main references and additional references in the post-closure safety assessment.

³ For SKB reports without named authors, the report number is used instead of publication year when referring to them in the text.

Table 1-1. Post-closure safety report and main references for the post-closure safety assessment. The reports are available at www.skb.se.

Abbreviated title by which the reports are identified in this report and in the main references Report number	Content
Post-closure safety report SKB TR-23-01	The main report of the PSAR post-closure safety assessment for SFR.
Initial state report SKB TR-23-02	Description of the expected conditions (state) of the repository at closure. The initial state is based on verified and documented properties of the repository and an assessment of its evolution during the period up to closure.
Waste process report SKB TR-23-03	Description of the current scientific understanding of the processes in the waste form and in the packaging, that have been identified in the FEP processing as potentially relevant for the post-closure safety of the repository. Reasons are given as to why each process is handled in a particular way in the safety assessment.
Barrier process report SKB TR-23-04	Description of the current scientific understanding of the processes in the engineered barriers that have been identified in the FEP processing as potentially relevant for the post-closure safety of the repository. Reasons are given as to why each process is handled in a particular way in the safety assessment.
Geosphere process report SKB TR-14-05	Description of the current scientific understanding of the processes in the geosphere that have been identified in the FEP processing as potentially relevant for the post-closure safety of the repository. Reasons are given as to why each process is handled in a particular way in the safety assessment.
Climate report SKB TR-23-05	Description of the current scientific understanding of climate and climate-related issues that have been identified in the FEP processing as potentially relevant for the post-closure safety of the repository. Description of the current scientific understanding of the future evolution of climate and climate-related issues.
Biosphere synthesis report SKB TR-23-06	Description of the present-day conditions of the surface systems at Forsmark, and natural and anthropogenic processes driving the future development of those systems. Description of the modelling performed for landscape development, radionuclide transport in the biosphere and potential exposure of humans and non-human biota.
FEP report SKB TR-14-07	Description of the establishment of a catalogue of features, events and processes (FEPs) that are potentially relevant for the post-closure safety of the repository.
FHA report SKB TR-23-08	Description of the handling of inadvertent future human actions (FHA) that are defined as actions potentially resulting in changes to the barrier system, affecting, directly or indirectly, the rate of release of radionuclides, and/or contributing to radioactive waste being brought to the surface. Description of radiological consequences of FHAs that are analysed separately from the main scenario.
Radionuclide transport report SKB TR-23-09 (this report)	Description of the radionuclide transport and dose calculations carried out for the purpose of demonstrating compliance with the radiological risk criterion.
Data report SKB TR-23-10	Description of how essential data for the post-closure safety assessment are selected, justified and qualified through traceable standardised procedures.
Model tools report SKB TR-23-11	Description of the model tool codes used in the safety assessment.

1.3 This report

1.3.1 Purpose

This report is the main document for reporting the radionuclide transport and dose calculations conducted for the PSAR. As such, this report provides key information for the subsequent assessment of compliance to the regulatory requirements on the capability to protect human health and the environment presented in the **Post-closure safety report**, Chapter 10.

The assessment of the protective capability is based on a set of scenarios that together illustrate the most important courses of development of the repository and its environs (**Post-closure safety report**). To estimate radiological consequences, the scenarios are evaluated with the aid of calculation cases that

are analysed with mathematical models. The radionuclide transport and dose modelling are performed with different models representing different parts of the disposal system; the near-field (repository), the geosphere (host rock) and the biosphere (surface system).

The modelling of radionuclide transport in the near-field and geosphere is described in detail in this report. Further, modelling of radionuclide transport in the surface system and annual doses to humans, is described in less detail to provide a complete overview. A fully detailed description related to doses to humans, and dose rates to non-human biota, is given in the **Biosphere synthesis report**. Supporting calculation cases with conditions that do not affect the near-field and geosphere are only presented in the **Biosphere synthesis report**.

1.3.2 Main developments since the SR-PSU

Updates to the radionuclide transport and dose calculations in the PSAR compared with the SR-PSU (SKB TR-14-09) involve changes in both input data and models. These changes have been made to incorporate modifications in the repository design, as well as new information from ongoing research and development (**Post-closure safety report**, Section 1.5.2). The radionuclide transport models for the near-field have also been updated following SSM's review comments on the SR-PSU. This concerns, in particular, the documentation which has been expanded with a separate report describing the near-field models (Åstrand et al. 2022). Models have also, to some extent, been simplified to avoid overly detailed implementation of features that are of minor importance for the overall performance of the repository. The set of scenarios, calculation cases and supporting calculation cases has been updated to include updated information on external conditions and internal processes. The handling of data uncertainty has also been extended with probabilistic handling of uncertainties in the radionuclide inventory, concentration of complexing agents and groundwater flow in the repository and geosphere.

The main differences in dose due to the updates and differences in the near-field, geosphere and biosphere modelling in the PSAR compared to the SR-PSU are discussed in Appendix C. Further details about the updates made in the near-field modelling can be found in Appendix D in Åstrand et al. (2022). The updates in the biosphere modelling are discussed in the **Biosphere synthesis report**.

1.3.3 Contributing experts

Project leader for the PSAR safety assessment has been Jenny Brandefelt (SKB). A number of people from various fields of expertise have been involved in the development of models and preparation of data for the radionuclide transport and dose calculations. The most involved in preparation of this report are listed below in alphabetical order:

Name	Affiliation	Contribution to this report
Katrin Ahlford	SKB	waste properties
Patrick Bruines	SKB	geosphere hydrogeology
Per-Anders Ekström	Kvot AB	numerical modelling and report co-author
Svante Hedström	SKB	near-field chemistry and report co-author
Olle Hjerne	SKB	biosphere modelling and report co-author
Thomas Hjerpe	Kemakta Konsult AB	collective dose and report co-author
Johan Liakka	SKB	climate data and report co-author
Sari Peura	SKB	biosphere data
Maria Rasmusson	SKB	hydrological data and report co-author
Jan Rosdahl	SKB	near-field chemistry
Peter Saetre	SKB	biosphere modelling and report co-author
Ola Wessely	SKB	near-field modelling and report co-author
Per-Gustav Åstrand	SKB	numerical modelling and report editor

This report has been significantly improved at different stages by adjustments in accordance with comments provided by informal and factual reviewers. Informal reviewers have been; Anna-Maria Jakobsson (SKB), Lindsay Krall (SKB), Maria Lindgren (Kemakta Konsult AB), Olli Nummi (Fortum) and Russell Alexander (Bedrock geosciences). Factual reviewers have been; Mike Thorne (Mike Thorne and Associates Ltd.) and Jordi Bruno (Amphos 21 Consulting).

1.4 Structure of this report

This report contains descriptions of models, calculation cases and results from the radionuclide transport and dose calculations. The following is a brief description of the contents.

Chapter 1 – Introduction. This chapter describes the background and the role of the report. Furthermore, definitions are provided as are explanations of the abbreviations used.

Chapter 2 – Assessment methodology and modelling approach. This chapter describes the contribution of the radionuclide transport and dose calculations to the overall safety assessment methodology as well as the modelling approach and handling of uncertainties.

Chapter 3 – Repository and radionuclide inventory. This chapter describes the repository design and the radionuclide inventory used in the calculations. This includes the initial selection performed to identify radionuclides potentially relevant for the post-closure safety and, thus, considered in the radionuclide transport modelling.

Chapter 4 – Model description. This chapter presents the radionuclide transport models representing the near-field (repository), the geosphere (host rock) and the biosphere (surface system) used in the post-closure safety assessment.

Chapter 5 – Calculation cases in the main scenario – *base case* and supporting calculation cases. This chapter describes the handling in the modelling of the *present-day climate calculation case*, used as the *base case* in the PSAR, as well as two supporting calculation cases. Furthermore, the results of these calculation cases, i.e. activity releases from near-field and the geosphere and annual doses, are presented in this chapter.

Chapter 6 – Calculation cases in the main scenario – climate evolution. This chapter describes the handling in the modelling and results for two calculation cases that, together with the *base case*, represent the range of probable evolution of external conditions: the *warm* and *cold climate calculation cases*.

Chapter 7 – Calculation cases in the less probable scenarios. This chapter describes the handling in the modelling and results for the calculation cases identified for less probable scenarios.

Chapter 8 – Calculation cases in the residual scenarios. This chapter describes the handling in the modelling and results for the calculation cases identified for residual scenarios.

Chapter 9 – Collective doses. This chapter describes the methodology, calculations and results for collective dose for the *base case* and calculation cases in the main and less probable scenarios with releases that are different from the *base case* for the first 1 000 years.

Chapter 10 – Summary and conclusions. This chapter presents a summary of doses to the most exposed group and collective doses as well as conclusions.

Appendix A, Input data and quality assurance. This appendix describes how data and models have been handled to ensure the quality of the assessment.

Appendix B – Modelling of radionuclide transport through cracks in the concrete structures. This appendix describes the handling of cracks in the concrete structures in the near-field and motivate the way cracks are represented in the radionuclide transport modelling.

Appendix C – Comparison with SR-PSU. This appendix summarises the main differences in annual dose calculated for the *base case*, resulting from updates in the near-field, geosphere and biosphere modelling in the PSAR compared to the SR-PSU.

Appendix D – Sensitivity analysis. This appendix presents results from a sensitivity analysis of four selected radionuclides relevant to dose.

Appendix E – Analytical expressions for the near-field. This appendix describes simplified analytical estimates of the releases from the near-field. These estimates provide scoping calculations and illustrate how barrier properties impact the transport resistance and overall performance of the barriers in the different vaults.

1.5 Terms and abbreviations

Terms and abbreviations used in this report are listed in Table 1-2.

Table 1-2. Explanations of terms and abbreviations used in this report.

Term or abbreviation	Description
1–2BTF	Vaults for concrete tanks in SFR1.
1BLA	Vault for low-level waste in SFR1.
1BMA	Vault for intermediate-level waste in SFR1.
1BRT	Vault for reactor pressure vessels in SFR3.
2–5BLA	Vaults for low-level waste in SFR3.
2BMA	Vault for intermediate-level waste in SFR3.
AD	Anno Domini.
Annual dose	Assessment endpoint calculated as the annual effective dose to an adult, where the annual effective dose is defined as the effective dose from external exposure in a year, plus the committed effective dose from intakes of radionuclides in that year.
Barrier	In the safety assessment context, a barrier is a physical feature, engineered or natural, which in one or several ways contributes to the containment and retention or prevention of dispersion of radioactive substances, either directly or indirectly by protecting other barriers.
<i>Base case</i>	The <i>base case</i> constitutes the basis for the radionuclide transport and dose calculations. The <i>present-day climate calculation case</i> is selected as the <i>base case</i> for the analysis of the main scenario. Models built and assumptions made for the other calculation cases are only described if they deviate from the <i>base case</i> and results from these cases are compared with those for the <i>base case</i> .
Bedrock	In the safety assessment context, the solid rock beneath the regolith also including the groundwater in the rock.
Best estimate (BE)	A single value for a parameter, describing a property or a process, used in deterministic calculations. Best estimates are typically derived from site and/or literature data and often correspond to mean values of the underpinning datasets.
Biosphere object	A part of the landscape that will potentially receive radionuclides released from a repository, directly or indirectly via other biosphere objects.
Biosphere system	In the safety assessment context, refers to the part of the repository system that is above the geosphere, with all its abiotic and biotic processes and features, as well as humans and human behaviour. Synonymous with Surface system.
BioTE _x	The Biosphere Transport and Exposure model. Used to calculate concentrations and subsequent transport of radionuclides in different environmental media in a biosphere object and potential doses to human and dose rates to non-human biota.
Bulk density	The bulk density of a porous medium is defined as the mass of the solid particles that make up the medium divided by the total volume they occupy. The total volume includes particle volume, inter-particle void volume and internal pore volume (cf. "particle density").
Calculation case (CC)	Used for the quantitative assessment of the scenarios selected in the safety assessment, typically by calculating doses.
Cautious	Indicates an expected overestimate of annual effective dose that follows from assumptions made, or models and parameter values selected, within the reasonably expected range of possibilities.
Climate domain	A climatically determined environment with a specific set of characteristic processes of importance for post-closure safety.
Clab	Central interim storage facility for spent nuclear fuel in Simpevarp, Sweden.
Collective dose	In the safety assessment context, equal to the collective effective dose, which is the sum of all the individual effective doses to members of a population. The special name of the unit of the collective effective dose is the man sievert (man Sv).
COMSOL Multiphysics	Commercial software for finite element analysis, solver and multi-physics simulation.
Conceptual model	A qualitative description of a physical system, including important processes and components and interactions between these components.
CR	Concentration ratio. Used to calculate uptake of radionuclides by biota, defined as the element-specific ratio between the concentration in biota and in the surrounding medium (soil or surface water).
Crushed rock	Mechanically crushed rock material with varying grain size distribution and hydraulic properties. The selected grain size distribution is dependent on the required properties. See also macadam.
Data uncertainty	Uncertainties concerning all quantitative input data, that is parameter values, used in the assessment.
Deterministic analysis	Analysis using single numerical values for parameters (taken to have a probability of one), which leads to a single value for the result, at each time point.
DFN	Discrete fracture network.

Term or abbreviation	Description
Discharge locations	Locations/areas where groundwater reaches the surface ecosystem. In the safety assessment context, this term refers to discharge of groundwater that has passed through the repository volume in the geosphere and hence could bring radionuclides to the surface. Synonymous with Discharge points.
DM	Drained-mire farmers. Refers to self-sustained agriculture in which wetlands are drained and cultivated (both crop and fodder production). It is one of four potentially exposed groups (PEGs) in this safety assessment.
EC	Electron capture (a mode of radioactive decay).
Effective dose	Effective dose is a measure of dose designed to reflect the amount of radiation detriment likely to result from the dose. It is defined as a weighted summation of the tissue or organ equivalent doses, that is the summation of the absorbed dose in each tissue or organ multiplied by appropriate radiation weighting factor, each multiplied by the appropriate tissue weighting factor.
Exposure	The act or condition of being subject to irradiation (not to be used as a synonym for dose, which is a measure of the effects of exposure).
External exposure	Exposure to radiation from a source outside the body.
FARF31	Semi-analytical computer code for modelling of radionuclide transport in the geosphere.
FARFCOMP	Compartment-based computer code for modelling of radionuclide transport in the geosphere.
FEP	Features, events and processes.
FHA	Future human actions.
Geosphere	The bedrock, including groundwater, surrounding the repository, bounded above by the surface system.
GP	Garden-plot households. Refers to a type of household that is self-sustained with respect to vegetables and root crops produced through small-scale horticulture. It is one of four potentially exposed groups (PEGs) in this safety assessment.
Harmful effects	Cancer (fatal and non-fatal) as well as hereditary effects in humans caused by ionising radiation, in accordance with paragraphs 47–51 in ICRP Publication 60 (ICRP 1991).
HCP	Hydrated cement paste.
HG	Hunter-gatherers. Refers to a community that uses the undisturbed surface ecosystems as living space and to obtain food. It is one of four potentially exposed groups (PEGs) in this safety assessment.
IAEA	International Atomic Energy Agency.
ICRP	International Commission on Radiological Protection.
Infilling	Infilling describes the combined process of sedimentation and organogenic deposition, which turns lakes into wetlands.
Initial state	The expected state of the repository and its environs at closure of the repository, including uncertainties.
Insolation	The amount of solar radiation received per unit area at the top of the Earth's atmosphere.
Intermediate-level waste	Radioactive waste that requires final disposal in a geological repository and shielding during handling. Cooling of the waste is not required.
Internal exposure	Exposure to radiation from a source within the body.
IO	Infield–outland farmers. Refers to a self-sustained agriculture in which infield farming of crops is dependent on nutrients from wetlands for haymaking (outland). It is one of four potentially exposed groups (PEGs) in this safety assessment.
IPCC	Intergovernmental Panel on Climate Change.
ISA	Isosaccharinate, a complexing agent that is a cellulose degradation product.
ISO	International Organization for Standardization.
IT	Isomeric transition.
Long-lived radionuclide	In the safety assessment context, radionuclides with a half-life exceeding 31 years.
Low-level waste	Radioactive waste that requires final disposal in a geological repository. Shielding during handling and cooling are not required.
Macadam	Crushed rock sieved in fractions 2–65 mm. Macadam has no or very little fine material (grain size < 2 mm). The fraction is given as intervals, for example "Macadam 16-32" is crushed rock comprising the fraction 16–32 mm.
Mathematical model	A quantitative description of a physical system, where important processes and components, and interactions between components, are represented by parameters and equations.
MIKE SHE	Computer code used to simulate groundwater and surface water flow.
Model waste package	A simplified representation of waste used in the near-field models.
Modelling uncertainty	Uncertainties arising from a necessarily imperfect understanding of the nature of processes involved in repository evolution which leads to imperfect conceptual models. The mathematical representation of conceptual models and imprecision in the numerical solution of mathematical models are other sources of uncertainty which fall into this category.

Term or abbreviation	Description
Near-field	Typically used for the model domain representing the repository, which may contain part of the nearby bedrock to obtain boundary conditions.
NHB	Non-human biota.
NPP	Nuclear power plant.
NTA	Nitrilotriacetic acid, a complexing agent.
Packaging	The outer container, such as a mould, drum or ISO-container, protecting the waste form (synonymous with Waste packaging).
Particle density	The particle density of a porous medium is the intrinsic density of the solid particles that make up the medium, i.e. the density the medium would have if it had zero porosity (cf. "bulk density").
PDF	Probability density function.
Pessimistic	Indicates an expected overestimate of annual effective dose that follows from assumptions made, or models and parameter values selected, beyond the reasonably expected range of possibilities.
PFL	Posiva Flow Logging method.
Potentially exposed group (PEG)	Groups of individuals potentially subjected to the highest exposure during any time of the assessment period.
Protective capability	The capability to protect human health and the environment from the harmful effects of ionising radiation.
PSAR	Preliminary Safety Analysis Report.
PSU	Programme SFR extension.
PWR	Pressurised water reactor.
QA	Quality assurance.
Radiotoxicity	The product of the activity of a radionuclide and its corresponding dose coefficient for intake.
RCP4.5	Emission scenario from IPCC in which radiative forcing is stabilised at approximately 4.5 W m ⁻² at 2100 AD.
RCP6.0	Emission scenario from IPCC in which radiative forcing is stabilised at approximately 6.0 W m ⁻² at 2100 AD.
Reference evolution	The probable post-closure evolution of the repository and its environs, including uncertainties in the evolution that may affect the protective capability of the repository.
Regolith	All matter overlying the bedrock. This includes both minerogenic and organogenic (i.e. derived from organic substances) deposits.
Relative sea level (RSL)	The vertical position of the sea relative to land, as measured in the reference height system RH 2000. The relative sea level is determined by the net effect of eustasy and isostasy.
Repository	The disposed waste packages, the engineered barriers and other repository structures.
Repository system	The repository, the bedrock and the biosphere surrounding the repository. Synonymous with repository and its environs.
Risk	Refers in the post-closure safety assessment to the radiological risk, defined as the product of the probability of receiving a radiation dose and the harmful effects of that radiation dose.
Risk dilution	In the context of the radionuclide transport, dose and risk calculations, risk dilution in a broad sense refers to a situation in which an increase in the uncertainty of the values of important input parameters, or in the assumptions with respect to the timing of an event, leads to a decrease in the calculated annual dose and associated annual radiological risk.
RNT	Radionuclide transport.
RPV	Reactor pressure vessel.
SAFE	Post-closure safety assessment for SFR1 reported to the regulatory authorities in 2001.
Safety analysis	In the context of the present safety assessment, the distinction is generally not viewed as important and therefore safety analysis and safety assessment are used interchangeably. However, if the distinction is important, safety analysis should be used as a documented process for the study of safety and safety assessment should be used as a documented process for the evaluation of safety.
Safety assessment	The safety assessment is the systematic process periodically carried out throughout the lifetime of the repository to ensure that all the relevant safety requirements are met and entails evaluating the performance of the repository system and quantifying its potential radiological impact on human health and the environment. The safety assessment corresponds to the term <i>safety analysis</i> in the Swedish Radiation Safety Authority's regulations.
Safety function	A role through which a repository component contributes to post-closure safety.
SAR	Safety Analysis Report.
SAR-08	Post-closure safety assessment for SFR1 reported to the regulatory authorities in 2008.
Scenario	A description of a potential evolution of the repository and its environs, given an initial state and specified external conditions and their development and how the protective capability of the repository is affected.

Term or abbreviation	Description
Scenario uncertainty	Uncertainties with respect to external conditions and internal processes in terms of type, degree and time sequence, resulting in an uncertainty in the future states of the repository system.
SE-SFL	The evaluation of post-closure safety for a proposed repository concept for SFL.
SFL	Final repository for long-lived radioactive waste.
SFR	Final repository for short-lived radioactive waste at Forsmark.
SFR1	The existing part of SFR.
SFR3	The extension part of SFR.
Shoreline displacement	The movement of the shoreline, that is the variation in time of the spatial location of the shoreline.
Shoreline regression	Migration of the coastline away from the land as the relative sea level decreases, which in turn increases the extent of the land area.
Short-lived radionuclide	In the safety assessment context, radionuclides with a half-life shorter than 31 years.
Silo	Cylindrical vault for intermediate-level waste (part of SFR1).
SKB	Swedish Nuclear Fuel and Waste Management Company.
SKBdoc	Internal document management system at SKB.
Sorption coefficient	Element-specific sorption coefficient, defined as the ratio between the elemental concentrations in the solid and liquid phases.
SR-PSU	Post-closure safety assessment that was a reference to the F-PSAR for the extended SFR, reported to the regulatory authority in 2014.
SRC	Standardised regression coefficients.
SRF	Sorption Reduction Factor (due to complexing agents).
SRF group	Group of radionuclides with analogous complexation properties and thus same SRF values.
SR-Site	Post-closure safety assessment for a spent nuclear fuel repository in Forsmark, reported to the regulatory authority in 2011.
SSM	Swedish Radiation Safety Authority.
SSMFS	Regulations of the Swedish Radiation Safety Authority.
SVN	Subversion. A version handling system used for code and data in the PSAR SFR.
Surface ecosystem	The surface ecosystem refers to the part of the environment above the bedrock, with all its abiotic and biotic processes and features.
Surface system	In the safety assessment context, refers to the part of the repository system that is above the geosphere, with all its abiotic and biotic processes and features, as well as humans and human behaviour. Synonymous with Biosphere system.
System component	A physical component of the repository system; a sub-system.
System uncertainty	Uncertainties concerning comprehensiveness issues, i.e. the question of whether all aspects important for the safety evaluation have been identified and whether the assessment is capturing the identified aspects in a qualitatively correct manner.
UNSCEAR	United Nations Scientific Committee on the Effects of Atomic Radiation.
Waste domain	Part of waste vaults where waste is placed (inside the engineered barriers).
Waste form	Waste in its physical and chemical form after treatment and/or conditioning.
Waste package	The waste (form) and its packaging.
Waste packaging	The outer container, such as a mould, drum or ISO-container, protecting the waste form (synonymous with Packaging).
Waste stream	The pathway of a specific waste, from its origin through to its disposal in a defined waste type.
Waste type	SKB's systematic classification of wastes according to a developed code system.
Waste vault	Part of repository where waste is disposed.

2 Assessment methodology and modelling approach

2.1 Introduction

Chapter 2 in the **Post-closure safety report** describes the methodology used in the overall safety assessment. The methodology specifically related to radionuclide transport and dose calculations is presented in this chapter. In Section 2.2, the role of these calculations in the safety assessment methodology is described. The main objective of the radionuclide transport calculations is to calculate radiation doses used in the assessment of risk, supporting the demonstration of compliance with regulatory requirements on radiological risk. To this end, several calculation cases are defined for each safety assessment scenario, described in Section 2.3. Finally, Section 2.4 briefly discusses the modelling approach, input data and their uncertainties.

2.2 Overview of the methodology

The overall methodology applied for the assessment of post-closure safety in the PSAR consists of ten main steps, described in the **Post-closure safety report**, Sections 2.6.1 to 2.6.10, and summarised in Figure 2-1. This report contributes to step 9: scenario analysis. This step comprises the selection and description of calculation cases, the radionuclide transport and dose calculations as well as the assessment of annual risk and protection of the environment.

A prerequisite for the radionuclide transport and dose calculations is that an initial state is defined, describing the expected state of the repository and its environs at repository closure. This is accomplished in step 2 in the methodology and is described in the **Post-closure safety report**, Chapter 4. Further, the reference evolution needs to be described, defined as the probable post-closure evolution of the repository and its environs, including uncertainties in the evolution that may affect the capability of the repository to protect human health and the environment. This is accomplished in step 7 in the methodology and is described in the **Post-closure safety report**, Chapter 6. The reference evolution starts from the initial state (step 2), and then follows the reference external conditions for the next 100 000 years (step 3), accounting for FEPs that are likely to influence the evolution (step 1). The description builds on the knowledge gained in the previous steps of the assessment methodology (step 1–6), as well as dedicated studies performed in order to assess the post-closure evolution of the repository and its environs. Three *variants* of the reference external conditions (the *present-day climate variant*, *warm climate variant* and *cold climate variant*) are considered. These represent the range of probable evolution of the external conditions at Forsmark over the next 100 000 years (**Post-closure safety report**, Section 2.6.3).

The final prerequisite step for the radionuclide transport and dose calculations concerns the selection of scenarios, which is accomplished in step 8. Following the general advice to the regulations (SSMFS 2008:21), three types of scenarios are selected: a main scenario, less probable scenarios and residual scenarios. These are described in the **Post-closure safety report**, Section 2.6.8 and summarised in the following.

- The main scenario (**Post-closure safety report**, Chapter 7) takes into account the most probable changes within the repository and its environs based on the initial state (step 2), the reference external conditions (step 3) and the reference evolution (step 7). It is used as the starting point for the analysis of the impact of uncertainties.
- Less probable scenarios (**Post-closure safety report**, Chapter 8) evaluate uncertainties related to alternative evolutions of the repository and its environs, or variations in the specified initial state or external conditions, that are not evaluated within the framework of the main scenario.
- Residual scenarios (**Post-closure safety report**, Chapter 9) are selected to illustrate the significance of individual barriers and barrier functions, detriment to humans intruding into the repository, and the consequences of an unsealed repository that is not monitored.

To estimate radiological consequences, the scenarios are evaluated with the aid of calculation cases, most of which are analysed in this report (see further Section 2.3). The calculated doses from the calculation cases in the main scenario and less probable scenarios are carried on to the assessment of annual risk (step 9) where they are compared with criteria stipulated in SSM's regulations (**Post-closure safety report**, Chapter 10). Calculations of residual scenarios are not propagated to the risk assessment. Uncertainty management is an integral part of the post-closure assessment methodology (**Post-closure safety report**, Section 2.5). An overview of the handling of uncertainties in the radionuclide transport and dose calculations is given in Section 2.5 in this report.

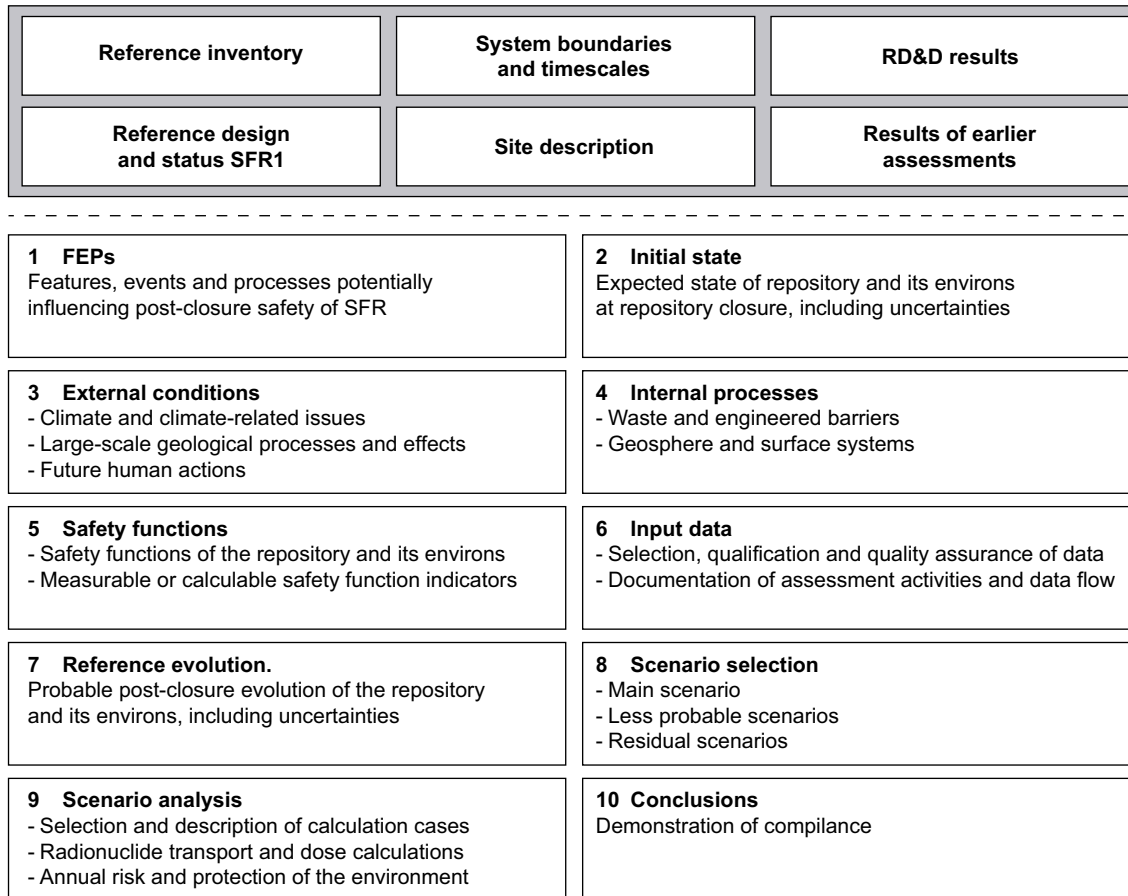


Figure 2-1. An outline of the ten main steps of the present post-closure safety assessment. The boxes above the dashed line are prerequisites for the methodology and its implementation, described in the **Post-closure safety report**, Sections 2.2 to 2.4. The contents of each step are described in detail in the **Post-closure safety report**, Sections 2.6.1 to 2.6.10. This report contributes to step 9: scenario analysis.

2.3 Calculation cases

The radionuclide transport and dose calculations aim to provide a quantitative assessment of radiological consequences for the selected scenarios, in terms of the annual effective dose to a representative individual in the group exposed to the greatest risk. To this end, calculation cases are defined for each scenario (**Post-closure safety report**, Section 2.6.9). Often, only a single calculation case is selected per scenario. For some scenarios, however, several calculation cases are considered necessary in order to evaluate all uncertainties identified by the scenario description. A calculation case may also include variants, selected to evaluate the impact of alternative assumptions within the framework of the calculation-case description. An overview of the calculation cases included in the present safety assessment is given in Table 2-1.

Three calculation cases are selected for the main scenario based on the reference external conditions. The *present-day climate calculation case* is selected as *base case* in the present safety assessment. The descriptions for all other calculation cases are based on differences from the *base case* regarding external conditions as well as handling of FEPs for the repository (near-field), the bedrock surrounding the repository (geosphere) and the surface systems above the repository (biosphere). The *warm climate calculation case* and *cold climate calculation case* of the main scenario represent the range of probable evolution of the external conditions.

A set of calculation cases is also defined to evaluate less probable and residual scenarios. In addition, the main scenario is complemented with a set of supporting calculations (Table 2-1), providing sensitivity analyses of specific aspects coupled to external conditions and internal processes potentially important for radionuclide transport through the repository system. The objective of these calculations is to support the selection of assumptions in the *base case* and to improve the confidence in the results of the main scenario. These calculations are not propagated to the summation of radiological risk (**Post-closure safety report**, Section 2.6.9). Two supporting calculation cases are evaluated in this report (Table 2-1).

Some of the calculation cases are described in other PSAR references rather than in this report. These include supporting calculations designed to evaluate the effects of specific uncertainties and assumptions in the biosphere models (indicated by superscripted “a” in Table 2-1), as well as calculation cases related to future human actions (FHA; indicated by superscripted “b” in Table 2-1), which are evaluated in residual scenarios. The supporting calculations for the biosphere and the FHA calculation cases are described in the **Biosphere synthesis report** and the **FHA report**, respectively.

Table 2-1. Scenarios and calculation cases analysed in the PSAR.

Scenario		Calculation case
Main scenario	Present-day climate (<i>base case</i>)*	
	Warm climate*	
	Cold climate	
	<i>Supporting calculation cases</i>	Timing of shoreline regression
		Delayed release from repository
		Subhorizontal fracture ^a
		Alternative landscape configurations ^a
		Ecosystem properties ^a
		Alternative delineation ^a
		Mire object properties ^a
Calcite depletion ^a		
Less probable scenarios	Glaciation	Glaciation
	High concentrations of complexing agents	High concentrations of complexing agents*
	Alternative concrete evolution	Alternative concrete evolution*
	Earthquake	Earthquake
Residual scenarios	Hypothetical early permafrost	No effect on engineered barriers Effect on engineered barriers
	Loss of engineered barrier function	No sorption in the repository No hydraulic barriers in the repository
	Loss of geosphere barrier function	No sorption in the geosphere No transport retention in the geosphere
	Alternative radionuclide inventory	Extended operation of reactors Increased fuel damage frequency Extended use of molybdenum-alloy fuel spacers
	Oxidising conditions	Oxidising conditions
	Initial concrete cracks	Initial concrete cracks
	Unrepaired 1BMA	Unrepaired 1BMA
	Unsealed repository	Unsealed repository
	Drilling into the repository	Drilling event ^b Construction on drilling detritus landfill ^b Cultivation on drilling detritus landfill ^b
	Intrusion well	Intrusion well ^b
	Water management	Construction of a water impoundment ^b
	Underground constructions	Rock cavern in the close vicinity of the repository ^b Mine in the vicinity of the repository ^b

Included in the risk assessment.

a Described in the Biosphere synthesis report.

b Described in the FHA report.

* Included in the calculations of collective dose.

2.4 Modelling approach

2.4.1 Modelling chain and general methodology

Figure 2-2 presents a schematic diagram of the main flow of data within the model chain. The chain starts with the near-field model that describes the transport, retention and release of radionuclides in the waste domain and the surrounding engineered barriers in a vault. The radionuclide release to the geosphere at the waste vault-bedrock interface is also calculated. The geosphere model describes the subsequent transport and retention of radionuclides through and in the fractured bedrock towards the surface. Finally, the biosphere model describes transport and accumulation of radionuclides in aquatic and terrestrial ecosystems. To calculate exposure from cultivation, the biosphere model also includes stylised representations of agricultural systems. The endpoints of the calculations are the annual doses to humans and dose rates to non-human biota. In this report, only annual doses to humans are presented (see further Section 2.4.3). Dose rates to non-human biota are analysed in the **Biosphere synthesis report**.

The models calculating radionuclide transport and dose are built using the compartment approach. All calculations for the near-field and the biosphere are performed with models implemented in Ecolego (**Model tools report**), which is a tool for creating compartment models for deterministic or probabilistic simulations of material transport. The radionuclide transport model for the geosphere is implemented in a Matlab program that was originally developed for the safety evaluation SE-SFL (SKB TR-19-06). In this report, an overview of the models used for the calculations is presented (Chapter 4). The near-field models are described in detail in Åstrand et al. (2022), the geosphere model in SKB TR-19-06 and the biosphere model in Saetre et al. (2013) and the **Biosphere synthesis report**.

The radionuclide transport calculations are carried out as dynamic simulations, where the output from one model, in terms of the annual activity release for each radionuclide, is used as input for the next. The modelling tools are coupled indirectly, i.e. the model chain has not been executed in continuous mode, but rather for one entity at a time followed by a semi-automatic transfer of files to the calculation tool for the subsequent model. To ensure functional coupling between the three models, the models have been designed to use compatible definitions of the parameters, so that the inputs and outputs are not only numerically compatible, but also so that the same FEPs are represented consistently over the whole modelling chain. Time-dependent releases from the geosphere are fed directly into the biosphere transport model. This enables the dose calculation to take the release history and the evolution of the biosphere system into account.

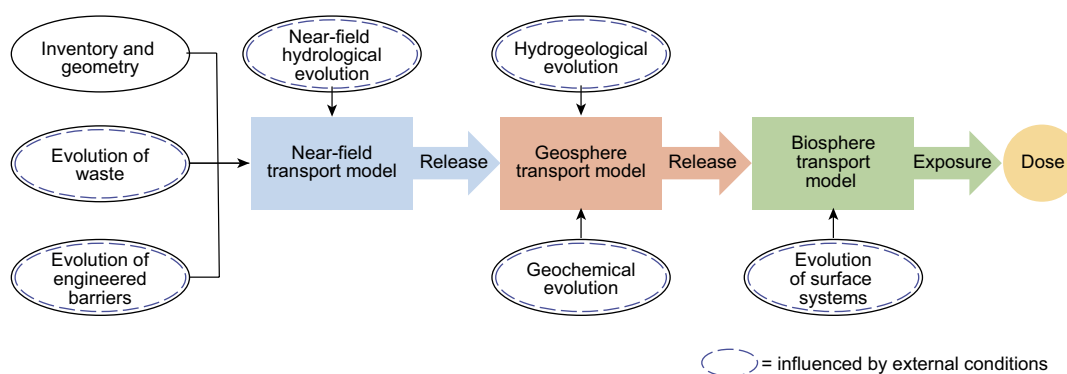


Figure 2-2. Models and data used for the radionuclide transport and dose calculations. Rectangles represent modelling activities and ovals represent data. Blue dashed ovals indicate that the data are influenced, directly or indirectly, by external conditions.

The calculations are time-dependent and cover the entire assessment period of 100 000 years, starting from the closure of the repository⁴. Calculations are performed both deterministically and probabilistically for most calculation cases. The probabilistic calculation cases are analysed using 1 000 simulations selected using Monte Carlo methods. For each simulation, random parameter values are sampled from pre-defined ranges that capture the uncertainties in the data. Parameters that are used in several transport models are only sampled once in order to ensure consistency in the handling between the models.

2.4.2 Overview of input data

The radionuclide transport and dose modelling use input data from several sources (Figure 2-2). The radionuclide activity at closure (i.e. the radionuclide inventory) constitutes the starting point for the calculations. To calculate transport and retention of radionuclides from the near-field to the surface, spatiotemporal data describing the post-closure evolution of the three sub-systems are used. Near-field data describe how the physical and chemical conditions change in the repository, which affects e.g. the groundwater flow and sorption in the engineered barriers and the waste. Characteristics of groundwater flow, water-bearing fractures and sorption properties in the bedrock matrix are important for the geosphere transport. Transport and accumulation of radionuclides in the biosphere are evaluated using representative data for the surface systems, including landscape development, ecosystem properties and characteristics of the discharge area (see further the **Biosphere synthesis report**, Chapter 8).

The input data in all transport models are also influenced by the evolution of external conditions (Figure 2-2). Important aspects of external conditions include the timing of the shoreline regression in the area above the repository and the temporal succession of climate domains (temperate, periglacial and glacial; see the **Climate report**, Section 1.4.3).

It should be emphasised that Figure 2-2 only illustrates the input data to radionuclide transport and dose modelling at a basic level and thus many dependencies of data are not highlighted in the figure. An overview of the various assessment activities used in the evaluation of repository evolution and radionuclide transport, as well as the connection between them in the form of data flow, is presented in the **Post-closure safety report**, Appendix H. The data used in the radionuclide transport calculations for the near-field and the geosphere are described in the **Data report** and in Appendix A. Input data used in the biosphere modelling are described in the **Biosphere synthesis report**, Chapter 8.

Each calculation case contains slightly modified sets of input data to reflect the uncertainty in the post-closure evolution of the repository and its environs, or to illustrate the sensitivity of the results to certain parameters. A summary of how input data for each of the calculation cases evaluated in this report are modified in the near-field, geosphere and biosphere models as compared to the *base case* is given in Table 2-2.

⁴ Note that most figures in this report present releases and doses from 2000 AD to 100 000 AD. This is a simplification as the planned closure of the repository is at 2075 AD and the assessment period in the calculations is 100 000 years. Thus, the figures present the first 98 000 years after closure and 2000 AD represents the time of closure.

Table 2-2. Summary of calculation-case implementations in the three transport models.

Scenario		Calculation case	Motivation	Near-field	Geosphere	Biosphere
Main scenario	Reference external conditions	Present-day climate	Basis for the calculations; selected as <i>base case</i> .	<i>Base case.</i>		
		Warm climate	Uncertainty in climate evolution.	Delayed increase of the groundwater flow due to 3500 years longer submerged conditions than in the <i>base case</i> .	Delayed increase of the groundwater flow due to 3500 years longer submerged conditions than in the <i>base case</i> .	Delayed emergence of terrestrial biosphere objects by 3500 years with respect to the <i>base case</i> . Ecosystem and hydrological parameters adjusted for increased air temperature and CO ₂ . Irrigation and effect of dry summers on hydrological parameters and plant water deficit are evaluated.
		Cold climate		Evaluated in two variants. <i>Permafrost with talik</i> variant: <i>base case</i> . <i>Continuous permafrost</i> variant: groundwater flow and radionuclide transport ceases during periglacial conditions.	<i>Permafrost with talik</i> variant: <i>base case</i> release redirected to a talik. <i>Continuous permafrost</i> variant: groundwater flow and radionuclide transport ceases during periglacial conditions.	Both variants: ecosystem and hydrological parameters adjusted, exposure only to hunter-gatherers during periglacial conditions. <i>Permafrost with talik</i> variant: dose evaluated in taliks. Accumulated activity in taliks evaluated also in the subsequent temperate period.
	Supporting calculation cases	Timing of shoreline regression	Uncertainty in future sea-level rise.	Delayed increase in groundwater flow due to submerged conditions for up to 20000 years longer than in the <i>base case</i> .	Delayed increase in groundwater flow due to submerged conditions for up to 20000 years longer than in the <i>base case</i> .	Delayed emergence of biosphere objects by up to 20000 years with respect to the <i>base case</i> .
		Delayed release from repository	Uncertainty in timing of releases.	Radionuclide transport and release delayed until 1000 years after closure.	<i>Base case.</i>	<i>Base case.</i>
Less probable scenarios	Glaciation	Glaciation	Uncertainty in climate evolution.	Periglacial: groundwater flow and radionuclide transport cease. Glacial: changes in groundwater flow rate. Sorption coefficients for oxidising conditions, affecting Np, Pa, Pu, Se, Tc and U. Engineered barriers completely degraded. Post-glacial: engineered barriers completely degraded.	Periglacial: groundwater flow and radionuclide transport cease. Glacial: changes in groundwater flow rate. Sorption coefficients for oxidising conditions. Post-glacial: groundwater flow as submerged conditions, interpolation to terrestrial conditions follows shoreline displacement.	Periglacial: see the continuous permafrost of the cold climate (in main scenario; see above). Glacial: dose evaluated for discharge to coast. Post-glacial: submerged conditions followed by terrestrial conditions, groundwater flow follows emergence of biosphere objects from the sea.

Scenario		Calculation case	Motivation	Near-field	Geosphere	Biosphere	
Less probable scenarios	High concentrations of complexing agents	High concentrations of complexing agents	Uncertainty in the amount and effect of complexing agents.	Tenfold increase of cement sorption reduction factors.	<i>Base case.</i>	<i>Base case.</i>	
	Alternative concrete evolution	Alternative concrete evolution	Uncertainty in timing and rate of concrete degradation.	Earlier and/or greater increase in concrete hydraulic conductivity, diffusivity and porosity.	<i>Base case.</i>	<i>Base case.</i>	
	Earthquake	Earthquake	Uncertainties in occurrence of earthquakes capable of damaging concrete structures.	After earthquake: increased groundwater flow due to damage of the silo structure.	After earthquake: near-field release discharged directly to the biosphere.	<i>Base case.</i>	
Residual scenarios	Hypothetical early permafrost	Effect on engineered barrier	Radiological consequences of a hypothetical permafrost event during the first 50 000 years after closure.	Water flow and radionuclide transport ceases during periglacial conditions. Frozen concrete variant: completely degraded concrete after 12 000 AD. Bentonite degradation variant: formation of an ice lens around the silo at 12 000 AD.	<i>Base case.</i>	<i>Base case.</i>	
		No effect on engineered barriers		<i>Cold climate calculation case.</i>	<i>Cold climate calculation case.</i>	<i>Cold climate calculation case.</i>	
	Loss of engineered barrier function	No sorption in the repository	Illustrate significance of the engineered barriers.		All sorption coefficients set to zero.	<i>Base case.</i>	<i>Base case.</i>
		No hydraulic barriers in the repository			No flow-resistance from structural concrete and bentonite.	<i>Base case.</i>	<i>Base case.</i>
	Loss of geosphere barrier function	No sorption in the geosphere	Illustrate significance of the geosphere barrier function		<i>Base case</i>	All sorption coefficients set to zero.	<i>Base case.</i>
		No transport retention in the geosphere			<i>Base case</i>	Near-field release discharged directly to the biosphere.	<i>Base case.</i>
	Alternative radionuclide inventory	Extended operation of reactors	Illustrate consequences of higher radionuclide inventory based on alternative events.		Radionuclide inventory representative for 80 years NPP operation (60 years in <i>base case</i>).	<i>Base case.</i>	<i>Base case.</i>
		Increased fuel damage frequency			Radionuclide inventory representative for extensive fuel damage during remaining NPP operation.	<i>Base case.</i>	<i>Base case.</i>

Scenario	Calculation case	Motivation	Near-field	Geosphere	Biosphere	
Residual scenarios	Alternative radionuclide inventory	Extended use of molybdenum-alloy fuel spacers	Illustrate consequences of higher radionuclide inventory based on alternative events.	Tenfold increase of Mo-93 inventory for affected waste streams.	Base case.	Base case.
	Oxidising conditions	Oxidising conditions	Illustrate consequence of hypothetical oxidising conditions in near-field and geosphere.	Sorption coefficients and 1BRT corrosion rates for oxidising conditions.	Sorption coefficients for oxidising conditions.	Base case.
	Initial concrete cracks	Initial concrete cracks	Illustrate significance of hypothetical initial cracks in the concrete barriers.	Initial cracks and higher hydraulic conductivity in all concrete barriers.	Base case.	Base case.
	Unrepaired 1BMA	Unrepaired 1BMA	Illustrate consequences of omitting the planned repair and strengthen measures of 1BMA.	No external concrete structure is added to 1BMA.	Base case.	Base case.
	Unsealed repository	Unsealed repository	Illustrate consequences of an unsealed repository.	No closure components.	Not modelled.	Human exposure via drinking tunnel-entrance water.

2.4.3 Assessment endpoints

The methodology for estimating the annual risk of harmful effects is part of the overall assessment methodology (Figure 2-1 and the **Post-closure safety report**, Section 2.6.9) and is not part of radionuclide transport calculations. To facilitate the risk estimation, the primary endpoint for humans in the radionuclide transport calculations is *annual dose* to a representative individual in the group exposed to the greatest risk. Annual dose is calculated as the annual effective dose for an adult, where the annual effective dose is defined as the effective dose from external exposure in a year, plus the committed effective dose from intakes of radionuclides in that year (**Biosphere synthesis report**, Section 2.3.5).

The dose is calculated for each point in time by summing the dose over all 1 000 simulations, giving each simulation the probability of 0.001. This time-dependent probability weighted average is the expected value of the dose for each fixed point in time. As it is equivalent to the mean of the 1 000 simulations, it is referred to as the mean total (or radionuclide specific) annual dose. In the present report, only the mean annual dose from the 1 000 simulations is presented in the calculation-case specific results. The spread in dose across the simulations is briefly discussed in the Section 10.2. A more comprehensive statistical analysis of the dose across the probabilistic simulations is specifically conducted for the *base case*; this is documented in the **Biosphere synthesis report**, Section 9.4.

Predictions of future human behaviour are inherently uncertain, especially on the timescales addressed in the present assessment. In the SR-PSU, exposure pathways of relevance within ecosystems of interest were reviewed. Land-use variants, which resulted in relatively high exposure, and the associated potentially exposed groups (PEGs) were then identified from historically self-sustainable communities (SKB R-14-02). Following this approach, ecosystems created by humans have a more simplified representation than natural ecosystems and PEGs are to be interpreted as credible bounding cases with respect to the identified exposure pathways. The PEGs used in this assessment are further described in Section 4.4.3.

As required in SSMFS 2008:37 Section 4, the collective dose is calculated as a result of the expected outflow of radioactive substances over a period of 1 000 years after closure of SFR. The approach in the present safety assessment is to calculate collective dose for the calculation cases in the main scenario and less probable scenarios, i.e. those that are propagated to the radiological risk assessment. However, some of these calculation cases are identical to the *base case* during the first 1 000 years after closure, so they are excluded from the collective dose calculations (Table 2-1). Moreover, the *earthquake calculation case* is excluded due to its extremely low probability of occurrence during the first 1 000 years. The collective dose calculations are presented in Chapter 9.

2.4.4 Simplifying assumptions

This section briefly summarises basic and simplifying assumptions that are made in the radionuclide transport modelling for most calculation cases. These include:

- The modelling assumes that resaturation of the repository occurs instantaneously upon repository closure, i.e. the repository is fully water saturated during the whole assessment period (**Post-closure safety report**, Chapter 4).
- Steel waste packages are expected to start corroding already during the operational period (**Initial state report**, Chapter 12). Any potential transport limiting effect of the steel waste packages is therefore disregarded in the modelling.
- The potential transport limiting effect of bitumen in bituminised waste is not taken into account (**Waste process report**, Section 3.6).
- Radionuclides are assumed to be fully soluble in water, i.e., no solubility limits are taken into account (**Waste process report**, Section 3.6).
- Potential sorption of radionuclides on corrosion products is not taken into account (**Waste process report**, Section 3.5.3).
- Potential sorption of radionuclides on various materials in the 1–5BLA vaults is not taken into account. This is particularly pessimistic for 2–5BLA where the amount of concrete waste amounts to about 14 000 tonnes (SKB R-18-07).
- In the geosphere transport calculations, no sorption in the fractures is considered, either on their walls or in possible fracture fill (**Geosphere process report**, Section 5.4.7). Thus, sorption is only accounted for in the bedrock matrix.
- All radionuclides that reach the terrestrial biosphere are discharged into a single biosphere object (**Biosphere synthesis report**, Chapter 5).

In general, these assumptions lead to an overestimation of the calculated dose in comparison to alternative, more realistic, assumptions. However, it is not obvious that an overestimation of release rates is always pessimistic in terms of risk. This is particularly true for releases that occur during the initial submerged period as the release to submerged receptors during this period may result in lower releases during subsequent periods of terrestrial conditions. The effect of this situation on the radionuclide transport and dose is addressed in the *delayed release from repository calculation case* (Section 5.8.3).

The simplifying assumptions inevitably also result in different degrees of pessimism depending on the waste vault and radionuclide considered. For example, the assumption of no sorption in the BLA vaults may be considered more pessimistic for the radionuclide release than for the other vaults. Further, the omission of solubility limits will affect some radionuclides more than others, e.g. U-235 and U-238 in the BLA vaults. Hence, the calculations should be seen as valid only for the purpose to show compliance with regulatory limits, but they do not necessarily exhibit a precise ranking of the actual contributions from individual vaults and radionuclides.

2.5 Management of uncertainties

The management of uncertainties is an important aspect of any safety assessment, but there are many possible ways in which to classify the uncertainties. Here, a classification is adopted that is similar to the classification suggested in the general advice to SSMFS 2008:21 and captures the aspects relating to uncertainty in the general advice as noted in SSMFS 2008:37, and international practice in this type of analysis (e.g. IAEA 2012, NEA 2012). The following broad definitions are used (**Post-closure safety report**, Section 2.5):

- *Scenario uncertainty* refers to uncertainty with respect to external conditions and internal processes in terms of type, degree and time sequence, resulting in an uncertainty in the future states of the repository system. It includes uncertainty in for example the evolution of the repository system, and climatic and other long-term processes.
- *System uncertainty* concerns comprehensiveness issues, i.e. the question of whether all aspects important for the safety evaluation have been identified and whether the assessment is capturing the identified aspects in a qualitatively correct way. In short, have all factors, features, events and processes been identified and included in a satisfactory manner or has their exclusion been appropriately justified?
- *Modelling uncertainty* arises from a necessarily imperfect understanding of the nature of processes involved in repository evolution which leads to imperfect conceptual models. The mathematical representation of conceptual models will have involved some simplification, also contributing to modelling uncertainty. Imprecision in the numerical solution of mathematical models is another source of uncertainty falling into this category.
- *Data uncertainty* concerns all quantitative input data, i.e. parameter values, used in the assessment. There are several aspects to consider in the management of data uncertainty. These include correlations between data, the distinction between uncertainty due to lack of knowledge (epistemic uncertainty) and due to natural variability (aleatoric uncertainty) and situations where modelling uncertainty is treated by broadening the range of input data. The input data required by a particular model is in part a consequence of the conceptualisation of the modelled process, meaning that modelling uncertainty and data uncertainty are to some extent intertwined.

Another element of the uncertainty management in the radionuclide transport and dose calculations, addressing especially modelling and data uncertainties, is to opt for *cautious* or *pessimistic* choices in order to ensure that calculation results, with a high degree of certainty, do not underestimate any potential radiological consequences. In the present safety assessment, these two terms are defined as follows (**Post-closure safety report**, Section 2.5):

- *Cautious* indicates an expected overestimate of annual effective dose that follows from assumptions made, or models and parameter values selected, *within* the reasonably expected range of possibilities.
- *Pessimistic* indicates an expected overestimate of annual effective dose that follows from assumptions made, or models and parameter values selected, *beyond* the reasonably expected range of possibilities.

Calculations that serve as input to the radiological risk assessment are, when possible, based on cautious rather than pessimistic assumptions, models or parameter values. Deliberate pessimistic assumptions, models or parameter values may be used in e.g. residual scenarios, i.e. calculations that are intended to illustrate and/or bound the effect of a certain process or hypothetical event, but that are not included in the radiological risk assessment. The choice of cautious or pessimistic approaches may also indicate availability of data, or lack thereof.

The handling of each type of uncertainty in the radionuclide transport and dose calculations is summarised in the following. An overview on how the uncertainties are accounted for calculation-case specific results is given in Section 10.3.

2.5.1 Scenario uncertainties

Scenario uncertainties are implicitly accounted for in the range of possible future developments covered by the calculation cases evaluated in the main scenario and less probable scenarios.

2.5.2 System uncertainties

System uncertainties were dealt with in the analysis of FEPs, which resulted in the selection of scenarios and calculation cases evaluated in this report. The FEP analysis is presented in detail in the **FEP report** and the scenario selection is described in the **Post-closure safety report**, Chapters 7 to 9.

2.5.3 Modelling uncertainties

Modelling uncertainties related to a potentially imperfect conceptual model are handled by ensuring that the simplifications made in the conceptual model do not lead to an underestimation of radiological risk. Cautious or pessimistic assumptions (see above), such as those exemplified in Section 2.4.4, are made when the real system is conceptualised and, subsequently, parameterised into a mathematical model. If it is not clear whether a simplification leads to an underestimation of the dose, several model alternatives are analysed to bracket the uncertainty.

Furthermore, it is also important to assess the contribution to the overall uncertainty from the numerical approximations and the accuracy of the numerical tools. This uncertainty, however, is typically several orders of magnitude smaller than the uncertainty from other sources. This is particularly true when appropriate numerical methods are used, e.g. the solver must be able to deal with states evolving at different rates (e.g. slow versus fast radioactive decay and ingrowth, sometimes referred to as system stiffness) and avoid numerical instability (oscillation).

Several comparisons with results obtained from other tools have been carried out to verify the numerical accuracy of the models implemented in Ecolego (**Model tools report**). In the safety assessment SR-Site, a comparison between biosphere compartment models implemented in Ecolego and Simulink/Pandora was performed (Avila et al. 2010, SKB TR-10-51). This comparison showed that the difference between the model tools was less than 1 % for all considered cases. This accuracy is considered reasonable as different numerical methods are used in Simulink/Pandora and Ecolego. The compartment model for the geosphere, FARFCOMP, is implemented in Matlab and was compared with both analytical and other numerical codes in the safety evaluation SE-SFL (Appendix B in SKB TR-19-06). It was concluded that the compartment implementation of FARFCOMP is fit for purpose for the spatial discretisation used in the PSAR.

Another uncertainty that falls into this category concerns human errors in the modelling. Potential consequences of this uncertainty are mitigated by the implementation of a robust quality assurance (QA) system. The QA handling in the radionuclide transport and dose calculations is described in Appendix A and in the **Biosphere synthesis report**, Section 8.5, following the overarching processes of quality management documented in the **Post-closure safety report**, Section 2.8.

2.5.4 Data uncertainty

Data uncertainty is accounted for by assigning probability distributions over a range of possible values for individual parameters. As described above, these probability distributions are considered in probabilistic Monte Carlo simulations in the modelling. Values of the sampled parameters are drawn from their probability distributions, as described by (parameterised) probability distribution functions (PDFs). The effects of data uncertainties are quantified by propagating uncertainties in parameters through the entire modelling chain, thereby contributing to the probability distributions of the assessment endpoints, i.e. dose to humans and dose rates to non-human biota.

For some input parameters, the probabilistic approach is not considered feasible. This is the case, for example, for parameters that are already handled cautiously or pessimistically in the radionuclide transport and dose modelling. Other parameters that are typically not handled probabilistically are those that are subject to a considerable modelling or scenario uncertainty. The former includes, for example, uncertainties in parameters that are derived from underlying modelling activities, for which a probabilistic approach was not considered feasible. This concerns e.g. the modelling of the landscape development and the surface hydrology in the biosphere analysis (**Biosphere synthesis report**, Chapter 5). Scenario uncertainties are, for example, related to significant changes in external conditions and/or the timing of an event. To maintain internal consistency in parameters depending on the external conditions and to avoid risk dilution (Section 10.6), such uncertainties are most appropriately handled by considering alternative sets of input data that bracket the potential variability. These uncertainties include e.g. the timing of concrete degradation in the engineered barriers.

3 Repository and radionuclide inventory

The models developed and input data selected for the radionuclide transport and dose modelling rely on the descriptions of the expected state of the repository and its environs at closure of the repository (the *initial state*, see the **Post-closure safety report**, Chapter 4) and the probable post-closure evolution of the repository and its environs (the *reference evolution*, see the **Post-closure safety report**, Chapter 6). Important data for the initial state includes the repository geometry and the radionuclide inventory, which are presented in this chapter. Not all radionuclides initially present in the waste or produced by radioactive decay (ingrowth) during the assessment period are considered in the post-closure safety assessment. The selection of radionuclides to be included in the radionuclide transport and dose calculations is therefore also presented in this chapter.

3.1 Repository layout

This section gives an overview description of the layout and post-closure functioning of each waste vault. Plugs and other closure components in SFR are also described. For a more comprehensive description, see the **Initial state report**, Chapter 11. The facility currently in operation (SFR1) consists of four 160-metre-long waste vaults (1BMA, 1–2BTF and 1BLA) and one waste vault with a concrete silo, see Figure 1-1. The extension (SFR3) consists of six 255–275-metre-long waste vaults (2BMA, 1BRT and 2–5BLA). The SFR facility will be decommissioned and closed when all waste has been disposed. Closure of SFR includes installation of backfill material and plugs in the underground facility. The waste vaults in SFR1 are located about 60 m deep in the bedrock. The bottom of the silo is located much deeper, however, about 130 m deep in the bedrock. When SFR3 is built it will comprise six waste vaults located about 120 m deep in the bedrock, which means that they are at approximately the same level as the bottom of the silo, see Figure 3-1.

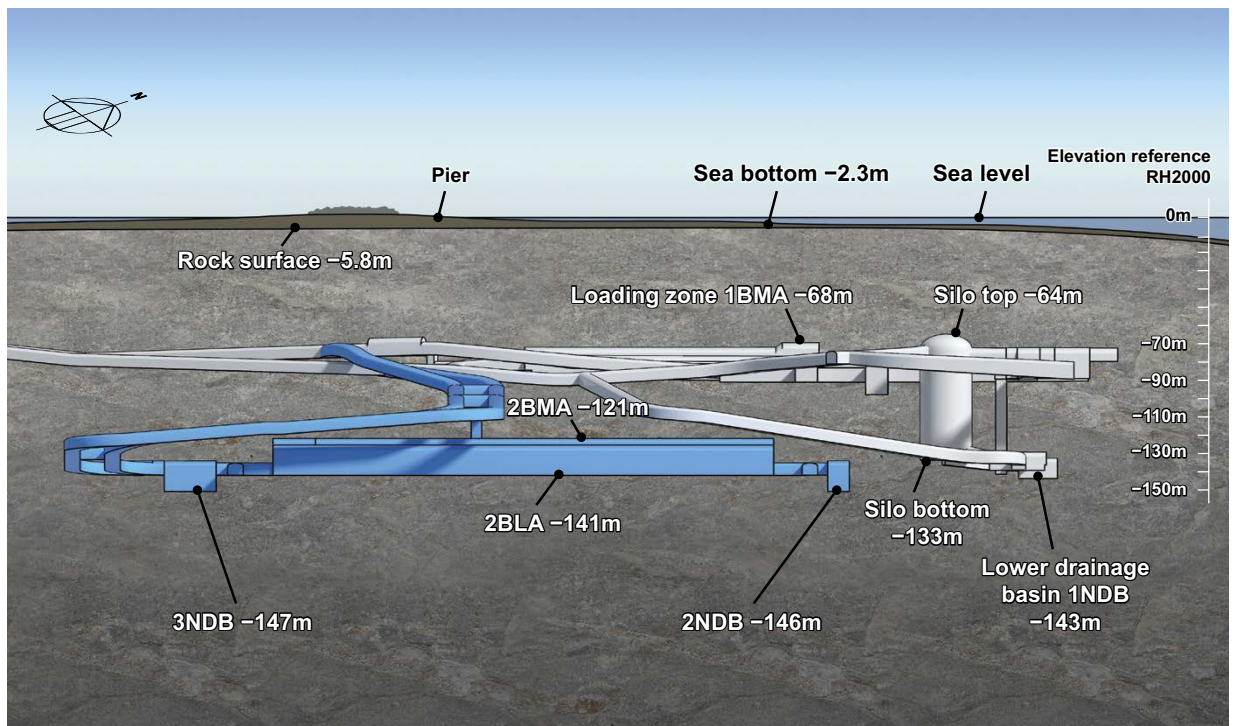


Figure 3-1. View of SFR with designated levels in RHB2000 (the Swedish geographical height system). View is towards the northwest, approximately perpendicular to the waste vaults. Note that stipulated elevations for the top surface of the rock and the sea floor are to be regarded as approximate since they are point data and vary in the plane above SFR. The grey part is SFR1 and the blue part is SFR3.

3.1.1 Silo, vault for intermediate-level waste

The silo in SFR1 is a cylindrical vault with a free-standing concrete cylinder, intended for conditioned intermediate-level waste in concrete and steel moulds or in steel drums. The vault is about 70 m high with a diameter of about 30 m. The concrete cylinder is made of *in situ* cast concrete and the concrete bottom is founded on a bed of 90 % sand and 10 % bentonite. The concrete cylinder is divided into several vertical shafts into which the waste packages are disposed. Grouting of waste packages in the shafts is done progressively during operations. The approximately 0.9 m wide gap between the concrete cylinder and the rock is filled with bentonite. The walls of the vault are lined with shotcrete.

In an initial step of the closure, the shafts are to be covered with cement grout up to the top rim of the concrete silo. A concrete lid provided with a gas evacuation system is cast and the silo top above the lid is filled with different layers of backfill material. Figures 3-2 and 3-3 show a schematic illustration and a vertical cross-section of the silo.

Most (about 75 %) of the radioactivity content in SFR is disposed in the silo and the layout of the waste vault was chosen to achieve post-closure safety for this waste. To this end, the bentonite surrounding the concrete silo limits the water flow through the waste and thus the advective transport of radionuclides from the waste to the repository environs. Furthermore, all cement-based materials in the waste, waste packaging, grouting and the concrete silo itself provide material surfaces for sorption, which leads to retention of radionuclides.

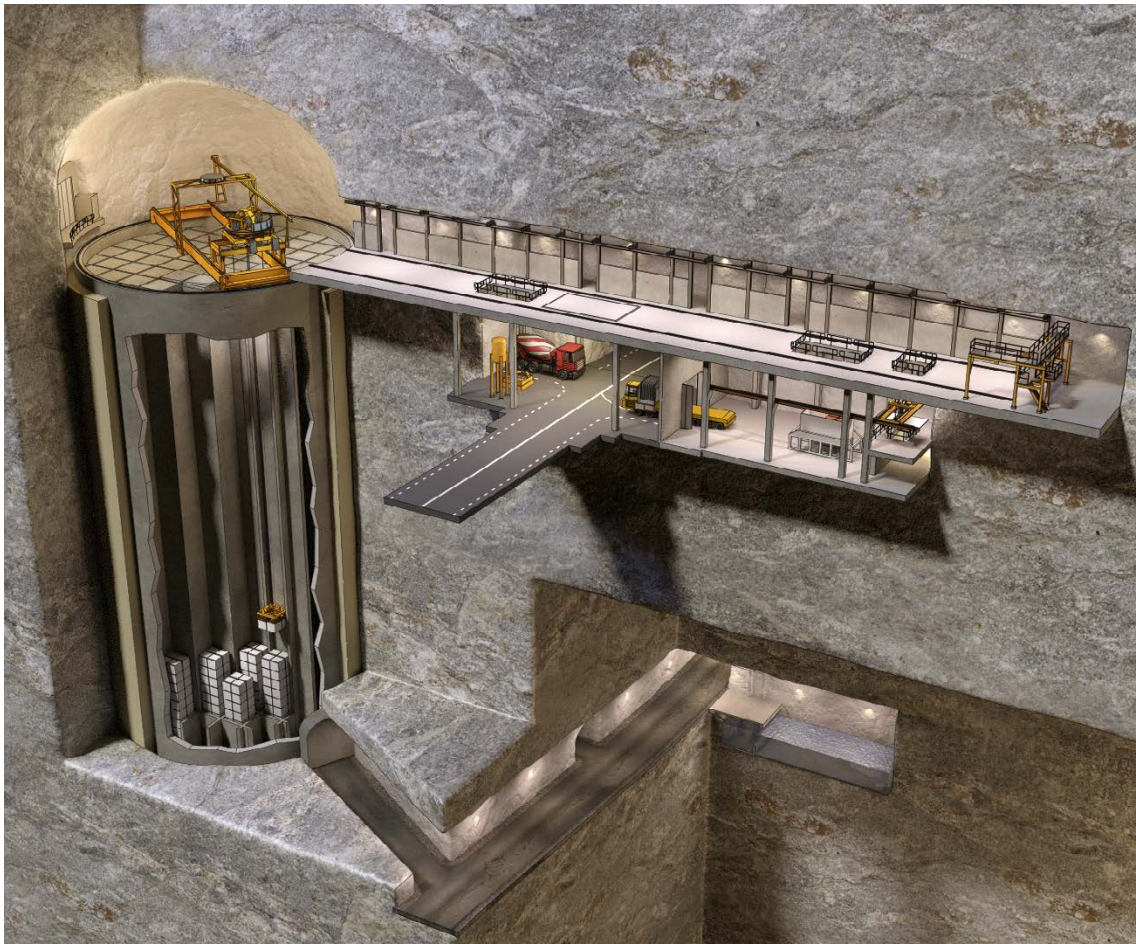


Figure 3-2. Illustration of the silo during the operational period.

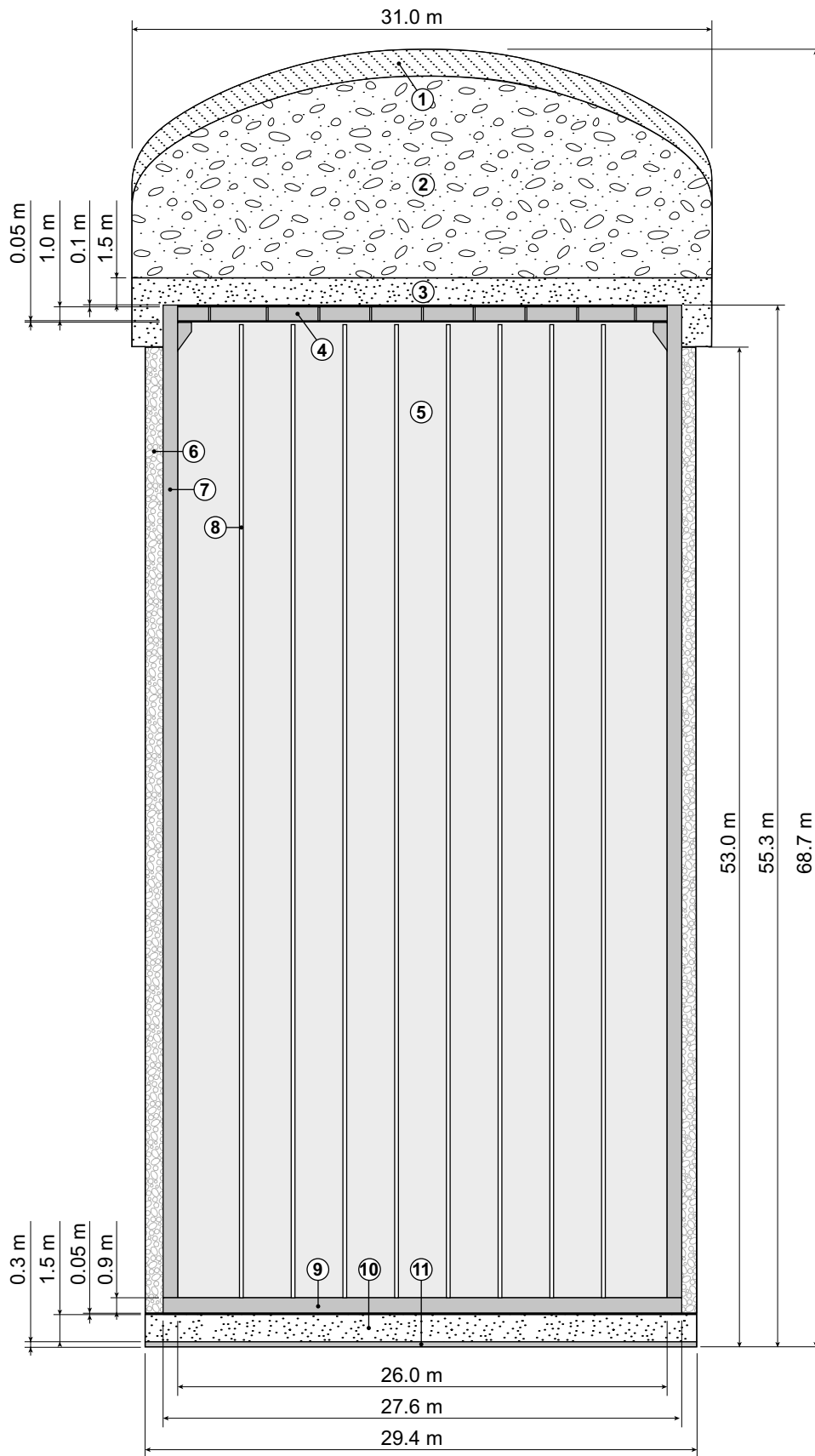


Figure 3-3. Schematic vertical cross-section of the silo at closure. The waste packages are surrounded by grout in this waste vault. Key to numbering 1) Cement-stabilised sand 2) Crushed rock backfill 3) Compacted fill with a mixture of 10 % bentonite and 90 % sand 4) Reinforced concrete slab with sand layer and gas evacuation channels 5) Waste 6) Side bentonite layer 7) Outer concrete wall 8) Inner (shaft) walls of concrete 9) Concrete slab 10) Bottom sand-bentonite layer 11) Bottom drainage system.

3.1.2 1-2BMA vaults for intermediate-level waste

1BMA in SFR1 is an approximately 20 m wide, 17 m high and 160 m long waste vault, intended for conditioned intermediate-level waste in steel drums, steel moulds and concrete moulds. The waste packages are disposed in an approximately 140 m long reinforced concrete structure divided into 13 large compartments and two smaller compartments. The concrete structure is founded on solid rock and the slab on a base of crushed rock. The roof and walls of the vault are lined with shotcrete. The steel and concrete moulds with waste are stacked six high and drums with waste eight high. Prefabricated concrete elements are placed over full compartments.

Prior to closure of 1BMA, repair and strengthening measures of the concrete structure are planned to improve its hydraulic and mechanical properties. The measures include new reinforced external concrete walls erected on the outside of the existing ones. A thick reinforced concrete lid will be cast on top of the prefabricated concrete elements and the space between the concrete structure and the vault roof and walls will be backfilled with macadam. Figure 3-4 and Figure 3-5 show a schematic illustration and a vertical cross-section of 1BMA.

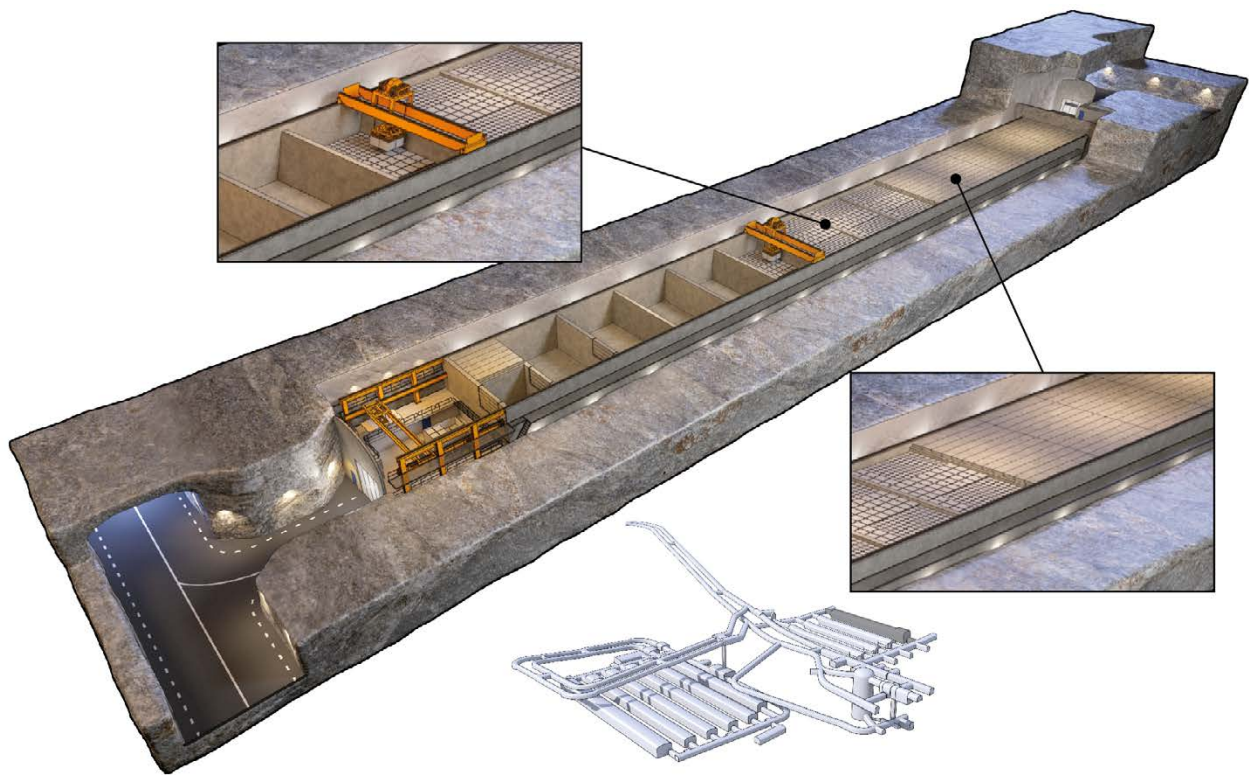


Figure 3-4. Illustration of 1BMA during the operational period. The upper inset shows the emplacement of waste packages, the lower inset shows the concrete lid. In addition, there is a view of SFR with the position of 1BMA highlighted in dark grey.

2BMA in SFR3 is an approximately 23 m wide, 19 m high and 275 m long waste vault, intended for intermediate-level waste in steel moulds, concrete moulds or drums. The waste packages are disposed in 13 free-standing unreinforced concrete caissons with inner walls of prefabricated reinforced concrete. The concrete caissons are founded on a macadam layer, and the walls and roof of the vault are lined with shotcrete. The steel and concrete moulds with waste are stacked six high and drums with waste eight high. Prefabricated concrete elements are placed over full caissons.

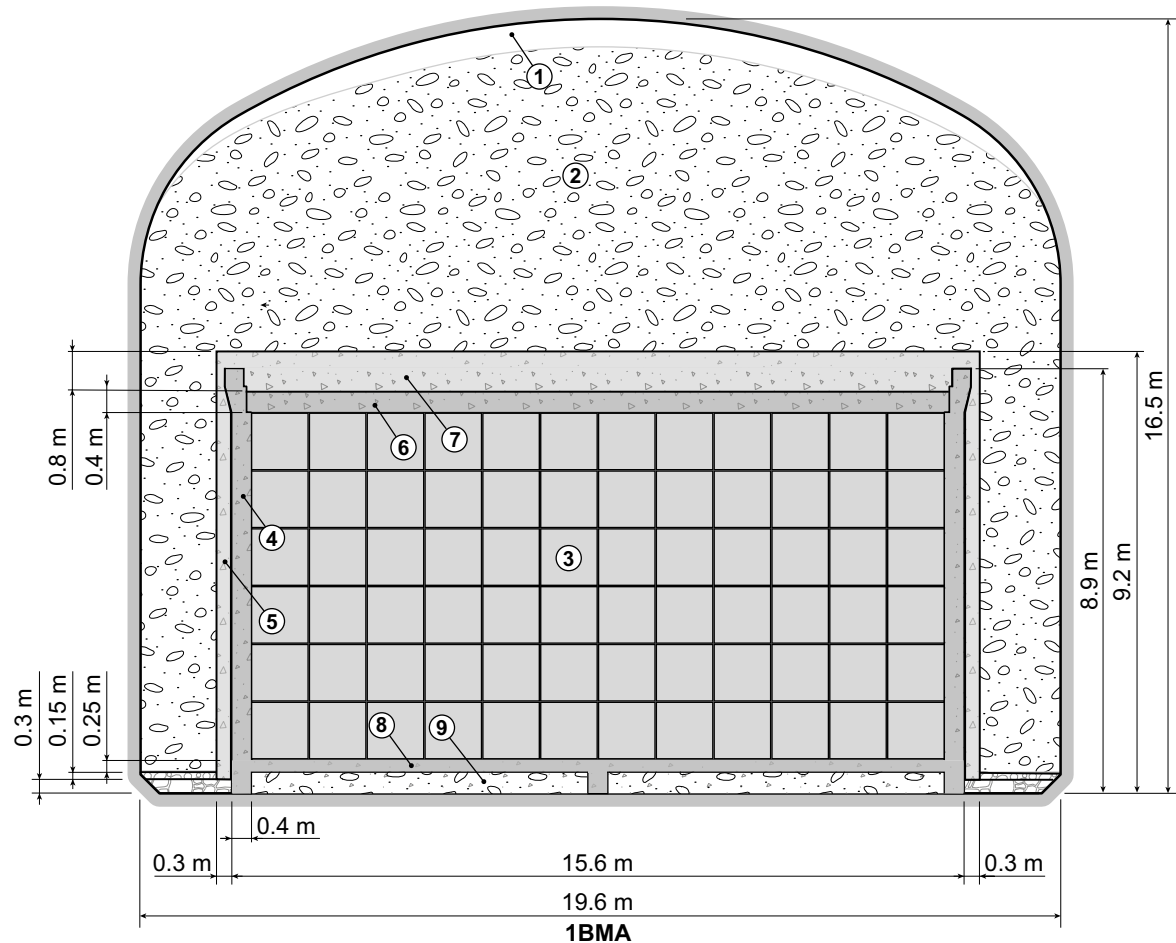


Figure 3-5. Schematic cross-section of 1BMA at closure. Key to numbering: 1) Void 2) Macadam backfill 3) Waste domain 4) Existing outer wall 5) New outer wall 6) Pre-fabricated concrete element 7) New concrete lid 8) Slab 9) Crushed rock.

At closure of the 2BMA, at latest, a gas evacuation system will be installed and a thick layer of concrete will be cast on top of the prefabricated concrete elements. The space between the concrete structures and the walls and roof of the vault will be backfilled with macadam. Figure 3-6 and Figure 3-7 show a schematic illustration and a vertical cross-section of 2BMA at closure.

Following the silo, the BMA waste vaults contain most of the total radioactivity in SFR, with approximately 10 % of the total radioactivity disposed in each of these vaults. The layout of the waste vaults is chosen to achieve post-closure safety for this waste. To this end, the combination of high permeability backfill with less permeable concrete structures limits the water flow through the waste and thus the advective transport of radionuclides from the waste to the repository environs. Furthermore, all cement-based materials in the waste, waste packaging and the concrete structures provide material surfaces for sorption, which will lead to retention of radionuclides following their release from the waste.

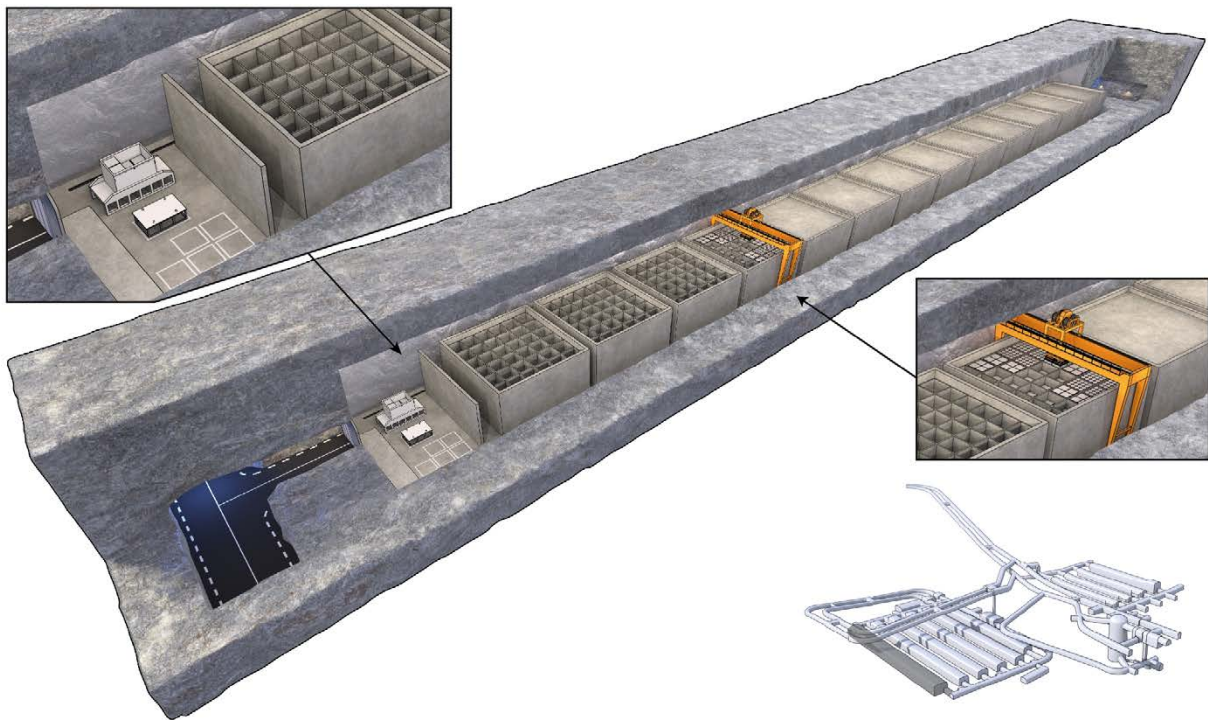


Figure 3-6. Illustration of 2BMA during the operational period. The upper inset shows the reloading zone the lower inset shows the emplacement of waste packages. In addition, there is a view of SFR with the position of 2BMA highlighted in dark grey.

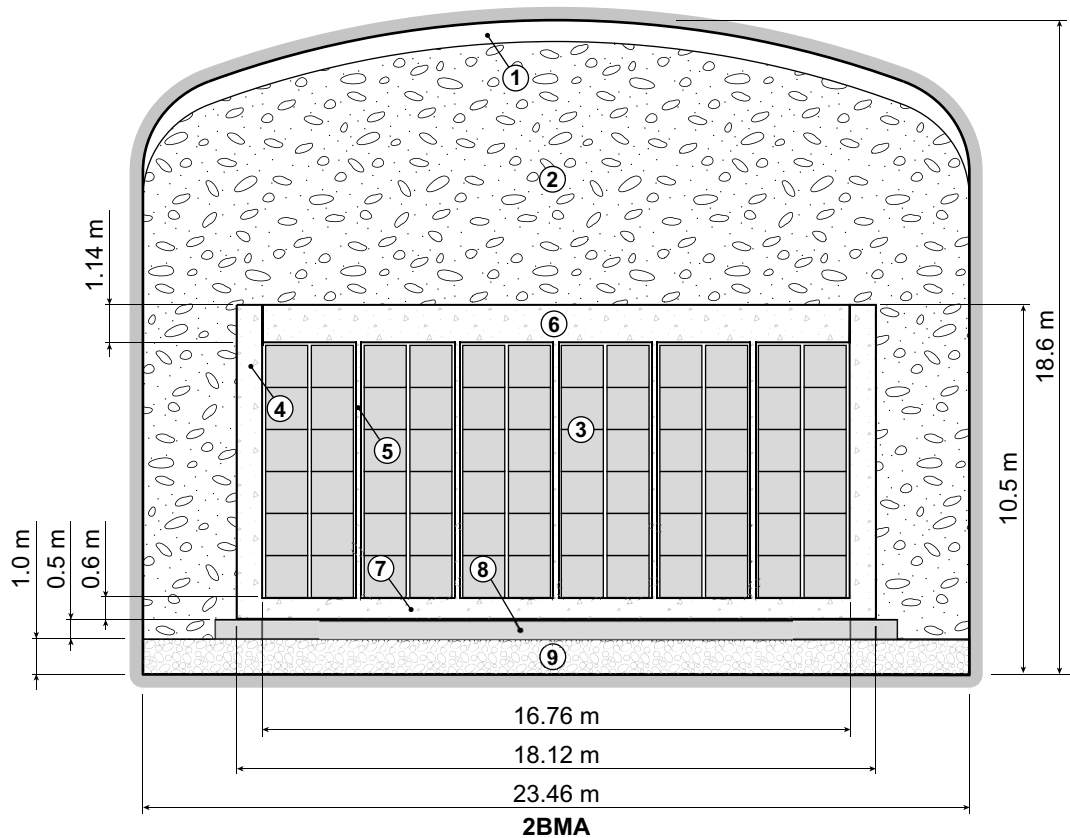


Figure 3-7. Schematic cross-section of 2BMA at closure. Key to numbering: 1) Void 2) Macadam backfill 3) Waste domain 4) Outer wall 5) Inner wall 6) Lid 7) Caisson slab 8) Slab 9) Crushed rock.

3.1.3 1BRT, vault for segmented reactor pressure vessels

1BRT in SFR3 is an approximately 17 m wide, 15 m high and 255 m long waste vault, intended mainly for segmented reactor pressure vessels in double moulds. The waste packages are to be disposed in an approximately 250 m long reinforced concrete structure which is divided into compartments by inner walls. The slab of the structure is founded on a macadam layer. The roof and walls of the vault are lined with shotcrete. The double moulds are stacked six high. Prefabricated concrete elements are placed over full compartments.

The waste packages are embedded in grout. A reinforced concrete lid is cast on top of the concrete elements and the space between the concrete structure and the walls and roof is backfilled with macadam. Figure 3-8 and Figure 3-9 show a schematic illustration and a vertical cross-section of 1BRT at closure.

The 1BRT vault contains about 1 % of the total radioactivity in SFR. The layout of the waste vault is chosen to achieve post-closure safety for this waste. To this end, all cement-based materials in the waste, waste packaging, grout and the concrete structures provide high pH, which limits corrosion of the waste and thus limits release of radioactivity in the steel. Furthermore, all cement-based materials provide material surfaces for sorption, which will lead to retention of radionuclides following their release from the waste.

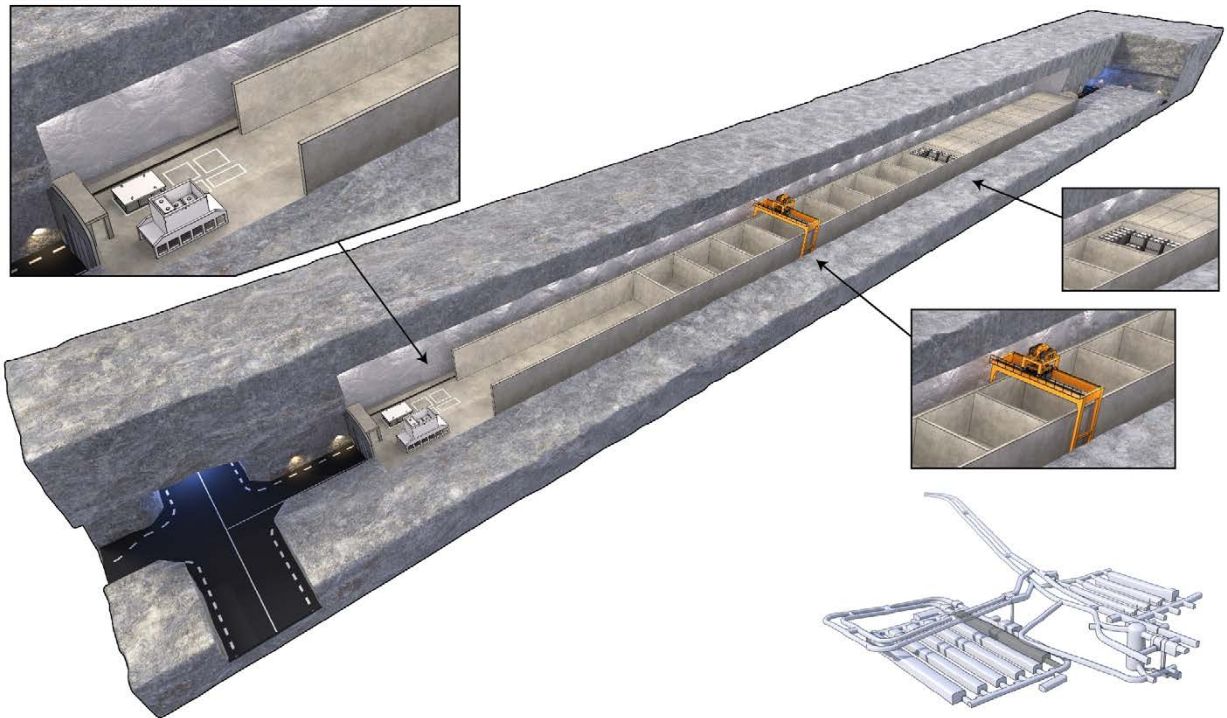


Figure 3-8. Illustration of IBRT during the operational period. The lower detail shows SFR with the position of IBRT in dark grey.

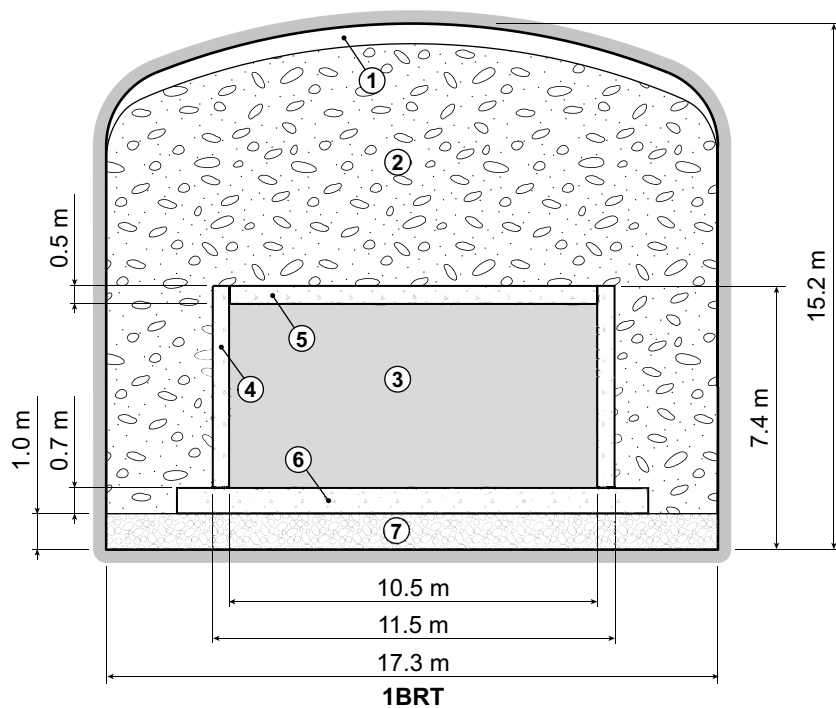


Figure 3-9. Schematic cross-section of IBRT at closure. Key to numbering: 1) Void 2) Macadam backfill 3) Waste domain 4) Outer wall 5) Lid 6) Slab 7) Crushed rock.

3.1.4 1–2BTF, vaults for concrete tanks

1–2BTF in SFR1 are approximately 15 m wide, 10 m high and 160 m long waste vaults intended primarily for dewatered ion-exchange resins in concrete tanks. Besides the concrete tanks, drums containing ash from incineration of waste are disposed in 1BTF. The waste packages are placed on a concrete slab that rests on a foundation with inbuilt drains. The roof and walls of the vaults are lined with shotcrete. Grouting around the ash-containing drums is done progressively during the operational period. The concrete tanks are positioned four abreast and two high, after which prefabricated concrete elements are placed on top.

At closure, the space between concrete tanks and the wall of the vault will be filled with grout and a concrete slab will be cast on top of the grout and the prefabricated concrete elements. The space above the concrete slab is backfilled with macadam up to the roof of the vault. Figure 3-10 to Figure 3-12 show schematic illustrations and vertical cross-sections of 1–2BTF at closure.

The BTF waste vaults contain less than 1 % of the total radioactivity in SFR. The layout of the waste vaults was chosen to achieve post-closure safety for this waste. The concrete tanks and the backfill limit the water flow through the waste and thus the advective transport of radionuclides from the waste to the repository environs. Furthermore, all cement-based materials provide material surfaces for sorption, which will lead to retention of radionuclides following their release from the waste.

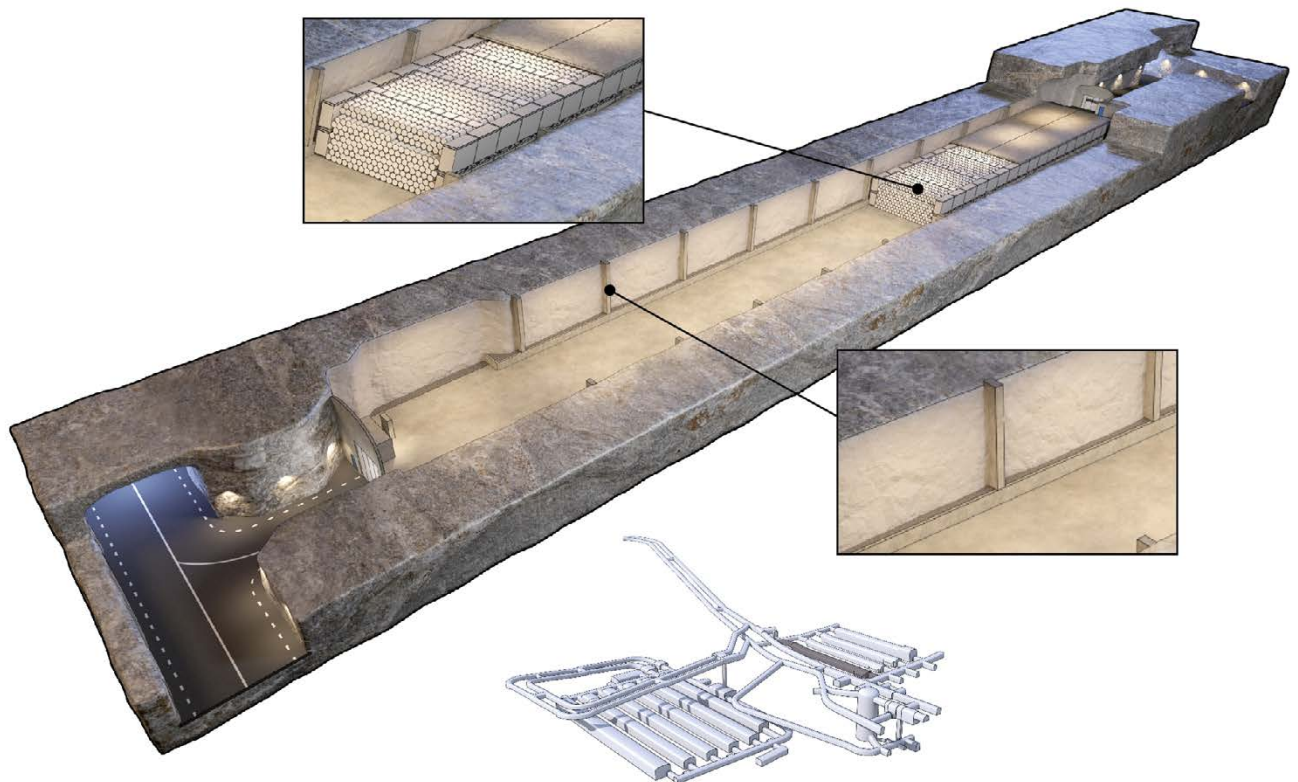


Figure 3-10. Illustration of 1BTF during the operational period. The upper detail shows the emplacement of the ash drums between concrete tanks, the lower detail shows the skirting and concrete pillars. In addition, there is a view of SFR with the position of 1BTF highlighted in dark grey.

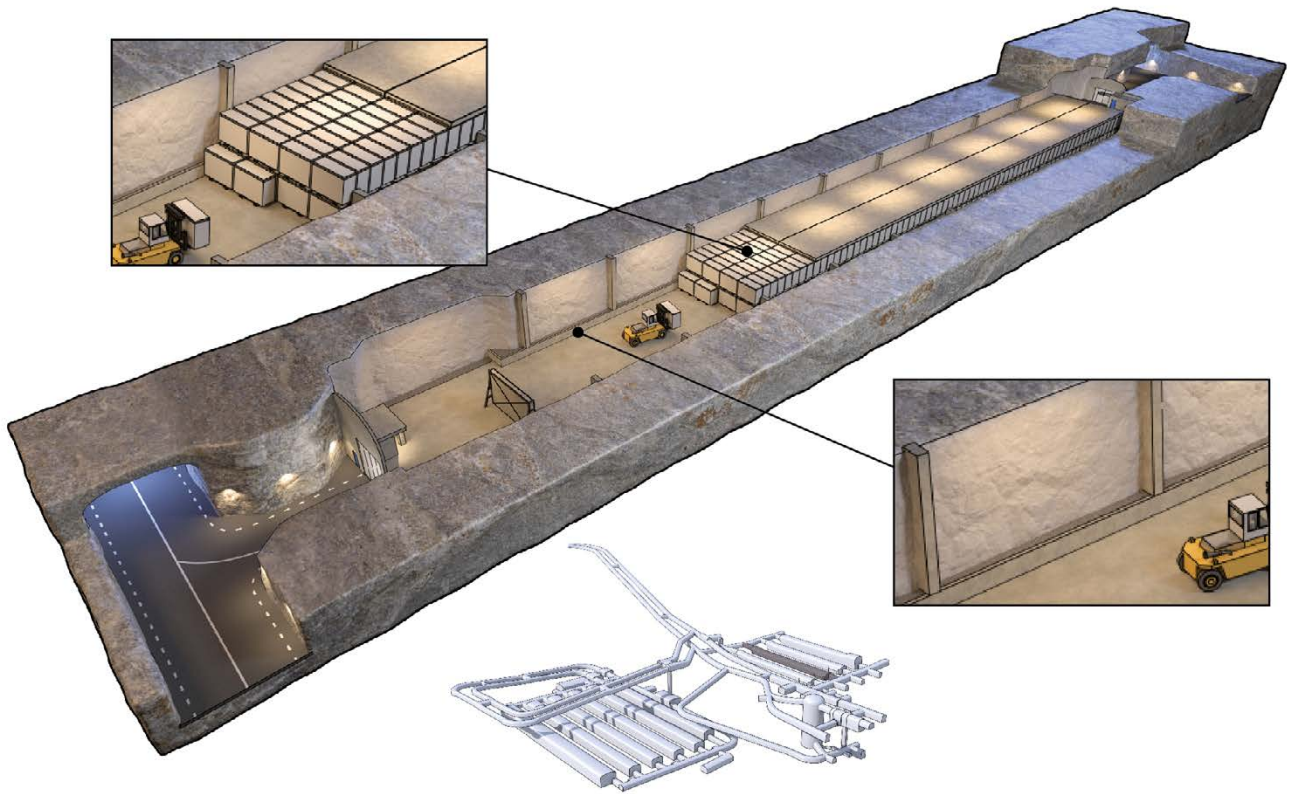


Figure 3-11. Illustration of 2BTf during the operational period. The upper detail shows the emplacement of concrete tanks, the lower detail shows the skirting and concrete pillars. In addition, a view of SFR is shown with the position of 2BTf highlighted in dark grey.

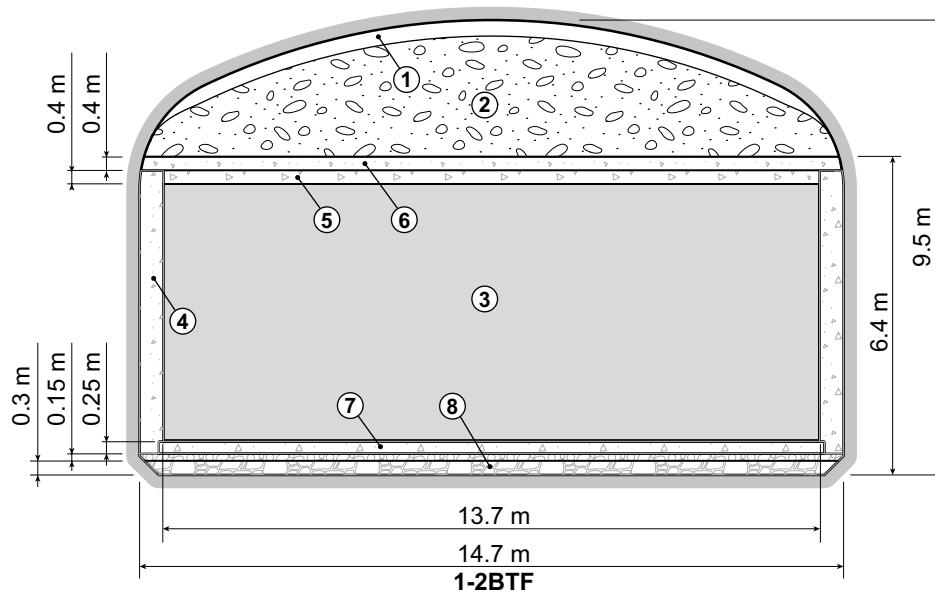


Figure 3-12. Schematic cross-section of 1BTf and 2BTf at closure. Key to numbering: 1) Void 2) Macadam backfill 3) Waste domain 4) Cementitious backfill 5) Pre-fabricated concrete elements 6) Cast concrete lid 7) Slab 8) Crushed rock (0.3 + 0.15 m).

3.1.5 1–5BLA, vaults for low-level waste

1BLA in SFR1 is an approximately 15 m wide, 13 m high and 160 m long waste vault, intended for disposal of low-level waste in ISO containers. The vault has a concrete slab cast on a layer of crushed rock and the vault roof and walls are lined with shotcrete. The ISO containers are stacked two abreast and three to six high, depending on their size.

The 1BLA vault is not backfilled except for the vault section that connects to the tunnel, which is filled with macadam to provide support for the plug. Figure 3-13 and Figure 3-14 show a schematic illustration and a vertical cross-section of 1BLA at closure.

The four vaults, 2–5BLA in SFR3 are approximately 18 m wide, 12 m high and 275 m long waste vaults, intended for low-level waste in ISO containers. The vaults have a concrete slab cast on a layer of macadam, and the vault roof and walls are lined with shotcrete. The ISO containers are stacked two abreast and three to six high, depending on their size.

The 2–5BLA vaults are not backfilled except for the vault sections that connect to tunnels, which are filled with macadam to provide support for the plugs. Figure 3-15 and Figure 3-16 show a schematic illustration and a vertical cross-section of 2–5BLA at closure.

The BLA waste vaults contain (at closure) less than 0.5 % of the total radioactivity in SFR. There are no specific barriers in 1–5BLA other than the common plugs, see Section 3.1.6.

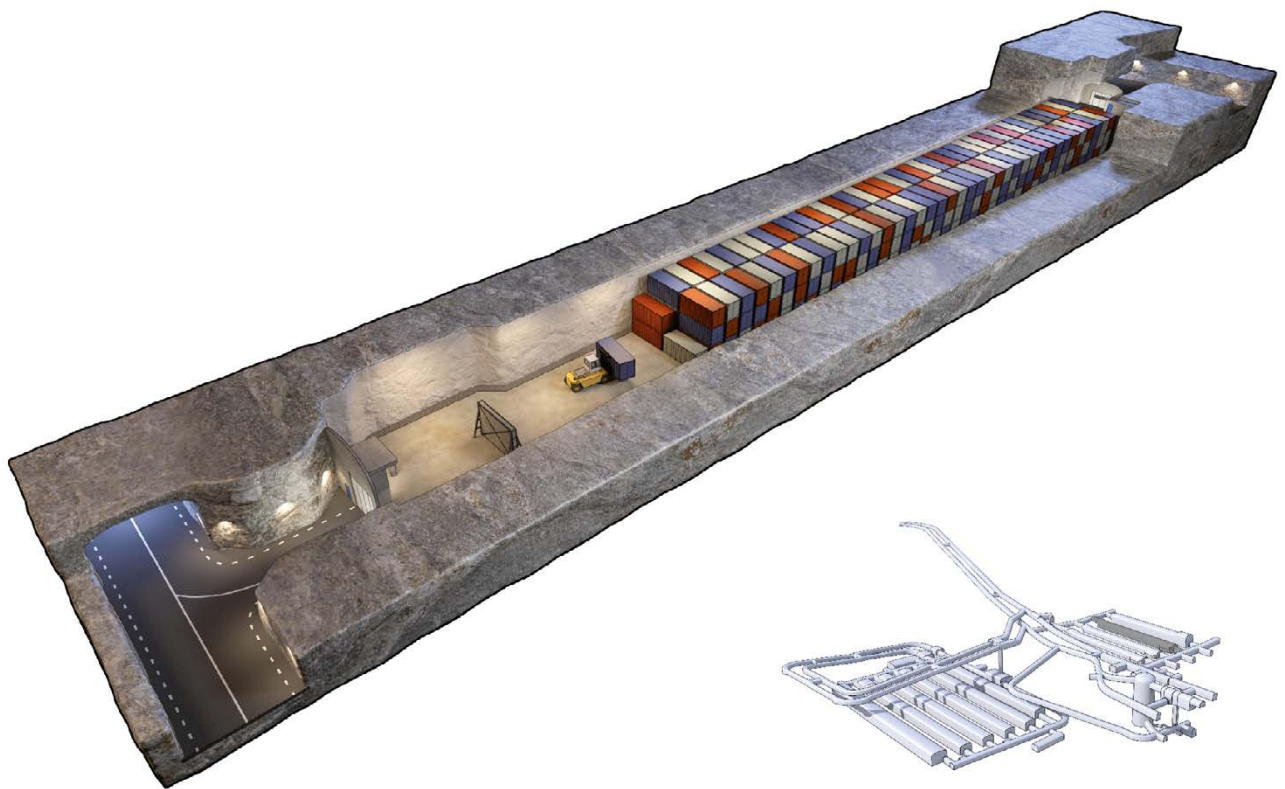


Figure 3-13. Illustration of 1BLA during the operational period and below there is a view of SFR with the position of 1BLA highlighted in dark grey.

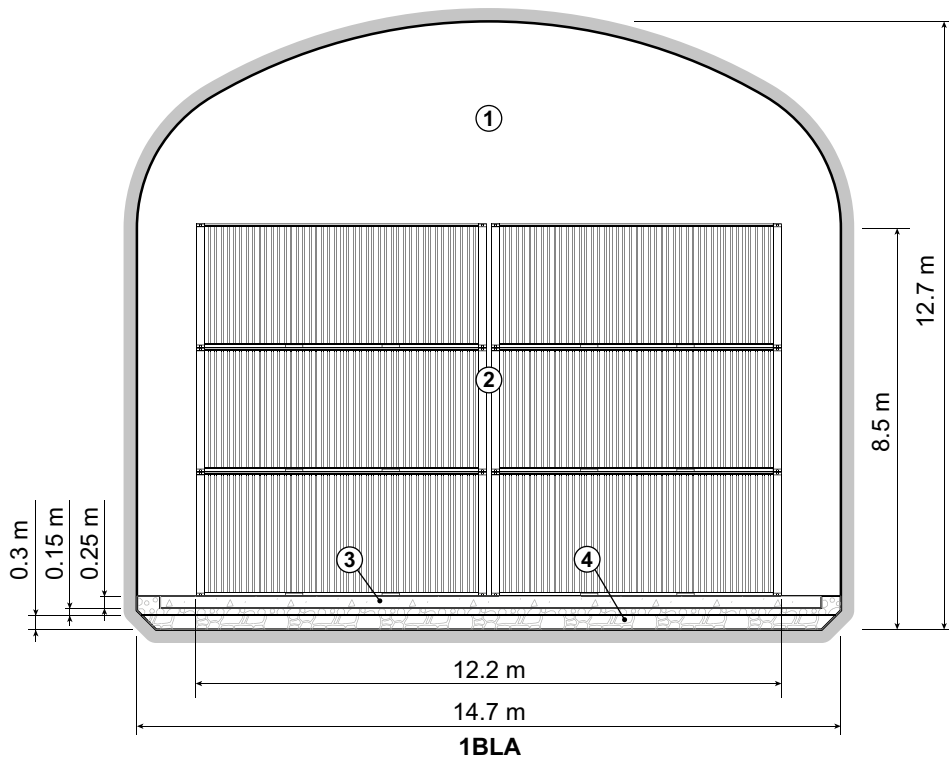


Figure 3-14. Schematic cross-section of 1BLA at closure, exemplified with full-height containers. Key to numbering: 1) Void 2) Waste domain 3) Slab 4) Crushed rock (0.3 + 0.15 m).

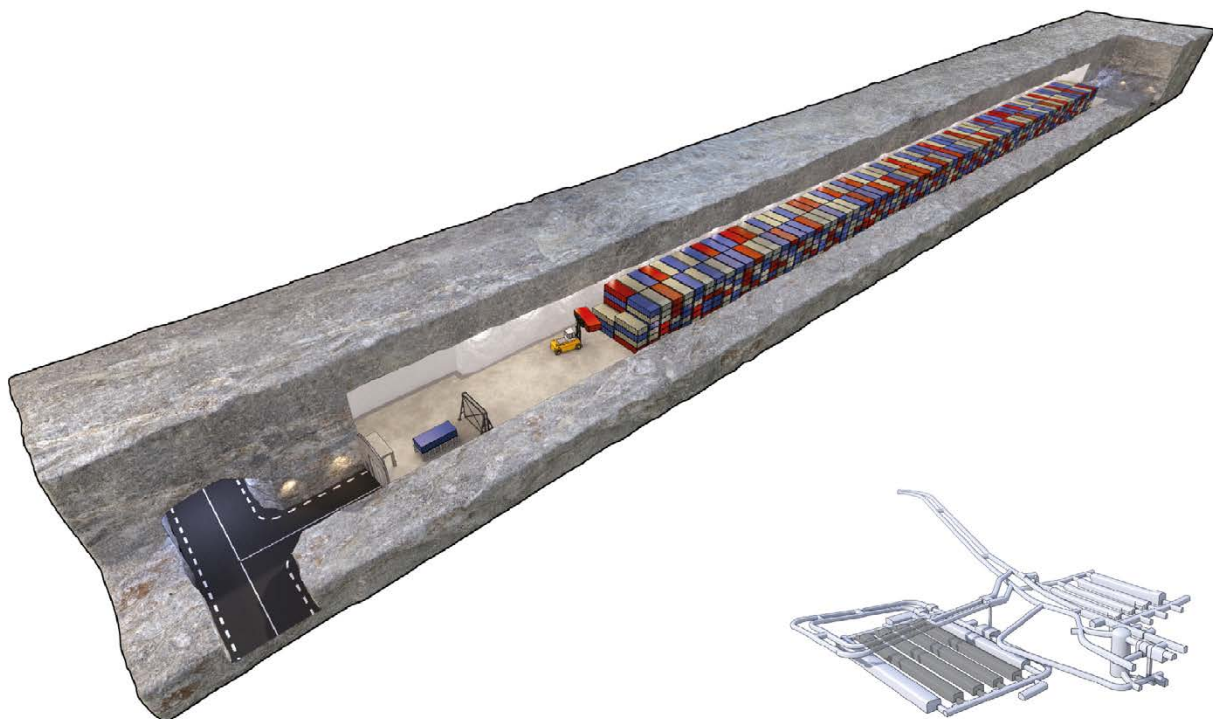


Figure 3-15. Illustration of 2-5BLA during the operational period and below there is a view of SFR with the positions of 2-5BLA highlighted in dark grey.

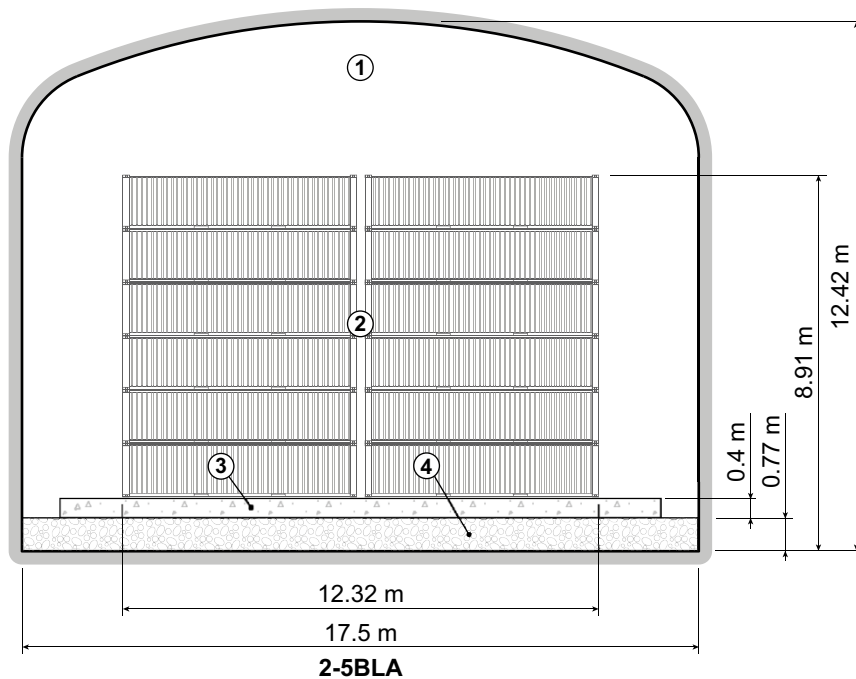


Figure 3-16. Schematic cross-section of 2–5BLA at closure, exemplified with half-height containers. Key to numbering: 1) Void 2) Waste domain 3) Slab 4) Crushed rock.

3.1.6 Plugs and other closure components

The closure components in SFR include the backfill in the waste vaults (described above) as well as the plugs in the underground facility and other closure components e.g. the backfill in tunnels, shafts and access ramps. A total of eight plug sections are to be installed to seal all the waste vaults in SFR from the connecting tunnels (**Initial state report**, Chapter 11). The aim of these plugs, that consist of hydraulically tight sections of bentonite and sections of concrete that provide mechanical support, is to limit the groundwater flow through the waste vaults. Plugs of concrete and bentonite are also to be installed in the access tunnels to minimise water flow along these tunnels. Tunnels, shafts and access ramps are to be backfilled with macadam.

3.2 Initial radionuclide inventory

The waste and associated properties such as the reference radionuclide inventory at repository closure are described in the **Initial state report** and in the **Post-closure safety report**, Section 4.3.7. The waste deposited in SFR mainly originates from the operation and decommissioning of the Swedish nuclear power plants and from the interim storage facility for spent nuclear fuel, Clab. SFR will also accommodate waste from the operation and decommissioning of the nuclear facilities at the Studsvik site, some of which contain radioactive waste from conventional industry, research institutions and medical care.

Most of the radionuclide activity in the operational waste from nuclear power plants comes from decontamination and deionisation of reactor water. The decontamination is mainly done by ion-exchange resins and particle filters that are later deposited in SFR. A smaller portion of the activity in the operational waste originates from contaminated clothing, cloth, scrap and refuse.

The decommissioning waste consists primarily of contaminated steel and concrete from decommissioned nuclear facilities and will mainly be deposited in the BLA waste vaults in SFR3 (2–5BLA). Reactor pressure vessels from the nine Swedish boiling water reactors will be disposed in a dedicated vault (1BRT) in SFR3. The calculated radionuclide inventory has been updated since SR-PSU, a comparison with this previous assessment is presented in Section 3.3.5. The reference activity for the 51 radionuclides listed in the **Initial state report** planned to be disposed in each waste vault is illustrated in Figure 3-17.

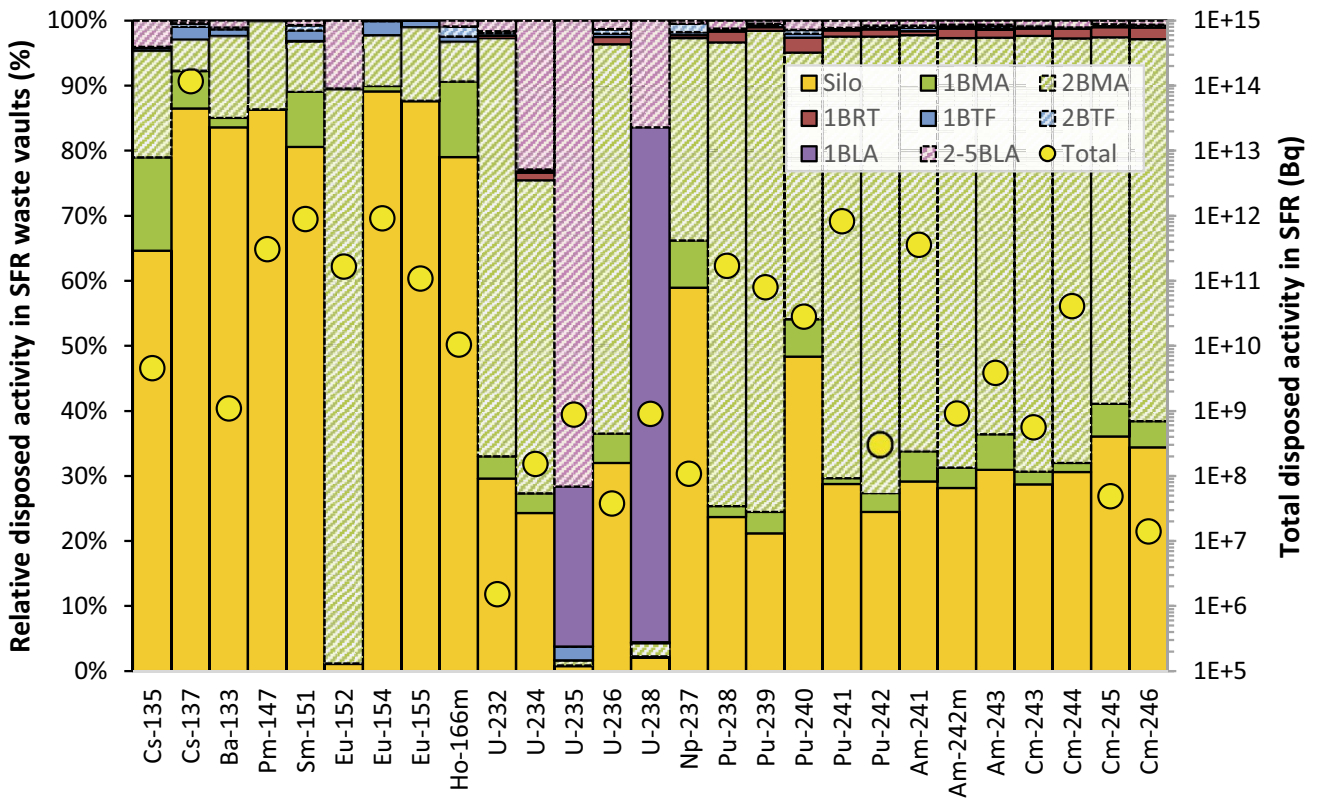
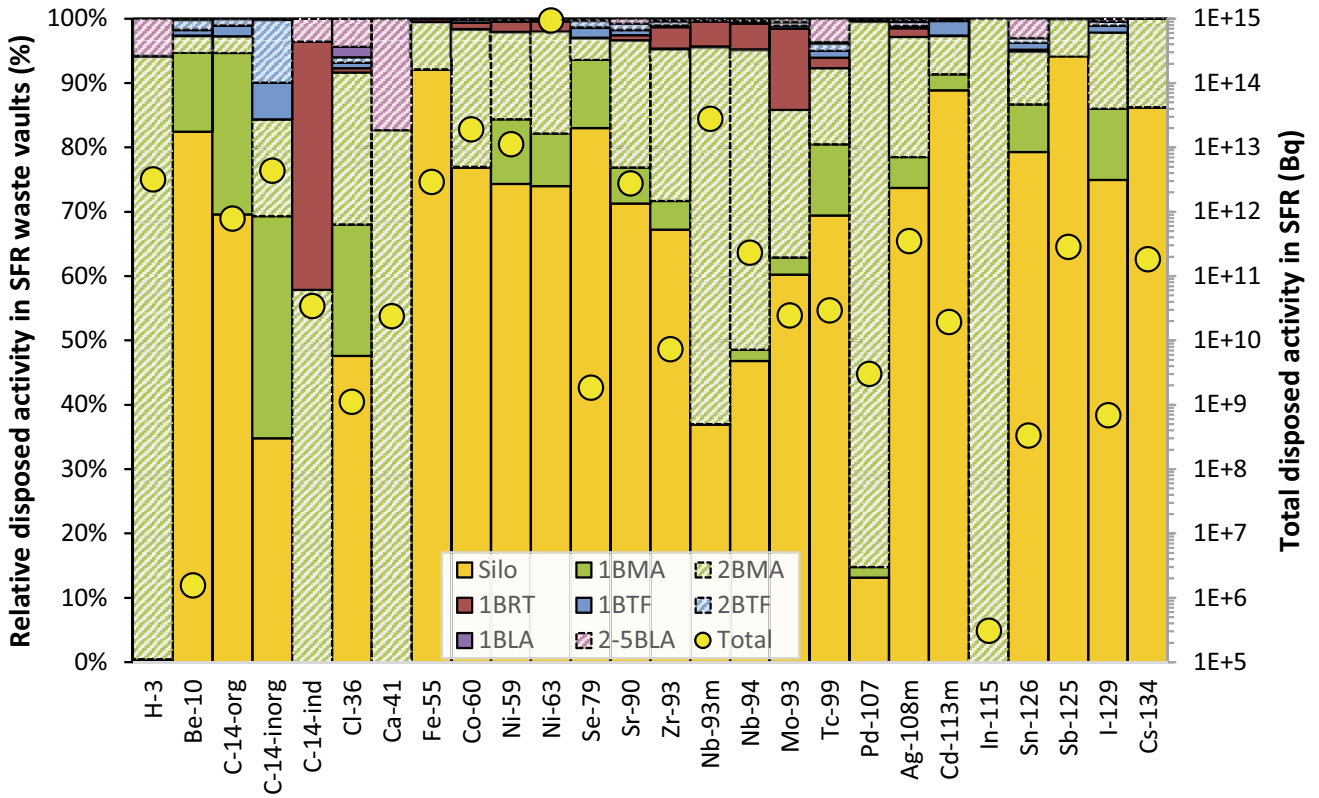


Figure 3-17. Reference radionuclide inventory in SFR at repository closure (Initial state report). Relative disposed activity in waste vaults illustrated as coloured columns (%) and total disposed activity in the extended SFR shown as yellow-coloured circles (Bq, right vertical axis). C-14 is presented in three forms: organic, inorganic and irradiation-induced (C-14-org, C-14-inorg and C-14-ind).

3.3 Selection of radionuclides

The radionuclide activity at closure is given in the **Initial state report** and illustrated in Figure 3-17. Not all radionuclides in the waste are relevant in a long-term safety perspective and so do not need to be included in the radionuclide transport and dose calculations.

The initial selection of relevant radionuclides is done in a consistent manner and is based on activity, toxic effect of radiation, half-life, and on the (shortest) time after repository closure that a potential exposure may commence, taking the assessment context into account.

The screening of radionuclides with respect to their relevance in the long-term safety assessment is based on the concepts of half-life and ingestion radiotoxicity, denoted *radiotoxicity*, which serves to quantify and compare radiological impacts in a simplified way (ingestion is generally assessed to be the main route of exposure⁵). Regulations for the risk of exposure for humans from disposed radionuclides are considered stricter than for non-human biota (NHB). In addition, internal exposure is considered the dominant exposure route for NHB and estimated maximum dose-rates to NHB were orders of magnitude below the screening dose-rate in the previous safety assessment. Therefore, ingestion radiotoxicity is considered a valid measure for screening radionuclides, also in the context of NHB.

The radiotoxicity of a radionuclide is hereby defined as the product of activity and the dose conversion coefficient for ingestion:

$$Rt^n(t) = DCC_{ing}^n \times A^n(t)$$

where:

$Rt^n(t)$ is the radiotoxicity for radionuclide n at time t , (Sv),

$A^n(t)$ is the activity of radionuclide n at time t , (Bq), and

DCC_{ing}^n is the ingestion dose conversion coefficient for radionuclide n , (Sv Bq⁻¹).

In other words, radiotoxicity is measured by the effective dose received from eating or drinking the radionuclide. The ingestion dose conversion coefficients are from ICRP (2012) and are tabulated in Appendix A.

Selection of safety-relevant radionuclides included in the reference inventory at closure is presented next and is followed by a section on the selection of safety-relevant decay products.

3.3.1 Safety-relevant initial inventory radionuclides

An initial screening of relevant radionuclides from the given reference inventory at closure to be considered in the radionuclide transport calculations is based on the following two criteria:

- the half-life of a radionuclide is 10 years or longer, and
- the radiotoxicity by ingestion at the time of repository closure exceeds 10 mSv.

The criteria were applied to select relevant radionuclides in previous safety assessments, namely in SR-Site and SR-PSU (SKB TR-10-50 and Chapter 3 in SKB TR-14-09). Any non-chain radionuclide that does not fulfil these criteria can be excluded from the calculations according to the previously adopted methodology. At least ten half-lives will pass within a period of 100 years after closure (during which knowledge about the repository is expected to be preserved, see the **FHA report**), reducing the activity of radionuclides with a half-life of less than 10 years by more than three orders of magnitude. Also, the repository is expected to be submerged for at least 1 000 years after closure (**Climate report**, Section 3.5.3), and submerged conditions are associated with low groundwater flow and high dilution in the surface system. After 1 000 years, the activities of radionuclides with half-lives less than 10 years are reduced by more than 30 orders of magnitude compared with their initial activity. The second criterion constitutes a reasonably low screening limit for radionuclides with negligible radiological impact relative to other radionuclides disposed in SFR, as can be seen in Figure 3-18.

⁵ For a discussion about screening based on other exposure pathways, see Section 3.3.4.

The blue circles in Figure 3-18 show the half-life versus the radiotoxicity for each radionuclide in the reference inventory, alongside the two above-mentioned selection criteria (red vertical and green horizontal lines, respectively). Seven radionuclides fall on the left side of the screening line due to their short half-life. In addition, two radionuclides (Be-10 and In-115) have a very low initial radiotoxicity of only about 2 mSv and just below 10 mSv, respectively. This allows their exclusion from the modelling, despite their long half-lives. Thus, radionuclides that fall above the green line and on the right side of the vertical red line in Figure 3-18 are included in the radionuclide transport calculations. In addition, due to its relatively high radiotoxicity at repository closure (fourth highest radiotoxicity), Co-60 with a half-life of about five years is also included.

3.3.2 Safety-relevant decay products

Regardless of the given reference inventory, decay products must be considered for their safety-relevance. The activity of these radionuclides results from ingrowth or a combination of reference inventory and ingrowth. Radiotoxicity can be calculated for decay products in the same way as for primary radionuclides. The radiotoxicity might increase with time due to ingrowth caused by radioactive decay before finally reaching a maximum value. Thereafter the radiotoxicity of the decay products decreases with time as decay dominates over ingrowth (and the parent radionuclide decays). The orange diamonds in Figure 3-18 show the maximal radiotoxicity over the full 100 000-year assessment period, due to ingrowth only (thus not including initial activity), for decay products.

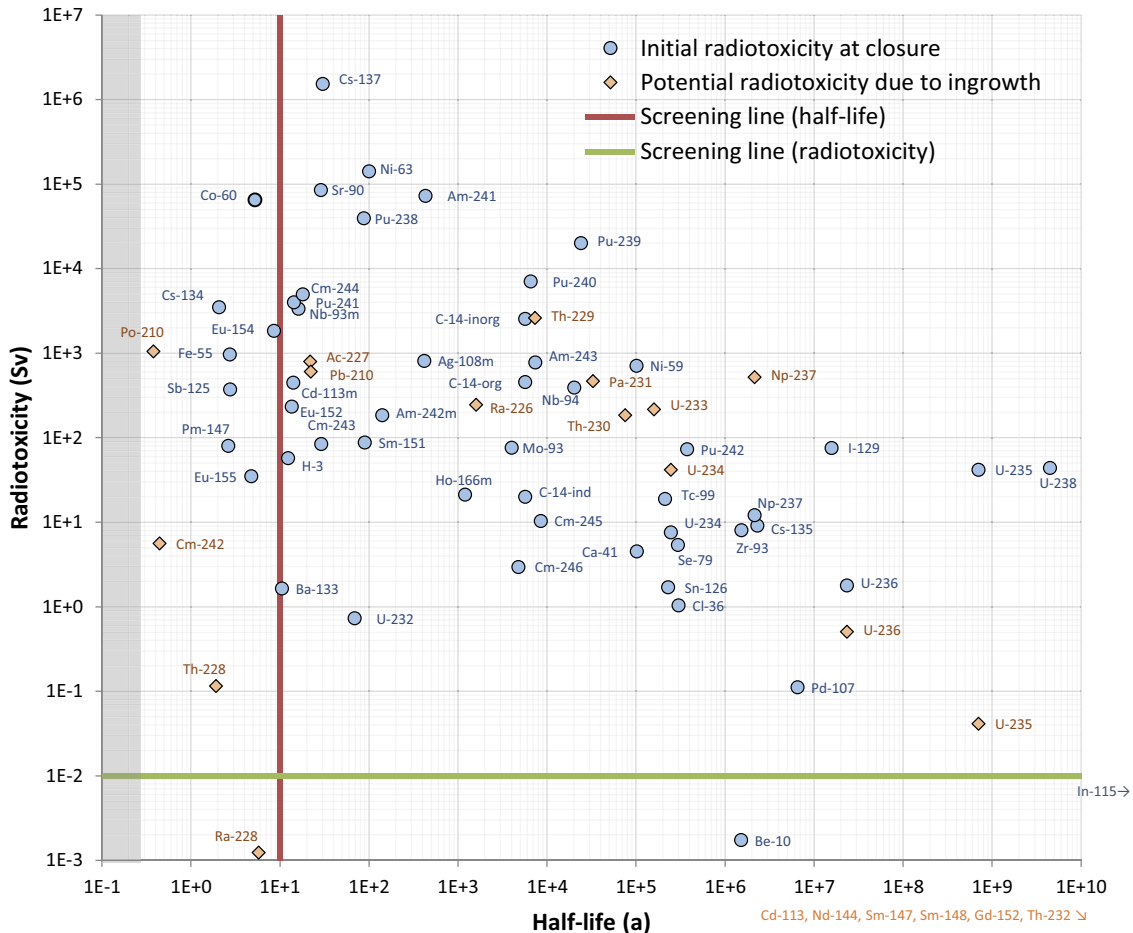


Figure 3-18. Radiotoxicity (Sv) versus radionuclide half-life (a): initial radiotoxicity of radionuclides (with a half-life exceeding one year) at repository closure (blue circles) and maximum radiotoxicity due to ingrowth of decay products over 100 000 years (orange diamonds). The vertical red line at 10 years shows the limit of the selection criterion of radionuclides in the waste based on half-life. The horizontal green line at 10 mSv shows the limit for the selection criterion of radionuclides in the waste due to radiotoxicity. The grey shading highlights the area of decay products with a half-life less than 100 days that are assumed to be in secular equilibrium with parent radionuclides (not shown), their radiotoxicities are instead added to that of their parents.

The criterion used for explicitly taking secondary radionuclides into account in the radionuclide transport calculations is that their half-life is longer than 100 days (in contrast to the half-life criterion in Section 3.3.1). Decay products with a half-life less than 100 days are not explicitly modelled in the transport calculations but are implicitly accounted for in the dose calculation, assuming that they are in secular equilibrium with their parent radionuclides when calculating the dose conversion coefficient of that parent (see Appendix A5 for details). Such short-lived decay products would fall within the grey shaded area on the left side of Figure 3-18.

Another rule for excluding decay products is if their half-life indicates that no dose-relevant activity could possibly build up during the assessment period. Thus, decay products not present in the initial inventory with a half-life greater than 10^{10} years are excluded in the radionuclide transport and dose calculations.

Two relatively short-lived decay products are pessimistically assumed to be in secular equilibrium with their parent radionuclides and thus not explicitly modelled to reduce the number of radionuclides modelled. These are Th-228 and Cm-242, both of which have parent radionuclides with half-lives of a few hundred years and are more radiotoxic than their decay products.

To reduce computation time, explicitly modelled decay chains are truncated at appropriate positions. An explicitly modelled decay chain is limited to decay products with half-lives shorter than 10^{10} years (assumed stable). This is the case for the thorium decay series ($4n$ chain), truncating the modelled decay chain at Th-232 which is assumed to be a stable isotope in this context. In addition, decay chains between parent radionuclides that do not contribute significantly to the activity of their decay products are not modelled. This is the case when a parent radionuclide, that itself is not a decay product, has a much shorter half-life than its decay products as well as similar or less initial activity. As a result, ingrowth of Pu-240 from Cm-244, Pu-242 from Cm-246, U-238 from Pu-242, Am-243 from Cm-243, and Pu-239 from either Cm-243 or Am-243 are not considered in the radionuclide transport modelling. The cuts in the decay chains are illustrated in Figures 3-19 to 3-21 as strikethrough arrows.

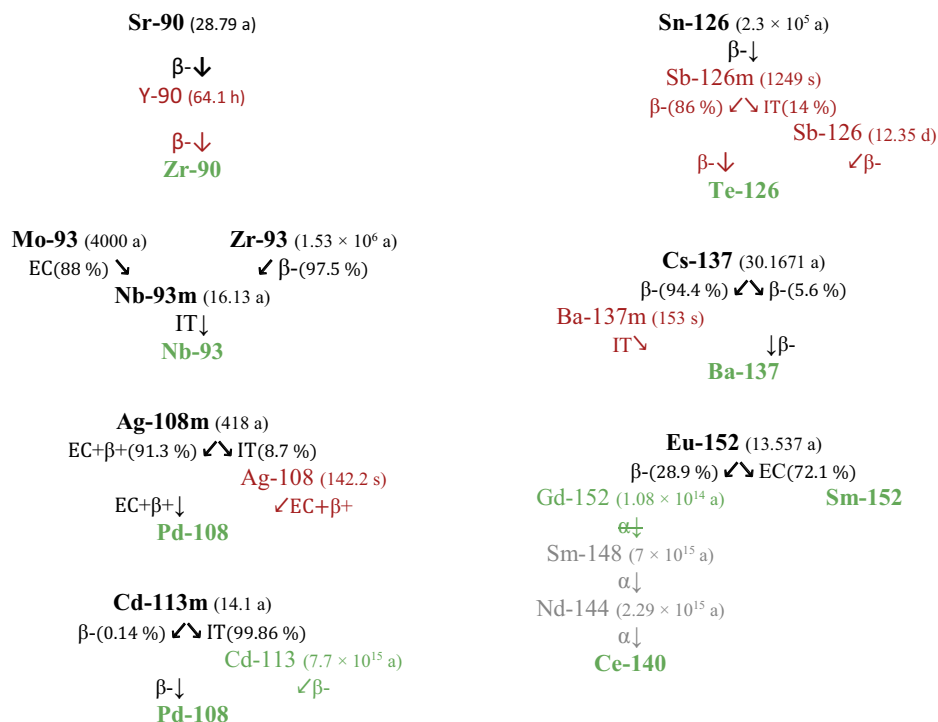


Figure 3-19. Radionuclide decay chains and half-lives for short decay series considered in the radionuclide transport calculations in the PSAR: explicitly modelled radionuclides defined in the reference inventory (black bold), explicitly modelled ingrown radionuclides (black), short-lived decay products accounted for by being assumed to be in secular equilibrium with parent radionuclide (red), stable isotope or radionuclide, i.e., half-life greater than 10^{10} years (green). Strikethrough decay chain arrow illustrates that ingrowth of decay products are excluded. Radionuclides ignored due to break in decay chain (grey). Illustrated decay modes are α : alpha decay, β^- : beta minus decay, β^+ : beta plus decay, EC: electron capture, and IT: isomeric transition.

3.3.3 Selected radionuclides

Radionuclide decay chains included in the radionuclide transport modelling are presented in Figures 3-19 to 3-21 and single radionuclides (radionuclides not part of a decay chain) explicitly modelled in the radionuclide transport calculations are presented in Table 3-1. In total 53 radionuclides are explicitly considered in the radionuclide transport modelling. Of these, C-14 is included in the calculations in three forms in the waste: organic, inorganic and irradiation-induced. Also, in the geosphere transport calculations, Rn-222, which is a member of the $4n + 2$ -chain is explicitly considered (see Section 5.5.1).

Table 3-1. Single radionuclides (not part of a decay chain) explicitly modelled in the radionuclide transport calculations in the PSAR. Radionuclide half-lives in parenthesis.

Radionuclide			
H-3 (12.32 a)	Ni-59 (1.01×10^5 a)	Nb-94 (2.03×10^4 a)	Ba-133 (10.52 a)
C-14 ¹ (5700 a)	Co-60 (5.27 a)	Tc-99 (2.11×10^5 a)	Cs-135 (2.3×10^6 a)
Cl-36 (3.01×10^5 a)	Ni-63 (100.1 a)	Pd-107 (6.5×10^6 a)	Sm-151 (90 a)
Ca-41 (1.02×10^5 a)	Se-79 (2.95×10^5 a)	I-129 (1.57×10^7 a)	Ho-166m (1200 a)

¹ C-14 is included in the calculation in three forms: organic, inorganic and irradiation-induced (C-14-org, C-14-inorg and C-14-ind).

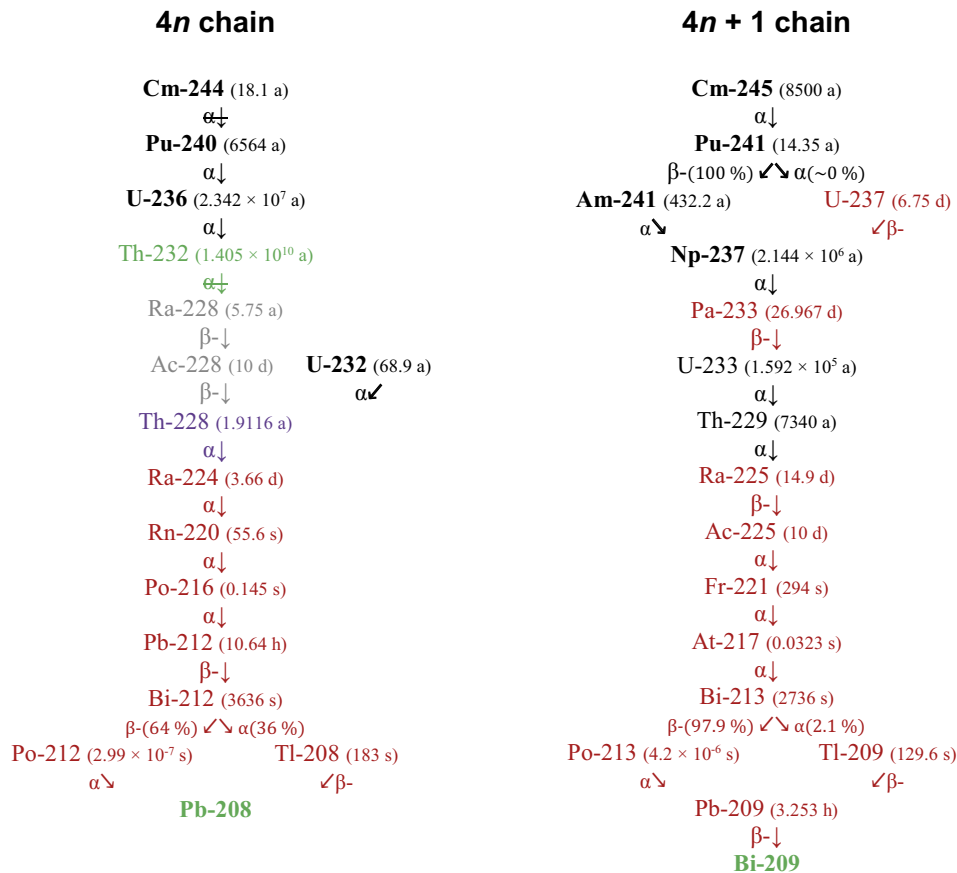
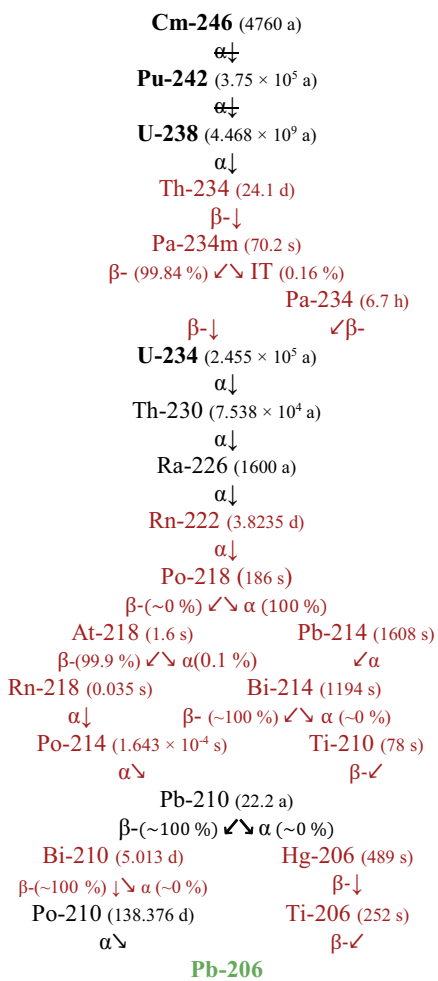


Figure 3-20. Radionuclide decay chains and half-lives considered in the thorium ($4n$) and neptunium ($4n + 1$) series for the radionuclide transport calculations in the PSAR: explicitly modelled radionuclides defined in the reference inventory (black bold), explicitly modelled ingrown radionuclides (black), short-lived decay products accounted for by being assumed to be in secular equilibrium with parent radionuclide (red), other decay products accounted for by being assumed to be in secular equilibrium with parent radionuclide (purple), stable isotope or radionuclide, i.e., half-life greater than 10^{10} years (green). Strikethrough decay chain arrow illustrates that ingrowth of decay products are excluded. Radionuclides ignored due to break in decay chain (grey). Illustrated decay modes are α : alpha decay, β -: beta minus decay, β +: beta plus decay, EC: electron capture, and IT: isomeric transition.

4n + 2 chain



4n + 3 chain

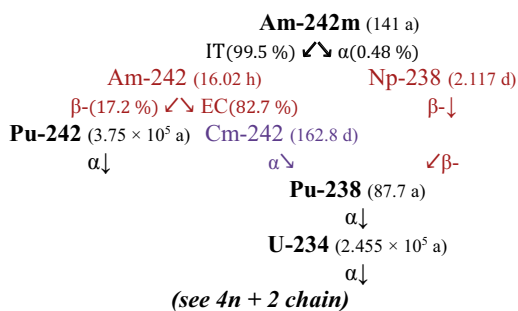
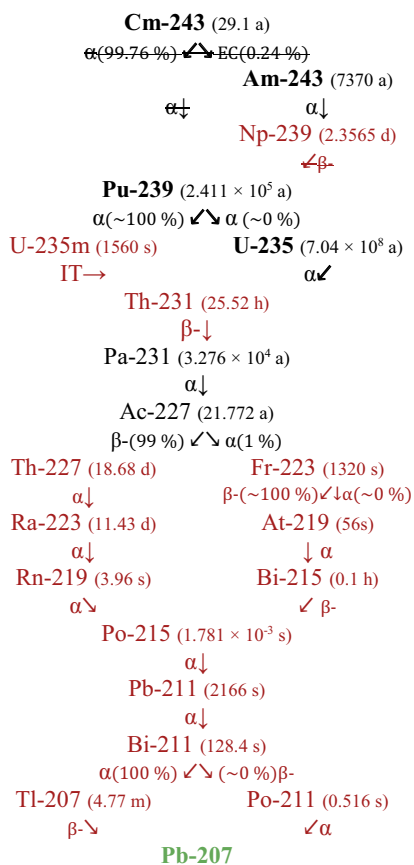


Figure 3-21. Radionuclide decay chains and half-lives considered in the radium ($4n + 2$) and actinium ($4n + 3$) series for the radionuclide transport calculations in the PSAR: explicitly modelled radionuclides defined in the reference inventory (black bold), explicitly modelled ingrown radionuclides (black), short-lived decay products accounted for by being assumed to be in secular equilibrium with parent radionuclide (red), other decay products accounted for by being assumed to be in secular equilibrium with parent radionuclide (purple), stable isotope or radionuclide, i.e., half-life greater than 10^{10} years (green). Strikethrough decay chain arrow illustrates that ingrowth of decay products are excluded. Radionuclides ignored due to break in decay chain (grey). Illustrated decay modes are α : alpha decay, β^- : beta minus decay, β^+ : beta plus decay, EC: electron capture, and IT: isomeric transition.

3.3.4 Other exposure pathways

In Section 3.3.1, radiotoxicity by ingestion was defined as one of the criteria to select the radionuclides for the radionuclide transport and dose calculations. However, intake through the digestive system may not dominate exposure from specific radionuclides in the biosphere. To identify radionuclides with high radiotoxicity that were mistakenly screened out, similarly designed screening calculations were also performed for exposure through inhalation as well as external exposure. In the calculations for inhalation, the entire activity is assumed to be inhaled for one year, whereas in the calculation of external exposure, the activity is assumed to be located on a surface area of 1 m² and exposure from external radiation is assessed for 1 year. Inhaling the radionuclide activity results, on average, two orders of magnitude higher radiotoxicity than the exposure through ingesting the activity. However, all radionuclides that would be included based on inhalation are already included based on ingestion, except for Be-10 (a factor 5 above the radiotoxicity screening line) and almost stable In-115 and Th-232. Several radionuclides with half-lives longer than 10 years have higher external radiotoxicity than for ingestion (Ho-166m, Ag-108m, Eu-152 and Ba-133). However, all of these are already included when screening based on ingestion. Furthermore, no long-lived radionuclides have greater radiotoxicity through external exposure than inhalation. Only a very small fraction of released Be-10 (which is an earth metal) is expected to be accessible in the air compared to the activity in the soil (activity air:soil is less than 1×10^{-10})⁶. Thus, as the radiotoxicity on inhalation for Be-10 was only slightly above the radiotoxicity criterion, Be-10 is not considered relevant to be included in further transport and dose modelling. Similarly, long-lived In-115 and Th-232 are not considered to be relevant to propagate to the transport and dose modelling.

3.3.5 Handling of uncertainties in the radionuclide reference inventory

Uncertainties in the radionuclide reference inventory are shown in the **Post-closure safety report**, Figure 4-2. The uncertainties are handled differently in the PSAR as compared with the SR-PSU. In the SR-PSU, uncertainties were accounted for by the high inventory scenario (SKB TR-14-01), which contributed to the risk assessment as a less probable scenario with a fixed probability. In the present assessment, an improved methodology is applied where uncertainties instead are handled in a probabilistic manner. In summary, PDFs of the inventory are constructed from information about the uncertainty in e.g., measurements and models (see also the **Data report**, Chapter 4). The probabilistic representation of the uncertainty in the radionuclide inventory is achieved through sampling these PDFs. This results in 1 000 samples (or realisations) of the inventory that are propagated to the radionuclide transport calculations.

In addition to the probabilistic handling of uncertainties, alternative inventories representing hypothetical changes in operational conditions are evaluated in three calculation cases in the *alternative radionuclide inventory scenario*, see Section 8.8.

3.3.6 Comparison with previous assessments of SFR


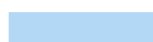




The post-closure safety of SFR has been assessed several times before (Section 1.2), and the assessment of inventory and safety is based on this experience. The set of radionuclides considered in the reference inventory in the PSAR assessment is the same as in the SR-PSU and is similar to the set of radionuclides considered in the assessment SAR-08 (Thomson et al. 2008). As in the SR-PSU and contrary to previous assessments, Ru-106 and Pu-244 were excluded (due to short half-life (Ru-106) and low inventory (Pu-244)), whereas Ca-41 and In-115 were included in the reference inventories representing decommissioning waste. Comparison of the reference inventories in previous assessments shows that U-233 and most thorium isotopes were excluded from SAR-08 but were included in the (previous) SAFE assessment (Lindgren et al. 2001). Also, they were not included in the following transport and dose modelling in either of the two assessments. In the SR-PSU, they were excluded in the reference inventory but included in the transport and dose modelling as decay products.

⁶ Concentration of fine soil particles in the air above agricultural land is around 5×10^{-8} kg_{DW} m⁻³ and the agricultural soil density is approximately 700 kg_{DW} m⁻³ in BioTE_x, **Biosphere synthesis report**.

Table 3-2 shows a comparison of which radionuclides were included in the inventory for the assessments SAFE, SAR-08 for SFR1, and the SR-PSU and the PSAR for SFR1 and SFR3. The number of safety-relevant radionuclides considered in the SAFE and SAR-08 assessments was significantly lower. Four decay products that were explicitly modelled in the SR-PSU are now excluded in the PSAR. Two of these (Th-228 and Cm-242) are pessimistically added to the parent radionuclide assuming secular equilibrium. The other two (Th-232 and Ra-228) are now screened out due to the long half-life of Th-232.

Table 3-2. Comparison of radionuclides in the SFR assessments SAFE, SAR-08, SR-PSU and the PSAR (Lindgren et al. 2001, Almkvist and Gordon 2007, Thomson et al. 2008, SKB R-13-37).

Radionuclide	SAFE	SAR-08	SR-PSU	PSAR	Radionuclide	SAFE	SAR-08	SR-PSU	PSAR
H-3					Ho-166m				
Be-10					Pb-210				
C-14					Po-210				
Cl-36					Ra-226				
Ca-41					Ra-228				
Fe-55					Ac-227				
Co-60					Th-228				
Ni-59					Th-229				
Ni-63					Th-230				
Se-79					Th-232				
Sr-90					Pa-231				
Zr-93					U-232				
Nb-93m					U-233				
Nb-94					U-234				
Mo-93					U-235				
Tc-99					U-236				
Ru-106					U-238				
Pd-107					Np-237				
Ag-108m					Pu-238				
Cd-113m					Pu-239				
In-115					Pu-240				
Sn-126					Pu-241				
Sb-125					Pu-242				
I-129					Pu-244				
Cs-134					Am-241				
Cs-135					Am-242m				
Cs-137					Am-243				
Ba-133					Cm-242				
Pm-147					Cm-243				
Sm-151					Cm-244				
Eu-152					Cm-245				
Eu-154					Cm-246				
Eu-155									

-  Not included in the reference inventory.
-  Included in the reference inventory, but not in the transport and dose modelling.
-  Implicitly included (reference inventory added to decay product).
-  Included.
-  Only included as decay product in the transport and dose modelling.
-  Implicitly included (decay product assumed to be in secular equilibrium with parent radionuclide in the transport and dose modelling).

The difference of the radionuclide inventory between the PSAR and the SR-PSU is presented as the quotient between the two projects for each waste vault and each radionuclide in Table 3-3. The changes in disposal strategy and methodology that resulted in these differences are described in detail in the **Post-closure safety report**, Section 4.2.5. Examples of alterations that contribute to a relocation of the radioactivity in the different repositories or waste vaults comprise e.g. that non-activated parts of the PWR RPV's (reactor pressure vessels) have been directed to 1BRT instead of SFL and conversely, smoke detectors previously allocated to the silo have instead been directed to SFL (the Am-241 and Np-237 inventory has therefore been substantially reduced in the silo). The radionuclide inventory in decommissioning waste from the Studsvik site was previously missing in the SR-PSU and has been included in the PSAR. Forecast operational waste has been allocated to 2BMA in the PSAR whereas, in the SR-PSU, only decommissioning waste was planned to be included in this waste vault.

Table 3-3. Quotient of the radionuclide reference inventory in the PSAR and in SR-PSU. Non-existing/insignificant activity levels shown as not applicable (N/A).

Radionuclide	Total	Silo	1BMA	2BMA	1BRT	1BTF	2BTF	1BLA	2-5BLA
H-3	0.91	1.51	0.41	0.90	N/A	2.44	0.46	0.02	0.94
Be-10	1.24	1.32	0.88	1.89	N/A	0.94	1.02	1.25	1.68
C-14-org	0.85	0.72	1.34	5.20	N/A	1.30	1.33	1.93	1.00
C-14-inorg	0.86	0.56	0.80	45.6	N/A	1.32	1.58	2.10	1.01
C-14-ind	2.09	N/A	N/A	3.91	1.30	N/A	N/A	N/A	1.04
Cl-36	0.73	0.59	0.68	1.31	1.02	0.67	0.56	0.86	1.06
Ca-41	1.23	N/A	N/A	1.27	N/A	N/A	N/A	N/A	1.06
Fe-55	1.01	0.99	0.0003	2.06	0.98	13.3	0.003	0.03	1.15
Co-60	1.24	1.14	0.05	2.06	0.98	5.10	0.08	0.33	1.22
Ni-59	1.12	1.22	0.54	1.61	1.11	0.44	0.65	0.78	1.11
Ni-63	1.17	1.28	0.53	1.62	1.06	0.48	0.65	0.74	1.07
Se-79	1.42	1.47	0.94	8.7	N/A	1.81	1.27	1.44	1.04
Sr-90	0.60	0.55	0.28	1.52	0.96	0.61	0.47	0.44	0.92
Zr-93	1.19	1.10	0.88	1.64	1.33	0.93	1.01	1.25	1.04
Nb-93m	1.18	1.11	0.54	1.25	1.01	2.03	0.58	1.01	0.95
Nb-94	1.21	1.25	1.11	1.18	1.17	0.84	1.01	1.16	1.10
Mo-93	0.84	0.75	0.44	1.24	1.03	0.33	0.58	0.09	1.55
Tc-99	0.47	0.41	0.52	2.46	1.07	0.13	0.65	0.04	2.10
Pd-107	1.05	1.45	0.94	1.01	N/A	1.81	1.27	1.44	1.30
Ag-108m	1.19	1.13	0.87	1.63	2.97	0.79	1.00	1.23	1.02
Cd-113m	1.83	1.80	0.61	12.6	N/A	5.76	0.53	1.46	5.14
In-115	0.99	N/A	N/A	0.99	N/A	N/A	N/A	N/A	N/A
Sn-126	1.29	1.30	0.94	1.60	1.08	1.81	1.27	1.44	1.27
Sb-125	2.17	2.04	0.04	62.9	1.61	16.2	0.004	0.03	0.99
I-129	0.59	0.52	0.52	10.7	N/A	0.33	0.43	0.56	1.45
Cs-134	0.84	0.72	0.0001	113	N/A	22.6	0.0001	0.01	1.02
Cs-135	0.80	0.66	0.78	14.0	N/A	0.19	0.31	0.65	1.05
Cs-137	1.68	1.72	0.83	6.41	N/A	3.32	0.95	1.52	0.98
Ba-133	1.32	1.49	0.33	0.97	N/A	2.75	0.37	0.82	0.98
Pm-147	0.86	0.74	0.003	104	1.00	57.3	0.00	0.03	3.18
Sm-151	1.49	1.56	0.92	1.95	1.04	2.25	1.18	1.48	1.03
Eu-152	1.09	2.15	0.51	1.10	0.90	1.00	0.50	0.90	1.00
Eu-154	1.64	1.56	0.34	10.5	0.87	9.91	0.19	1.64	1.34
Eu-155	1.09	0.97	0.08	33.1	0.87	22.4	0.02	0.55	1.62
Ho-166m	1.17	1.23	0.88	1.23	1064	0.95	1.01	1.25	1.06
U-232	1.72	0.74	0.59	6.77	1.05	0.35	0.72	0.07	2.68
U-234	3.27	1.05	0.70	24.6	N/A	0.39	0.85	0.09	81.0
U-235	1.35	0.49	0.33	88.5	2548	1.00	0.90	0.73	1.96
U-236	1.47	0.77	0.65	3.80	1.10	0.44	0.76	0.08	2.42
U-238	0.95	0.57	0.36	14.6	N/A	0.41	0.57	0.98	0.84
Np-237	0.19	0.12	0.29	4.42	1.11	0.43	0.75	0.15	1.78
Pu-238	1.30	0.56	0.38	2.77	1.05	0.24	0.56	0.04	1.38
Pu-239	2.86	1.00	0.96	8.74	1.14	0.43	1.06	0.10	1.38
Pu-240	0.73	0.57	0.42	1.26	1.11	0.32	0.62	0.07	1.36

Radionuclide	Total	Silo	1BMA	2BMA	1BRT	1BTF	2BTF	1BLA	2-5BLA
Pu-241	1.59	0.78	0.31	3.39	0.91	0.31	0.33	0.03	1.61
Pu-242	1.50	0.61	0.45	4.27	1.09	0.30	0.59	0.06	1.37
Am-241	0.02	0.005	0.58	5.63	1.15	0.29	0.67	0.12	1.45
Am-242m	1.60	0.81	0.66	3.34	1.03	0.33	0.68	0.07	1.34
Am-243	1.50	0.75	1.04	3.56	1.14	0.40	0.78	0.40	1.38
Cm-243	1.73	0.85	0.58	3.66	0.96	0.33	1.96	0.05	1.43
Cm-244	1.89	1.36	0.87	2.52	0.94	0.27	0.73	0.05	1.45
Cm-245	1.74	1.20	1.24	2.76	1.11	0.38	0.78	0.13	1.30
Cm-246	1.65	1.13	1.07	2.48	1.11	0.43	0.95	0.12	1.26
							x < 0.9	0.9 > x < 1.1	x > 1.1

3.4 Inventory and radiotoxicity over time

Total reference activity of each radionuclide, and the reference activity in each waste vault, are illustrated in Figure 3-17 and listed in Table 3-9 and Table 3-10 (95th percentile) of the **Initial state report**. The radionuclide reference activity in each waste package type is given in the inventory report (SKB R-18-07).

Figures 3-22 and 3-23 illustrate the development over time of the reference activity plus its decay products relative to the sum of the reference activity at repository closure, for each waste vault and radionuclide, respectively. It includes the activity of all radionuclides in SFR, including those rejected from the transport modelling according to the criteria in Section 3.3.1. Most of the activity in SFR is disposed in the silo and the two BMA waste vaults. Most of the radionuclide inventory in SFR is relatively short-lived and the activity decays to less than 1.5 % of the initial activity within 1 000 years. The largest contribution to the total activity during the initial period comes from Ni-63. As shorter-lived radionuclides decay, Ni-59 dominates the total activity from about 500 years after closure until the end of the assessment period of 100 000 years.

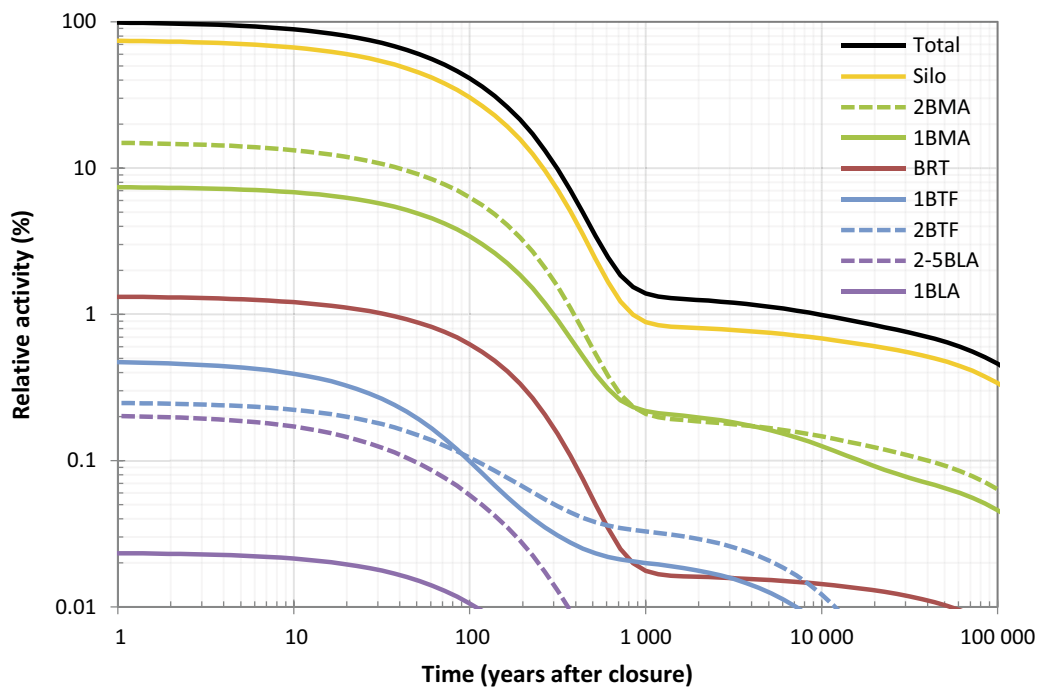


Figure 3-22. Contributions from each waste vault to total activity as a function of time.

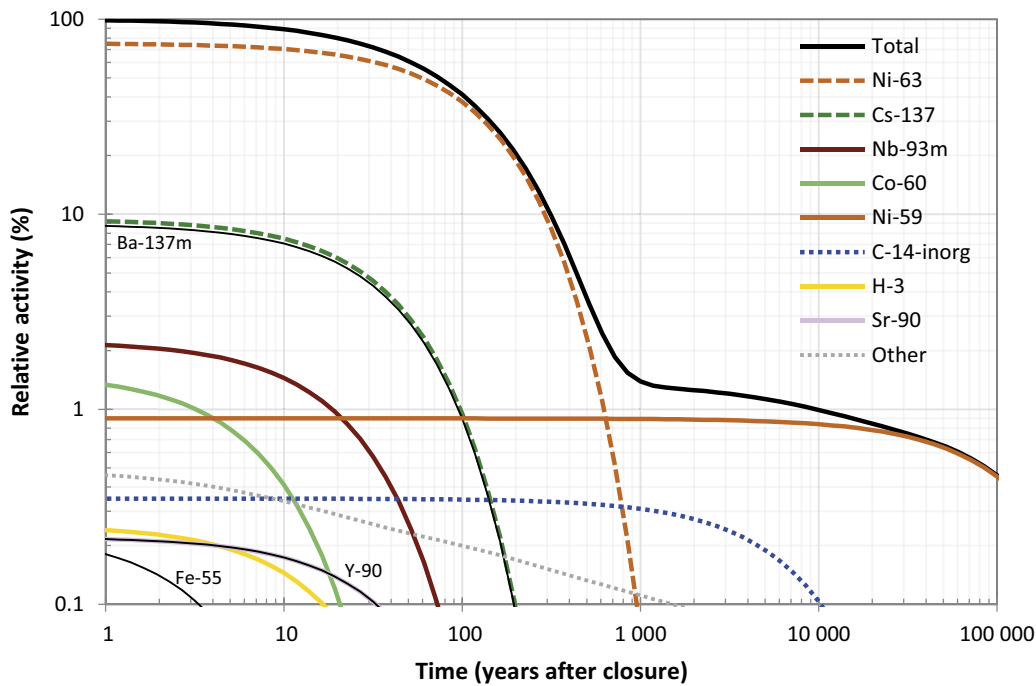


Figure 3-23. Contributions from radionuclides to total activity as a function of time. Other (grey dotted line) includes contributions from all radionuclides not visible in the figure. Implicitly modelled radionuclides (in the radionuclide transport and dose modelling, Ba-137m and Y-90 are assumed to be in secular equilibrium with Cs-137 and Sr-90, respectively, Section 3.3.2) and Fe-55 that is not included in the radionuclide transport and dose modelling are illustrated with thin black lines.

Figures 3-24 and 3-25 show the time dependent radiotoxicity from each waste vault and from each radionuclide as based on the reference activity of the waste. The radiotoxicity of all radionuclides in SFR are shown, including those rejected from the transport modelling according to the criteria in Section 3.3.1. As with the activity, the total radiotoxicity decreases with time as shorter-lived radionuclides decay. By 1 000 years post-closure, less than 2.5 % of the initial radiotoxicity remains and by the end of the assessment period, less than 0.2 % of the initial radiotoxicity remains.

Initially, the silo inventory contributes about 80 % of the total radiotoxicity, primarily due to the amount of Cs-137 and Ni-63. Between 200- and 100 000-years post-closure, the radiotoxicity is dominated by two actinides, Am-241 and Pu-239. Contrary to the previous assessment of SFR (SR-PSU), it may be noted that the large amounts of Am-241, in the form of waste packages containing discarded smoke detectors, which were previously planned to be disposed in the silo, are now planned to be directed to SFL (see Section 3.1.3 in SKB R-18-07). In the SR-PSU, Am-241 in the silo dominated the radiotoxicity in SFR during the first 4 000 years with a contribution of almost 100 % of the total radiotoxicity.

After the assessment period, ingrowth of short-lived and very radiotoxic decay products (mainly Ac-227 and Po-210), originating from long-lived uranium isotopes (U-235 and U-238) disposed in the BLA waste vaults, upholds and increases the total radiotoxicity (not shown in figures). At 1 000 000 years post-closure, the radiotoxicity is still approximately 0.2 % of the radiotoxicity of the initially disposed inventory.

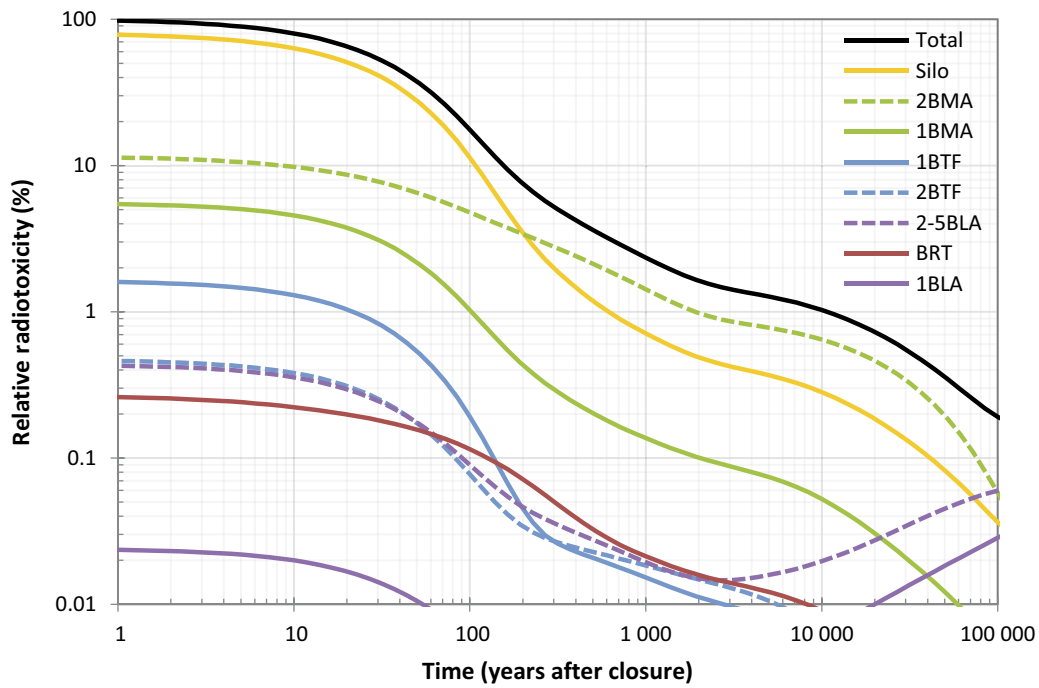


Figure 3-24. Contributions from each waste vault to total radiotoxicity as a function of time.

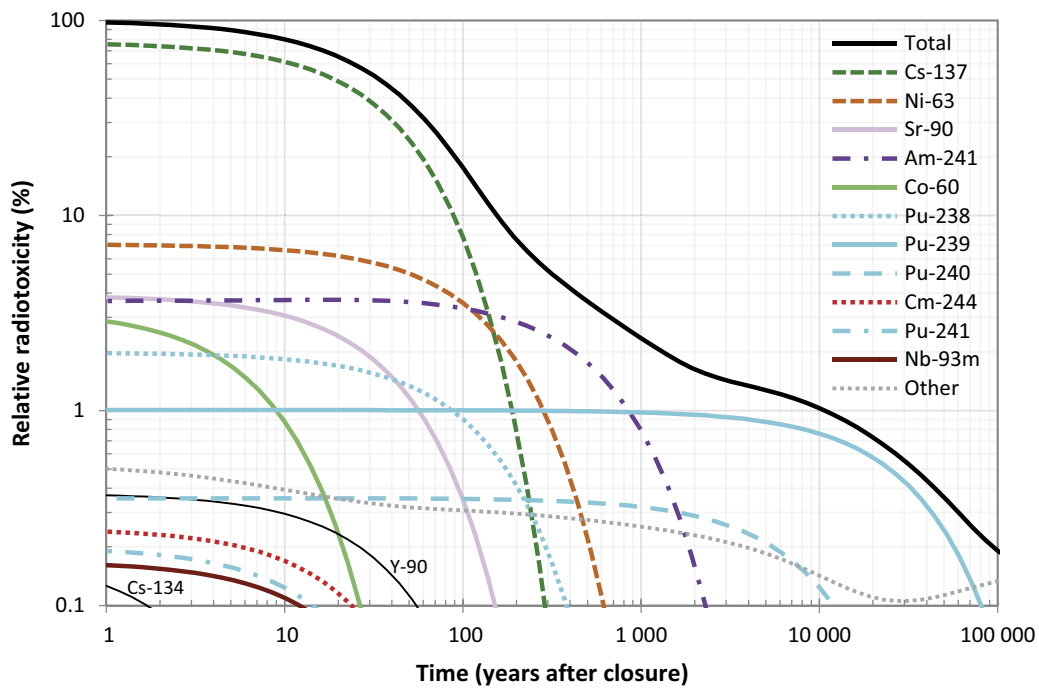


Figure 3-25. Contributions from radionuclides to total radiotoxicity as a function of time. Other (grey dotted line) include contributions from all radionuclides, but not shown here individually. Note that Y-90 is implicitly modelled (assumed to be in secular equilibrium with Sr-90 in the radionuclide transport and dose modelling) and Cs-134 that is not included in the transport and dose modelling (due to short half-life) are illustrated with thin black lines.

4 Model description

4.1 Introduction

This chapter presents the radionuclide transport models that represent the different parts of the repository and its environs, i.e. the near-field, the geosphere and the biosphere, in the PSAR. The models form a chain in which the release of radionuclides from the near-field model constitutes the source of radionuclides to the geosphere model and the release from the geosphere model constitutes the source to the biosphere model. All models are implemented as compartment models (Section 4.1.1). The near-field radionuclide transport models are presented in detail in Åstrand et al. (2022). The geosphere model is presented in detail in SKB (TR-19-06) and the biosphere model is presented in detail in the **Biosphere synthesis report**, Chapter 7. A brief overview of the models is given here. The near-field models and the biosphere model are implemented in the Ecolego (version 6.5) compartment modelling software (**Model tools report**). The geosphere compartment model is implemented in Matlab (**Model tools report**).

4.1.1 The compartment modelling approach

Compartment models are used in this safety assessment to simulate the transport of radionuclides from the waste packages, through the engineered barriers and the geosphere, and to the surface system/biosphere. This approach assumes that the system can be adequately represented by discretisation into a limited number of compartments, each of which is internally homogeneous (each compartment is assigned uniform transport properties) and connected to other compartments. However, the number and size of the compartments, and the connectivity between them, must be chosen so that the representation is suitable for the assessment context (optimised such that the representation is sufficiently detailed while remaining computationally feasible).

The partitioning of the system into model compartments often, but not always, coincides with physical entities in the real system, e.g. a waste form, a barrier or a sediment layer. A physical region with homogenous radionuclide concentration can often be adequately represented by one single model compartment. However, if the concentration of radionuclides within one region cannot be assumed to be homogenous, then that region is represented using several compartments. The latter approach is particularly applicable to the concrete and bentonite walls in the repository (Section 4.2, Åstrand et al. 2022), which are usually represented by five compartments. This number of compartments has been considered a reasonable compromise between accuracy and computing time (Åstrand et al. 2022). The geosphere is, likewise, represented by a large number of compartments (see Section 4.3), and the deepest two of the six regolith layers in the biosphere models are divided into five sub-compartments each (Section 4.4).

4.2 Near-field transport models

For radionuclide transport modelling, one separate model has been developed for each of the 11 waste vaults in SFR1 and SFR3 (shown in Figure 1-1). The level of detail used in the models varies for the waste vaults depending on the character of their barriers and their expected relative importance to the overall system performance. The vault models have been developed to take into account the main retaining properties of the barriers in the vault but, depending on the vault, some retaining abilities are neglected. For example, sorption is not considered in the 1-5BLA vault models, despite the presence of significant amounts of cement and other sorbents.

To limit radionuclide releases from the repository, different barriers have been designed. The vaults that will contain the highest activity will have engineered barriers with highest retention capabilities, whereas vaults containing very little activity will be enclosed only by the vault plugs, the natural barrier of the surrounding rock and the subsea siting.

The engineered concrete barriers (all non-BLA vaults) and bentonite barriers (only the silo) limit the release of radionuclides from the near-field by reducing the groundwater flow through the waste and by providing sorption capacity for many radionuclides. The macadam backfill (non-BLA vaults) provides only minor sorption and negligible flow resistance. These barriers are explicitly represented in the radionuclide transport models.

The access tunnels and plugs are also important for post-closure safety. However, they are not explicitly represented in the radionuclide transport models. Instead, their impact on radionuclide transport is considered through their effect on groundwater flow because plug flow resistance affects water flow in the vaults.

Calculations of water flow in the near-field have been performed for the geometry depicted in Figure 4-1. The calculated flow of water through the barriers and waste is used as input to the radionuclide transport models.

4.2.1 Control volumes and compartments

In the near-field flow modelling, the vaults are divided into control volumes (Abarca et al. 2013, 2020), i.e. model-specific entities that allow evaluation of the annual vault-water balance, including calculation of (directional) annual water flow through bounding surfaces (faces). Annual water flow is assigned to the faces of the control volumes such that the flow is balanced for each control volume. The control volumes and their faces are mapped to compartments or to groups of compartments in the radionuclide transport model as described in Åstrand et al. (2022). Hence, control volumes are used to facilitate transfer of results from the hydrological models to the radionuclide transport models.

Dimensions SFR 1 model:

X : 370 m [6255, 6625]
Y : 485 m [9850, 10335]
Z : 205 m [-25, -230]

Dimensions SFR 3 model:

X : 400 m [6490, 6890]
Y : 500 m [9690, 10190]
Z : 205 m [-25, -230]

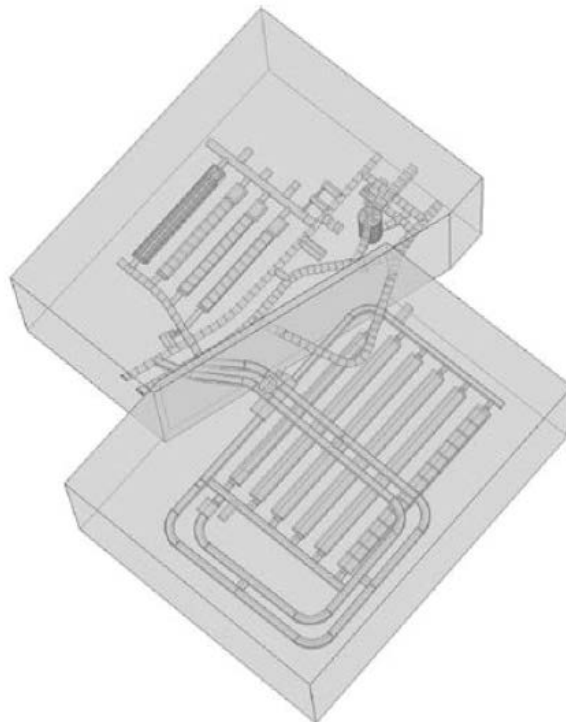


Figure 4-1. The geometry of SFR 1 (on the upper left) and SFR 3 (on the lower right) as defined in the hydrological model (Abarca et al. 2020). Note that the SFR1 and SFR3 water flows are calculated in two separate models.

4.2.2 Processes handled in the near-field model

A large number of physical and chemical processes have been identified and analysed in the near-field of SFR (see the **Waste process report** and the **Barrier process report**). However, only a few of these processes have a significant impact on radionuclide transport and these are summarised below.

Radioactive decay and in-growth

Radioactive decay and in-growth are well-understood physical processes with accurate mathematical descriptions. These processes are explicitly modelled as decay and in-growth rates that are proportional to the inventory of the corresponding radionuclide (or its parent) at a given time and parameterised using decay constants and branching ratios (Equation 4-1).

Speciation

Speciation of radionuclides is implicitly included in near-field models as pre-calculated, time-dependent sorption coefficients and diffusivities. These coefficients are determined for each vault based on chemical and physical conditions that will change with time, as external and internal processes drive the evolution of the near-field chemical conditions.

Advection

Advection is explicitly included in the radionuclide transport modelling (Equation 4-3). The groundwater flow rates between control volumes obtained from near-field hydrological model simulations are used to calculate advective transport of radionuclides in solution. The possible future occurrence of larger cracks in the concrete barriers is also addressed by modelling the impact of advective transfer directly through the cracks without crediting the sorption potential of crack surfaces (Appendix B).

Diffusion

Diffusion is explicitly included in the radionuclide transport modelling (Equation 4-4). The radionuclide transport calculation takes into account the material-specific effective diffusivities of radionuclides, as well as the porosities and compartmental geometries (diffusion lengths and cross section areas) of the waste packages and barriers. The effective diffusivities increase over time to reflect a gradual degradation of the concrete barriers. Diffusive resistance is, pessimistically, neglected for waste matrices. This is particularly important for bitumen-solidified wastes which can be assumed to have a large diffusive resistance initially. Diffusion from the near-field into the surrounding bedrock is accounted for in the silo model but not in the other vault models, because transport from the near-field to the geosphere is dominated by advection due to the highly conductive backfill in those vaults.

Dispersion

Dispersion, as discussed here, refers to dispersive effects caused by the pore- and crack-structure of the barrier materials. In contrast to diffusion, dispersion is not represented explicitly in the model. However, the representation of transport through a compartment model of, e.g., a concrete wall, gives rise to a certain degree of numerical dispersion. The numerical dispersion is on the same order of magnitude as the expected physical dispersion, and thus justifies the omission of an explicit dispersion term in the model equations (see Åstrand et al. 2022, for further details).

Sorption

Sorption on an immobile solid phase has a retarding effect on transport of many radionuclides. Sorption is here used to describe the combined effect of all processes resulting in attachment of dissolved species to solid surfaces, including adsorption, absorption and ion-exchange. Sorption on near-field materials, mainly cement but also bentonite in the silo and crushed rock, is explicitly included in the radionuclide transport modelling using a linear approach, based on sorption coefficients (K_d values) specific to the chemical species (**Data report**, Chapter 7). K_d is also dependent on the chemical conditions which vary over time, as well as on the solid-material properties which vary in time for cementitious materials but

not for bentonite and crushed rock. Relevant parameters include redox potential, pH (which relates to changes in the cement mineralogical properties, represented with four different degradation states, see Section 5.3.1), complexing agent concentrations (see below) and chemical speciation of the radionuclides.

Complexation

Organic complexing agents present in the repository tend to associate with cationic radionuclides, forming soluble coordination complexes (**Post-closure safety report**, Section 6.2.8). This decreases the effective sorption coefficient of these radionuclides. Hence, due to the presence of complexing agents in the repository, the K_d values of several radionuclides are divided by a unitless sorption reduction factor (SRF) before application in the transport calculations (Equation 4-2). The SRF is a dynamic parameter that changes over time, as it is dependent on the concentrations of complexing agents that change due to cellulose degradation and outflow of soluble complexing agents. An SRF value of unity corresponds to fully intact sorption, unaffected by complexing agents.

Corrosion-controlled radionuclide release

Some wastes contain radionuclides produced because of neutron activation. In particular, the steel from the reactor pressure vessels in 1BRT becomes significantly neutron-activated during the operation of the reactor⁷. These radionuclides are assumed to be released congruently with the corrosion products as the steel corrodes. The corrosion rate of the steel in the reactor pressure vessels changes with time, depending on the evolution of pH and redox conditions in the vault. This process is explicitly included in the 1BRT transport model as described in Equation 4-10 and 4-11. For other vaults, the induced activity is assumed to be instantly available for transport upon repository closure.

4.2.3 Modelling of transport through cracked concrete

Advective transport through concrete barriers is modelled in two ways, either as transport through a homogenous porous medium or a cracked medium (possible future cracking of the concrete barriers is described in the **Post-closure safety report**, Chapter 6). The latter approach applies for cases when degradation has caused cracks in the concrete, and the water flow can be expected to be localised to a few larger cracks.

For the radionuclides transported by advection in cracks, the sorbing surface will be smaller (per unit water volume) in the case of a few larger cracks than for many smaller cracks. This will limit the validity of a homogenous representation in the model and when the crack is sufficiently large sorption is neglected in the modelling. An analysis of the conditions under which modelling of the concrete barriers as homogenous media is valid can be found in Appendix B. The conclusion drawn there is that it is appropriate to model intact and moderately degraded concrete as homogenous media whereas severely and completely degraded concrete (defined in Section 5.3.1) should be modelled as cracked media. This approach is also applied in the present safety assessment.

4.2.4 Mathematical model description

Activity transport equation

The state of a compartment, i.e. the radionuclide inventory at a given time, depends on local processes such as radioactive decay and in-growth, as well as exchange processes (e.g. advective and diffusive transport) between compartments. The concepts “transfer” and “transfer coefficient” are used here to describe the exchange processes between compartments, and are defined as:

Transfer N_{jk}^i (Bq a^{-1}): The transfer rate of radionuclide i from compartment j to compartment k .

⁷ During the operational lifetime of the reactors, the surface of the vessels is also contaminated by radionuclides present in the reactor water. This surface contamination is assumed to dissolve in the surrounding pore water immediately after closure of the repository.

Transfer coefficient μ_{jk}^i (a^{-1}): The rate coefficient, i.e., the factor of proportionality between the transfer N_{jk}^i and the radionuclide inventory \mathbb{A}_j^i in source compartment j . The transfer coefficient can be applied for transfers depending linearly on the inventory of the source compartment, $N_{jk}^i = \mu_{jk}^i \mathbb{A}_j^i$. The linear model is applied for all transfer processes considered in this report (advection, diffusion and corrosion-controlled radionuclide release), see also Section 4.2.2.

The rate of change of a compartment's inventory can be described by the following equation⁸.

$$\frac{d}{dt} \mathbb{A}_j^i = \sum_{k \in n_j} \left(\overbrace{\mu_{kj}^i \mathbb{A}_k^i}^{N_{kj}^i} - \overbrace{\mu_{jk}^i \mathbb{A}_j^i}^{N_{jk}^i} \right) + \sum_{p \in P_i} \lambda^i B r_p^i \mathbb{A}_j^p - \lambda^i \mathbb{A}_j^i + r_j^i \quad \text{Equation 4-1}$$

where:

\mathbb{A}_j^i = inventory of radionuclide i in compartment j , (Bq),

n_j = set of indices of transfers connected to compartment j , (-),

N_{jk}^i = transfer rate of radionuclide i from compartment j to k , (Bq a^{-1}),

μ_{jk}^i = transfer coefficient of radionuclide i from compartment j to k , (a^{-1}),

P_i = set of indices of parents of radionuclide i , (-),

λ^i = decay rate of radionuclide i (a^{-1}),

$B r_p^i$ = branching ratio from parent radionuclide p to radionuclide i , (-),

r_j^i = sink/source term (representing external connections) for radionuclide i in compartment j , (-).

Capacity

The sorption of radionuclides is dependent on several physical and chemical processes described in the process reports for the PSAR (**Waste process report** and **Barrier process report**). These processes are represented by a simplified linear model for the partitioning of radionuclides dissolved in the water and sorbed to the matrix of the porous medium. In this model, the sorption coefficient, K_d , is defined as the ratio of the quantity of the radionuclide sorbed per unit mass of porous medium to the amount remaining in solution at equilibrium.

The concept of capacity (m^3) has been used in this work to condense the mathematical expressions used in the models and report. The capacity can be interpreted as a fictive volume consisting of the pore volume plus the effective volume of sorption sites. Hence, the pore-water concentration of a radionuclide in a compartment is obtained by dividing the total amount of the radionuclides in the compartment with the capacity of the compartment.

The capacity (m^3) of a compartment j to store radionuclide i is defined as:

$$\text{Cap}_j^i = V_j \left(\phi + (1 - \phi) f_m \rho_c \frac{K_d^i}{\text{SRF}_j^i} \right) \quad \text{Equation 4-2}$$

where:

V_j = volume of the compartment j (m^3),

ϕ = porosity of the medium in the compartment (-),

f_m = mass fraction of the sorbent medium in the solid medium in the compartment (-),

ρ_c = particle density of the (total) solid medium in the compartment (kg m^{-3}),

K_d^i = sorption coefficient for radionuclide i in the sorbent medium ($\text{m}^3 \text{kg}^{-1}$),

SRF_j^i = sorption reduction factor due to complexing agents for radionuclide i in compartment j (-).

The mass fraction f_m is smaller than unity for concrete and sand/bentonite mix, and $f_m = 1$ for bentonite and macadam.

⁸ Note that the radionuclide inventory is expressed in (Bq) in Equation 4-1. This affects the form of the in-growth term. Considering that the in-growth expressed in number of nuclei per time unit of the decay product is given by $\frac{d}{dt} M^i = B r_p^i \lambda^p M^p$ (where M denotes the number of atoms), and by definition $\mathbb{A} \equiv \lambda M$, the time derivative of the radionuclide inventory is given by $\frac{d}{dt} \mathbb{A}^i \equiv \lambda^i \frac{d}{dt} M^i = \lambda^i B r_p^i \lambda^p M^p \equiv \lambda^i B r_p^i \mathbb{A}^p$.

Advection

The advective transfer coefficient between compartments is expressed as:

$$\mu_{adv,jk}^i = \frac{Q_{jk}}{Cap_j^i} \quad \text{Equation 4-3}$$

where:

- $\mu_{adv,jk}^i$ = advective transfer coefficient for radionuclide i from compartment j to k (a^{-1}),
- Q_{jk} = water flow from compartment j to compartment k ($m^3 a^{-1}$),
- Cap_j^i = capacity of compartment j to store radionuclide i (m^3).

The model is implemented with advective transfer in or out over selected compartment surfaces. At a given point in time, only a unidirectional advective transfer over a surface is considered. This arrangement makes it possible to consider changes in the direction of water flow over time.

Diffusion

The total diffusive transfer between compartments is expressed as a combination of a forward and a backward diffusive transfer, each in the form expressed in Equation 4-4.

$$\mu_{diff,jk}^i = \frac{1}{0.5(R_j + R_k)Cap_j^i} \quad \text{Equation 4-4}$$

where:

- $\mu_{diff,jk}^i$ = diffusive transfer coefficient for radionuclide i from compartment j to k (a^{-1}),
- R_j = diffusive resistance in the direction of diffusion in compartment j ($a m^{-3}$),
- Cap_j^i = capacity of compartment j to store radionuclide i (m^3).

Diffusive resistance in a particular direction of a compartment is defined as:

$$R_j = \frac{L_j}{A_j D_e} \quad \text{Equation 4-5}$$

where:

- L_j = length of compartment in the direction of diffusion in compartment j (m),
- A_j = diffusion area i.e. cross-sectional area of compartment j perpendicular to the direction of diffusion (m^2),
- D_e = effective diffusivity in the porous medium in the compartment ($m^2 a^{-1}$).

Note that R_j refers to the diffusive resistance of the full length of the compartment. The transport between two adjacent compartments experience on average half of the diffusive resistance of each of the compartments, hence the factor 0.5 in the denominator in Equation 4-4.

The diffusive net transfer rate $N_{diff,jk}^{i,net}$ ($Bq a^{-1}$) from compartment j to k is driven by the difference in concentration of a particular radionuclide between the compartments:

$$N_{diff,jk}^{i,net} = \frac{1}{0.5(R_j + R_k)} \left(\frac{A_j^i}{Cap_j^i} - \frac{A_k^i}{Cap_k^i} \right) \quad \text{Equation 4-6}$$

A model compartment in a near-field model can represent multiple physical waste packages in the repository. The concept used here is similar to parallel coupling of equal resistances in electronic circuits. In this case the expression for the diffusive resistance of the model compartment becomes:

$$R_j = \frac{L_j}{nA_j D_e} \quad \text{Equation 4-7}$$

where:

- n = actual number of waste packages represented by the model compartment,
- A = surface area of one waste package.

Diffusion into bedrock

The diffusive transport of radionuclides from the silo bentonite into the bedrock occurring at the interface of these distinct compartments is represented by the equivalent water flow, Q_{eq} (Neretnieks et al. 1987). For other vaults in SFR, diffusion to bedrock is not considered, because transport from the near-field to the geosphere is dominated by advection due to the highly conductive backfill in those vaults.

The Q_{eq} flow transports dissolved radionuclides, with concentrations equal to the concentrations in the compartment releasing radionuclides to the bedrock. The value of Q_{eq} ($m^3 a^{-1}$) depends on the size of the contact area, the Darcy velocity of water in the adjacent bedrock, the flow porosity in the bedrock and the diffusivity as follows:

$$Q_{eq} = A_w \varepsilon_{rock} \sqrt{\frac{4D_w}{\pi t_{res}}} \quad \text{Equation 4-8}$$

where:

A_w = area of interface between bentonite and rock (m^2),

ε_{rock} = flow porosity in rock (-),

D_w = diffusivity of radionuclides in water ($m^2 a^{-1}$),

t_{res} = residence time of the water in contact with the bentonite (a).

where:

$$t_{res} = \frac{\varepsilon_{rock} L}{q} \quad \text{Equation 4-9}$$

where:

L = distance over which flowing water in the rock is in contact with the bentonite (m),

q = Darcy velocity of water in the rock ($m a^{-1}$).

Corrosion-controlled radionuclide release

Radiation-induced radionuclides in the steel in the reactor pressure vessels are released congruently with corrosion products as the metal corrodes. This is modelled as a yearly release of radionuclides from steel to grout, with a rate corresponding to the amount of radionuclides in a thin layer of the steel corroding each year. The transfer is modelled with the following expressions:

$$\mu_{corr} = \begin{cases} \frac{1}{\max(1, t_{corr1} - t)} & ; t < t_0, \text{ alkaline} \\ \frac{1}{\max(1, t_{corr2} + (1 - \frac{t_{corr2}}{t_{corr1}}) t_0 - t)} & ; t \geq t_0, \text{ near-neutral} \end{cases} \quad \text{Equation 4-10}$$

$$\begin{cases} t_{corr1} = \frac{d_{steel}}{2k_{corr1}} & ; \text{ alkaline conditions} \\ t_{corr2} = \frac{d_{steel}}{2k_{corr2}} & ; \text{ near-neutral conditions} \end{cases} \quad \text{Equation 4-11}$$

where:

μ_{corr} = transfer coefficient for corrosion (a^{-1}),

d_{steel} = steel thickness (m),

k_{corr1} = corrosion rate for alkaline conditions ($m a^{-1}$),

k_{corr2} = corrosion rate for non-alkaline conditions ($m a^{-1}$),

t_0 = time when conditions change from alkaline to near-neutral (a),

t_{corr1} = time for complete corrosion of a steel piece under alkaline conditions (a),

t_{corr2} = time for complete corrosion of a steel piece under near-neutral conditions (a).

Note that the corrosion rate increases significantly under non-alkaline (near-neutral) conditions (**Data report**, Chapter 5). When the reactor pressure vessel is fully corroded, the denominator in Equation 4-10 is set to 1. This is done to prevent errors in the calculation resulting from division by zero or negative transfer coefficients.

The steel from the reactor pressure vessels is assumed to corrode from both sides, hence the division by two in Equation 4-11. Furthermore, the activation of the steel is assumed to be homogenous. The transfer coefficient increases over time (Equation 4-10). At the same time the thickness of the steel decreases due to corrosion. As a result, radionuclides are released in proportion to the corrosion rate of the steel.

4.2.5 Analytical estimates of the residence time based on flow and vault capacity

A coarse estimate of the release of radionuclides from the vaults can be done with analytical estimates. The approach is shortly summarised here.

In Appendix E, simplified analytical expressions for the residence time are given for each vault. The expressions are used in Section 5.3 to illustrate how time-dependent barrier properties, such as effective diffusivity, impact the performance of the different vaults.

The residence time, T_{res} (a), of a radionuclide in a vault is a quantity that gives an estimate of the time until the majority (approximately 60 %) of its activity has been released from the vault. A long residence time ensures that the annual release is only a small fraction of the initial inventory, such that the release is diluted over time. This section introduces an approximative way of estimating the residence time where many simplifications compared to the RNT model used to calculate the release from the vaults are made. A more detailed description of how to calculate the residence time is given in Appendix E. The residence time is commonly defined as the total inventory A_{vault} (Bq) in the vault divided by the annual release N_{vault} (Bq a⁻¹) obtained from transport modelling, assuming no decay, using a steady-state solution of the radionuclide transport model for the vault:

$$T_{\text{res}}^{\text{transp}} = \frac{A_{\text{vault}}}{N_{\text{vault}}} \quad \text{Equation 4-12}$$

An alternative estimate of the residence time not based on explicit transport modelling (but still on hydrological modelling), in terms of water flow rates and diffusive resistance is given by:

$$T_{\text{res}}^{\text{Cap}} = \frac{Cap_{\text{vault}}}{Q_{\text{tot}}} \quad \text{Equation 4-13}$$

Where Cap_{vault} (m³) is the capacity of the vault and Q_{tot} (m³ a⁻¹) is the total effective volume flow rate, i.e. the sum of the diffusive and advective volumetric flow rate through the barriers:

$$Q_{\text{tot}} = Q_{\text{diffusive}} + Q_{\text{advective}} = \frac{1}{R_{\text{barrier}}} + Q_{\text{waste}} \quad \text{Equation 4-14}$$

The advective water flow rate through the barriers $Q_{\text{advective}}$ (m³ a⁻¹) is approximated by the flow through the waste, Q_{waste} , based on hydrogeological simulations given in Abarca et al. (2020).

The diffusive flow rate, $Q_{\text{diffusive}}$, is calculated from the transport resistance of a vault, R_{barrier} , by considering the vault subdivided into different paths through different parts. The division is made so that the geometry of each part is simple enough to enable its diffusive resistance to be calculated, see Equation 4-5. Each part can be a model compartment but any sub-volume with sufficiently simple shape can be used.

The radionuclides can be considered to migrate through each path in parallel and for, a specific path, the radionuclides diffuse sequentially through different segments, e.g. the waste package, inner barrier and outer barrier, see Equation E-4 and Equation E-5.

The capacity of a vault, Cap_{vault} , is given by the summed capacities of the different parts of the vault, see Equation 4-2. However, since only a fraction of the water flowing through the macadam/crushed rock backfill also flows through the waste, the capacity of the backfill is omitted when summing over capacities.

4.3 Geosphere transport model

Radionuclide transport in the geosphere is modelled with FARFCOMP, a tool developed and used within the safety evaluation SE-SFL (SKB TR-19-01). Like the near-field model, the implemented radionuclide transport model is a compartment model. The calculation code is written in Matlab and based on the geosphere model used in the SR-PSU (SKB TR-14-09). A detailed description of FARFCOMP is provided in SKB (TR-19-06, Appendix B), while an overview of the main features of the model is presented here.

In general, the geosphere model relies on the dual-porosity concept and reflects transport of radionuclides in discrete parallel fractures situated in a porous rock matrix. In the dual-porosity approach, the rock is divided into two distinct domains with different types of porosity: 1) fractures with flowing water and 2) rock matrix with porosity accessible only by diffusion. The approach furthermore assumes that the properties of the two porosity domains are averaged and that transfer between the two domains is averaged (Elert et al. 2004). Figure 4-2 illustrates the conceptual parallel fracture-matrix system.

The geosphere model incorporates a compartmental representation of the fracture-matrix system to approximate the solution to the same dual-porosity problem previously obtained by the semi-analytical Fortran code FARF31 (Norman and Kjellbert 1990). The model solves radionuclide transport in one single discrete fracture with constant properties. The required flow-related input data are the total advective travel time t_w (a) of a water particle passing through the fracture network and the transport resistance, F (a m^{-1}), along the full fracture length. The flow-related input data are based on calculations using a particle-tracking algorithm in Darcy Tools (Öhman and Odén 2018). Further details of the parametrisation of the model are discussed in Section 5.5.

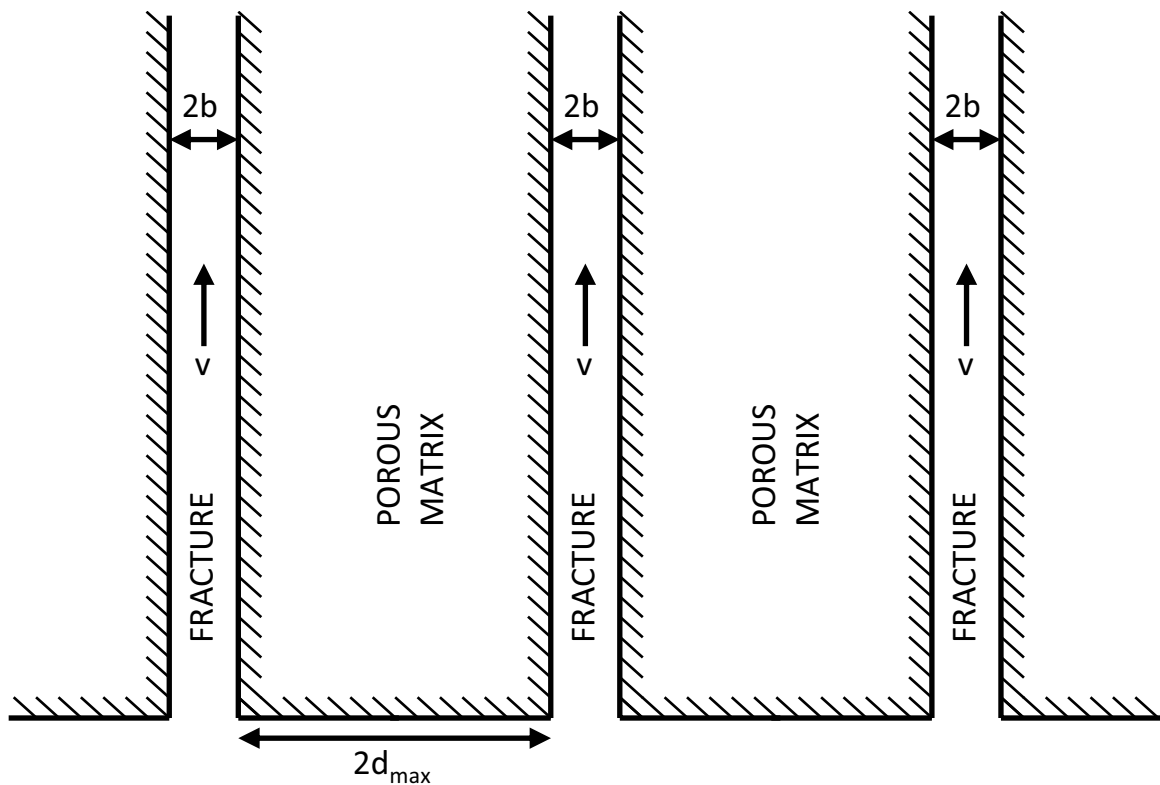


Figure 4-2. Conceptual parallel-fracture-matrix system used in the geosphere model. After Tang et al. (1981). For each fracture ($i-k$) the groundwater velocity v (m a^{-1}), and the fracture aperture $2 \times b$ (m) are constant. Two times the maximum penetration depth ($2 \times d_{\max}$, m) corresponds to the distance between fractures.

4.3.1 Processes handled in the geosphere model

All the physical and chemical processes identified in the geosphere are discussed in the **Geosphere process report**. However, only a few of them are relevant for radionuclide transport modelling in the geosphere and are described here:

Radioactive decay and ingrowth

Radioactive decay and ingrowth are included in the same way as described for the near-field models (Section 4.2.2).

Advection

Advection is explicitly included in the geosphere model (Equation 4-15). The regional hydrogeological simulations are described in Öhman and Odén (2018). The groundwater flow data used in the radionuclide transport calculations are based on the results of these simulations, see further Section 5.5.

Dispersion

In the geosphere model, longitudinal hydrodynamic dispersion along the individual trajectories is explicitly modelled (see Equation 4-15) by means of the constant Péclet number that quantifies the ratio between advective and dispersive transport. The transverse dispersion is neglected.

Rock-matrix diffusion

The rock matrix is porous, and radionuclides can enter the stagnant water in the pores of the rock matrix by diffusion and thereby be retarded by sorption on the pore surfaces. The exchange between the flowing water in the fracture compartment and the adjacent rock matrix is included in the geosphere model. Fickian diffusion is assumed in the rock matrix, where a finite penetration depth is considered (see Appendix A).

Sorption

Radionuclides are retarded by sorption onto the internal surfaces of the rock matrix. Sorption in the rock matrix is accounted for and is parametrised by the linear sorption coefficient, K_d . However, sorption on the fracture surface, or possible fracture fill, is pessimistically omitted.

4.3.2 Conceptual model and mathematical model description

The modelled physical fracture-matrix system is illustrated in Figure 4-2. A constant groundwater velocity is applied to each fracture. The transport processes in such a system can be described by the following two coupled, one-dimensional governing equations, one for the fracture (Equation 4-15) and one for the porous matrix (Equation 4-16). The coupling is provided by the continuity of concentrations along the interface (C^i).

$$\frac{\partial C_f^i}{\partial t} = -v \frac{\partial C_f^i}{\partial z} + D_L \frac{\partial^2 C_f^i}{\partial z^2} - \lambda^i C_f^i + \sum_{p \in P_i} \lambda^n C_f^p B r_p^i + \frac{D_e^i}{b} \frac{\partial C_m^i}{\partial x} \Big|_{x=0} \quad \text{Equation 4-15}$$

$$R_m^i \frac{\partial C_m^i}{\partial t} = D_e^i \frac{\partial^2 C_m^i}{\partial x^2} - R_m^i \lambda^n C_m^i + \sum_{p \in P_i} R_m^p \lambda^i C_m^p B r_p^i \quad \text{Equation 4-16}$$

In the above equations:

C_f^i = Activity concentration of radionuclide i in the flowing water of the fracture (Bq m^{-3}),
 C_m^i = Pore-water activity concentration of radionuclide i in the matrix adjacent to the fracture (Bq m^{-3}).

t = Time (a).

v = Mean water velocity in water-bearing fracture (m a^{-1}).

z = Distance in the flow direction (m).

D_L = Longitudinal dispersion coefficient ($\text{m}^2 \text{a}^{-1}$).

b = Half-aperture of the fracture (m).

D_e^i = Effective diffusivity of radionuclide i in the rock matrix ($\text{m}^2 \text{a}^{-1}$).

x = Distance into the rock matrix (m).

λ^n = Decay rate for radionuclide n (a^{-1}).

P_i = Set of indices of parents of radionuclide i (-).

Br_p^i = Branching ratio from parent radionuclide p to radionuclide i (-).

R_m^i = Capacity factor for radionuclide i in rock matrix (-), defined as:

$$R_m^i = \varepsilon_m + K_{d,m}^i \rho_m \quad \text{Equation 4-17}$$

where:

ε_m = Porosity of the rock matrix (-).

$K_{d,m}^i$ = Sorption coefficient in rock matrix for radionuclide i ($\text{m}^3 \text{kg}^{-1}$).

ρ_m = Bulk density of the rock matrix (kg m^{-3}).

The initial conditions are:

$$C_f^i \Big|_{t=0} = 0 \quad \text{Equation 4-18}$$

$$C_m^i \Big|_{t=0} = 0 \quad \text{Equation 4-19}$$

The boundary conditions are given by:

$$C_f^i \Big|_{z \rightarrow \infty} = 0 \quad \text{Equation 4-20}$$

$$Q_{\text{tube}} \left(C_f^i - \frac{D_L}{v} \frac{\partial C_f^i}{\partial z} \right) \Big|_{z=0} = F_{\text{in}}^i \quad \text{Equation 4-21}$$

$$C_m^i \Big|_{x=0} = C_f^i \quad \text{Equation 4-22}$$

$$\frac{\partial C_m^i}{\partial x} \Big|_{x=d_{\text{max}}} = 0 \quad \text{Equation 4-23}$$

Q_{tube} = Volume flow of water in the fracture ($\text{m}^3 \text{a}^{-1}$).

F_{in}^i = Inlet activity flow of radionuclide i to fracture (Bq a^{-1}).

d_{max} = Maximum penetration depth into the rock matrix (m).

The desired quantity is the output release F_{out}^i (Bq a^{-1}) for radionuclide i at the end of the fracture z_{tot} (m):

$$F_{\text{out}}^i = Q_{\text{tube}} \left(C_f^i - \frac{D_L}{v} \frac{\partial C_f^i}{\partial z} \right) \Big|_{z=z_{\text{tot}}} \quad \text{Equation 4-24}$$

F_{out}^i = Output release of radionuclide i from the fracture (Bq a^{-1}).

z_{tot} = Total length of the fracture (m).

In the geosphere model, the rock matrix and advective transport paths, i.e., trajectories, are divided into one-dimensional compartments to approximate the solution to the dual-porosity problem. Figure 4-3 and Figure 4-4 show a schematic view of the fracture–matrix system implemented in the geosphere model. Each box represents a compartment, and the arrows represent the flow paths of radionuclides between these compartments. Solid blue arrows represent advective transport, dashed blue arrows represent transport by dispersion, and yellow arrows represent transport by diffusion.

The advective transport path through fractures in the rock is represented by fracture compartments of equal length that have constant properties. For the rock-matrix compartments, on the other hand, the thicknesses increase exponentially from the fracture-matrix interface into the matrix (Figure 4-4) because a higher numerical resolution is required near the rock-matrix-fracture interface, due to the high concentration gradient there. This is done by using a constant factor adjusted so that the total thickness of the rock matrix equals the maximum penetration depth d_{max} (m). The level of discretisation along the trajectories, thickness of the first matrix compartment, maximum penetration depth and the level of discretisation in the porous matrix are input parameters to the geosphere model.

In the geosphere model, transport of radionuclides within and between compartments is described by defining transfer rates (a^{-1}) as described in Section 4.2.4. Details on the derivation of the transfer rates incorporated in the geosphere model are presented in Appendix B of SKB (TR-19-06).

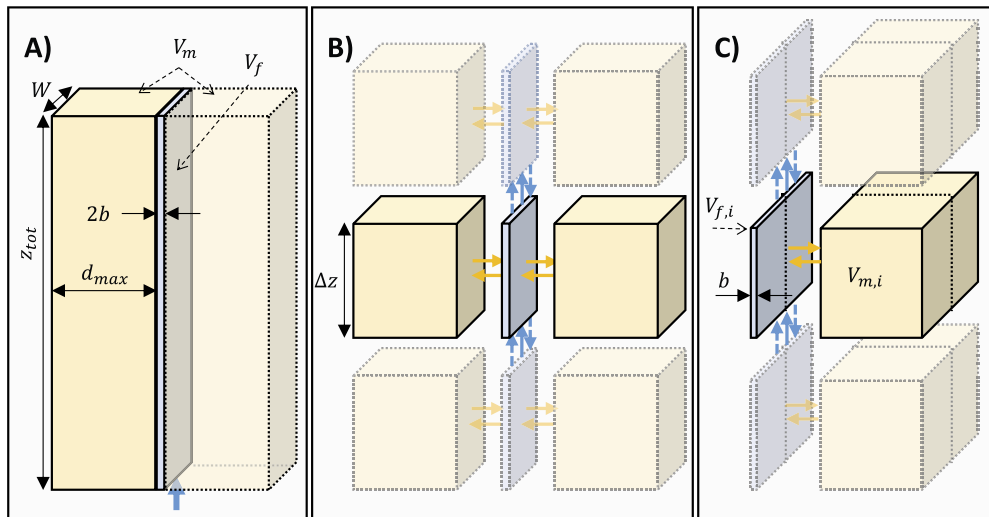


Figure 4-3. Schematic view of the fracture-matrix system implemented in the geosphere model. Discretising the simple volumes in, (A) sections along the fracture, (B) by rearranging the volumes so that only one rock-matrix volume needs to be considered per discretised fracture volume, (C) V_f and V_m , the modelled fracture and porous rock matrix volumes, respectively. z_{tot} is the total length of the fracture and Δz is the length of fracture compartment i . Blue arrows represent advective (solid) and dispersive (dashed) transport along the fracture and yellow arrows represent diffusive transport in the rock matrix. See further details in SKB (TR-19-06).

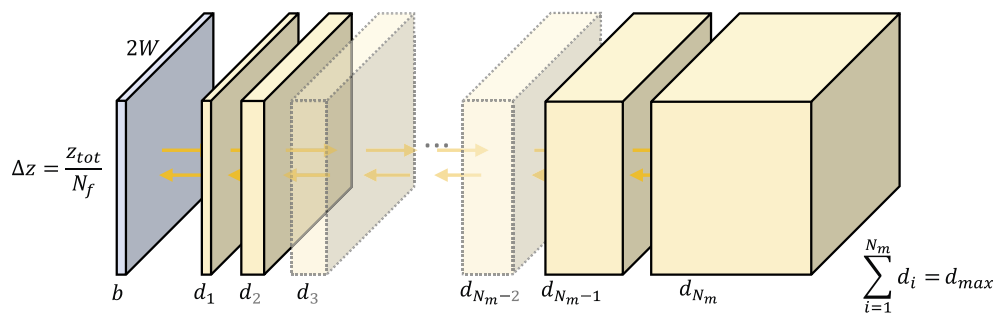


Figure 4-4. Schematic view of the rock-matrix discretisation. d_1 (m) is the depth of the first matrix compartment adjacent to the fracture compartment and N_m is the number of rock-matrix compartments (-) and N_f is the number of compartments in the advective flow path (-).

4.4 Biosphere transport and exposure model

The radionuclide transport in the biosphere is described by the **biosphere transport and exposure model (BioTEx)**. The BioTEx model describes radionuclide transport and accumulation in the near-surface environment and ecosystems and calculates potential doses to humans and dose rates to non-human biota.

Given the requirements of the safety assessment (**Biosphere synthesis report**, Chapter 2), the biosphere model needs to handle relevant FEPs for transport and accumulation of radionuclides and address important exposure pathways so that it is consistent with the descriptions of the site and its development (**Biosphere synthesis report**, Chapters 3–6). Moreover, transport, accumulation and decay (including in-growth of decay products) of radionuclides with different biogeochemical behaviour need to be handled consistently. As SFR is located in a coastal area which is experiencing isostatic rebound and because the evaluation period covers 100 000 years, both aquatic and terrestrial ecosystems need to be represented by the model and capabilities are needed to handle temporal development of the system.

The biosphere model used in the SR-PSU, which was developed from the model used in SR-Site (Avila et al. 2010) has the above-mentioned capabilities. However, as a result of reviews of SR-Site and SR-PSU by SSM (e.g. SSM 2017, 2018, Walke et al. 2017), as well as SKB's own development and research programmes, the BioTEx model was somewhat modified in SE-SFL (SKB TR-19-05). Most of these updates are included in the BioTEx model adopted for the PSAR. For further details on the updates since SR-PSU, see the **Biosphere synthesis report**, Section 7.5.

4.4.1 Biosphere objects

A biosphere object is an area in the modelled landscape that is predicted to receive a substantial portion of the radionuclides following release from the geosphere, i.e. it is the spatial unit for the coupled aquatic-terrestrial ecosystem described in the BioTEx model (Section 4.4.2).

Parameters describing the properties of biosphere objects (and their evolution over time) were derived using extensive site investigations and landscape development modelling (**Biosphere synthesis report**, Chapters 3 and 4). The biosphere objects identified in the SR-PSU (SKB TR-14-06) are also used in the PSAR; these are shown in Figure 4-5. They were identified by mapping simulated flow paths from the repository in hydrogeological simulations to present marine basins and the postulated locations of future lake basins (Odén et al. 2014).

Following the completion of the SR-PSU, new hydrogeological simulations were carried out under temperate conditions to address uncertainties in the bedrock modelling (Öhman and Odén 2018). The simulations consisted of 30 sets of parameterisation variants (referred to as bedrock cases). Results of the modelling study of Öhman and Odén (2018) largely confirmed the pattern of discharge locations reported in the SR-PSU (Odén et al. 2014); for 22 of the 30 bedrock cases, almost all particles released from SFR1, and most particles from SFR3, were discharged into biosphere object 157_2 (**Biosphere synthesis report**, Section 5.1.3)⁹.

The results from the hydrogeological study presented in Öhman and Odén (2018) thus indicated that the objects defined in the SR-PSU are also useful in the PSAR. Furthermore, the results from this study, as well as the results from the hydrogeological modelling conducted for the SR-PSU (Odén et al. 2014), indicated that for most calculation cases, it is sufficient to use biosphere object 157_2 as the primary discharge area for examining the effects of a geosphere release. In the marine period, the surface water in all seven basins (Figure 4-5) will receive radionuclides via advective fluxes of the surface water across the basin boundaries. During the terrestrial period, the two objects downstream of 157_2, i.e. 157_1 and 116, are assumed to receive radionuclides via surface and/or groundwater flow from object 157_2.

⁹ In the remaining eight bedrock cases of Öhman and Odén (2018), an anomalous low probability realisation of the bedrock was used, representative of a large subhorizontal fracture under object 157_2. Radiological consequences of such a fracture are evaluated in the **Biosphere synthesis report**, Section 10.5.

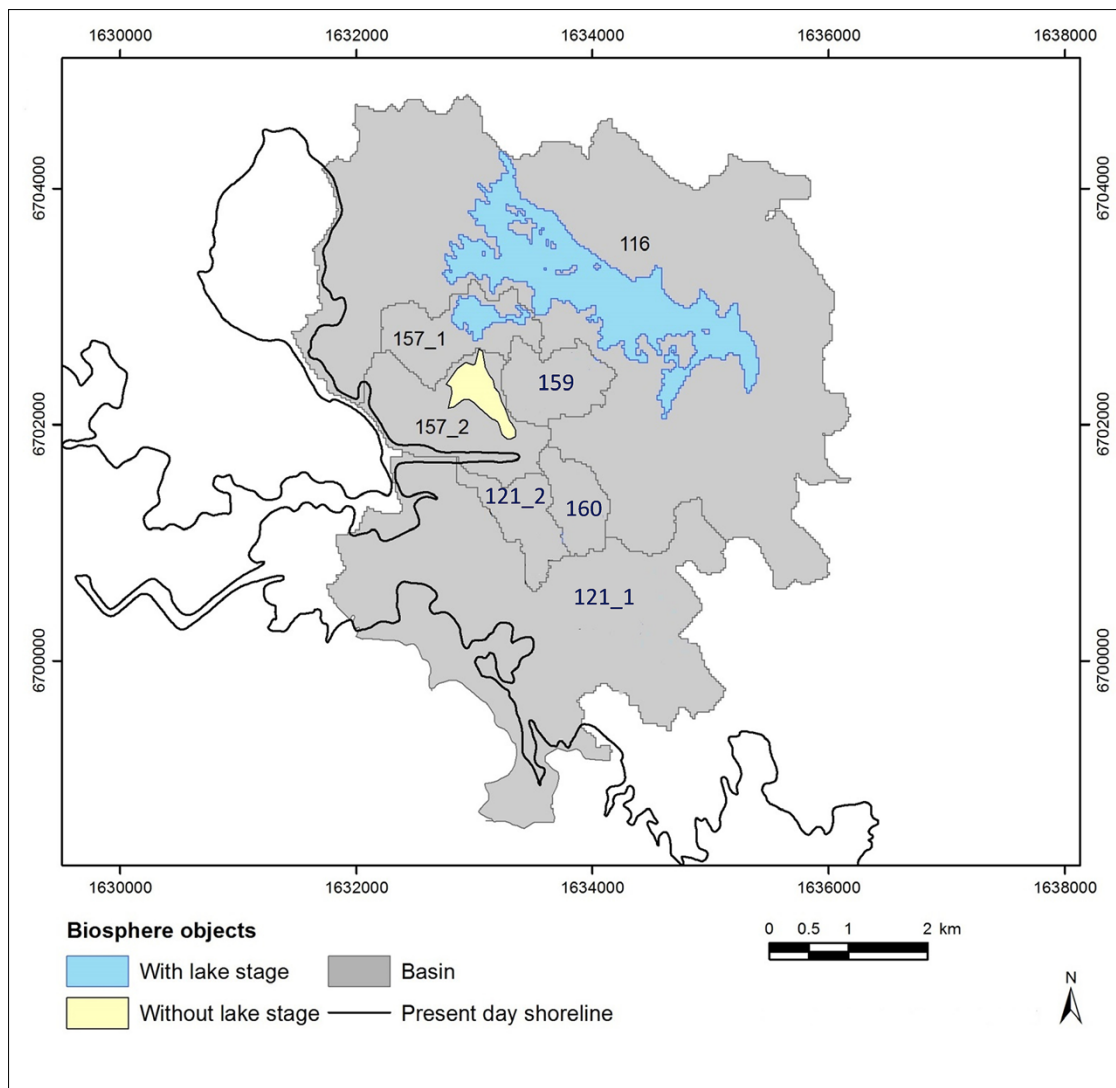


Figure 4-5. Map of biosphere objects. When the area is submerged, the biosphere objects are in their marine stage and all the delineated objects are used simultaneously in order to assess the potential exposure dose from the marine object. However, significant fractions of the geosphere release are only expected to be discharged to basin 157_2 in most calculation cases evaluated in this report. In the terrestrial stage, the biosphere object is defined as the original lake basin (blue) or the mire (yellow).

Under periglacial conditions, it is postulated that only pathway available for groundwater to reach the surface ecosystem will be via so-called “through taliks”. A through talik is defined as an area of unfrozen ground in an otherwise frozen landscape, wherein a hydrogeological connection between the surface and the deep groundwater exists. Through taliks most often occur below lakes where thermal conditions may prevent permafrost development. Given the right conditions, the entire thickness of the permafrost may thaw thus producing a hydraulically conductive regime in the regolith and bedrock which connects the deep groundwater to the surface water of the lake. Results of the hydrological modelling studies conducted for the SR-PSU indicate that object 157_1 and lake 114 could potentially evolve to become through taliks (Bosson et al. 2010, 2013, Odén et al. 2014, Vidstrand et al. 2014a). These objects are therefore considered in the BioTEx modelling under periglacial conditions.

Different types of water wells and well locations are considered. Dug wells are considered as an exposure pathway for agricultural, self-sustained communities existing within in the biosphere objects. Drilled wells, placed outside of the repository footprint, are also considered in the analyses as water pumped from these wells could be contaminated by radionuclides. The likelihood of this water being contaminated by radionuclides is assessed based on the location of these wells relative the location

of a plume of radionuclide contaminated groundwater downstream of the repository. The area covered by this plume, combined with the area of influence of any potential well drilled around the plume, is deemed the *well interaction area* (Werner et al. 2013, Öhman and Vidstrand 2014). The spatial coverage of the well interaction area in the PSAR is the same as in the SR-PSU (Werner et al. 2013).

The probability of drilling a well into the well interaction area is not taken into account. Following the review of the SR-PSU, the method of calculating the dose from the well interaction area is updated to reflect the recommendations of SSM (**Biosphere synthesis report**, Section 7.5.4). In the PSAR, the drilled well is treated as an exposure pathway (with the probability of one) and the dose from this pathway is evaluated considering a small exposed group that uses the water for household needs (the garden-plot household, see Section 4.4.3). The spatial variability of the radionuclide concentration in the well interaction area is accounted for as data uncertainty (**Biosphere synthesis report**, Section 8.2.4). Drilled wells which directly penetrate the repository are addressed in the **FHA report** and are not included in this report.

The identification and development of biosphere objects are described in detail in Chapter 5 of the **Biosphere synthesis report**.

4.4.2 Radionuclide transport model

Discharge of radionuclides into the biosphere is evaluated over thousands of years. The discharge area is considered at the scale of a coastal basin or a lake–mire complex (Section 4.4.1) and the annual dose to future inhabitants is calculated over an adult lifetime of 50 years (Section 2.4.3). At these temporal and spatial scales, it is assumed that most biogeochemical interactions can be approximated by equilibrium or steady-state conditions. Thus, ecosystem states are represented by average conditions and fluxes of water, solid matter and gas are typically described as functions of empirical parameters that capture the combined outcome of the underlying processes.

In the calculation cases, radionuclides released from the repository enter the surface system through deep groundwater discharge and then reach the soil, sediments, water and air. Two main types of ecosystems are simulated, namely aquatic ecosystems (including sea basins, lakes and streams) and terrestrial ecosystems (including mires). The distribution of radionuclides in aquatic ecosystems is represented by six compartments associated with several regolith layers, two compartments associated with the water, and one compartment associated with aquatic primary producers (Figure 4-6, Table 4-1). Correspondingly, the distribution of radionuclides in mire ecosystems is represented by eight compartments associated with several regolith layers and one compartment associated with the mire vegetation (Figure 4-6, Table 4-1). In addition, a garden plot is used to evaluate consequences of irrigation with water from a drilled well in the bedrock and combustion of wood and peat (see further Section 4.4.3).

In the models, radionuclides are released to the deepest regolith layer (RegoLow) of a biosphere object. The dynamic change in the radionuclide content of each compartment is the result of radionuclide fluxes and ingrowth/decay. The fluxes are associated with mass fluxes of water, solids (including organic matter) or gas, together with diffusion and/or with the transformation between inorganic and organic forms (Table 4-2). The processes considered in the model have been checked against the SKB FEP list (SKB R-13-43, Chapter 6) and they are fully described in the **Biosphere synthesis report**, Section 7.3.

The endpoints of the transport calculations are the concentrations of radionuclides in environmental surface media. The identification of potential areas reached by radionuclides (i.e. biosphere objects; Section 4.4.1) is a prerequisite for this modelling. The final step in the biosphere modelling consists of calculating annual doses to humans and dose rates to non-human biota that are exposed to repository derived radionuclides in the environment. The assessment endpoints for humans are further described in Section 4.4.3. As dose rates to non-human biota are not analysed in this report, the endpoints of that analysis are described in the **Biosphere synthesis report**, Section 6.3.

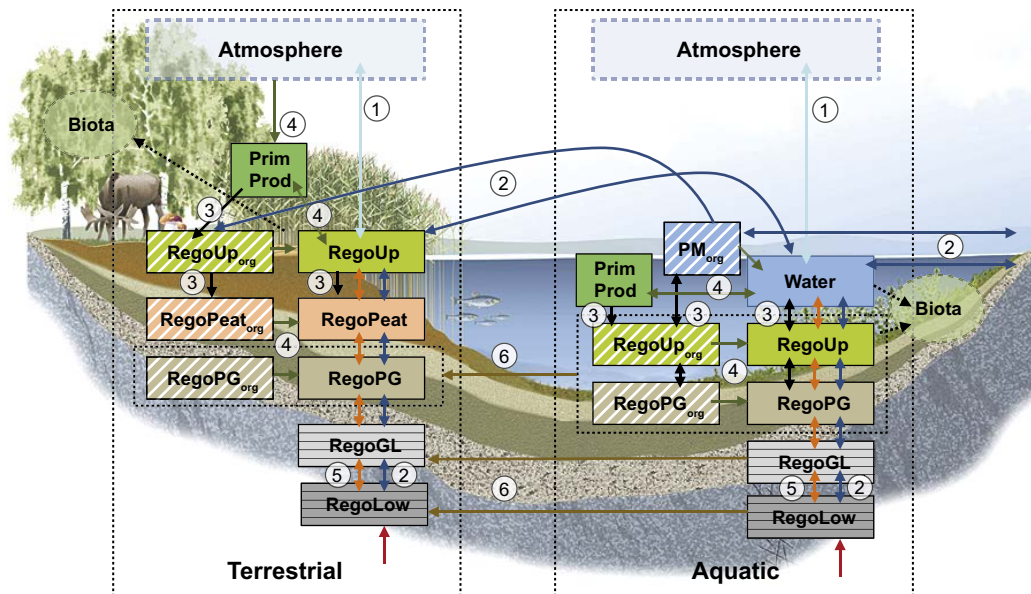


Figure 4-6. Conceptual model corresponding to the BioTEx model used to simulate transport and accumulation in a discharge area with two natural ecosystems (delimited by thin dotted black lines). Each box in the two ecosystems corresponds to a radionuclide inventory associated with a physical or biological compartment. Note that in the PSAR, the two lowermost regolith layers are represented by five compartments each. Arrows represent fluxes of radionuclides between compartments and fluxes into and out of the system. Radionuclide fluxes are linked to mass fluxes of gas (1, light blue), water (2, dark blue) and solid matter (3, black), to transformation between inorganic and organic forms of radionuclides (4, green), to diffusion in soil pore water (5, orange) and to ingrowth of wetland vegetation (6). The red arrow indicates that the geosphere release enters the biosphere via groundwater discharge to the till layer (compartments RegoLow). Dotted boxes (atmosphere and biota) are assumed to be in equilibrium with the corresponding environmental media and the uptake of radionuclides into biota (dotted arrow) is not included in the mass balance of the BioTEx model. Figure from SKB (TR-19-05).

Table 4-1. Summary description of compartments representing radionuclide inventories in the BioTE_x model (see also Figure 4-6).

Ecosystem/Name	Description
Aquatic	
Water	Radionuclides in open water of sea basins, lakes and streams, including radionuclides dissolved in water and adsorbed to particulate matter.
PM _{org} ¹	Radionuclides stored in refractory organic particulate matter suspended in the water column.
PrimProd	Radionuclides stored in aquatic primary producers, including radionuclides in pelagic, microbenthic and macrobenthic primary producers.
RegoUp	Radionuclides in the upper oxic and biologically active layer of aquatic sediments, including radionuclides in pore water and adsorbed on sediment particles.
RegoUp _{org}	Radionuclides incorporated into organic particulate matter in the upper oxic and biologically active layer of aquatic sediments.
RegoPG	Radionuclides in post-glacial aquatic sediments (clay gyttja) below the biologically active layer, including radionuclides in pore water and adsorbed on sediment particles.
RegoPG _{org}	Radionuclides incorporated into organic particulate matter in post-glacial aquatic sediments (clay gyttja) below the biologically active layer.
RegoGL	Radionuclides in glacial clay (typically overlain by post-glacial deposits), including radionuclides in pore water and adsorbed on sediment particles. Note that this layer is vertically discretised and represented by five sub-compartments in the BioTE _x model.
RegoLow	Radionuclides in till (typically overlain by glacial clay), including radionuclides in pore water and adsorbed on sediment particles. Note that this layer is vertically discretised and represented by five sub-compartments in the BioTE _x model.
Mire	
PrimProd	Radionuclides stored in mire vegetation biomass, including both above- and below-ground biomass of bryophytes, vascular plants, dwarf shrubs and trees.
RegoUp	Radionuclides in the upper oxic and biologically active layer of peat (acrotelm peat), including radionuclides in pore water and adsorbed on peat.
RegoUp _{org}	Radionuclides incorporated into organic matter in the upper aerobic and biologically active layer of peat (acrotelm peat).
RegoPeat	Radionuclides in deep, permanently anoxic peat (catotelm peat), including radionuclides in pore water and adsorbed on peat.
RegoPeat _{org}	Radionuclides incorporated into organic matter in the deep, permanently anoxic peat (catotelm peat).
RegoPG	Radionuclides in post-glacial sediments (clay gyttja) overlain by peat, including radionuclides in pore water and adsorbed on sediment particles.
RegoPG _{org}	Radionuclides incorporated into particulate organic matter in post-glacial sediments (clay gyttja) overlain by peat.
RegoGL	Radionuclides in glacial clay buried under peat and typically overlain by post-glacial deposits. Inventory includes radionuclides in pore water and adsorbed on sediment particles. Note that this layer is vertically discretised and represented by five sub-compartments in the BioTE _x model.
RegoLow	Radionuclides in till, buried under peat and typically overlain by glacial clay. Inventory includes radionuclides in pore water and adsorbed on sediment particles. Note that this layer is vertically discretised and represented by five sub-compartments in the BioTE _x model.
Agricultural	
RegoUp	Radionuclides in the upper (ploughed) unsaturated soil layer of cultivated land, including radionuclides in pore water and adsorbed on soil.
RegoUp _{org}	Radionuclides incorporated into organic matter in the upper aerobic and biologically active layer of the soil.

¹ = The PM_{org} compartment is also referred to as Water_{org} in the earlier technical description (Saetre et al. 2013).

Table 4-2. Overview of radionuclide fluxes (processes) included in the BioTE_x model (see Figure 4-6). The processes have been categorised with respect to the underlying mechanism, namely mass flow-flux of solids (MS), water (MW) or gas (MG), diffusion in water (DW) or in gas (DG), or incorporation into or release from organic matter due to photosynthesis (PP) or mineralisation (Min). “Y” indicates that the process is included as a dynamic flux between compartments in the aquatic, mire or agricultural sub-model. * indicates that only the steady-state outcome of the process is taken into account. Superscripts indicate that fluxes can occur between ecosystems (BTW), that the initial inventory in agricultural soil is conditioned on environmental concentrations in natural ecosystems (INIT). Superscripts also specify the system(s) of cultivation; drained mire (DM), infield–outland agriculture (IO) or a garden plot (GP). ** Indicates that the process is restricted to warm climate for DM and IO.

Process	Type	Radionuclide flux		
		Aqua	Mire	Agri
Biological				
Bioturbation	MS	Y		Y ^{DM}
Plant (root) uptake	PP	Y	Y	*
Leaf retention/translocation	PP			Y ^{**}
Litter respiration/release	Min	Y	Y	Y ^{IO}
Litter production	PP	Y	Y	
Regolith Mineralisation	Min	Y	Y	Y
Vegetation ingrowth ^{BTW}	MS	Y	Y	
Water bound				
Advective horizontal ^{BTW}	MW	Y	Y	
Advective vertical	MW	Y	Y	Y
Diffusion (vertical)	DW	Y	Y	
Water uptake	MW			Y ^{DM}
Solid liquid phase dissociation		*	*	*
Sediment dynamics				
Sedimentation	MS	Y		
Resuspension	MS	Y		
Burial	MS	Y	Y	
Gas transport/transition				
Degassing	MG/DG	Y	Y	Y
Gas uptake	MG	Y	Y	
Human behaviour				
Drainage/cultivation ^{BTW, INIT}	MS			Y ^{DM}
Fertilisation ^{BTW}	MS			Y ^{GP, IO}
Irrigation	MW			Y ^{**}
Radiological				
Radionuclide decay/ingrowth		Y	Y	Y

4.4.3 Assessment endpoints for humans

The primary assessment endpoint for humans in the biosphere assessment is the annual dose to a representative individual in the group exposed to the greatest risk (Section 2.4.3). To select an appropriate group, or groups, to address in the analysis, all exposure pathways relevant for the post-closure safety must be identified. These include doses from external exposure (radiation from the ground, air and seawater), inhalation of radionuclides and, most importantly, by ingestion of radionuclides through food and water, depending on the type of ecosystem (Figure 4-7).

A comprehensive pathway analysis for exposure of humans was conducted for the SR-PSU (SKB R-14-02) and this is also valid for the present assessment. The outcome of that analysis was that 22 exposure route cases were identified as important for post-closure safety and that they could be covered in the dose calculations by establishing four potentially exposed groups (PEGs). These groups are briefly summarised below and are considered credible to use as bounding cases for a representative individual in the group exposed to the greatest risk, with respect to exposure through all relevant exposure pathways (**Biosphere synthesis report**, Chapter 6).

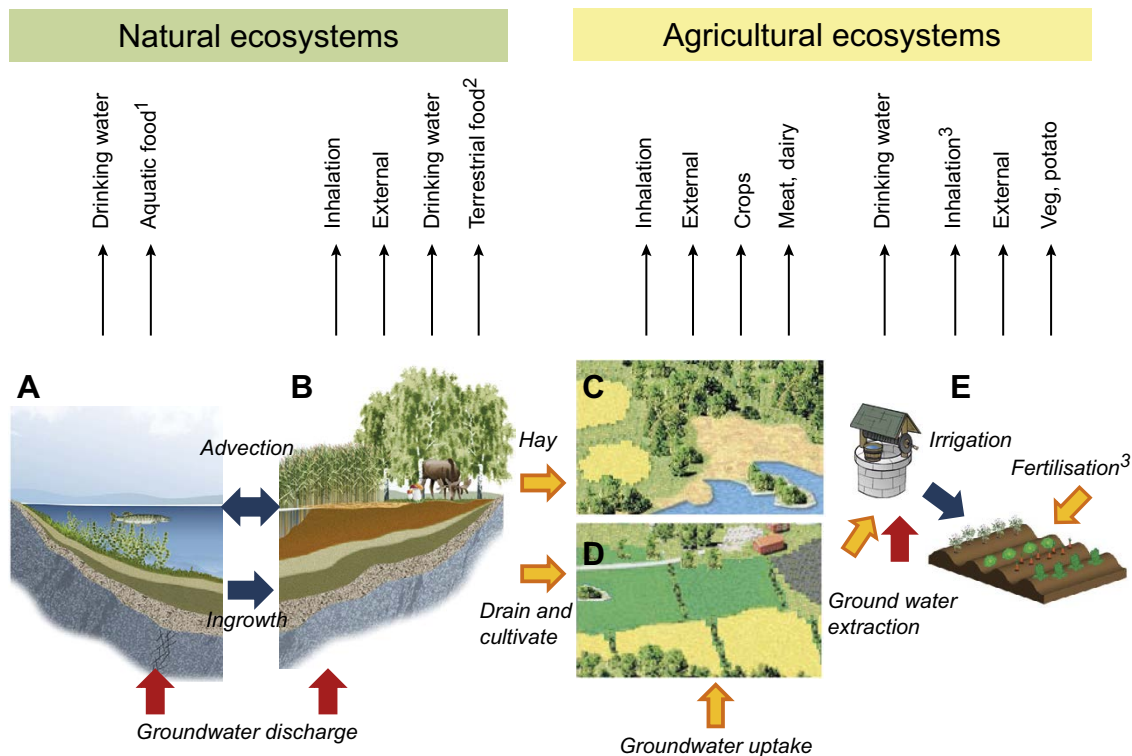


Figure 4-7. Exposure pathways included in the dose calculations for exposed populations using natural resources and/or living in biosphere objects. Hunter-gatherers use natural aquatic (A) and mire (B) ecosystems. The other three exposed populations represent different uses of arable land, namely infield–outland agriculture (C), draining and cultivating the mire (D) and small-scale horticulture on a garden-plot I. Bold arrows represent input of radionuclides from the bedrock (red), from natural ecosystems or deep regolith deposits (orange), or water-bound transfer of radionuclides within the biosphere (blue). The thin arrows (top) represent exposure routes: 1 = fish and crayfish, 2 = game, berries and mushroom, 3 = inhalation and fertilisation that include radionuclides from combustion of biofuel.

Hunter-gatherers (HG) – A hunter and gatherer society uses the undisturbed biosphere for living space and food. The major exposure pathways to a hunter-gatherer are related to foraging (fishing, hunting and collecting berries and mushrooms) discharge areas in the landscape and from drinking water from surface water (streams or lakes). Land use and habits of a typical hunter-gatherer community have been extracted from historical records (Saetre et al. 2013 and the associated electronic supplementary material), and the group is assumed to be made up of 30 individuals that forage an area of approximately 20 km².

Infield–outland farmers (IO) – Self-sustained agriculture in which infield farming of crops is dependent on nutrients from mires (outland). Radionuclides in wetland hay reach the cultivated soil through fertilisation with manure. The major exposure pathways are from growing food and raising livestock and from drinking water either from a dug well or surface water. A self-sufficient community of infield–outland farmers is assumed to be made up of 10 persons. A wetland area of 0.1 km² (10 ha) is needed to supply winter fodder to the herd of livestock corresponding to the amount of manure needed to support infield crop production for this group.

Drained mire farmer (DM) – Self-sustained agriculture on a former lake or wetland, where both crops and fodder are cultivated on organic soils. Radionuclides that have accumulated for an extended time prior to drainage is the main source of activity, but radionuclides reaching the cultivated soil through groundwater uptake are also taken into account. The major exposure pathways are from growing food and raising livestock and from drinking water from a dug well (or from surface water). A self-sufficient community of drained-mire farmers is assumed to be made up of 10 persons. A wetland area of 6 ha is needed to support food production for this group, assuming a level of technology similar to that from the turn of the nineteenth century.

Garden-plot households (GP) – A household that is self-sustained with respect to vegetables and root crops produced through small-scale horticulture. Radionuclides reach the cultivated soil through fertilisation (with algae or biomass ash) and irrigation. The major exposure pathways are from growing food and from drinking water from a dug or drilled well (or from surface water). A garden-plot household is assumed to be made up of five persons and a 270 m² area garden plot is assumed to be sufficient to support the family with vegetables and root crops. The garden-plot is also associated with support areas providing fertilizers. These depend on the productivity of seaweed, the productivity of wood, or the depth of the peat layer in the biosphere object. The productivity of the garden-plot and the diet for this group have been determined from present-day habits.

The annual dose (see Section 2.4.3) is calculated for all PEGs. Doses are evaluated continuously over the assessment period, but for the drained-mire farmers, doses arise from an event (the draining and cultivation of a natural wetland). Exposure is evaluated and averaged over a 50-year period following the drainage event, assuming that the mire has not been drained previously. However, the consequences of draining the mire are cautiously evaluated for all times when cultivation is feasible.

The HG society uses undisturbed ecosystems, whereas the other three groups actively cultivate the land. For the HG and DM groups, exposure occurs within the boundaries of the biosphere object or objects. However, for the IO and GP groups, exposure occurs due to utilising resources from the biosphere object (e.g. organic fertilisers, biofuel or irrigation water) and the location of the cultivated land is not explicit.

During marine conditions, natural ecosystems can be used for food gathering (fishing) and as a source for organic fertilisers (seaweed), but no cultivation of the biosphere object is possible. The possibility to drain and cultivate the biosphere object and to extract water from a well increases as more land becomes available due to the shoreline regression. Hay and surface waters can be used as soon as an object has been isolated from the sea. Wells can be dug and mires can be drained when the risk of saltwater intrusion has been reduced, which is assumed to occur when the land is at least 1 m above sea level.

It follows from the description above that the four PEGs represent four different types of future land use. In the remainder of this report, especially in the description of modelling results, the groups are frequently referred to as “land use variants”.

5 Calculation cases in main scenario – *base case* and supporting calculation cases

5.1 General description

The *base case* constitutes the basis for the analysis of the main scenario, and thus the radionuclide transport and dose calculations (**Post-closure safety report**, Chapter 7). External conditions follow from the *present-day climate variant* of the reference evolution, which assumes that present-day climate conditions prevail for the entire assessment period of 100 000 years (**Post-closure safety report**, Sections 6.2 and 6.3). Although this assumption is not realistic per se, this case is considered to give a reasonable description of the evolution of the repository and its environs. This is due to the assessment that the Forsmark climate will likely remain temperate for the next 100 000 years if current, or higher, levels of anthropogenic greenhouse-gas emissions continue for the next few decades (**Climate report**, Section 4.3). Hence, despite its simplicity, the anticipated small changes in the Forsmark climate over the next 100 000 years are adequately captured by the *base case*. This calculation case also fulfils the regulatory requirement that an assessment of a repository's protective capability should include a case where the biosphere conditions prevailing at the time of the application will not change (SSMFS 2008:37, Section 10).

The conditions in the repository and its environs at closure and post closure are chosen based on the initial state (**Post-closure safety report**, Chapter 4) and the *present-day climate variant* of the reference evolution (**Post-closure safety report**, Sections 6.2 and 6.3).

Models configured for the other calculation cases are only described if they deviate from the *base case* and results from these cases are compared to those of the *base case*. Therefore, the description of the *base case* is far more detailed than the descriptions of the other calculation cases. A comparison of the results between the *base case* and the SR-PSU *base case*, the global warming calculation case, is given in Appendix C. External conditions in the two cases are identical for the first 50 000 years after closure.

This chapter begins with a short description of the external conditions (Section 5.2). Thereafter, the description of *base case* follows the structure established by the radionuclide transport modelling chain (Figure 2-2), starting with the near-field (Section 5.3), followed by the interface between the near-field and the geosphere (Section 5.4), the geosphere (Section 5.5), the interface between the geosphere and the biosphere (Section 5.6) and the biosphere (Section 5.7). The results of the *base case* from the near-field, geosphere and biosphere modelling are included in Sections 5.3, 5.5 and 5.7, respectively. Radiological consequences of specific uncertainties in external conditions and the future evolution of the repository and its environs are analysed in two supporting calculation cases in Section 5.8. Finally, the chapter ends with a summary and conclusions in Section 5.9.

5.2 External conditions

The *base case* describes a future development where present-day climate conditions prevail for the complete assessment period. Thus, 100 000 years of temperate conditions are assumed in this calculation case (Figure 5-1).

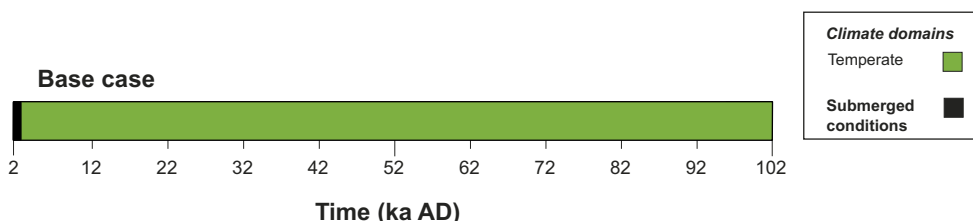


Figure 5-1. Succession of climate domains and submerged conditions in the *base case*.

The present-day climate is defined by the initial state (**Post-closure safety report**, Section 4.5), which is based on locally measured meteorological data during the year between October 2003 to September 2004 (referred to as the “normal year”, see Bosson et al. 2010). During this year, the average annual air temperature was 6.4 °C and the accumulated precipitation was 583 mm. The annual potential evapotranspiration of this year is estimated to have been 421 mm. These values are similar to the average annual air temperature and precipitation during the 1986–2005 reference period (**Climate report**, Section 3.3) as well as the period 2004–2010 when the site investigations were carried out (Bosson et al. 2010, Werner et al. 2013).

The initial shoreline displacement in the *base case* follows from the *present-day climate variant* of the reference evolution (**Post-closure safety report**, Section 6.2.1), amounting to 1 000 years of initial submerged conditions above the repository. This variant assumes that the contribution of future sea-level rise is negligible and, thus, that the shoreline displacement at Forsmark is almost completely dominated by the post-glacial isostatic adjustment (as described in Brydsten and Strömberg 2013). The same representation of the shoreline displacement was also used in the SR-PSU *base case* (SKB TR-14-09, Section 4.1.1). Radiological consequences of using longer submerged periods consistent with contemporary projections future sea-level rise (**Climate report**, Section 3.5), are illustrated in the *timing of shoreline regression calculation case* (Section 5.8.2).

5.3 Near-field

5.3.1 General handling and conditions

The repository near-field is the starting point of the radionuclide transport calculations, as described in Chapter 2. A general overview of the repository layout and functioning is given in Chapter 3. As the repository becomes saturated, the radionuclides may dissolve in the groundwater. The dissolved radionuclides are then slowly transported, by diffusion and advection, from the waste form, through the packaging to the surrounding materials and structures and finally out from the repository and to the geosphere.

The near-field radionuclide transport calculations rely on data for flow-related, and non-flow-related, migration properties, which may vary over time. For instance, degradation of the concrete structures and evolution of the chemical environment are considered. The near-field development, and the migration properties of the concrete structures in the *base case* are described in the following subsections. Unless otherwise specified, parameter values presented here are best estimates, i.e. reference values. The full statistical distribution delimited by upper and lower bounds is not presented here, although it is used in the probabilistic modelling and presented in the **Data report**, where all input data are further described. In the following sections the input parameters used in the radionuclide transport calculations are presented and the importance of the different parameters is illustrated by discussing how they affect the residence times of the radionuclides. A thorough description of the near-field models is given in Åstrand et al. (2022).

Radionuclide inventory and speciation

The inventory and selection of radionuclides included in the modelling are described in Chapter 3. The uncertainty in the radionuclide inventory is handled by means of probabilistic transport calculations based on pre-sampled values obtained with the methodology described in Chapter 2 of SKB (R-18-07).

Steel waste is present in most waste vaults to some extent. The largest quantities are found in 1BRT, where much of it contains irradiation-induced activity. As such, corrosion-controlled radionuclide release is considered for the corresponding 1BRT waste, but not elsewhere.

The speciation of radionuclides is important since it affects their sorption and diffusivity (considered in the PSAR), and in some cases couples to their solubility (solubility limits are not considered within the PSAR). Speciation of radionuclides is discussed further in the **Waste process report**, Section 3.6.1 and the **Post-closure safety report**, Section 6.2.8. The expected speciation and oxidation state of radionuclides in the near-field (**Post-closure safety report**, Section 6.2.8) determines the choice of sorption coefficients (**Data report**, Chapter 7), since the sorption of a radionuclide generally is sensitive to its speciation.

Hydrology

The repository is assumed to become instantly saturated with groundwater upon closure and to remain so for the full assessment period (Section 2.4.4).

The radionuclide transport model uses values of steady-state groundwater flow obtained from near-field and regional hydrological modelling. The near-field hydrological model (Abarca et al. 2020) uses boundary conditions and hydraulic properties of the bedrock obtained from the regional hydrogeological modelling (Öhman and Odén 2018). The two repository parts (SFR1 and SFR3) are represented by separate near-field hydrological models (Figure 4-1). The sizes of the model domains (the interior of the boundaries of the SFR1 model and the SFR 3 model) have been chosen large enough so that changes in hydraulic properties in the waste vaults do not impact conditions at the model boundaries. The vaults in SFR are represented in both the regional and near-field models, but the near-field models represent the interior of the vaults in greater detail. The results from the near-field hydrological model are calculated over surfaces of a large number of control volumes representing key parts of the barriers and wastes. The calculated fluxes are exported and used as input for the calculation of radionuclide transport and release from the vaults.

The steady-state groundwater flow through the repository over time is obtained from simulations that reflect various shoreline positions and concrete degradation states (Table 5-1). These shoreline positions are referred to as 1, 2, 3 and 4 and correspond, respectively, to the years 2000 AD, 2500 AD, 3500 AD and 5000 AD in the *base case* (Abarca et al. 2020). Changes in groundwater flow between the time intervals are handled by linear interpolation up to the steady state which is used to the end of the simulation (further details in Åstrand et al. 2022). Although this approach utilises steady-state input data in transient transport calculations, it adequately captures the transition from lower water flow during the initial submerged period to higher water flow when terrestrial conditions prevail above the repository. This is summarised under (A) in Table 5-1 (details for (B) and (C) are found under respective subheadings below). During the submerged period, the flow is so low that, for most vaults, diffusion dominates the transport from the waste to backfill.

Table 5-1. Summary of influence of the three uncorrelated developments of: (A) shoreline position, (B) concrete physical degradation and (C) cement chemical degradation on conditions affecting radionuclide releases.^a

A	Conditions above SFR	Submerged	Shoreline right above SFR	Terrestrial	Terrestrial
	Time (AD)	2000	2500	3500	5000
	Shoreline position ^b	1	2	3	4
	Groundwater flow rates ^c	~0.1 % of maximum flow	~10 % of maximum flow	~Maximum stationary flow	Maximum stationary flow
B	Concrete physical degradation state^{d,e}	Intact	Moderately degraded	Severely degraded	Completely degraded
	Hydraulic conductivity K (m s ⁻¹)	10 ⁻⁹	10 ⁻⁷	10 ⁻⁵	10 ⁻³
	Cracks	1BMA slab	1BMA slab	1–2BMA, 1BRT	1–2BMA, 1BRT
C	Cement chemical degradation state	State I	State II	State IIIa	State IIIb
	Main dissolving minerals	NaOH, KOH	Ca(OH) ₂	C-S-H, (CaO) _x (Al ₂ O ₃) _y	C-S-H
	pH (-)	> 12.5	12.5	12	10.5

^a The three evolutions are uncorrelated, and the timings of chemical degradation and physical degradation vary between vaults.

^b Abarca et al. (2020).

^c Estimated from Figure 6-11 in Öhman and Odén (2018).

^d The physical degradation varies between different concrete barriers within a vault, the given hydraulic conductivity is for the main barrier.

^e In addition, the porosity and effective diffusivity increase over time, but in steps that do not coincide with the hydraulic conductivity steps (Tables 5-4 to 5-6, 5-8 to 5-10).

The regional hydrogeological models calculate the groundwater flow through the vaults from steady-state flow solutions at nine points in time (time slices: 2000 AD, 2100 AD, 2250 AD, 2500 AD, 2750 AD, 3000 AD, 3500 AD, 5000 AD and 9000 AD) representing different shoreline positions, see further Section 5.5. To ensure that the flow rates from the near-field models are consistent with those from the regional models, the near-field flow rates within each vault are rescaled with the vault-specific flow rates obtained from the regional models, see Table A-1 in Appendix A2. Since the regional models are solved for more time slices than the near-field models, the vault-specific flows from the regional models are used in the interpolation of the flow from the near-field model between different time slices, as described in Section 5.5. The shoreline position at 9000 AD is assumed to prevail for the remainder of the assessment period.

Moreover, to account for uncertainties in the fracture network of the host rock, the near-field flow rates are rescaled. The rescaling is done by applying a probabilistic factor stochastically drawn from a probability density function (PDF) based on the flow rates through the vaults for different fracture realisations generated in the regional model. Uncertainties in flow-related migration properties are discussed further in Section 5.5 and Appendix A4.

As described in the **Initial state report**, Chapter 11, several closure components will be installed when the repository closes. These components include plugs with low hydraulic conductivity ($K = 1 \times 10^{-12} \text{ m s}^{-1}$). In the *base case*, these plugs are considered to remain intact during the whole assessment period (**Post-closure safety report**, Section 6.3.9).

Concrete physical properties

Over time, as concrete chemically degrades, the physical properties of the concrete structure, such as the hydraulic conductivity, change from values representative of intact concrete to moderately degraded concrete, severely degraded concrete and, finally, to values representative of completely degraded concrete (Abarca et al. 2020, summarised in Table 5-1). The diffusion-available porosity and the effective diffusivity of radionuclides in the concrete also increase as it degrades.

The transition between these concrete degradation states occurs at different times, depending on the vault design (**Post-closure safety report**, Section 7.4.2). Furthermore, different concrete structures in a vault, e.g. concrete waste package *versus* a concrete vault barrier, can degrade at different rates and so can exist in distinct degradation states (**Data report**, Chapter 10). The transitions are assumed to be practically instantaneous in the modelling; only a short transition period of 100 years is included for numerical reasons.

Cracks

As concrete degrades, cracks may form (**Post-closure safety report**, Section 6.3.9). Cracks are treated as preferential flow paths for dissolved radionuclides that channel radionuclide advection through the concrete barrier. This is implemented in the model by adding an advective transfer directly from the waste domain to the gravel backfill without taking any sorption in the concrete structure into account. However, as diffusive transfer through the concrete structure occurs, sorption sites are still available for the radionuclides that diffuse into the concrete structure. For 1-2BMA and 1BRT, advective transport through the concrete structures has been modelled using a crack (a transfer directly from the waste domain to the gravel) during periods with severely and completely degraded concrete (Table 5-1). For all other time periods and vaults, advective transport through the concrete structures has been modelled as transport through a homogenous porous medium (Section 4.2.4). This way of modelling cracks is discussed further in Appendix B.

Cement sorption properties

Like the physical-hydrological properties of concrete, the chemical-mineralogical properties change over time as the cement minerals in the concrete undergo chemical degradation. The physical and chemical degradation processes are, in reality, coupled, but are here treated separately, without direct coupling. Initially, all cementitious materials are in chemical degradation state I, characterised by dissolution of sodium- and potassium-hydroxide minerals and $\text{pH} > 12.5$ in the porewater. Thereafter follows degradation state II (dissolution of portlandite, $\text{pH} \approx 12.5$), degradation state IIIa (incongruent

dissolution of C-S-H phases, presence of Ca-aluminates, $\text{pH} \approx 12$) and degradation state IIIb (incongruent dissolution of C-S-H phases, absence of Ca-aluminates, $\text{pH} \approx 10.5$). This is summarised in Table 5-1 (C). It is assumed that pH evolves at the same rate in all cementitious materials within a single vault, i.e., at a given time all cementitious materials within a vault are assumed to be in the same chemical degradation state. The evolution of chemical degradation states for each waste vault is further discussed in the **Post-closure safety report**, Section 7.4.2.

Cement degradation affects its sorption capacity (**Post-closure safety report**, Sections 6.2.8 and 6.3.8). Therefore, different sorption coefficients, K_d values, are used for different materials and time periods. The sorption coefficients for cement paste of different chemical degradation states are presented in Tables 7-4 to 7-7 in the **Data report**. To account for the uncertainty in the sorption capacity of cementitious materials, the K_d values are implemented in the form of probability density functions. In the following vault-specific subsections, the handling of cement-degradation-related transport properties is presented with a focus on a few select radionuclides. In those sections, only the best-estimate values (used in deterministic calculations) of the K_d statistical distributions are discussed. For some radionuclides, K_d values are independent of the chemical degradation state, e.g. the cement-paste K_d value of I-129 ($10^{-3} \text{ m}^3 \text{ kg}^{-1}$) and C-14-org ($10^{-5} \text{ m}^3 \text{ kg}^{-1}$); these values are not repeatedly discussed in the vault-specific sections. Furthermore, sorption is not credited in the BLA vaults that lack dedicated concrete barriers.

To account for the fact that cement paste constitutes only a small fraction of the concrete, the K_d values for cement paste are multiplied with the corresponding mass fractions presented in Table 5-2 to obtain an effective K_d value for the various cementitious materials. Over time, chemical degradation leads to depletion of cement paste from the concrete and a simultaneous porosity increase.

According to the reference evolution, reducing redox conditions will prevail in the near-field shortly after closure and throughout the analysis period (**Post-closure safety report**, Sections 6.2.8 and 6.3.8). Hence, radionuclide oxidation states and sorption coefficients that correspond to reducing conditions are selected for the *base case*, see the **Data report**, Chapter 7.

Table 5-2. Mass fraction of cement paste in structural concrete and grout (Table 7-8 in the Data report).

Material	Cement paste mass fraction (kg kg^{-1})
Structural concrete (general recipe)	0.219
Structural concrete, 1BMA* and 1-2BTF	0.182
Structural concrete, 2BMA	0.197
Grout, silo	0.267
Grout, 1-2BTF** sides	0.235
Grout, 1-2BTF (waste)	0.171
Grout, 1BRT	0.174

* The outer concrete structure is cautiously assumed to have the same cement paste mass fraction as the inner concrete.

** The concrete used to backfill the space between the outer concrete tanks and the rock walls.

Complexing agents

The sorption-reducing effect of organic complexing agents is implemented in the form of sorption reduction factors (SRF, see Section 4.2). SRF values are strongly dependent on the type and concentration of the complexing agent (Table 7-12 in the **Data report**, Table 4-1 in Keith-Roach et al. 2021). The complexing-agent effect and thus the SRF values are also element-specific. As such, SRF values are defined for five groups of elements (SRF Groups), within each of which complexation properties are similar (Table 5-3). Note that only the SRF value is assumed identical within an SRF Group, whereas other properties such as the K_d value are not (Tables 7-4 to 7-7 in the **Data report**).

Table 5-3. Radionuclides grouped by assumed analogous complexation properties and thus SRF values. Denoted by their oxidation states and relevant isotopes, respectively. Some oxidation states are judged irrelevant and thus excluded from the transport calculations.

SRF Group	Elements by oxidation state	Relevant isotopes in the transport modelling
Group 1	Ac(III), Eu(III), Am(III), Cm(III), Ho(III), Sm(III), Po(IV)	Ac-227, Am-241, Am-242m, Am-243, Cm-243, Cm-244, Cm-245, Cm-246, Eu-152, Ho-166m, Po-210, Sm-151
Group 2	Pb(II), Pd(II)	Pb-210, Pd-107
Group 3	Th(IV), Np(IV), Pa(IV), Tc(IV), Zr(IV), Sn(IV), Pa(V)	Np-237, Pa-231, Sn-126, Tc-99, Th-229, Th-230, Zr-93
Group 4	Pu(IV)	Pu-238, Pu-239, Pu-240, Pu-241, Pu-242
Group 5	U(VI)	U-232, U-233, U-234, U-235, U-236, U-238
Other	Elements assumed unaffected by complexing agents	Ag-108m, Ba-133, C-14-ind, C-14-inorg, C-14-org, Ca-41, Cd-113m, Cl-36, Co-60, Cs-135, Cs-137, H-3, I-129, Mo-93, Nb-93m, Nb-94, Ni-59, Ni-63, Ra-226, Se-79, Sr-90

Two complexing agents have been found to dominate the sorption reduction in SFR: isosaccharinate (ISA) and nitrilotriacetate (NTA) (Keith-Roach et al. 2021). ISA and NTA differ in several ways. First, ISA is a degradation product of cellulose, so its concentration in SFR grows slowly as cellulose degrades. Second, it sorbs to cement minerals, increasing its longevity in the repository; zero outflow of ISA is pessimistically assumed. NTA, on the other hand, is cautiously assumed to be instantly and fully dissolved, but its negligible sorption permits outflow from the repository. Finally, the different SRF groups are differently affected by ISA and NTA.

The amounts and ranges of dissolved concentrations of ISA and NTA have been estimated for each part of the repository: silo, 1–2BMA, 1–2BTF as well as for the individual waste compartments in 1BMA (Table 3-6 in Keith-Roach et al. 2021). The BLA vaults, where sorption is not credited, are excluded. IBRT, which exclusively contains metallic waste, does not contain any complexing agents. Based on the properties of ISA and NTA and their estimated concentrations (ranges characterised by reference value, minimum and maximum bound), sets of SRFs were determined for each complexing agent (Tables 4-2 and 4-3 in Keith-Roach et al. 2021). The SRF values used in the probabilistic transport modelling follow a triangular distribution but in the following vault-specific subsections, only the best estimates (reference values) of these probability density functions are discussed.

Radionuclide complexation is mainly a solution-phase process, so the sorption reduction is not much affected by the nature of the sorbent surface. Therefore, the same SRFs are applied to sorption on bentonite as to cement. The same approach was followed in the SR-PSU, although it was not explicitly discussed.

Other material properties

Macadam/Crushed rock

All vaults (except the BLA vaults) are backfilled with macadam/crushed rock, which is assigned an effective diffusivity, porosity and solid density of $6 \times 10^{-10} \text{ m}^2 \text{ s}^{-1}$ (SKB R-01-14, Table 6-10), $0.3 \text{ m}^3/\text{m}^3$ (**Initial state report**) and 2700 kg m^{-3} (SKB R-01-14, Table 6-10), respectively.

Solid density

The particle or solid density of all bentonite and concrete materials is approximately 2700 kg m^{-3} (SKB R-01-14, Table 6-10), and this is the value used in the radionuclide transport calculations.

Analytical estimate of residence time and annual release from the near-field

Radionuclide transport through the near-field is simulated using the radionuclide transport model described in more detail in Chapter 4 and in Åstrand et al. (2022). In the following, the simplified analytical estimates of the residence time based on diffusion, flow and vault capacity (introduced in Section 4.2.5 and further described in Appendix E) are used to illustrate how barrier properties impact the transport through individual vaults. However, the presented annual releases from the near-field from the vaults is the mean release values calculated using the radionuclide transport model.

5.3.2 Silo calculations and results

Handling in the silo model

The silo contains most of the activity in SFR (see Figure 3-17) and therefore has engineered barriers with the highest retention capabilities, e.g. being the only vault with a bentonite buffer, see Section 3.1. A detailed description of this vault is given in Chapter 4 in the **Initial state report**.

Hydrology

In the silo, groundwater flow through the waste is limited mainly by the bentonite barrier that surrounds the silo. As explained in Section 5.3.1, the hydraulic conductivity of the concrete structures evolves through four defined physical states in response to degradation. This results in different groundwater flow rates for different time periods through different parts of the silo. Figure 5-2 shows the hydraulic-conductivity values applied for the silo, corresponding to intact concrete (Abarca et al. 2020), and Table 5-4 shows the evolution of the hydraulic conductivity over time. The bentonite is assumed to retain its initial-state properties during the entire assessment period (**Post-closure safety report**, Section 6.3.9). The hydraulic conductivity of the bentonite wall is height-dependent due to self-compaction, ranging from $9 \times 10^{-12} \text{ m s}^{-1}$ to $9 \times 10^{-11} \text{ m s}^{-1}$ (**Initial state report**), increasing from the bottom towards the top according to the formula:

$$K(z) = az + b \quad \text{Equation 5-1}$$

where:

K = hydraulic conductivity (m s^{-1}),

z = depth (m), where the uppermost part of the silo concrete structure is located at $z = -79.6 \text{ m}$

a = height-dependence (s^{-1}) = $1.54 \times 10^{-12} \text{ s}^{-1}$

b = height-independent term (m/s) = $2.11 \times 10^{-10} \text{ m s}^{-1}$

The hydraulic conductivity of the sand–bentonite mix in the bottom and top of the silo is set to 10^{-9} m s^{-1} (**Initial state report**). The waste is assigned a conductivity derived from the average conductivity of the waste packages and the grout.

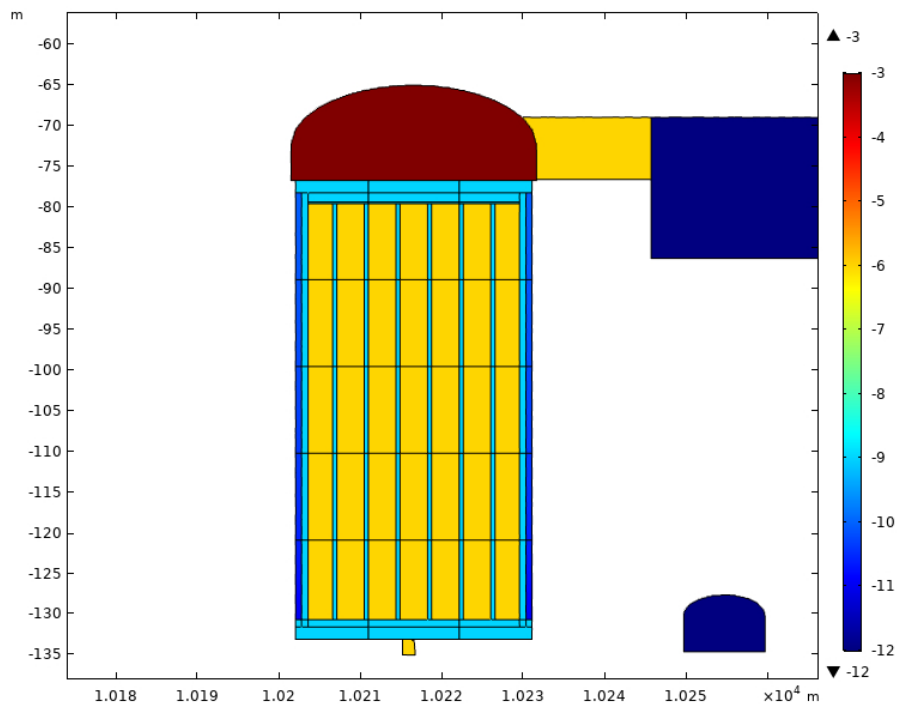


Figure 5-2. Cross section of the silo vault showing the logarithm $\log_{10}(K)$ of the hydraulic conductivity K (m s^{-1}) (colour scale) for the initial state corresponding to the intact concrete physical degradation state (Abarca et al. 2020).

In addition to the groundwater flow ($\text{m}^3 \text{s}^{-1}$) through the silo, the Darcy velocity (m s^{-1}) of the flow through the surrounding rock has been calculated using an older version of the repository near-field hydrological model, see Abarca et al. (2014), Appendix E. The Darcy velocity is used to estimate the *equivalent water flow*, Q_{eq} ($\text{m}^3 \text{s}^{-1}$), which represents the diffusive transport of radionuclides from the silo bentonite to the host rock, see Section 5.4.

Concrete structures and bentonite

Over time, as the silo concrete degrades, the effective diffusivity, D_e , and the diffusion-available porosity of the concrete structure evolve as shown in Table 5-4 and in Chapter 9 and 10 of the **Data report**. Initially, deterministic values are assigned to the effective diffusivity of the structural concrete but, as the concrete degrades, a probability density function with a variance that increases with time is used. The cementitious materials other than structural concrete are assigned deterministic properties throughout. The porosities, given in Table 5-4 for structural concrete and Table 5-5 for bentonite, are not handled probabilistically.

In addition to the physical evolution, concrete undergoes chemical–mineralogical degradation. This entails a decrease in the pH of the porewater and altered mineralogical properties affecting the sorption capacity. Table 5-4 shows the pH and K_d values that follow from the simplified chemical-degradation development of the silo. The sorption strength for some radionuclides, e.g. Mo-93 expected to occur as molybdate, will be unaffected by the chemical–mineralogical degradation and its K_d value ($3 \times 10^{-3} \text{ m}^3 \text{ kg}^{-1}$, see Chapter 7 in the **Data report**) will remain constant throughout the assessment period.

In the silo, the amount of ISA-producing cellulose is so small that the ISA effect on sorption is negligible; the SRF rather derives from the presence of NTA (Keith-Roach et al. 2021). The SRF values for sorption on cement in the silo interior and on bentonite in the outer bentonite wall are shown in Table 5-4. These data are described in more detail in Keith-Roach et al. (2021).

Table 5-4. Development of base-case silo barrier-material properties: concrete hydraulic conductivity K , diffusivity D_e , porosity ϕ , pH, cement sorption coefficients K_d for selected species and sorption reduction factors SRF in the cementitious silo interior and in the bentonite barrier.

Time (AD)	Concrete structure			All cement				Bentonite wall		
	K (m s^{-1})	D_e ($\text{m}^2 \text{s}^{-1}$)	ϕ (-)	pH	K_d ($\text{m}^3 \text{kg}^{-1}$)		SRF (-)		SRF (-)	
					C-inorg	Ni	Group 3	Group 4	Group 3	Group 4
2000–3000	$1.0 \times 10^{-7\text{a}}$	3.5×10^{-12}	0.11	> 12.5	2.0	2.68×10^{-1}	1.79×10^2	9.80×10^1	5.30×10^1	4.90×10^1
3000–17 000	1.0×10^{-5}	5.0×10^{-12}	0.14	> 12.5	2.0	2.68×10^{-1}				
17 000–22 000	1.0×10^{-5}	5.0×10^{-12}	0.14	> 12.5	2.0	2.68×10^{-1}			1 ^c	1 ^c
22 000–34 000	1.0×10^{-5}	1.0×10^{-11}	0.18	> 12.5	2.0	2.68×10^{-1}	1 ^b	1 ^b	1	1
34 000–52 000	1.0×10^{-5}	1.0×10^{-11}	0.18	12.5	5.0	1.66×10^0	1	1	1	1
52 000–102 000	1.0×10^{-3}	1.0×10^{-10}	0.30	12.5	5.0	1.66×10^0	1	1	1	1

^a The structural concrete is pessimistically assumed to be moderately degraded already from 2000 AD.

^b Linear interpolation gives a unity value (no sorption reduction) at 22 450 AD.

^c Linear interpolation gives a unity value (no sorption reduction) at 17 450 AD.

The bentonite material properties are assumed to not change over time during the assessment period, but most of its transport-related properties are dependent on the nature of the transported radionuclide. K_d values in the bentonite for selected radionuclides are shown in Table 5-5, whereas the rest are presented in Table 7-9 in the **Data report**. The effective diffusivity, D_e , and the diffusion available porosity, ϕ , are presented in Table 5-5 for anions, cations and neutral species, respectively.

Table 5-5. Base-case silo barrier-material properties assumed to be time-independent: bentonite hydraulic conductivity K , diffusivity D_e , porosity ϕ , and sorption coefficients K_d for selected radionuclides.

Bentonite wall			Sand-Bentonite bottom	Bentonite			
K (m s ⁻¹)	D_e (m ² s ⁻¹)	ϕ (-)	K (m s ⁻¹)	K_d (m ³ kg ⁻¹) ^c			
				C-org	Mo	Ni	I
9.0×10^{-12} ^a	4.00×10^{-11} (anion)	0.24 (anion)	1.00×10^{-9}	0	0	3.00×10^{-1}	0
9.0×10^{-11} ^b	7.50×10^{-10} (cation)	0.61 (cation)					
	4.00×10^{-10} (neutral)	0.61 (neutral)					

^a Bottom of bentonite wall, see Equation 5-1.

^b Top of bentonite wall, see Equation 5-1.

^c For sand/bentonite the K_d is assumed to be the average, weighted to the mass proportions of the two materials in the mix.

Analytical estimate of residence time

The residence time for radionuclides in the silo is estimated using Equation E-12. The equation only approximates the true residence time because of the simplifying approximations made, for example, neither the diffusive resistance of waste packages nor diffusive transport to the backfill on top of the silo is included (see Appendix E2). Neglecting the resistance of the waste packages is motivated by the fact that the diffusive resistance of the waste packages is much lower than the diffusive resistance of the concrete structure since the waste packages have a large area to thickness ratio (as exemplified in more detail for the concrete tanks in 2BTF in Section 5.3.6). It is important to note that the simplifying approximations made in Equation E-12 are not made in the compartment model. However, estimating the residence time using these simplifications gives some understanding of the relative importance of different transport processes and how different barriers and their properties contribute to the retention of radionuclides.

All variables included in Q_{tot} , see Equation E-3 and E-10, are plotted in Figure 5-3a. The Q_{eq} term represents water flow in the rock outside the bentonite barrier, i.e. it carries away the radionuclides that diffuse from the bentonite into the fractures. The Q_{eq} is the limiting factor for silo diffusive transport, since $1/R_{tot}$ is larger than Q_{eq} , see Figure 5-3a. That is $1/Q_{eq}$ is larger than the total diffusive resistance $R_{tot} = R_{concrete\ side} + R_{bentonite\ side}$, which means that the diffusive resistance of the concrete and the bentonite is negligible compared to the limitation imposed by the diffusion into the slowly moving water in the adjacent fractured rock. From Figure 5-3a it can be seen that flow through the waste, Q_{waste} , is larger than Q_{eq} , which means that advection is the dominating transport mechanism throughout the assessment period. In addition, the flow through the silo vault, Q_{vault} , is plotted in Figure 5-3a. This flow is larger than Q_{waste} because it also includes the flow through the relatively permeable silo top backfill. Most of the water flows horizontally through the top and is never in direct contact with the waste.

Many transport-related parameters, such as e.g. the various Q s in Figure 5-3, are influenced by the regional hydrological conditions and concrete properties. These conditions and properties are summarised in Table 5-1 and included in the form of horizontal bars in Figure 5-3 and subsequent figures throughout Section 5.3 to visualise their correlation with the transport-parameter and activity-release curves presented in the figures.

To estimate the residence time, the total capacity (cf. Section 4.2.4) of the vault is needed (Equation 4-2 and Equation E-11). The total capacity of the silo depends on the sorption properties of the cementitious materials which evolve in time as the cement degrades (Figure 5-3b).

The residence time in the silo for a few relevant radionuclides is shown in Figure 5-3c. For all radionuclides, the residence time decreases by several orders of magnitude during the first 3 000 years after closure. The decrease is due to the increased flow of groundwater through the waste caused by the receding shoreline above the repository. The physical state of degraded concrete has a negligible impact on the residence time, as seen in Figure 5-3c, because bentonite is the main hydraulic barrier in the silo. The residence time for the strongly sorbing radionuclide Ni-59 increases after 34 000 AD

due to the increased cement K_d and decreased solubility as $\text{Ni}(\text{OH})_3^-$ becomes less favoured by a less basic pH (Section 7.9 in the **Data report**). This is illustrated by the increased capacity in Figure 5-3b. A few other radionuclides also have higher sorption coefficients on cement after 34 000 AD, although most sorb more weakly.

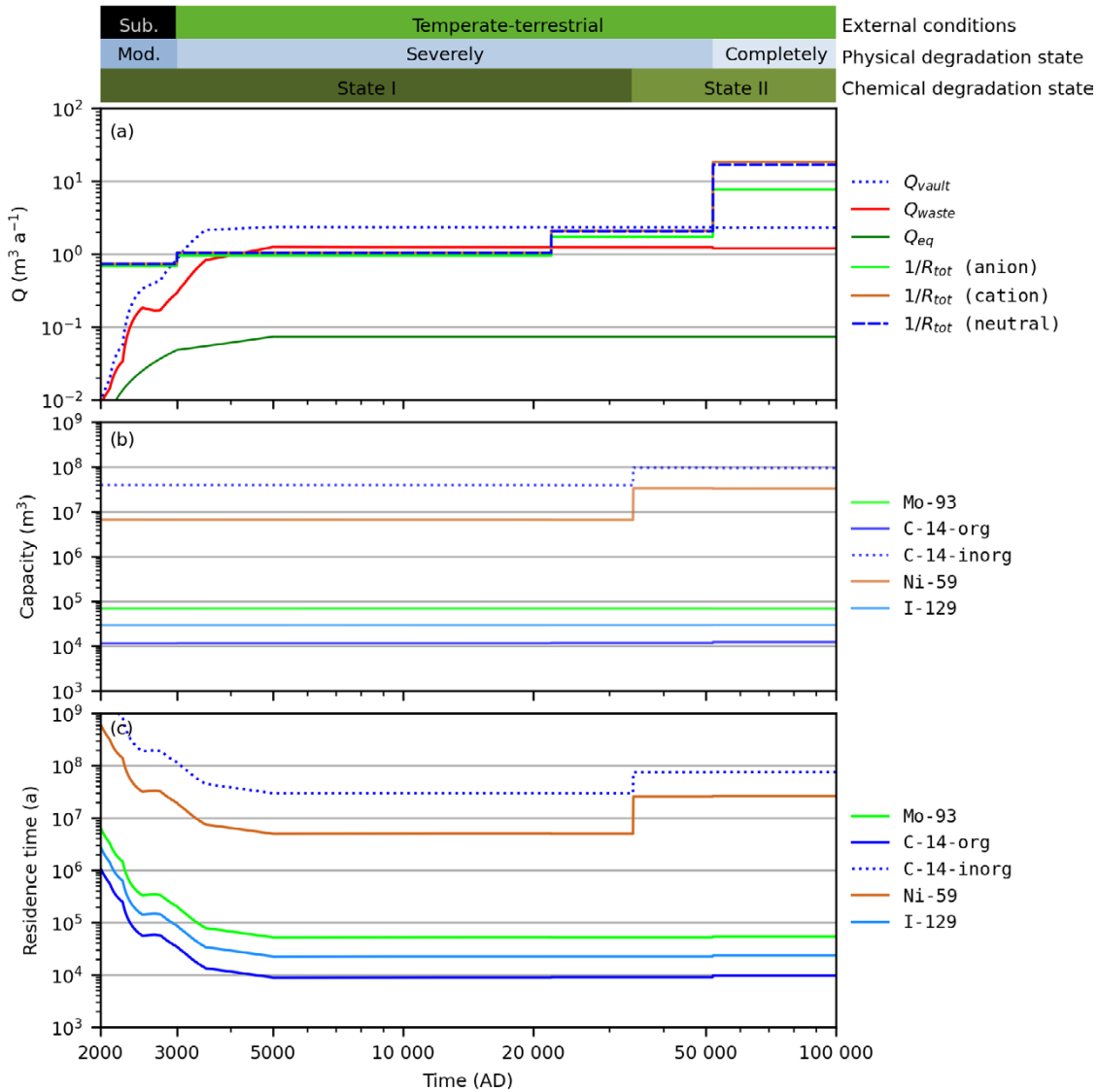


Figure 5-3. (a): Water flow through the waste Q_{waste} , equivalent flow Q_{eq} and inverse diffusive resistance of the concrete and bentonite silo structures, $R_{\text{tot}} = R_{\text{concrete side}} + R_{\text{bentonite side}}$, as a function of time. The effective diffusivity and thus the diffusive resistance are different for cationic, anionic and neutral radionuclide species. Q_{vault} is the flow through the whole silo vault including the top backfill. (b): The total capacity (cf Section 4.2.4) of the waste, concrete structure and bentonite for select radionuclides as a function of time. (c): Residence time in the silo vault for select radionuclides as a function of time. Coloured horizontal bars (top) show the evolution of the external conditions and of the concrete physical and chemical degradation, respectively, briefly explained in Table 5-1.

Annual release from the near-field from the silo

The total annual activity released from the silo vault to the geosphere as calculated by probabilistic radionuclide transport simulations is shown in Figure 5-4. The release of all radionuclides initially increases until a maximum release rate is reached. The time until maximum release rate is determined by the time it takes for the radionuclides to travel from the waste to the geosphere, in turn depending on various transport-related parameters in the repository such as e.g. the hydraulic conductivities of the various structures. The travel time also differs between radionuclides depending on their retention properties, e.g. the peak release of Ni-59 occurs much later than the peak release of Cl-36 since Ni-59 has a much larger K_d value. After peaking, the release rate starts to decrease mainly due to decreasing radionuclide inventory and decay. Based on the analytical expressions it is expected that the release will be dominated by long-lived radionuclides with high release rates, i.e., half-lives longer than 1 000 years and release rates higher than $100\,000\text{ Bq a}^{-1}$ in Figure E-1.

The release is initially dominated by weakly sorbing radionuclides with the largest inventory and half-lives longer than a few hundred years, e.g. C-14-org and Mo-93. The release of most of these radionuclides peak within a few thousand years. During the second part of the assessment period, the release is dominated by longer-lived radionuclides such as Ni-59, whose release is retarded by sorption on cementitious materials.

The cement chemical degradation only has a minor impact on the release during the first 32 000 years after closure. At 34 000 AD, cement chemical degradation induces stronger sorption of Ni onto cement and, therefore, a lower release of Ni-59¹⁰.

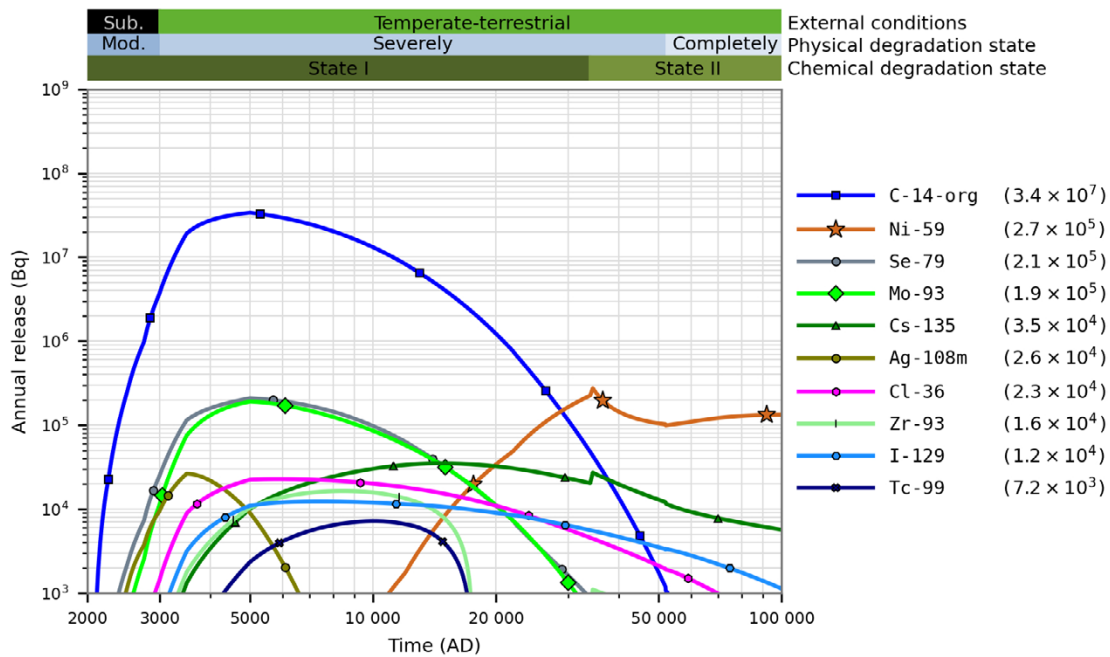


Figure 5-4. Annual activity releases (Bq) from the silo in the base case. The annual release maxima (Bq) are shown in parentheses in the key. Coloured horizontal bars (top) as in Figure 5-3.

¹⁰ Despite a higher K_d for Ni after 34 000 AD a sudden increase of the mean release can be seen shortly after the K_d transition. This is due to the fact that the K_d values are sampled probabilistically and, since the samples are uncorrelated, this results in a few combinations of K_d values for the first and second period where the first K_d value is higher than the second.

5.3.3 1BMA calculations and results

Handling in the 1BMA model

The existing 1BMA waste vault consists of a concrete structure into which waste packages are disposed, see Section 3.1. At closure, the concrete structure will be covered with a lid. The *base case* considers the concrete structure in 1BMA to have undergone repair measures (Chapter 5 in the **Initial state report**). As such, the modelled structure consists of two parts: an inner part with the original concrete and an outer part with the new concrete from the repair measures. An unrepaired 1BMA is analysed in a dedicated calculation case described in Section 8.7. A detailed description of 1BMA is given in Chapter 5 in the **Initial state report**.

Hydrology

The groundwater flow rate through the waste is limited by the concrete structure surrounded by a high hydraulic conductivity backfill. In the near-field hydrological model, the different parts of 1BMA are assigned different hydraulic conductivities for different physical degradation states as shown in Figure 5-5 (Abarca et al. 2020). The modelled evolution of the hydraulic conductivity of the inner (original) and outer (new) parts of the concrete structure surrounding the waste is shown in Table 5-6 (also described in Chapter 9 in the **Data report**). The two parts are most easily distinguished in the moderately degraded state in Figure 5-5, where the outer part is shown in cyan and the inner part is shown in yellow (light red represents waste and the dark red represents backfill). Due to the new concrete in the outer part, the conductivity is initially assigned a value several orders of magnitude lower than in the inner part. The conductivity of both parts increases over the successive physical degradation states and finally reaches the same value of 10^{-3} m/s for completely degraded concrete. In the concrete structure interior, a higher conductivity is applied based on the average conductivity of the waste packages and the void that surrounds them.

For radionuclide transport in 1BMA, both magnitude and direction of the water flow are important. The water flow through the different waste compartments at 2000 AD is shown in Figure 5-6. The flow in the vertical (z) direction corresponds to the flow through the slab and the y-direction is along the long side of the vault. The flow changes both in magnitude and direction between different waste compartments, but is, in general, low. The spatial variation of the flow is determined by the hydraulic properties (fracture zones) of the surrounding bedrock.

The water flow changes direction and magnitude over time. This is illustrated in Figure 5-7 which shows the flow when the concrete has become moderately degraded and the shoreline has moved away from the repository (i.e. terrestrial conditions at 5000 AD, see Section 5.3.1). The flow is directed along the long side of the vault and is highest in compartment 12 and 13. This maximum flow coincides with the fracture zone that intersects the vault (Abarca et al. 2020).

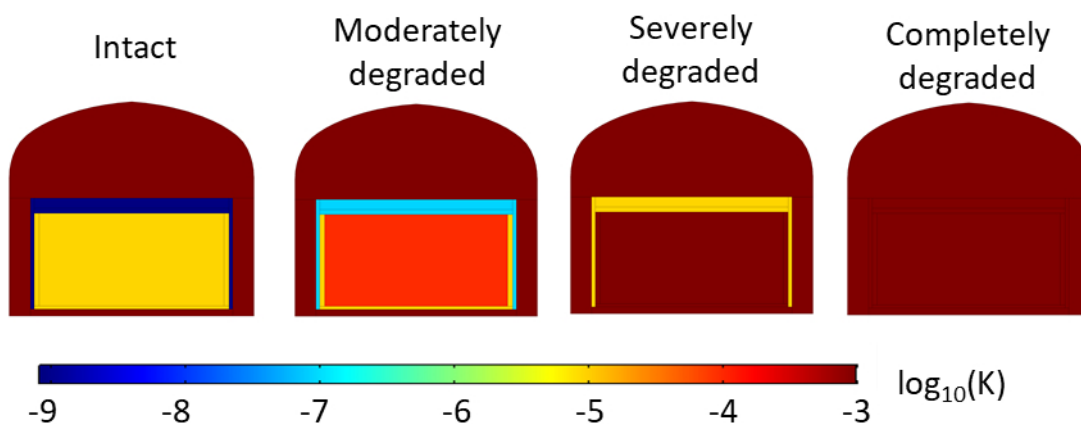


Figure 5-5. Cross sections of the 1BMA vault showing the logarithm $\log_{10}(K)$ of hydraulic conductivity K (m/s), (colour scale) for different physical degradation states. Adapted from Abarca et al. (2020).

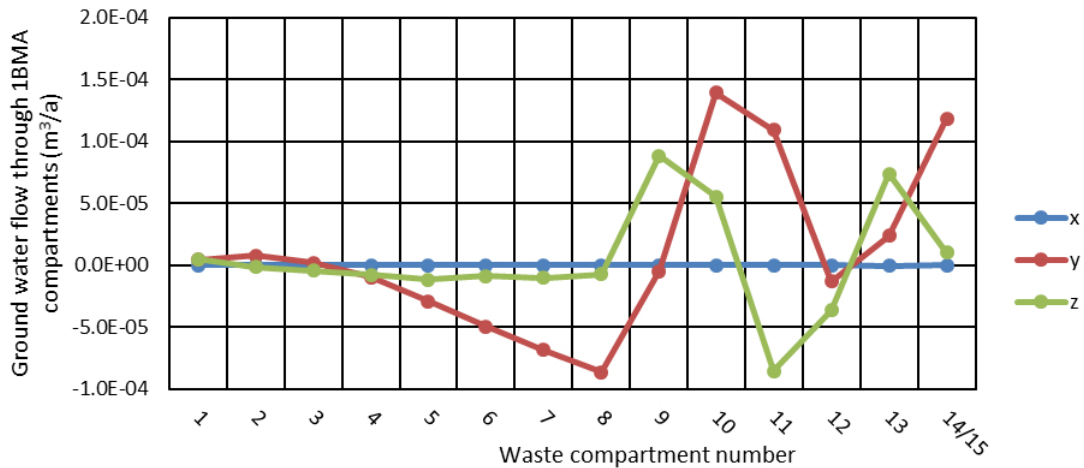


Figure 5-6. Flow through the 15 waste compartments in IBMA for intact concrete at 2000 AD (i.e. submerged conditions), decomposed into three cartesian directions, where y is along the long side of the vault and z is upwards (Abarca et al. 2020). The two half size compartments 14/15 are lumped together.

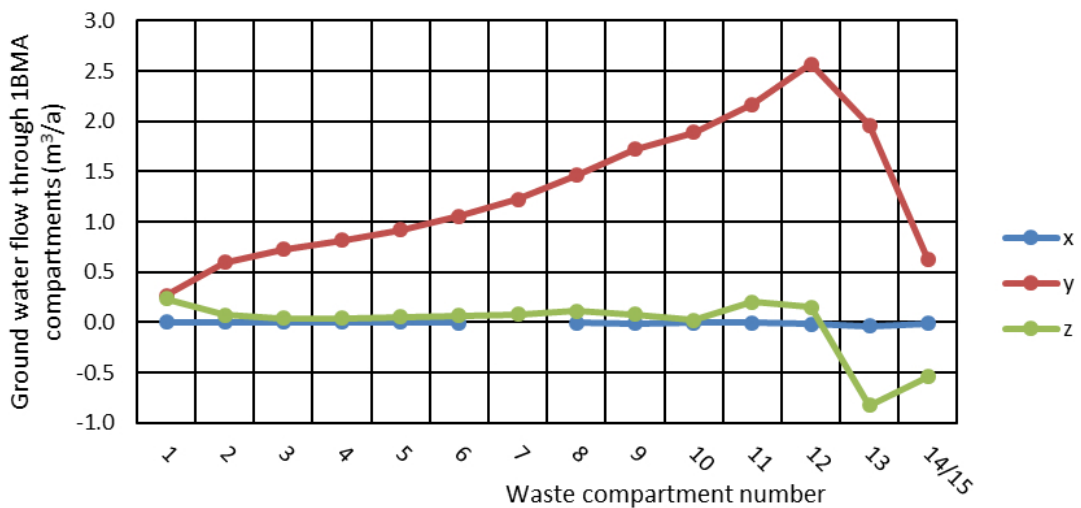


Figure 5-7. Flow through the 15 waste compartments in IBMA for moderately degraded concrete at 5000 AD (i.e. terrestrial condition), decomposed into three cartesian directions, where y is along the long side of the vault and z is upwards (Abarca et al. 2020). The two half size compartments 14/15 are lumped together.

Concrete barriers

Unlike the hydraulic conductivity, both the porosity and the effective diffusivity are assumed to be the same in the inner and outer parts of the concrete structure, where the value for the inner part is cautiously applied for both parts. The porosity evolution is presented in Table 5-6 (Chapter 9 in the **Data report**). The porosity is not treated probabilistically. The effective diffusivity is implemented as an initially single (deterministic) value that, as the concrete degrades, increases over time via probability density functions with increasing variances (see Chapter 10 in the **Data report**). The evolution of the effective diffusivity is shown in Table 5-6.

The development of pH and of the sorption coefficients for selected radionuclides are shown in Table 5-6. The sorption capacity for some radionuclides will be unaffected by cement degradation; for example, Mo has a K_d that remains constant throughout the assessment period ($3 \times 10^{-3} \text{ m}^3 \text{ kg}^{-1}$). The 15 waste compartments in IBMA have different content of different waste types and thus also different SRFs due to complexing agents as shown in Table 5-7, taken from Keith-Roach et al. (2021, Chapter 4).

Table 5-6. Development of base-case 1BMA barrier-material properties: concrete hydraulic conductivity K , diffusivity D_e , porosity ϕ , pH and cement sorption coefficient K_d for selected radionuclides.

Time period (AD)	Outer concrete structure	Inner concrete structure	Inner and outer concrete structure ^a		All cement	
	K (m s ⁻¹)	K (m s ⁻¹)	D_e (m ² s ⁻¹)	ϕ (-)	pH	K_d (m ³ kg ⁻¹) C-inorg Ni
2000–3000	8.30×10^{-10}	1.00×10^{-5}	5.00×10^{-12}	0.14	> 12.5	2.0 2.68 × 10 ⁻¹
3000–12000	1.00×10^{-7}	1.00×10^{-5}	5.00×10^{-12}	0.14	> 12.5	2.0 2.68 × 10 ⁻¹
12000–22000	1.00×10^{-7}	1.00×10^{-5}	5.00×10^{-12}	0.14	ca 12.5	5.0 1.66
22000–52000	1.00×10^{-5}	1.00×10^{-3}	1.00×10^{-11}	0.18	ca 12.5	5.0 1.66
52000–102000	1.00×10^{-3}	1.00×10^{-3}	2.00×10^{-10}	0.3	ca 12.5	5.0 1.66

^a The outer concrete structure is cautiously assumed to have the same diffusivity and porosity as the inner concrete.

Table 5-7. Base-case 1BMA SRF values (-) used for different groups of radionuclides (see Table 5-3) and waste compartments.^a

Compartment	SRF Group						
	1 2 3			4			
	Start SRF ^b	End SRF	End time (AD)	Start SRF	End SRF	End time (AD)	
1	1	1	1	1	1	1	-
2	1	10	1	1	1	1	-
3	1	100	653	1	11 100	141	11 100
4	1	100	842	4	11 400	158	11 400
5	1	1	20	1	5900	18	5900
6	1	1	1661	1	12 500	233	12 500
7	1	100	1	1	-	1	-
8	2	100	32	17	6950	29	6950
9	2	100	60	14	8550	56	8550
10	2	100	455	17	10 700	123	10 700
11	4	100	36	36	-	33	-
12	1	1	7	1	4200	7	4200
13	1	1	1	1	-	1	-
14, 15	1	1	32	1	6950	30	6950

^a SRF Group 5 has SRF = 1 in 1BMA throughout the assessment period.

^b The SRF value varies linearly between the given start (at closure) and end SRF and becomes constant (= end SRF) after the given end time.

Cracks

In the 1BMA model, the transport through cracks in the concrete barriers is modelled explicitly. The slab is cautiously assumed to be cracked directly after closure. The side walls (both the inner and outer parts), slab and lid of all waste compartments in 1BMA are modelled using cracks after the concrete structure transitions from the moderately degraded to the severely degraded physical degradation state, see Figure 5-8 and Tables 5-1 and 5-6.

Analytical estimate of residence time

The 1BMA residence time is estimated from Equation E-15, where, as for the silo (Section 5.3.2), the diffusive resistance of waste packages is neglected. All factors included in the total effective volume flow rate in 1BMA (the denominator in Equation E-15) are plotted in Figure 5-8a.

Figure 5-8a shows that either the diffusive resistance (here the inverse, $1/R_{\text{barrier}}$, is shown) or the groundwater flow through the waste (Q_{waste}) can limit the release of radionuclides. At the beginning of the assessment period (intact concrete and submerged conditions), water flow through the concrete structure is very low (0.1 % of max flow) and diffusion is the dominating transport mechanism

($1/R_{\text{barrier}} > Q_{\text{waste}}$). As the shoreline advances past the repository and the concrete degrades, water flow increases and, at 3000 AD, the advective transport becomes equally important as the diffusive transport ($1/R_{\text{barrier}} \approx Q_{\text{waste}}$). At 22 000 AD, the severely degraded physical degradation state results in increasing water flow through the waste making advection the dominating radionuclide transport mechanism. When the concrete structure eventually reaches its completely degraded state at 52 000 AD and the effective diffusivity of radionuclides in the concrete structure increases, diffusion again becomes the dominating transport mechanism. Groundwater flow through the vault, Q_{vault} , is larger than that through the waste because the former includes flow through the relatively permeable backfill (Figure 5-8a).

In order to estimate the residence time, the combined capacity of the waste and the concrete structure needs to be estimated (Equations 4-2 and E-14). This combined capacity depends on the sorption properties of the cementitious materials, which, in turn, depend on the evolution of the concrete (Figure 5-8b).

The residence time in 1BMA for selected radionuclides is shown in Figure 5-8c. The residence time decreases after 3000 AD for all radionuclides and is due to the increased flow of water through the waste caused by the shoreline movement and degradation of the hydraulic properties of the concrete structure. The residence times for Ni-59 and C-14-inorg increases at 12 000 AD, which can be explained by the increased capacity (Figure 5-8b) which is due to the increase in K_d values for nickel and C-14-inorg.

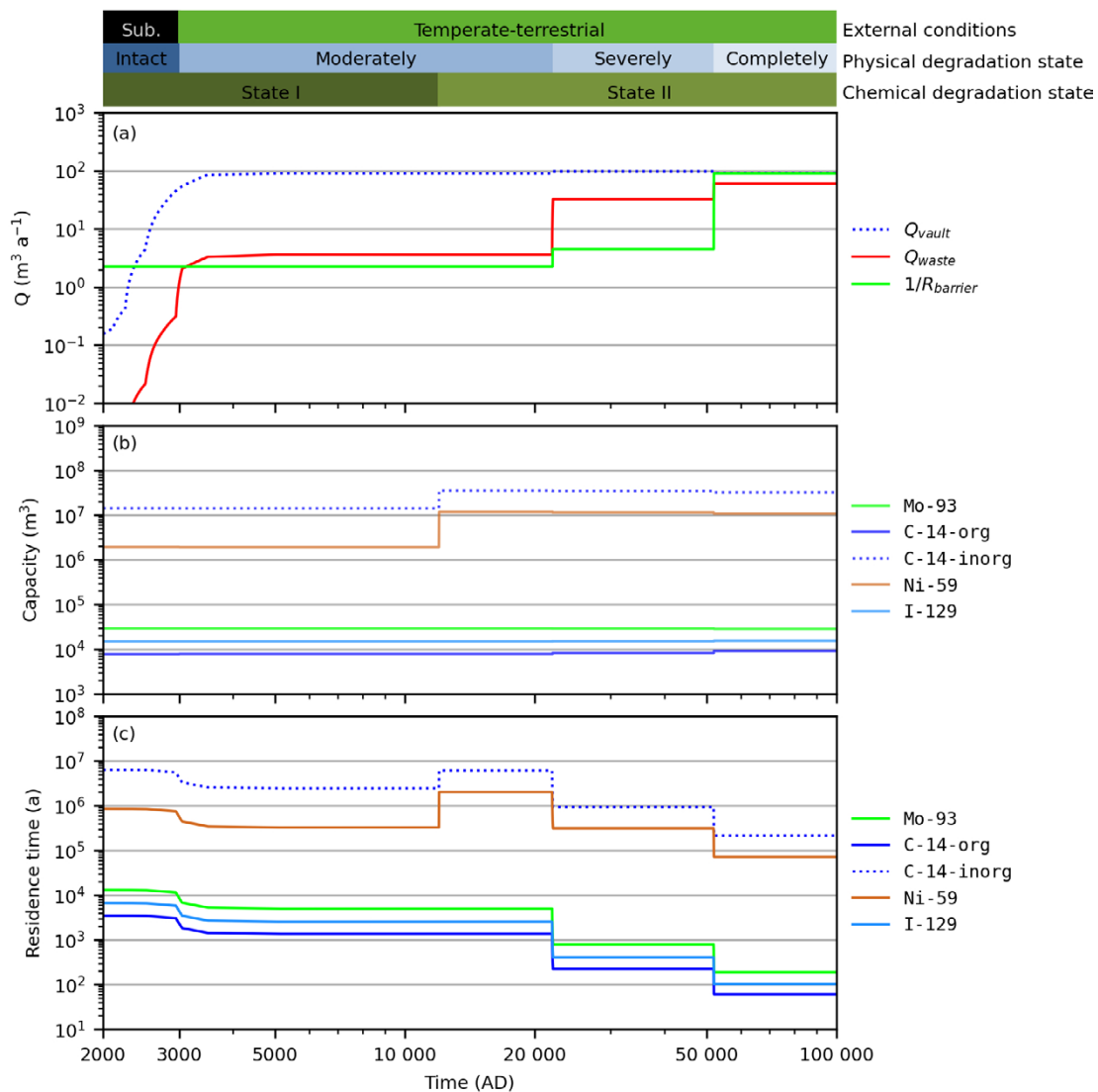


Figure 5-8. (a): Water flow through the waste Q_{waste} , and inverse diffusive resistance of the concrete structure R_{barrier} as a function of time. R_{barrier} is defined in Equation E-13 Q_{vault} is the flow through the whole 1BMA vault including the backfill. (b): The combined capacity of the waste and the concrete structure for select radionuclides as a function of time. (c): Residence times in the 1BMA vault as functions of time. Coloured horizontal bars (top) as in Figure 5-3.

For radionuclides that are non- or very weakly sorbing onto cement, e.g. C-14-org, a porosity increase slightly increases the capacity, seen at 22 000 AD and 52 000 AD in Figure 5-8b. Conversely, the capacity of sorbing radionuclides such as Ni-59 and C-14-inorg decrease at the same time points due to porosity increase. The small capacity change has an insignificant impact on the residence time, but the increased flow through the waste at 22 000 AD and the increased effective diffusivity of radionuclides in the concrete structure at 52 000 AD have a large impact (Figure 5-8c).

As seen in Figure 5-6, water flow differs between the waste compartments. In addition, the types of waste packages and their cement content differs between compartments (**Initial state report**). For compartments with low flow and high cement content, the residence time is greater compared to compartments with high flow and low cement content.

Annual release from the near-field from 1BMA

The total annual activity releases from 1BMA, as calculated by probabilistic radionuclide transport simulations, are shown in Figure 5-9. The 1BMA release curves are similar to those of the silo: the initial increase, as the radionuclides travel through the near-field, is followed by a decrease due to depletion and decay. Three exceptions are the sorbing radionuclides C-14-inorg, Tc-99 and Ni-59, whose release rates are strongly affected by the concrete evolution. The release is initially dominated by weakly sorbing radionuclides with a large inventory, i.e., C-14-org and Ag-108m. The release of these radionuclides typically peaks within a few thousand years. The sharp peak of C-14-inorg at 3000 AD is due to a combination of increased water flow as the concrete changes its physical degradation state and the presence of cracks in the slab. After a few thousand years, the release is dominated by more strongly sorbing radionuclides with larger inventories such as C-14-inorg and Ni-59. During the latter part of the assessment period, i.e. after 52 000 AD, the release is dominated by long-lived, strongly sorbing radionuclides such as Ni-59, whose releases are delayed due to sorption but which still remain with significant activity in the vault.

When compared with the silo, the releases from 1BMA change more irregularly with time, resulting in less smooth shapes of the curves in Figure 5-9 than in Figure 5-4 for the silo. This difference is explained by a more variable evolution of the residence time for 1BMA than for the silo (cf. Figures 5-3 and 5-8).

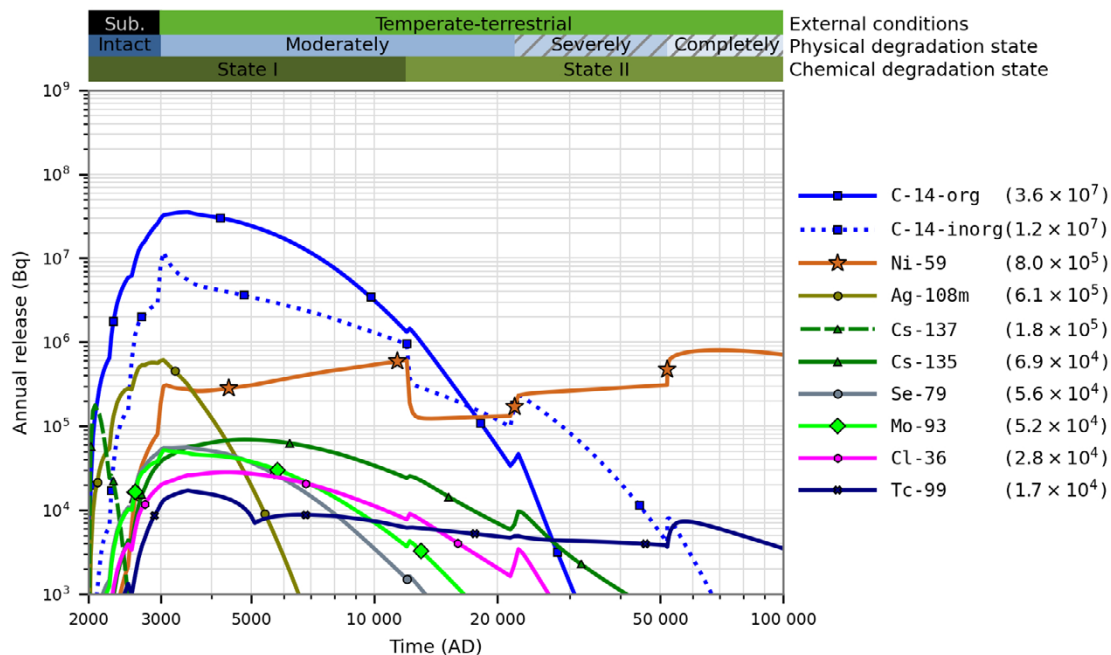


Figure 5-9. Annual activity releases (Bq) from 1BMA in the base case. Only the 10 radionuclides with the highest annual release are shown. The annual release maxima (Bq) are shown in parentheses in the key. Coloured horizontal bars (top) as in Figure 5-3; hatched pattern indicates explicitly modelled barrier crack flow.

As for the silo, the chemical concrete degradation has some impact; the transition to chemical cement degradation state II at 12 000 AD induces increased sorption and lower annual releases of nickel and C-14-inorg. Transitions in physical degradation state increase the release of all radionuclides at 22 000 AD and 52 000 AD.

5.3.4 2BMA calculations and results

Handling in the 2BMA model

The 2BMA vault consists of 13 concrete caissons in which waste packages will be emplaced, see Section 3.1. A detailed description of 2BMA is given in the **Initial state report**.

Hydrology

Groundwater flow through the waste is limited by the concrete caissons surrounded by a permeable backfill. In the near-field hydrological model, the different parts of 2BMA are assigned different hydraulic conductivities as shown in Figure 5-10 (Abarca et al. 2020). Table 5-8 shows the evolution of the hydraulic conductivity of the concrete structure surrounding the waste in the *base case*. Inside the concrete structure, a higher conductivity is applied based on the average conductivity of the waste packages and the inner walls.

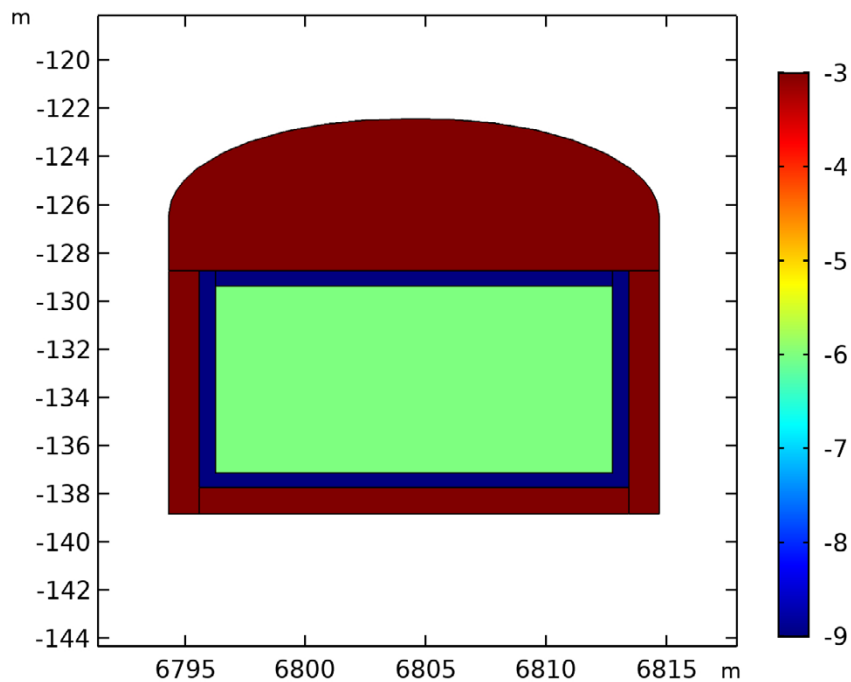


Figure 5-10. Cross section of the 2BMA vault showing the logarithm $\log_{10}(K)$ of the hydraulic conductivity K (m/s) (colour scale) for the initial state corresponding to the intact concrete physical degradation state (Abarca et al. 2020).

Concrete barriers

The evolution of porosity and the effective diffusivity of the concrete caissons in 2BMA are shown in Table 5-8. Like 1BMA, probability density functions with variances that increase with time are assigned to the effective diffusivity (see Chapter 10 in the **Data report**), whereas porosity is treated deterministically.

The same chemical-degradation evolution (pH and sorption coefficients) of the cementitious materials is applied as for the cementitious materials in 1BMA (Table 5-6). Ca-41 is present in large amounts in the decommissioning waste deposited in 2BMA (and 2–5BLA). The sorption of Ca-41 is thus particularly relevant to 2BMA and its sorption coefficients are shown in Table 5-8, see Chapter 7 in the **Data report** for details. No sorption reduction factors are applied in 2BMA in the *base case* due to the assumption of sufficiently low concentrations of complexing agents (Keith-Roach et al. 2021).

Table 5-8. Development of base-case 2BMA barrier-material properties: concrete hydraulic conductivity K , diffusivity D_e , porosity ϕ , and cement sorption coefficient K_d of Ca(II).

Time (AD)	Concrete structure/barrier			Gas evacuation channels	All cement
	K (m s^{-1})	D_e ($\text{m}^2 \text{s}^{-1}$)	ϕ (-)	D_e ($\text{m}^2 \text{s}^{-1}$)	Ca K_d ($\text{m}^3 \text{kg}^{-1}$)
2000–3000	1.00×10^{-9}	3.50×10^{-12}	0.11	3.50×10^{-10}	3.54×10^{-2}
3000–12 000	1.00×10^{-7}	5.00×10^{-12}	0.14	3.50×10^{-10}	3.54×10^{-2}
12 000–22 000	1.00×10^{-7}	5.00×10^{-12}	0.14	5.00×10^{-10}	3.09×10^{-3}
22 000–52 000	1.00×10^{-5}	1.00×10^{-11}	0.18	1.00×10^{-9}	3.09×10^{-3}
52 000–102 000	1.00×10^{-3}	2.00×10^{-10}	0.3	1.00×10^{-9}	3.09×10^{-3}

Cracks

In the 2BMA model, transport through cracks in the side walls, slab and lid of all caissons is explicitly modelled after the concrete transitions from the moderately degraded to the severely degraded physical degradation state at 22 000 AD, see Tables 5-1 and 5-8.

Analytical estimate of residence time

The 2BMA residence time is estimated from Equation E-18, by neglecting the diffusive resistance of waste packages. All factors included in the total effective volume flow rate given in the denominator in Equation E-18 are shown in Figure 5-11a. From this figure it can be seen that the limiting factors for the release of radionuclides can be either the diffusive resistance or the groundwater flow through the waste. At the beginning of the assessment period (intact concrete and submerged conditions), the flow of water through the caissons is very low and diffusion is the dominating transport mechanism ($1/R_{\text{barrier}} > Q_{\text{waste}}$), see also corresponding section for 1BMA. As the shoreline moves past the repository and the concrete degrades, the water flow increases and, at 22 000 AD when the concrete structure is considered to have severely degraded hydraulic properties, advective transport becomes the dominant transport mechanism ($1/R_{\text{barrier}} < Q_{\text{waste}}$). At 52 000 AD, the effective diffusivity of the concrete structure is considered to increase (Table 5-8) and diffusive transport becomes equally as important as advective transport ($1/R_{\text{barrier}} \approx Q_{\text{waste}}$). The vault flow (Q_{vault} in Figure 5-11a) should be greater than the waste flow since it also includes flow through the relatively permeable backfill. However, at 52 000 AD the waste flow in Figure 5-11a becomes higher than the vault flow since water leaving one caisson can enter another caisson and will thus be counted several times.

The residence time (Equation E-18) depends on the combined capacity of the waste and the concrete caissons. This in turn depends on the sorption properties of the cementitious materials that evolve with time as the caissons degrade (Figure 5-11b).

The residence time in 2BMA for selected radionuclides is shown in Figure 5-11c. For these radionuclides, the residence time decreases at 3000 AD mainly due to the increased diffusivity in the concrete caissons. The residence times for Ni-59 and C-14-inorg increase at 12 000 AD due to the increased cement sorption for nickel and C-14-inorg assumed for cement chemical degradation state II at this time, also seen as an increased capacity in Figure 5-11b. For Ca-41 conversely, the sorption is weaker on cement in degradation state II, resulting in a lower capacity and shorter residence time.

For radionuclides that are non- or very weakly sorbing onto cement, e.g. C-14-org, a porosity increase slightly increases the capacity, seen at 22 000 AD and 52 000 AD in Figure 5-11b. Conversely, that the capacity of sorbing radionuclides such as Ni-59 and C-14-inorg decreases at the same time is due to the porosity increase. The small capacity change has an insignificant impact on the residence time, but the increased flow through the waste at 22 000 AD significantly decreases the residence time. The increased diffusivity in concrete at 52 000 AD also causes a decrease of the residence time.

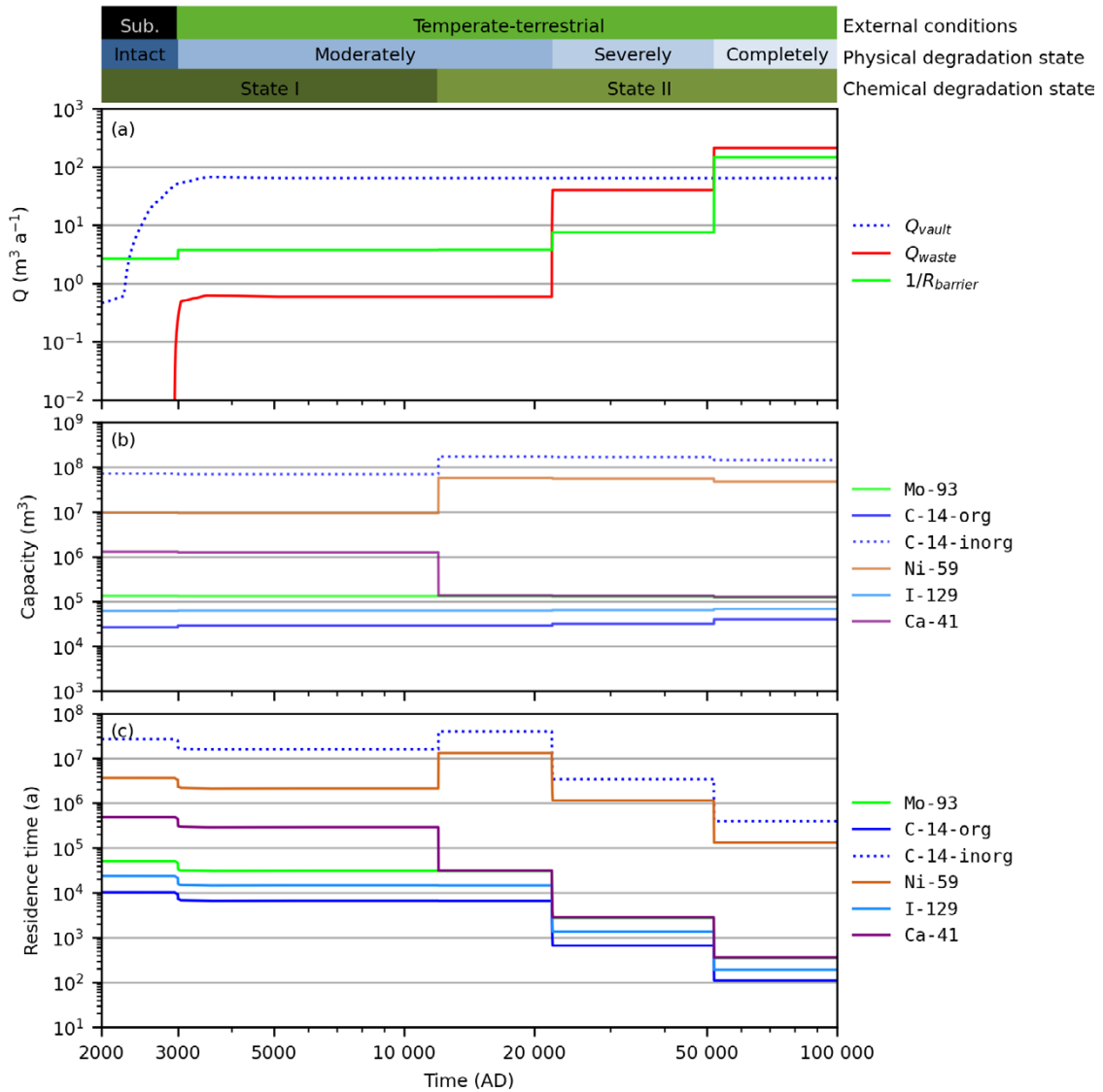


Figure 5-11. (a): Water flow through the waste, Q_{waste} and inverse diffusive resistance of the concrete structure $R_{barrier}$ as a function of time. $R_{barrier}$ is defined in Equation E-16. Q_{vault} is the flow through the whole 2BMA vault including the backfill. (b): The combined capacity of the waste and the concrete caissons for selected radionuclides as a function of time. (c): Residence time in the 2BMA caissons for select radionuclides as a function of time. Coloured horizontal bars (top) as in Figure 5-3.

Annual release from the near-field from 2BMA

The total annual activity releases from the 2BMA vault as calculated by probabilistic radionuclide transport simulations are shown in Figure 5-12. The 2BMA release curves show an initial increase as the radionuclides travel through the near-field, followed by a decrease due to depletion and decay. Exceptions to this general response can be observed for sorbing radionuclides such as Ca-41 and Ni-59 whose releases are strongly affected by the concrete evolution.

The release is initially dominated by weakly sorbing radionuclides with high inventory, i.e., C-14-org, C-14-ind and Ag-108m. The release of these radionuclides typically peaks within a few thousand years. After 22 000 AD, releases are dominated by long-lived, strongly sorbing radionuclides such as Ca-41 and Ni-59, whose releases are delayed due to sorption but they still retain a significant inventory in the vault. Ca-41, originating in cementitious decommissioning waste, is assumed to be present only in 2BMA and 2-5BLA (SKB R-18-07).

The similar concrete evolution displayed by the 2BMA and 1BMA vaults results in similar trends of releases. The sharp breaks in the release curves correlate with changes in residence time, see Figure 5-11c. The transition to chemical cement degradation state II at 12 000 AD in 2BMA, is associated with stronger sorption of Ni and weaker sorption of Ca, decreasing and increasing their annual releases respectively. The higher releases at 22 000 AD and 52 000 AD, are caused by increased groundwater flow due to physical concrete degradation and by increased diffusivity, respectively. The explicit representation of cracks at 22 000 AD amplifies the effect of the increased flow at this time.

5.3.5 1BRT calculations and results

Handling in the 1BRT model

The 1BRT waste vault will contain nine segmented RPVs and some additional steel waste placed in moulds and embedded in concrete. The waste packages will be placed in a concrete structure and surrounded by grout, see Section 3.1. A more detailed description of 1BRT is given in the **Initial state report**.

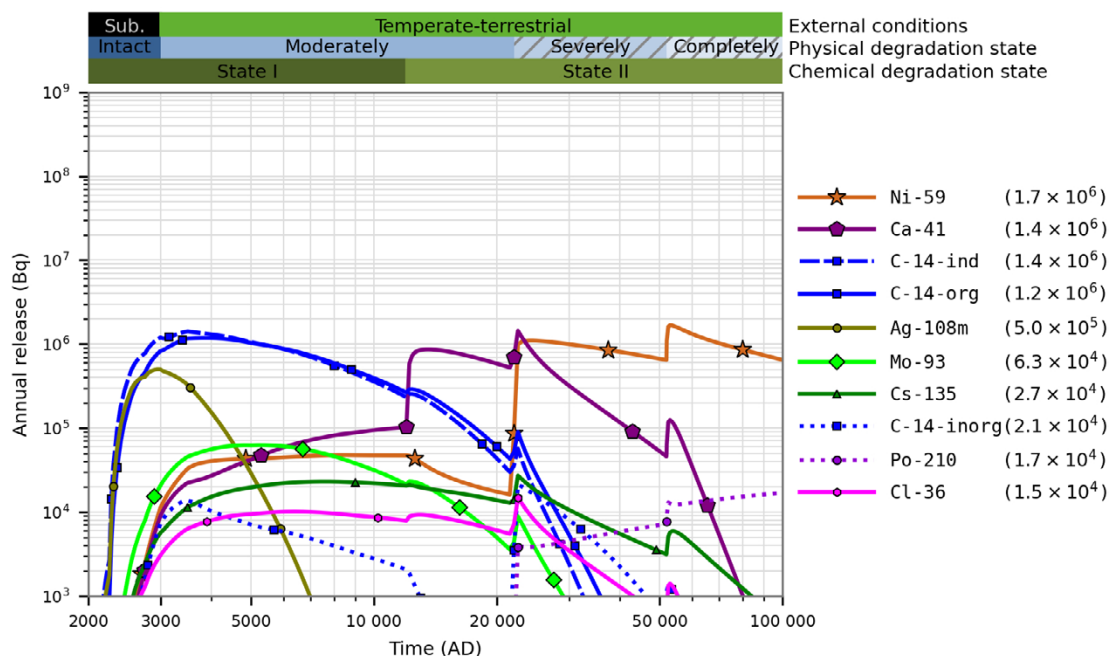


Figure 5-12. Annual activity releases (Bq) from 2BMA in the base case. Only the 10 radionuclides with the highest annual release are shown. The annual release maxima (Bq) are shown in parentheses in the key. Coloured horizontal bars (top) as in Figure 5-9.

Hydrology

In the 1BRT near-field hydrological model, the different parts of the vault are assigned different hydraulic conductivities as shown in Figure 5-13 (Abarca et al. 2020). Table 5-9 shows the evolution of the hydraulic conductivity of the concrete structure and its interior in the *base case*.

Concrete barriers

The concrete evolution in 1BRT is similar to that of 1BMA. The porosity and effective diffusivity of the concrete structure in 1BRT are shown in Table 5-9. The effective diffusivities are given by probability density functions with variances that increase with time (see Chapter 10 in the **Data report**), while porosity is treated deterministically. The applied evolution of pH as well as the sorption coefficients of selected radionuclides for the cementitious materials are also shown in Table 5-9. These data are described in detail in the **Data report**. The K_d of induced carbon-14 (C-14-ind) is set to zero $\text{m}^3 \text{kg}^{-1}$.

1BRT contains purely metallic waste, so sorption reduction factors are not applied due to the absence of complexing agents.

Table 5-9. Development of base-case 1BRT material properties: concrete hydraulic conductivity K , diffusivity D_e , porosity ϕ , pH and cement sorption coefficient K_d for selected radionuclides.

Time period (AD)	Concrete structure		Concrete structure and waste domain ^a	Waste	All cement			
	D_e ($\text{m}^2 \text{s}^{-1}$)	ϕ (-)	K (m s^{-1})	ϕ (-)	pH	K_d ($\text{m}^3 \text{kg}^{-1}$)		C-inorg
						Mo	Ni	
2000–4000	5.00×10^{-12}	0.14	1.00×10^{-4b}	0.3	> 12.5	3.00×10^{-3}	2.68×10^{-1}	2.0
4000–12000	5.00×10^{-12}	0.14	1.00×10^{-4}	0.3	ca 12.5	3.00×10^{-3}	1.66	5.0
12000–22000	5.00×10^{-12}	0.14	1.00×10^{-4}	0.4	ca 12.5	3.00×10^{-3}	1.66	5.0
22000–52000	1.00×10^{-11}	0.18	1.00×10^{-4}	0.5	ca 12	3.00×10^{-3}	1.66	2.0
52000–87000	2.00×10^{-10}	0.3	1.00×10^{-3}	0.5	ca 12	3.00×10^{-3}	1.66	2.0
87000–102000	2.00×10^{-10}	0.3	1.00×10^{-3}	0.5	ca 10.6	0.00	1.66	7.0×10^{-1}

^a Average hydraulic conductivity of the concrete structure surrounding the waste and its interior (**Data report**).

^b As the concrete structure in 1BRT is not considered to constitute a hydraulic barrier, it is pessimistically assumed to be severely degraded already from 2000 AD.

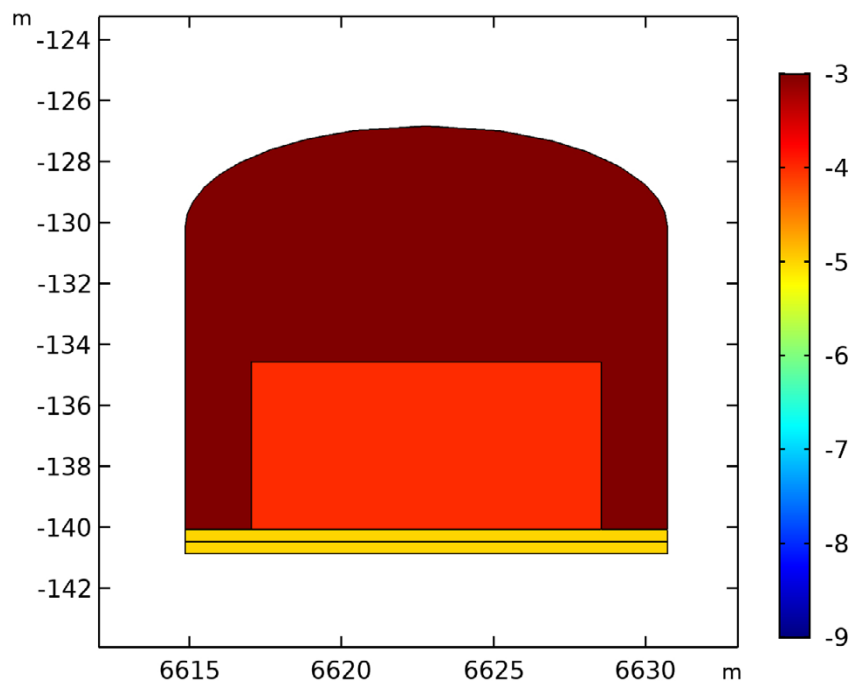


Figure 5-13. Cross section of the 1BRT vault showing the logarithm $\log_{10}(K)$ of the hydraulic conductivity K (m/s), (colour scale) for the severely degraded physical degradation state (Abarca et al. 2020).

Cracks

The concrete structure in 1BRT is not considered to constitute a hydraulic barrier and is assumed to be in the severely degraded physical degradation state directly after closure (**Post-closure safety report**, Chapter 7). In addition, cracks are already included explicitly in the model at the beginning of the assessment period.

Corrosion-controlled release

Metallic waste can exhibit both surface-contamination activity, which is cautiously assumed to be released immediately at the start of the assessment period, as well as irradiation-induced activity which is gradually released as the metal corrodes (**Post-closure safety report**, Section 6.2.8). A slow corrosion-controlled release of irradiation-induced radionuclides in steel from reactor pressure vessels is accounted for in the modelling (the activity in the extra RPV lids that are currently stored in 1BTF and on the Ringhals site is pessimistically assumed to be released immediately after closure).

The corrosion is considered to progress at a constant anoxic-corrosion rate (Chapter 5 in the **Data report**), and the activity is considered to be evenly distributed within the metal (Section 4.2.2), so the release rate is constant during the period. The rates are based on statistical analyses of literature data resulting in a log-normal distribution with a mean value of $0.025 \mu\text{m a}^{-1}$ for carbon steel under high pH conditions (Table 5-13 in the **Data report**). This distribution is applied in the probabilistic radionuclide transport calculations.

Based on the amount of concrete in 1BRT, a decreasing pH evolution is applied according to Table 5-9. Although the corrosion rates are expected to remain low even as the pH approaches ~ 9 , the distributions of rates for near-neutral, anoxic conditions are pessimistically applied from 22 000 AD, during this period a log-triangular distribution with a mode value of $10 \mu\text{m a}^{-1}$ is applied (Table 5-14 in the **Data report**). Note that the pessimistic corrosion-rate increase at 22 000 AD results in complete corrosion and dissolution of all induced activity within a few thousand years thereafter. Nevertheless, the speciation of radionuclides is still assumed to follow the reference redox evolution based on the more realistic expectation that metallic steel is present over the entire assessment period (Section 6.3.8 in the **Post-closure report**).

Analytical estimate of residence time

The transport of radionuclides from the irradiation-activated steel waste (segmented RPVs) to the backfill surrounding the concrete structure can be considered as a two-step process. The first step is the corrosion-controlled release of radionuclides from the RPV steel to the embedment material (grout) within the waste packages (moulds) and the grout surrounding the waste packages. The transport resistance of the waste package itself is neglected, as is the resistance of the grout. The second step is the migration of radionuclides through the concrete structure to the surrounding backfill. For the fraction of the inventory that is assumed to be instantaneously released from the waste, only the second step is relevant. As the radionuclides reach the backfill, they will be transported further by the groundwater flowing into the host rock.

The residence time for radionuclides in the grout surrounding the RPV (both embedment material within the waste moulds and the grout surrounding the moulds) and concrete structure is estimated using Equation E-21. All factors included in the total effective volume flow rate (Equation E-21) are plotted in Figure 5-14a. From Figure 5-14a it can be seen that the limiting factor for the release of radionuclides from the grout surrounding the waste to the vault backfill is either the diffusive resistance of the concrete structure or the groundwater flow through the waste. At the beginning of the assessment period (severely degraded concrete and submerged conditions), groundwater flow through the concrete structure is very low and diffusion is the dominating transport mechanism ($1/R_{\text{barrier}} > Q_{\text{waste}}$ in Figure 5-14a). As the shoreline moves past the repository, groundwater flow increases and, at about 3000 AD, advective transport becomes the dominating transport mechanism ($1/R_{\text{barrier}} < Q_{\text{waste}}$). At 52 000 AD the effective diffusivity of the concrete structure increases and diffusive transport once again becomes the dominating transport mechanism. In addition, flow through the vault, Q_{vault} , is plotted in Figure 5-14a.

The residence time (Equation E-21) also depends on the combined capacity of the waste, grout and the concrete structure, and is, in turn, dependent on the sorption properties of the cementitious materials which evolve in time as they degrade (Figure 5-14b).

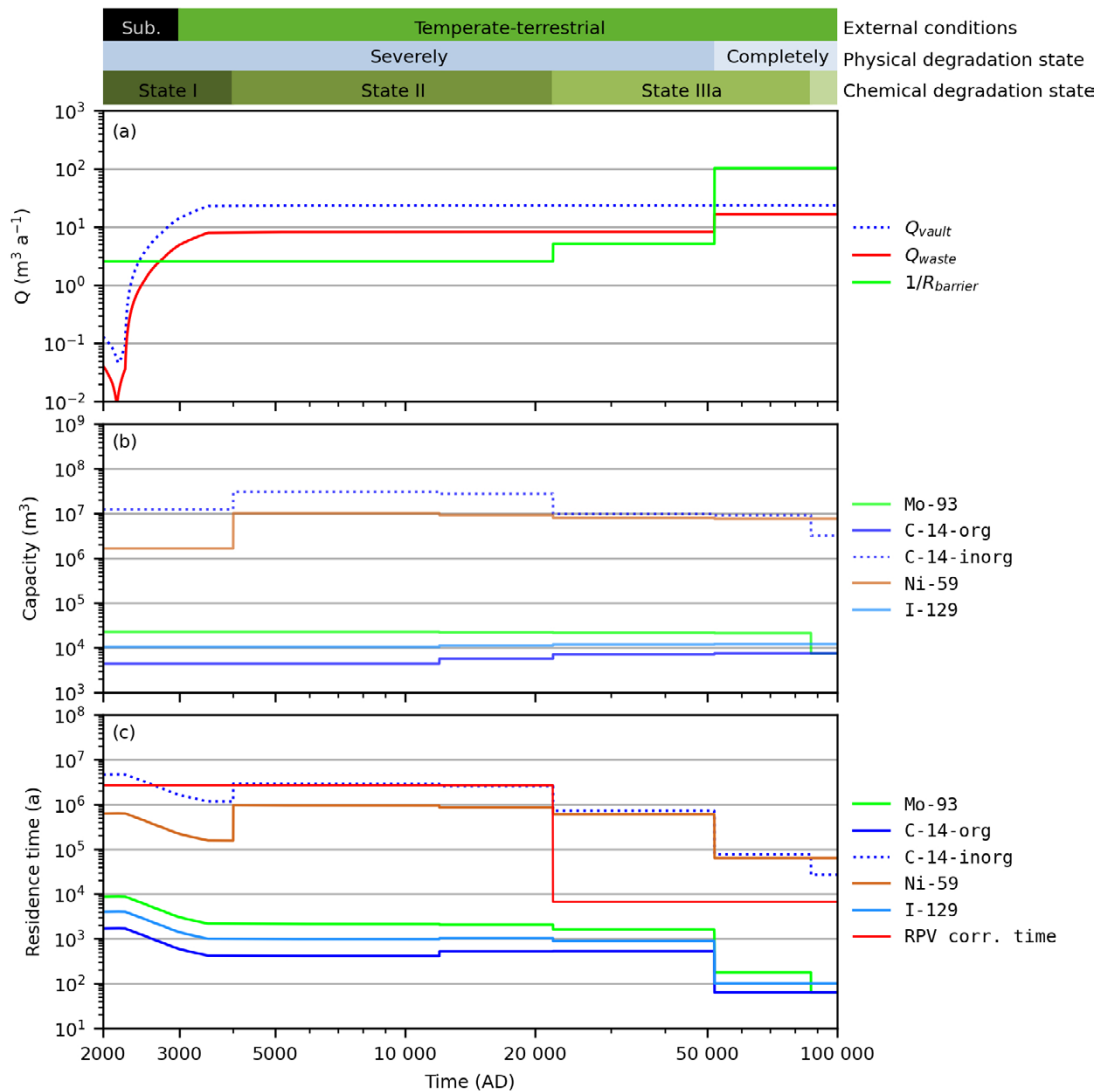


Figure 5-14. (a): Water flow through the waste, Q_{waste} , and inverse diffusive resistance of the concrete structure $R_{barrier}$ as a function of time. $R_{barrier}$ is defined in Equation E-19. Q_{vault} is the flow through the whole IBRT vault including the backfill. (b): The combined capacity of the waste, grout and concrete structure for selected radionuclides as a function of time. (c): Residence time in the grout and concrete structure in IBRT for selected radionuclides as a function of time, the time for complete corrosion of the RPVs is also shown (RPV corr. time). Coloured horizontal bars (top) as in Figure 5-3.

The residence time in IBRT for a few relevant radionuclides is shown in Figure 5-14c together with the time for complete corrosion of the RPV (RPV corr. time). The decrease in corrosion time at 22000 AD is due to a higher corrosion rate, caused by the decrease of pH at this time (see Table 5-9). For corrosion times longer than the residence time, corrosion is the limiting process for the release of induced radionuclides from the vault. This is the case for the weakly sorbing activation products C-14-ind, Mo-93 and Cl-36. For strongly sorbing radionuclides, such as Ni-59, the retention due to sorption is of similar importance as that of corrosion.

In Figure 5-14c, the residence time decreases during the first 2000 years after closure for all radionuclides. This response is explained by an increase in groundwater flow rates caused by the initial shore-line regression. The residence time for Ni-59 increases at 4000 AD due to the increased cement sorption for nickel under cement chemical degradation state II (Table 5-9), also seen as an increased capacity in Figure 5-14b. After 12000 AD, the gradual degradation of the concrete structure and the grout causes a stepwise decrease in capacity and residence time since the chemical degradation affects the K_d values. For example, the K_d value for C-14-inorg decreases with the transition to chemical degradation states IIIa and IIIb at 22000 AD and 87000 AD, respectively. The residence time is further reduced by the increase of the effective diffusivity of radionuclides in the concrete structure at 52000 AD (Table 5-9).

Annual release from the near-field from 1BRT

The total annual activity releases from the 1BRT vault calculated by probabilistic radionuclide transport simulations are shown in Figure 5-15. The 1BRT release curves show an initial increase as the radionuclides travel through the near-field, followed by a decrease due to depletion and decay. An exception is the second peak at 22 000 AD for some radionuclides. This peak coincides with an increase of corrosion rates and altered sorption properties, i.e. the release of C-14-ind and Mo-93 is determined by the corrosion rate.

The release is initially dominated by weakly sorbing radionuclides with a high, instantaneously available, inventory and half-lives longer than a few hundred years, e.g. Ag-108m and C-14-org. The release of these radionuclides typically peaks within a few thousand years. Mo-93, even though mainly induced and with a small instant release, still provides a large contribution to the total release until 5000 AD due to its weak sorption. After 5000 AD, Ni-59 mainly dominates the release. However, C-14-ind released from the corroding RPVs also contributes to the release, especially after 22 000 AD when the corrosion rate of the RPVs increases.

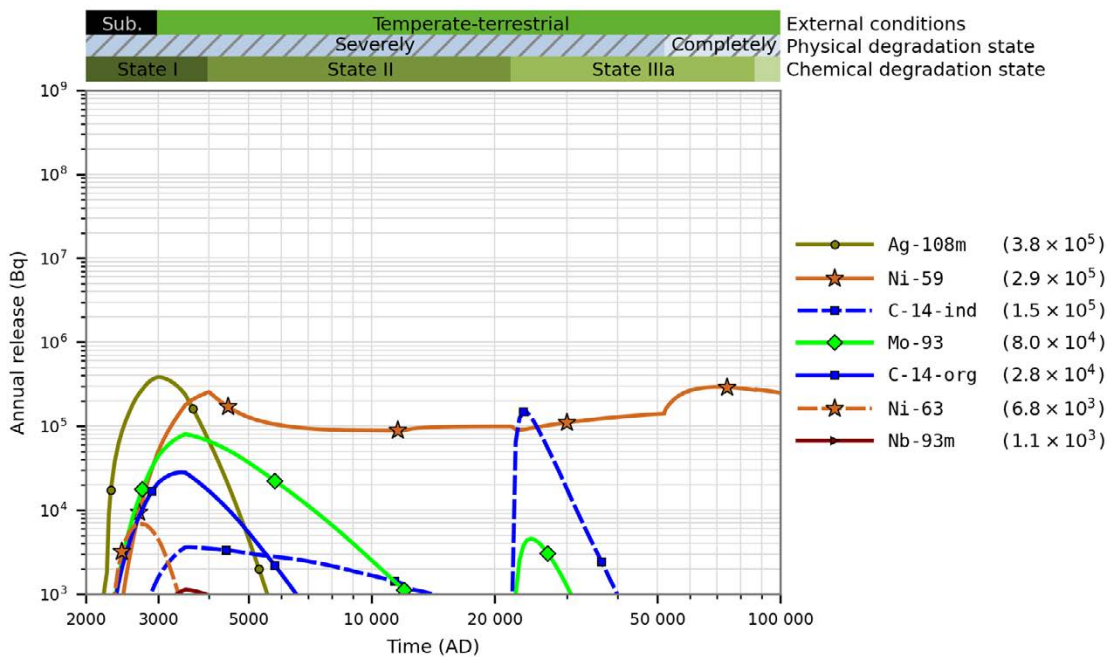


Figure 5-15. Annual activity releases (Bq) from 1BRT in the base case. The annual release maxima (Bq) are shown in parentheses in the key. Coloured horizontal bars (top) as in Figure 5-9.

5.3.6 1–2BTF calculations and results

Handling in the 1–2BTF models

In the BTF vaults, the waste is stored in concrete tanks, drums and concrete moulds. The space between the waste packages, rock walls and the slab is grouted with concrete and a lid of concrete is placed on top of the waste, see Section 3.1. A detailed description of 1BTF and 2BTF is given in the **Initial state report**.

Hydrology

In the 1BTF and 2BTF near-field hydrological models, the different parts of the vaults are assigned different hydraulic conductivities as shown in Figure 5-16 (Abarca et al. 2020). The evolution of the hydraulic conductivity of the concrete tanks, the concrete lid on top of the waste and the concrete slab is shown in Table 5-10. The waste domain is assigned a conductivity based on the average conductivity of the waste packages (tanks) and the grout that surrounds them.

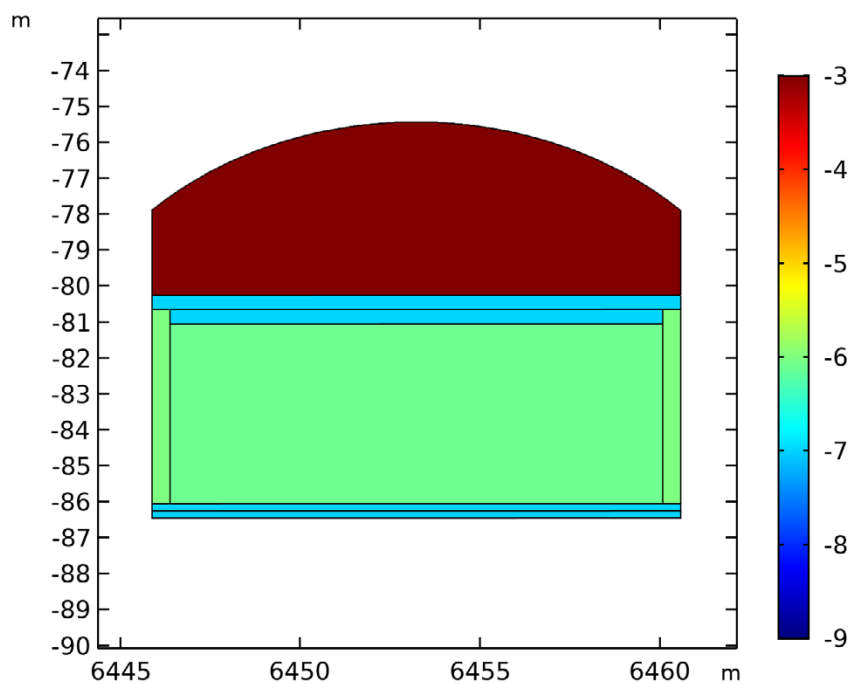


Figure 5-16. Cross section of a BTF vault showing the logarithm $\log_{10}(K)$ of the hydraulic conductivity K (m/s), for the moderately degraded concrete physical degradation state (Abarca et al. 2020).

In the near-field hydrological and radionuclide-transport models, the waste domain (waste packages and grout) is divided into 10 model sections. The groundwater flow through each of these sections for the severely degraded concrete state is shown in Figures 5-17 and 5-18 for the 1BTF and 2BTF vaults, respectively. The corresponding water flow rates through the sections for the completely degraded concrete case are shown in Figure 5-19 and 5-20, respectively. For all concrete degradation states, except for completely degraded concrete, flow through the waste is mainly in the (vertical) z-direction. Different sections have different z-component values of the flow, due to a fracture zone that intersects the vault. For the completely degraded concrete degradation state, flow through the waste is mainly directed along the long side of the vault, i.e., in the y-direction. This is because the concrete no longer constitutes a hydraulic barrier.

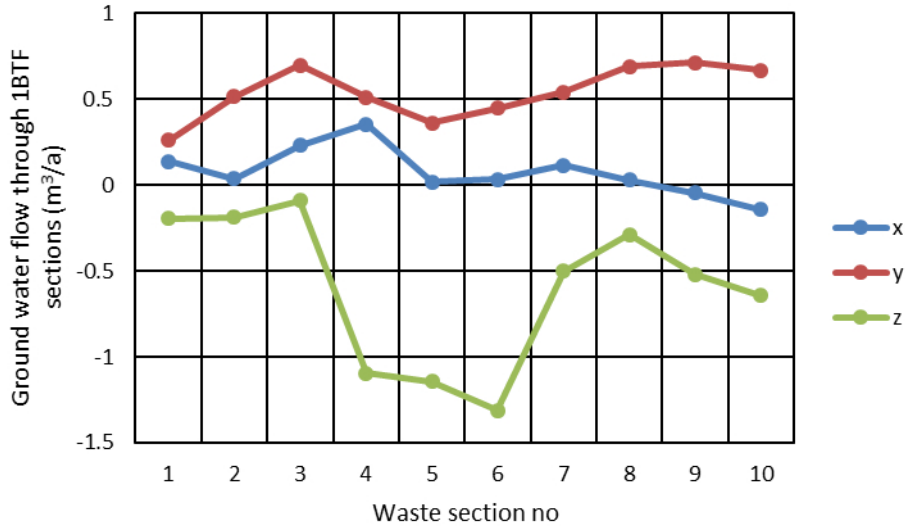


Figure 5-17. Flow through the 10 waste-domain sections in 1BTF for severely degraded concrete and terrestrial conditions, decomposed into three cartesian directions, where y is along the long side of the vault and z is upwards (Abarca et al. 2020).

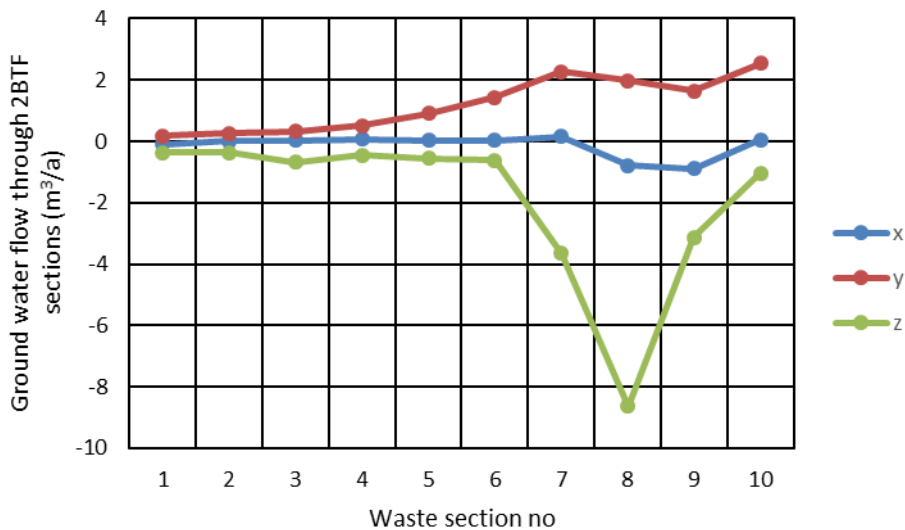


Figure 5-18. Flow through the different waste-domain sections in 2BTF for severely degraded concrete and terrestrial conditions. The y-direction is along the long side of the vault and the z-direction is upwards (Abarca et al. 2020).

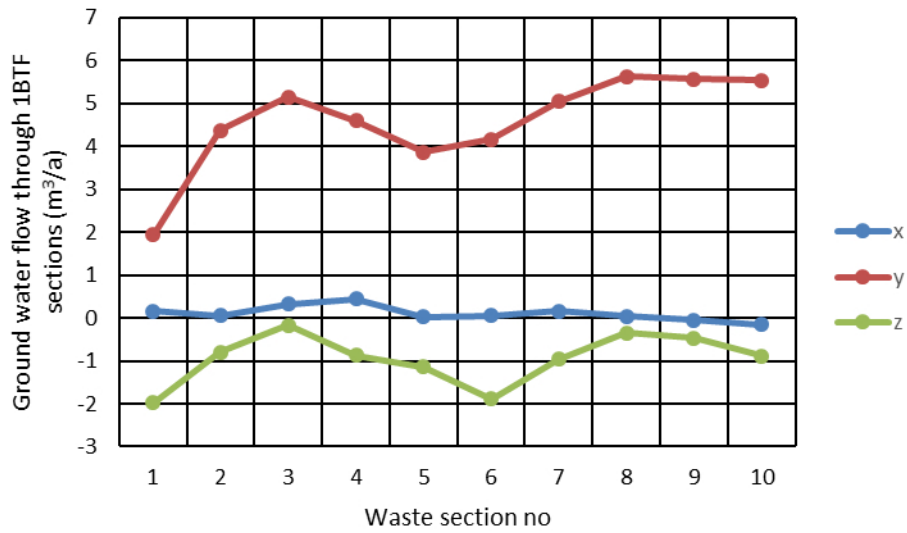


Figure 5-19. Flow through the different waste-domain sections in 1BTF for completely degraded concrete (> 12 000 AD) and terrestrial conditions. The y-direction is along the long side of the vault and the z-direction is upwards (Abarca et al. 2020).

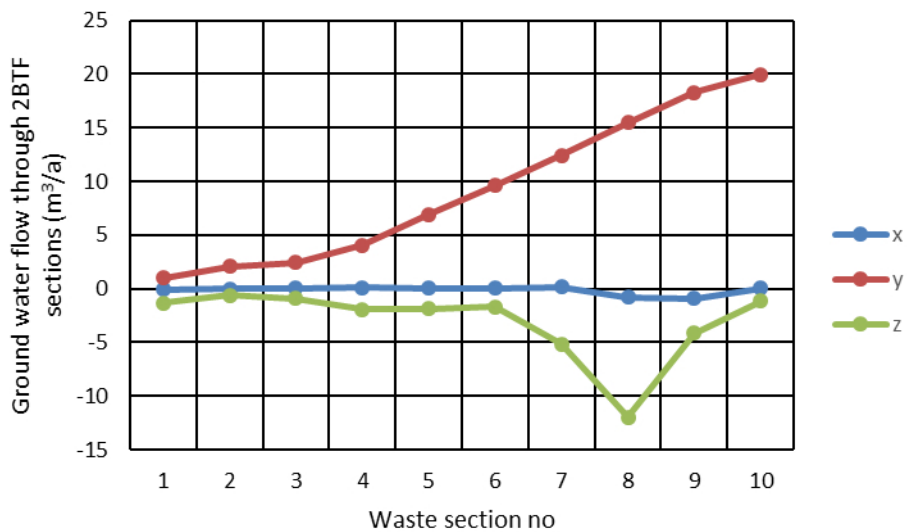


Figure 5-20. Flow through the different waste-domain sections in 2BTF for completely degraded concrete (> 12 000 AD) and terrestrial conditions. The y-direction is along the long side of the vault and the z-direction is upwards (Abarca et al. 2020).

Concrete barriers

The porosity and effective diffusivity of the concrete structures (vault slab and prefabricated lid on top of the waste domain) and concrete tanks in 1–2BTF are shown in Table 5-10. These parameters are treated deterministically. The applied pH evolution and the cement-sorption coefficients for selected radionuclides are also shown in Table 5-10. The SRF used for different groups of radionuclides is shown in Table 5-11. These data are described further in the **Data report**.

Table 5-10. Development of base-case 1–2BTF barrier-material properties: hydraulic conductivity K , diffusivity D_e , porosity ϕ and cement sorption coefficients K_d for selected radionuclides.

Time (AD)	Structural concrete					Waste-domain ^a	All cement			
	All	Vault lid, slab		Concrete tanks			pH	K_d ($\text{m}^3 \text{kg}^{-1}$)		C-inorg
	K (m s^{-1})	D_e ($\text{m}^2 \text{s}^{-1}$)	ϕ (-)	D_e ($\text{m}^2 \text{s}^{-1}$)	ϕ (-)	K (m s^{-1})	Mo	Ni		
2000–2100	1.0×10^{-7b}	3.5×10^{-12}	0.14	3.5×10^{-12}	0.11	6.33×10^{-7}	> 12.5	3.0×10^{-3}	2.68×10^{-1}	2
2100–2500	1.0×10^{-7}	2.0×10^{-11}	0.14	5.0×10^{-11}	0.11	6.33×10^{-7}	> 12.5	3.0×10^{-3}	2.68×10^{-1}	2
2500–3000	1.0×10^{-7}	2.0×10^{-11}	0.14	5.0×10^{-11}	0.11	6.33×10^{-7}	> 12.5	3.0×10^{-3}	2.68×10^{-1}	2
3000–4000	1.0×10^{-5}	2.0×10^{-11}	0.2	5.0×10^{-11}	0.2	6.03×10^{-5}	> 12.5	3.0×10^{-3}	2.68×10^{-1}	2
4000–12 000	1.0×10^{-5}	2.0×10^{-11}	0.2	5.0×10^{-11}	0.2	6.03×10^{-5}	~12.5	3.0×10^{-3}	1.66×10^0	5
12 000–22 000	1.0×10^{-3}	1.0×10^{-10}	0.3	2.0×10^{-10}	0.3	1.00×10^{-3}	~12.5	3.0×10^{-3}	1.66×10^0	5
22 000–52 000	1.0×10^{-3}	5.0×10^{-10}	0.3	8.0×10^{-10}	0.3	1.00×10^{-3}	~12	3.0×10^{-3}	2.68×10^{-1}	2
52 000–58 000	1.0×10^{-3}	5.0×10^{-10}	0.3	8.0×10^{-10}	0.3	1.00×10^{-3}	~12	3.0×10^{-3}	2.68×10^{-1}	2
58 000–102 000	1.0×10^{-3}	5.0×10^{-10}	0.3	8.0×10^{-10}	0.3	1.00×10^{-3}	~10.6	0	2.68×10^{-1}	0.7

^a Average hydraulic conductivity of concrete tanks and surrounding grout (Abarca et al. 2020).

^b All structural concrete is pessimistically assumed to be already moderately degraded from 2000 AD.

Table 5-11. Sorption reduction factors (SRF) used in 1–2BTF for different groups of radionuclides (see Table 5-3) in the base case (Keith-Roach et al. 2021).^a

Vault	SRF Group 3			SRF Group 4		
	Start SRF ^b	End SRF	End time (AD)	Start SRF	End SRF	End time (AD)
1BTF	9	1	2850	8	1	2850
2BTF	6673	1	7600	688	1	7600

^a SRF Groups 1, 2 and 5 have SRF = 1 in 1–2BTF throughout the assessment period.

^b The SRF value varies linearly between the given start and end SRF and becomes constant (= end SRF) after the given end time.

Analytical estimate of residence time

The residence time for radionuclides in 1–2BTF is estimated from Equation E-26 and Equation E-27. The equations are simplifications, because the diffusive transport through the grout on the sides and through the concrete slab is neglected. In addition, the diffusive resistance of the grout surrounding the waste packages is not considered. It is important to emphasise that these simplifications are not made in the radionuclide transport model because the waste package walls are explicitly represented in the radionuclide transport model for the vaults that is used to calculate the release (Åstrand et al. 2022).

A reason for estimating the residence time is to gain a better understanding which transport process dominates and how the properties of different barriers contribute to the retention of radionuclides. This can be done by comparing the different quantities included in Equations E-26 and E-27. All factors included in the total effective volume flow rate (given in the denominator in Equations E-26 and E-27) are plotted in Figures 5-21a and 5-22a for 1BTF and 2BTF, respectively. As shown in Figure 5-22a, the diffusive resistance of the tanks in 2BTF is negligible compared to the diffusive resistance of the lid ($R_{\text{tanks}} \ll R_{\text{lid}}$) and can therefore be disregarded. The concrete tanks in 2BTF exhibit the largest diffusive resistance of all types of waste packages in SFR. Diffusive resistance of other types of waste packages in 1–2BTF are neglected, in the analytical expressions.

Figure 5-22a also shows that the limiting factor for the release of radionuclides from the concrete tanks to the grout surrounding the tanks is the diffusive resistance of the tank walls ($1/R_{\text{tanks}} > Q_{\text{waste}}$). However, for the radionuclides to exit the vault, they must migrate from the grout either transported by the water flow (Q_{waste}) or by diffusion through the concrete lid or slab. This implies that, even though the diffusive resistance of the tanks limits the transport to the grout, it is not the limiting factor for the release of radionuclides from the vault.

During the initial period of submerged conditions, groundwater flow through the waste is very low and diffusion is the dominating transport mechanism within the vault ($1/R_{\text{lid}} > Q_{\text{waste}}$ in Figures 5-21a and 5-22a). As the shoreline moves past the repository and the concrete degrades, groundwater flow increases and, between 2500 AD and 22 000 AD, advective transport becomes the dominating transport mechanism within the vault. However, as the porosity and effective diffusivity of the concrete lid increases after 22 000 AD, the diffusive contribution to transport also becomes significant.

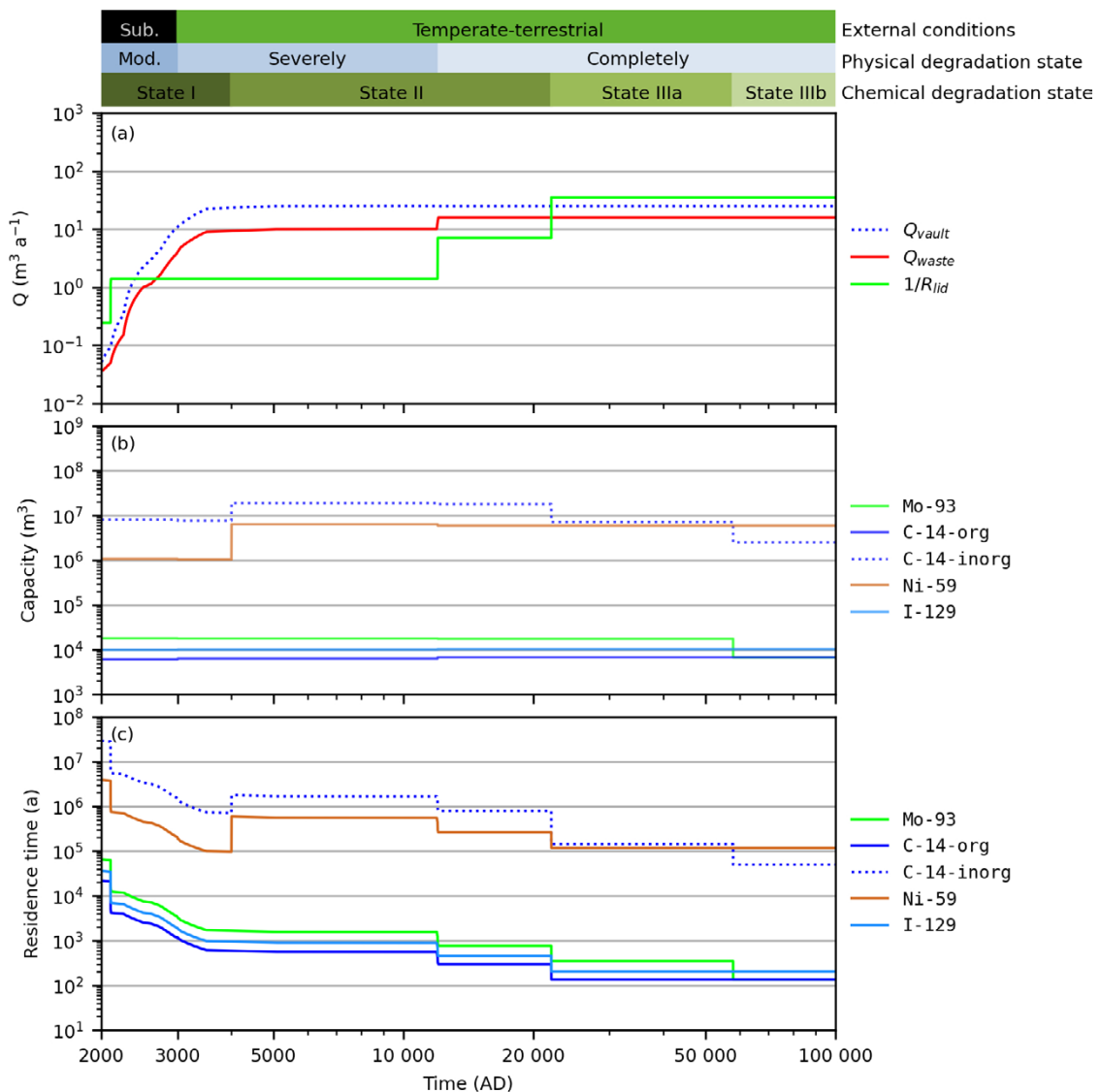


Figure 5-21. (a): Water flow through the waste, Q_{waste} , and inverse diffusive resistance of the concrete lid, R_{lid} for IBTF as a function of time. Q_{vault} is the flow through the whole vault including the backfill. (b): The combined capacity of the waste (the waste packages and the grouting surrounding the packages) and the concrete structures in IBTF for some radionuclides as a function of time. (c): Residence time in IBTF for some radionuclides as a function of time. Coloured horizontal bars (top) as in Figure 5-3.

The residence time in 1–2BTF for a few relevant radionuclides is shown in Figure 5-21c and 5-22c respectively. It can be seen that the residence time decreases by several orders of magnitude until around 3500 AD for all selected radionuclides. The main reason for this is the increased water flow caused by shoreline regression. The increase in residence time at 4000 AD for Ni-59 and C-14-inorg is a result of increased capacity (Figures 5-21b and 5-22b), which in turn is explained by increased cement sorption under cement chemical degradation state II. The capacity of C-14-inorg decreases at chemical degradation states IIIa and IIIb.

The increased effective diffusivity of radionuclides in the concrete lid at 12 000 AD and 22 000 AD in combination with increased porosity in the concrete tanks and concrete structures, cause a stepwise decrease in the residence time.

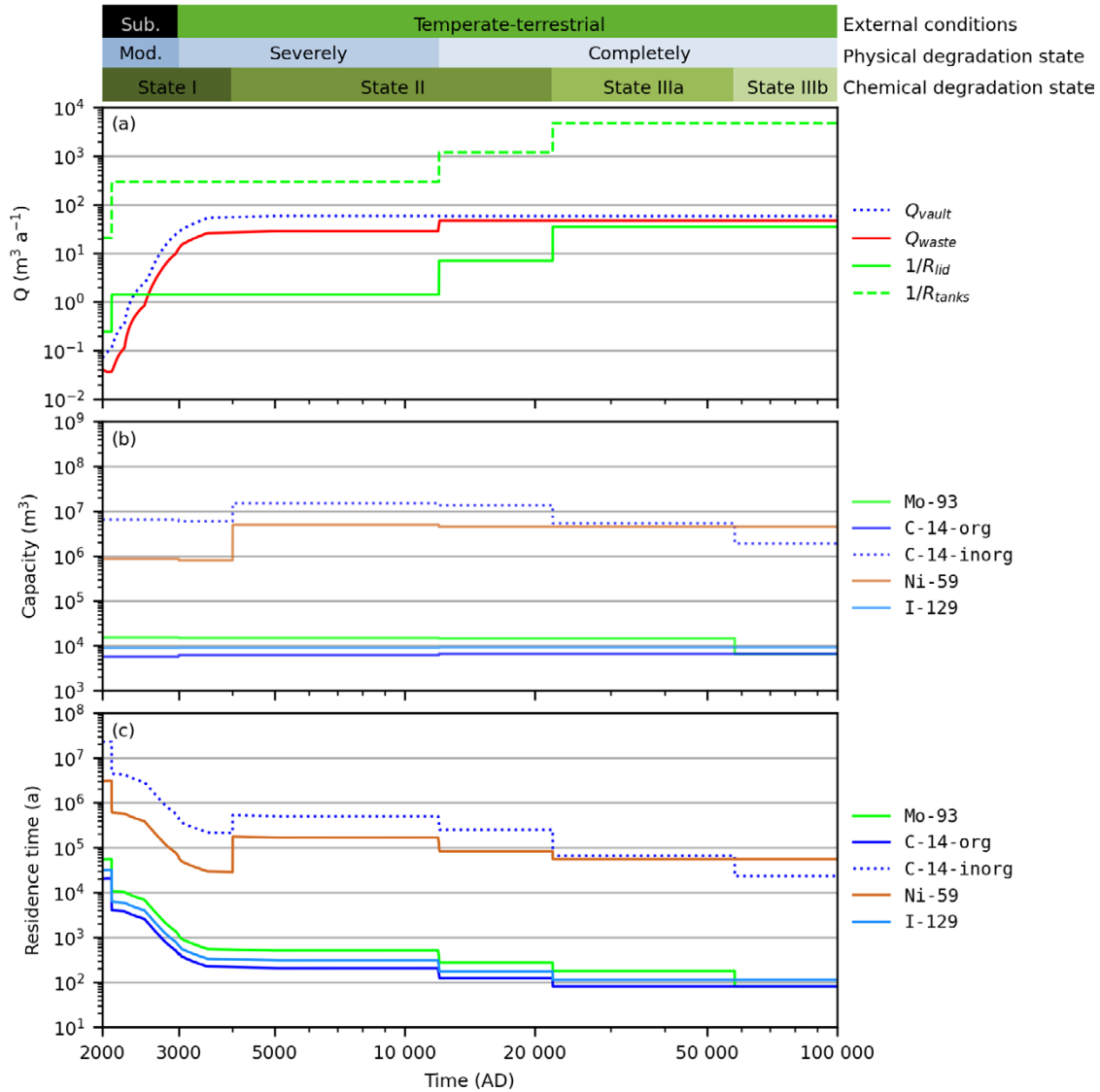


Figure 5-22. (a): Water flow through the waste, Q_{waste} , and inverse diffusive resistance of the concrete lid and tanks, R_{lid} and R_{tanks} respectively for 2BTF as a function of time. R_{tanks} is defined in Equation E-22. Q_{vault} is the flow through the whole vault including the backfill. (b): The combined capacity of the waste (the waste packages and the grouting surrounding the packages) and the concrete structures in 2BTF for some radionuclides as a function of time. (c): Residence time in 2BTF for some radionuclides as a function of time. Coloured horizontal bars (top) as in Figure 5-3.

Annual release from the near-field from 1-2BTF

The total annual activity releases from the two BTF vaults based on probabilistic radionuclide transport simulations are shown in Figures 5-23 and 5-24. The release curves first show an increasing trend as the radionuclides travel through the near-field and then decreasing due to depletion and decay. The sharp breaks in the release curves (Figure 5-21c and 5-22c) are caused by changes in residence time.

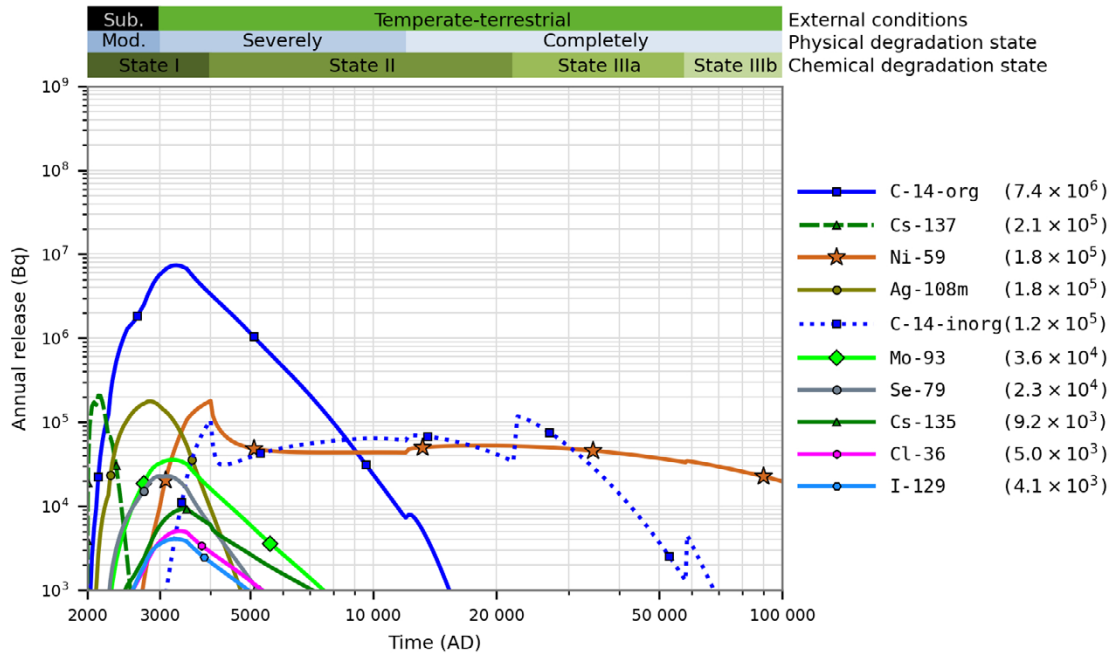


Figure 5-23. Annual activity releases (Bq) from 1BTF in the base case. The annual release maxima (Bq) are shown in parentheses in the key. Coloured horizontal bars (top) as in Figure 5-3.

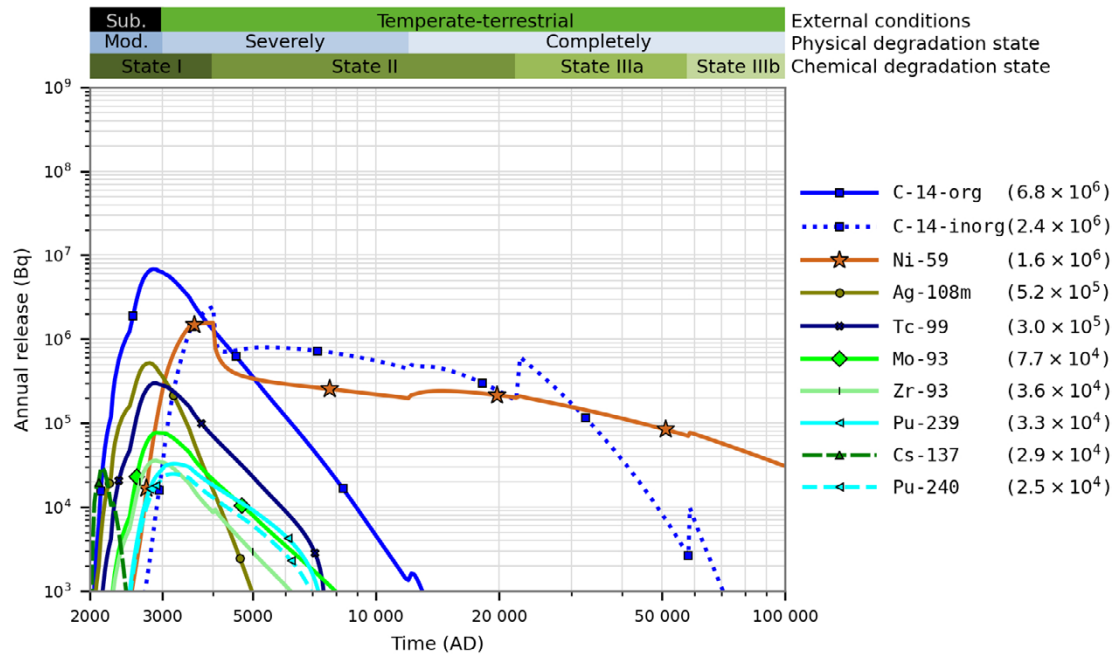


Figure 5-24. Annual activity releases (Bq) from 2BTF in the base case. Only the 10 radionuclides with the highest annual release are shown. The annual release maxima (Bq) are shown in parentheses in the key. Coloured horizontal bars (top) as in Figure 5-3.

The release is initially dominated by weakly sorbing radionuclides with high inventory, i.e., C-14-org and Ag-108m. The release of these radionuclides typically peaks within a thousand years. After a few thousand years, the release is dominated by strongly sorbing radionuclides such as Ni-59 and C-14-inorg. The transition to chemical cement degradation state II occurs at 4000 AD, associated with stronger sorption of Ni and C-14-inorg, decreasing their annual release. Furthermore, transition in physical and chemical concrete degradation states increase the release of all radionuclides at 12 000 AD, 22 000 AD and 52 000 AD.

5.3.7 1–5BLA calculations and results

Handling in the 1–5BLA models

The low-activity waste in 1–5BLA is disposed in ISO-containers, see Section 3.1. A detailed description of 1–5BLA is given in the **Initial state report**.

Radionuclide inventory

As no decision has yet been taken on the distribution of the different waste streams in vaults 2–5BLA, for the modelling, the radionuclide inventory is assumed to be equally distributed between them (**Initial state report**). The radionuclide inventory in 1–5BLA is described in Chapter 3.

Hydrology

In the near-field hydrological models of 1–5BLA, the interior of the vaults is assigned a hydraulic conductivity of 10^{-3} m/s as shown in Figures 5-25 and 5-26 (Abarca et al. 2020). The slabs of the vaults have a lower hydraulic conductivity, but the hydraulic properties of the slabs have an insignificant influence on the total flow through the vaults.

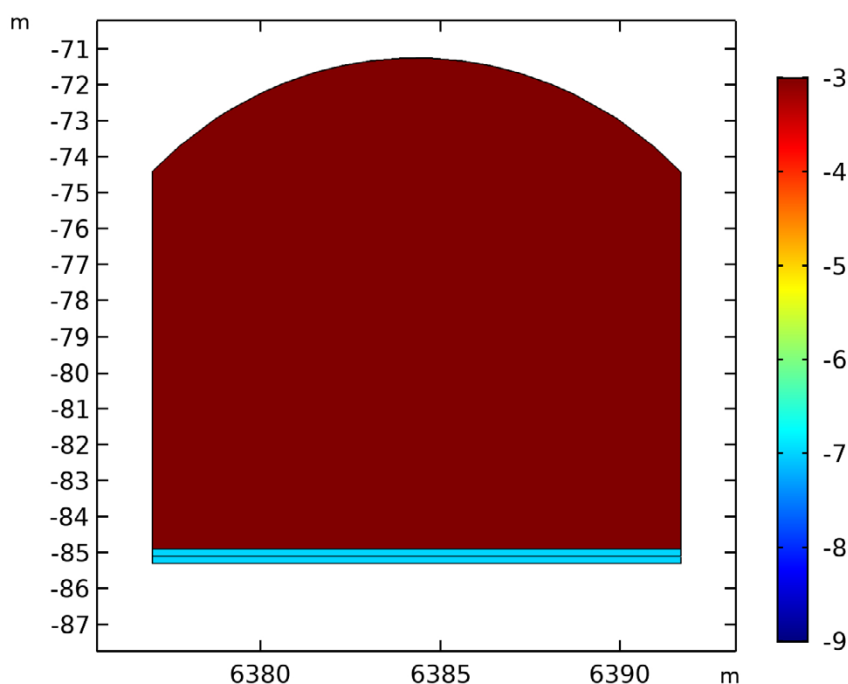


Figure 5-25. Cross section of the 1BLA vault showing the logarithm $\log_{10}(K)$ of the hydraulic conductivity K (m/s), for the moderately degraded concrete physical degradation state (Abarca et al. 2020).

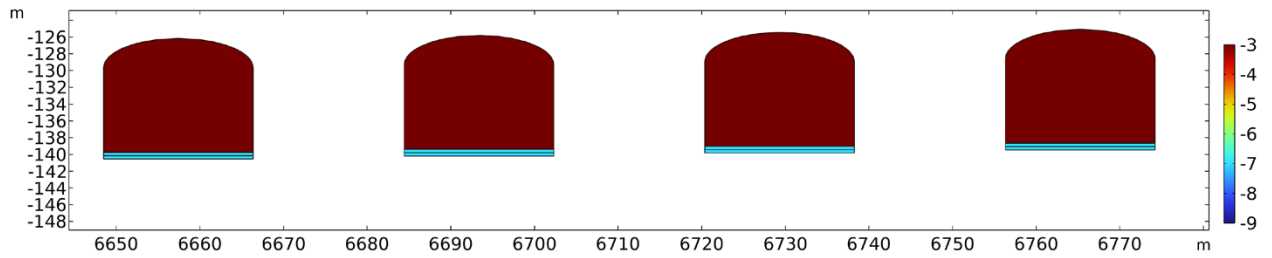


Figure 5-26. Cross section of the (identical) 2–5BLA vaults showing the logarithm $\log_{10}(K)$ of the hydraulic conductivity K (m/s), for the moderately degraded concrete physical degradation state (Abarca et al. 2020).

Engineered barriers

No dedicated engineered barriers are to be installed inside the 1–5BLA vaults and sorption of radionuclides onto waste form and waste packaging is pessimistically disregarded.

Analytical estimate of residence time

The 1–5BLA residence times are estimated from Equation E-28. Porosities of 0.77 and 0.76 are considered for the 1BLA and the 2–5BLA vaults, respectively, and the corresponding total pore volumes are 20 700 m³ in 1BLA and on average 46 400 m³ per vault in 2–5BLA (**Initial state report**). The total flow through the vaults and the corresponding residence times are shown in Figure 5-27. The significant increases in groundwater flow through the vaults after a few hundred years are caused by shoreline regression. An increase in flow decreases the residence time.

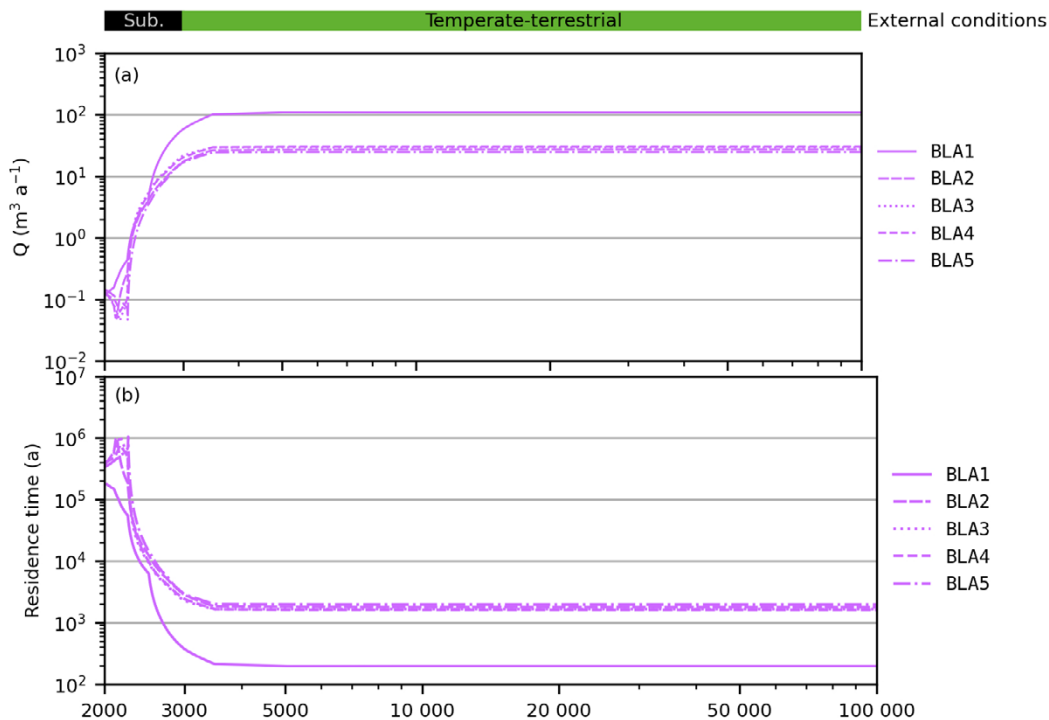


Figure 5-27. (a): Water flow through the 1–5BLA vaults (Q) as a function of time. (b): Residence time in the 1–5BLA vaults as a function of time. All radionuclides have the same residence time because sorption is not considered. Coloured horizontal bar (top) shows the evolution of the external conditions.

Annual release from the near-field from 1-5BLA

The total annual activity releases from the BLA vaults as calculated by probabilistic radionuclide transport simulations are shown in Figure 5-28 and 5-29. Advection is the dominating transport mechanism; initially, radionuclide release rates increase with groundwater flow through the vault, then decrease as the inventory in the vault is depleted through outflow and radioactive decay.

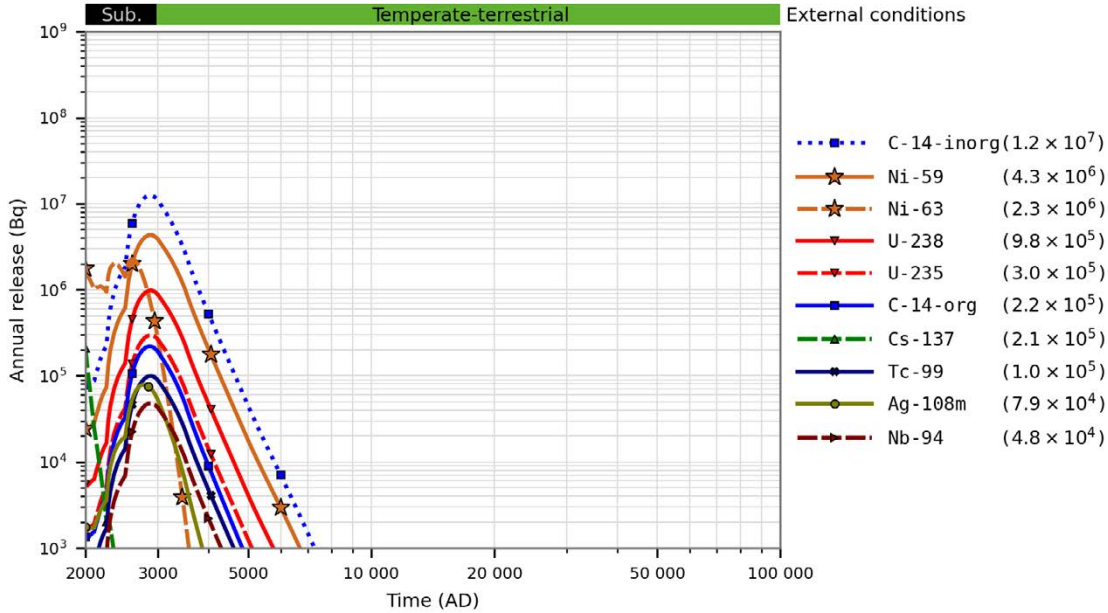


Figure 5-28. Annual activity releases (Bq) from 1BLA in the base case. Only the 10 radionuclides with the highest annual release are shown. The annual release maxima (Bq) are shown in parentheses in the key. Coloured horizontal bar (top) shows the evolution of the external conditions.

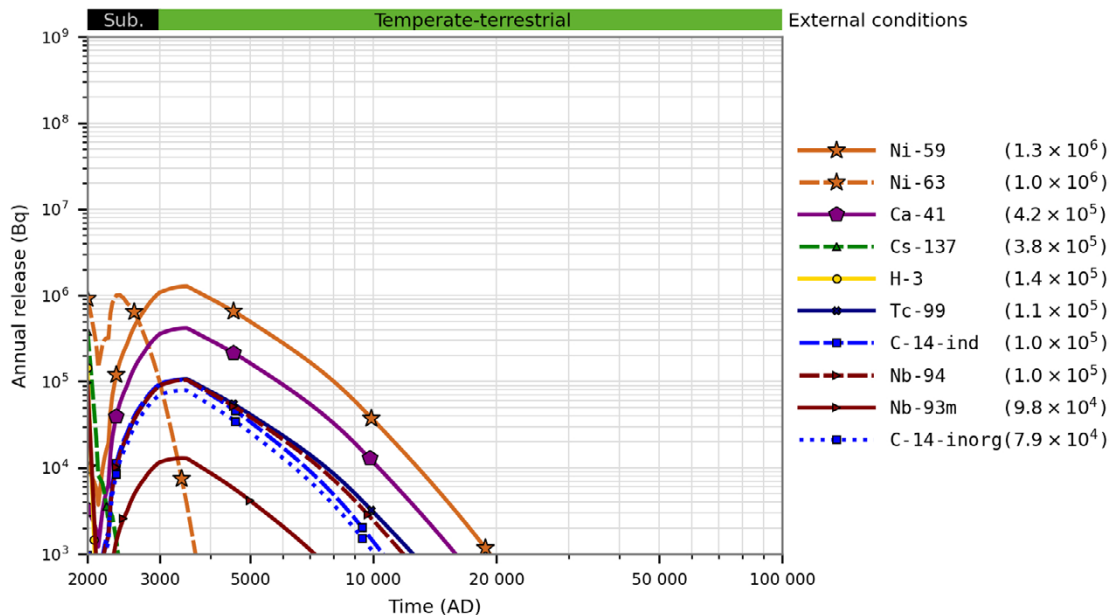


Figure 5-29. Annual activity releases (Bq) from 2BLA in the base case, the annual release from each of the other BLA-vaults in SFR3 is almost identical. Only the 10 radionuclides with the highest annual release are shown. The annual release maxima (Bq) are shown in parentheses in the key. Coloured horizontal bar (top) shows the evolution of the external conditions.

The annual activity release from 1BLA is dominated by the radionuclides with high inventory. For the radionuclides with half-lives longer than 1 000 years, the peak release occurs at approximately 3000 AD when flow through the vault reaches its maximum.

Since 2–5BLA contain identical inventories, the annual activity releases from these waste vaults are essentially the same. Therefore, in Figure 5-29, only the release from 2BLA is shown as a representative for 2–5BLA. The releases are dominated by the radionuclides with high inventory. This includes Ca-41, which is only present in 2–5BLA and 2BMA (SKB R-18-07). Compared with the releases from 1BLA the releases from 2–5BLA are significantly more dispersed in time, due to the lower water flow at the depth of SFR3.

For the radionuclides with half-lives longer than 1 000 years, the releases peak at approximately 3500 AD when the flow through the vaults has reached a maximum.

5.3.8 Vault comparison for key radionuclides

The retention properties vary between vaults and radionuclides and are dependent on the properties of the radionuclides (e.g. speciation) and the barriers (e.g. sorption properties). Retention leads to a reduction of releases over time and reduces the release most effectively for radionuclides with half-lives shorter than the residence time.

The purpose of this section is to assess barrier performance in the *base case* by analysing the near-field releases from each vault for four select radionuclides with different half-lives and sorption properties. The near-field models are developed to take into account the main retention properties of the barriers in the vaults, but some secondary retention properties are neglected. As an example, sorption in the 1–5BLA vaults is neglected due to a lack of dedicated sorption barriers, despite the presence of significant amounts of cement and other sorbents. In addition, the calculated releases are also affected, to varying extents, by the assumptions and degree of pessimism inherent in the input data and model representation of transport processes.

It is thus very important to note that comparisons between calculated vault releases are inherently insufficient for a fair judgement of barrier efficacy (see also Section 2.4.4). For instance, calculated releases from 1–5BLA are probably more overestimated than from other vaults. In consequence, the present comparison serves mainly as an explanation of the results of the radionuclide transport calculations, but not as an accurate comparison of the relative performance of different vault designs (see the **Post-closure safety report**, Chapter 10 for further details). Nevertheless, the results show that even though the vaults have very different inventories of radionuclides, their releases are of similar magnitudes, see below. This indicates that in the *base case*, the barrier performance of each vault is adequate with respect to its inventory, which is one requirement for the overall safety performance of the repository. The effect of the vault-specific releases on the annual dose is documented in Section 5.9.

The set of radionuclides for the vault comparison, chosen to represent both strongly/weakly sorbing and long/short half-life radionuclides, respectively, is shown in Table 5-12.

Table 5-12. Half-life and sorption coefficient, K_d , for cement in chemical degradation state II for key radionuclides included in the vault comparison.

Radionuclide	Half-life (a)	Cement K_d (m ³ /kg)
C-14-inorg	5.70×10^3	5.0
Ni-59	1.01×10^5	1.66
Mo-93	4.00×10^3	0.003
I-129	1.57×10^7	0.001

C-14-inorg

The total activity inventory at closure in each vault is presented and discussed in the **Initial state report**. After closure, the activity starts to decay and some portion is transported out of the vault. Hence, at a given time after closure, the activity can be divided into three groups: still present in the vault, decayed within the vault and escaped from the vault, where the sum of the three groups equals the initial inventory. This distribution is shown in a stacked area chart in Figure 5-30 for C-14-inorg. The opaque areas represent the activity remaining in the vaults, which at 2000 AD adds up to 100 % of the initial activity but then decrease. The pale areas represent the amount of C-14-inorg that has decayed inside each vault, and they grow with time at a rate corresponding to the half-life of C-14. After about half of the assessment period, most C-14-inorg has decayed, as evident from the disappearance of the opaque areas in Figure 5-30. The topmost, white area in Figure 5-30 represents the fraction of C-14-inorg released to the geosphere. This area amounts to less than 1 % of the total activity, and thus shows that the vaults are good at retaining C-14-inorg.

The BLA and 1BRT C-14-inorg activities are too small to be visible in Figure 5-30, so this subset is shown separately in Figure 5-31. The figure shows that, for BLA, the released fraction (white area) is substantially larger than for the vaults presented in Figure 5-30, which have engineered barriers with higher retention capabilities.

Figure 5-32 shows the annual release of C-14-inorg from each vault. The flanking vertical bar on the left y-axis shows the fraction of initial activity in each vault, identical to Figure 5-30 at 2000 AD. The flanking vertical bar on the right y-axis shows the fraction of accumulated activity released from the vaults, corresponding to the white area in Figure 5-30 divided by the contribution from each vault.

As shown in Figure 5-32, the annual release is initially dominated by the release from 1BLA and 1BMA. Comparing the two flanking vertical bars showing initial activity (left y-axis) and accumulated released activity (right y-axis), it is evident that the relative fraction of C-14-inorg released from the different vaults differs from their relative fraction of the initial inventory. For example, the C-14-inorg fraction released from the silo is much smaller than the fraction in the initial inventory thanks to engineered barriers with higher retention capabilities, providing a long residence time in the vault compared to the C-14 half-life. For the same reason, but at the other end of the barrier-sophistication scale, the C-14-inorg accumulated release from 1BLA is large relative to its initial activity in this vault.

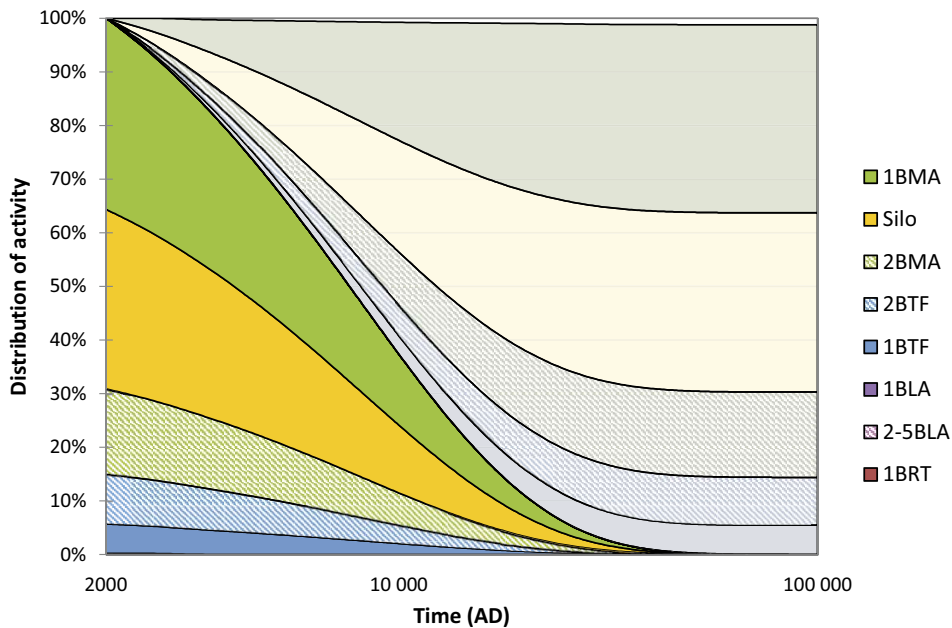


Figure 5-30. Development of the near-field C-14-inorg activity, by vault as a proportion of initial activity in the entire SFR. The opaque areas (left) represent the activity present inside each vault, which at 2000 AD correspond to the full initial inventory of C-14-inorg. The corresponding pale areas in the same vertical order (right) represent the activity that has decayed within the respective vaults. The small white area (top) represents activity that is likely to have escaped the near-field, i.e. neither still retained nor decayed in the vaults.

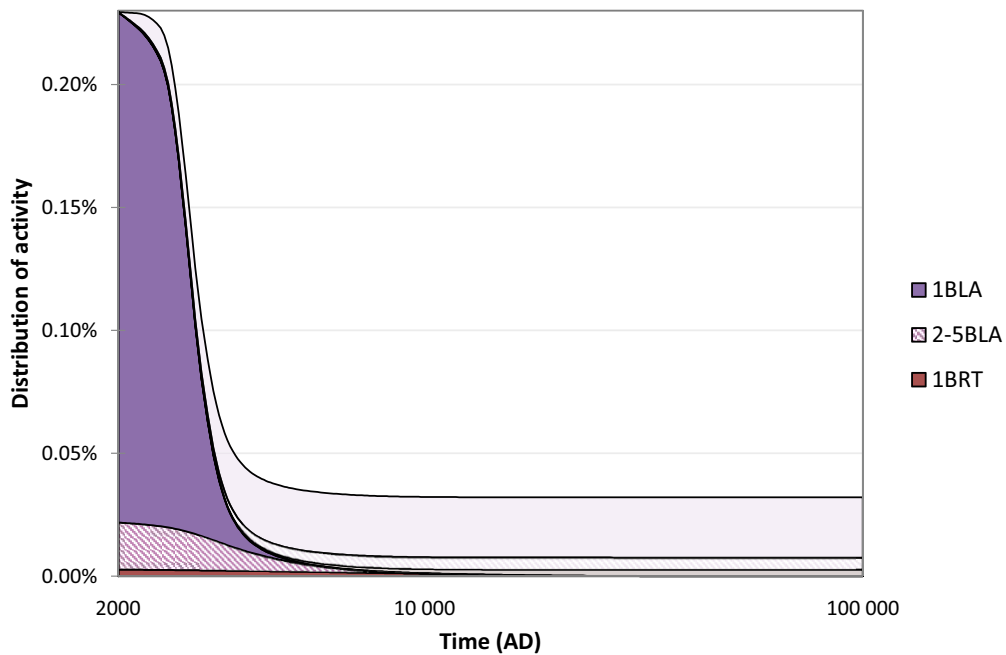


Figure 5-31. Development of the near-field C-14-inorg activity in only the 1–5BLA and 1BRT vaults as a proportion of initial activity in the entire SFR (1BRT barely visible on this scale). The opaque areas (left) represent the activity present inside each vault, which at 2000 AD corresponds to the initial inventory of C-14-inorg in these vaults. The corresponding pale areas in the same vertical order (middle) represent the activity that has decayed within the respective vaults. The white area (top–right) represents activity that has escaped the near-field, i.e. neither still present nor decayed in the vaults.

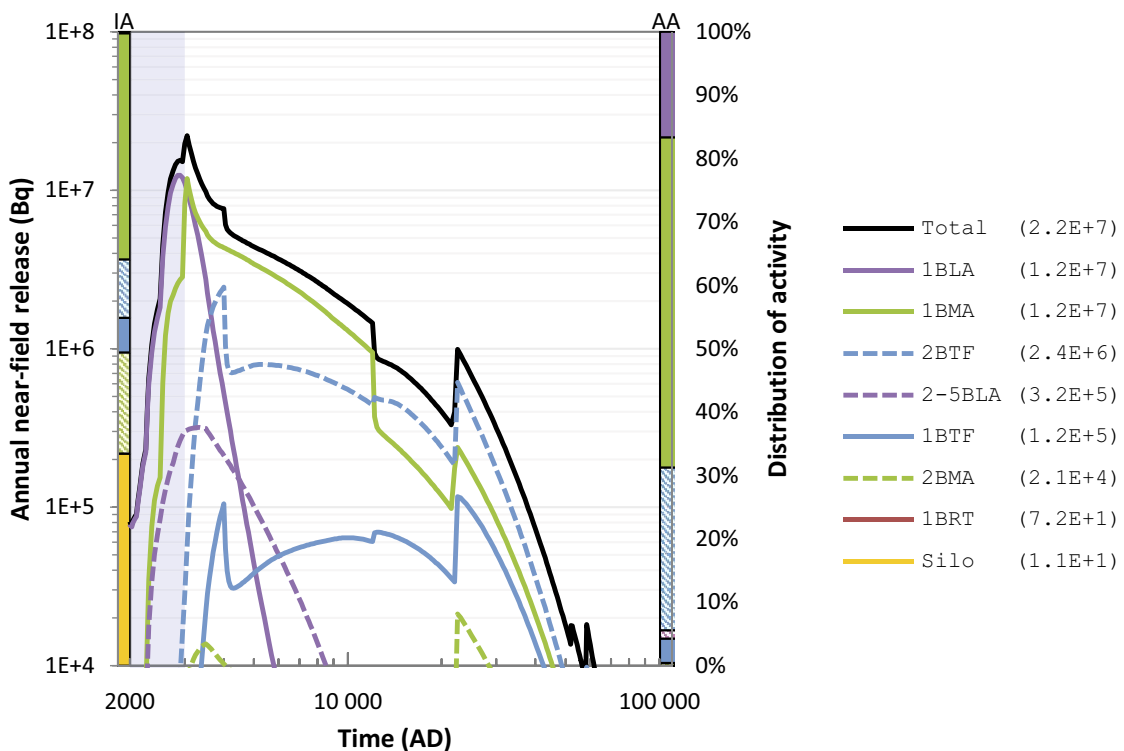


Figure 5-32. Annual activity release of C-14-inorg (Bq, left y-axis) from the entire SFR (black line) and from specific vaults (coloured lines) in the base case. The flanking vertical bars on the left and right represent the distribution of initial activity (IA) between the vaults and of all released activity accumulated over 100 000 years (AA), respectively (right y-axis, colours are the same as those given by the key and the hatched areas in the bar correspond to the dashed lines in the key). The total and vault-specific release maxima are shown in parentheses in the key. The submerged period is illustrated by the blue shading.

Ni-59

Most of the Ni-59 inventory is found in the waste disposed in the silo, 2BMA and 1BMA. As shown in Figure 5-33, most of the Ni-59 disposed in these vaults is expected to remain within the vaults during the whole assessment period. A substantial part of the Ni-59 is expected to decay within the vaults prior to the end of the assessment period and a very small fraction is likely to escape the repository.

The BLA, 1-2BTF and 1BRT Ni-59 activities are too low to be visible in Figure 5-33, so this subset is shown separately in Figure 5-34. The figure shows that, for 1BRT, the decrease in remaining activity (red area) is not fully compensated for by the increase in decayed activity in the vault (pale red-grey area). As a result, the accumulated release to the geosphere (white area) at the end of the assessment period amounts to less than 25 % of the initial inventory of Ni-59 in 1BRT, 1-2BTF and 1-5BLA.

Even though the silo, 1BMA and 2BMA vaults contain most of the Ni-59 inventory, the total annual release of Ni-59 is not exclusively dominated by the releases from these vaults as shown in Figure 5-35. As a consequence, the relative fraction of Ni-59 released from the silo is substantially smaller than its relative fraction in the initial inventory, as is evident from comparing the left and right y-axis flanking vertical bars in Figure 5-35.

The reason for the good Ni-59 retention ability of the silo, 1BMA and 2BMA vaults is that this radionuclide sorbs strongly to both cement and bentonite, resulting in long residence times in these vaults.

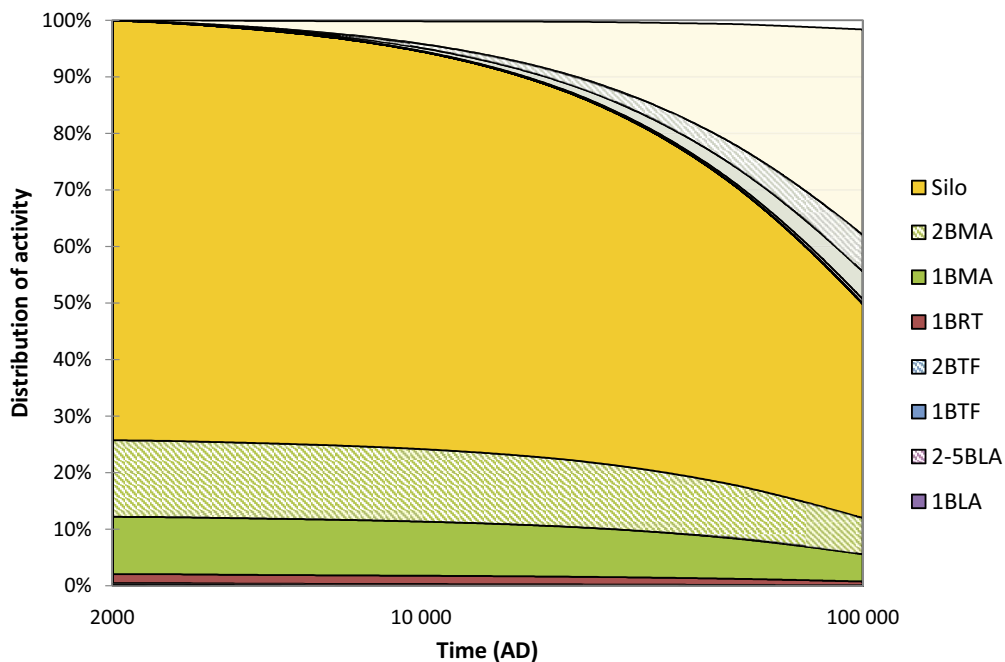


Figure 5-33. Development of the near-field Ni-59 activity, by vault as a proportion of initial activity in the entire SFR. The opaque areas (bottom of left y-axis) represent the activity present inside each vault, which at 2000 AD correspond to the full initial inventory of Ni-59. The corresponding pale areas in the same vertical order (top of right y-axis) represent the activity that has decayed within the respective vaults. The white area (very top right, barely visible on this scale) represents activity that is likely to have escaped the near-field, i.e. neither still retained nor decayed in the vaults.

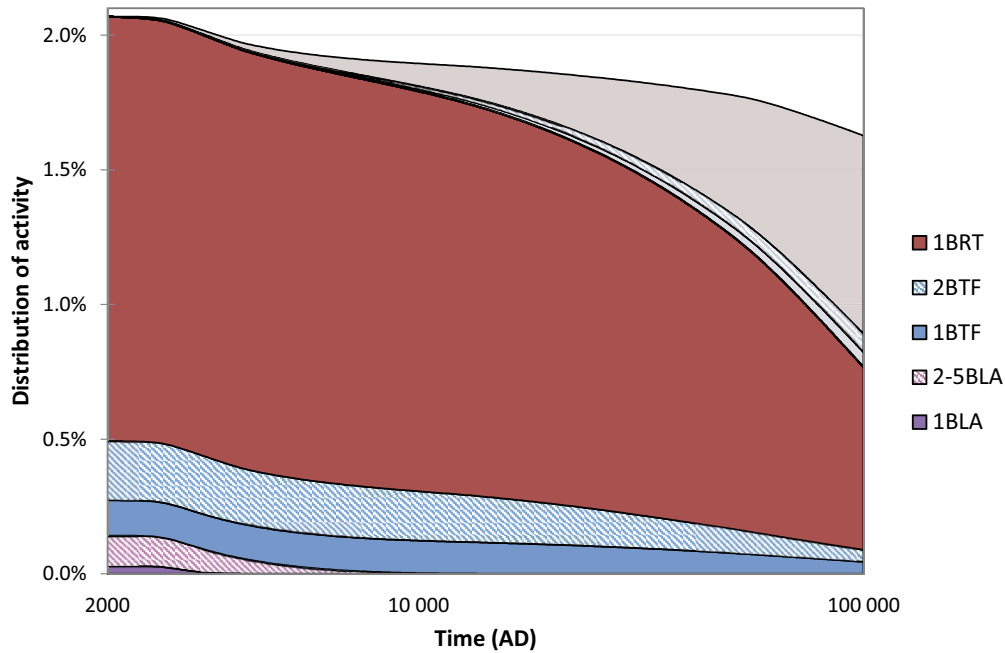


Figure 5-34. Development of the near-field Ni-59 activity, in only the 1BRT, BTF and BLA vaults as a proportion of initial activity in the entire SFR. The opaque areas (left-bottom) represent the activity present inside each vault, which at 2000 AD corresponds to the initial inventory of Ni-59 in these vaults. The corresponding pale areas in the same vertical order (middle) represent the activity that has decayed within the respective vaults. The white area (top) represents activity that has escaped the near-field, i.e. neither still present nor decayed in the vaults.

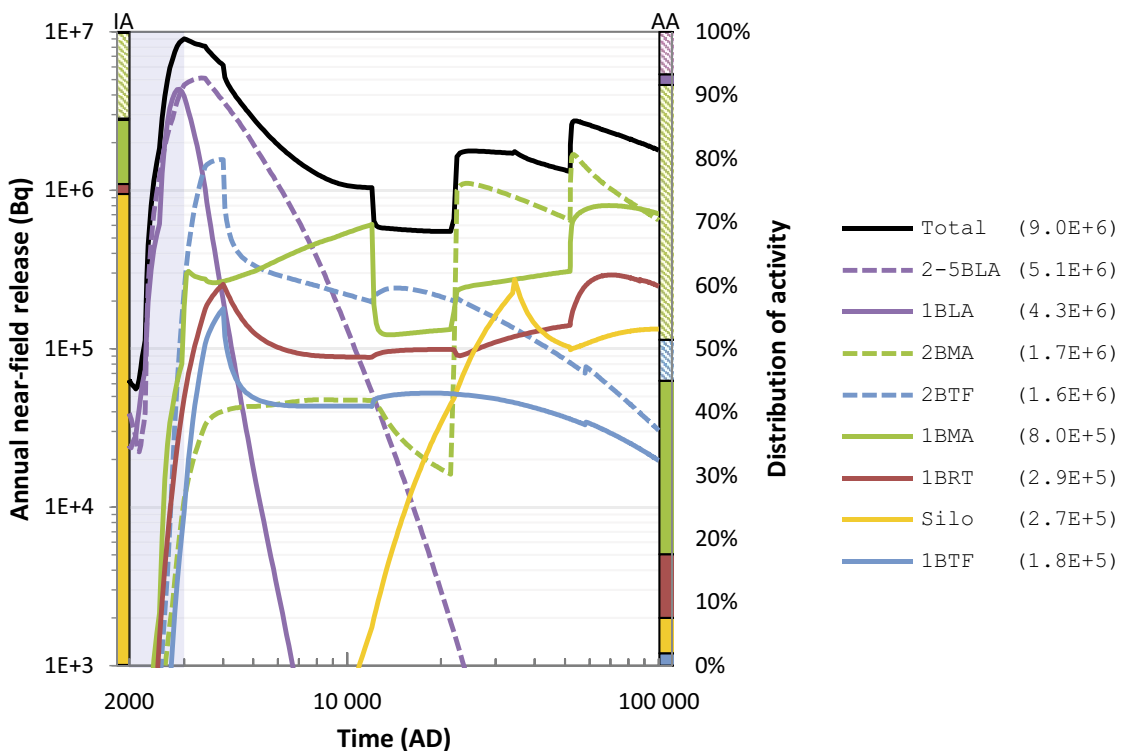


Figure 5-35. Annual activity release of Ni-59 (Bq, left y-axis) from the entire SFR (black line) and from specific vaults (coloured lines) in the base case. The flanking vertical bars on the left and right represents the distribution of initial activity (IA) between the vaults and of all released activity accumulated over 100 000 years (AA), respectively (right y-axis, colours are the same as those given by the key and the hatched areas in the bar correspond to the dashed lines in the key). The total and vault-specific release maxima are shown in parentheses in the key. The submerged period is illustrated by the blue shading.

Mo-93

Most of the Mo-93 inventory is found in the waste disposed in the silo, 2BMA and 1BRT. As shown in Figure 5-36 about 90 % of the Mo-93 will decay within the vaults and not be released to the geosphere.

The BLA and BTF Mo-93 activities are too low to be visible in Figure 5-36, so this subset is shown separately in Figure 5-37. Although the initial Mo-93 activities in these vaults are low, a large fraction of their inventory is released (Figure 5-37), because the engineered barriers in these vaults have less retention capabilities than those of the other SFR vaults with respect to hydraulic resistance.

The silo and 2BMA, followed by 1BRT contain most of the Mo-93 that will be disposed in SFR (> 95 %), and the accumulated annual release of Mo-93 comes mainly from these vaults (Figure 5-38). However, the maximum annual release (see Figure 5-38) does not fully follow this trend, as 1BRT and 2BTF show the second highest maximum annual release after the silo.

Figure 5-38 shows that the release from the silo, 1-2BMA and 1BRT is distributed over a longer time period compared to the other vaults, which will clearly reduce the total annual release of Mo-93 from the repository. The retardation of the release from the silo and BMA vaults is due to the high retention capabilities of the engineered barrier systems of these vaults. The Mo-93 release from 1BRT is limited by a long corrosion time relative to the Mo-93 half-life.

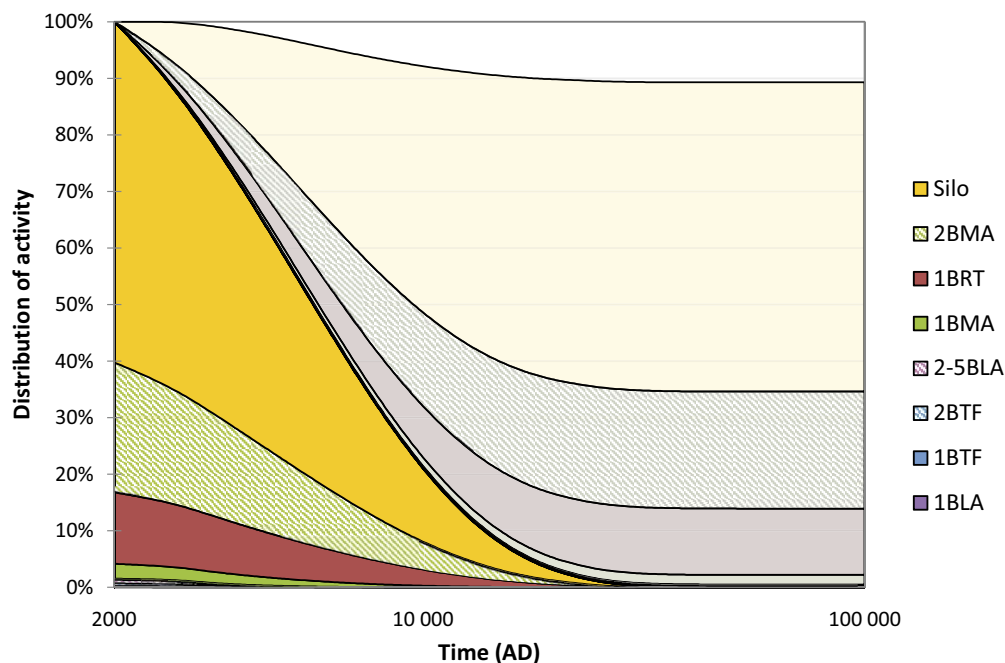


Figure 5-36. Development of the near-field Mo-93 activity, by vault in order of initial activity in the entire SFR. The opaque areas represent the activity present inside each vault, which at 2000 AD correspond to the full initial inventory of Mo-93. The corresponding pale areas in the same vertical order (right) represent the activity that has decayed within the respective vaults. The white area (top) represents activity that has escaped the near-field, i.e. neither still present nor decayed in the vaults.

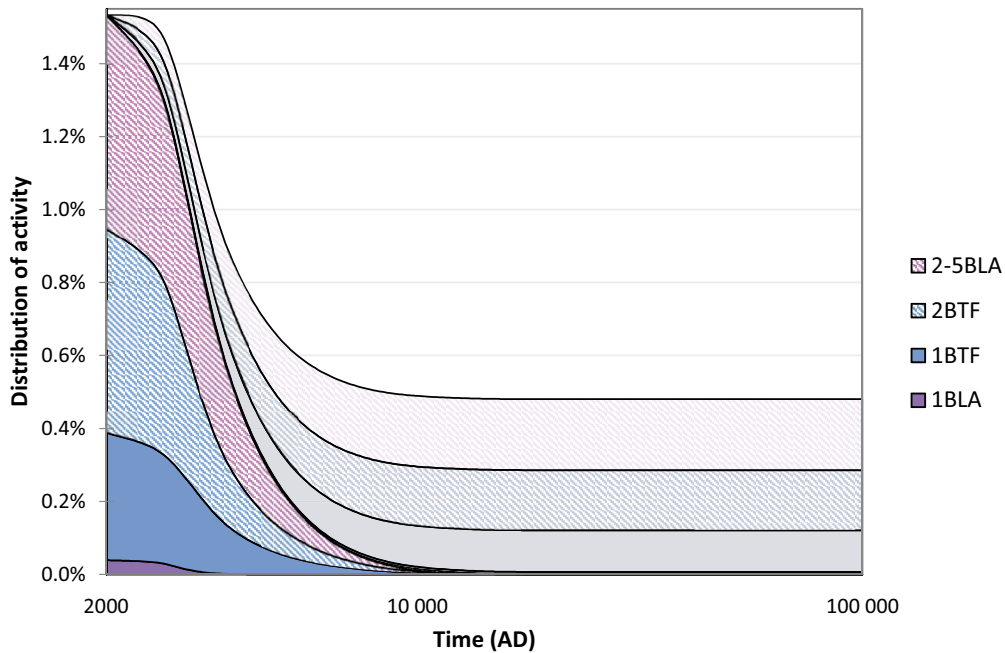


Figure 5-37. Development of the near-field Mo-93 activity, in only the 1–2BTF and 1–5BLA vaults as a proportion of initial activity in the entire SFR. The opaque areas (left) represent the activity present inside each vault, which at 2000 AD corresponds to the initial inventory of Mo-93 in these vaults. The corresponding pale areas in the same vertical order (middle) represent the activity that has decayed within the respective vaults. The white area (top) represents activity that has escaped the near-field, i.e. neither still present nor decayed in the vaults.

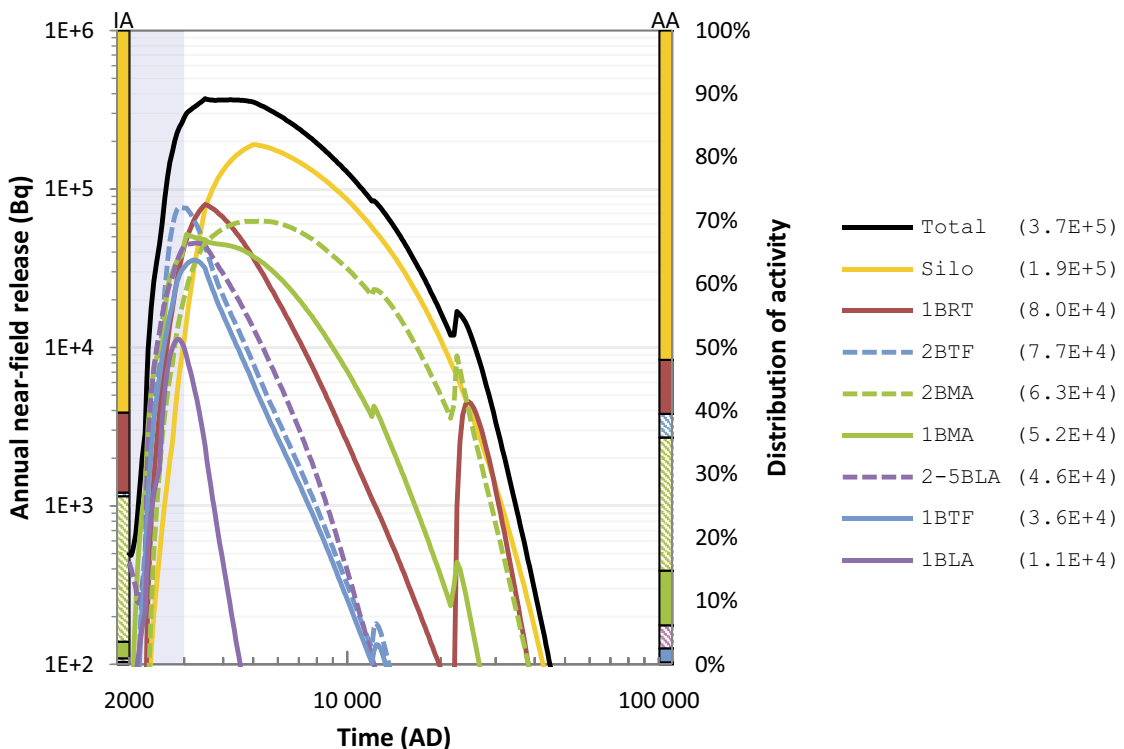


Figure 5-38. Annual activity release of Mo-93 (Bq, left y-axis) from the entire SFR (black line) and from specific vaults (coloured lines) in the base case. The flanking vertical bars on the left and right represents the distribution of initial activity (IA) between the vaults and of all released activity accumulated over 100 000 years (AA), respectively (right y-axis, colours are the same as those given by the key and the hatched areas in the bar correspond to the dashed lines in the key). The total and vault-specific release maxima are shown in parentheses in the key. The submerged period is illustrated by the blue shading.

I-129

About 98 % of the I-129 inventory is found in the waste disposed in the silo, 1BMA and 2BMA. Since the half-life of I-129 is very long and its sorption is negligible (Table 5-12), most of its inventory will be released and only a negligible amount will decay in the near-field, as evident from the fact that the corresponding areas in Figure 5-39 are too thin to be visible. Thus, only a small amount of I-129 will remain in the silo at the end of the assessment period.

The BLA, BTF and 1BRT I-129 activities are too small to be visible in Figure 5-39, so this subset is shown separately in Figure 5-40. As for the previous radionuclides, the figure shows that the vaults with engineered barriers that has less retention capabilities release their I-129 inventory more rapidly than the silo and BMA vaults.

The silo, 1BMA and 2BMA are the vaults that contribute the most to the maximum annual release of I-129 (Figure 5-41). The figure also shows that the release from these vaults is distributed over a relatively long time of many millennia, whereas in the BLA, BTF and 1BRT vaults, the residence times of I-129 are only a couple of millennia. Thus, the repository also provides a degree of retardation for this poorly sorbing and long-lived radionuclide and its release is distributed over a long time period, albeit less than for sorbing radionuclides with longer residence times.

Unlike for C-14-inorg, Ni-59, and Mo-93 above, the distribution of the initial I-129 inventory between vaults shows a strong resemblance to the distribution of accumulated releases (left versus right flanking vertical bars on the y-axes in Figure 5-41). This too can be explained by the lack of sorption and long half-life of I-129, which reduces the impact of all barrier systems.

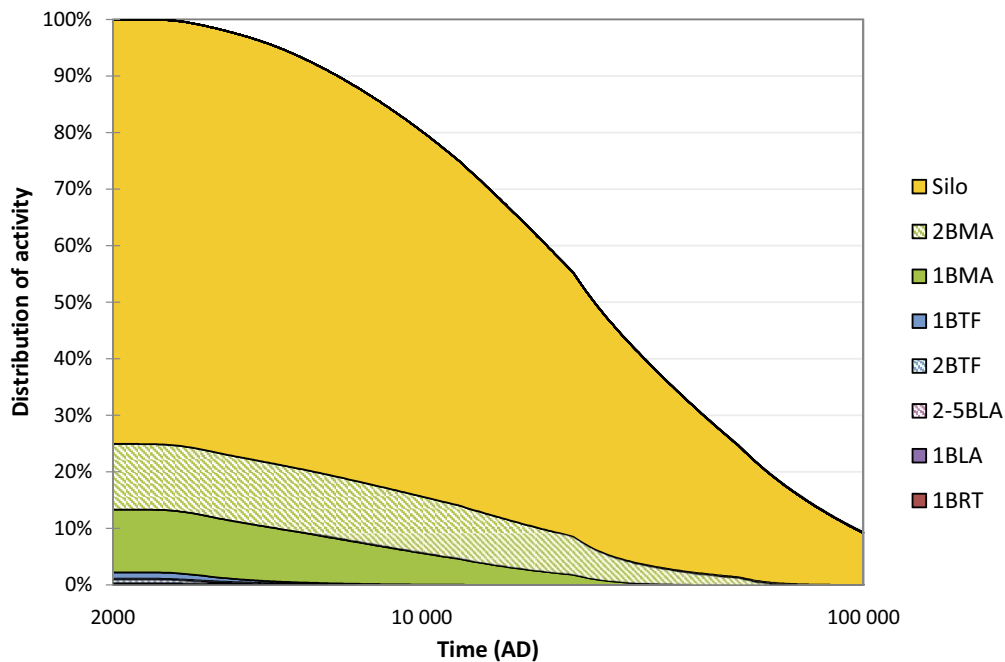


Figure 5-39. Development of the near-field I-129 activity, by vault in order of initial activity in the entire SFR. The opaque areas (left-bottom) represent the activity present inside each vault, which at 2000 AD correspond to the full initial inventory of I-129. The corresponding pale areas (too thin to be visible) represent the activity that has decayed within the respective vaults. The white area (top-right) represents activity that has escaped the near-field, i.e. neither still present nor decayed in the vaults.

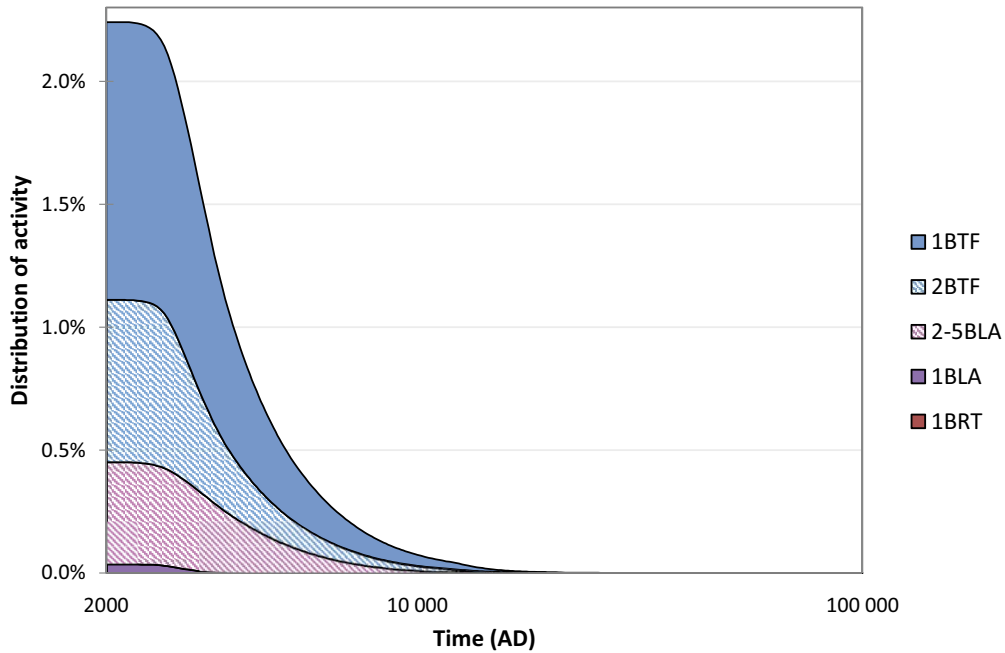


Figure 5-40. Development of the near-field I-129 activity, in only the 1BRT (too small to be visible), 1–2BTF and 1–5BLA vaults as a proportion of initial activity in the entire SFR. The opaque areas (left) represent the activity present inside each vault, which at 2000 AD corresponds to the initial inventory of I-129 in the vaults. The corresponding pale areas (too thin to be visible) represent the activity that has decayed within the respective vaults. The white area (right) represents activity that has escaped the near-field, i.e. neither still present nor decayed in the vaults.

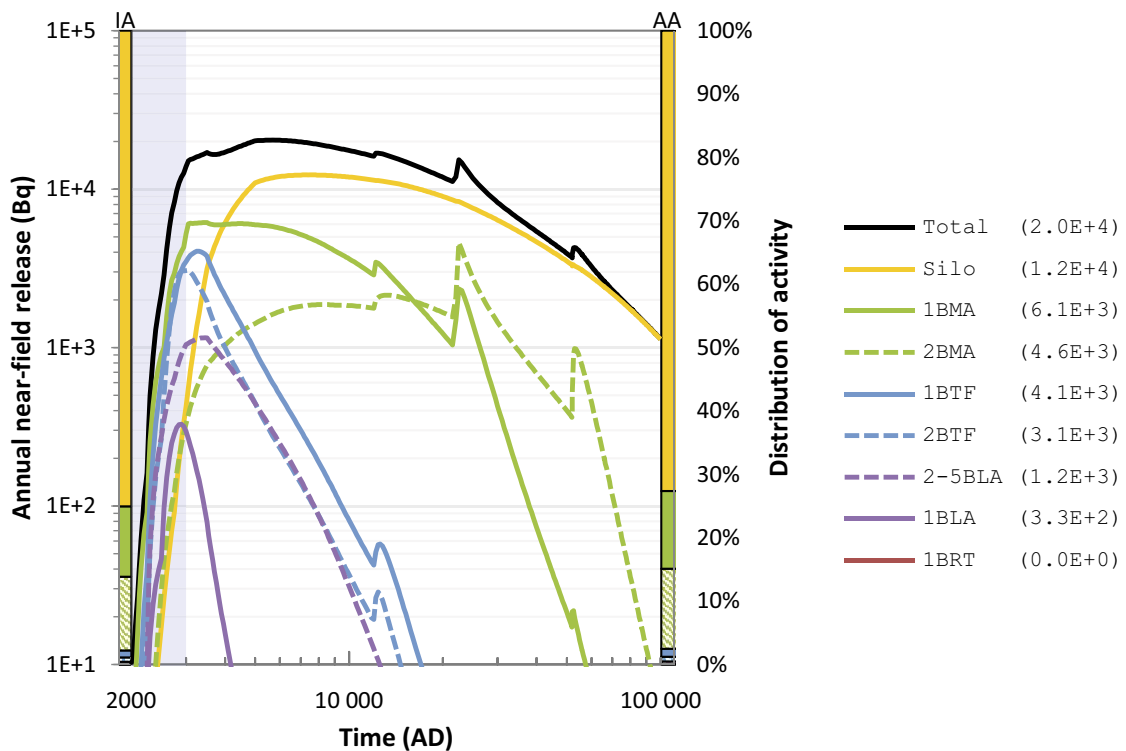


Figure 5-41. Annual activity release of I-129 (Bq, left y-axis) from the entire SFR (black line) and from specific vaults (coloured lines) in the base case. The flanking vertical bars on the left and right represents the distribution of initial activity (IA) between the vaults and of all released activity accumulated over 100 000 years (AA), respectively (right y-axis, colours are the same as those given by the key and the hatched areas in the bar correspond to the dashed lines in the key). The total and vault-specific release maxima are shown in parentheses in the key. The submerged period is illustrated by the blue shading.

Barrier performance

The conclusion of the analysis above is that a substantial part of the C-14-inorg, Ni-59 and Mo-93 inventory will decay within the vaults with engineered barriers (i.e. all except 1-5BLA) instead of being released. An exception is the very long-lived and very weakly sorbing radionuclide I-129, for which most of the inventory is released during the assessment period.

The analysis shows that even though the silo has a substantially larger initial inventory of Ni-59, Mo-93 and I-129 than the other waste vaults (Chapter 3), its concrete and bentonite barriers ensure release rates of similar magnitude to the other waste vaults. The silo also has a large C-14-inorg inventory but, due to its barriers once again, the annual release of this radionuclide is very small compared to the other vaults.

After the silo, the 1-2BMA vaults generally contain the most activity, except Mo-93 which is more prevalent in 1BRT than in 1BMA. 1-2BMA releases are earlier than from the silo, but are nevertheless strongly reduced by the concrete barriers, resulting in release rates of similar magnitude to the other waste vaults.

Most of the activity in 1BRT is in the form of induced activity in the RPVs and 1BRT is the vault that contains the third largest inventory of Mo-93. The annual release of Mo-93 from 1BRT is limited by the slow corrosion rate of the RPV and so is of similar magnitude to those of the other vaults.

In general, the inventories of 1-2BTF and 1-5BLA are substantially smaller than those of the other vaults. Compared to the BLA vaults, 1-2BTF are better at retaining radionuclides that sorb to the concrete barriers, e.g. Ni-59 and C-14-inorg. An example of this is that even though 1-2BTF contain significantly more C-14-inorg than 1-5BLA, the maximum annual release is lower from the former.

The 1-5BLA vaults do not have credited engineered barriers and their release is determined by the groundwater flow rate set by the regional hydrological conditions. 2-5BLA are more efficient at delaying the release of radionuclides compared to 1BLA, due mainly to lower groundwater flow at their greater depths and the associated impact this has on the site hydrogeology.

5.3.9 Summary of the near-field radionuclide transport

In Figure 5-42, radionuclides with the highest release from the entire SFR are shown. The annual release is initially very small due mainly to the low-flow, submerged conditions above SFR. The releases increase as the radionuclides travel through the waste and barrier systems of the near-field. At some point, the annual releases start decreasing due to depletion and decay. The annual releases are also affected by the concrete evolution, where sorbing radionuclides are more strongly affected.

The total near-field releases in Figure 5-42 are summed over all vaults, so certain features in the curves can have several underlying causes. The inventories in the different waste vaults are very different since each vault is designed to handle specific types of waste. For instance, Ca-41 is mainly found in decommissioning waste and the total release of Ca-41 originates from the 2-5BLA and 2BMA vaults. Also, these vaults are very different from each other due to differences in vault and barrier design. The fact that Ca-41 is found in the inventory of only 2-5BLA and 2BMA (SKB R-18-07 and Table 3-9 in the **Initial state report**) makes it quite unique among the radionuclides in this assessment. As a comparison, the initial inventory of the radionuclides discussed in Section 5.3.8 is largest in 1BMA (C-14-inorg) or the silo (Ni-59, Mo-93, I-129).

C-14-org dominates the release until ~22 000 AD because of a high initial inventory in the vaults, an assumed lack of sorption, and a moderate half-life of 5 700 years.

The Mo-93 release curve is similar in shape to that of C-14-org due to its similar half-life, but its annual release is consistently lower due to a smaller initial inventory and to weak, albeit non-zero, sorption.

Ni-59 is also deposited in significant amounts in all vaults. Its total initial inventory is even larger than that of C-14-org. However, its tendency to sorb strongly to cement decreases its maximum release and enhances its longevity in the vaults, which together with a longer half-life makes it release-dominant at later times.

The C-14-inorg release curve is intermediate between C-14-org and Ni-59, explained by a stronger cement sorption than C-14-org and shorter half-life than Ni-59.

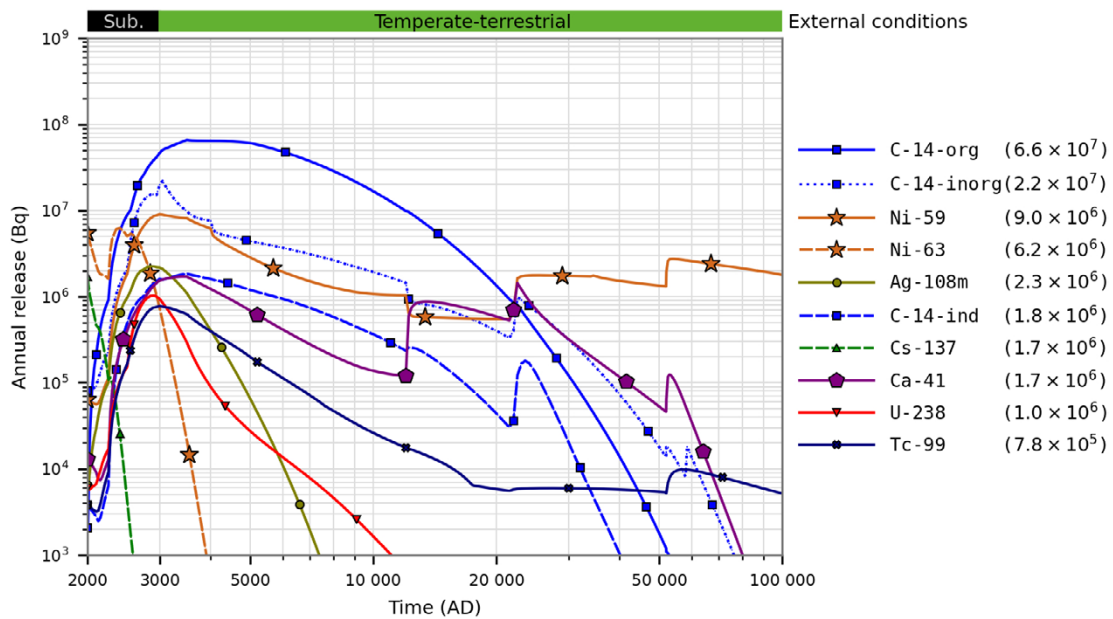


Figure 5-42. Annual activity releases (Bq) from the entire SFR in the base case. Only the 10 radionuclides with the highest annual release are shown. The annual release maxima (Bq) are shown in parentheses in the key. Coloured horizontal bar (top) shows the evolution of the external conditions.

As illustrated above, the factors that affect the annual release of radionuclides from the near-field are (in arbitrary order) (a) the initial inventory, (b) low flow through the vaults as afforded by naturally low groundwater flow and engineered barriers with low hydraulic conductivity, (c) sorption on cement and bentonite and (d) radioactive decay. Factors (b) and (c) together cause retardation which leads to a distribution of releases over long times. (d) can even cause the releases to become insignificant if the half-life is shorter than the residence time determined by (b) and (c).

5.4 Near-field – geosphere interface

The radionuclides are assumed to be released from the vaults by advection, except in the silo model (Section 5.3.2). The radionuclides released from each vault are fed into an effective trajectory representing an average trajectory for particles released from the vault and transported through fractures in the geosphere, to the surface systems, see Section 5.5.

The release of radionuclides from the near-field is, for all vaults except the silo, calculated as the sum of the advective transfers (because transport in the macadam backfill is driven by advection) from the near-field model compartments to the geosphere, see Section 4.1. Transfer of radionuclides from the geosphere to the vault is cautiously disregarded. That is, even though groundwater flowing out from a vault potentially could re-enter the same vault or another vault, it is assumed that radionuclides are fully transferred to the geosphere model as soon as they have left a vault model. That is, the models form a chain, in which the sum of the releases of radionuclides from the near-field models constitutes the source of radionuclides to the geosphere model.

5.4.1 The interface between the silo and the geosphere

In addition to advective radionuclide transfer to the geosphere, diffusion from the near-field into the surrounding host rock is accounted for in the silo. The *equivalent water flow*, Q_{eq} , represents the diffusive transport of radionuclides from the silo bentonite to the water flowing along the bentonite–rock interface. The Q_{eq} is estimated using Equation 4-8 and Equation 4-9. The parameters for Q_{eq} are shown in Table 5-13, as well as the Darcy velocity of the flow through the rock surrounding the silo which has been calculated using a model similar to the repository near-field hydrogeological model (see Abarca et al. 2014, Appendix E).

Table 5-13. Parameter values for calculation of the equivalent flow Q_{eq} , (Abarca et al. 2014, Appendix E).

Parameter	Value	Description
A_w (m ²)	5×10^3	Area of interface between bentonite and rock
ϵ_{rock} (-)	2.3×10^{-5}	Flow porosity in rock
D_w (m ² s ⁻¹)	2×10^{-9}	Diffusivity of radionuclides in water
L (m)	50	Approximate path length for water seeping along the silo wall
Parameter	Time (AD)	Darcy velocity of water in the rock q (m s ⁻¹)
q (m s ⁻¹)	2000	1.54×10^{-13}
q (m s ⁻¹)	3000	7.83×10^{-11}
q (m s ⁻¹)	5000	1.83×10^{-10}

The Q_{eq} is evaluated at three different shoreline positions corresponding to 2000 AD, 3000 AD and 5000 AD. As the shoreline changes, the Q_{eq} is calculated using linear interpolation between modelled Q_{eq} at these fixed shoreline positions, the result is shown in Figure 5-3a.

5.5 Geosphere

The geosphere radionuclide transport calculations require both flow and non-flow related migration properties as input. Flow-related migration properties are calculated using a site-specific hydrogeological model (Odén et al. 2014, Öhman and Odén 2018). The non-flow-related migration properties are primarily based on the SR-PSU parameters. Updated input data that are not presented in the **Data report** or in this chapter are presented in Appendix A. For details about changes in the geosphere modelling since SR-PSU, as well as the potential effect of these changes on the geosphere releases, see Appendix C.

5.5.1 Handling in the geosphere model

Flow-related migration properties

In accordance with the *base variant* of the reference evolution, the groundwater flow through the bedrock and the repository is expected to increase as the shoreline regresses over the repository further seawards (Figure 5-43; see also **Post-closure safety report**, Section 6.2). This projection is based on hydrogeological modelling at the repository site. In the most recent hydrogeological study, three bedrock cases (model-parameterisation variants), namely 1, 11, and 15, were considered representative of future flow conditions: a reference case and two bounding cases with low and high flow, respectively (Öhman and Odén 2018). This is consistent with the SR-PSU, where the variation in vault flow (Q) between these three cases was similar to, or greater than, the variation across all bedrock cases used in that safety assessment (Öhman et al. 2014).

For each of the three bedrock cases, steady-state flow solutions at nine stages of shoreline retreat were evaluated (time slices at 2000 AD, 2100 AD, 2250 AD, 2500 AD, 2750 AD, 3000 AD, 3500 AD, 5000 AD and 9000 AD). These are considered representative for resolving the transition from submerged conditions into fully matured terrestrial conditions in the *base case* (Section 5.2). The simulations showed that groundwater flow through the geosphere increases from very low levels, less than 1 % of the maximum flow, during fully submerged conditions, until about 3000 AD, when a transition towards a maximum stationary flow occurs. At around 3500 AD, the flow regime around SFR approaches stationary conditions, i.e. the flow regime is largely unaffected by the continued shoreline regression (Figure 5-43 and Öhman and Odén 2018).

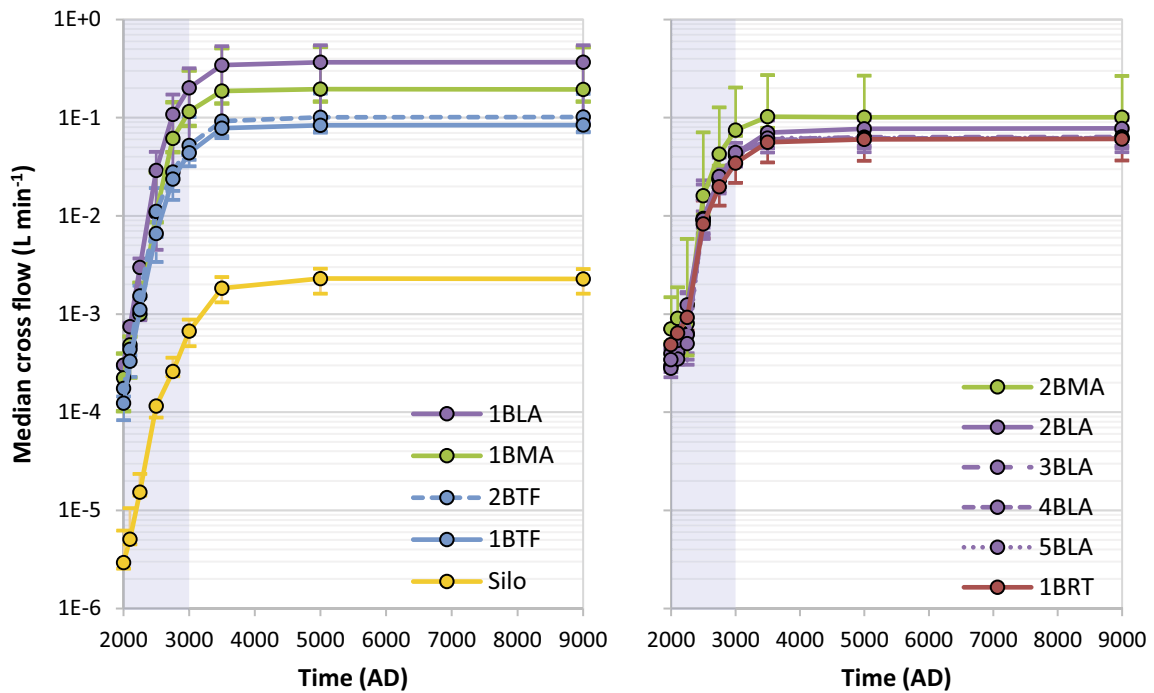


Figure 5-43. Vault cross flow (Q) from 2000 AD to 9000 AD in the base case (Section 5.2) for SFR1 (left) and SFR3 (right). Circles indicate the median values of the three representative bedrock cases (1, 15, and 11), and bars indicate the variability between these cases. The submerged period is illustrated by the blue shading. Figure reproduced from Figure 6-34 in Öhman and Odén (2018).

For each time-slice, particle tracking was performed with 10 000 particles starting at the bedrock entry (i.e. the vault-rock passage) of each waste vault and terminating at its exit (i.e. the regolith interface passage). The particle tracking was initiated with particles uniformly distributed over the waste vaults under stationary flow conditions for all model permutations (see Öhman and Odén 2018). The trajectories collectively describe the potential macro-dispersion¹¹ in the transport through the geosphere. As the shoreline regresses over the repository, the flow is not stationary (Öhman and Odén 2018). Since the particles are released independently for each time slice, it is not appropriate to synchronise particle trajectories over time.

The shallow granite rock surrounding SFR is fractured. As a result, reported advective travel times of the groundwater through the shallow geosphere are relatively short, typically a couple of years for terrestrial conditions above the repository (see Table 5-14 at 3500 AD and beyond)¹². Thus, radionuclide residence times in the geosphere are generally considerably shorter than those in the engineered barriers of the waste vaults. Therefore, a simplified approach describing the transport of radionuclides through the geosphere is adopted here, using so-called “effective trajectories”. For each bedrock case, waste vault and time slice, these trajectories are computed as the median values of the advective travel time (t_w , in units a) and the flow-related transport resistance (F , in units of a m^{-1}) for all the 10 000 trajectories. The distributions of these two performance measures are approximately log-normal. Thus, the geometric means over the three bedrock cases are used as the best estimates for the parameter values (see subsection *Uncertainties in flow-related migration properties* below for details of the probabilistic handling of flow-related parameters). Between the time-slices, linear interpolation is used to estimate parameter values. The effective trajectory for the last shoreline position is considered representative for the time beyond 9000 AD.

¹¹ Macro dispersion is here defined as the dispersion due to splitting up the release into different pathways with varying lengths, transport times and flow-related transport resistances.

¹² Note that travel times for the groundwater are considerably shorter than the travel times for elements that sorb onto the rock matrix, see further Section 5.5.2.

In Appendix A3, the geosphere transport calculations with effective trajectories are compared to a more comprehensive approach, where all the individual trajectories are used. For this comparison, the geosphere activity release of five dose-relevant radionuclides with different transport properties are analysed by describing the flow-related properties t_w and F with all particle trajectories in the reference bedrock case and with their median values (Öhman and Odén 2018). In summary, the analysis in Appendix A3 shows that the geosphere activity releases of the key radionuclides using effective trajectories are in close agreement with the mean release using all trajectories. Therefore, the use of effective trajectories is considered a reasonable simplification of the radionuclide transport calculations in the geosphere. Another result in Appendix A3 is that the effect of macro-dispersion on the geosphere activity release is limited, at least for the key radionuclides.

Depending on the waste vault, estimated median travel times range from 260 years to 1 500 years during fully submerged conditions at repository closure, to approximately 8 months to 4 years when the area above the repository is fully terrestrial (Table 5-14).

Table 5-14. Median travel times (a) as a function of waste vault and shoreline position. The values are the geometric mean over median values for the three representative bedrock cases, where each case is represented by one effective trajectory (see text for details).

Time (AD)	1BLA	1BMA	1BTF	2BTF	Silo	1BRT	2BMA	2BLA	3BLA	4BLA	5BLA
2000	550	610	690	450	1500	640	260	580	560	550	510
2100	280	310	310	190	710	450	180	350	330	330	300
2250	99	110	80	60	210	270	120	210	200	170	140
2500	11	10	20	13	38	69	36	61	46	35	29
2750	3.6	2.2	13	8.3	14	24	13	18	13	8.7	8.3
3000	2.0	1.1	6.6	4.5	6.7	11	4.9	8.6	5.9	3.9	3.8
3500	1.4	0.7	2.3	2.1	1.8	5.1	4.0	4.3	4.6	3.2	3.1
5000	1.4	0.7	2.2	2.1	1.7	4.6	4.3	4.1	4.8	3.5	3.2
9000	1.5	0.7	2.2	2.1	1.7	4.4	4.3	4.0	4.7	3.4	3.2

During submerged conditions, topography has a minor effect on the groundwater flow. Thus, during this period flow components are mainly vertical, and particles follow fracture paths directed upwards (**Post-closure safety report**, Section 6.2.5). As the shoreline regresses over the repository, conductive fractures and hydraulic pressure gradients due to the surface terrain also influence the path of the particles. As the horizontal flow components successively increase, the trajectory paths are expected to be directed mainly towards the mire in biosphere object 157_2 situated north of the repository (Section 4.4.1 and Chapter 5 in the **Biosphere synthesis report**). Therefore, in the *base case*, it is cautiously assumed that all paths are directed towards biosphere object 157_2 (see further Section 5.6). The effect on radionuclide transport and dose of a large subhorizontal fracture beneath object 157_2, causing some of the released radionuclides from the geosphere to be distributed to other biosphere objects, is evaluated in the **Biosphere synthesis report**, Chapter 10.

In Table 5-15, estimated average rock fracture apertures are listed. These are based on the calculated flow paths for each time slice; they are calculated from the geometric means of the median travel times and flow-related transport resistances from the three representative bedrock cases (aperture [m] = $2 \times t_w/F$), see also Section 4.3. This results in average fracture apertures, ranging from 0.16 mm to 0.39 mm.

Table 5-15. Average aperture of the rock fractures (mm) as a function of waste vault and shoreline position. The aperture is calculated from the geometric mean of the median travel times (a) and the median flow-related transport resistances (a m⁻¹) from three representative bedrock cases.

Time (AD)	1BLA	1BMA	1BTF	2BTF	Silo	1BRT	2BMA	2BLA	3BLA	4BLA	5BLA
2000	0.38	0.36	0.38	0.37	0.32	0.21	0.29	0.23	0.19	0.21	0.23
2100	0.38	0.37	0.37	0.36	0.31	0.19	0.28	0.21	0.18	0.19	0.22
2250	0.39	0.36	0.34	0.35	0.29	0.18	0.19	0.17	0.16	0.17	0.16
2500	0.37	0.35	0.31	0.35	0.24	0.20	0.24	0.19	0.22	0.20	0.19
2750	0.29	0.32	0.23	0.23	0.18	0.19	0.22	0.18	0.20	0.20	0.17
3000	0.26	0.32	0.23	0.22	0.19	0.19	0.18	0.17	0.19	0.21	0.17
3500	0.26	0.31	0.21	0.22	0.16	0.18	0.16	0.16	0.17	0.18	0.16
5000	0.25	0.30	0.20	0.21	0.17	0.17	0.17	0.16	0.17	0.17	0.16
9000	0.25	0.31	0.20	0.21	0.17	0.17	0.16	0.16	0.17	0.17	0.17

Uncertainties in flow-related migration properties

The variation of the properties (Q , t_w , and F) from flow trajectories at different stages (time slices) of shoreline retreat is correlated between time slices, waste vaults and each other. For example, a bedrock case with high groundwater flow at 2500 AD tends to have high flow rates at later time points and co-varying groundwater flow in neighbouring vaults. Moreover, realisations with a short travel time (t_w) tend to have a low transport resistance (F) and a high vault cross flow (Q) (Figure 5-44). In the PSAR, the uncertainties in t_w , F and Q are derived from the variations between the three bedrock cases that are considered to be representative (Öhman and Odén 2018, cases 1, 11, and 15).

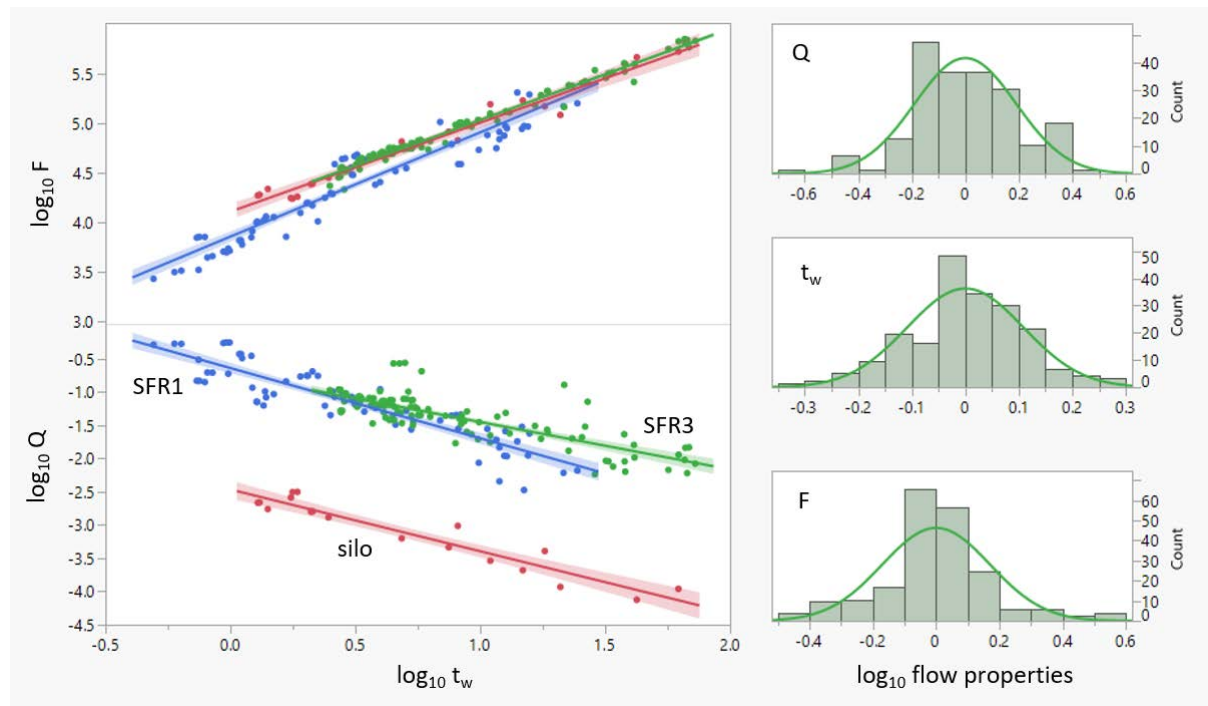


Figure 5-44. Correlation between flow-related properties (left) and variation of properties for individual waste vaults and time points(right). Displayed data represents flow-conditions for all waste vaults in the period between 2500 AD to 9000 AD given the three representative bedrock cases (1, 11 and 15; Öhman and Odén 2018). Left top, transport resistance (F) and left bottom, vault cross flow (Q) as a function of travel time (t_w) for the repository units SFR1(blue), silo (red), and SFR3 (green). Right, histograms showing random deviations (residuals) from the geometric mean for all waste vaults at six time points (2500, 2750, 3000, 3500, 5000 and 9000 AD). Note that the deviations are approximately normally distributed (green curve) on a logarithmic scale.

To describe the patterns of variation and co-variation of the flow-related properties, the three representative bedrock cases are analysed with a mixed linear model for 2500 AD and later times (Appendix A4). In this analysis, the variation in the flow properties in SFR1 (without the silo), the silo and SFR3, are treated as independent. This assumption is reasonable based on the physical distance between the repository units and it is partly supported by previously reported patterns of vault cross flows (Odén et al. 2014).

For each of the three repository units (SFR1, silo and SFR3), the total random variation¹³ is first estimated for t_w , F and Q from the residuals around the geometric values for each property with respect to waste vault and time (right panels in Figure 5-44). This variation is then partitioned into three variance components:

- a component describing how a random bedrock case affects all three properties in all vaults at all times ($\sigma_{BC,shared}^2$),
- a component describing how a bedrock case affect each property independently in all vaults at all times ($\sigma_{BC,ind}^2$), and
- a residual variance component describing how a flow-related property varies randomly around its average value with respect to vault and time point (σ_{res}^2) (Table 5-16).

To mimic this variation structure in the input data used for radionuclide transport calculations in the PSAR, random error terms (e) were drawn from log-normal distributions in Monte-Carlo simulations. Flow characteristics that were correlated across time, repository unit and property type were then generated by adding the error terms from all three sources to the geometric mean for each waste vault and time (see Appendix A4 for details). Thus, for a specified repository unit (SFR1, silo or SFR3), random error terms (e) were summed as follows:

$$\begin{aligned} e_{totalQ} &= -e_{BC,shared} + e_{BC,ind,Q} + e_{res,Q,jk} \\ e_{totalF} &= e_{BC,shared} + e_{BC,ind,F} + e_{res,F,jk} \\ e_{totalt_w} &= e_{BC,shared} + e_{BC,ind,t_w} + e_{res,t_w,jk} \end{aligned}$$

Where $e_{BC,shared}$ is $N(0, \sigma_{BC,shared}^2)$ distributed, $e_{BC,ind}$ is $N(0, \sigma_{BC,ind}^2)$ distributed and $e_{res,Q,jk}$ is $N(0, \sigma_{res}^2)$ distributed (Table 5-16, lower panel). These total error terms (e_{total}) were then scaled back with the corresponding standard deviation, s_i (Table 5-16, upper panel). Thus, the error term is expressed as a scale factor (Sf) which is multiplied with the best estimate for each property, vault and time, respectively. For SFR1 this is expressed as:

$$Sf_{ijk} = 10^{s_i e_{total,ijk}}$$

$i = Q, t_w, F$; $j = 1BMA, 1BTF, 2BTF, 1BLA$; $k = 2500, \dots, 9000$

Note that the three repository units are considered to vary independently. Thus, a Monte-Carlo realisation that is associated with high groundwater flow in SFR1, yields a relatively high Q , and relatively low t_w and F values in *all* SFR1 waste vaults (at all times), but not necessarily in the silo or in SFR3.

Table 5-16. Random variation of flow properties for three units of the SFR repository as captured by the three representative bedrock cases. The measures of uncertainties are expressed on a logarithmic scale. See text and Appendix A4 for a detailed explanation of its derivation and application in Monte-Carlo simulations.

Repository unit	Total standard deviation (s)		
	Q	F	t_w
SFR1	0.24	0.26	0.15
Silo	0.12	0.13	0.12
SFR3	0.16	0.07	0.07

Repository unit	Variance components (σ^2)		
	$\sigma_{BC,shared}^2$	$\sigma_{BC,ind}^2$	σ_{res}^2
SFR1	0.76	0.02	0.70
Silo	0.34	0.51	0.57
SFR3	0.26	0.23	1.00

¹³ As opposed to the systematic variation caused by time and waste vault.

Non-flow-related migration properties

The non-flow-related migration properties used in the radionuclide transport modelling are summarised in Table 5-17. The density and porosity of the rock matrix as well as the Peclet number use the same values as in the SR-PSU. Hence, the density is 2700 kg m⁻³ (SKB TR-10-52, Chapter 6), the porosity is set to 0.18 % (SKB TR-10-52, Table 6-90) and the Peclet number is selected to be 10 (SKB R-01-14, Table 7-3). The penetration depth of the radionuclides, i.e. how far they are allowed to diffuse up into the rock matrix, is updated to 0.9 m in the PSAR from 1.4 m in the SR-PSU. This updated distance corresponds to half the average spacing between conductive fractures in the area around the SFR site (Appendix A3).

Table 5-17. Non-flow related migration properties.

Name	Unit	Value	Probabilistic
Rock matrix porosity	-	0.0018	No
Rock matrix density	kg m ⁻³	2700	No
Maximum penetration depth in the rock matrix	m	0.9	No
Peclet number	-	10	No
Effective diffusivity ^a	m ² s ⁻¹	3.2 × 10 ⁻¹⁴ ^b	Yes
Element-specific K_d values for the rock matrix	m ³ kg ⁻¹	See Table 5-18	Yes

^a The effective diffusivity (D_e) for anions is cautiously selected to be representative for all radioelements. The D_e values are obtained from Löfgren (2014).

^b Lognormal distribution describes parameter uncertainty for effective diffusivity with assigned value as geometric mean and geometric standard deviation of 1.78. One set of parameter samples is used in the probabilistic simulation, these being shared by all species.

Rock matrix sorption coefficients (K_d) are obtained from Table 8-8 in the **Data report**. Some radionuclides exhibit different sorption characteristics depending on the prevailing pH, redox conditions and groundwater salinity. For these radionuclides, K_d corresponding to pH < 10 and reducing conditions are selected for the *base case*, and the lowest K_d values are cautiously selected with respect to the salinity conditions (temperate saline groundwater conditions). Table 5-18 presents the resulting element-specific K_d values for the rock matrix used in the calculations.

The impact of complexing agents from the near-field on K_d values in the geosphere has been evaluated by Crawford (2017), with scoping-level thermodynamic calculations based on a mixing model of regional groundwater with cement-leachate water from the near-field. A conclusion is that the effect of complexing agents reaching the geosphere via water from the near-field is tightly coupled to the high pH of the same water. The reason for this coupling is the significant pH sensitivity of sorption coefficients and particularly of the interactions between radionuclides and complexing agents. In consequence, evaluation of SRFs in the geosphere would require knowledge of the pH evolution along the whole flow path(s), including the dilution of cement-leachate water containing complexing agents as a function of distance from the repository. Nevertheless, the scoping-level calculations indicate that the effect of complexing agents in the geosphere is minor, see further details in Sections 8.6 and 8.9 of the **Data report**.

Crawford (2017) further notes that a case corresponding to the *no sorption in the geosphere calculation case* can be seen as a pessimistic upper bound of complexing-agent impact in the geosphere, which in Section 8.4 is shown to have only a marginal effect on dose. This is mainly because the dose-dominating radionuclides Mo-93, C-14-org and Ca-41 have minimal or zero assumed bedrock sorption even in the absence of complexing agents (**Data report**, Section 8.6). Stable Fe ions from minerals in the bedrock compete with certain cationic radionuclides for complexation, further reducing the impact in the geosphere of many complexing agents. In light of the minor impact on dose and the lack of detailed investigation, the effect of both complexing agents and the pH plume is neglected in the geosphere modelling in this assessment.

Rn-222 ($t_{1/2} \sim 3.8$ days) is modelled in the geosphere as a short-lived decay product of Ra-226 and a parent of Pb-210. A noble gas, Rn-222 is expected to be dissolved with no sorption in the rock matrix. As this noble gas is not considered in the near-field models (due to its short half-life), only ingrowth during transport through the geosphere is considered.

Po-210 is not modelled in the geosphere. Instead, the activity release of Po-210 from the geosphere to the biosphere is assumed to be the same as activity release of its parent Pb-210, under the assumption that radioactive polonium in groundwater wells is in secular equilibrium with its parent (**Data report**, Chapter 8). Releases of Po-210 from the waste vaults are therefore ignored.

Table 5-18. Element-specific sorption coefficients (K_d , $m^3 kg^{-1}$) for the rock matrix, sorted by sorption strength. Log-normal distributions describe parameter uncertainties with the added restriction on samples to be within a 95 % confidence interval (this is somewhat different for Mo and Se, see the Data report, Chapter 8). For all elements, the best estimate (BE) is the same as the assigned geometric mean, except for Mo and Se, for which the BE is assumed to be $0 m^3 kg^{-1}$ (Table 8-6 in Data report). Each element has a unique set of parameter samples in the Monte-Carlo simulation.

Radionuclides	Geometric mean	Geometric std dev
Sn	1.6×10^{-1}	1.9
Pa	5.9×10^{-2}	3.0
Np, Tc, Th, U	5.3×10^{-2}	4.5
Pb	2.5×10^{-2}	3.6
Zr	2.1×10^{-2}	2.2
Nb	2.0×10^{-2}	4.4
Ac, Am, Cm, Eu, Ho, Pu, Sm	1.5×10^{-2}	5.3
Ba, Ra	1.0×10^{-3}	2.9
Cs	8.9×10^{-4}	3.8
Cd, Co, Ni	7.4×10^{-4}	6.2
Se	3.5×10^{-4}	4.2
Sr	1.5×10^{-5}	4.0
Mo	5.2×10^{-7}	4.2
Ag, Ca, C*, Cl, H, I, Pd	0	-

*All three forms of C-14 in the waste are cautiously assumed to exhibit no sorption in the geosphere.

5.5.2 Releases from the geosphere

Figure 5-45 shows the total annual geosphere activity releases from SFR. For several radionuclides with high releases from the near-field, no or almost no sorption in the geosphere is assumed. As a result, the near-field and geosphere releases are very similar for these radionuclides (C-14, Ag-108m, Ca-41 and Mo-93). For longer-lived radionuclides which display relatively weak sorption in the geosphere (Ni-59, Se-79, and Cs-135), transport through the geosphere results in a minor delay and a small decrease in the maximum release (less than one order of magnitude). However, for radionuclides which display strong sorption in the geosphere (U-238, Tc-99, U-235, Nb-94, Am-241, Pu-239 and Pu-240), and/or relatively short-lived radionuclides that are released mainly during the submerged period (H-3, Cs-137, Ni-63 and Am-241), the retardation during transport through the geosphere serves to reduce the maximum annual geosphere releases by at least one order of magnitude when compared with the near-field releases. Geosphere transport also reduces the release rates of radionuclides that have activity releases of less than $100 kBq a^{-1}$ (represented by “Other” in Figure 5-45), particularly during the first 10000 years after closure.

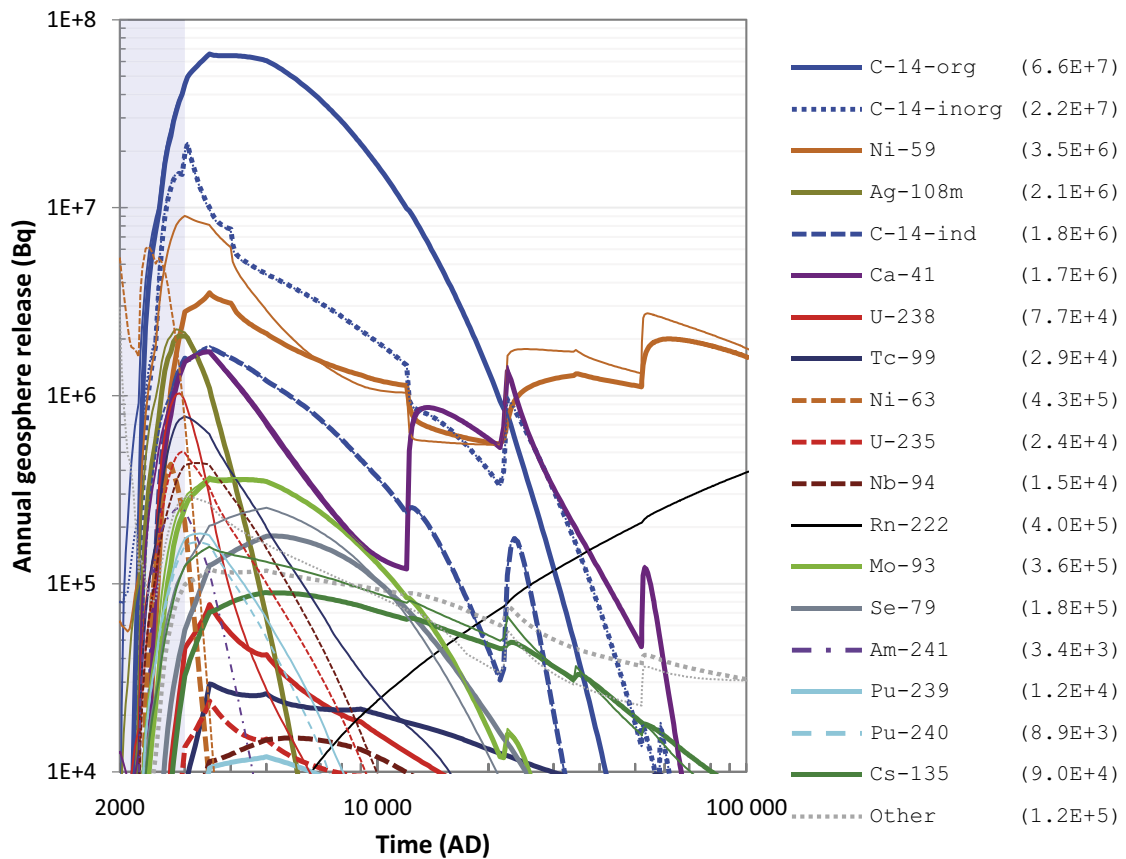


Figure 5-45. Annual activity releases (Bq) from the geosphere (thick lines) and the near-field (thin lines) from the entire SFR in the base case. The combined activity of radionuclides not shown is indicated by the grey dotted lines. Note that Rn-222 is not modelled in the near-field, but generated due to radioactive decay in the geosphere, and is therefore only illustrated for geosphere release (thin black line). The annual geosphere release maxima (Bq) are shown in parentheses in the key, data are sorted in the key by maximum annual near-field or geosphere release after the submerged period, which is illustrated by the blue shading.

5.5.3 Additional analysis

The radionuclide release from the near-field depends mainly on the initial activity of the waste, the ability of the engineered barriers to retard the migration and the shoreline position and its regression (Section 5.3). During submerged conditions, radionuclide releases from the waste vaults are low due to intact engineering barriers, small hydraulic gradients in the surrounding rock and, consequently, limited water flow through the waste vaults (see e.g. Figure 5-42). As the shoreline regresses over the repository and the engineered barriers deteriorate, an increase in groundwater flow occurs and the radionuclide release from the waste vaults increases. The radionuclides released from the waste vaults are then expected to be affected by retardation in the geosphere, as discussed in the following sub-sections.

Retardation in the geosphere

One important effect of the transport through the geosphere is that the geosphere will disperse the near-field release over time, independently of decay and ingrowth. This dispersion is illustrated in Figure 5-46, which shows the time evolution of releases from the geosphere of a species with the same properties as stable nickel, resulting from 1 000 years of unit annual release (1 mole a⁻¹) from the near-field. An integral effect of the dispersion is that the maximum release rate from the geosphere may be effectively lower than the maximum release rate from the near-field as a result of retardation in the geosphere (~0.4 in the figure). If the dispersion were more limited, the geosphere release would be confined to a period more similar to the near-field release and the maximum geosphere release would thus be higher. If the effect of dispersion were even more pronounced, the geosphere release would be spread over a longer period of time, resulting in a lower maximum release rate. It is also important to note that the dispersion results in a skewed temporal distribution of the geosphere release. The maximum release rate in the simplified example (Figure 5-46) occurs slightly beyond the release time from the near-field. This is because the sorption strength is low and the advective travel time is only a couple of years (this effect is more apparent in the expanded linear section of Figure 5-46, in the grey box). After the maximum annual release rate occurs, the geosphere release gradually declines. As a result of this skewed distribution, the average residence time in the geosphere is not considered an appropriate metric for when the most relevant (in a dose aspect) geosphere release occurs. As illustrated in Figure 5-46, the average residence time overestimates the timing of most of the release compared to the timing of the maximum geosphere release rate. The maximum release rate is thus of greater importance for dose than the lower release rates corresponding to the average residence time, which occurs up to tens of thousands of years after the maximum annual geosphere release.

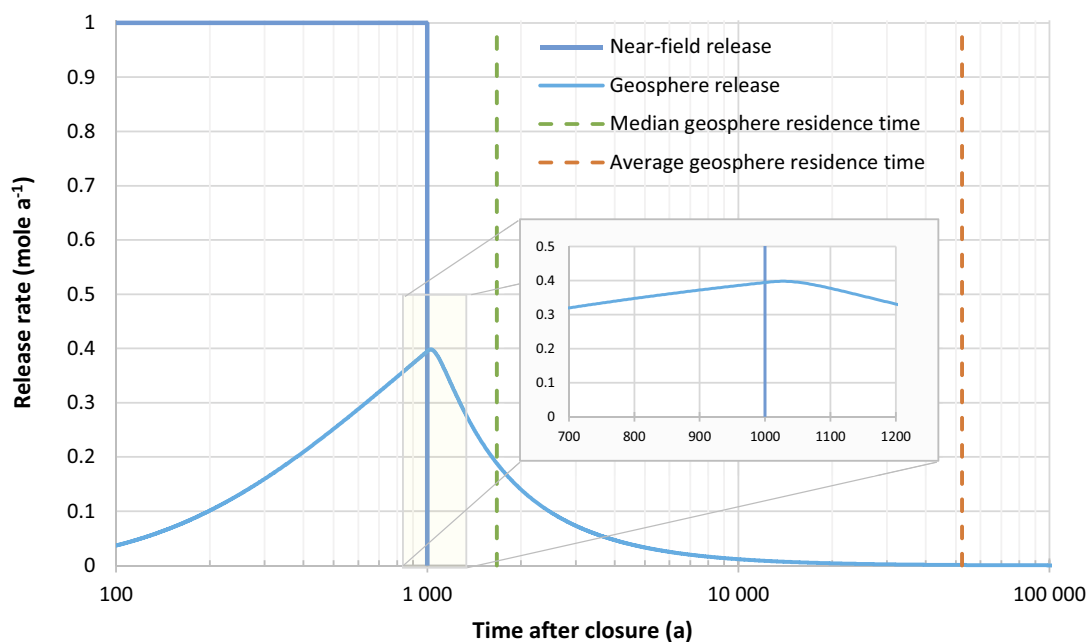


Figure 5-46. Illustrative example of the effect of dispersion for a species sharing the properties of stable nickel. The light blue curve shows the release from the geosphere in response to 1 000 years of a unit annual release from the near-field (dark blue curve). The median and average residence times in the geosphere are indicated by the green and orange vertical dashed lines, respectively. In this example, the area above the repository is assumed to be fully terrestrial using flow-related migration variables for an average fracture in the SFR-area (0.20 mm, resulting in a travel time of 2.9 years). Grey box shows an expanded area of the geosphere release curve.

The dispersion depends on the flow-related properties, such that longer travel times (as during the initial submerged period) and fractures with smaller apertures (reducing the diffusion path into the rock matrix) would result in a stronger dispersion. The appearance of dispersion also depends on several other features, including retardation and longitudinal dispersion in the fracture during advective transport. For a specific fracture, however, dispersion is mostly dependent on the duration of the release from the near-field (d_r) and the sorption strength in the rock matrix (K_d). The effect of these two features on dispersion are illustrated in Figure 5-47. The contours in the figure represent the maximum geosphere release rate resulting from a unit release rate from the near-field (i.e. corresponding to the maximum release in Figure 5-46). To facilitate the discussion related to Figure 5-47, this unitless parameter is hereafter referred to as r , which may vary between 0 and 1. If r is close to 1, after transport through the geosphere release rates similar to that of the near-field are reached, i.e. the effect of dispersion on the maximum geosphere release rate is limited. This situation emerges for radionuclides with low sorption coefficients and long release times. Conversely, if r is low, closer to zero, the effect of dispersion is high. This occurs when sorption is high and the release time is short. It is important to note that, whilst the release time sets an upper limit of r , the same is not true for the sorption coefficient. Thus, in the limit of $d_r \rightarrow \infty$ (i.e. at steady-state), the effect of dispersion on the maximum geosphere release rate will disappear, and thus $r = 1$. If $K_d = 0$, however, some effect of dispersion will still occur (for non-infinite d_r) since retardation in the rock matrix is still present due to the porosity of the rock and the longitudinal dispersion during advective transport in the fracture (see discussion in Rasmuson and Neretnieks 1981). For this situation, r may be close to, but never exactly, 1.

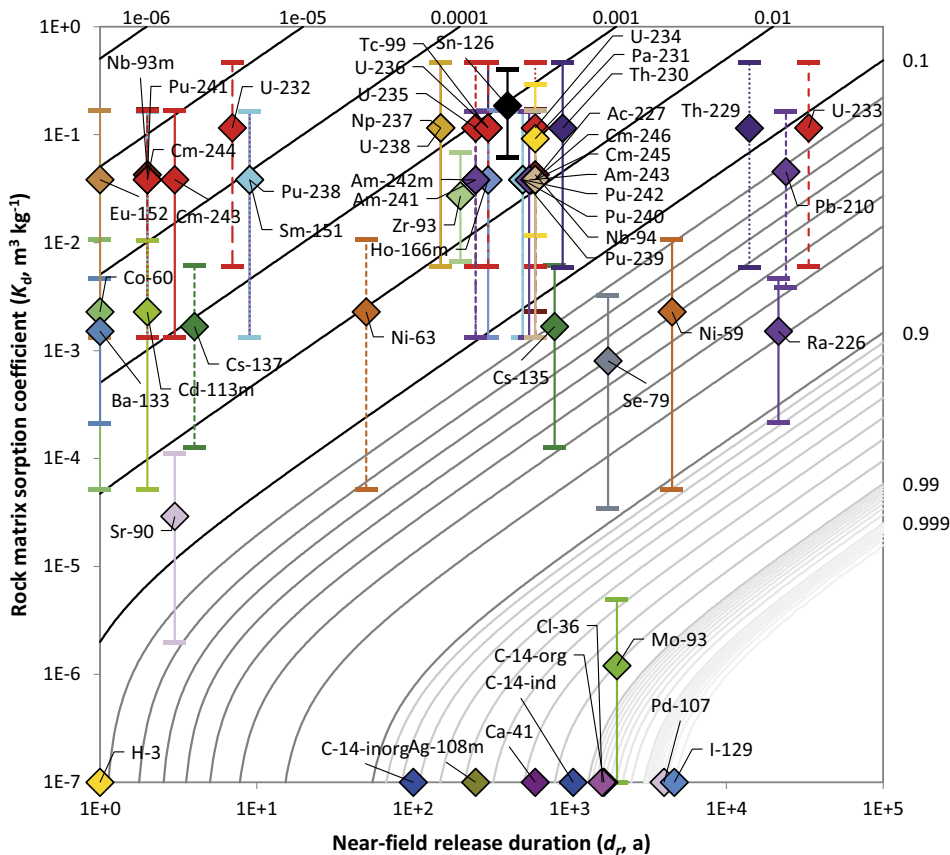


Figure 5-47. The maximum geosphere release resulting from unit release from the near-field (r ; contours in light grey and black) through an average fracture during fully terrestrial conditions as a function of release duration from the near-field (d_r) and the sorption coefficient (K_d). This illustrates the effect of dispersion of radionuclides during transport through the geosphere. The contours are plotted in steps of a factor 10 (black lines), higher contour resolutions are shown with lighter grey lines. Radionuclides have been placed on the K_d -axis according to summary statistics of the PDF (average value and 90 % confidence span), note that non-sorbing radionuclides (with a $K_d = 0$) have been placed on the x-axis. Radionuclide positions on the release time-axis are selected based on the duration of near-field maximum release (i.e. selected as release rate within 10 % of its maximum value). Note that, as in Figure 5-46, no radioactive decay in the geosphere is accounted for in the calculations.

Properties of the radionuclides are also included in the figure based on the duration of maximum near-field releases (x-axis) and their average K_d values in the rock matrix (y-axis and Table 5-18). For radionuclides (I-129, Pd-107, Cl-36, C-14-org, C-14-ind, Mo-93, Ca-41, Ag-108m and C-14-inorg) with very low or zero K_d values, and a near-field release duration of at least one hundred years, only a limited effect of dispersion is expected, corresponding to a decrease in maximum releases of less than 10 % ($r > 0.9$) from the geosphere relative to the near-field. Consequently, the effect of dispersion in the geosphere on those radionuclides is negligible in the radionuclide transport calculations. However, since most radionuclides released from the waste vaults have K_d values for the rock matrix greater than zero, the effect of dispersion on the maximum geosphere release is expected to be at least 10 % ($r < 0.9$) for typical release durations. For many of the released radionuclides, an effect of one, or even several, orders of magnitude due to dispersion is expected as a result of a strong sorption in the rock matrix ($r < 0.1$). Several radionuclides disposed in SFR are relatively short-lived (less than a couple of hundred years) and are not significantly affected by ingrowth (e.g. Co-60, Ba-133, H-3, Eu-152, Cd-113m, Pu-241, Nb-93m, Cm-244, Sr-90, Cm-243, Cs-137, U-232, Pu-238, Sm-151, Ni-63 and Am-242m) and these will have a very short release time from the near-field. Consequently, most of the release of these radionuclides will occur during the submerged period when a considerably larger dispersion effect is expected due to longer travel times.

A large dispersion combined with a short half-life also leads to an increased effect of radioactive decay due to the retardation in the geosphere. Thus, activity releases from the geosphere of these radionuclides are considerably lower than the corresponding near-field releases. This effect is most prominent for radionuclides with a half-life shorter than the transport time through the geosphere.

Annual radiotoxicity

As large activity releases of one radionuclide may lead to less harmful effects than lower activity releases of another radionuclide, it is important to not only consider activity releases when evaluating geosphere transport. Another way to illustrate the effect of the geosphere on radionuclide transport is to consider how the maximum annual radiotoxicity¹⁴ from the near-field changes during transport through the geosphere (Figure 5-48). Radionuclides located in the vicinity of the black line in Figure 5-48 have a similar maximum annual radiotoxicity from the geosphere as from the near-field, i.e. a value of r close to unity. The distance from the black line indicates how much the maximum annual geosphere radiotoxicity deviates from that of the near-field. Hence, radionuclides located below the line indicate that the maximum annual radiotoxicity decreases during transport through the geosphere and vice versa.

The grey circles in Figure 5-48 show the maximum annual geosphere radiotoxicity considering only the effect of dispersion (i.e. ignoring the effect of decay and ingrowth). The orange transparent circles show the effect of dispersion plus decay. Blue circles include the combined effects of dispersion, decay and ingrowth. Hence, the distance between the blue and orange circles represents the effect of ingrowth on the maximum annual geosphere radiotoxicity.

Figure 5-48 shows that the effect of the geosphere on the radiotoxic release varies widely depending on the radionuclide. In summary, however, radionuclides affected by geosphere transport can chiefly be grouped into the following four categories:

- 1) Radionuclides for which the maximum annual radiotoxicity from the near-field is marginally affected by the transport through the geosphere, i.e. those that are represented by only blue circles and located in the vicinity of the black line in Figure 5-48 (Cl-36, Ca-41, Cs-135, Se-79, Ni-59, Mo-93, I-129, Ag-108m as well as the different species of C-14). These radionuclides are not short-lived and display weak or zero sorption in the rock matrix. In addition, they may be associated with long near-field release times (see Figure 5-47).
- 2) Radionuclides that are only affected by dispersion due to stronger sorption together with longer half-lives and/or short release periods. These are represented by blue circles and positioned below the black line in Figure 5-48 (U-236, Sn-126, Np-237, Pu-242, Tc-99, Nb-94, U-235, U-238, Pu-239).

¹⁴ Annual radiotoxicity (Sv a^{-1}) is here defined as the activity release rate (Bq a^{-1}) multiplied by the dose coefficient for ingestion (Sv Bq^{-1}).

- 3) Radionuclides that are affected by both dispersion and radioactive decay, but not by ingrowth. These are indicated by blue circles located below a grey circle in Figure 5-48 (H-3, Eu-152, Ho-166m, Cm-245, Co-60, Ni-63, Pu-238, Sr-90, Cs-137, Am-241, Am-243, Pu-240).
- 4) Radionuclides for which the effects of dispersion and decay are partially or fully compensated by ingrowth from parent radionuclides (relevant decay chains are indicated by blue arrows in Figure 5-48). The impact of the compensation due to ingrowth can be measured by the relative distance between the blue and orange circles. For Pu-241, for example, located between the grey and orange circles, ingrowth does not fully compensate for decay during transport. For Th-230, Ra-226, Pb-210 and Ac-227, the effect of ingrowth even exceeds the combined effect of dispersion and decay, resulting in a slight increase of the maximum annual radiotoxicity of these radionuclides during transport through the geosphere.

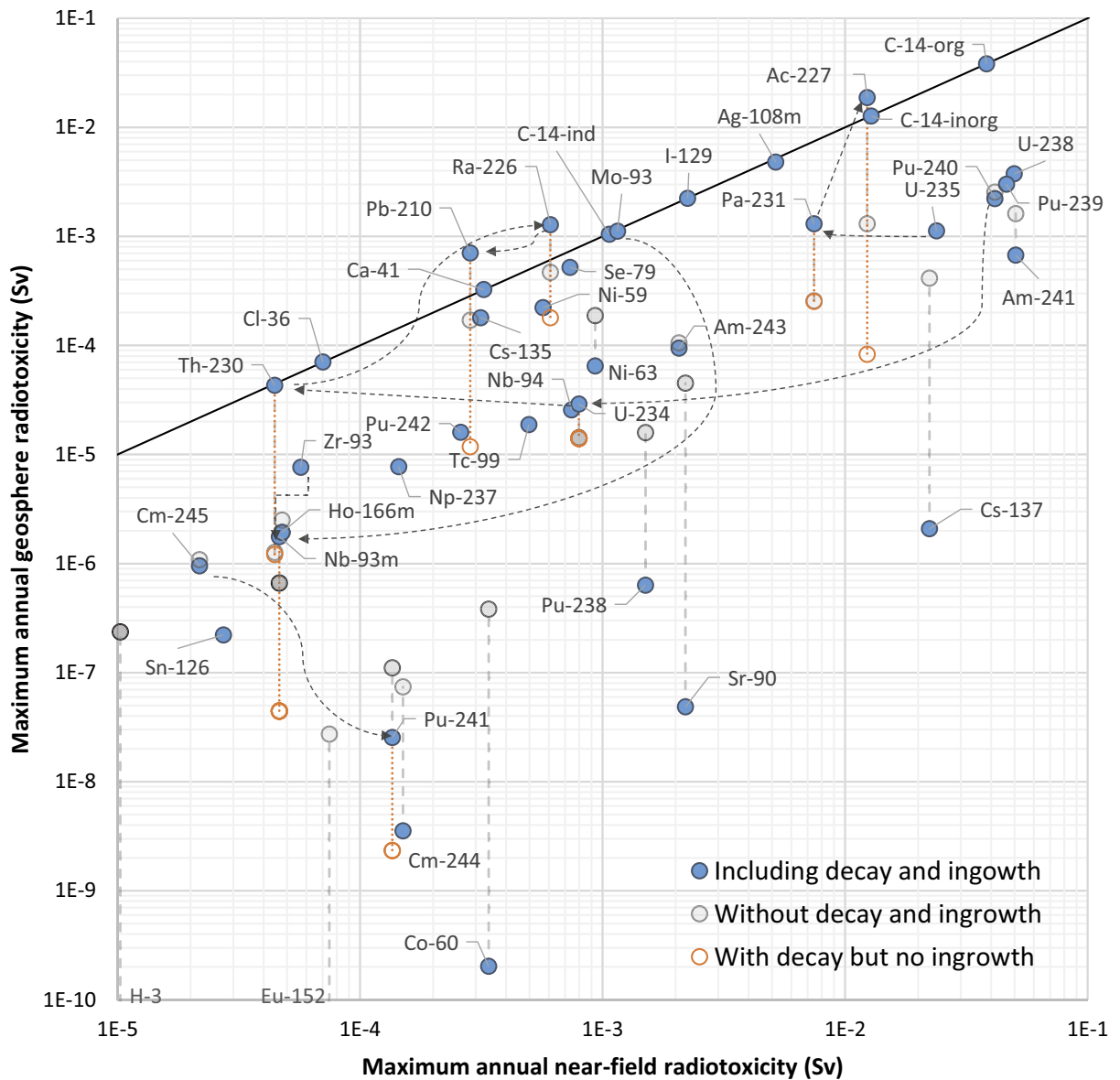


Figure 5-48. Maximum annual geosphere radiotoxicity as a function of maximum annual near-field radiotoxicity. Blue circles correspond to the total radiotoxicity, grey semi-transparent circles to the geosphere radiotoxicity without the effects of radioactive decay and ingrowth, and orange circles to the geosphere radiotoxicity without the effect of ingrowth. Grey and/or orange circles that would fall on the corresponding blue circles (within 10 % uncertainty) are omitted from the figure. The arrows indicate decay chains from parent radionuclides to decay products.

It should be noted that potential exposures to radionuclides after release from the geosphere are not necessarily correlated with the *maximum* annual radiotoxicity. Instead, for many radionuclides, dose consequences are often better correlated with the *accumulation* of radionuclides in the regolith layers in the surface system over time (**Biosphere synthesis report**). The potential effect of accumulation of radionuclides in the surface systems is examined by integrating the annual radiotoxicity released from the geosphere over the full assessment period. This exercise also reveals the scale of the source and sink terms of radionuclides in the geosphere. As can be seen in Figure 5-49, source terms of radionuclides in the geosphere are either releases from the near-field or ingrowth from parent radionuclides, whereas sink terms either represent radioactive decay or release from the geosphere to the biosphere.

Figure 5-49 shows the accumulated radiotoxicity (integrated over the whole 100 000-year assessment period) released from the near-field and the geosphere as well as the accumulated radiotoxicity produced within the geosphere (yellow square, circle and triangle symbols respectively) for radionuclides with an accumulated near-field release or geosphere production that has a radiotoxicity larger than 1 Sv. The figure also shows the fraction of radionuclides that at the end of the assessment period either 1) still reside within the geosphere (dark grey), 2) have decayed during transport through the geosphere (light transparent grey), or 3) have been released from the geosphere into the biosphere (diagonal grey stripes). The maximum possible accumulated radiotoxicity in the biosphere, when also taking decay and ingrowth into account, is illustrated by the green diamonds. Order of radionuclides, from left to right, are based on the magnitude of the accumulated radiotoxicity released from the geosphere (circles).

Of the 28 radionuclides in Figure 5-49, the eight rightmost ones display more than five orders of magnitude lower accumulated radiotoxicity release from the geosphere than the total initial radiotoxicity. As a result of radioactive decay and/or retardation in the near-field and the geosphere, these radionuclides reach the biosphere at very low radiotoxicity levels within the assessment period of 100 000 years. The remaining 20 radionuclides in Figure 5-49 all respond differently during retardation in the geosphere. Broadly, however, they can be grouped into three categories.

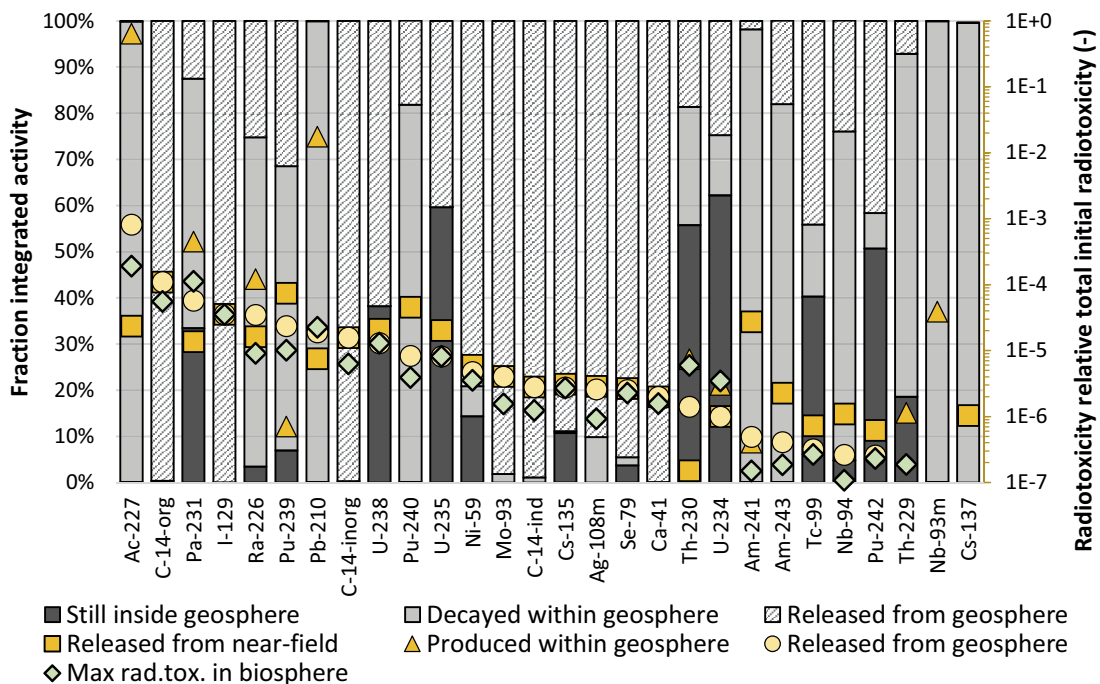


Figure 5-49. Fates of radionuclides in the geosphere in the base case. Radionuclides are sorted from the left to right by the integrated radiotoxicity release from the geosphere to the biosphere. Left y-axis: fraction of radionuclides (released to geosphere + produced within the geosphere) that 1) remain within the geosphere at the end of the 100 000-year assessment period (dark grey bar), 2) have decayed within the geosphere (light transparent grey), or 3) have been released from the geosphere within the assessment period (diagonal grey stripes). Right y-axis: integrated radiotoxicity over the assessment period relative to the total initial radiotoxicity as released from the near-field (squares), produced within the geosphere (triangles), released from the geosphere (circles) and the maximum radiotoxicity possibly existing in the biosphere at any point in time (diamonds).

The first category concerns radionuclides for which the radiotoxicity is not significantly altered by the retardation in the geosphere i.e. virtually the entire release from the near-field will end up in the biosphere. This includes C-14-org which has the second highest accumulated radiotoxicity releases to the biosphere, but also other zero or weakly-sorbing radionuclides such as Mo-93, C-14-inorg, I-129, C-14-ind and Ca-41. Further, even though some decay and dispersion of the activity of Se-79 may occur in the geosphere¹⁵, the effect of the geosphere transport on the radiotoxicity is limited for this radionuclide.

In the second category, belong eight radionuclides for which the geosphere retardation considerably decreases the accumulated radiotoxicity from the near-field and/or from ingrowth. The radiotoxicity decrease is attributed to either a slow transport through the geosphere, significant radioactive decay or a combination of both. For long-lived radionuclides U-235, U-238 and Cs-135, the decreased radiotoxicity is predominately a result of a slow transport through the geosphere. For the remaining radionuclides within this category, i.e. Pu-239, Pu-240, Ni-59, and Ag-108m, radioactive decay is also important. This effect is particularly evident for the sorbing and highly radiotoxic plutonium isotopes, Pu-239 and Pu-240, for which only 10–20 % of the released activity from the near-field ends up in the biosphere.

Finally, in the third category belong radionuclides that are predominately produced within the geosphere. This includes two of the three radionuclides with largest accumulated radiotoxicity releases to the surface system, Ac-227 and Pa-231, both of which originate from U-235 during transport, but also Ra-226, Pb-210, Th-230, U-234 that are products of the U-238 decay chain (see also Figure 5-48). As a result of ingrowth, most of the radionuclides within this category become more radiotoxic during transport through the geosphere. The only exception is U-234, for which the increased radiotoxicity from ingrowth is compensated by slow transport through the geosphere.

5.5.4 Summary geosphere

The influence of the geosphere on the retardation of radionuclides in the SFR area depends mainly on (1) the duration of the near-field release (2) the degree of sorption in the rock matrix, (3) radioactive decay and (4) ingrowth of decay products. Of these processes, sorption and duration of the near-field release contribute greatly to the dispersion of radionuclides, as illustrated in Figure 5-47. Some of the radionuclides, with half-lives longer than some millennia and which display weak sorption in the rock matrix and are not significantly dispersed over time, will not be significantly affected by geosphere retardation. Many of the radionuclides that contribute most to the dose in the subsequent biosphere analysis fall into this category (e.g. C-14, Mo-93, Ni-59 and Ca-41, see Section 5.7).

It is also important to note that transport through the geosphere has an important effect on mitigating the release of long-lived radionuclides from SFR that could otherwise end up being most relevant for dose consequences in the future. This concerns mainly radionuclides that are associated with long transport times and significant dispersion due to strong sorption in the rock matrix, including certain isotopes of uranium and plutonium (U-235, U-236 and U-238, Pu-239 and Pu-242). The long transport times of these radionuclides, however, enable ingrowth of decay products. For example, two of the three radionuclides with the highest accumulated annual radiotoxicity are decay products of U-235 (Pa-231 and Ac-227). These radionuclides are expected, on average, to be among the most toxic from direct ingestion (e.g. through drilling of wells) over the next 100 000 years. Finally, relatively long transport times in the geosphere also serve to reduce the radiotoxicity of certain shorter-lived radionuclides (e.g. Ni-63, Cs-137 and Am-241) before they reach the biosphere.

¹⁵ Se-79 has a median K_d value that is relatively small, but also the largest K_d variation of all radionuclides. Thus, for a limited number of iterations the transport through the geosphere may be slower, resulting in some activity and decay in the geosphere.

5.6 Geosphere – biosphere interface

Most of the geosphere release is likely to be discharged into biosphere object 157_2 (see Figure 4-5) given the reference bedrock case (BC1, Öhman and Odén 2018). Moreover, hydrogeological modelling of release locations in the landscape in 22 bedrock cases showed that more than 80 % (and in most cases more than 90 %) of particles released from SFR would end up in the basin of biosphere object 157_2 (Figure 5-50). In addition, less than 3 % of the released particles typically reach other biosphere objects after the submerged period (which ends at 3000 AD in the *base case*).

In the *base case*, the entire geosphere release is assumed to be discharged to biosphere object 157_2, and, subsequently, radionuclides are transported to other biosphere objects through water exchange or stream water (Sections 2.2 and 5.7).

Extraction of radionuclides in groundwater from wells drilled into the geosphere downstream of the repository is evaluated in the area where groundwater is expected to have the highest concentrations of radionuclides, i.e. the *well interaction area* (Section 4.4). The average fraction of the release from the geosphere that reaches such a well is expected to be between 3.4 % (1BRT) and 9.6 % (silo), accounting for variability due to the position of the well. In the PSAR, this fraction was handled probabilistically, accounting for differences between waste vaults and co-variation caused by the spatial position of the well (**Biosphere synthesis report**, Section 8.2). The concentration of the extracted well water is simply calculated by dividing this fraction of the release by the postulated water extraction rate of 700 litres per day (Grolander 2013, Section 12.1.1).

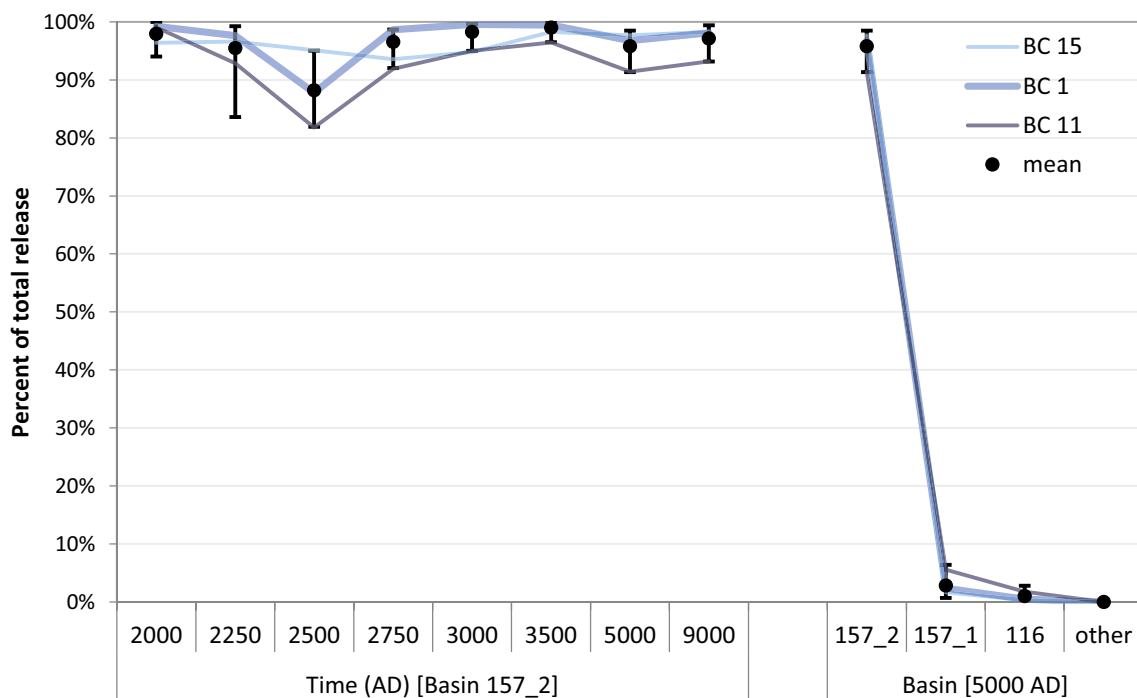


Figure 5-50. Fractions (%) of total potential release from SFR that are discharged into the basin of biosphere object 157_2 over time (left) or at 5000 AD (right, also including other basins). The bold blue line represents the reference bedrock case (BC1), whereas the thin lines represent the other two representative bedrock cases (BC11 and BC15) according to Öhman et al. (2014). Surface positions for discharging particles are taken from Öhman and Odén (2018). Mean (black circles) and 90 % confidence interval (vertical bars) are given for the 22 bedrock cases.

5.7 Biosphere

This section summarises how the biosphere is handled in the *base case* and presents a summary of key results. A more detailed biosphere description of the *base case*, as well as a more comprehensive analysis of the results, is presented in Chapter 9 of the **Biosphere synthesis report**.

5.7.1 Handling in the biosphere models

Landscape description

The evolution of biosphere object 157_2 and the *well interaction area* above sea level resulting from the shoreline regression in the *base case* are summarised in Table 5-19. The deepest parts of object 157_2 are presently approximately 6 m below sea level and, when the object emerges from the sea, the shallowest (southern) parts of the object will emerge first. During the submerged period, radionuclides are expected to reach all basins in direct or indirect contact with basin 157_2, through lateral exchange of water between basins (Figure 5-51). However, during periods of fully terrestrial conditions (after ~4500 AD for object 157_2), radionuclides will only reach objects that are connected with the primary discharge area via surface runoff (Figure 5-52).

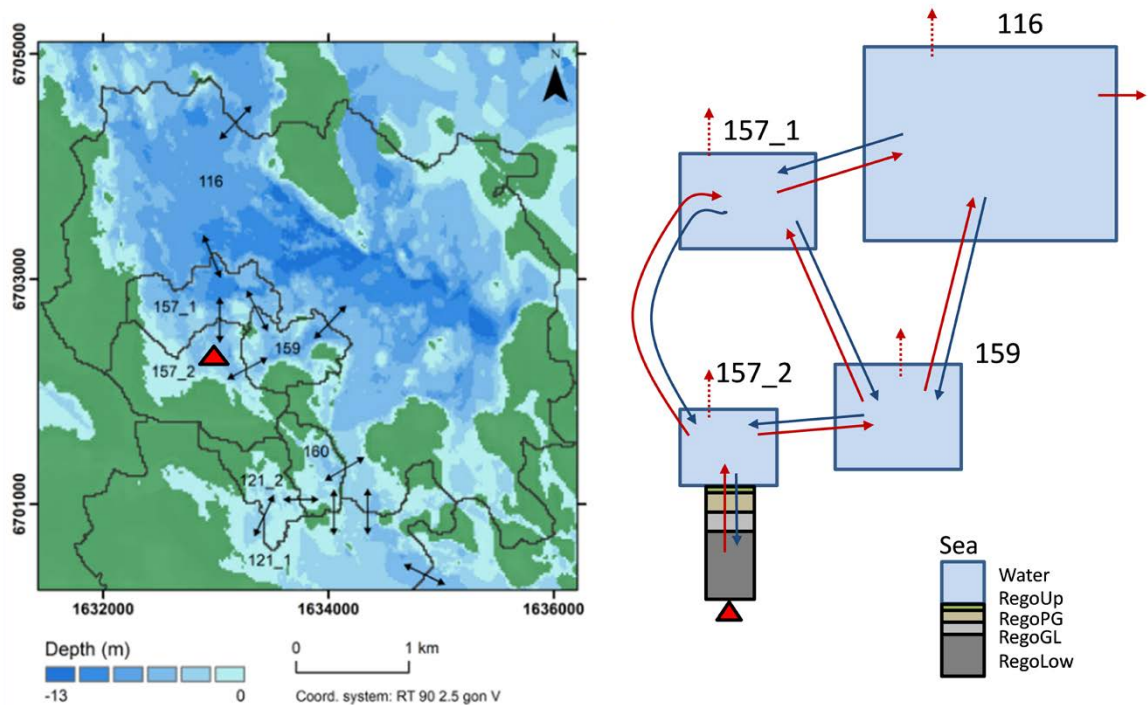


Figure 5-51. Conceptual model of discharge and dispersion of radionuclides that reach the biosphere via groundwater from the geosphere during the marine stage. The red triangle represents the location of the geosphere release (object 157_2). Left) Water depth and dispersion routes of radionuclides between basins at 3000 AD. Biosphere object 157_2 receives radionuclide-containing groundwater from below. All biosphere objects receive radionuclides via lateral seawater flow during the marine stage. Right) Schematic sketch of the dispersion of radionuclides between regolith layers and surface seawater volumes within and between biosphere objects. The light blue boxes represent seawater. Red arrows show transport of radionuclides along a declining solute concentration gradient. Blue arrows show the transport of radionuclides in the opposite direction. The regolith layers included are (from below); till (RegoLow), glacial clay (RegoGL), post-glacial clay-gyttja (RegoPG), biologically active surface sediments (RegoUp). Dashed arrows represent loss of C-14 to the atmosphere. Note that the figure represents a snapshot in time and that exchange with basins south of 116 has been excluded for clarity.

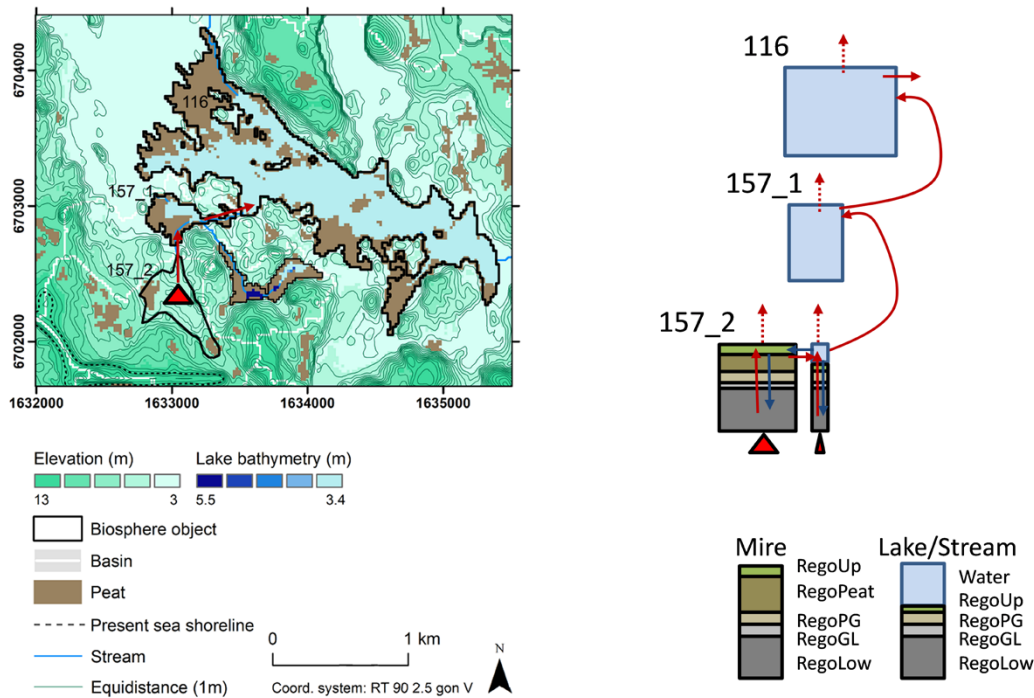


Figure 5-52. Conceptual model of discharge and dispersion of radionuclides that reach the biosphere via groundwater from the geosphere during the terrestrial stage. The red triangle represents the location of the geosphere release (object 157_2). Left) Ground surface elevation and water depths in lakes at 5000 AD. Downstream objects 157_1 and 116 receive radionuclides via surface water during the terrestrial stage. Right) Schematic sketch of the transport of radionuclides between regolith layers and surface waters within and between biosphere objects. In both the panels, red arrows show transport of radionuclides along a declining solute concentration gradient. Blue arrows show transport in the opposite direction. The regolith layers for aquatic ecosystems are labelled as in Figure 5-51. In terrestrial parts deep peat (RegoPeat) and surface peat (RegoUp) are stratified on top of clay-gyttja. The light blue boxes represent lake and stream water. Dashed arrow represents loss of C-14 to the atmosphere. Note that the figure represents a snapshot in time and that the lake basins in 157_1 and 116 will ultimately be infilled with peat so that the lakes disappear and only a stream remains.

In the *base case*, the biosphere description is focused on the primary discharge area. Transport and accumulation of radionuclides in regolith layers and water bodies are described for both the marine and terrestrial periods of biosphere object 157_2. Exposure from downstream objects is also evaluated but, for these recipients, water is the only environmental transport medium considered.

The transport and accumulation of radionuclides is simulated in a landscape that is undisturbed by humans. Only after the biosphere object has emerged sufficiently above sea level to prevent intrusion of saline water are the consequences of draining and cultivating the mire complex and extraction of water from a dug well, evaluated in parallel. Similarly, the effects of water extraction from a well drilled into the geosphere are evaluated when the *well interaction area* is sufficiently elevated above sea level. The threshold for cultivation and extraction of well water has been set to one metre above the prevailing sea level, approximately corresponding to the highest storm-surge levels in the area (**Climate report**, Section 3.5 and Grolander 2013, Werner et al. 2013). The upland parts of object 157_2 and of the *well interaction area* will, in the *base case*, have emerged one metre above the sea level around 3200 and 3000 AD, respectively (Table 5-19).

Table 5-19. Overview of the evolution of biosphere object 157_2 and the well interaction area, resulting from the initial shoreline displacement assumed in the *base case* (Section 5.2).

Year AD	Surface above SFR	Biosphere object 157_2	Well interaction area
2000	Submerged	Submerged	Submerged
2500	Shoreline located directly above SFR	Submerged	Submerged
3000	> 75 % terrestrial	Highest point (southern part) above sea level ¹	Highest area > 1 m above sea level
3500	Terrestrial	20 % of the object above sea level, and highest point > 1 m, above sea level	25 % of area > 1 m above sea level
4000	Terrestrial	90 % of the object above sea level	67 % of area > 1 m above sea level
4500	Terrestrial	Whole object > 1 m above sea level, mire fully developed.	Whole area > 1 m above sea level
5000	Terrestrial	Whole object > 1 m above sea level, mire fully developed	Whole area > 1 m above sea level

¹ = dug well and draining possible.

Surface hydrology

Water balances of the future biosphere objects (areas potentially affected by releases) were modelled at three points in time: 3000 AD (end of submerged period), 5000 AD (terrestrial period, when objects are either lake-mire complexes or mires) and 11 000 AD (terrestrial period, all objects are mires). Temperature, precipitation and potential evapotranspiration from present-day condition, i.e. the normal year (Section 5.2), were used as input data to the simulations. Hydrological modelling and parameter values are further described in Chapters 4 and 8 of the **Biosphere synthesis report**.

It is assumed that the runoff from object 157_2 reaches the downstream object 157_1 via a stream (Section 7.5.2 in Werner et al. 2013). The effects of assuming diffuse overland-water transport, rather than stream transport, are examined in the *alternative landscape configuration calculation case* (**Biosphere synthesis report**, Section 10.6).

Ecosystem parameters

Ecosystem parameters are based on site data from lakes, wetlands and marine basins in the area, and they are applied to future ecosystems by assuming present-day conditions concerning nutrients and temperatures. The parameters updated since SR-PSU include those used to describe the accumulation of organic carbon and those describing the crop and water regime of the GP exposed group (Section 4.4.3). In addition, new parameters for chlorine were derived from recent field measurements in Forsmark. These are described in the **Biosphere synthesis report**, Section 8.2.

Potentially exposed groups and populations

The annual dose to a representative human is calculated for the four different exposed populations, described in Section 4.4. Exposure pathways included are the ingestion of food and drinking water, the inhalation of air, and direct external irradiation (see Section 6.2 in the **Biosphere synthesis report** for details).

The exposure from a well drilled in the area where groundwater is expected to have the highest concentrations of radionuclides originating from SFR (i.e. the *well interaction area*, Section 4.4.1) is only considered to be relevant for a small group. The pathways considered for this group are the ingestion of water and small-scale irrigation (GP). As the group is small, a risk criterion of 10^{-5} is considered appropriate. To make the dose comparable to that of other exposed populations, it is divided by a factor of ten (**Biosphere synthesis report**, Section 7.5.4).

5.7.2 Annual doses

Annual doses to the potentially exposed groups

The resulting annual doses, from the total geosphere release to the potentially exposed groups (PEGs) in the *base case* are presented in Figure 5-53. During the initial submerged period when agriculture in object 157_2 is not possible, HG is the most exposed group and the resulting doses are low. Note that during this period, the GP group also receives doses, albeit at very low levels, as they are assumed to collect seaweed from object 157_2 and use it to fertilise a kitchen garden. Beginning from 3000 AD, when drilling of wells becomes possible (Table 5-19), the GP group utilising the well has the highest dose and this situation persists for 200 years.

At 3200 AD, it is considered feasible to drain the peat land in object 157_2 and to extract water from a dug well, resulting in the DM farmers becoming the most exposed group for the rest of the assessment period. The following presentation and discussion of the results therefore focuses mainly on this group. For this group, released radionuclides are considered to accumulate continuously in the mire ecosystem up to the point of drainage. The average annual dose from early cultivation (50 years following drainage, approximately corresponding to a human lifetime) is evaluated for each point in time, cautiously assuming that the mire has not been disturbed prior to the point of drainage. The potential exposure from consumption of water from a well dug in the till is also evaluated for this exposure group.

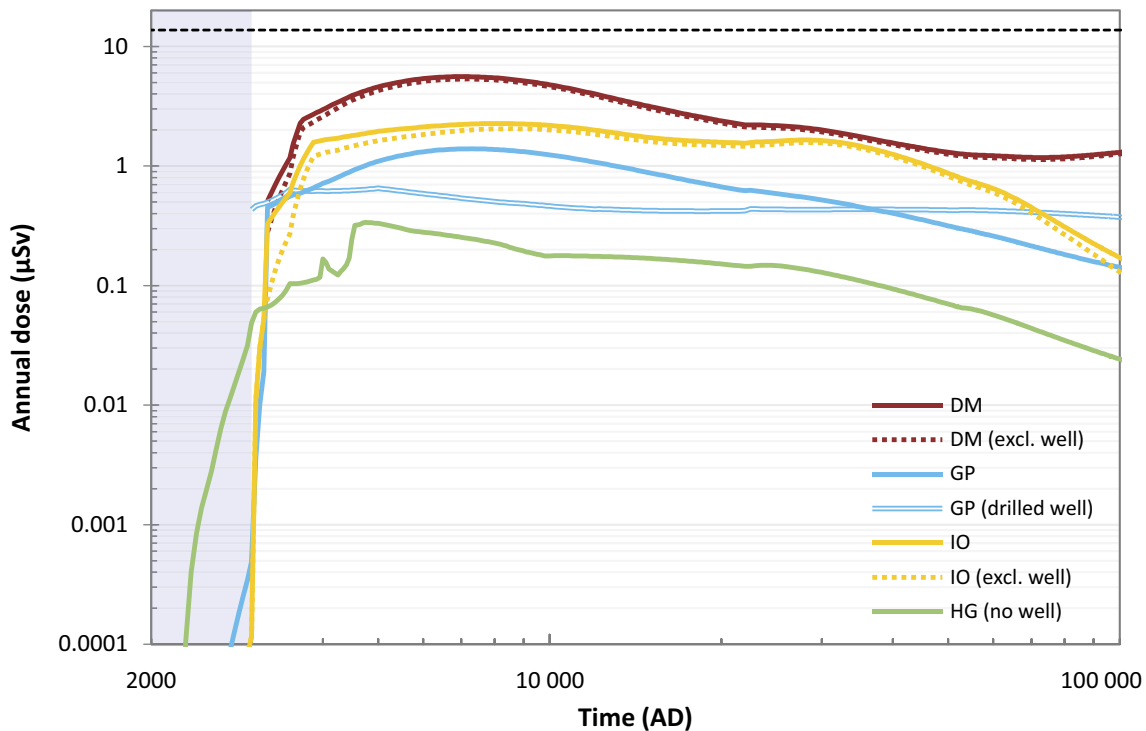


Figure 5-53. Annual doses for different exposed groups in the base case, that is to hunter-gatherers (HG), infield–outland farmers (IO), drained-mire farmers (DM) and garden-plot households (GP). The dose contribution from well water is highlighted by including results where exposures of DM and IO from dug wells are replaced with exposures from stream water (dashed coloured lines). The doses to GP from a dug and from a drilled well are shown separately (single and double blue lines respectively). The annual dose corresponding to the regulatory risk criterion (14 µSv) is indicated by the black dashed line and the submerged period is illustrated by the blue shading.

Radionuclide-specific annual doses

Radionuclide-specific annual doses to the most exposed group¹⁶ are shown in Figure 5-54. Mo-93 and C-14, especially in organic form in the waste, contribute most to the total annual dose during the first 20 000 years, with some contributions from U-238, I-129 and Ca-41. The dose maximum, ca 5.6 μSv , occurs 5 000 years after closure of the repository (i.e. around 7000 AD), where Mo-93 and C-14-org contribute with 60 % and 15 % to the total annual dose.

Ca-41 is the radionuclide contributing most to the total annual dose during the period between 20 000 and 60 000 AD. The total annual dose decreases during this period (with an initial dose of approximately 2.4 μSv) as contributions from Mo-93, I-129 and uranium isotopes gradually decrease with time. The decline in total annual dose is partly compensated by increased contributions from Ca-41 and decay products of U-235 (Ac-227 and Pa-231) in the middle of the period.

Ni-59, which is rather immobile in the near-field and geosphere, becomes increasingly important towards the end of the assessment period and becomes the radionuclide contributing most to the total annual dose after 60 000 AD. At this time, the total annual dose is ca 1 μSv , but increases slightly at the end of the assessment period. Ni-59 contributes a third of the total annual dose at the end of the assessment period, with contributions of about 30 % and 15 % from Cs-135 and Ac-227, respectively.

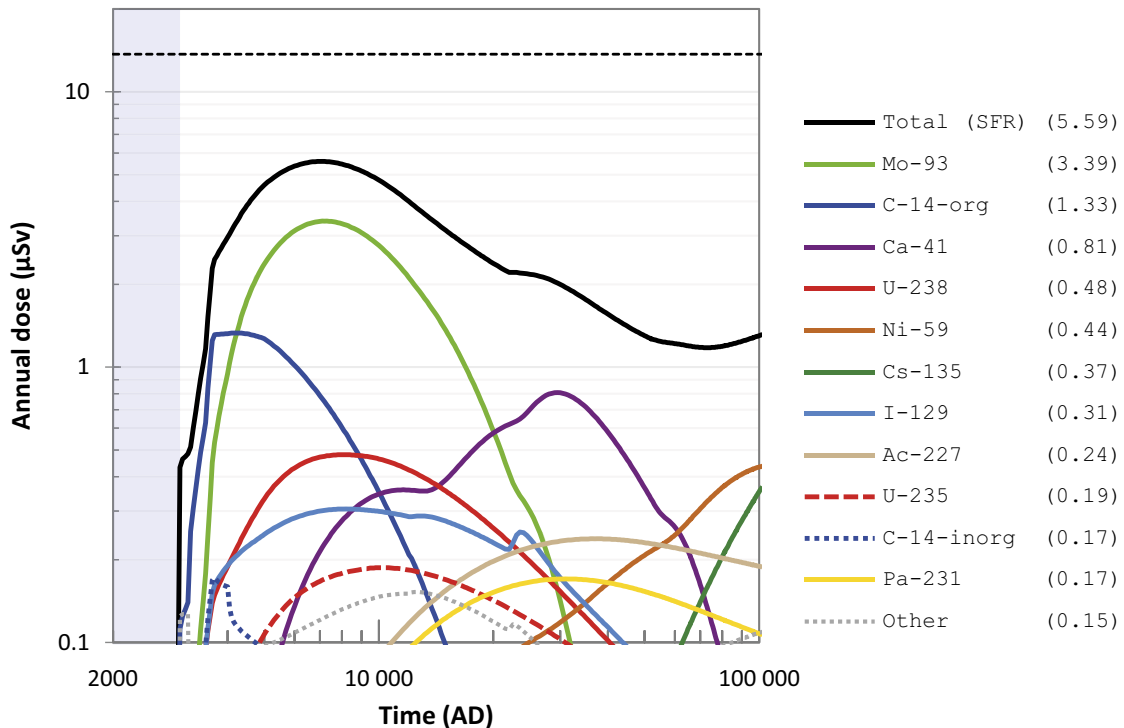


Figure 5-54. Annual dose (μSv) to the most exposed group in the base case (black line) including radionuclide-specific contributions (coloured lines). The combined contribution from the radionuclides not shown is indicated by the grey dotted line. The total and radionuclide-specific annual dose maxima (μSv) are shown in parentheses in the key. The annual dose corresponding to the regulatory risk criterion (14 μSv) is indicated by the black dashed line and the submerged period is illustrated by the blue shading.

¹⁶ “Most exposed group” refers to the PEG receiving the highest dose at each point in time. Thus, the PEG corresponding to the most exposed group may vary with time over the assessment period.

Both Ni-59 and Cs-135 show an increasing dose trend at the end of the assessment period. As they both are long-lived and move slowly in the regolith layers, they are relevant to dose in a very long time-perspective. Thus, to investigate the behaviour of these radionuclides, simulations were performed for an additional 900 000 years for the *base case*. These simulations show that, while the doses from Ni-59 and Cs-135 continue to increase for some time after the end of the assessment period, their contributions remain well below the dose corresponding to the risk criterion. Specifically, Ni-59 reaches a maximum of about 0.5 μSv at 120 000 AD and decreases continuously after that. Cs-135 reaches a maximum of about 1.5 μSv at 450 000 AD after which it gradually decreases.

The temporal behaviour of the radionuclide-specific annual doses is strongly influenced by the geosphere releases (Figure 5-45). However, there are also other factors affecting the temporal patterns and the relations between the magnitudes of geosphere releases and doses for the different radionuclides. These include radionuclide- and element-specific properties that influence their transport and accumulation in the biosphere, transfers to plants and foodstuffs and the magnitude of potential radiological consequences arising from unit exposures of humans, either by intake or as external irradiation.

Properties of key radionuclides

To illustrate and understand how radionuclide properties influence the assessment results in terms of doses and environmental activity concentrations, the following discussion focuses specifically on the four radionuclides that contribute most to the annual dose, i.e. C-14-org, Mo-93, Ca-41 and Ni-59. These four radionuclides also cover a wide range of isotopic- and element-specific properties (Table 5-20). A more comprehensive analysis of these four radionuclides is given in the **Biosphere synthesis report**, Section 9.3.

In the biosphere, properties related to transport, sorption, accumulation and radioactive decay determine environmental activity concentrations in the regolith profile, in relation to the geosphere releases. Figure 5-55 shows the relative distribution of the activity concentration in the regolith layers at dose maxima for the four key radionuclides, as well as the proportion of the total activity that has been removed from the biosphere object, either by export out of the system via surface water, degassing or by radioactive decay.

In the biosphere, the non-sorbing radionuclide C-14-org mainly follows the groundwater flow. C-14-org is quickly transported through the regolith layers (~ 10 years) and is only marginally affected by radioactive decay within this time period. It is, as seen in Figure 5-55, to a large degree exported out of the system, by water exchange with surrounding basins during the submerged stage, or by degassing to the atmosphere during the terrestrial stage. The overall environmental concentrations closely follow the geosphere release (Figure 5-45), meaning that the maximum geosphere release is strongly correlated with potential dose consequences.

The sorbing radionuclides are retained in the regolith and the accumulation of activity and the average transport (or residence) times are positively correlated to the degree of sorption. For Mo-93 and Ni-59, the average transport time in the biosphere is in the same order as their physical half-lives and thus a noticeable amount of the released activity decays within the biosphere (Figure 5-55). For Ca-41, the half-life is almost an order of magnitude greater than the average transport time, so export out of the system with water is a dominant removal mechanism, despite retention in the regolith.

Mo-93, Ca-41 and Ni-59 all sorb fairly strongly in the regolith (Table 5-20). At the time of maximum radionuclide-specific doses, approximately 40 % of the accumulated releases are stored in the regolith profile of the biosphere object (Figure 5-55). This activity inventory corresponds to an accumulation of releases over several thousands and tens of thousands of years for Mo-93 and Ca-41, respectively. However, the distribution of the accumulated activity differs between radionuclides (Figure 5-55). Ca-41 and Ni-59 are strongly sorbed to inorganic regolith layers and so are retained within the lowest regolith layer. Mo-93, on the other hand, sorbs more strongly in the organic-rich upper regolith layers, meaning that most of the accumulated Mo-93 activity will become accessible for exposure when the object is drained and cultivated. For C-14-org, radionuclide accumulation is of minor importance for exposure during cultivation. Instead, groundwater uptake is the primary source for C-14-org in the drained and cultivated mire.

Table 5-20. Selected properties of radionuclides contributing significantly to the dose. K_d is the sorption coefficient in the regolith layers, CR the soil-to-plant concentration ratio, TC the transfer coefficients to animal products and DC the ingestion dose coefficient. The colours and their intensities reflect the magnitude of each parameter, where blue shades symbolise lower values and yellow larger values.

Parameter	Unit	Specification	C-14-org	Mo-93	Ca-41	Ni-59
Half-life	years		5 700	4 000	102 000	101 000
$K_d^{(a)}$	$m^3 kg_{DW}^{-1}$	RegoUp_ter	0	4.3	0.31	1.9
		RegoPeat	0	3.9	0.38	2.6
		RegoPG	0	3.4	0.037	1.1
		RegoGL	0	0.22	0.95	17
		RegoLow	0	0.021	0.29	0.79
		RegoUp (DM)	0	0.74	0.11	0.83
$CR^{(a)}$	$kg_{DW}^{-1} kgC^{-1}$	cereals	-(b)	1.2	0.23	0.016
		tubers	-(b)	0.90	0.39	0.14
		fodder	-(b)	0.26	1.5	0.14
$TC^{(a)}$	$day kg_{FW}^{-1}$ $day L^{-1}$	meat	-(b)	0.001	0.013	0.16
		milk	-(b)	0.0011	0.02	0.00095
$DC^{(c)}$	$Sv Bq^{-1}$	ingestion	5.8×10^{-10} (d)	3.1×10^{-09}	1.9×10^{-10}	6.3×10^{-11}

a) Geometric mean.

b) Parameter not relevant since a specific activity approach is used for C-14-org.

c) Constant value.

d) The dose coefficient for C-14-org due to ingestion of water is $2.9 \times 10^{-11} Sv Bq^{-1}$.

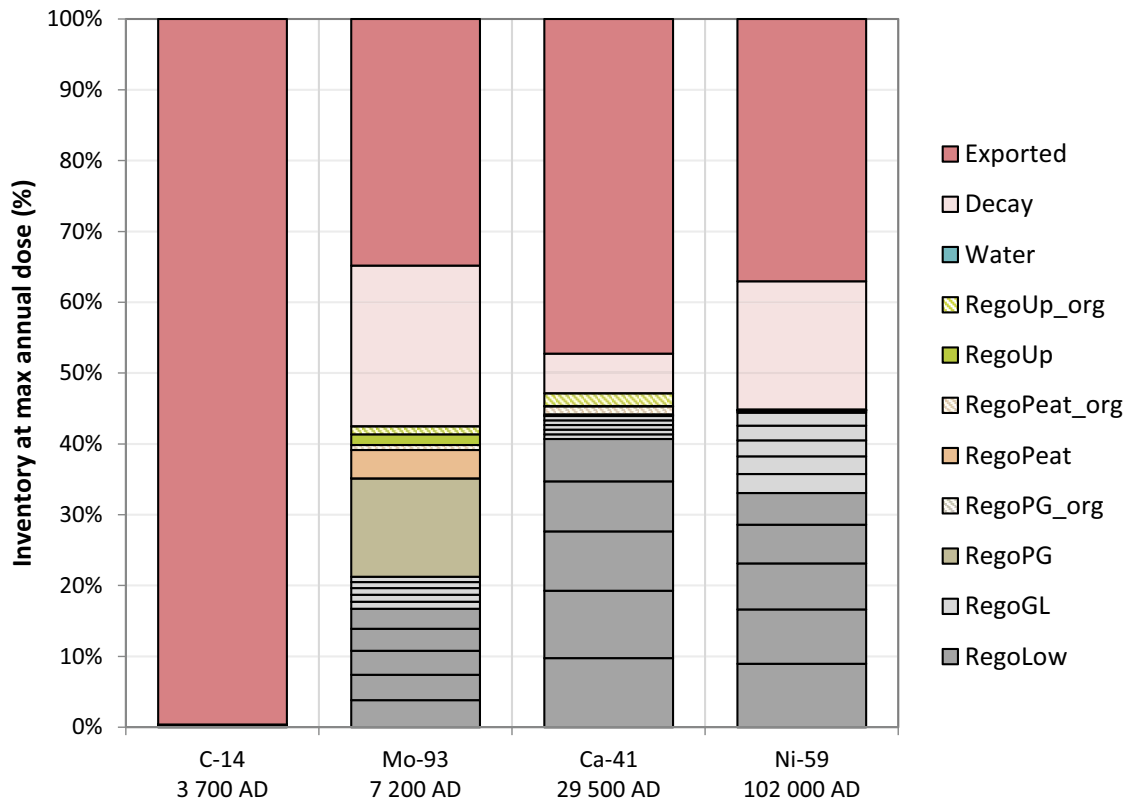


Figure 5-55. Relative distribution of the radionuclide inventories at the time of the radionuclide-specific dose maxima in the different regolith compartments, as well as the relative amounts that have decayed within the discharge object and have been exported out of the system. The two lowermost regolith layers are represented by five compartments each.

Exposure pathways

The most important exposure pathways from the drained mire are through ingestion of cultivated crops and ingestion of animal products (Figure 5-56). These pathways are linked to uptake of radionuclides by plants, either directly in edible crops or indirectly via fodder consumed by livestock. Carbon is the main structural component of life and the bioavailability of C-14 is particularly high. Both Mo-93 and Ca-41 are essential plant nutrients and plant uptake of these two radionuclides is also high (in cereal for Mo-93 and in fodder for Ca-41) as compared with the uptake of Ni-59 (Table 5-20). Ingestion of cereals is the most important exposure pathway during the entire assessment period and explains between 30 to 70 % of the total dose. At the time of the dose maximum, ingestion of cereals contributes about 70 % of the dose. The radionuclide-specific annual doses also depend on the ingestion radiotoxicity of the radionuclides (i.e. the product of the activity of a radionuclide and its corresponding ingestion dose coefficient). Of the four radionuclides discussed here, Mo-93 is the most radiotoxic, having an ingestion dose coefficient about one order of magnitude higher than C-14-org and Ca-41 and two orders of magnitude higher than Ni-59 (Table 5-20).

Exposure from drinking water from the dug well is important early in the assessment period when the extent of the emergent land area may be limiting the other exposure pathways or at times before the radionuclides have had time to accumulate in the upper regolith layers where the plant uptake occurs (Figure 5-56). Exposure to radionuclides in the deep groundwater is also considered. However, this pathway is only relevant for a small group (Section 4.4.1), so the dose from a drilled well becomes lower than from the dug well when a scaling factor of ten is employed (Section 5.7.1). In summary, the contribution of exposure via drinking water to the total dose maximum is marginal.

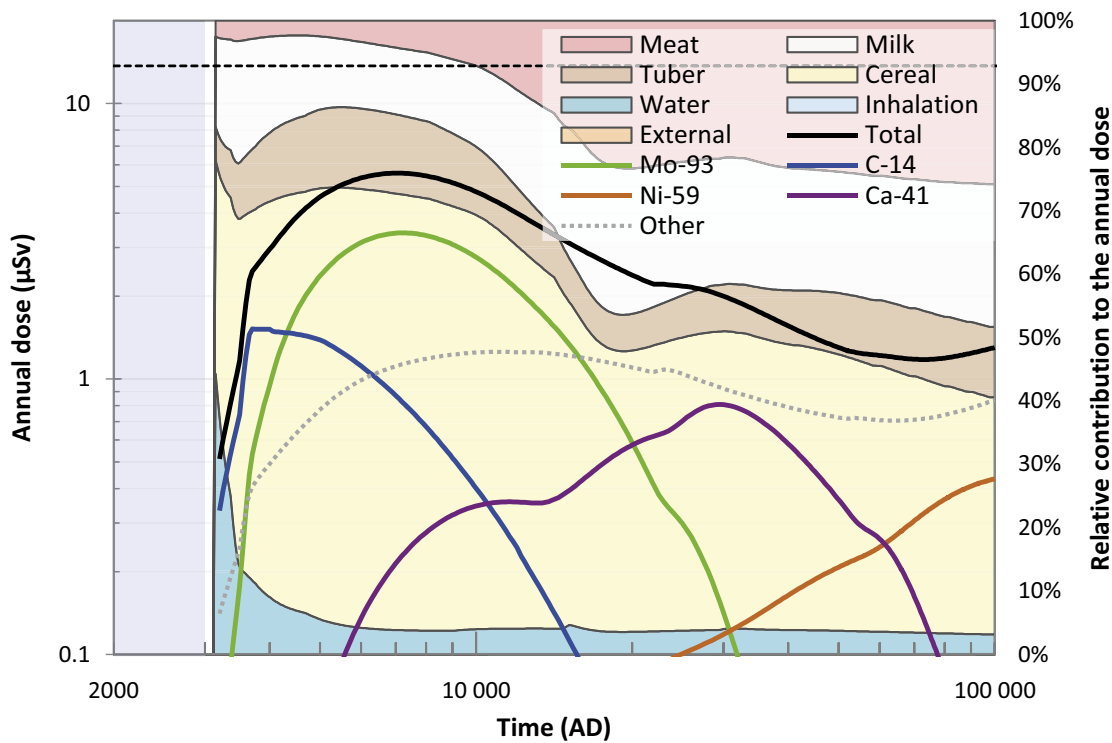


Figure 5-56. Relative contribution to the annual dose to DM farmers from different exposure pathways during terrestrial conditions (coloured areas linked to the right y-axis and corresponding total annual dose as well as radionuclide-specific annual doses for C-14, Mo-93, Ca-41 and Ni-59 (left y-axis) in the base case. Note that the doses due to inhalation and external irradiation are too small to be visible in the figure. The annual dose corresponding to the regulatory risk criterion (14 μ Sv) is indicated by the black dashed line and the submerged period is illustrated by the blue shading.

5.7.3 Summary biosphere

In the *base case*, the total annual dose throughout the entire 100 000-year assessment period is below the dose corresponding to the regulatory risk criterion, 14 μSv , with a maximum of 5.6 μSv occurring around 7000 AD. Draining and cultivation of a mire (DM group) in biosphere object 157_2 is the land use variant resulting in the highest doses. This is primarily because of accumulation of radionuclides in peat over long periods of time prior to drainage and subsequent exposure and because the cultivated ecosystems are highly productive.

In the biosphere, properties related to transport, sorption, accumulation and radioactive decay determine environmental activity concentrations in the regolith, in relation to the geosphere releases. Uptake in plants and transfer to animal products and radiotoxicity are other key properties affecting the radionuclide-specific doses. Four radionuclides are of specific interest in the PSAR, namely Mo-93 and C-14-org that contribute the most to the total dose from the time of repository closure up until the time of dose maximum, Ca-41 that contributes the most in the middle of the assessment period, and Ni-59 that contributes the most at the end of the assessment period.

The most important exposure pathways from the drained mire are through ingestion of cultivated crops and ingestion of animal products. These pathways are linked to uptake of radionuclides by plants, either directly in the edible crops or indirectly via the fodder consumed by livestock. Ingestion of cereals is the most important exposure pathway during the entire assessment period and explains between 30 and 70 % of the total dose.

5.8 Supporting calculation cases

5.8.1 Introduction

The main scenario also includes a set of supporting calculation cases, selected to provide a sensitivity analysis of specific uncertainties in external conditions and internal processes that are important for radionuclide transport through the repository system (Section 2.3). The supporting calculations serve to support the selection of assumptions for the *base case* and improve the confidence in the results of the main scenario. As the *base case* constitutes the basis for all radionuclide transport and dose calculations in the present safety assessment, evaluating the sensitivity to specific uncertainties in this case also contributes to increasing the confidence of the other scenarios and calculation cases in the assessment. Therefore, the supporting calculation cases are configured with respect to the conditions in the *base case*.

Two supporting calculation cases are presented in this section, covering uncertainties in future sea-level rise (*timing of shoreline regression calculation case*, Section 5.8.2) and the timing of initial releases from the repository (*delayed release from repository calculation case*, Section 5.8.3). In addition to the calculation cases presented in this report, seven supporting calculation cases have been identified specifically for the biosphere analysis (**Biosphere synthesis report**, Chapters 10 and 11). In addition, some simplified and deterministic supporting calculations have been carried out specifically for the near-field and these are reported in Åstrand et al. (2022).

5.8.2 Timing of shoreline regression

During the transition from submerged to terrestrial conditions above SFR, the continuous shoreline regression will result in a gradual increase of the hydraulic gradient in the parts emerging from the sea and, consequently, in gradually higher groundwater flow rates. Thus, the timing of the shoreline regression affects the transport of radionuclides in the near-field and the geosphere, as well as the timing of ecosystem succession and the potential for exposure in the biosphere.

In the *base case*, the initial period of submerged conditions is 1 000 years based on the assumption that the global sea-level rises until repository closure and immediate post closure will be negligible. Although this simplification facilitates comparison with the results in the SR-PSU, where the same duration of the submerged period was used, it is arguably not fully realistic when taking the ongoing and anticipated future sea-level rise into account. At present, sea-level rise due to melting of Earth's ice sheets and glaciers and thermal expansion of sea water offsets about 40 % of the post-glacial

isostatic rebound at Forsmark, and the influence of sea-level rise on the shoreline displacement at Forsmark is expected to continue for several thousands of years after repository closure (**Climate report**, Section 3.5).

The uncertainty in projected global sea-level rise over the coming millennia is very large, ranging from a couple of metres to more than 50 m depending on the degree of global warming and how Earth's ice sheets and glaciers will respond to that warming (**Climate report**, Section 3.5). At Forsmark, this uncertainty translates to between 1 300 and 18 300 years of initial submerged conditions above the repository (**Climate report**, Section 3.5). One case within this interval, corresponding to a 3 500-year delayed shoreline regression compared with the *base case*, is evaluated in the *warm climate calculation case* (Table 2-2 and Section 6.2). The *timing of shoreline regression calculation case* covers the remaining uncertainty. In this calculation case, dose consequences are evaluated for delayed shoreline regressions of 5 000, 10 000, 15 000 and 20 000 years relative to the *base case*, in addition to the 3 500-year delay of the *warm climate calculation case*.

Handling in the transport models

The delayed shoreline regression is handled by letting the shoreline position corresponding to 2000 AD in the *base case* prevail for the duration of the delay, after which the initial shoreline development of the *base case* is assumed to follow (**Data report**, Chapter 12). The delayed shoreline regression is considered to only influence the progression of the groundwater flow and the landscape development. Thus, the *base case* groundwater flow rates and development of biosphere objects are also used in this calculation case, but they are shifted forward in time according to the delayed shoreline regression. Aside from these changes, the handling in the near-field, geosphere and biosphere models is identical to the *base case*. Thus, the potential of a slower concrete degradation due to the delayed increase of the groundwater flow is cautiously omitted in this calculation case.

Depending on its properties related to retention, accumulation and exposure, the maximum dose of a certain radionuclide may depend more on its maximum release from the near-field and the geosphere than the accumulated release up until the time of the dose maximum, or vice versa. Since only longer periods of submerged conditions than in the *base case* are evaluated in this calculation case, groundwater flow will not be higher than in the *base case* at any point during the assessment period. In consequence, the accumulated releases of radionuclides over the assessment period will also not be higher than in the *base case*, except for decay products that can accumulate due to ingrowth. Therefore, results related to changes in the maximum releases rather than the accumulated releases are mainly discussed in this calculation case.

Annual release from the near-field

In the *base case*, three of the 15 radionuclides with the highest near-field releases exhibit their maximum releases before the end of the submerged period (Ni-63, Cs-137 and H-3, see Figure 5-42). A delayed shoreline regression, thus, has virtually no effect on the maximum releases of these radionuclides. For most of the other radionuclides, including the remaining 12 radionuclides with the highest releases in the *base case*, the timing of the maximum release is largely controlled by the change in groundwater flow which, in turn, is closely linked to the timing of the shoreline regression. As a result, maximum releases of these radionuclides occur when the groundwater flow has increased after terrestrial conditions have been established above the repository. Thus, for most radionuclides, a specific delay in the shoreline regression will typically result in a comparable delay of the maximum release from the near-field.

A consequence of the delayed release is that the maximum release relative to the *base case* will be reduced for most radionuclides. The greatest reduction is obtained for radionuclides that experience a significant decay in the waste vaults during the extended submerged period. This primarily concerns radionuclides with half-lives slightly shorter than, or within the range of, the durations of the submerged periods evaluated in the calculation (e.g. Ag-108m, C-14-org and Mo-93, see Figure 5-57).

For radionuclides with longer half-lives, the maximum release may either decrease or increase depending on the properties of the radionuclides and waste vaults. In most waste vaults, the transport from the waste form to the backfill is dominated by diffusion (or corrosion in 1BRT) during the submerged period. In combination with the low groundwater flow that limits the releases from the near-field, this results in an increased accumulation of radionuclides in the backfill. The accumulated radionuclides

are subsequently released to the geosphere as the groundwater flow increases and this might result in higher maximum near-field releases than in the *base case*. Furthermore, the longest periods of submerged conditions extend beyond the time points associated with degradation of the concrete in these vaults, resulting in even higher near-field releases when the groundwater flow increases. This effect is however not present in the BLA vaults which have no credited barriers. As a result, radionuclide releases that originate from the BLA vaults, e.g. of Ni-59 and uranium isotopes, exhibit a marginal decrease due to depletion and radioactive decay during the prolonged submerged period (exemplified by U-238 in Figure 5-57).

Two radionuclides with notable increases in the maximum-release for longer submerged periods are Ca-41 and I-129 (Figure 5-57). The increased releases of these radionuclides are partly explained by the accumulated activity in the backfill in 1BMA (I-129) and 2BMA (both Ca-41 and I-129) that is released when the water flow increases. However, another explanation is that the longest periods of submerged conditions extend beyond the time points associated with degradation of the concrete in these vaults. Specifically, this concerns the chemical degradation at 12 000 AD (for Ca-41) and, for the longest extended submerged period, also the physical degradation at 22 000 AD (Tables 5-6 and 5-8). Thus, when the groundwater flow increases after the longer submerged periods (> 10 000 years), a higher activity of these radionuclides will be released from 1BMA and 2BMA due to the higher remaining inventory at this time compared with the *base case* in combination with a lower retention capacity of the waste vaults.

Other radionuclides that exhibit an increased maximum near-field release as a result of the delayed shoreline regression are primarily decay products. A longer submerged period increases the retention of their parents and enables a higher activity of these radionuclides to accumulate in the waste vaults due to ingrowth. Examples of such radionuclides are the decay products of U-235 in the BLA vaults, i.e. Pa-231 and Ac-227. For the longest submerged period evaluated in this calculation case, the maximum near-field release of these radionuclides increases by more than one order of magnitude relative to the *base case* (exemplified by Ac-227 in Figure 5-57).

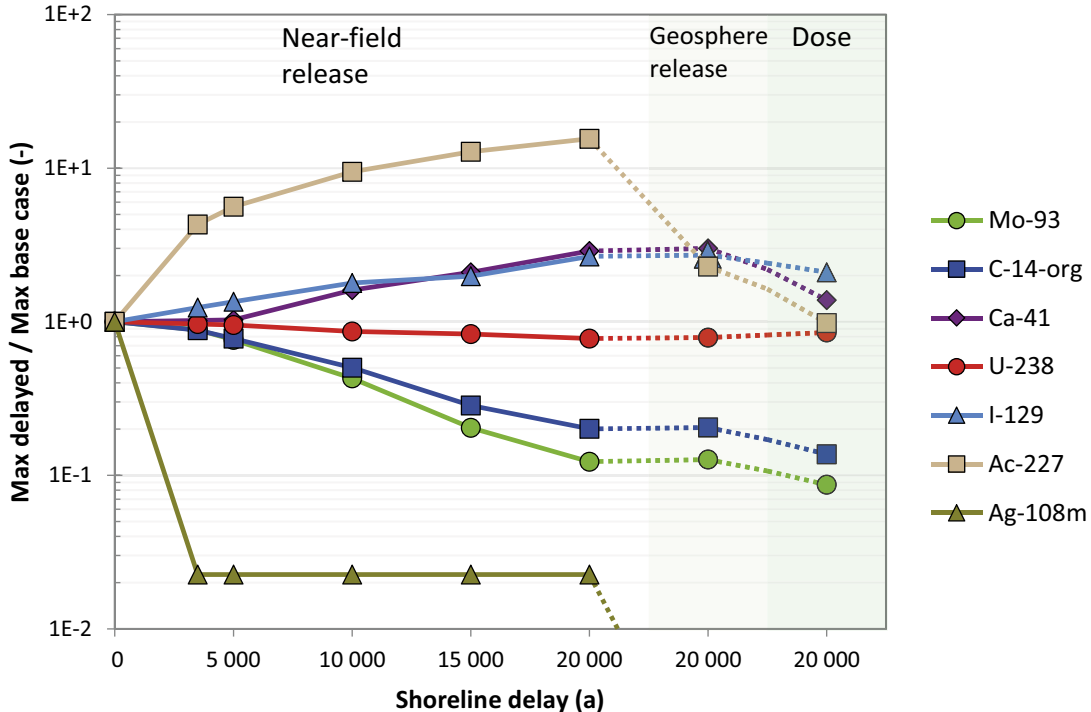


Figure 5-57. Quotient between the maximum near-field release of select radionuclides in the calculations with delayed shoreline regression and the maximum near-field releases in the base case (left panel, white background, solid lines). The middle and right panels show the corresponding quotient for the maximum geosphere releases (middle panel, pale green background, dotted lines) and the annual doses (right panel, green background, dotted lines) for the longest delay of the shoreline regression considered (20 000 years). Note that the dotted lines do not indicate a time progress, they are only included to facilitate identifying related radionuclides in different models.

Annual release from the geosphere

For most of the radionuclides, changes in the maximum releases from the near-field as a result of the delayed shoreline regression are accompanied by similar changes in the geosphere (Figure 5-57). An exception concerns the decay products of U-235 (Pa-231 and Ac-227). Although the maximum geosphere release of these radionuclides is slightly higher than in the *base case*, the increase is much more modest than the corresponding increase from the near-field (cf. Ac-227 in Figure 5-57). In the *base case*, releases from the geosphere of these decay products gradually increase for a relatively long time (until ~40 000 AD) due to high sorption in the rock matrix of the parent radionuclide (U-235). Thus, for longer submerged periods, the geosphere releases of these decay products are primarily due to ingrowth in the geosphere and, to a lesser extent, dependent on the near-field releases.

Annual doses

The main effect of the longer submerged periods is a lower total maximum dose compared with the *base case*. The main reason is that the radionuclides that dominate the maximum annual dose in the *base case*, Mo-93 and C-14-org, have decayed more before they reach the biosphere and are available for exposure (Figure 5-57). Consequently, maximum doses from those two radionuclides occur later and decrease with increasing duration of the delay of the shoreline regression (Figure 5-58).

As a result of the lower doses from Mo-93 and C-14-org, longer-lived radionuclides become more important for the total dose for increasingly longer submerged periods. Owing to the elevated releases of Ca-41 from the near-field and the geosphere (Figure 5-57), this radionuclide dominates the total dose maximum for the longest shoreline-regression delays (15 000 and 20 000 years) (Figure 5-58).

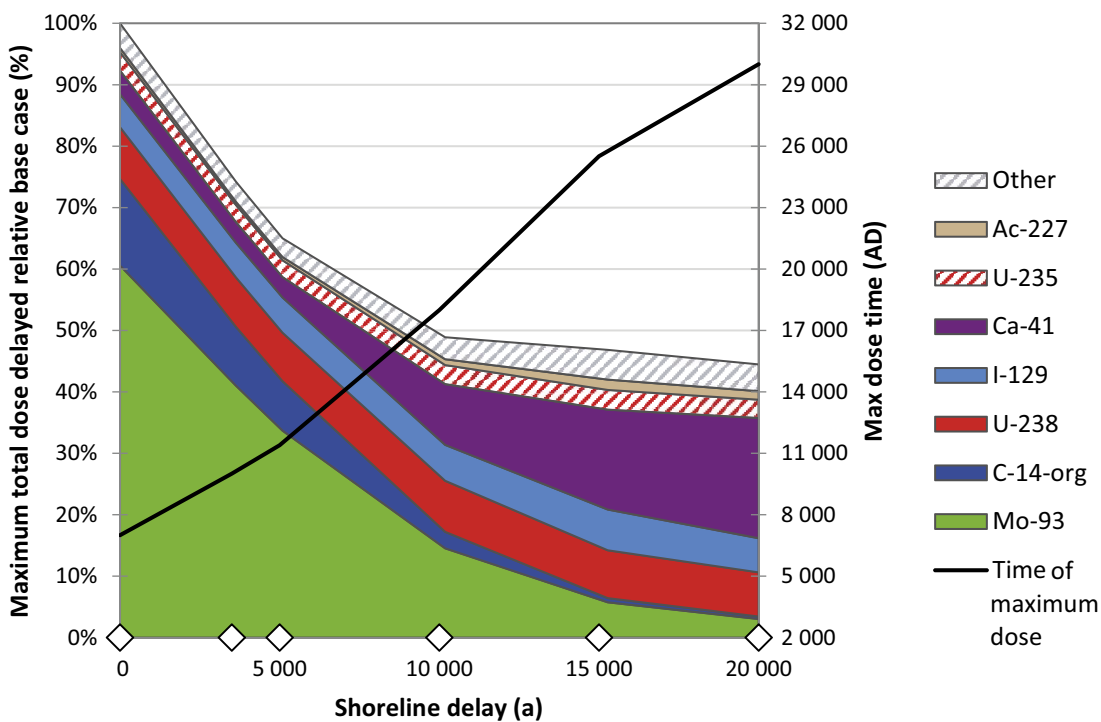


Figure 5-58. Percentage of total maximum and radionuclide specific annual doses relative to the base case (left y-axis) and timing of total maximum annual doses (right y-axis) as a function of the delay in shoreline regression in the timing of shoreline regression calculation case relative to the base case (x-axis). A shoreline delay of 0 years corresponds to the base case; this case and the calculations with delayed shoreline regression are indicated by white diamonds on the x-axis. The total height of the stacked areas shows the maximum dose relative to the base case and the height of the individual-coloured areas show the radionuclide specific dose contribution to the maximum doses. The black line illustrates the time of the total maximum dose.

However, Ca-41 is sorbed effectively in the regolith layers that contribute to exposure and thus accumulated geosphere releases are also important for exposure to this radionuclide in the biosphere. In contrast to the maximum geosphere release, the accumulated geosphere release of Ca-41 does not change substantially compared with the *base case*. The increase in the maximum dose from Ca-41 is therefore limited (c 50 % higher with 20 000 years delay, see Figure 10-7 in the **Biosphere synthesis report**) in relation to the maximum release, and the total maximum dose with a delayed shoreline regression never exceeds the total maximum dose in the *base case*.

Maximum near-field and geosphere releases of I-129 increase, similarly to Ca-41, by up to about 200 % for the longest submerged period (Figure 5-57). Since iodine is more mobile in the regolith, the release maximum is more effectively propagated to increased doses (~ 100 % higher with 20 000 years delay) than Ca-41. However, this has a small effect on total maximum doses, since its contribution to the total dose is limited (Figure 5-58).

Elevated near-field releases of the decay products Pa-231 and Ac-227 (Figure 5-57) never reach the regolith layers exposed by cultivation since they are effectively retained and decay in the till. Instead, exposure from Pa-231 and Ac-227 primarily originates from ingrowth from U-235 in the regolith.

Summary and conclusions

This calculation case evaluates radiological consequences of a delayed shoreline regression compared with the *base case*. It includes five calculations with gradually increasing delays of the shoreline regression until a maximum of 20 000 years.

The timing of the shoreline regression largely determines the magnitude of the groundwater flow, with generally several orders of magnitude higher flow rates prevailing during terrestrial conditions than during submerged conditions. For increasing delays in the shoreline regression, this means that the timing of the maximum dose is gradually shifted forward in time with the corresponding delay of the shoreline regression. This results in reduced maximum dose compared with the *base case* due to increased radioactive decay of C-14-org and Mo-93. In contrast to those radionuclides, the contribution of Ca-41 to the maximum dose increases somewhat with the delayed shoreline regression, such that it becomes the radionuclide contributing most to the maximum dose for shoreline-regression delays greater than 10 000 years. This is due to the long half-life (102 000 years) of Ca-41, the tendency for increased releases due to accumulation in the backfill and the larger remaining inventory at the time for degradation of the barriers (in 2BMA). In conclusion, the assumption of a relatively short submerged period in the *base case* is pessimistic, as using longer, more realistic, submerged periods result in lower annual doses.

5.8.3 Delayed release from repository

As mentioned in Chapter 2, handling of uncertainties is of key importance for the safety assessment. Uncertainties are in most cases addressed by choosing pessimistic or cautious parameter values so that the calculated dose is not underestimated. When it comes to radionuclide release, faster and earlier releases are typically regarded as more pessimistic than slower and later. However, in some situations this is not the case. An early start of radionuclide releases from the near-field results in an early release from the geosphere to the biosphere. During the first ca 1 000 years of the assessment period, releases to the biosphere are highly diluted and have low radiological impact because of the submerged conditions of the discharge area. Assuming a later onset of radionuclide releases in the near-field might hence cause higher doses in the biosphere after the area has emerged from the sea and the potential for dilution is much lower. It is, therefore, not obvious which timing of releases to the biosphere leads to higher maximum doses and how significant the effect will be.

The *delayed release from repository calculation case* illustrates the effect of preventing releases for a set amount of time after closure. The results are intended to permit judgement about whether the *base case* assumptions can be considered reasonably cautious with respect to dose and risk consequences.

This *delayed release from repository calculation case* is developed to evaluate radiological consequences of simplifying assumptions whereby several processes are omitted in the near-field modelling. The overall consequence of these simplifications is an earlier release from the near-field compared to if more realistic parameterisations were to be used. Thus, the simplifications could possibly result in an

exaggerated release during the submerged period in the *base case*, when doses to humans are significantly lower than during the subsequent period when land has emerged. A delay period of 1 000 years is therefore chosen based on the length of the submerged period above the repository.

The omitted processes, as first introduced in Chapter 2, are summarised in the following together with a short discussion on their release-delaying timescales, sorted roughly from longest to shortest upper-bound delay estimate.

- Steel waste packaging could keep radionuclides contained. A fully intact and sealed carbon steel mould or drum of 5 mm wall thickness could provide containment for up to 50–5 000 ka, given uniform corrosion from only the outside at a rate of 0.001–0.1 $\mu\text{m a}^{-1}$ (Table 5-13 in the **Data report**). In a few cases, stainless steel packages are used, with even lower corrosion rates (Table 5-16 in the **Data report**). More likely, the packaging could be damaged, and corrosion initiated during the operational period and localised corrosion could be faster in certain areas of the package e.g. around welds, joints, and seals, which decreases the containment time.
- The very high diffusive resistance of bitumen hinders uptake of water that is required for radionuclide dissolution and, even after water uptake, it retards transport of radionuclides out from bituminised waste, primarily ion-exchange resins. This could delay the release from bitumen-conditioned wastes for many millennia but is not taken into account in the modelling (Section 3.6 in the **Waste process report**). Swelling and cracking decreases the transport resistance in the bitumen, and these generally occur as a result of water uptake of the pre-dried ion-exchange resins within the bitumen matrix, exacerbated by possible hygroscopic salts in the waste, e.g. from evaporator concentrates, and by radiolytic gas production (Section 3.5.7 in the **Waste process report**). However, the steel packaging, if it is intact, could hinder both water uptake and subsequent swelling since it is expected to withstand the swelling pressure to some extent.
- Radionuclides incorporated inside solid materials must dissolve before becoming available for transport. This is accounted for in the case of the irradiation-induced activity in the 1BRT steel waste, but not in other wastes whose radionuclide inventory is rather assumed to be instantly released from the waste form and available for transport. This concerns certain metal and cementitious waste fractions in most vaults, which must degrade via oxidation and leaching, respectively, for these radionuclides to dissolve. This degradation is gradual and generally slow, on the order of many millennia for steel and concrete. The gradual release of solid-incorporated activity has the strongest impact on retention at early times, while most of the activity remains incorporated.
- Several radionuclides have limited solubility under repository conditions, which limits their dissolved concentrations and thus lowers the transport rate. This is not taken into account in the PSAR (Section 3.6 in the **Waste process report**). An important example is $\text{Ni}(\text{OH})_2$, whose very low solubility product of about 10^{-16} M^3 (SenGupta 2017) limits the dissolved Ni concentration. However, Ni can also speciate into $\text{Ni}(\text{OH})_3^-$ with very high solubility. The resulting maximum allowed total dissolved concentration of Ni is approximately equal to that of Ni-59 plus Ni-63 in the transport model; i.e. solubility limits would not affect the Ni-59 and Ni-63 transport. However, when considering that the significant amount of stable Ni isotopes in e.g. steel and cement wastes also compete for the total dissolved Ni concentration, the radioisotope concentrations are indeed affected. In addition to Ni(II), similar solubility limit considerations could affect Co(II), Ca(II), Pu(IV) and possibly Mo(VI). Solubility limits retard rather than block the near-field releases; their omission from the modelling has most impact during early times when radionuclide activity concentrations are highest.
- The 1–5BLA vaults contain no credited engineered barriers but do include substantial amounts of cementitious materials in the waste, vault slab and shotcrete lining of the vault walls. Despite this, sorption in 1–5BLA is pessimistically disregarded in the modelling. The residence time of sorbing radionuclides in the BLA vaults could thus be underestimated by up to roughly 1 000 years, crudely estimated based on the observation that 1BLA near-field releases peak around 3000 AD (Figure 5-28), whereas in 1–2BTF credited with sorption, non-sorbing radionuclides peak at around 3000 AD and sorbing Ni-59 and C-14-inorg peak around 4000 AD (Figures 5-23 and 5-24). However, the impact on total SFR releases is expected to be small due to the low activity content of the BLA vaults.

- Sorption of radionuclides is generally accounted for on cementitious materials and bentonite, but not on other potential sorbents such as metals and particularly their corrosion products (Section 3.5.3 in the **Waste process report**). This affects the release rates of certain radionuclides with appreciable sorption coefficients on the neglected sorbent materials. This effect may have a greater impact over time, concomitantly with build-up of metal corrosion products.
- Groundwater flow through the waste packages is likely to be a fraction of the flow through the waste domain. However, the resolution of the near-field hydrological model is on a coarser level than individual waste packages, so the flow rate through the waste packages is not determined. In the radionuclide transport modelling it is therefore pessimistically assumed that the calculated flow through the entire waste domain also applies to each model waste package. This could overestimate the waste-package flow by up to about an order of magnitude, depending on where in the waste domain the package is located (Section 2.5 in Ekström et al. 2017). However, high flow through the waste packages mainly affects the transport rate within the waste domain and not out from it. Thus, the effect of this assumption is largest initially, when all radionuclides are still inside the packages. The maximum near-field release is not expected to be noticeably affected, since it is mainly determined by the flow through the entire vault rather than through the waste packages.
- The rock walls in all vaults are lined with shotcrete but this is not considered in the transport model, which rather assumes that the radionuclide-containing groundwater in the vaults is directly connected to water-bearing bedrock fractures (Section 5.4). The shotcrete could act as a barrier in terms of advection, diffusion and sorption. This could both delay the onset of the near-field release somewhat and decrease the subsequent annual release until the shotcrete degrades.
- In the period just after closure, the vaults are still unsaturated, preventing radionuclide transport. This period is neglected in the modelling which assumes instant saturation (Chapter 12 in the **Initial state report**). The impact on releases is small, however, since the saturation time is expected to be on the order of years to decades (Börgesson et al. 2015, Holmén and Stigsson 2001).

Handling in the near-field model

In this calculation case the radionuclide release from the waste is set to zero for the first 1 000 years and thus does not begin until the conditions above SFR change to terrestrial. This is implemented by not activating any transport processes during the first 1 000 years. Prior to this, the only process affecting the size of the inventory is radioactive decay and in-growth.

Other processes within the vaults are assumed to proceed unimpeded as in the *base case*, such as dissolution of induced activity in the 1BRT steel, and degradation of cement and of cellulose to ISA. The concentration of the complexing agent NTA is, in the *base case*, assumed to decrease linearly due to outflow and, for simplicity, the same assumption is made in the *delayed release case*, even though some of the processes that delay radionuclide release would also delay complexing-agent outflow.

Handling in the geosphere/biosphere model

The handling of the geosphere and the biosphere is identical to the *base case*.

Releases from the near-field

The near-field releases in the *delayed release from repository calculation case* compared with the *base case* are shown for 1BMA in Figure 5-59 and for the entire SFR in Figure 5-60. In the *delayed release from repository calculation case*, all transport processes and thus releases are stopped for the first 1 000 years after closure. During the same period in the *base case*, radionuclides move from the waste, primarily via diffusion since advective flow is very low under submerged conditions. A fraction of the radionuclides diffuses to the vault edge and is slowly released to the geosphere, while another fraction moves into the cementitious barriers where sorbing radionuclides become retained, potentially for a long time which lowers their subsequent release.

Conversely in the *delayed release from repository calculation case*, all radionuclides are still inside the waste at 3000 AD and not inside the engineered barriers. In 1BMA, a large fraction of sorbing radionuclides including C-14-inorg originates in the bituminised waste (Figure 7-5 in Åstrand et al.

2022). Since neither the bitumen matrix nor its steel packaging are credited with transport resistance, those radionuclides are readily transported from the waste via assumed cracks in the 1BMA waste-compartment slabs (Section 5.3.3), through the conductive backfill and into the geosphere. This explains why the release spike from 1BMA just after 3000 AD for sorbing radionuclides C-14-inorg and Ni-59 is much larger in the *delayed release from repository calculation case* than in the *base case* (Figure 5-59); that is, they have not had the same chance to diffuse into the retaining barriers before 3000 AD as in the *base case*.

For non-sorbing radionuclides such as C-14-org the trend is the opposite, with releases just after 3000 AD that are higher in the *base case* than in the present case. This is attributed to the fact that the majority of C-14-org in 1BMA is present in cement-conditioned waste in concrete moulds (Figure 7-5 in Åstrand et al. 2022). The transport resistance of these waste types shifts the release pulse to later times in the *delayed release from repository calculation case* and, because of the relatively short C-14 half-life of 5730 years, the peak is also lowered due to decay (Figure 5-59).

The response from 1BMA of a *delayed release from repository* largely explains the release response of C-14-inorg, Ni-59 and Mo-93 from SFR as a whole (Figure 5-60), although the differences between the two cases are less pronounced due to dilution from the other vaults less affected by a *delayed release from repository*. The release of U-238 and U-235 becomes a little higher during terrestrial conditions in the *delayed release from repository calculation case* than in the *base case*. As these radionuclides are found mainly in the BLA vaults (no sorption assumed for these vaults), a significant fraction in the *base case* is released to the marine environment before 3000 AD. In the *delayed release from repository calculation case*, the entire inventory of these is instead released during terrestrial conditions when dose consequences are much higher given the same activity release. At longer times, all releases become practically identical to the *base case*.

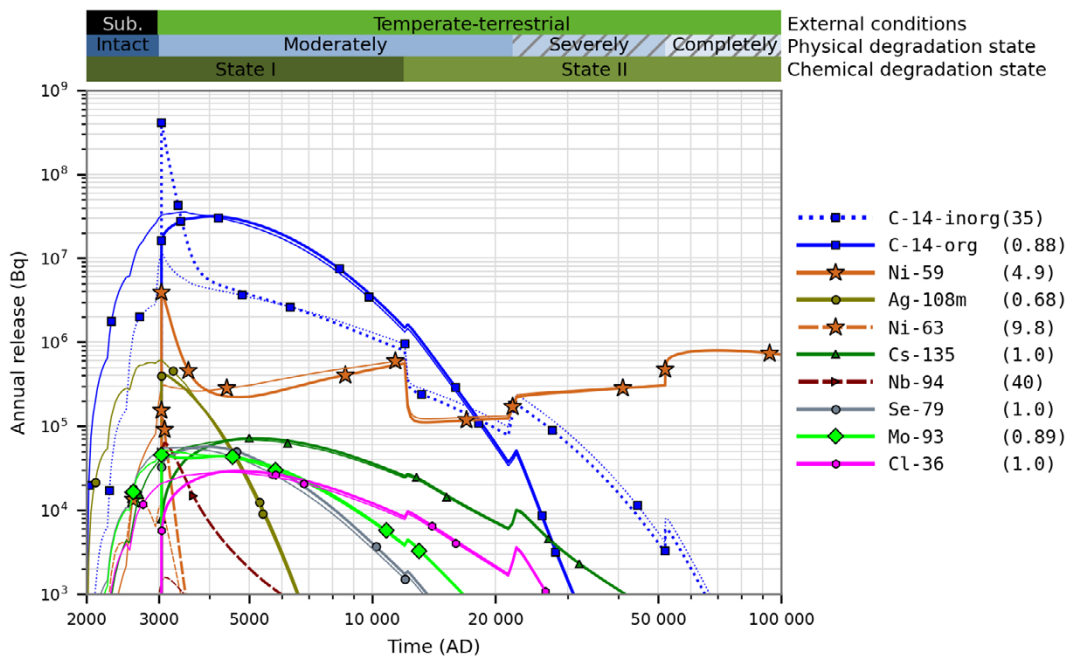


Figure 5-59. Annual activity releases (Bq) from 1BMA in the *delayed release from repository calculation case* (thick lines) and the *base case* (thin lines). Only the 10 radionuclides with the highest annual release are shown. The ratio between the maximum releases in the present calculation case and the base case are shown in parentheses in the key. Coloured horizontal bars (top) as in Figure 5-9.

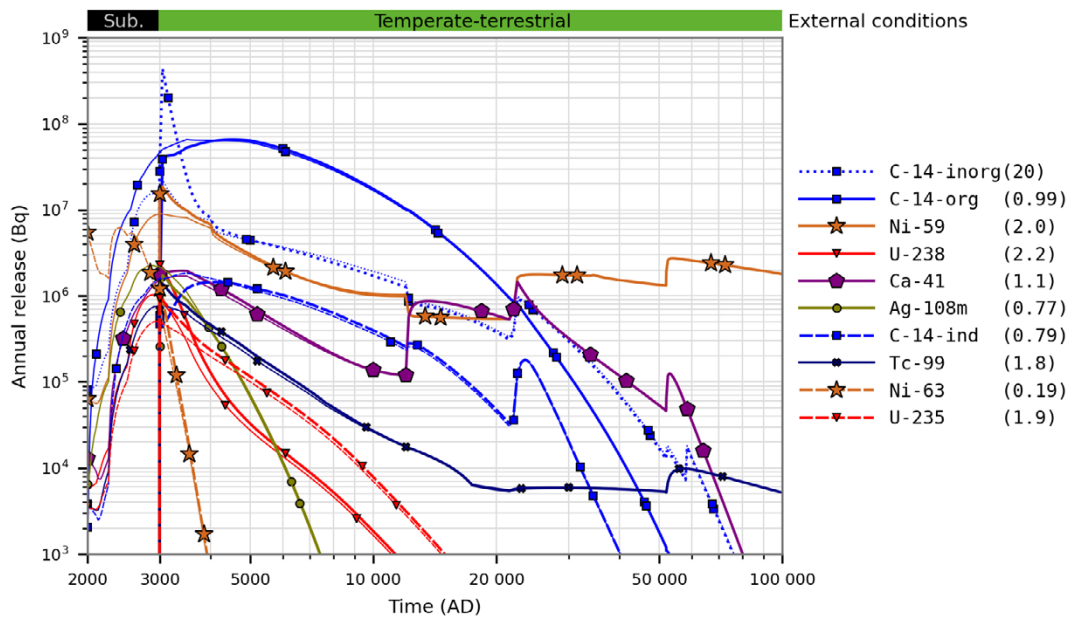


Figure 5-60. Annual activity releases (Bq) from the entire SFR in the delayed release from repository calculation case (thick lines) and the base case (thin lines). Only the 10 radionuclides with the highest annual release are shown. The ratio between the maximum releases in the present calculation case and the base case are shown in parentheses in the key. Coloured horizontal bar (top) shows the evolution of the external conditions.

Annual doses

The doses to the most exposed group are shown in Figure 5-61. The largest difference between the *delayed release from repository calculation case* and *base case* is seen just after 3000 AD where the dose response from C-14-inorg is a direct consequence of the near-field release response explained above. The C-14-inorg difference is large during the spike for a few centuries post 3000 AD. After this time, the C-14-inorg difference is marginal and the small difference in total dose is instead mainly due to C-14-org and Mo-93, the dose pulses of which are shifted to later times in the present case due to the delayed transport onset. This shift is larger for Mo-93 due to more efficient retention in regolith layers in the biosphere and, because of the relatively short half-life of Mo-93, the shift entails a lower peak dose due to decay. After about 10 000 AD, no discernible difference in total dose remains between the two cases.

Concluding remarks

In conclusion, the results from the *delayed release from repository calculation case* shows that the potential effects of uncertainties with respect to near-field retention processes during the first 1 000 years after closure are unlikely to have any significant effects on the dose used to evaluate the post-closure safety. Thus, the simplistic representation in the *base case*, where several processes are omitted, is considered to be adequate.

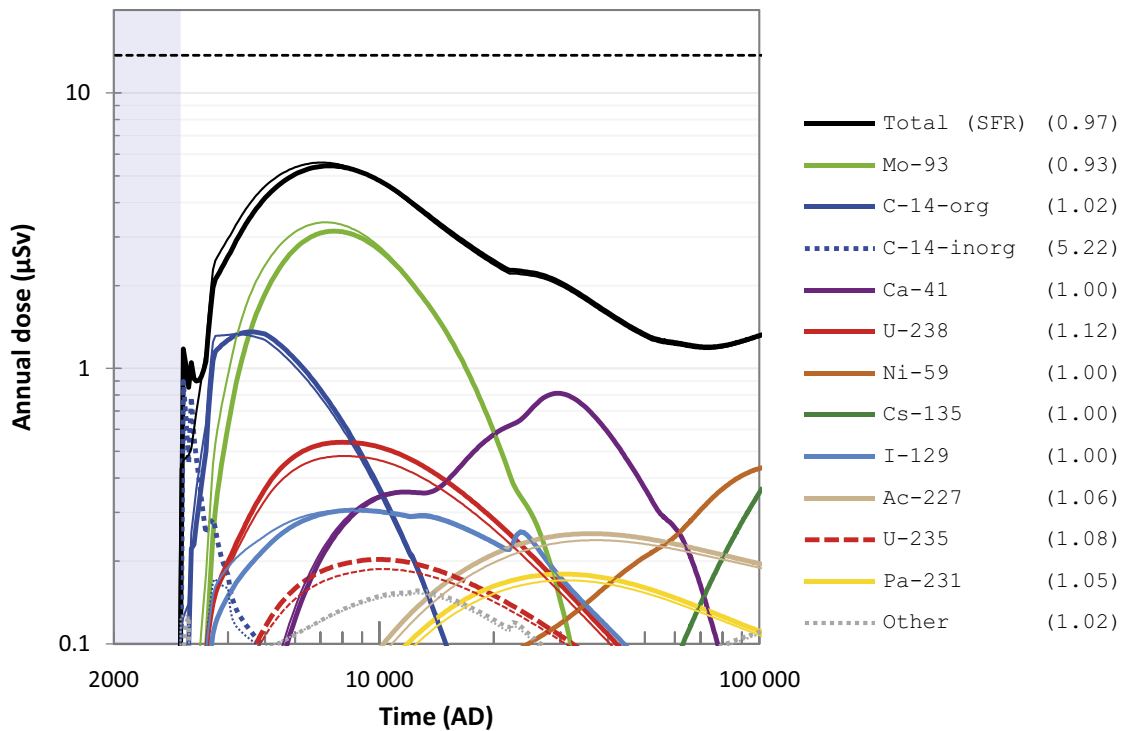


Figure 5-61. Annual dose (μSv) to the most exposed group (black line), including radionuclide specific contributions (coloured lines), in the delayed release from the repository calculation case (thick lines) and the base case (thin lines). The combined contribution from radionuclides not shown is indicated by the grey dotted line. The ratio between the maximum doses in the present calculation case and the base case are shown in parentheses in the key. The annual dose corresponding to the regulatory risk criterion ($14 \mu\text{Sv}$) is indicated by the black dashed line and the submerged period is illustrated by the blue shading.

5.9 Summary and conclusions

5.9.1 Introduction

The *base case* constitutes the basis for the analysis of the main scenario and, thus, for the radionuclide transport and dose calculations. External conditions follow from the *present-day climate variant* of the reference evolution. It assumes that present-day climate conditions prevail for the entire assessment period and that the initial rate of shoreline regression is dominated by the post-glacial isostatic uplift, resulting in 1 000 years of submerged conditions above the repository.

During the initial submerged period, annual doses are negligible due to slow transport through the near-field and geosphere, and a lack of recipients in terrestrial ecosystems. After terrestrial conditions have been fully established in the area, the conditions in the geosphere and the biosphere are assumed to remain constant for the rest of the assessment period, and all the geosphere release is cautiously assumed to be discharged to biosphere object 157_2 just north of the repository. During this period, temporal changes in the transport conditions for the radionuclides are confined to the near-field, primarily as a result of physical and chemical degradation of the concrete barriers in the waste vaults.

5.9.2 Retention in the waste vaults

Retention of radionuclides in the near-field is primarily achieved by the engineered barriers, as these promote low groundwater flow through the waste and retain many radionuclides by sorption. As a result, most of the initial activity has decayed or is still present within the waste vaults by the end of the assessment period, with only a small fraction having been released. This is illustrated in Figure 5-62, which shows how much of the initial radiotoxicity in the *base case* (including radiotoxicity produced due to ingrowth in the waste vaults) is eventually released to the geosphere at some point during the assessment period. Such a comparison should arguably be interpreted with some caution as the simplifying assumptions adopted in the modelling (Section 2.4.4) may affect individual radionuclides

differently. However, as the strategy in the modelling is to opt for the cautious or pessimistic choices for uncertain parameters (Section 2.5), the releases shown in Figure 5-62 are more likely overestimated than underestimated. The figure shows that for most of the radionuclides considered in the analysis, especially those with the highest radiotoxicity, more than 90 % of the initial or produced radiotoxicity remains or decays within the waste vaults during the assessment period. Importantly, most radionuclides that have a large fraction of their inventory released from the near-field also have a relatively low initial or produced radiotoxicity, typically less than 0.1 % of the total initial radiotoxicity in SFR (Figure 5-62).

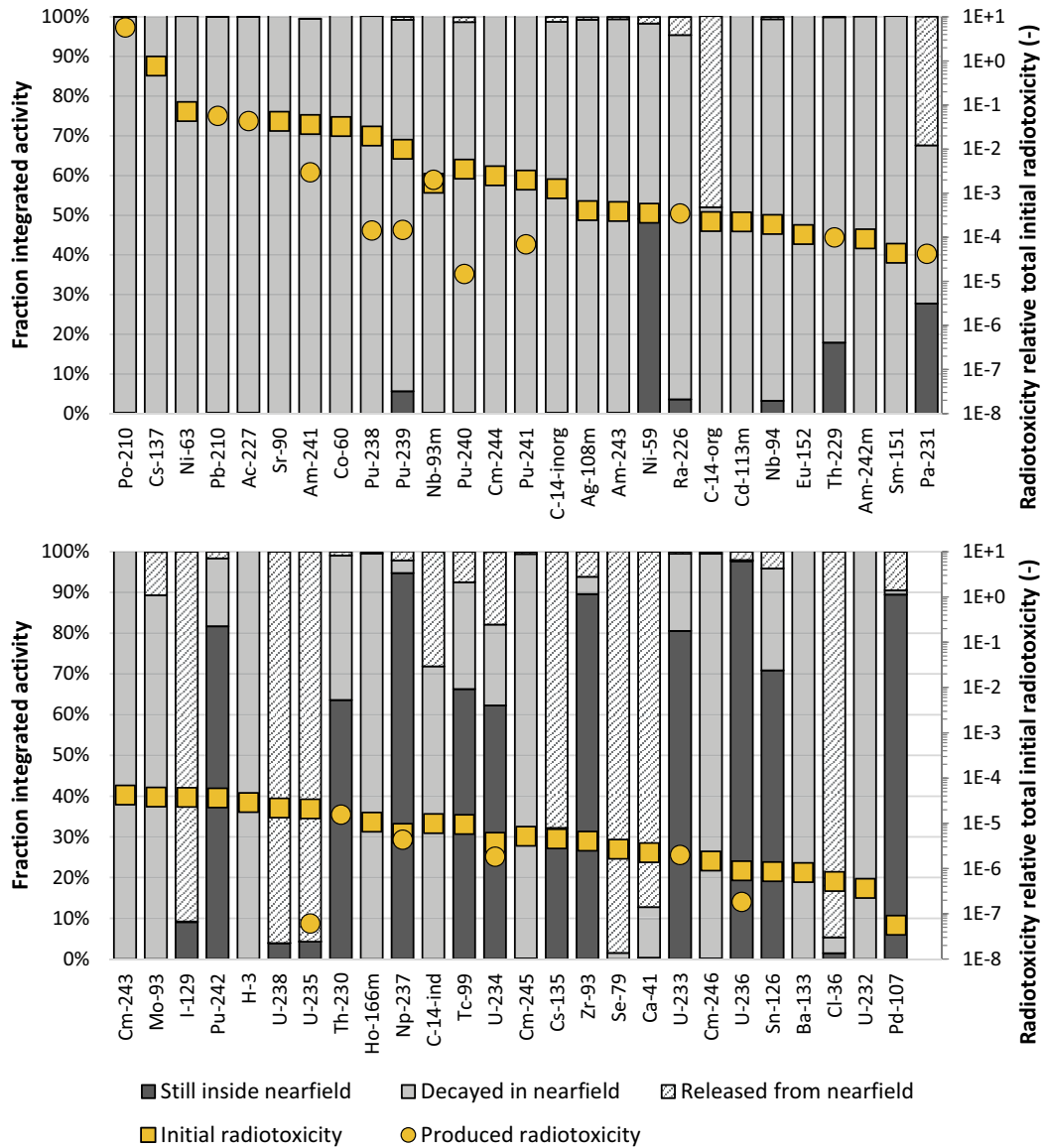


Figure 5-62. Fates of radionuclides in the near-field in the base case. The radionuclides are sorted from the top-left to the bottom-right in descending order of initial (yellow squares) or ingrown radiotoxicity within the SFR repository summed over the whole assessment period (yellow circles). Both the yellow squares and circles are shown as fractions of the total initial radiotoxicity in the entire SFR (right vertical axis). The bars illustrate the retention capacity of the repository for different radionuclides (left vertical axis); dark grey shows the fraction of the integrated activity (i.e. the initial disposed activity plus the activity produced by ingrowth) still contained in the SFR repository at 100 000 AD, light grey shows the fraction that has decayed inside the SFR repository and the hatched part shows the fraction that has been released.

The efficacy of containment also varies depending on the properties of the waste vaults, generally correlating positively with the effectiveness of the engineered barriers in the waste vaults. However, the engineered barriers were designed based on the total radiotoxicity in the waste vaults, such that the waste with the highest initial radiotoxicity typically is disposed in the vaults with the most effective barriers and vice versa (**Post-closure safety report**, Section 1.3). For example, the silo is the most robust waste vault and contains about 80 % of the total initial radiotoxicity, but a much smaller fraction of the total near-field release comes from this vault (Section 5.3.8). This stands in contrast to the BLA vaults, whose release to the geosphere constitutes a disproportionately large portion of the initial activity, such that most of the disposed radionuclides with half-lives longer than ~1 000 years are released at some point. As a result, despite large differences in the initial inventory between the waste vaults, each of the vaults has a relatively similar contribution to the total dose, with only one-order-of-magnitude difference between the vault with the highest maximum contribution (silo) and the vault with the lowest contribution (1BTF) (Figure 5-63). This result indicates that the initial radiotoxicity of the waste is appropriately distributed between the individual waste vaults.

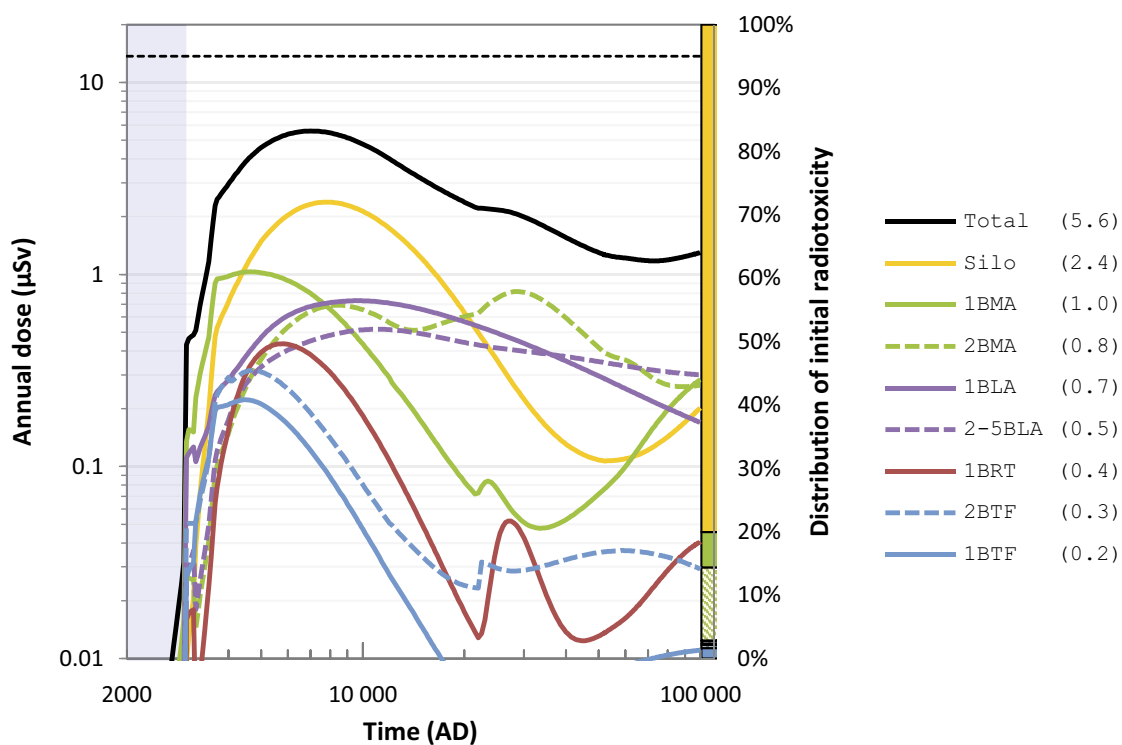


Figure 5-63. Annual dose (μSv , left y-axis) to the most exposed group in the base case (black line) including vault-specific contributions (coloured lines). The flanking vertical bar on the right represent the distribution of initial radiotoxicity between the vaults (right y-axis, colours are the same as those given by the key, and the hatched areas in the bar correspond to the dashed lines in the key). The total and vault-specific dose maxima (μSv) are shown in parentheses in the key. The annual dose corresponding to the regulatory risk criterion ($14 \mu\text{Sv}$) is indicated by the black dashed line and the submerged period is illustrated by the blue shading.

5.9.3 Radionuclide contributions to dose

In the *base case*, the total annual dose throughout the assessment period is below the dose corresponding to the regulatory risk criterion of 14 μSv , with a maximum of 5.6 μSv occurring around 7000 AD. Draining and cultivation of a mire in the biosphere object 157_2 is the land-use variant resulting in the highest doses.

Most radionuclides have only modest dose contributions to the total dose, illustrated by the fact that only 11 of the 53 radionuclides explicitly considered in the analysis contribute at any point with more than 0.1 μSv ¹⁷ to the total dose (Figure 5-54). One important reason for the minor dose contributions from these radionuclides is the high retention in the waste vaults (see above). However, other radionuclide-specific properties are also important for the dose, namely (i) initial radiotoxicity of the inventory, (ii) radioactive decay and ingrowth, (iii) retention in the geosphere and the biosphere and (iv) uptake in plants and transfer to animal products.

Four radionuclides were found to be particularly important for the dose throughout the assessment period: Mo-93 and C-14-org that contribute most during the period of maximum dose, Ca-41 that contributes most in the middle of the assessment period and Ni-59 that contributes most at the end of the assessment period.

¹⁷ 0.1 μSv is approximately 0.7 % of the dose corresponding to the regulatory risk criterion.

To illustrate the properties of these dose-dominating radionuclides, as well as their transport through the repository system, Figure 5-64 shows their relative activity remaining in each repository-system component (including that which has left the modelled system, denoted “Export” in Figure 5-64) at the time point of their respective dose maxima to the DM group (circles). The figure also shows the corresponding distribution between repository-system components of the activity that has decayed until the same point in time (triangles). In addition to the four dose-dominating radionuclides, I-129 and U-238 are included in the figure. These contribute less to the total dose but serve as illustrative examples of radionuclides that exhibit different half-lives, decay chains and sorption coefficients than the dose-dominating radionuclides. Also, the dose maxima of both I-129 and U-238 to the DM group coincide roughly with the timing of the maximum total annual dose¹⁸ (Figure 5-54). The properties of the six radionuclides in Figure 5-64, as well as their transport and retention in the repository system, are further discussed in the following.

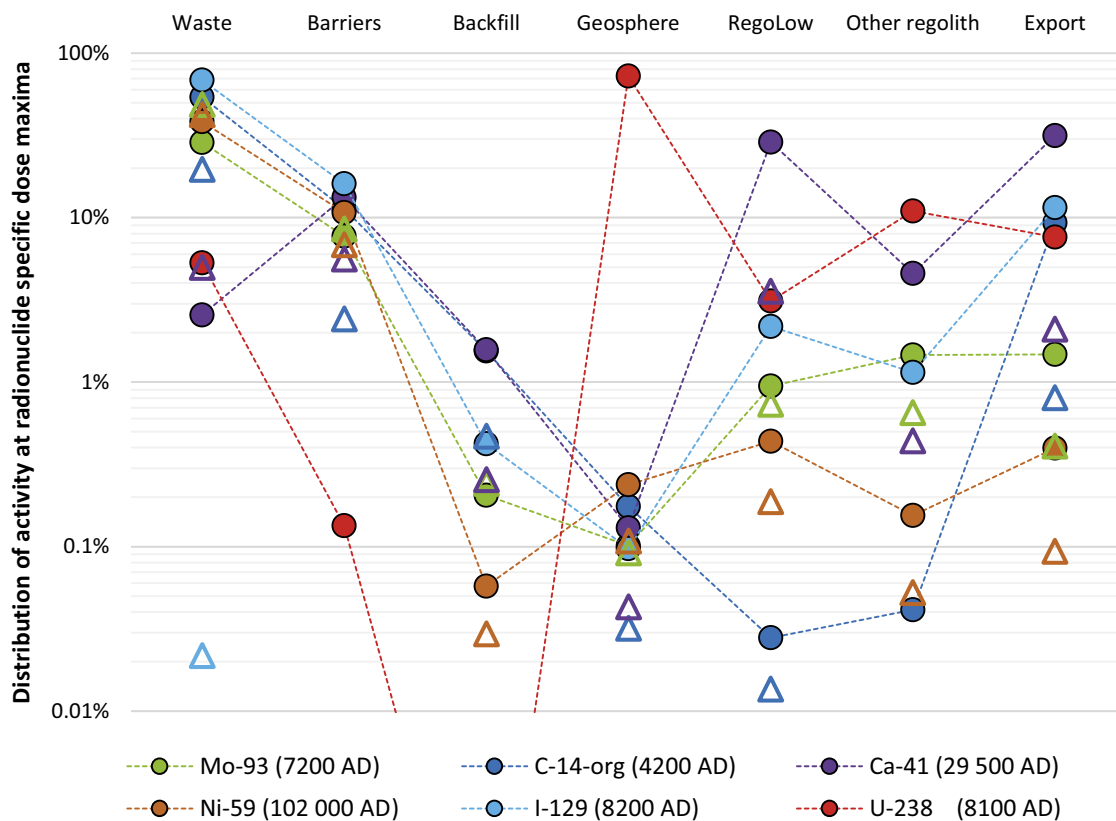


Figure 5-64. Distribution of activity between repository-system components in the base case, including outside the model (Export, far right), of the remaining activity (circles) and accumulated decay (triangles) of six key radionuclides at the time of their respective dose maxima to the DM group (the time of maximum dose for each radionuclide is noted in the legend). The dashed lines are included to better visualise changes in the relative activity between the repository-system components.

¹⁸ In contrast to the other radionuclides in Figure 5-64 whose dose contribution is dominated by exposure to DM farmers, the I-129 dose is larger (factor ~3) to IO farmers and peaks far later in the assessment period (~20 000 AD). However, as the total dose at 20 000 AD is significantly lower than the total dose maximum, it is considered more relevant to illustrate doses of I-129 to DM farmers, especially since their dose maximum roughly coincides with the total dose maximum (~7000 AD).

C-14-org

C-14-org has a high initial inventory in the silo and 1BMA, and displays negligible sorption in all repository-system components as modelled here. As a result, it is relatively quickly transported through the repository, the geosphere and the regolith layers. It is ultimately exported out of the system, by degassing to the air or downstream via surface water. Owing to its mobile nature and relatively short half-life, the dose maximum occurs relatively early for this radionuclide, about only 2000 years after repository closure. The total dose contribution from each waste vault correlates positively with the initial activity within the vaults, but 1-2BTF have disproportionally large releases compared to their inventory. Residence times of C-14-org are slightly shorter in 1BMA than in the silo, implying that releases from 1BMA contribute more to dose for the first few thousands of years, whereas the silo contributes more for the remainder of the assessment period (Figure 5-65). Thus, the fact that most of the C-14-org is still present within the waste and barriers at the time of its dose maximum, as seen in Figure 5-64, is primarily due to the strong retention properties of the silo. In addition, owing to its mobile nature, accumulation is of minor importance for exposure. Instead, groundwater uptake is the primary source for C-14-org in the drained and cultivated mire.

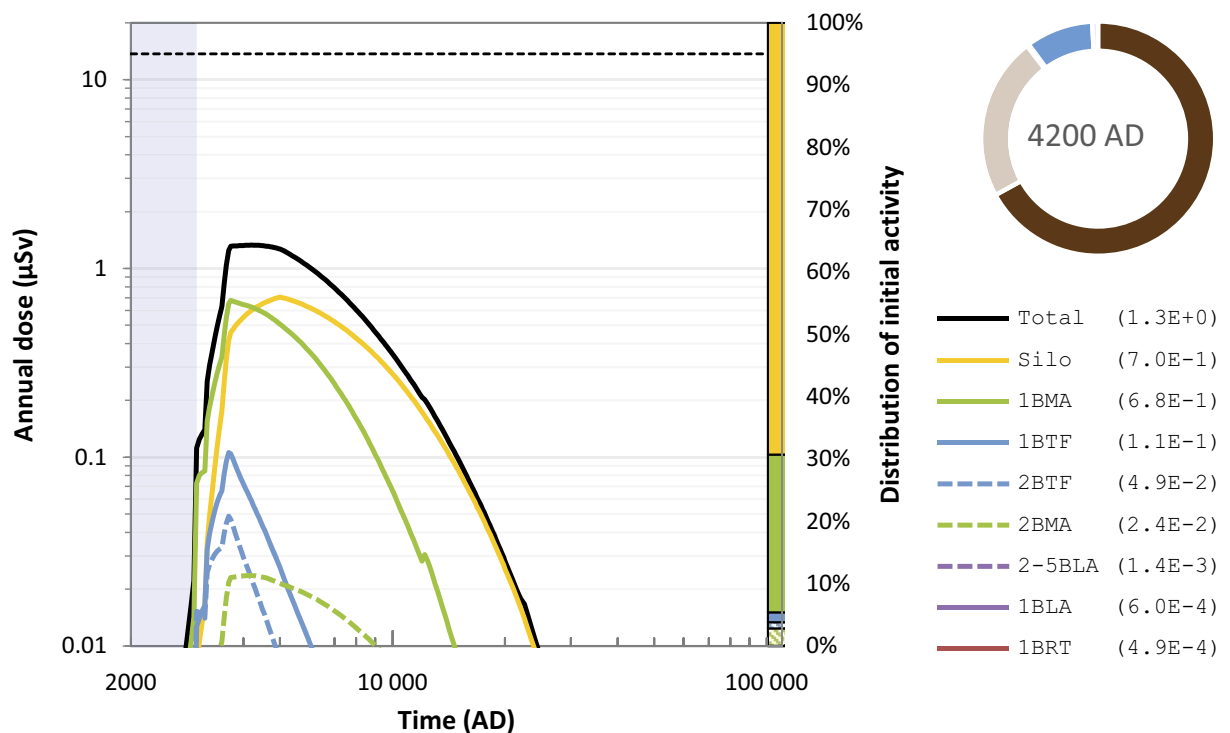


Figure 5-65. Annual dose from C-14-org (μSv , left y-axis) to the most exposed group in the base case (black line) including vault-specific contributions (coloured lines). The flanking vertical bar on the right represents the distribution of initial activity between the vaults (right y-axis, colours are the same as those given by the key), and the hatched areas in the bar correspond to the dashed lines in the key). The total and vault-specific dose maxima from C-14-org (μSv) are shown in parentheses in the key. The annual dose corresponding to the regulatory risk criterion ($14 \mu\text{Sv}$) is indicated by the black dashed line and the submerged period is illustrated by the blue shading. The circle diagram shows the distribution of the activity (opaque colours) between the near-field (brown) and the export from the system (blue), together with the cumulative decay in the near-field (pale brown), at the time for maximum annual dose from C-14-org (data from Figure 5-64). Note that the activities in the geosphere and biosphere are too small to be visible in the circle diagram.

Mo-93

Most of the initial activity of Mo-93 is found in the silo, with significant, albeit lower, activities also in 2BMA and 1BRT. These waste vaults also contribute most to the dose from this radionuclide (Figure 5-66). Doses from Mo-93 are significant in the *base case*, contributing more than 50 % to the total dose maximum (Figure 5-54). Nevertheless, the engineered barriers inhibit Mo-93 transport; the analysis demonstrates that, despite a relatively weak sorption to cement, only a couple of percent of the total Mo-93 inventory has been released to the geosphere by the time of its dose maximum (7200 AD, Figure 5-64)¹⁹. Further, Mo-93 has a half-life of 4000 years, implying that more than half of its initial activity has decayed in the vaults at the time of dose maximum.

Mo-93 sorbs weakly to the rock matrix, so it is virtually unaffected by transport through the geosphere. It sorbs more strongly in the biosphere, particularly in the organic-rich upper regolith layers (cf. “Other regolith” versus “RegoLow” in Figure 5-64). Most of the accumulated activity of Mo-93 in the biosphere will be exposed when those layers are cultivated by drained-mire farmers. The doses from Mo-93 are dominated, almost entirely, by ingestion of cultivated crops.

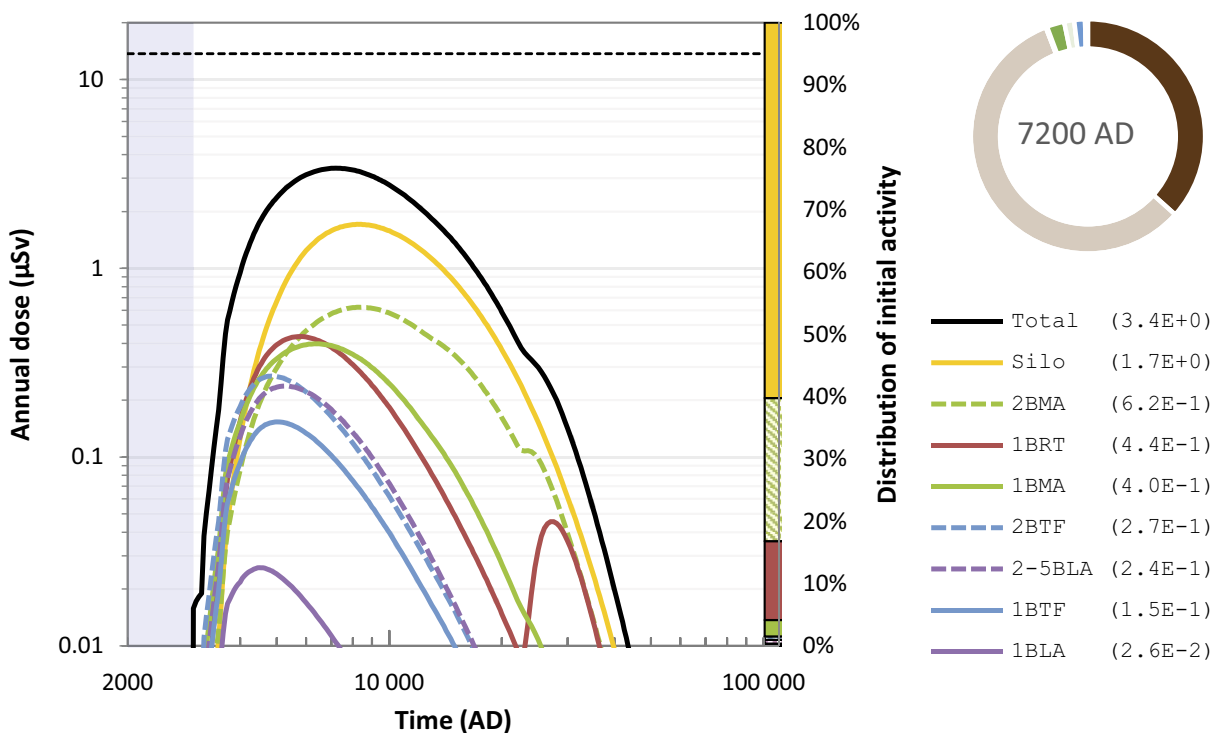


Figure 5-66. Annual dose from Mo-93 (μSv , left y-axis) to the most exposed group in the base case (black line) including vault-specific contributions (coloured lines). The flanking vertical bar on the right represents the distribution of initial activity between the vaults (right y-axis, colours are the same as those given by the key), and the hatched areas in the bar correspond to the dashed lines in the key). The total and vault-specific dose maxima from Mo-93 (μSv) are shown in parentheses in the key. The annual dose corresponding to the regulatory risk criterion ($14 \mu\text{Sv}$) is indicated by the black dashed line and the submerged period is illustrated by the blue shading. The circle diagram shows the distribution of the activity (opaque colours) between the near-field (brown), biosphere (green), and the export from the system (blue), together with the cumulative decay (pale colours), at the time for maximum annual dose from Mo-93 (data from Figure 5-64). Note that the activity in the geosphere is too small to be visible in the circle diagram.

¹⁹ Over the entire assessment period, ~10 % of the total Mo-93 inventory is released to the geosphere, while the remaining ~90 % decays in the waste vaults (Figure 5-36).

Ca-41

The initial Ca-41 activity is present only in 2BMA and in 2-5BLA, which have very different transport properties. The waste containers in the BLA vaults are not credited with any transport retention capability and significant releases of Ca-41 from those vaults to the geosphere thus start immediately after the shoreline recedes past the repository and groundwater flow becomes appreciable. This results in a relatively early dose contribution of Ca-41 from 2-5BLA (Figure 5-67). In 2BMA, on the other hand, the residence time of Ca-41 in the concrete caissons is relatively long until 12 000 AD and 22 000 AD, when the concrete undergoes chemical and physical degradation, respectively (Figure 5-11c). Given its long half-life (102 000 years), Ca-41 releases from 2BMA increase significantly in response to these two degradation events. Thus, 2BMA contributes considerably more to the later dose of Ca-41 than the BLA vaults (Figure 5-5). A further consequence of the sorption to cementitious materials in 2BMA is that the Ca-41 activity inside the barriers is higher than in the waste at the time of maximum dose (Figure 5-64).

Sorption of Ca-41 is not considered in the geosphere (**Data report**, Section 8.6), so the geosphere release of this radionuclide is similar to its near-field release. In the biosphere, Ca-41 is strongly sorbing to inorganic regolith layers and is primarily retained within the lowest regolith layer (Figure 5-64). At the time of maximum dose, ca 30 000 AD, a similar amount of activity has decayed as remain in the near-field (ca 15 %). However, twice as much activity has accumulated in the biosphere or has left the surface system (ca 30 % each; Figure 5-64). Ingestion of food, especially animal products, is the dominant exposure pathways for this radionuclide.

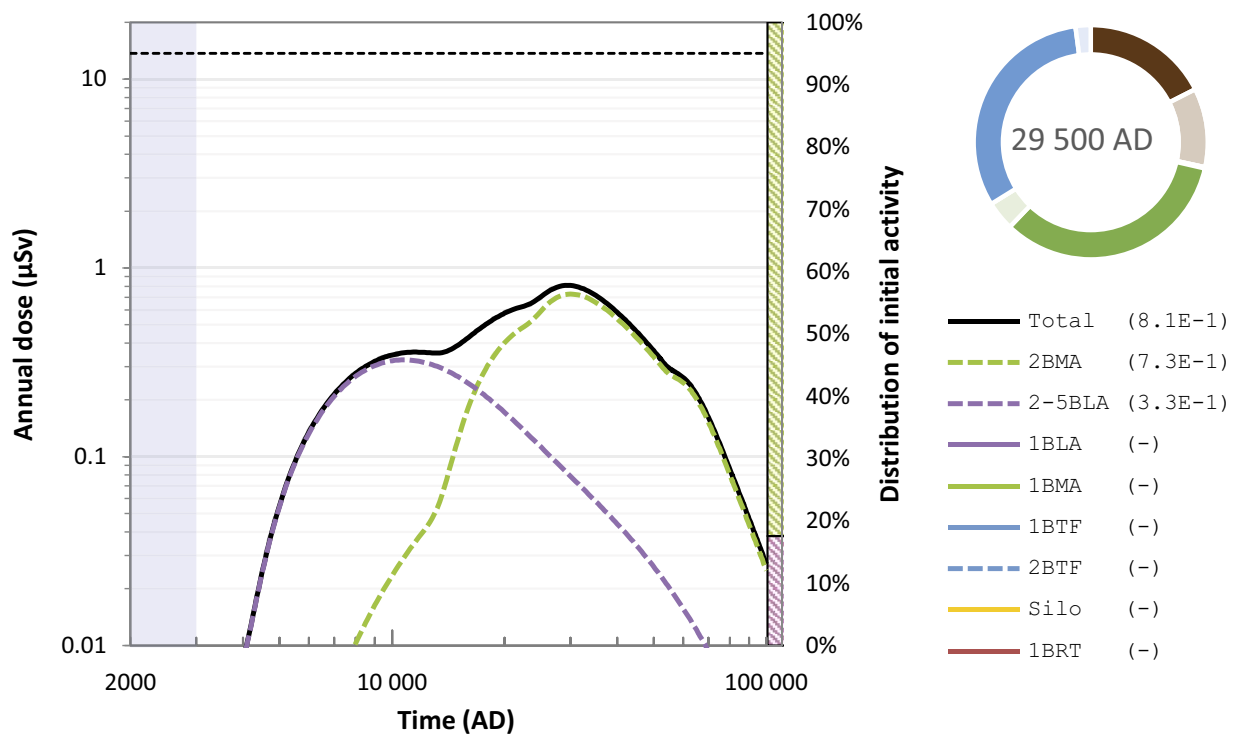


Figure 5-67. Annual dose from Ca-41 (μSv , left y-axis) to the most exposed group in the base case (black line) including vault-specific contributions (coloured lines). The flanking vertical bar on the right represents the distribution of initial activity between the vaults (right y-axis, colours are the same as those given by the key, and the hatched areas in the bar correspond to the dashed lines in the key). The total and vault-specific dose maxima from Ca-41 (μSv) are shown in parentheses in the key. The annual dose corresponding to the regulatory risk criterion ($14 \mu\text{Sv}$) is indicated by the black dashed line and the submerged period is illustrated by the blue shading. The circle diagram shows the distribution of the activity (opaque colours) between the near-field (brown), biosphere (green), and the export from the system (blue), together with the cumulative decay (pale colours), at the time for maximum annual dose from Ca-41 (data from Figure 5-64). Note that the activity in the geosphere is too small to be visible in the circle diagram.

Ni-59

Although most of the Ni-59 inventory is present in the silo, 1BMA and 2BMA, other waste vaults with relatively small inventories contribute notably to the annual Ni-59 dose (Figure 5-68). The reason is that the activity disposed in the silo and the BMA vaults is effectively retained by sorption to cement and bentonite. Therefore, 98 % of the total Ni-59 activity either decays or remains in the repository by the end of the assessment period (which coincides with its dose maximum, see Figure 5-64). Ni-59 is a long-lived radionuclide (half-life is 101 000 years), so releases from the near-field to the geosphere are largely controlled by concrete degradation in 1BMA and 2BMA at later stages in the assessment. Overall, however, annual releases of Ni-59 from SFR are relatively constant throughout the assessment period (Figure 5-42).

In contrast to the other dose-dominating radionuclides, Ni-59 sorbs, albeit relatively weakly, to the rock matrix (Table 5-18). Consequently, about 20 % of its accumulated activity either decays or remains in the geosphere during the assessment period (Figure 5-49), and the mean release from the geosphere is slightly lower than that from the near-field (Figure 5-45).

As with Ca-41, Ni-59 sorbs more strongly to the inorganic lower regolith layers than to the organic upper layers (Figure 5-64). However, Ni-59 sorption in these layers is substantially stronger than for Ca-41 (Table 5-20), resulting in longer biosphere residence times. This together with the relatively constant release of Ni-59 results in higher doses towards the end of the assessment period.

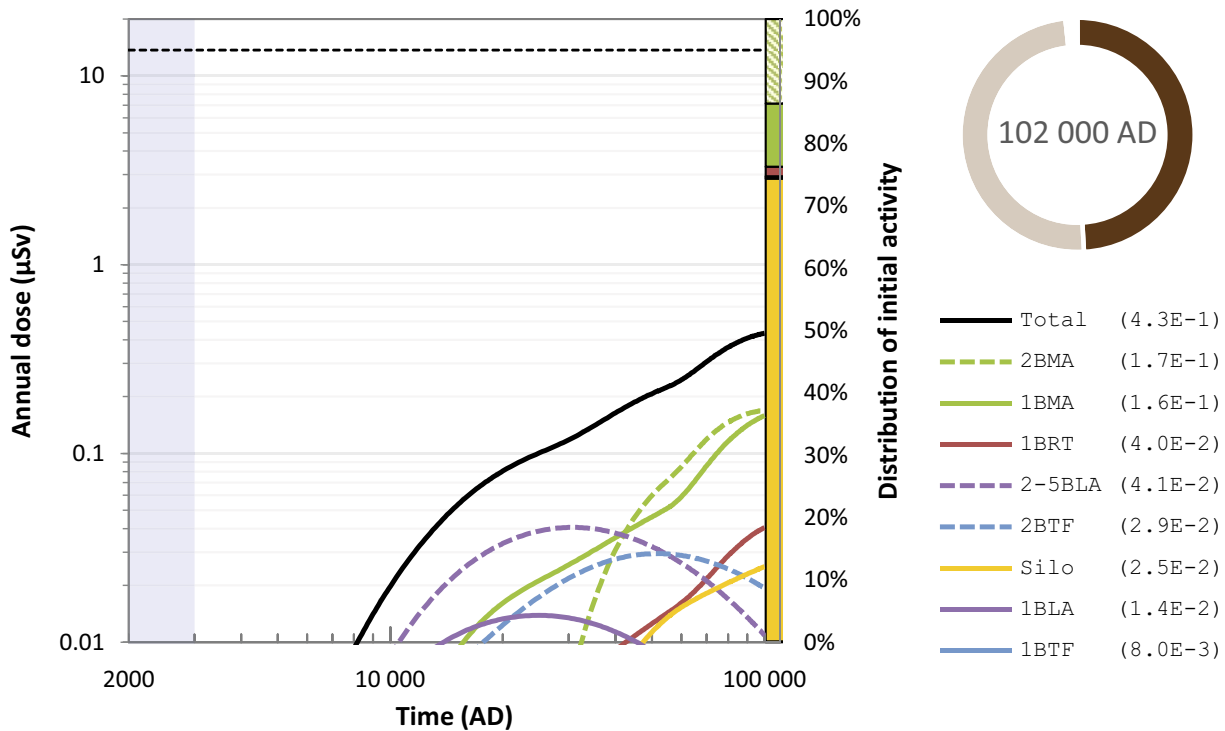


Figure 5-68. Annual dose from Ni-59 (μSv , left y-axis) to the most exposed group in the base case (black line) including vault-specific contributions (coloured lines). The flanking vertical bar on the right represents the distribution of initial activity between the vaults (right y-axis, colours are the same as those given by the key), and the hatched areas in the bar correspond to the dashed lines in the key). The total and vault-specific dose maxima from Ni-59 (μSv) are shown in parentheses in the key. The annual dose corresponding to the regulatory risk criterion ($14 \mu\text{Sv}$) is indicated by the black dashed line and the submerged period is illustrated by the blue shading. The circle diagram shows the distribution of the activity (opaque colours) between the near-field (brown) and other components (too small to be visible), and the cumulative decay (pale colours), at the time for maximum annual dose from Ni-59 (data from Figure 5-64). Note that the activities in the geosphere and biosphere as well as the activity exported from the system are too small to be visible in the circle diagram.

I-129

The majority (75 %) of the I-129 inventory is disposed in the silo with smaller contributions from 1BMA and 2BMA (11 % and 12 % respectively). The total activity of its inventory is one-to-four orders-of-magnitude lower than for the dose-dominating radionuclides (**Post-closure safety report**, Section 4.3.7). Despite the relatively low inventory, it contributes more than 5 % to the total dose maximum (Figure 5-54). The high dose contribution relative to its initial inventory is partly explained by its high radiotoxicity. Moreover, it has an extremely long half-life (1.57×10^7 years) and sorbs weakly to cement. As a result, decay in the near-field is negligible and more than 90 % of its initial inventory is released from the repository by the end of assessment period (Figure 5-39). The near-field mobility of I-129 results in a strong correspondence between the initial inventory distribution and accumulated vault-specific releases (left versus right vertical bars in Figure 5-41) and vault-specific doses (Figure 5-69). The depletion of the I-129 inventory occurs at a relatively constant rate throughout the assessment period. Therefore, and because the maximum dose from I-129 occurs relatively early in the assessment period (8200 AD), most of the I-129 activity will still be present in the waste vaults at the time of its maximum dose contribution to the DM group (Figure 5-64).

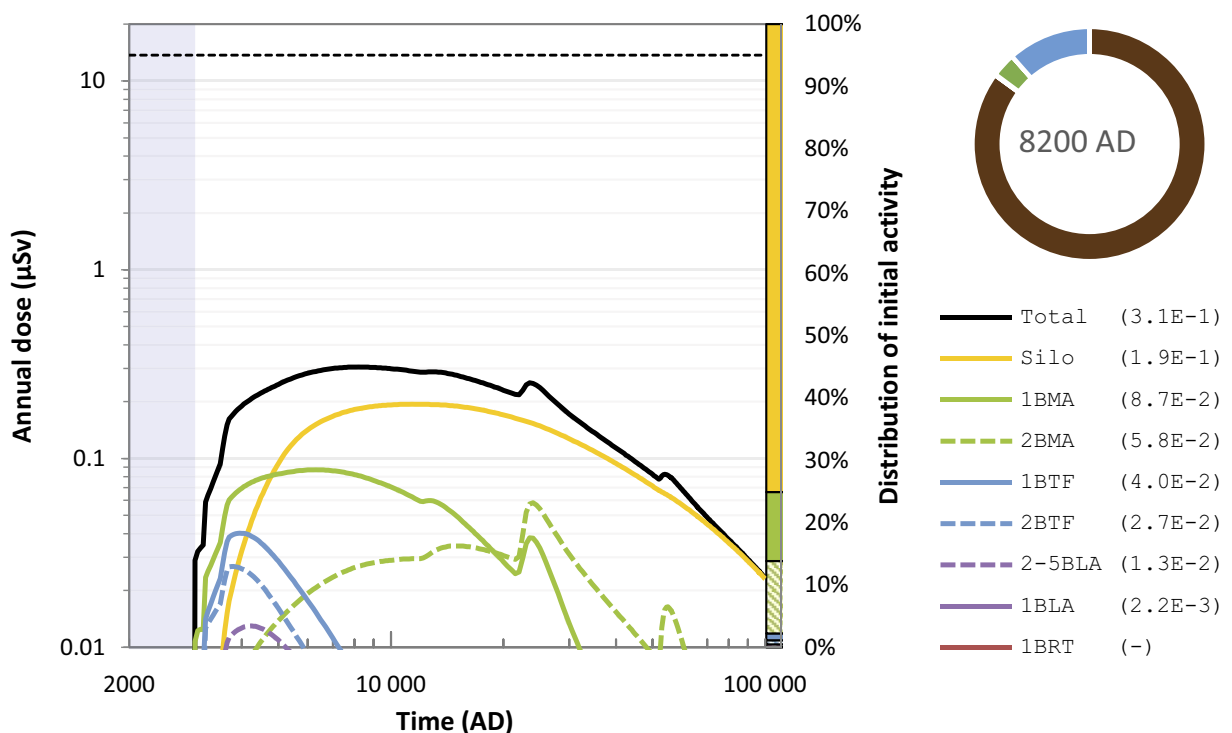


Figure 5-69. Annual dose from I-129 (μSv , left y-axis) to the most exposed group in the base case (black line) including vault-specific contributions (coloured lines). The flanking vertical bar on the right represents the distribution of initial activity between the vaults (right y-axis, colours are the same as those given by the key, and the hatched areas in the bar correspond to the dashed lines in the key). The total and vault-specific dose maxima from I-129 (μSv) are shown in parentheses in the key. The annual dose corresponding to the regulatory risk criterion ($14 \mu\text{Sv}$) is indicated by the black dashed line and the submerged period is illustrated by the blue shading. The circle diagram shows the distribution of the activity between the near-field (brown), biosphere (green), and the export from the system (blue) at the time for maximum annual dose from I-129 (data from Figure 5-64). Note that the activity in the geosphere as well as the cumulative decay in all repository-system components are too small to be visible in the circle diagram.

U-238

Most of the U-238 inventory is disposed in 1BLA with some smaller quantities in 2–5BLA. As sorption of radionuclides onto waste form and waste packaging in 1–5BLA is neglected in the modelling (Section 5.3.7), the contribution from these vaults to the U-238 dose is roughly proportional to their initial U-238 inventory (Figure 5-70). U-238 has an extremely long half-life (4.5×10^9 years), so only a negligible amount will decay within the assessment period.

U-238 contributes only ca 10 % to the total dose maximum (Figure 5-54) but is included in this summary to illustrate the retention properties of the geosphere for uranium. In contrast to the other radionuclides discussed here, uranium sorbs strongly to the rock matrix, so the majority of the U-238 activity is retained in the geosphere at the time of maximum dose (Figure 5-64). Thus, for this radionuclide, the natural bedrock is the primary transport barrier.

Despite the strong retention in the geosphere, the dose maximum of U-238 occurs relatively early compared to other long-lived radionuclides like Ca-41 and Ni-59. This difference has a two-fold explanation. First, releases from BLA-vaults to the geosphere occur much earlier than from 2BMA and the silo, where most of the Ca-41 and Ni-59 inventories are present, respectively. Second, Ca-41 and Ni-59 sorb relatively strongly in the lower regolith layers, but uranium is relatively mobile in those layers and sorbed strongly in the upper organic layers (cf. “Other regolith” versus “RegoLow” in Figure 5-64). This implies that most of the U-238 activity accumulated in the biosphere will be exposed when those layers are cultivated by the farmers in the DM group.

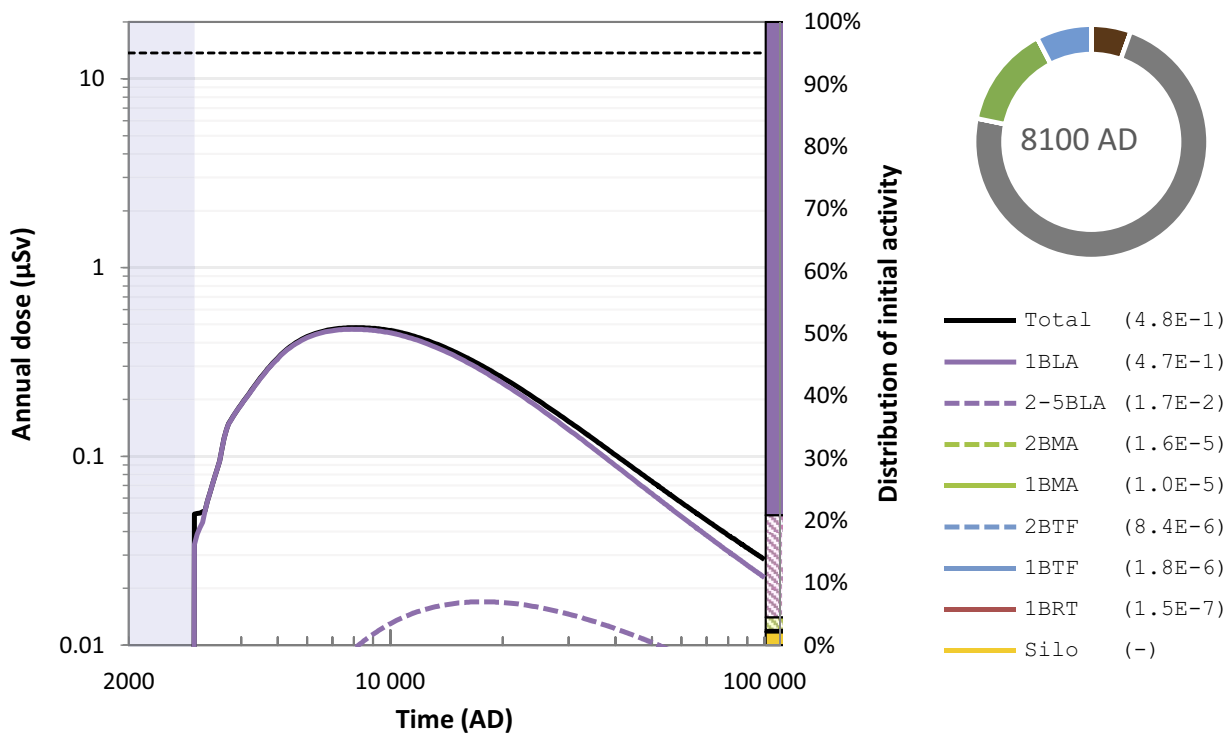


Figure 5-70. Annual dose from U-238 (μSv , left y-axis) to the most exposed group in the base case (black line) including vault-specific contributions (coloured lines). The flanking vertical bar on the right represents the distribution of initial activity between the vaults (right y-axis, colours are the same as those given by the key), and the hatched areas in the bar correspond to the dashed lines in the key). The total and vault-specific dose maxima from U-238 (μSv) are shown in parentheses in the key. The annual dose corresponding to the regulatory risk criterion ($14 \mu\text{Sv}$) is indicated by the black dashed line and the submerged period is illustrated by the blue shading. The circle diagram shows the distribution of the activity between the near-field (brown), geosphere (grey), biosphere (green), and the export from the system (blue) at the time for maximum annual dose from U-238 (data from Figure 5-64). Note that the cumulative decay in all repository-system components is too small to be visible in the circle diagram.

Due to the strong geosphere sorption of uranium, their consequently long transport times in the geosphere will enable ingrowth of radiotoxic decay products. Two of the three radionuclides with the highest accumulated radiotoxic release from the geosphere are decay products of U-235 (Pa-231 and Ac-227; Figure 5-49). These radionuclides are expected to be among the most hazardous to direct ingestion, e.g. through drilling of wells, over the next 100 000 years.

5.9.4 Uncertainties

Uncertainties in most parameters are handled through a probabilistic approach that draws stochastic parameter values from a PDF. Potential consequences of using this probabilistic approach in the *base case* are analysed in the **Biosphere synthesis report**, Section 9.4. In summary, this analysis shows that data uncertainty does not lead to an underestimation of the dose.

The probabilistic approach has not been applied to all input parameters used in the *base case*, so these parameters are handled deterministically in the calculations using best-estimate values. This is the case, for instance, for parameters that are subject to a considerable modelling or scenario uncertainty (Section 2.5.4). The impact of such uncertainties on the resulting dose are handled in the less probable scenarios (Chapter 7) or in dedicated supporting calculation cases. Two supporting calculation cases are included in this report evaluating uncertainties in the initial shoreline regression and timing of initial releases from the repository (Section 5.8). As with the *base case*, the maximum dose in the supporting calculations is well below the dose corresponding to the regulatory risk criterion. This supports the notion that the assumptions in the *base case* are reasonable and do not underestimate doses.

5.9.5 Conclusions

The outcome of the analysis of the *base case* is consistent with SKB's general understanding, acquired from previous safety assessments, of radionuclide transport through the SFR repository system. Differences in transport patterns of individual radionuclides are explained by radionuclide-specific properties and by properties of individual waste vaults. Uncertainties in specific assumptions, evaluated in the supporting calculation cases, are shown to have only a small influence on the calculated doses. Taken together, the analysis of the *base case* helps to build confidence that the model results are reliable, robust and that they serve as a credible starting point for the analysis of uncertainties in other calculation cases evaluating the main scenario, less probable scenarios and residual scenarios.

6 Calculation cases in main scenario – climate evolution

6.1 Introduction

The *base case* was defined, in part, to enable straightforward evaluation of differences with respect to other calculation cases. To this end, a simplified climate evolution characterised by present-day climate conditions for the entire assessment period was assumed for the *base case*.

In this chapter, the other two calculation cases of the main scenario besides the *base case* are described. These represent the range of probable climate evolutions as defined by the reference external conditions (**Post-closure safety report**, Section 2.6.3 and Chapter 6). Two calculation cases have been identified to analyse the effects of future climate evolution in the main scenario:

- The *warm climate calculation case* is defined based on the *warm climate variant* of the reference evolution, representing warmer-than-present climate conditions including the effect of a delayed shoreline regression (Section 6.2).
- The *cold climate calculation case* is defined based on the *cold climate variant* of the reference evolution, representing a development towards colder climate conditions including the effect of periglacial conditions during the last 50 000 years of the assessment period (Section 6.3).

The difference in underlying assumptions between the *warm climate calculation case* and the *cold climate calculation case* relates to the amount of anthropogenic greenhouse gases emitted to the atmosphere within the current and the next century (**Post-closure safety report**, Sections 6.4.1 and 6.5.1). The cumulative emissions within this relatively short time frame are expected to influence the evolution of climate and climate-related processes at Forsmark for the entire assessment period of 100 000 years, including the initial shoreline development and the potential emergence of periglacial conditions within the assessment period (**Climate report**, Chapter 3).

6.2 Warm climate

6.2.1 General description

The *warm climate calculation case* is selected to evaluate doses to humans for the *warm climate variant* of the reference evolution (**Post-closure safety report**, Sections 6.2 and 6.4). The *warm climate variant* represents a future development where similar-to-present levels of anthropogenic greenhouse-gas emissions continue for the next few decades, after which they gradually decline towards net-zero emissions within the next century. To this end, this variant represents a likely future development in line with recent forecasts of “business-as-usual” emissions and the Intergovernmental Panel on Climate Change (IPCC) medium emissions scenarios RCP4.5 and RCP6.0 (**Climate report**, Section 4.2). These assumptions result in considerable climate warming during the initial thousands of years and, similar to the *base case*, temperate climate conditions at Forsmark for the complete assessment period of 100 000 years after closure (**Post-closure safety report**, Section 6.4).

As compared with the *base case*, both the surface water availability and the shoreline development are affected by the warmer climate and hydrology and ecosystem parameters are adjusted accordingly. The geosphere and near-field conditions are not expected to be affected by a warmer climate in a way that significantly affects repository performance (**Post-closure safety report**, Section 6.4).

Annual precipitation at Forsmark is expected to increase in a warmer climate (**Climate report**, Section 3.4). However, analyses of climate model projections suggest that this increase may not be distributed equally throughout the year. According to these projections, precipitation will increase because of a warmer climate during the winter, spring and autumn seasons, but may either increase or decrease during the summer season (**Climate report**, Appendix B). As a result, the effects of a warmer climate are examined in two variants with, respectively, higher and lower summer precipitation compared to present: the *high summer precipitation* variant and the *low summer precipitation* variant.

In the *base case*, it is assumed that DM farmers cultivate crops that obtain the required water via groundwater uptake. However, as the climate becomes warmer, the potential evapotranspiration is projected to increase at a faster rate than the precipitation (**Post-closure safety report**, Section 6.4.1), resulting in increased water demand for crops and the potential use of irrigation water to satisfy this demand. In the *warm climate calculation case*, it is therefore assumed that the increased water demand is satisfied either by groundwater uptake or sprinkler irrigation. To this end, an additional exposed group is considered in the calculations: DM farmers practicing large-scale irrigation.

6.2.2 External conditions

External conditions correspond to the *warm climate variant* of the reference evolution, described in the **Post-closure safety report**, Sections 6.2 and 6.4. In summary, the evolution of climate domains is identical to the *base case* except for a longer initial duration of submerged conditions (Figure 6-1).

As described in Section 5.8.2, the future relative sea-level change at Forsmark is associated with a large uncertainty. Under business-as-usual anthropogenic greenhouse-gas emissions, this uncertainty is represented by two alternative developments that are considered to bracket the full range of possible relative sea-level change (left panel of Figure 6-2 and **Climate report**, Section 5.2.2). The mean value of the range is chosen for the *warm climate calculation case*, corresponding to 4 500 years of initial submerged conditions above SFR. This corresponds to 3 500 years delayed shoreline regression relative to the *base case*, which was included as one of the calculations in the *timing of shoreline regression calculation case* (Section 5.8.2). Thus, in this calculation case, the shoreline regression of the *base case* is assumed to be shifted 3 500 years forward in time, implying that biosphere object 157_2 begins to emerge above sea level around 6500 AD, instead of around 3000 AD in the *base case* (right panel of Figure 6-2). This simplified representation is considered to adequately capture the main features of a delayed shoreline regression (**Data report**, Chapter 12). The approach is arguably also cautious, as it does not account for the expected increase in water exchange between the assessed basins (Figure 4-5) and Öregrundsgrepen (which is in contact with the Baltic Sea). In addition, it does not account for the expected slow-down of the land uplift (due to the rate of land uplift decreasing with time) that could reduce the rate of uplift and the area of the biosphere object during emergence.

Under business-as-usual anthropogenic greenhouse-gas emissions, the annual average air temperature is projected to reach its maximum value within the first thousand years after closure, after which it slowly declines over the subsequent tens of thousands of years as the increased atmospheric CO₂ concentration declines (**Climate report**, Section 3.4.4). Changes in precipitation and potential evapotranspiration correlate with the air temperature, such that their maximum changes, both seasonally and annually, will coincide relatively closely in time with the change in maximum air temperature.

In the *warm climate calculation case*, the maximum changes in air temperature, precipitation and potential evapotranspiration are, for simplicity, assumed to persist for the complete assessment period (Table 6-1). This simplification is considered to be pessimistic as it overestimates the average difference between potential evapotranspiration and precipitation, i.e. the water demand at the surface, during the summer season compared with that arising if a more realistic temporal climate evolution were to be used. However, the maximum dose typically occurs during the early stages of the assessment period when the warming is expected to be relatively similar to its maximum value. Thus, the impact on maximum dose of a constant-in-time climate evolution is expected to be relatively small compared to a more realistic temporal climate evolution.

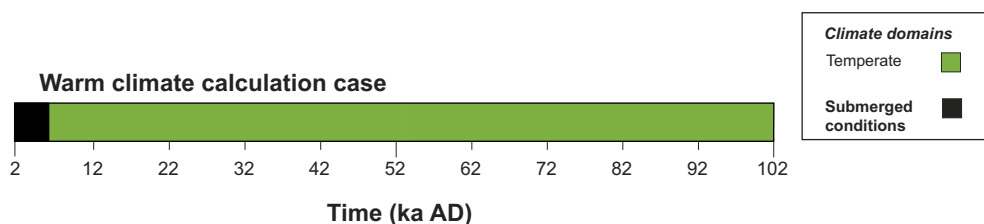


Figure 6-1. Succession of climate domains in the warm climate calculation case.

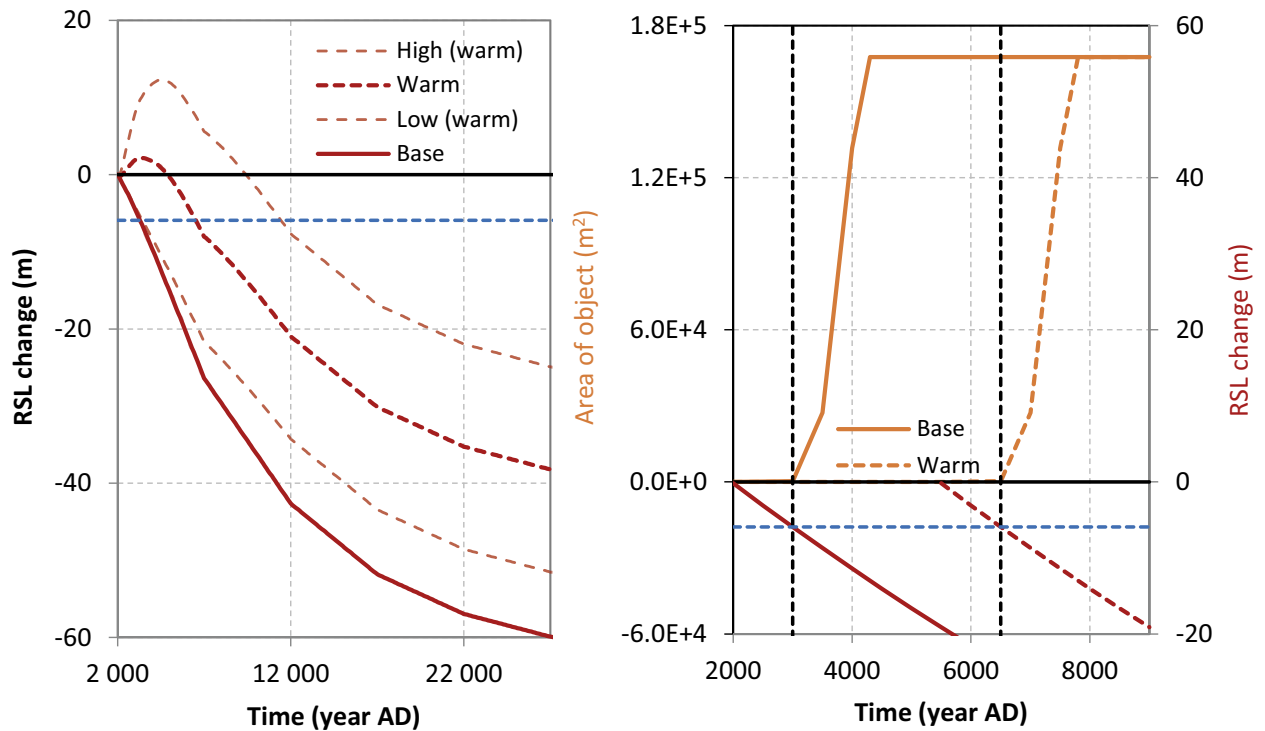


Figure 6-2. Temporal evolution of the shoreline at Forsmark. Left) Change in the relative sea level (RSL) in the present-day (base case) climate variant (solid) and the warm climate variant (dashed) of the reference evolution. Thin dashed lines represent the low- and high-end RSL estimates under the level of global warming assumed in the warm climate variant, and the thick dashed line represents the mean of those estimates. The horizontal blue dashed line represents the RSL corresponding to the end of the submerged period. Right) Simplified treatment of RSL as used in the base case and the warm climate calculation case (red lines) and the resulting emergence of object 157_2 above sea level (orange lines). The vertical black dashed lines indicate the time when the object starts to emerge above the sea.

Table 6-1. Changes in the climate conditions in the two variants of the *warm climate calculation case* with respect to the *base case*. Annual (without a subscript) and summer (June, July and August; denoted JJA) changes are given for temperature (ΔT), precipitation (ΔP), and potential evapotranspiration (ΔPET).

Variant	Air temperature		Precipitation		Potential evapotranspiration	
	ΔT	ΔT_{JJA}	ΔP	ΔP_{JJA}	ΔPET	ΔPET_{JJA}
High summer precipitation	+5.0 °C	+4.0 °C	19 %	17 %	34 %	18 %
Low summer precipitation	+5.0 °C	+4.0 °C	10 %	-13 %	34 %	18 %

6.2.3 Handling in the near-field and geosphere models

The handling in the near-field and geosphere models is identical to that of the *timing of shoreline regression calculation case* (Section 5.8.2). Thus, the progression of the groundwater flow in the near-field and geosphere is shifted 3 500 years forward in time compared with the *base case*. Except for this change, the handling in the near-field and geosphere is identical to the *base case*. Thus, the entire geosphere release is still assumed to be discharged to biosphere object 157_2.

6.2.4 Handling in the biosphere model

The modelling of the *warm climate calculation case* in the biosphere considers changes in surface hydrology and ecosystem parameters and includes an additional potentially exposed group (PEG): DM farmers practicing large-scale irrigation.

Surface hydrology

Ground- and surface-water flows for the mire state of biosphere object 157_2 in a warmer climate were simulated with the MIKE SHE tool (**Biosphere synthesis report**, Appendix F). The simulations are based on the climate description for the two variants set out above (*high/low summer precipitation*), and hydrological parameter values are derived from simulated water balances (**Biosphere synthesis report**, Section 8.3.1). In addition to object-specific flow, the net precipitation from the new hydrological simulations was used to characterise percolation in the unsaturated agricultural soils (left panel in Figure 6-3).

In a warmer climate, the projected increase in evapotranspiration is greater than the projected increase in precipitation leading to an increase of the plant water deficit during the vegetation period. This is true for both variants of the calculation case. An increased demand for water could either fully or partly be supplied by an increased groundwater uptake through capillary rise, and/or it could be satisfied by irrigation. A multi-model approach is used to forecast the response of crop water demand in agricultural systems (right panel in Figure 6-3)²⁰. Moreover, it is cautiously assumed that the crop water demand is fully compensated by water containing radionuclides originating from the repository, either from groundwater or from irrigation with surface water.

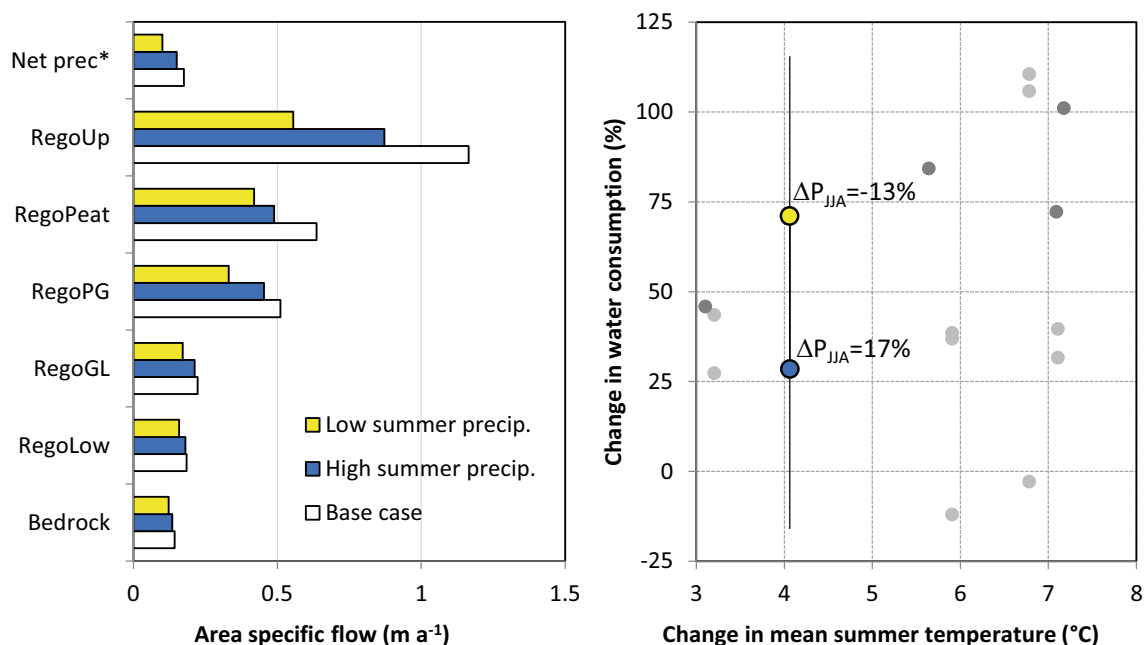


Figure 6-3. Response in surface hydrology and water demand for arable land for the two variants of the warm climate calculation case. Left) Area specific upward groundwater flow for the wetland in object 157_2 and net precipitation (*) at the landscape level, as predicted with hydrological modelling (*Biosphere synthesis report*, Appendix F). The regolith layers in the model are shown in Figure 4-6. Yellow represents flow in the variant with low summer precipitation, blue represents flow in the variant with high summer precipitation, and white the flow given present-day climate used in the base case. Right) Changes in crop water demand due to changes in summer temperature and precipitation as estimated from a global multi-model approach (Gosling et al. 2019). Coloured symbols represent the mean changes as compared to the demand in the base case. Error bars represent the standard deviation corresponding to the uncertainty in projections between hydrological models (*Biosphere synthesis report*, Appendix G). Dark grey circles correspond to results for the grid point closest to Forsmark, whereas light grey circles represent the average response for entire Scandinavia.

²⁰ For this purpose, output data for sixteen combinations of global climate and hydrological models were utilised (Gosling et al. 2019). The data were provided by the second phase of the Inter-Sectoral Impact Model Intercomparison Project (ISIMIP2, available at <https://www.isimip.org/>).

Ecosystem parameters

Values for ecosystem parameters, such as biomass, net primary production and crop yield are adjusted to increased air temperature based on literature data from warmer locations (Grolander 2013). The concentration of stable CO₂ in the atmosphere is adjusted to elevated levels in accordance with the RCP4.5 emissions scenario (540 ppm; **Climate report**, Section 3.4.1).

Large-scale irrigation of cereal and fodder production is not practiced in Forsmark under present conditions. Adding large-scale irrigation as an exposure pathway to DM farming thus requires the definition of new parameters describing this practice (**Biosphere synthesis report**, Section 8.3.1). Moreover, the processes for accumulation on edible parts of crop (cereals), element translocation to edible parts (potatoes) and weathering of intercepted radionuclides (fodder) are added to the models describing agriculture in warmer conditions. The amount and frequency of irrigation of a garden plot are also adjusted to reflect warmer conditions.

Owing to their different representations of the summer climate, the crop water deficit during the vegetation season, and thus the irrigation and plant groundwater uptake, is higher in the *low summer precipitation* variant than in the *high summer precipitation* variant.

Potentially exposed groups

In addition to the PEGs of humans defined in the *base case*, a variant of DM farmers practicing large-scale irrigation at a relatively low intensity is added (two irrigation events per season at a scale of several hectares, evaluated over 50 years of cultivation). Long-term large-scale irrigation (500 consecutive years) is assessed for the IO farming group (two irrigation events per season). The effects of short-term irrigation at higher intensities (ten irrigation events per season) with well water, either from a dug or a drilled well, are assessed for the GP household group.

6.2.5 Annual release from the near-field and the geosphere

Changes in annual releases from the near-field and the geosphere, resulting from a delayed shoreline regression, were analysed in the *timing of shoreline regression calculation case* (Section 5.8.2).

6.2.6 Annual doses

A warmer climate leads to a reduction of the maximum dose with respect to the *base case* as assessed by the exposed group receiving the highest dose (Figure 6-4). This result is primarily an effect of the prolonged period of submerged conditions as this serves to delay and reduce the geosphere release of C-14-org and Mo-93. Moreover, elevated CO₂ levels in the atmosphere (540 ppm versus 380 ppm in the *base case*) increase the atmospheric dilution of C-14-org (i.e. by lowering the atmospheric C-14 to C-12 ratio). However, this reduction is off-set by an increased groundwater uptake of C-14-org (for farming without irrigation) to compensate for the decreased net precipitation in a warmer climate and by an increased accumulation of sorbing radionuclides in regolith layers due to decreased groundwater flow in the mire ecosystem (Figure 6-3).

The dose from C-14-org is near proportional to the rate of groundwater uptake and its activity concentration, as this is the primary source for C-14-org in the drained mire (Section 5.7). In the *low summer precipitation* variant, the groundwater uptake increases by 70 % (right panel in Figure 6-3) and the dilution of groundwater decreases by ~15 % (RegoLow in Figure 6-3). Thus, almost twice as much of the radionuclides released from the geosphere reach the cultivated soil, which affects both root and foliar uptake of C-14-org proportionally. This results in even higher C-14-org doses in the *low summer precipitation* variant than in the *base case* despite a delayed release and an increased concentration of C-12 in the atmosphere (upper panel in Figure 6-5).

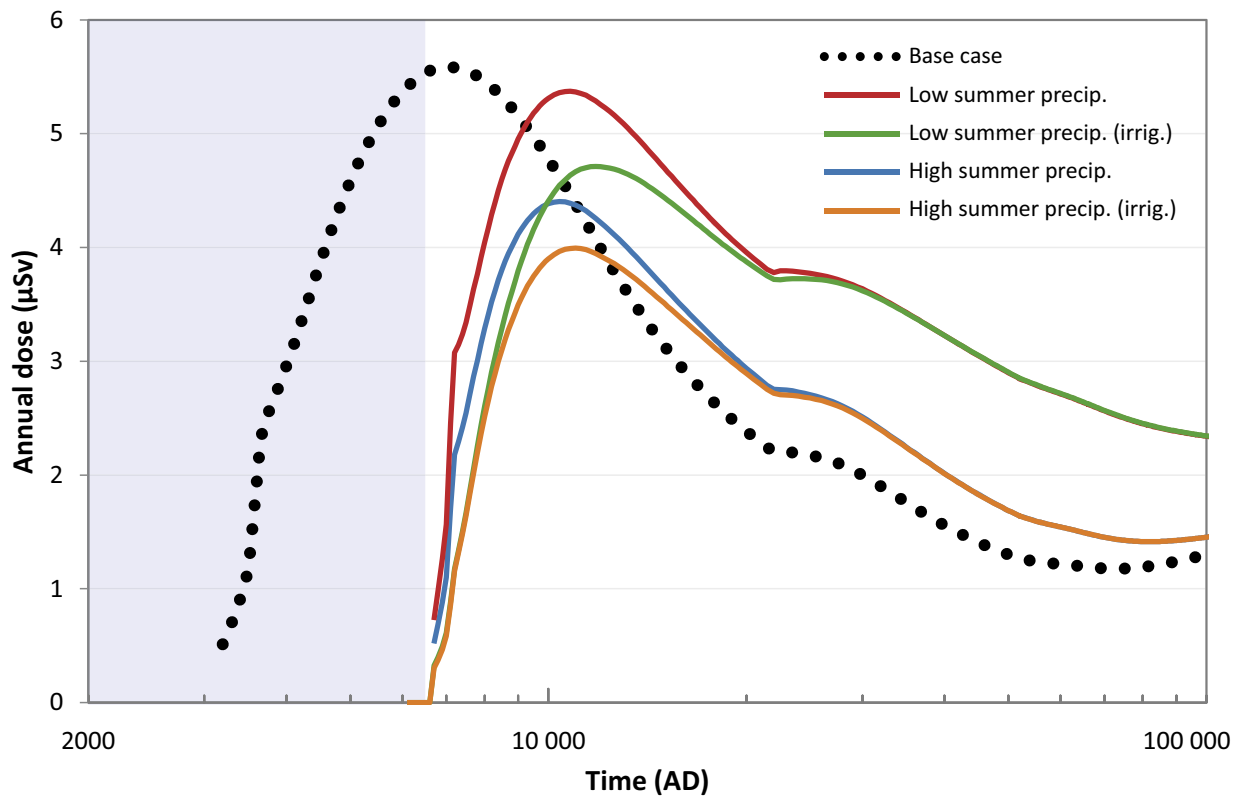


Figure 6-4. Annual dose to DM farmers (μSv), with and without large-scale irrigation, in the two variants of the warm climate calculation case (coloured lines). The annual dose in the base case is shown for comparison (black dotted line). The submerged period for the warm climate calculation case is illustrated by the blue shading.

The accumulation of radionuclides in the regolith layers is greatest in the *low summer precipitation* variant, where the upward groundwater flow is reduced by between $\sim 20\%$ (RegoGL glacial clay) and 35% (RegoPeat deep peat) in layers that are exposed when the mire is drained (left panel of Figure 6-3). The increased accumulation leads to a noticeable increase in the dose from, for example, Ca-41, Ni-59 and Ac-227, and the dose is consistently higher than in the *base case* for the period after 20 000 AD (upper panel of Figure 6-5). The annual dose after 20 000 AD varies between 2 to 4 μSv in the *low summer precipitation* variant, as compared to doses of 2 μSv (or lower) in the *base case*. It can be noted that the relative increase is most pronounced for Ac-227 and Pa-231. This is because accumulation of U-235 is the primary source of Ac-227 and its decay product. A decrease in the near-surface groundwater flow thus affects both the source and the dilution of Ac-227 and Pa-231.

The effect of irrigation is evaluated using stream water to compensate for the crop water deficit. This is reasonable because stream water is generated locally and is readily available in the discharge area. As stream water is diluted with the runoff generated in the catchment, the dilution is more than a factor four larger than in groundwater used to meet the crop water demand assuming capillary rise from the saturated lower regolith layer. The effect of surface water dilution is only noticeable in the early stage when C-14-org contributes to the dose (Figure 6-4), and, at this stage, the annual dose is consistently lower in variants with irrigation. However, after 20 000 AD, there is no difference in doses with respect to the source of water covering the crop water deficit. This is because accumulation in mire regolith layers is the dominating source of activity for the other dose contributing radionuclides (e.g. Mo-93, Ca-41, Ni-59 and Ac-227). Thus, accumulation of activity that ends up in the cultivated soil occurs prior to drainage and the activity in the cultivated soil is only marginally affected by groundwater uptake and irrigation.

A comparison of the dose between the exposed groups confirms the conclusions from the *base case*; long-term accumulation in natural ecosystems is also the most important exposure pathway in a warmer climate (Figure 6-5, lower panel). Thus, although the dose to IO farmers increases in the

warm climate as compared with the *base case* (~40 %), the potential dose contribution from long-term irrigation with surface water is marginal compared to accumulation in mire ecosystems or long-term addition of organic fertilizers (as seen by comparing IO-irrig with IO and DM in Figure 6-5).

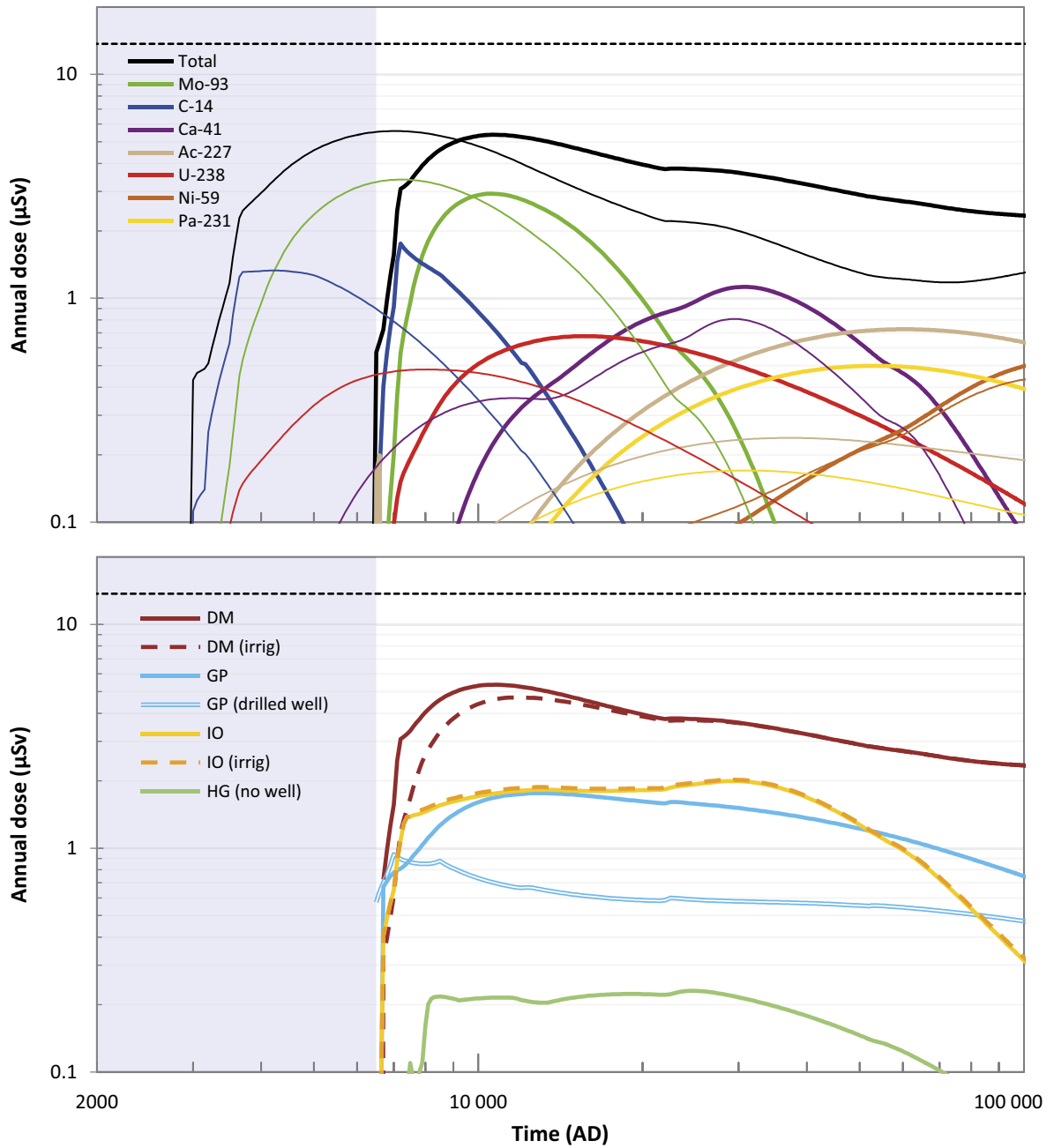


Figure 6-5. Annual doses (μSv) to the most exposed group (black line) including radionuclide specific contributions (coloured lines) (upper panel) and to the PEGs (lower panel) in the low summer precipitation variant of the warm climate case. For clarity, only the radionuclides contributing most to the total annual dose are shown. In the upper panel, the annual dose in the base case is shown for comparison (thin lines). In both panels, the annual dose corresponding to the regulatory risk criterion ($14 \mu\text{Sv}$) is indicated by the black dashed line and the submerged period is illustrated by the blue shading.

6.2.7 Summary and conclusions

The *warm climate calculation case* evaluates the radiological consequences under a future development consistent with business-as-usual scenarios of anthropogenic greenhouse-gas emissions. In a warmer climate, increased melting of land-based ice sheets and thermal expansion of seawater are expected to result in a prolonged submerged period with limited groundwater flow rates. This calculation case assumes that the regression of the shoreline in the Forsmark area is delayed by 3 500 years compared with the *base case* and is thus identical to the shortest delay of the shoreline regression evaluated in the *timing of shoreline regression calculation case* (Section 5.8.2). In that calculation case, it was concluded that a delayed shoreline regression results in lower near-field and geosphere releases of the radionuclides that contribute most to the maximum dose in the *base case* (C-14-org and Mo-93). Similar changes in the radionuclide release are also seen in the *warm climate calculation case*, resulting in a lower maximum dose in this calculation case than the maximum dose in *base case*.

The postulated changes in the biosphere associated with a warmer climate serve to increase doses from longer-lived radionuclides during the period subsequent to the dose maximum (i.e. after 20 000 AD). However, this increase is modest (approximately a factor of two) and the dose during this period does not exceed the maximum dose in the *base case*. Finally, it is concluded that the calculated doses are insensitive to assumptions of irrigation, as radionuclide accumulation prior to drainage and cultivation is found to be a more important source of activity in crops than being imported in with water during cultivation. The dose from C-14-org is an exception to this pattern. However, in this case, irrigation with surface water results in a lower dose than if the plant water deficit is covered by plant uptake of groundwater.

6.3 Cold climate

6.3.1 General description

The *cold climate calculation case* is selected to evaluate doses to humans for the *cold climate variant* of the reference evolution (**Post-closure safety report**, Sections 6.2 and 6.5). The *cold climate variant* represents a future development characterised by substantial reductions in anthropogenic greenhouse-gas emissions and/or removal of atmospheric CO₂ by technological measures. This development is projected to result in the termination of the current interglacial in conjunction with the next substantial minimum in incoming solar radiation (insolation) around 56 000 AD and in two periods of periglacial conditions at Forsmark within the latter half of the assessment period (**Post-closure safety report**, Section 6.5). A development characterised by ice-sheet advance over Forsmark within the assessment period is assessed to be considerably less likely (**Climate report**, Section 4.4), and is therefore evaluated as a less probable scenario in the *glaciation calculation case* (Section 7.2).

Periods of periglacial conditions are characterised by considerably lower air temperatures than at present, resulting in the development of permafrost and frozen bedrock conditions at Forsmark. There is a wide range of potential air temperatures that could influence the post-closure development of frozen conditions in the bedrock. For example, it is estimated that permafrost development in response to the insolation minimum at 56 000 AD could be accompanied by Forsmark air temperatures ranging from -11 °C to -1 °C depending on, for instance, the prevailing atmospheric CO₂ content and the Northern Hemisphere ice cover (**Post-closure safety report**, Section 6.5.3). Motivated by this uncertainty, two simplified bounding variants are selected to evaluate radiological consequences of periglacial conditions in this calculation case.

The *continuous permafrost* variant describes a situation where the climate becomes sufficiently cold to enable frozen bedrock conditions below repository depth. In this variant, frozen conditions are considered to hinder all release of radionuclides to the surface during periglacial conditions, and doses are evaluated in the active layer of the biosphere object (object 157_2) that receives geosphere release during temperate conditions.

In the *permafrost with talik* variant, the climate is assumed to be sufficiently cold to enable a shallow freezing of the bedrock, yet warm enough to maintain unfrozen conditions at repository depth. In this variant, the geosphere release is assumed to reach the surface ecosystem via a discharge talik, i.e. a local unfrozen part of the bedrock connecting the deep groundwater with the surface during periglacial conditions. Doses to humans are evaluated in different ecosystems: a mire and a lake. The properties of the biosphere objects are adjusted to represent the considered talik, and ecosystem and hydrological parameters are adjusted to reflect periglacial conditions.

Although these variants represent simplifications of the temporal and spatial development of a periglacial landscape, they are considered to bracket the uncertainty in radionuclide transport due to development of permafrost and frozen conditions in the geosphere and the biosphere. Freezing of pore water that could cause potential damage to the concrete barriers is not considered in this calculation case. In the *base case*, the concrete barriers are assumed to degrade to such an extent within the first 50 000 years (Section 5.3) that a potential subsequent freezing would no longer significantly influence the hydraulic properties of the concrete. Radiological consequences of a hypothetical earlier freezing of the concrete pore water are illustrated in a residual scenario with the *hypothetical early permafrost calculation case* (Section 8.2).

6.3.2 External conditions

External conditions correspond to the *cold climate variant* of the reference evolution, described in **Post-closure safety report**, Sections 6.2 and 6.5. In summary, the evolution of climate domains, including the initial duration of submerged conditions, is identical to the *base case* except for the occurrence of two periglacial periods within the latter half of the assessment period (Figure 6-6). Based on modelling of the future climate at Forsmark (Lord et al. 2019), the periglacial periods are defined to occur between 61 000 AD and 69 000 AD and between 81 000 AD and 102 000 AD (**Post-closure safety report**, Section 6.5). Periods of permafrost growth and decay are, for simplicity, neglected in the modelling. Thus, transitions to and from the periglacial landscapes described in this calculation case are assumed to be instantaneous. This simplification is considered to be cautious as it may result in elevated releases of decay products accumulated during periglacial conditions compared to a representation characterised by a more gradual and realistic transition (see further Section 6.3.5).

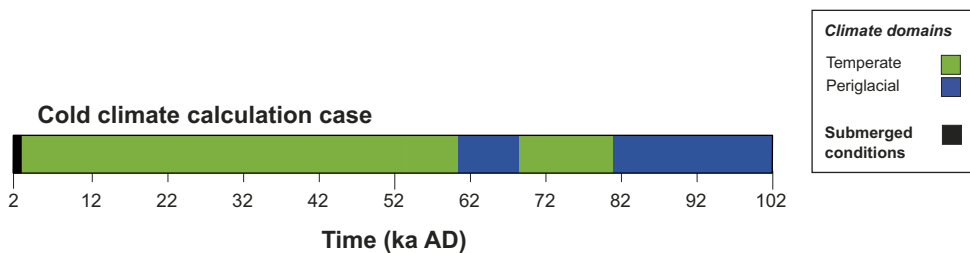


Figure 6-6. Succession of climate domains in the cold climate calculation case.

6.3.3 Handling in the near-field and geosphere models

During temperate conditions, including the initial period of submerged conditions, the handling in the near-field and the geosphere models is identical to the *base case*. In the *continuous permafrost* variant, the frozen conditions are considered to result in a complete cessation of the groundwater flow in the near-field and geosphere. As the geosphere release only occurs in temperate periods in the *continuous permafrost* variant, the entire release is directed to the one single discharge area, object 157_2, as in the *base case*.

In the *permafrost with talik* variant, which assumes unfrozen conditions at repository depth, the conditions in the near-field are considered to be the same as during temperate conditions, i.e. also identical to the *base case*. In this variant, the geosphere release during periglacial periods reaches the biosphere through a discharge talik. The distribution of unfrozen conditions in permafrost landscapes is influenced by several factors, including air temperature, topography, snow cover, availability of water bodies and vegetation (Johansson et al. 2006, Hartikainen et al. 2010). Unfrozen conditions and discharge taliks are typically formed below lakes. Results from regional hydrogeology modelling shows that groundwater from the extended repository could be discharged to large future lakes in Öregrundsgrepen (Odén et al. 2014). Furthermore, mire vegetation might inhibit permafrost development and discharge taliks below mires cannot be excluded (Cohen-Corticchiato and Zwinger 2021). Thus, in the *permafrost with talik* variant, the entire geosphere release during periglacial conditions is either directed to a future lake or a mire (see further Section 6.3.4).

In the *permafrost with talik* variant, the geosphere release is assumed to be equally large as in the *base case*. This simplification is overall considered to be cautious, as motivated in the following.

The expected groundwater composition under periglacial conditions is expected to be similar to that of temperate conditions (**Post-closure safety report**, Table 6-8). Moreover, reducing conditions are expected in the geosphere during periglacial conditions (**Post-closure safety report**, Section 6.5.6). Hence, just as in the *base case*, radionuclide K_d values for the rock matrix in this calculation case are chosen from Table 8-8 in the **Data report** based on $\text{pH} < 10$ and reducing conditions. For some elements, K_d values in the rock matrix may be higher during periglacial conditions than during temperate conditions (Crawford 2013). Since the radionuclides that contribute mostly to the dose generally sorb relatively poorly on the rock matrix, an increased K_d would result in lower releases to the biosphere and, consequently, to lower doses for most radionuclides. Therefore, the lowest K_d values for the rock matrix corresponding to the temperate saline groundwater conditions used in the *base case*, are cautiously chosen also for this calculation case.

In the regional hydrogeological modelling of periglacial conditions (Odén et al. 2014), it was concluded that the total flow through the waste vaults is lower, that path lengths are longer, and that travel times and flow-related transport resistance values are significantly higher than under temperate conditions. Furthermore, they showed that water flow is strongly dependent on the extent and number of taliks in the flow domain, with the weakest average flow obtained for the lowest number of taliks (Figure 5-5 in Odén et al. 2014). Using *base case* representations of the flow-related migration properties is thus considered to result in shorter path lengths and higher water flow than values representative for periglacial conditions. This choice is considered cautious as it serves to shorten the travel times in the geosphere for those radionuclides that contribute mostly to the dose.

6.3.4 Handling in the biosphere model

The biosphere model is adjusted to account for a lake and a mire talik in the biosphere objects. Furthermore, hydrological and ecosystem parameters are adjusted to reflect periglacial conditions (**Biosphere synthesis report**, Section 10.3.1).

Landscape description

The evolution of the landscape in the *cold climate calculation case* is identical to the *base case* up until the onset of the first periglacial period at 61 000 AD.

All lake-mire systems in the area above the repository are considered to have reached a mature state before 50 000 AD and a stationary representation of the mire in object 157_1 at its mature state is used to evaluate doses. Lake infilling is considered to be slow in periglacial conditions (Brydsten and Strömngren 2010) and thus a stationary representation of a hypothetical deep lake (i.e. a permanent lake without ingrowth and ecosystem succession) in object 114 farther out in Öregrundsgrepen is also used to evaluate doses (**Biosphere synthesis report**, Figure 5-12).

Surface hydrology

Permafrost has a major influence on hydrology and near-surface hydrogeology. The hydrologically active period is short and groundwater flow is restricted to a relatively thin active layer. Moreover, taliks may connect the unfrozen groundwater flow system in the bedrock with the surface system. In the SR-PSU, near-surface water-flow components were derived for the same potential future taliks as considered in this calculation case (Sections 4.3 and 5.5 in the **Biosphere synthesis report** and Odén et al. 2014). The hydrological modelling of taliks is described in Werner et al. (2013) and the hydrological parameters for the two taliks (biosphere objects 114 and 157_1) in Grolander (2013).

Biosphere object 157_2 is assumed to experience continuous permafrost during periglacial periods. Thus, in the biosphere modelling, all solute transport (advection and diffusion) in object 157_2 is terminated in the till layer (RegoLow). However, as the active layer thaws in summer, transport processes are assumed to be maintained to some extent in the regolith layers above the till. The net precipitation and runoff are assumed to increase by about 25 % in a future permafrost landscape (**Biosphere synthesis report**, Section 7.5.5).

Ecosystem parameters

The solubility of CO₂ is adjusted to reflect levels typical of a lower temperature and primary production, mineralisation, production of edible fish and crayfish are altered to better reflect permafrost conditions (**Biosphere synthesis report**, Section 8.3).

Potentially exposed groups

During periglacial conditions, cultivation is not possible due to permafrost and wells will not yield any water from the frozen ground. Thus, during periglacial periods, the PEG is HG foraging in the Forsmark landscape. HGs are assumed to collect food from a large area and can thereby utilise food from several biosphere objects at the same time (i.e. objects 157_2, object 157_1 and object 116). In the *permafrost with talik* variant with a lake talik (object 114), no additional downstream objects are considered.

During temperate conditions, the PEGs are identical to those assessed in the *base case* (Section 5.7).

6.3.5 Releases from the near-field and the geosphere

In the *permafrost with talik* variant, the total near-field and geosphere releases are identical to the *base case*. The same is also true for the *continuous permafrost* variant up until onset of the first periglacial period at 61 000 AD. At the onset of the first periglacial period, many radionuclides, including the dose-dominating Mo-93 and C-14-org, have decayed considerably and releases of more long-lived radionuclides dominate. In the *continuous permafrost* variant, the near-field and geosphere releases are prevented by the frozen bedrock conditions during the periglacial periods. Once groundwater flow again increases during the subsequent temperate period, releases of long-lived radionuclides are similar to those immediately prior the onset of the preceding periglacial period. This means that releases during the subsequent temperate period could be marginally higher than the releases during the corresponding time in the *base case* (Figure 6-7).

For decay products, the frozen conditions may lead to accumulation of radionuclides from their parents trapped in the frozen barriers and bedrock and the accumulated activity results in a subsequent period with elevated releases when groundwater flow occurs again. This effect results in relatively sharp increases of the geosphere release of some decay products (e.g. Ra-226 and Pb-210) at the onset of the post-periglacial temperate period, followed by a gradual decline of the releases for the remainder of the

temperate period (Figure 6-7). The sharp increases at the onset of the temperate period at 69 000 AD are also amplified by the instantaneous transitions between the periglacial and temperate domains that are assumed in the modelling (Section 6.3.2). A more realistic gradual transition between the climate domains would result in lower release peaks than those seen in Figure 6-7.

6.3.6 Annual doses

Before the first onset of periglacial conditions at 61 000 AD, the resulting doses in the *cold climate calculation case* are identical to the *base case*. The main result in the *cold climate calculation case*, in both variants, is at least an order of magnitude lower doses during periglacial periods than in the *base case* at the corresponding time (Figure 6-8). The main reason is that HG activities during periglacial conditions result in lower doses than cultivation and well water usage. While doses to DM farmers after 61 000 AD are dominated by radionuclides such as Ca-41 and Ni-59 that sorb and accumulate in regolith layers that become cultivated, I-129 dominates the dose to the HG group. This radionuclide is transported relatively quickly through the regolith and exposure is mainly through ingestion (wildlife and berries), but also by drinking surface water.

Doses to HGs are similar in the *continuous permafrost* and the *permafrost with talik* variants both in the temperate and periglacial periods. The reason for this is that the doses are generally dominated by exposure from a radionuclide (i.e. I-129) that accumulated in object 157_2 during the preceding temperate periods. In both the *continuous permafrost* and the *permafrost with talik* variants, the geosphere release to the biosphere object 157_2 stops during periglacial periods. In combination with continued leakage of radionuclides from the hydrologically active regolith layers in object 157_2, this results in a total dose to HGs that is lower during periglacial periods than in the *base case* (Figure 6-8).

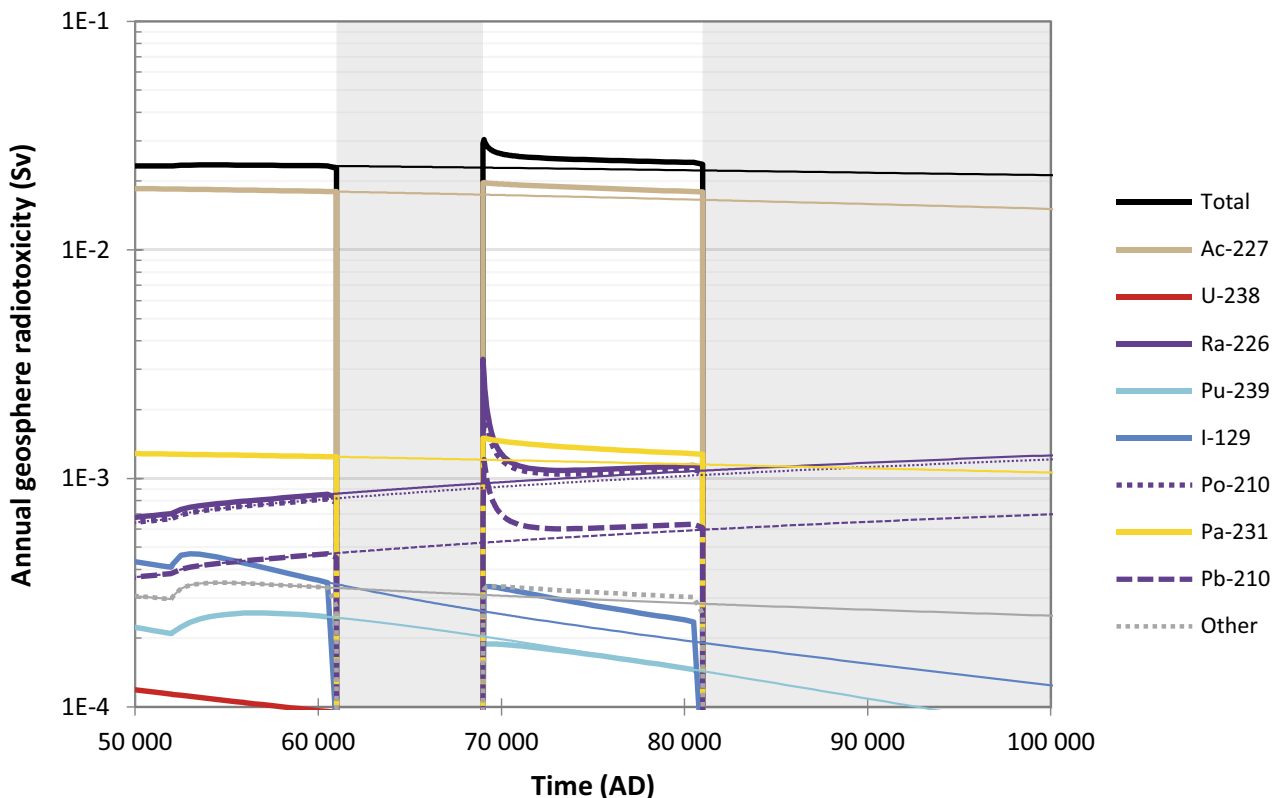


Figure 6-7. Annual geosphere radiotoxicity (Sv) from the entire SFR (black lines) in the continuous permafrost variant of the cold climate calculation case (thick lines) and the base case (thin lines), including radionuclide-specific contributions (coloured lines). The combined contribution from radionuclides not shown is indicated by the grey dotted lines. Grey shading indicates periods of periglacial conditions (cf Figure 6-6). Note that the timescale is shown only for the second half of the assessment period and is presented on a linear scale.

In the *permafrost with talik* variant, exposure from releases to a lake talik in object 114 is marginal compared to exposures to HGs foraging the landscape in the vicinity of the biosphere object 157_2 and the mire talik (object 157_1). Therefore, only results from the calculation with a talik in 157_1 are reported here. As radionuclides leach from the regolith layers in biosphere object 157_2, doses decrease during the periglacial periods (Figure 6-8). The geosphere release to the talik eventually reaches the upper regolith in object 157_1 and starts to contribute to the dose. This counteracts the decrease and doses become slightly higher than in the *continuous permafrost* variant (Figure 6-8). At the end of the second and slightly longer permafrost period, the dose contribution from object 157_1 is similar to the dose contribution from object 157_2.

As soon as farming is possible again during the post-periglacial temperate period, DM doses in object 157_2 exceed doses to HGs by more than one order of magnitude. Those DM doses are initially somewhat lower than in the *base case* due to the lack of releases to object 157_2 and the depletion of accumulated inventory in the regolith due to leaching during the preceding periglacial period, but eventually approach the levels of the *base case* doses. The marginally higher geosphere releases of radionuclides, including decay products, trapped in the near-field and geosphere by the permafrost in the *continuous permafrost* variant (Figure 6-7), do not affect doses significantly.

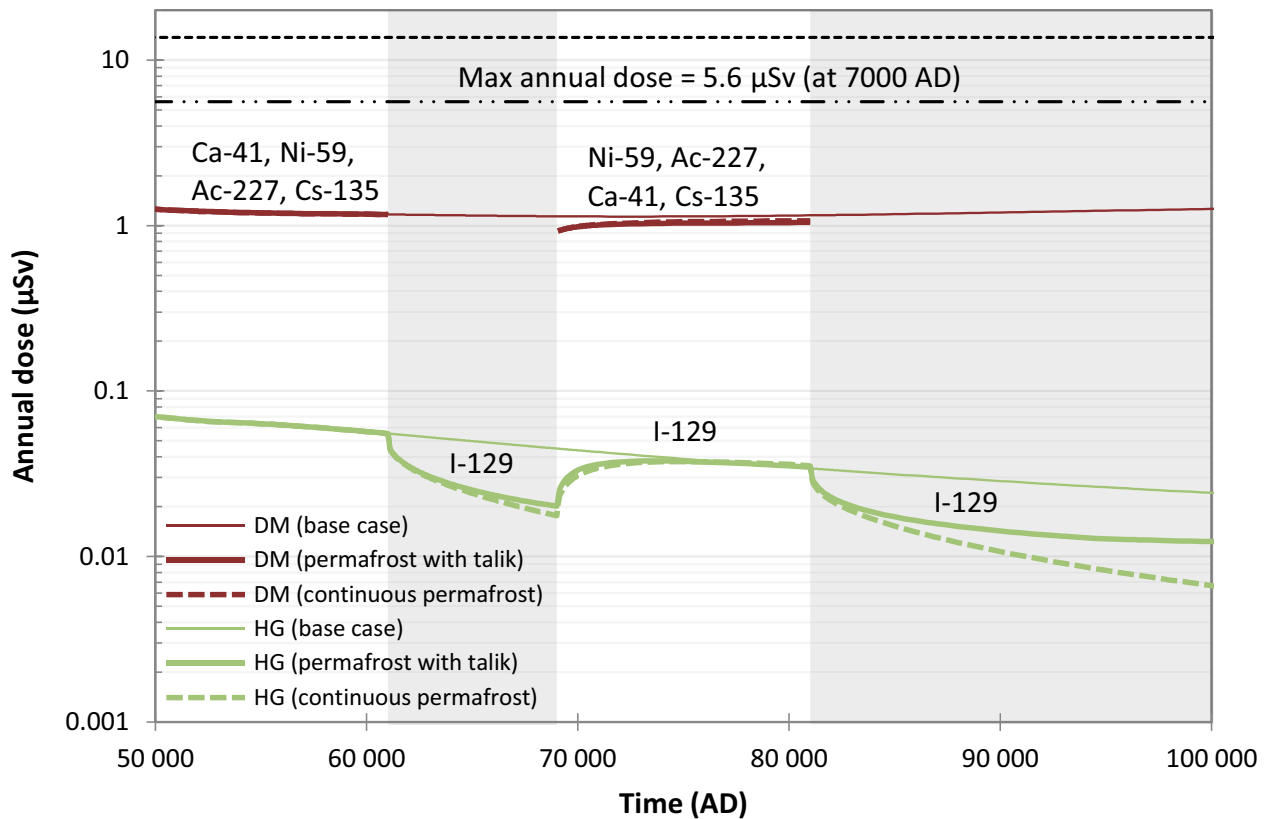


Figure 6-8. Annual doses (μSv) to the DM and HG groups in the continuous permafrost variant (dashed line) and permafrost with talik variant (solid line) of the cold climate calculation case. Doses from release through a talik into a lake in biosphere object 114 is below $0.001 \mu\text{Sv}$ and are therefore not shown. Base case doses are plotted for comparison as thin lines. During periglacial conditions (grey shading), when only hunting and gathering is possible (HG green line), doses drop by more than one order of magnitude compared with the base case doses (DM red line). The radionuclides contributing most to the doses to DM and HG groups are indicated in the plot. The maximum annual dose during the assessment period (same as the base case) is indicated by the black dashed-dotted line. The annual dose corresponding to the regulatory risk criterion ($14 \mu\text{Sv}$) is indicated by the black dashed line.

6.3.7 Summary and conclusions

The *continuous permafrost* and *permafrost with talik* variants of the *cold climate calculation case* cover a wide range of possible periglacial conditions that could influence radionuclide releases, transport, accumulation and exposure of humans. In the *continuous permafrost* variant, the near-field and geosphere releases cease during periglacial periods and, in the *permafrost with talik* variant, they are redirected through a discharge talik to either a mire (object 157_1) or a lake (object 114) ecosystem.

The main result, for both variants, is that doses during periglacial periods are at least one order of magnitude lower than in the *base case* at the corresponding time and at least two orders of magnitude lower than the maximum dose in the *base case* that occurs around 7000 AD (Section 5.7). The main reason is that the HG group face the only possible exposure pathways during this time and this results in lower doses than DM group. Despite the different transport pathways between the *continuous permafrost* and the *permafrost with talik* variants during periglacial periods, the doses are relatively similar. The reason is that exposure in both variants is dominated by radionuclides accumulated in object 157_2 during the temperate periods *prior to* the periglacial periods. The dose contribution from radionuclides released through the talik to object 157_1 is limited until the end of the second periglacial period. Furthermore, accumulation of decay products in the near-field and the geosphere in the *continuous permafrost* variant does not result in doses that exceed the dose in the *base case* during the post-periglacial temperate period.

7 Calculation cases in the less probable scenarios

7.1 Introduction

This chapter presents the calculation cases in the less probable scenarios. The aim of the less probable scenarios is to evaluate uncertainties related to alternative evolutions of the repository and its environs, or variations in the specified initial state or external conditions, that are not evaluated within the framework of the main scenario (Chapter 5 and 6). The reasoning underpinning the selection and detailed descriptions of the scenarios are presented in the **Post-closure safety report**, Chapter 8. Four less probable scenarios are selected for detailed examination:

- *Glaciation scenario* (Section 7.2).
- *High concentrations of complexing agents scenario* (Section 7.3).
- *Alternative concrete evolution scenario* (Section 7.4).
- *Earthquake scenario* (Section 7.5).

Each scenario is evaluated in one calculation case. The resulting releases and doses from the calculation cases are compared with the *base case* with regards to contributions from different waste vaults and radionuclides. The calculation cases in the less probable scenarios are analysed with probabilistic calculations in the same way as the calculation cases in the main scenario, with the exception of the *earthquake calculation case*. In this calculation case, many simulations are performed since the calculations are repeated for an earthquake occurring every 100 years throughout the assessment period. A full probabilistic approach would not be feasible considering the available computational capacity. Instead, a combination of a deterministic simulation approach using best estimate values and a probabilistic approach using random samples based on parameter PDFs is applied in the *earthquake calculation case*.

7.2 Glaciation calculation case

7.2.1 General description

The *glaciation calculation case* is selected to evaluate doses to humans from the *glaciation scenario* (**Post-closure safety report**, Section 8.3). Both this calculation case and the *cold climate calculation case* in the main scenario (Section 6.3) represent colder-than-present climate conditions due to substantial reductions in anthropogenic greenhouse-gas emissions and/or removal of atmospheric CO₂ by technological measures. In the *cold climate calculation case*, these developments result in two periods of periglacial conditions at Forsmark within the latter half of the assessment period (Section 6.3). In the *glaciation calculation case*, atmospheric CO₂ is projected to have decreased sufficiently within the first 50 000 years such that ice sheets start to grow in the Northern Hemisphere in response to the summer insolation minimum around 56 000 AD. This results in the development of colder climate conditions at Forsmark, including two periods of glacial conditions after 50 000 years. The likelihood of such development is assessed to be considerably lower than a development of periglacial conditions such as in the *cold climate calculation case* (**Climate report**, Section 4.4). Radiological consequences of a glaciation are of particular interest during post-glacial temperate conditions when the land around the repository can be fully exploited by human activities again.

7.2.2 External conditions

The development of external conditions in the *glaciation calculation case* is described by the glaciation climate case (**Climate report**, Section 5.3.1) and is summarised in Figure 7-1 and Table 7-1. The initial shoreline development is the same as in the *base case*. As discussed in Section 6.3.2, this is reasonable for a future development towards a colder climate. As a result, external conditions in the *glaciation calculation case* are the same as in the *base case* up until the onset of the first period of periglacial conditions at 56 600 AD. The development of external conditions for the remainder of the assessment period is summarised in the following subsections. A more detailed description of the glaciation climate case, representing the external conditions in this calculation case, is given in the **Climate report**, Section 5.3.1.

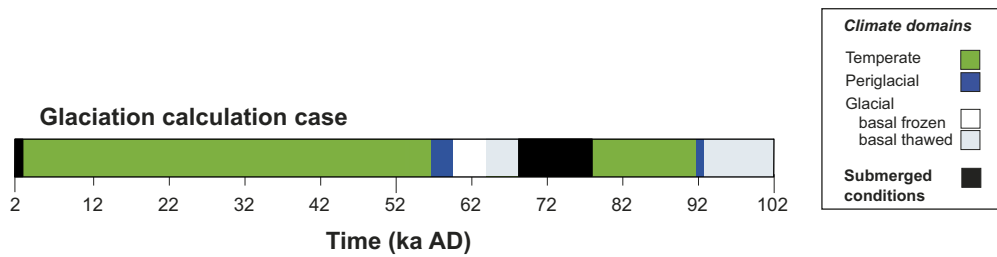


Figure 7-1. Succession of climate domains in the glaciation calculation case.

Table 7-1. Summary of the glaciation calculation case, including conditions in the repository and its environs during periods of different climate domains.

Time period	Duration (years)	Climate domain above repository	Thermal conditions at all repository depths	Repository barrier integrity	Repository and geosphere redox conditions	Geosphere groundwater flow ^a	Biosphere discharge area
2000–56 600 AD	54 600	Temperate	<i>base case</i>	<i>base case</i>	Reducing	<i>base case</i>	<i>base case</i>
Periglacial conditions 56 600–59 600 AD	3 000	Periglacial	Frozen bedrock	<i>base case</i>	Reducing	No flow	Cold climate (<i>continuous permafrost</i>)
Ice-sheet advance 59 600–63 900 AD	4 300	Glacial	Frozen bedrock	No barriers	Reducing	No flow	No recipient/no exposure
Peak glaciation 63 900–66 200 AD	2 300	Glacial	Thawed bedrock	No barriers	Oxidising	<i>base case</i> 9000 AD ^b	Deep sea basin
Ice-sheet retreat 66 200–68 150 AD	1 950	Glacial	Thawed bedrock	No barriers	Oxidising	Linear interpolation to 3 × <i>base case</i> 9000 AD ^b	Deep sea basin
Transition from glacial to submerged conditions 68 150–68 200 AD	50	Glacial	Thawed bedrock	No barriers	Oxidising	Linear interpolation to <i>base case</i> 2000 AD ^c	Deep sea basin
Submerged conditions 68 200–76 900 AD	8 700	Temperate, submerged conditions	Thawed bedrock	No barriers	Reducing	<i>base case</i> 2000 AD ^c	Historic reconstruction. <i>base case</i> 2000 AD
Transition from submerged to terrestrial conditions 76 900–77 900 AD	1 000	Temperate, submerged conditions	Thawed bedrock	No barriers	Reducing	<i>base case</i> 2000–3000 AD	<i>base case</i> 2000–3000 AD
Terrestrial conditions 77 900–91 800 AD	13 900	Temperate	Thawed bedrock	No barriers	Reducing	<i>base case</i> 3000–16 900 AD	<i>base case</i> 3000–16 900 AD
Periglacial conditions 91 800–92 800 AD	1 000	Periglacial	Frozen bedrock	No barriers	Reducing	No flow	Cold climate (<i>continuous permafrost</i>)
Ice-sheet advance 92 800–102 000 AD	9 200	Glacial	Thawed bedrock	No barriers	Oxidising	<i>base case</i> 9000 AD ^b	Shallow sea basin

^a The geosphere groundwater flow is based on the *base case* flow, scaled by a time-dependent factor. The repository groundwater flow is based on the *base case* and a “no barriers” flow case (Abarca et al. 2020) also used for the *no hydraulic barriers in the repository* calculation case (Section 8.3.3). The same scaling factor as for the geosphere groundwater flow is also applied for the near-field flow.

^b “*base case* 9000 AD” is taken as a representative for the flow under fully terrestrial temperate conditions.

^c “*base case* 2000 AD” corresponds to the flow under fully submerged temperate conditions.

Development of permafrost and frozen ground

Permafrost and frozen ground develop during periglacial conditions, but may, or may not prevail beneath an ice sheet during glacial conditions. For an ice sheet to advance over a region, below-freezing annual average air temperatures are required for some time prior to the arrival of the ice sheet (**Climate report**, Section 3.2.3). Thus, the landscape at Forsmark is considered to be dominated by periglacial conditions prior to the ice-sheet migration (Table 7-1). The duration of these periods is estimated based on modelling of the future climate at Forsmark (Lord et al. 2019), as further described in the **Climate report**, Section 5.3.1. In order not to underestimate the duration of the temperate period following the first glaciation at the site, pessimistic assumptions are employed to ensure that the second period of periglacial conditions was kept as short as possible (**Climate report**, Section 5.3.1).

Following the methodology adopted for the *cold climate calculation case* (Section 6.3), transitional periods of permafrost growth and decay are also neglected in this calculation case. Thus, the transition between frozen and unfrozen conditions deeper in the bedrock is assumed to occur simultaneously with the freezing and thawing at the surface, respectively. In this calculation case, it is further assumed that the frozen depth always exceeds the depth of the repository. The case of a shallower permafrost development, including the presence of taliks in the landscape, is analysed in the *cold climate calculation case* (Section 6.3).

Periods of glacial conditions

The timing and duration of the glacial periods, including the thermal conditions (frozen/unfrozen) beneath the ice sheet, are adopted from the Weichselian glacial cycle climate case in the SR-PSU (SKB TR-13-05, Section 4.4). The same glacial conditions were also used in the reference glacial cycle climate case in SR-Site (SKB TR-10-49, Section 4.5). These climate cases represent a projection into the future of conditions reconstructed for the last 120 000 years. Although changes in insolation over the next 100 000 years will be considerably different from those during the past 120 000 years, periods of glacial conditions in the climate cases coincide reasonably well with the timing of anticipated future periods of colder climate conditions and ice-sheet growth in the Northern Hemisphere (**Climate report**, Sections 3.4.5 and 4.4).

In accordance with the SR-PSU Weichselian glacial cycle climate case, the 100 000-year long assessment period encompasses two glacial periods at Forsmark. The first glacial period begins at 59 600 AD, a few thousand years after the summer insolation minimum at 56 000 AD, and the second glacial period begins at 92 800 AD (Figure 7-1 and Table 7-1). Further, frozen conditions beneath the ice sheet are considered to persist during the initial 4 300 years of the first glacial period. During the remaining time of the first glacial period (also 4 300 years), as well as the entire second glacial period, thawed conditions are considered at repository depth as well as at the surface (Table 7-1).

The inclusion of a second glaciation in this safety assessment conforms to the general understanding of climate and ice-sheet dynamics of the past ~800 000 years and is supported by contemporary projections of the future climate (**Climate report**, Sections 3.4.5 and 5.3.1).

Post-glacial submerged and temperate-terrestrial conditions

After the first glaciation, the Forsmark site is assumed to be submerged beneath the Baltic Sea for almost 10 000 years (Figure 7-1 and Table 7-1). The duration of this period is adopted from the SR-PSU Weichselian glacial cycle climate case (SKB TR-13-05, Section 4.4). The shoreline development during the last 1 000 years of this post-glacial submerged period and the subsequent terrestrial period of temperate conditions is assumed to follow the initial development of the *base case* (Table 7-1).

In order not to underestimate the radiological consequences of a glaciation, the period of temperate-terrestrial conditions after the first glacial period is assigned a relatively long duration of 13 900 years. Together with the preceding submerged period, this results in almost 24 000 years of uninterrupted temperate conditions after the first glaciation in this calculation case. Such a long sequence of temperate conditions embedded within a glacial cycle is considered to be pessimistic as it is neither supported by geological data from the last glacial (the Weichselian) nor by modelling (see further the **Climate report**, Section 5.3.1).

7.2.3 Handling in the near-field model

The handling in the near-field models is identical to the *base case* up until the onset of the first period of periglacial conditions at 56 600 AD. For the remainder of the assessment period, the sorption due to changes in redox and hydrological conditions is adjusted in the near-field with respect to the *base case*. The changes are summarised in Table 7-1 and described in the following.

Hydrology

The structural integrity of the engineered barriers cannot be expected to remain intact after a glaciation. However, at the time of the first ice-sheet advance over the site (59 600 AD), the concrete barriers are already completely degraded in the *base case* (**Post-closure safety report**, Section 7.4.2). This calculation case further pessimistically assumes that also the bentonite will become completely degraded due to the glaciation (**Post-closure safety report**, Chapter 8). Thus, the hydraulic conductivity of the bentonite in the silo is considered to be 10^{-3} m s^{-1} (as opposed to the *base case* where the conductivity given by Equation 5-1 is applied during the whole assessment period) from the first ice-sheet advance over the site until the end of the assessment period. Furthermore, the hydraulic resistance of the plugs is pessimistically neglected after the ice-sheet advance.

The influence of the changes described above on the hydrology was examined in the “no barriers” flow case by Abarca et al. (2020). It was concluded that groundwater flow through the waste increased for all waste vaults in comparison to a case with intact concrete and bentonite barriers. The most affected vault by far is the silo, for which the groundwater flow is increased by almost three orders of magnitude in the “no barriers” case with respect to the case with intact barriers (Abarca et al. 2020).

During periods of frozen conditions at repository depth, near-field groundwater flow and diffusion are considered insignificant and therefore set to zero. This concerns the periods of periglacial conditions that prevail prior to ice-sheet advance at the site as well as during the first 4 300 years of the first glaciation, i.e. between 59 600 AD and 63 900 AD. From the onset of thawed conditions beneath the ice sheet at 63 900 AD until the end of the first glacial period at 68 200 AD, the near-field groundwater flow will increase, being determined by the gradient of the ice-sheet surface, as described in the simulations of Vidstrand et al. (2013, 2014b). When the gradient of the ice-sheet surface is low over the repository site, i.e. when the ice-sheet margin is located far from Forsmark, the groundwater flow is comparable to that during temperate terrestrial conditions (Figure 9 in Vidstrand et al. 2014b). Around this time, i.e. at 68 200 AD, the groundwater flow in the repository is therefore assigned to be identical to the “no barriers” flow under temperate terrestrial conditions (Figure 7-2).

When the ice sheet retreats, its southward margin gradually propagates closer to the repository site, at which point the slope of the ice sheet becomes steeper. In the ice sheet used for this calculation case, which is assumed to be the same as reconstructed for the last glacial cycle (Section 7.2.2), the slope of the ice-sheet surface begins to steepen during approximately the last 2 000 years of the first glacial period (**Climate report**, Appendix E). In the radionuclide transport calculations, groundwater flow rates increase linearly to a maximum value between 66 200 and 68 150 AD and the maximum is achieved when the ice-sheet margin is located above the repository. This maximum change is derived from the simulations of Vidstrand et al. (2013), where the maximum increase of the groundwater flow during ice-sheet retreat varies in the range 3 to 20 times the magnitude simulated for present-day conditions. In order not to overestimate the amount of radionuclides that are transported out of the repository during the glacial period (when dose consequences are expected to be marginal), the lower value (3 times the “no barriers” flow) is selected as the maximum flow during ice-sheet retreat (Table 7-1 and Figure 7-2).

After the ice sheet has retreated from the site, the ice-free bedrock is isostatically depressed and thus the site is submerged beneath the Baltic Sea. Based on typical propagation rates of ice-sheet retreat from the last glacial cycle, the transition between glacial and submerged conditions at the Forsmark site is estimated to take approximately 50 years (**Climate report**, Table F-1). Thus, the transition from high to low groundwater flow is selected to occur during the last 50 years of the glacial period, i.e. between 68 150 AD and 68 200 AD (Table 7-1). During this short period, flow is reduced to “no barriers” flow under fully submerged conditions (i.e. conditions are assumed to be the same as at 2000 AD). This flow is then kept constant for 8 700 years of the post-glacial submerged period. For the remaining 1 000 years of the submerged period, as well as for the subsequent 13 900-year long period with temperate terrestrial conditions, the “no barriers” flow between 2000 AD and 16 900 AD is applied.

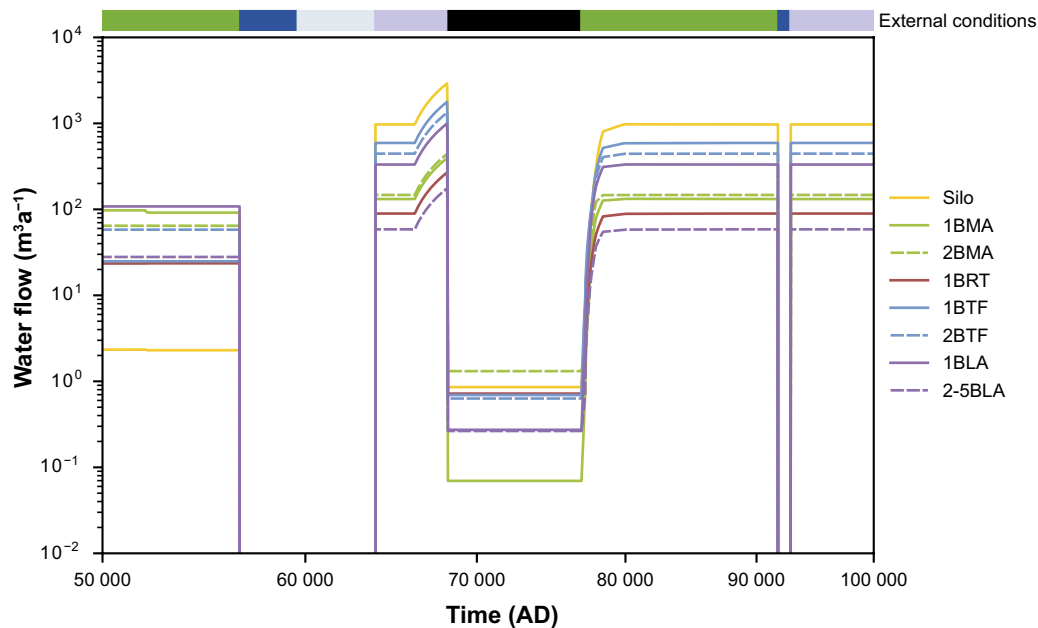


Figure 7-2. Groundwater flow rates through the vaults in the glaciation calculation case. Note that the time on the horizontal axis starts at 50 000 AD and that the flow for 2–5BLA is the average for these four vaults. The coloured bar in the upper part of the figure shows the evolution of external conditions (see Figure 7-1 and Table 7-1).

The second glacial period prevails beyond the assessment period of 100 000 years (Section 7.2.2). Thus, a potential increase in groundwater flow due to the retreat of this ice sheet is not considered in the modelling. For this glaciation, thawed conditions also prevail beneath the ice sheet at the time of its advance over the site, thus giving the possibility of increased groundwater flow around this time. However, even if thawed conditions are present in a layer of the bedrock close to the surface around this time, it is conceivable that the conditions in the remaining part of the bedrock will remain mostly frozen due to the preceding periglacial conditions. Thus, as opposed to the first glaciation at the site, the second glacial period is not expected to have a large influence on the groundwater flow within the assessment period, and the flow rate is chosen to be identical to the “no barriers” flow under temperate terrestrial conditions.

Sorption

The vault-specific concrete chemical degradation development in the *glaciation calculation case* is the same as in the *base case* (Section 5.3). This is a cautious choice since the degradation rate is expected to slow down or halt during periods of frozen repository conditions. Hence, this calculation case does not affect the sorbents. Sorption is instead affected in terms of the properties of the sorbates, particularly in terms of altered speciation of some radionuclides in response to altered redox conditions, see below.

Glacial meltwater is oxygen rich; Auqué et al. (2013, Tables 5-1 to 5-3) propose a redox potential E_h of +400 mV for glacial groundwater and around –225 mV for non-glacial groundwater. The combination of abundant meltwater supply and high water-pressures caused by the ice sheet may cause injection of glacial meltwater to greater depths than oxygen-rich waters would penetrate under non-glacial conditions. In addition, the consumption of oxygen close to the surface may be limited due to the lack of organic matter and microbiological activity (**Climate report**, Section 2.3).

During the periods with sub-glacial meltwater production (between 63 900 and 68 200 AD and between 92 800–102 000 AD), it is therefore cautiously assumed that oxygen-rich water penetrates from the surface to the repository, resulting in oxidising conditions in the repository and its environs. After the first glacial period, the surface groundwater becomes reducing again which in itself is sufficient to provide reducing conditions in the repository, even without any remaining reducing materials such

as metallic steel. Owing to the relatively slow vertical groundwater flow, the occurrence of oxidising conditions at repository depth would be somewhat delayed from that of the surface. However, a similar delay is expected when the surface groundwater production goes back from oxidising to reducing conditions as the ice sheet retreats from the site. Hence, the duration associated with oxidising conditions at repository depth is expected to be similar to that of the surface groundwater. For simplicity, oxidising conditions are considered to prevail at repository depth simultaneously with the meltwater production at the surface (Table 7-1).

Several redox-sensitive radionuclides are expected to change oxidation state during oxidising conditions in the near-field. This affects the speciation and consequently the sorption coefficients on bentonite and cement of Np, Pa, Pu, Se and Tc as discussed in Chapter 8 in the **Data report** and summarised in Table 7-2. For uranium, a recent study (Bruno et al. 2018) indicates that U(VI) is not reduced under cementitious, SFR-like conditions and this oxidation state is thus considered to prevail during both reducing and oxidising conditions. Of the five affected elements, four show weaker sorption during oxidising conditions. Only selenium, which is non-sorbing during reducing conditions, has a higher sorption coefficient during oxidising conditions, albeit still quite low (Table 7-2).

Plutonium can exist in various oxidation states in the solid phase and in solution, as explained in the Radionuclide speciation subsection in **Post-closure safety report**, Section 6.2.8. In the PSAR, K_d values for Pu(VI) are applied during oxidising conditions as this oxidation state is expected to be most prevalent.

Table 7-2. Oxidation state and sorption coefficients K_d on bentonite and on hydrated cement paste (HCP) in degradation states I–IIIb during reducing and oxidising conditions for affected radionuclides (Data report, Chapter 7).

Oxidation state	Bentonite	HCP			
Reducing	K_d (m ³ /kg)	K_d I–IIIb (m ³ /kg)			
Np(IV)	63	1 × 10 ²			
Pa(IV)	3	1 × 10 ²			
Pu(IV)	63	1 × 10 ²			
Se(–II)	0	0			
Tc(IV)	63	3			
Oxidising	K_d (m ³ /kg)	K_d I (m ³ /kg)	K_d II (m ³ /kg)	K_d IIIa (m ³ /kg)	K_d IIIb (m ³ /kg)
Np(V)	2 × 10 ^{–2}	1 × 10 ^{–1}	1 × 10 ^{–1}	1 × 10 ^{–1}	1 × 10 ^{–1}
Pa(V)	3	1 × 10 ¹	1 × 10 ¹	1 × 10 ¹	1 × 10 ¹
Pu(VI)	3	2	3 × 10 ¹	3 × 10 ¹	3 × 10 ¹
Se(VI)	0	3 × 10 ^{–3}	3 × 10 ^{–3}	3 × 10 ^{–3}	0
Tc(VII) ²¹	0	1 × 10 ^{–3}	1 × 10 ^{–3}	1 × 10 ^{–3}	1 × 10 ^{–3}

As a result of the altered speciation of these radionuclides under oxidising conditions, their interactions with complexing agents are expected to change in terms of moving to a different sorption reduction factor (SRF) group, where each SRF group has a certain sensitivity to complexing agents (Keith-Roach et al. 2021). Thus, the vault-specific SRF are altered upon changed redox conditions for Np, Pu and Tc, whereas Pa and Se remain in the same SRF group (Table 7-3).

²¹ During this work a preliminary version of the **Data report** was used. In that version the K_d value for Tc(VII) for cement paste, in degradation state IIIb, was set to 1 × 10^{–3}. In the current version this value has been changed to zero. However, this change has no significant impact on the safety assessment.

Table 7-3. Sorption reduction factor (SRF) groups and oxidation state of radionuclides affected by oxidising conditions.

SRF Group	Reducing conditions	Oxidising conditions	Modelled isotopes
1	-	Np(V)	Np-237
2	-	-	-
3	Np(IV), Pa(IV), Tc(IV)	Pa(V)	Pa-231
4	Pu(IV)	-	-
5	-	Pu(VI)	Pu-238, Pu-239, Pu-240, Pu-241, Pu-242
Other	Se(-II)	Se(VI), Tc(VII)	Se-79, Tc-99

7.2.4 Handling in the geosphere model

Groundwater flow is modified according to Table 7-1. The temporal evolution of the groundwater flow is described and justified in Section 7.2.3.

The handling of sorption coefficients during glacial conditions in the geosphere follows that of the near-field (Section 7.2.3). To this end, K_d -values from the *base case* are used for the entire assessment period, apart for the periods of sub-glacial meltwater production from 63 900 AD to 68 200 AD and from 92 800 AD to the 102 000 AD. During these periods, the groundwater is considered to be oxygen-rich (Table 7-2), resulting in a modified K_d for several elements (Table 7-4), and Chapter 8 of the **Data report**). For some of these elements, the altered redox conditions cause a change in oxidation state, whereas others change their K_d in response to the altered water composition and mineralogy without changing redox state, as shown by thermodynamic speciation calculations (Chapter 8 of the **Data report** and Crawford 2013).

Table 7-4. Sorption coefficients (K_d) in the geosphere of the elements that are affected by the oxidising conditions between 63 900 AD and 68 200 AD and from 92 800 AD to the end of the assessment period in the glaciation calculation case. The K_d for all other elements are the same as in the *base case* (Table 5-18).

Reducing	K_d (m ³ /kg), reducing	Oxidising	K_d (m ³ /kg), oxidising
Ba(II)	1.0×10^{-3}	Ba(II)	1.1×10^{-1}
Cs(I)	8.8×10^{-4}	Cs(I)	7.7×10^{-3}
Np(IV)	5.3×10^{-2}	Np(V)	4.1×10^{-4}
Ra(II)	1.0×10^{-3}	Ra(II)	1.1×10^{-1}
Sr(II)	1.5×10^{-5}	Sr(II)	1.6×10^{-3}
Tc(IV)	5.3×10^{-2}	Tc(VII)	0
U(IV)	5.3×10^{-2}	U(VI)	1.1×10^{-4}

Up until the onset of the first periglacial period, handling in the geosphere is identical to that of the *base case*. When the bedrock is considered to be frozen (56 600–63 900 AD and 91 800–92 800 AD), no groundwater flow is considered to occur and therefore no radionuclides are transported to the biosphere, i.e. the handling is the same as in the *continuous permafrost* variant of the *cold climate calculation case* (Section 6.3).

During the latter part of the first glacial period (63 900–68 200 AD), when the bedrock is thawed, radionuclides are transported from the geosphere to a single sea basin (see Section 7.2.5). Due to the isostatic depression of the bedrock at SFR, a substantial water depth is considered in this part of the Baltic Sea during the first glaciation. A similar approach is used during the second glaciation (92 800–102 000 AD). In contrast to the first glaciation, the second glaciation is characterised by thawed bedrock conditions already when the ice-sheet margin advances to the site. At this time, however, the isostatic depression of the bedrock is moderate, resulting in a significantly lower relative sea level compared to the time of thawed bedrock conditions during the first glacial period. Thus, during the second glaciation, radionuclides from the geosphere are assumed to be released to a shallow sea basin instead of deep-sea basin (see further Section 7.2.5).

During the post-glacial submerged period and the following temperate period (68 200–92 800 AD) radionuclides are transported through the geosphere to biosphere object 157_2, as in the *base case*.

7.2.5 Handling in the biosphere model

The handling in the biosphere model is identical to the *base case* up until the onset of the first period of periglacial conditions at 56 600 AD. For the remaining time of the assessment period, the development of the biosphere follows the sequence of external conditions (Table 7-1). Thus, the development of object 157_2 includes periods of permafrost conditions and a development from open-sea conditions to fully terrestrial conditions (see below). When the ice sheet retreats, most unconsolidated regolith layers on top of the till are expected to be removed by glacial erosion. Moreover, the remaining activity in the till is likely to be flushed out by large quantities of surface water when the ice retreats over the area above the repositories. Thus, the radionuclide inventories in all regolith layers of object 157_2 are assumed to be negligible at the start of the post-glacial submerged period. During glacial conditions, when the site is covered with ice and unfrozen conditions prevail beneath the ice sheet, radiological consequences are evaluated by releasing radionuclides to an open sea basin (see below).

Surface hydrology and ecosystem state

During periglacial periods, the handling of biosphere object 157_2 is identical to that of the periglacial periods in the *continuous permafrost* variant of the *cold climate calculation case*. In short, the lower part of the mire in object 157_2 will be permanently frozen, and the hydrology in the upper parts (i.e. the active layer) is modified according to permafrost conditions (Section 6.3.4).

When the bedrock is unfrozen during the first glacial period (59 600–63 900 AD), the historical sea basin of object 116 (dating to 10 500 before present) is used as open sea recipient. At this time of the development, the area of the basin is 1×10^7 m², the average water depth is 140 m, and the water exchange with outer sea basins is 3×10^{11} m³ a⁻¹ (corresponding to a turnover time of days; Grolander 2013). As the second glacial period is characterised by thawed bedrock conditions when the ice sheet advances over the site (Table 7-1), it is accompanied with a significantly lower relative sea level compared to the time of thawed bedrock conditions during the first glacial period (Section 7.2.4). Therefore, during the second glaciation, the same basin is used, but with a shallower water depth (corresponding to year 3000 AD). At this time of the development, the area of the basin is 7×10^6 m², the average water depth is 6 m, and the water exchange with outer sea basins is 3×10^9 m³ a⁻¹ (corresponding to a turnover time of days; Grolander 2013). For simplicity, these conditions are considered to be constant during the glacial periods and it is cautiously assumed that the geosphere release reaches the water directly, without passing through any seabed sediments. Since the historical accumulation in regolith is not accounted for in these calculations, it is not necessary to consider changes in regolith sorption coefficients due to oxidising conditions.

During the post-glacial period, biosphere object 157_2 develops from a deep-sea basin to a state corresponding to the present state and then the development follows that in the *base case*. The early post-glacial development of the object follows a historic reconstruction (Table C-5 in Grolander 2013). To get a period of 9 700 years that starts with submerged conditions and ends with the emergence of the object, historical data starting from 8 700 before present are used in the simulations. At the start of this time sequence, basin 157_2 is covered by more than 60 m of water. A matching description of water exchange between basin 157_2 and neighbouring basins is used for the period (Table D-5 in Grolander 2013). Groundwater flow rates for biosphere object 157_2 during the post-glacial submerged period are set to be identical to those of the marine period in the *base case*.

Calculations for secondary release

During ice-covered periods, most unconsolidated regolith layers on top of the till are expected to be removed by glacial erosion and the remaining regolith is assumed to be flushed by large quantities of surface water. Simplified calculations are used to evaluate potential effects of a secondary release of radionuclides from the biosphere due to these effects. In these calculations, the entire radionuclide inventory that has accumulated in object 157_2 during the temperate period (i.e. until 56 600 AD) is released, at a constant rate, into an open sea basin (see above) over a period of fifty years. The release period is set to the estimated time for the ice front to retreat across the area above the repository (Table 7-1) and equals the integration time for calculating annual doses to humans. As the time for

turnover is short (days) compared to the temporal resolution in the model (years), the water activity concentration is calculated from steady state conditions²². Doses to HGs are then calculated accounting for the primary exposure route, consumption of fish (see Saetre et al. 2013, Section 9.3).

Ecosystem parameters

The values of ecosystem parameters are adjusted during periglacial conditions as described in the *cold climate calculation case* (Section 6.3.4). That is, the concentration of stable CO₂ in the atmosphere and parameters on primary production and production of food foraged from terrestrial and aquatic ecosystems are altered to better reflect periglacial conditions.

Potentially exposed groups

During temperate conditions the potentially exposed groups are identical to those addressed in the *base case*. During periglacial and glacial periods HG is the only potentially exposed group. In the periglacial periods this is because cultivation is not possible due to permafrost (see Section 6.3.4). In the glacial period, the discharge area is covered by the sea, and catches from the postulated open sea basin provide the only source of food considered to contain radionuclides for the potentially exposed group (Saetre et al. 2013, Section 9.3).

7.2.6 Annual release from the near-field

No radionuclides are released from the repository during periods of periglacial conditions and the first period of ice-sheet advance. Many radionuclides, including e.g. the dose-dominating Mo-93 and C-14-org, have decayed considerably by the onset of the first glacial period. For other radionuclides, like Ca-41 and U-238, most of the activity has already been released during the temperate period (as they are to a large extent disposed in 1–5BLA). Thus, for these radionuclides, post-glacial releases are low and their maximum releases are not affected by the glaciation. In contrast, however, the near-field releases of long-lived radionuclides, such as I-129, Ni-59 and Pu-239, and decay products that accumulate during the frozen period (e.g. Ra-226 and Po-210), are significantly increased after the glaciation (Figure 7-3, upper panel). For some redox-sensitive radionuclides (e.g. Pu-239), part of the increased release is caused by a mobilisation (or decreased storage capacity) due to oxidising conditions.

An increased near-field release is particularly pronounced in the period of peak glaciation and ice-sheet retreat (Figure 7-3, upper panel). Due to the reduced function of the engineered barriers, mobile radionuclides are effectively flushed out of the repository when the bedrock thaws (visualised e.g. by a rapidly declining release of I-129 in the upper panel of Figure 7-3). For immobile/strongly sorbing radionuclides (e.g. Pu-239), only a tiny fraction of the inventory is accessible in porewater and consequently the changes in the release are much smaller. For all radionuclides, the release rates increase in the latter half of the glacial period due to the associated increase in the bedrock groundwater flow when the ice-sheet retreats over the repository (66 200–68 200 AD, see Table 7-1).

When the repository is submerged after the first glaciation, the radiotoxicity of near-field releases is significantly lower than in the *base case* (Figure 7-3, upper panel). This is because the bedrock groundwater flow is orders of magnitude lower than when the area above the repository is terrestrial (Figure 7-2). It can also be noted that the radiotoxicity of the near-field release is substantial after the submerged period, indicating that much of the activity of the contributing radionuclides remains in the repository despite the reduced function of the hydraulic barriers.

Of the above-mentioned radionuclides, the increased total release of Ni-59 is particularly significant as it dominates the activity release towards the end of the assessment period in the *base case* (Figure 5-42)²³ and contributes most to dose during that period (Figure 5-54). In this calculation case, the annual release of Ni-59 during the post-glacial temperate period increases by almost two orders of magnitude compared

²² At steady state, the water activity concentration simply equals the release rate (Bq a⁻¹) divided by the water exchange rate with outer basins (m³ a⁻¹)

²³ The near-field release of Po-210 is of little concern for transport to the surface, as this activity is lost through radioactive decay and geosphere release of Po-210 originates instead from ingrowth within the geosphere.

to the same time period in the *base case* (Figure 7-3, upper panel). The significantly increased release of Ni-59 during this period is primarily caused by the reduced function of the hydraulic barriers in the silo where most of Ni-59 inventory is disposed.

As in the first periglacial period, no radionuclides are released from the repository in the second periglacial period. During the second glacial period, Po-210, Pu-239, Ni-59 and Ra-226 contribute most to the released radiotoxicity from the near-field (Figure 7-3, upper panel).

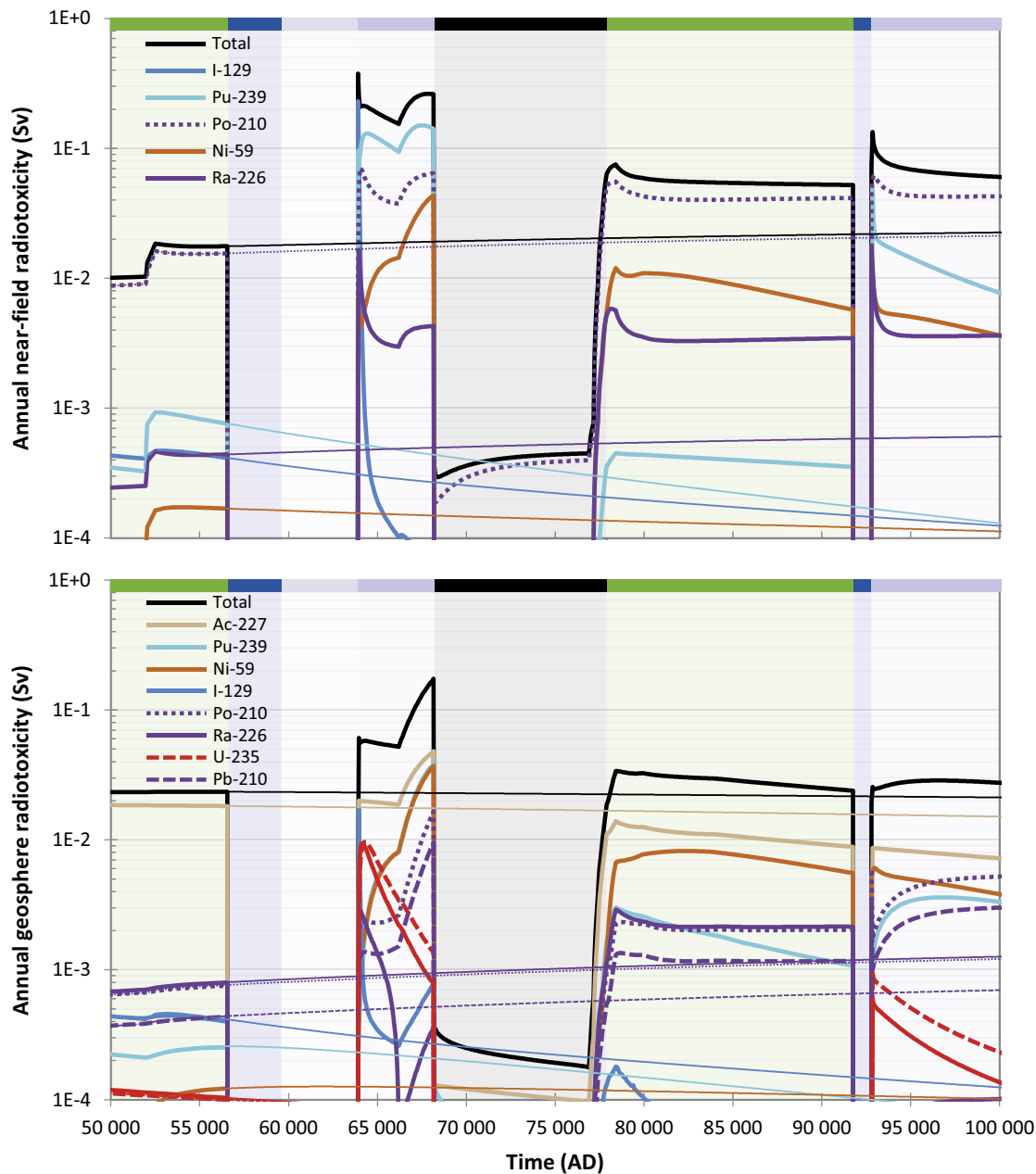


Figure 7-3. Annual radiotoxicity (Sv) released from the near-field (upper panel) and the geosphere (lower panel) from the entire SFR in the glaciation calculation case. Coloured lines represent the contribution from individual radionuclides and black lines are the total radiotoxicity. Thick lines illustrate results from the present case and thin lines are results from the base case. Coloured bars at the top of each panel with matching background shading represent the succession of climate domains in the glaciation calculation case (cf Figure 7-1 and Table 7-1). Note that the timescale is shown only for the second half of the assessment period and is presented on a linear scale.

7.2.7 Annual release from the geosphere

As in the *base case*, radionuclides with low sorption in the geosphere (e.g. Ni-59) typically have similar releases as from the near-field. However, for radionuclides that accumulate significantly in the geosphere and/or radionuclides that are primarily generated in the geosphere, the geosphere release may differ considerably from the near-field release. For example, while the near-field release of Pu-239 is relatively constant during the thawed glacial period, the activity in the geosphere is gradually building up, approaching a fifth of the near-field release levels towards the end of the period.

The geosphere releases of U-235 and U-238 during the first glacial period are virtually unaffected by the near-field releases at the time. This is because most of the uranium inventory (> 96 %) is stored in the BLA waste vaults and this activity is released to the geosphere within a few thousand years of the assessment period. Thus, the geosphere release is the result of a mobilisation of uranium that has accumulated in the geosphere during the initial temperate period. The mobilisation is caused by the oxidising conditions which lowers the geosphere's capacity for sorbing uranium as compared to reducing conditions (Table 7-4). The release of Ac-227 primarily originates from decay of U-235 and accumulation of the intermediate decay product Pa-231²⁴. Pa-231 is strongly sorbed in the geosphere and is not considered to be redox-sensitive. Therefore, the releases of its decay product, Ac-227, is relatively stable at peak glaciation, but increases with the higher groundwater flow as the ice sheet retreats (Figure 7-3, lower panel). Similarly, the releases of Ra-226, Pb-210 and Po-210 primarily originate from decay of U-238 and the accumulation of U-234 and Th-230 in the geosphere during the first temperate period.

In the post-glacial temperate period, the geosphere release of Ni-59 increases by almost two orders of magnitude as compared to the *base case* and the maximum release occurs around year 80 000 AD (Figure 7-3, lower panel). The cumulative geosphere release of Ni-59 up until this point is almost 20 times larger than in the *base case*. The release of Pu-239 during the post-glacial temperate period is also elevated by a factor of 20 with respect to the *base case*. Both increases are primarily caused by the elevated releases from the near-field (Section 7.2.6). The lower release of Ac-227 during the post-glacial temperate period than in the *base case* (Figure 7-3, lower panel) is explained by an increased export of Pa-231 from the geosphere after the first glaciation.

As during the first periglacial period, no radionuclides are released from the geosphere during the second periglacial period. Releases during the second glaciation are similar to those during the preceding temperate period, with the exception of radionuclides affected by the oxidising conditions. That is, the oxidising conditions serve to mobilise uranium isotopes, whereas Ra-226 is immobilised. The accumulation of Ra-226, in turn, leads to an increased release of its decay products.

7.2.8 Annual doses

During the first period of periglacial conditions, the doses are significantly lower than in the preceding temperate period (Figure 7-4). This is primarily because neither agriculture nor water extraction from a well are possible when permafrost prevails (i.e. HG is the most exposed group). The lack of release to the biosphere in combination with leaching of radionuclides from the upper soil layers also contribute to the decrease in the dose during this period. The radionuclide that contributes most to the dose at this time is I-129, which is consistent with the results for the *continuous permafrost* variant of the *cold climate calculation case* (Section 6.3.6).

When the ice sheet covers the site and the bedrock is frozen, there is no transport to, or exposure in, surface ecosystems. When the bedrock is unfrozen during the glacial period, the geosphere release is discharged to an open sea basin. Although the annual releases from the geosphere are significantly higher than during corresponding temperate period in the *base case*, the doses are very low during this period (Figure 7-4). This is mainly due to the high rate of water exchange in the sea basin; the geosphere release is mixed with 3×10^{11} m³ of water per year. Po-210 contributes by far the most to the dose during this period, in spite of higher radiotoxic releases of other radionuclides (e.g. I-129, Pu-239, Ac-227 and Ni-59, lower panel in Figure 7-3). This is because Po-210 is highly bioavailable and is easily taken up by marine organisms which are then consumed by humans.

²⁴ Ac-227 has a short half-life (~22 years) and therefore is in secular equilibrium with Pa-231.

The potential effect of flushing out radionuclides from object 157_2 is also evaluated by a release to an open sea basin over 50 years, when the ice-sheet margin retreats from the area above the repository (Table 7-1). The main contributing radionuclide is Po-210, reflecting the combined effect of relatively large regolith inventories and a high bioavailability in marine fish (Figure 7-4). The relatively fast release of radionuclides that have accumulated in the regolith for more than 50 000 years results in significantly higher doses than a geosphere release during glacial or submerged conditions. However, the doses are still very low during this short period and are more than two orders of magnitude below the dose corresponding to the regulatory risk criterion.

During the post-glacial submerged period, both near-field and geosphere releases are two to three orders of magnitude lower than during the temperate period. This, in combination with relatively high dilution in the developing sea basins and a low productivity, results in very low annual doses ($< 1 \times 10^{-5} \mu\text{Sv}$).

During the first ~5 000 years of the post-glacial temperate-terrestrial period, the total dose is similar to that of the temperate period just prior to the onset of the periglacial period and just below the levels at the corresponding time in the *base case* (~1 μSv). However, during this period, exposure from extracting water from a drilled well causes the maximum dose, which is somewhat elevated as compared with the same group in the *base case* (~factor 2 at similar times). The exposure to individual radionuclides from consuming well water is proportional to the radiotoxicity of the geosphere release. Thus, it is Ac-227 and Ni-59 that contribute most to the dose during this time with some contribution from Pu-239, Ra-226 and its decay products (Figure 7-3, lower panel). The concentration of Ac-227 is, however, lower than in the *base case* and thus the elevated total dose from the well is primarily due to the elevated contributions of the other radionuclides.

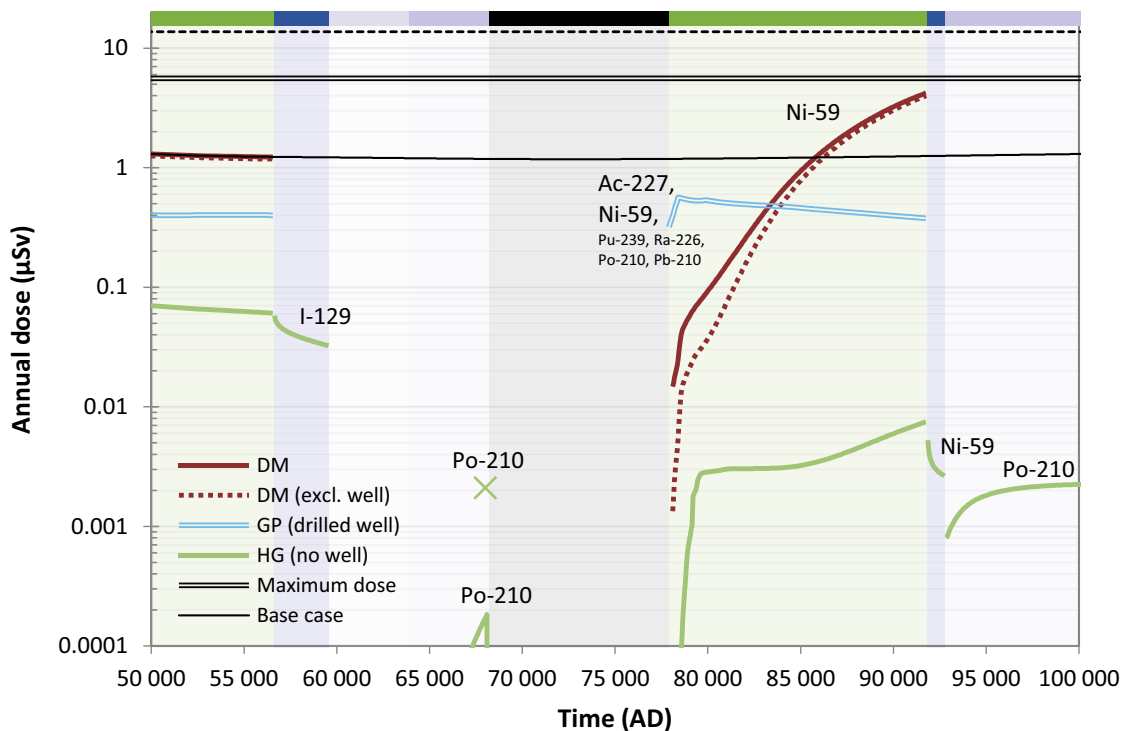


Figure 7-4. Annual doses (μSv) to the three most exposed groups in the glaciation calculation case. The potential annual dose (μSv) due to an outflow of radionuclides accumulated in object 157_2 as the ice-sheet margin retreats from the area, is marked with a green cross. Radionuclides contributing most to the total annual dose are indicated in the plot. The maximum annual dose (at ~7000 AD; same as in the base case) and the annual dose in the base case is shown with a double black line and a thin black line respectively. The annual dose corresponding to the regulatory risk criterion (14 μSv) is indicated by the black dashed line. Coloured bars at the top with matching background shading represent the succession of climate domains in the glaciation calculation case (cf Figure 7-1 and Table 7-1). Note that the timescale is shown only for the second half of the assessment period and is presented on a linear scale.

During the post-glacial temperate period, the geosphere release of Ni-59 is strongly elevated as compared with the *base case* (Section 7.2.7). Ni-59 sorbs strongly in the lower regolith and thus the transport to the glacial clay (and to regolith layers above it) is slow (see also Section 5.7.2). Due to the transport of Ni-59 from the lower regolith, draining and cultivating of the mire in object 157_2 gives the highest exposure after the initial 5 000 years of the post-glacial temperate period. From this time, the annual doses increase continuously and towards the end of the period the dose is $\sim 4 \mu\text{Sv}$. This is about 3 times higher than in the *base case* at this time (or later times) but is still lower than the maximum dose that occurs during the first temperate period.

During the second periglacial period, the doses are again reduced to very low levels when neither agriculture nor extraction of well water is possible and Ni-59 contributes most to the dose. Similarly, doses are also low during the second glacial period. As in the first glacial period, it is uptake of Po-210 in fish that causes the exposure. As the release is directed to a shallow rather than a deep-sea basin during this period, the doses are an order of magnitude higher than during the first glacial period, though the release of Po-210 is significantly reduced (Figure 7-3, lower panel).

7.2.9 Summary and conclusions

This calculation case evaluates radiological consequences of a glaciation above SFR within the assessment period. The underlying assumption is the same as in the *cold climate calculation case*, i.e. that the onset of the next glaciation in the Northern Hemisphere will occur in response to the next substantial minimum in summer insolation at 56 000 AD. However, in this calculation case, this development is assumed to result in the emergence of ice sheets and glacial conditions above the repository within the latter half of the assessment period.

At the time of the first ice-sheet advance over the area, the concrete barriers in the waste vaults are already completely degraded, as in the *base case*. In addition, a glaciation is considered to result in (i) a reduced hydraulic barrier function also for the bentonite, (ii) an altered sorption capacity for some radionuclides due to the intrusion of oxygen-rich glacial meltwater and (iii) elevated groundwater flow in the near-field and the geosphere in response to the ice-sheet retreat from the area. All these effects are considered in this calculation case.

Owing to the late arrival of ice sheets to the repository area, only the long-lived radionuclides and their potential decay products will be influenced by a glaciation. Doses resulting from a glaciation are highest during the subsequent period of temperate and terrestrial conditions when exposure to DM farmers in biosphere object 157_2 is possible. The duration of this period is pessimistically assigned to be relatively long (almost 14 000 years) considering it is embedded in a glacial cycle. Even under this pessimistic assumption, the maximum dose during this period remains below the dose maximum in the *base case*. Ni-59 is the radionuclide contributing most to the dose during this period. This is primarily caused by the reduced function of the hydraulic barriers in the silo induced by the overriding ice sheet. As a result, more than 30 % of the Ni-59 inventory is released from the near-field in this calculation case compared to only 2 % in the *base case*.

Since an increased oxygen content in the groundwater in this calculation case is caused by an intrusion of glacial meltwater, potential effects of oxidising conditions were only considered during periods of ice-sheet coverage over the area. During these periods, doses were found to be several orders of magnitude lower than during temperate conditions. Thus, it is concluded that glacially induced changes in redox conditions are of little relevance for the dose consequences.

Other potential effects of a glaciation on dose were also evaluated in this calculation case, including release of radionuclides accumulated in the regolith of object 157_2 up until the first ice-sheet retreat and exposure in a deep and shallow sea basin during periods of glacial conditions. These effects were, however, found to result in much lower doses than the doses resulting from exposure of Ni-59 during the post-glacial temperate period.

7.3 High concentrations of complexing agents calculation case

7.3.1 General description

The *high concentrations of complexing agents calculation case* is selected to evaluate doses to humans from the *high concentrations of complexing agents scenario* (**Post-closure safety report**, Section 8.4). The purpose of the scenario is to analyse uncertainties related to complexing agents and their potential impact on the safety function *sorb radionuclides* in the waste form, packaging and engineered barriers. The calculation case handles several sources of uncertainty and evaluates the effects of possible increases in the amounts of complexing agents and materials that degrade into complexing agents in the repository. These materials include water-reducing cement additives (superplasticisers), cellulose and paint hardeners. Further uncertainties arise from interactions between vaults, as well as possible yet undiscovered complexing agents in the waste, as expanded upon below. The effect of these uncertain complexing-agent concentrations is implemented in terms of an assumed additional tenfold reduction in sorption in this calculation case.

The first source of uncertainty relates to superplasticisers, a class of cement additives with potential for complexation. As discussed in the **Post-closure safety report**, Section 6.2.8, superplasticisers in structural concrete and their possible degradation products are expected to have a very small effect on radionuclide sorption. There is, however, a certain degree of uncertainty since the long timescales required for their degradation exceed the feasible timeframes for experiments. The sorption reductions in this calculation case are cautiously chosen to significantly exceed the expected effects of superplasticisers in SFR.

The second uncertainty relates to dissolved complexing agents that may potentially travel with the groundwater from 1BLA to 1BMA. This issue is discussed in the **Post-closure safety report**, Section 6.2.8, where several mitigating effects are mentioned: slow ISA formation, low ISA formation yield in 1BLA, Ca-ISA precipitation, concrete barriers in 1BMA and ISA sorption to cement. Disregarding these mitigating factors and pessimistically assuming completely degraded concrete barriers in 1BMA, it is judged that less than 10 % of the ISA formed in 1BLA could be transferred to 1BMA. This value is thus cautiously assumed in the following estimation of the ISA-transfer effect on 1BMA sorption.

If evenly divided between the 15 1BMA compartments, the amount of ISA would be about $337 \text{ tonnes} \times 10 \% / 15 = 2 \text{ tonnes}$ per compartment, corresponding to about 11 000 mol per compartment. For SRF Group 3 with the strongest ISA-concentration dependence (Table 4-1 in Keith-Roach et al. 2021), the pre-transfer best-estimate SRFs in 1BMA due to ISA range from SRF = 1 (compartments 1–3, 5–7, 12–15) to SRF = 36 in compartment 11 (Table 4-3 in Keith-Roach et al. 2021). Post transfer from 1BLA, the values are calculated to range from SRF = 5.8 (compartments 1 and 13–15 previously without any cellulose, assumed to have an average cement content), to SRF = 64 in compartment 11 with comparatively little cement, based on ISA concentrations calculated with consideration of its sorption isotherm on cement (van Loon et al. 1997). The cautiously estimated effect of interactions with 1BLA thus corresponds to SRF increases by factors of about 2–6 in 1BMA, which is lower than the tenfold SRF increase applied in this calculation case.

In the risk assessment, the *high concentrations of complexing agents scenario* is assigned a 10 % probability to occur and affects all vaults except 1–5BLA and 1BRT (**Post-closure safety report**, Section 8.4). While the probability in reality is higher that *some* complexing agents from 1BLA reach 1BMA, the expected amounts are substantially smaller than cautiously estimated above. Further, vault interactions are of significance only for 1BLA to 1BMA and the tenfold SRF increase in this calculation case is applied to many vaults. It is thus judged that the risk contribution of this scenario is cautiously estimated and that it is illustrative of the possible effects of vault interactions on 1BMA activity releases.

The third source of uncertainty that this calculation case is intended to cover, is possible complexing materials that reach the waste producers' waste streams but that have not yet been identified or accounted for in the SRF waste. Discoveries of such complexing-agent sources have occurred several times since SFR was commissioned and, when discovered, the new amounts are included in future assessments of complexing agents and of post-closure safety. Recent examples²⁵ were included in the latest complexing-agent assessment (Keith-Roach et al. 2021). Although it is difficult to assess the probability, timing and severity of possible yet undiscovered complexing agents, the sorption reductions resulting from earlier discoveries are generally smaller than those applied in this calculation case. Furthermore, the waste producers' understanding and avoidance of complexing agents have in recent years improved, so the SRFs applied in this calculation case are judged to be cautious with respect to this uncertainty.

The fourth and final source of uncertainty relates to polyamines from paints and their interaction with Ni(II) (**Post-closure safety report**, Section 6.2.8). The affinity of Ni(II) to the dominant complexing agents ISA and NTA is modest and Keith-Roach et al. (2021) place it in the SRF Group "Other" which comprises radionuclides that in the *base case* are considered unaffected by complexing agents (Section 5.3.1). However, due to its affinity to polyamines, the present calculation case applies the same tenfold SRF increase for Ni(II) as well, the only radionuclide from the SRF Group "Other" so treated.

7.3.2 Handling in the near-field models

In the near-field transport calculations, the SRF values for cement, bentonite and crushed rock in SRF Groups 1–5 are increased by a factor of 10 compared with the *base case*, including radionuclides whose *base case* SRF = 1 (see Section 5.3.1, Table 5-4). This tenfold increase is applied throughout the assessment period, regardless of whether ISA or NTA determines the *base case* SRF. As noted in Section 7.3.1, the Ni(II) SRF is also increased tenfold, while remaining radionuclides in SRF group "Other" are left unchanged at SRF = 1. The increased SRFs are applied to all waste vaults credited with the safety function *sorb radionuclides* and where complexing agents and/or cellulose are, or could be, disposed. As such, the waste vaults 1BRT and 1–5BLA are not affected in this calculation case.

Values for hydraulic conductivity and porosity of the cementitious materials (and bentonite in the silo), as well as the diffusivity of radionuclides, evolution of the pH and K_d values are identical to those applied in the *base case* (see Section 5.3.1, Table 5-4).

²⁵ Hedström S, Bultmark F, Sihm Kvenangen K, 2019. Konsekvensutredning – Komplexbildare i avfallstyper O.07 och F.17 och deras påverkan på säkerhet efter förslutning. SKBdoc 1877287 ver 3.0, Svensk Kärnbränslehantering AB. (In Swedish.) (Internal document.)

7.3.3 Annual release from the near-field

Release from the silo

The annual near-field silo releases are shown in Figure 7-5. Of the radionuclides with significant absolute releases, the one most affected by high concentrations of complexing agents is Ni-59, with a much earlier release onset and a maximum release increased by almost two orders of magnitude compared with the *base case*. This also leads to Ni-59 becoming release-dominant almost 20 000 years earlier than in the *base case*. The time of its maximum release is largely unchanged, however, occurring around 30 000 years after closure. Ni-59 also retains its position as the radionuclide with the second highest maximum release, behind C-14-org which is considered unaffected by complexing agents.

Pu-239 and Pu-240 show the greatest increases in annual release in this calculation case, but their absolute release is still small. Other radionuclides from SRF Groups 3 and 4 are also affected in terms of higher releases throughout, including Zr-93 and Tc-99.

Release from 1BMA

The 1BMA releases are shown in Figure 7-6, with Ni being most affected in this calculation case. Ni-59 shows an earlier release onset and the release is significantly greater throughout most of the assessment period. The maximum Ni-59 release becomes almost as large as the maximum C-14-org release. In addition, Ni-63 shows a significantly greater and earlier release in this case. As with the silo, radionuclides from SRF Groups 3 and 4 are also affected, of which Tc-99 contributes most to the 1BMA releases.

Release from 2BMA

The calculated 2BMA releases are shown in Figure 7-7. Generally, the same radionuclides as in 1BMA are affected here, with similar responses in their release curves.

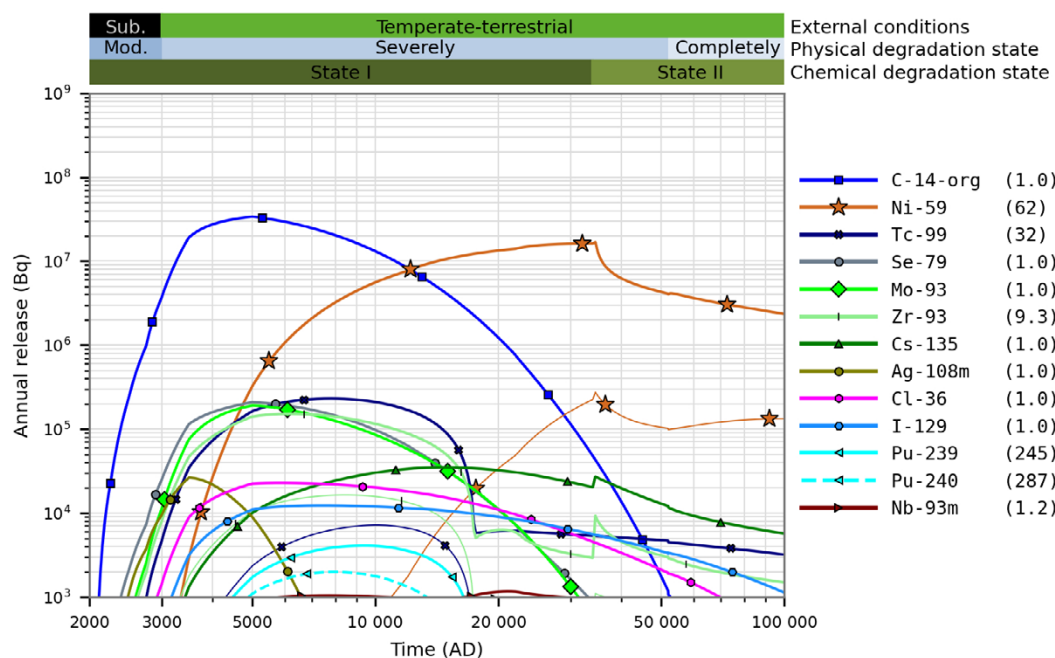


Figure 7-5. Annual activity releases (Bq) from the silo in the high concentrations of complexing agents calculation case (thick lines) and the base case (thin lines). The ratio between the maximum releases in the present calculation case and the base case are shown in parentheses in the key. Note that, for radionuclides not affected by complexing agents (SRF Group "Others" excluding Ni), the two cases cannot be distinguished in the plot. Coloured horizontal bars (top) as in Figure 5-3.

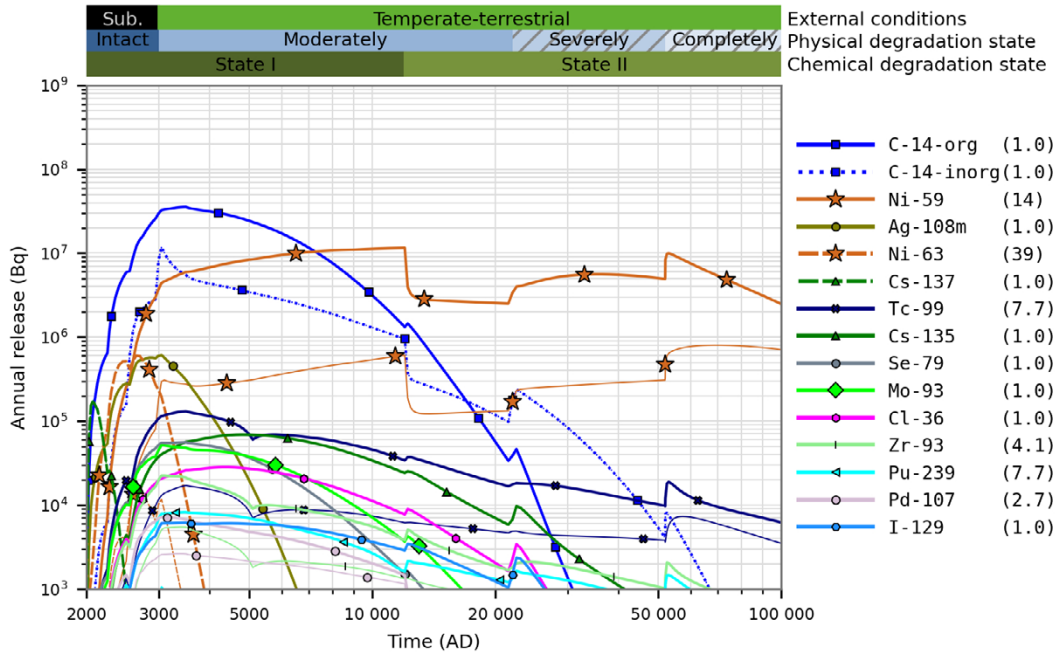


Figure 7-6. Annual activity releases (Bq) from 1BMA in the high concentrations of complexing agents calculation case (thick lines) and the base case (thin lines). Only the 15 radionuclides with the highest annual release are shown. The ratio between the maximum releases in the present calculation case and the base case are shown in parentheses in the key. Note that, for radionuclides not affected by complexing agents (SRF Group “Others” excluding Ni), the two cases cannot be distinguished in the plot. Coloured horizontal bars (top) as in Figure 5-9.

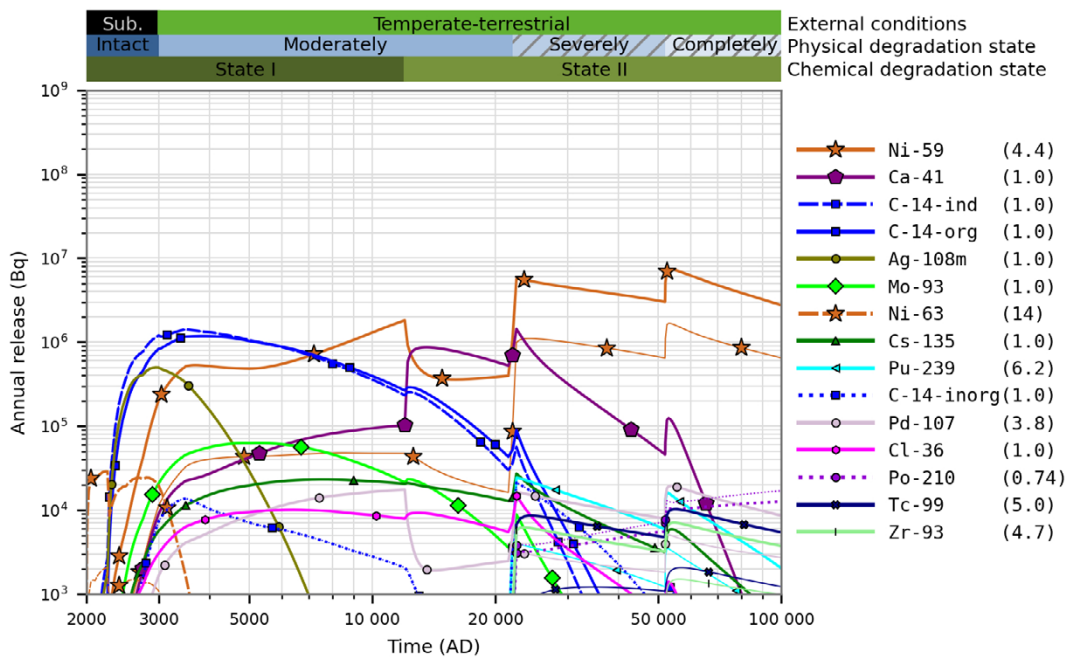


Figure 7-7. Annual activity releases (Bq) from 2BMA in the high concentrations of complexing agents calculation case (thick lines) and the base case (thin lines). Only the 15 radionuclides with the highest annual release are shown. The ratio between the maximum releases in the present calculation case and the base case are shown in parentheses in the key. Note that, for radionuclides not affected by complexing agents (SRF Group “Others” excluding Ni), the two cases cannot be distinguished in the plot. Coloured horizontal bars (top) as in Figure 5-9.

Release from 1-2BTF

In 1-2BTF (Figure 7-8 and Figure 7-9), the two isotopes of Ni are, once again, the radionuclides most affected in the *high concentrations of complexing agents calculation case*. They show an increase in annual release during early times when the release is highest, but Ni-59 falls below the *base case* release towards the end, due to depletion of its inventory. The increase is smaller in these vaults, particularly in 2BTF. The reason for the smaller effect of complexing agents in 1-2BTF compared to 1-2BMA and silo can be attributed to the lower retention capabilities of the engineered barriers with less capacity for sorption and thus potential for sorption reduction. In 2BTF, the two isotopes of Pu are also somewhat affected. It can be noted that the effect on Tc-99 in 2BTF is small because its SRF is high already in the *base case*, making it effectively non-sorbing in both cases.

Release from SFR

Figure 7-10 shows total releases from the near-field of SFR in the *high concentrations of complexing agents calculation case* compared with the *base case*. The changes in release in the present case are dominated by Ni-59 from all vaults affected by complexing agents (i.e. all vaults excluding 1BRT and 1-5BLA). A minor increase can also be seen in the Ni-63 and Tc-99 releases.

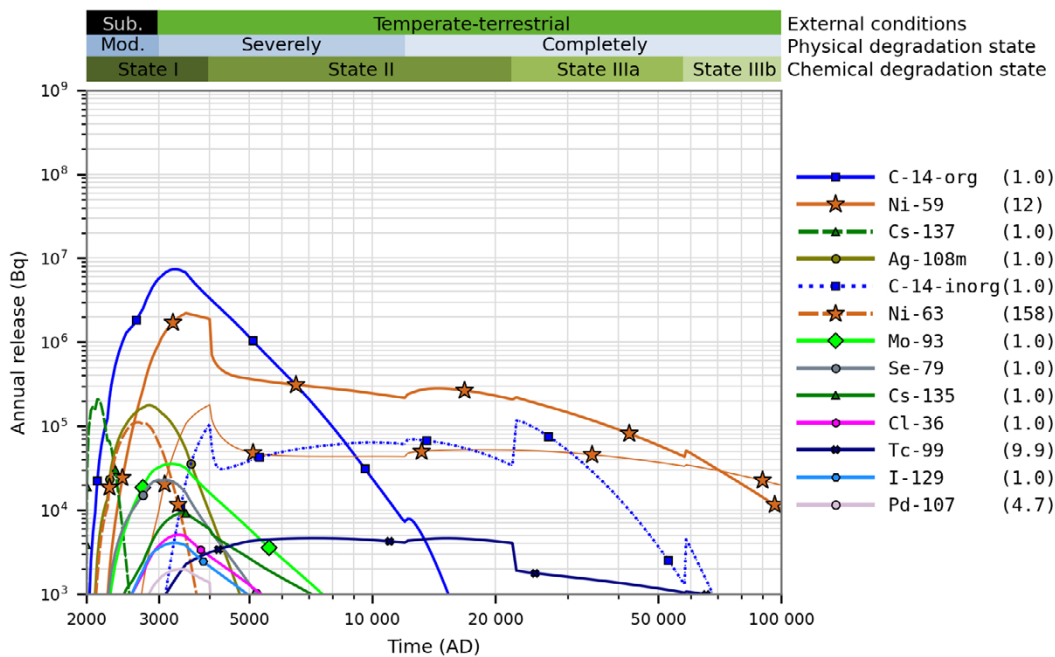


Figure 7-8. Annual activity releases (Bq) from 1BTF in the high concentrations of complexing agents calculation case (thick lines) and the base case (thin lines). The ratio between the maximum releases in the present calculation case and the base case are shown in parentheses in the key. Note that, for radionuclides not affected by complexing agents (SRF Group “Others” excluding Ni), the two cases cannot be distinguished in the plot. Coloured horizontal bars (top) as in Figure 5-3.

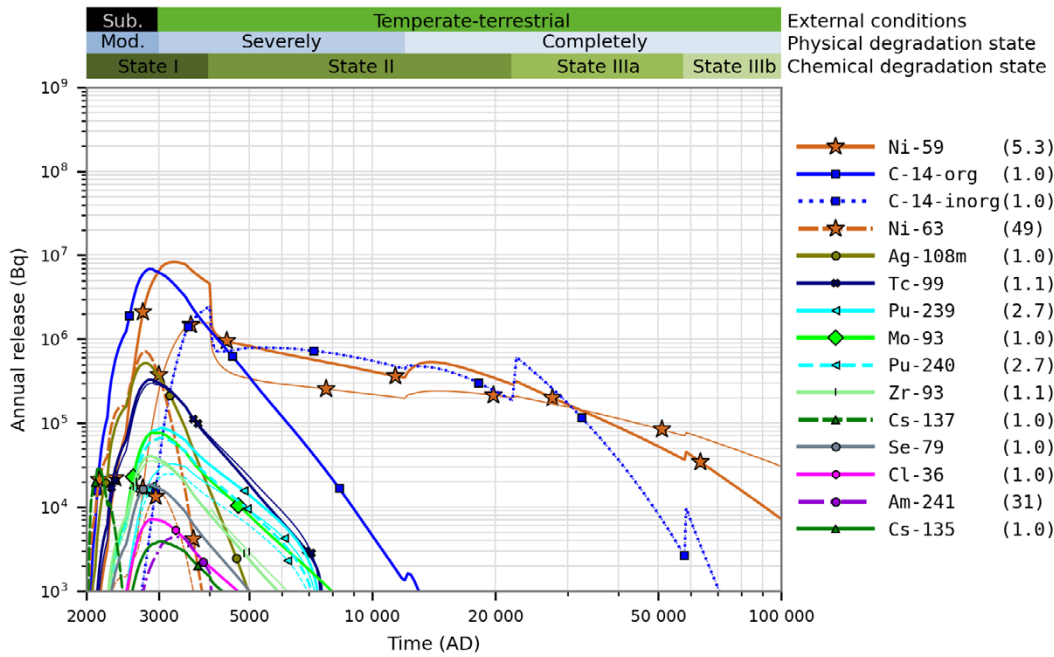


Figure 7-9. Annual activity releases (Bq) from 2BTF in the high concentrations of complexing agents calculation case (thick lines) and the base case (thin lines). Only the 15 radionuclides with the highest annual release are shown. The ratio between the maximum releases in the present calculation case and the base case are shown in parentheses in the key. Note that, for radionuclides not affected by complexing agents (SRF Group “Others” excluding Ni), the two cases cannot be distinguished in the plot. Coloured horizontal bars (top) as in Figure 5-3.

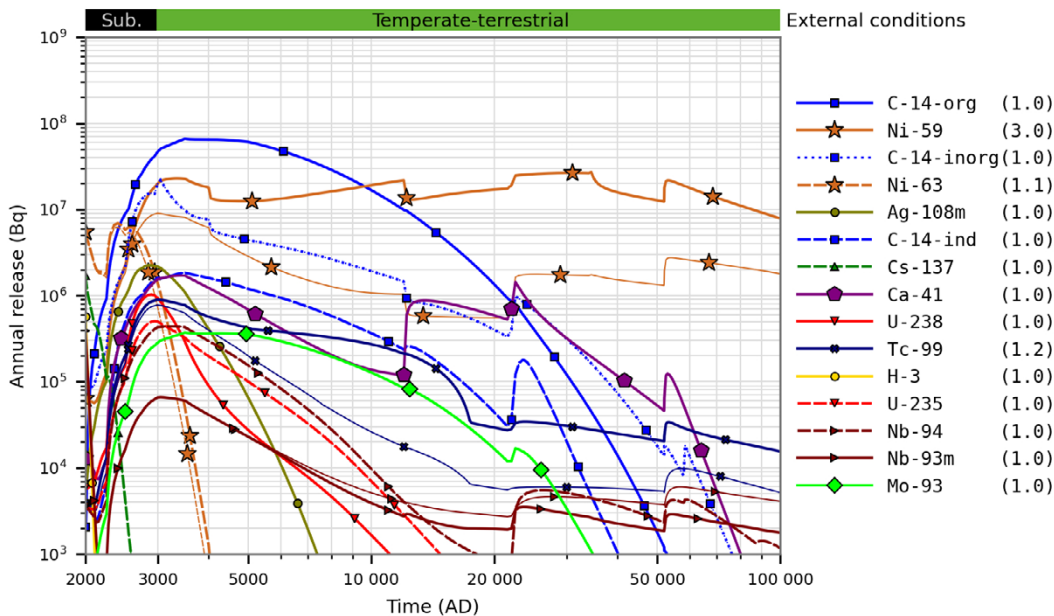


Figure 7-10. Annual activity releases (Bq) from the entire SFR in the high concentrations of complexing agents calculation case (thick lines) and the base case (thin lines). Only the 15 radionuclides with the highest annual release are shown. The ratio between the maximum releases in the present calculation case and the base case are shown in parentheses in the key. Note that, for radionuclides not affected by complexing agents (SRF Group “Others” excluding Ni), the two cases cannot be distinguished in the plot. Coloured horizontal bars (top) as in Figure 5-3.

Of the radionuclides with appreciable near-field releases, Ni-59 is evidently the one that is most affected by this calculation case. The difference in Ni-59 release between the two cases is modest initially, but increases to about an order of magnitude from ca 7000 AD. A break-down per vault of the Ni-59 near-field release is presented in Figure 7-11. The present case gives significantly increased releases from all vaults, apart from 1-5BLA where sorption is not credited and complexing agents thus have no effect and 1BRT where no complexing agents are foreseen. The silo shows the largest increase compared with the *base case*, followed by 1BMA.

7.3.4 Handling in the geosphere model

The handling of the geosphere is identical to the *base case*.

When radionuclide-organic complexes enter the geosphere where the complexing-agent concentration is smaller than in the repository, a large fraction of complexes is expected to dissociate, reaching new equilibrium concentrations as determined by their stability constants. As noted in the **Post-closure safety report**, Section 6.2.6, complexing agents from the repository may reduce the sorption of radionuclides in the geosphere. This effect has not been quantified but is judged to be smaller than in the near-field, since sorption is much stronger to cement than to bedrock for all radionuclides significantly affected in this calculation case: Ni(II), Pu(IV), Pd(II), Tc(IV), Zr(IV) (see Tables 7-6 and 8-8 in the **Data report**). Thus, the SRFs in the geosphere are, for simplicity, not altered in this calculation case.

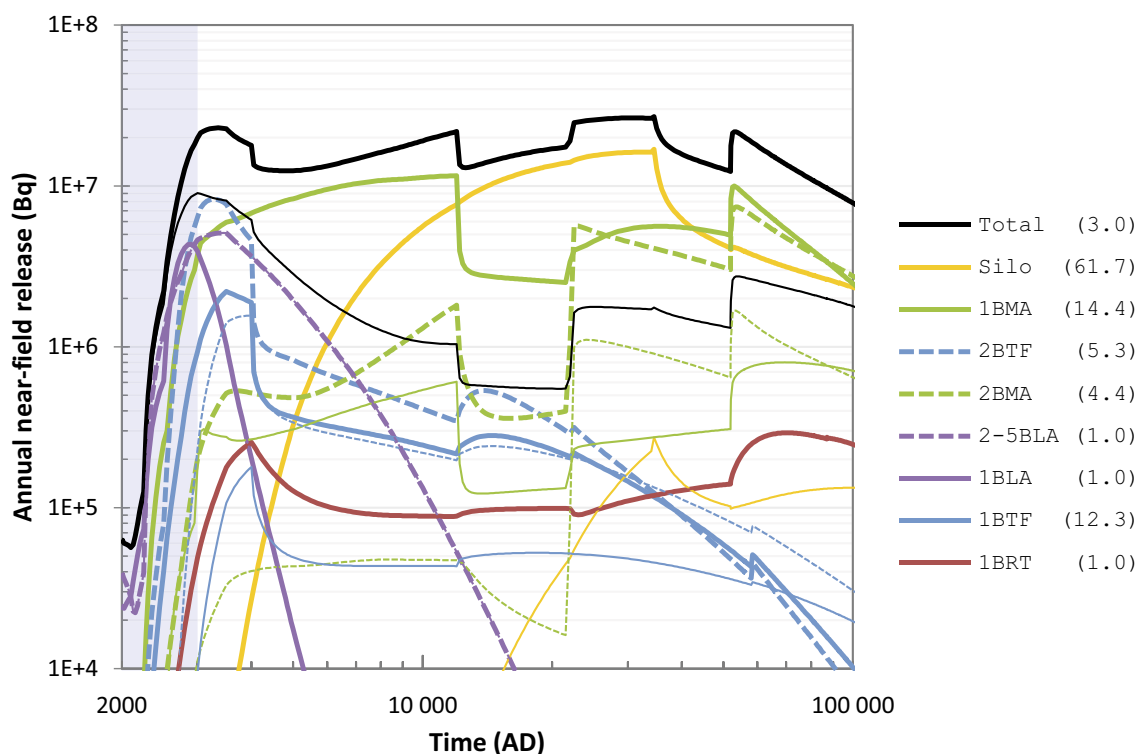


Figure 7-11. Annual activity releases of Ni-59 (Bq) from the entire SFR (black lines) including vault-specific contributions (coloured lines) in the high concentrations of complexing agents calculation case (thick lines) and the base case (thin lines). The ratio between the maximum releases in the present calculation case and the base case are shown in parentheses in the key. The submerged period is illustrated by the blue shading.

7.3.5 Handling in the biosphere model

The handling of the biosphere is identical to the *base case*.

7.3.6 Annual doses

The annual dose from the total release from SFR is presented in Figure 7-12. The dose maximum is unchanged in the present case, since it is dominated by two complexation-independent radionuclides: primarily Mo-93 and secondarily C-14-org. In addition, the significantly increased Ni-59 near-field release (Figure 7-11) results in a second dose peak around 80 000 AD that is only marginally lower than the Mo-93-dominated peak around 7000 AD.

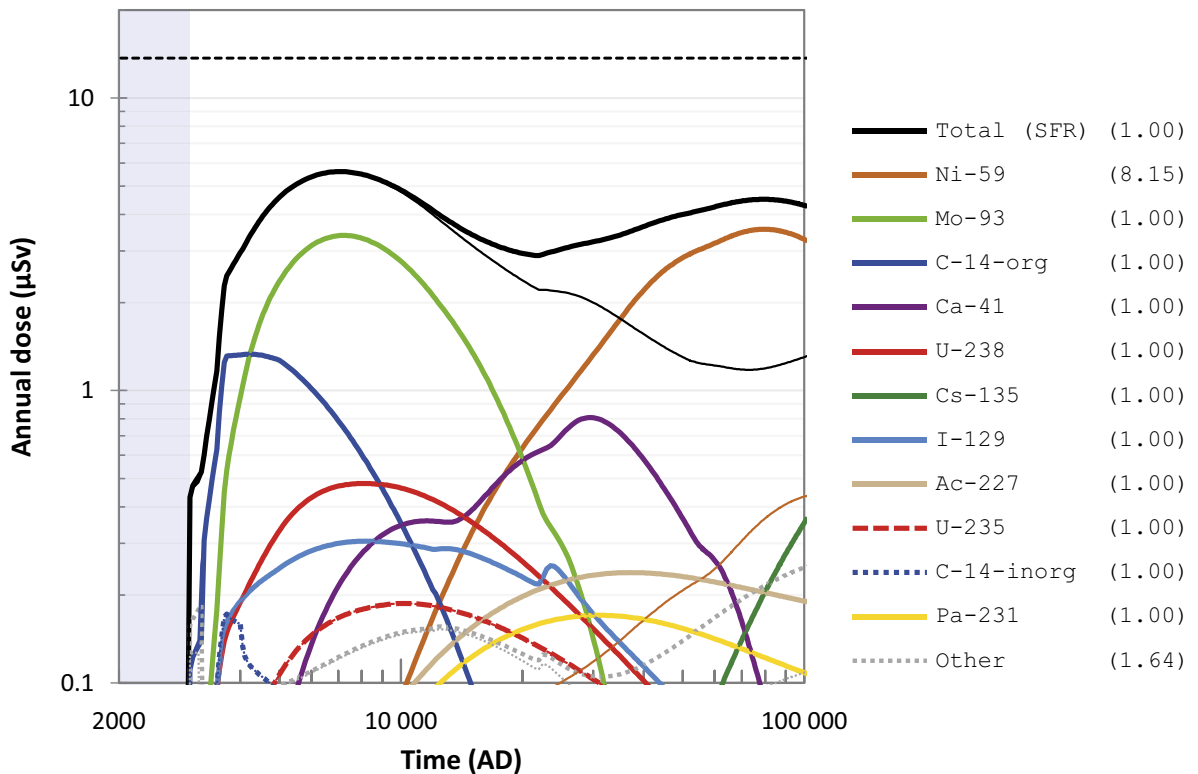


Figure 7-12. Annual dose (μSv) to the most exposed group (black line), including radionuclide specific contributions (coloured lines), in the high concentrations of complexing agents calculation case (thick lines) and the base case (thin lines). The combined contribution from radionuclides not shown is indicated by the grey dotted line. The ratio between the maximum doses in the present calculation case and the base case are shown in parentheses in the key. The annual dose corresponding to the regulatory risk criterion ($14 \mu\text{Sv}$) is indicated by the black dashed line and the submerged period is illustrated by the blue shading.

7.3.7 Summary and conclusions

Figure 7-13 gives an illustrative summary of the performance of the near-field in the case of *high concentrations of complexing agents*, for radionuclides substantially affected by this case. The vertical bars show the fraction of the initial activity that is released from the near-field over the assessment period, i.e. the accumulated release divided by the initial activity, in the present case and in the *base case*. Of the radionuclides included in the figure, the long-lived fission products Pd-107, Zr-93 and Tc-99 show the largest accumulated-release fractions in both cases, being significantly greater in the present case. For all other radionuclides, less than 15 % of their initial activity is ever released, in both calculation cases.

The quotient of accumulated release in the present case and the *base case* (black circles in Figure 7-13) show that Ni-59 is the radionuclide most affected by *high concentrations of complexing agents* in terms of accumulated release, with an almost tenfold greater accumulated release in the present case. Zr-93, Pd-107, Tc-99 and Pu-242 also show several times greater accumulated release in the present case. Conversely, Ni-63 is much less affected in this sense because the total release of Ni-63 is dominated by release from 1–5BLA which are unaffected by this calculation case. The figure also shows the corresponding quotient between cases for maximum annual release (yellow circles).

In terms of maximum dose, the presence of additional complexing agents has a minor effect because the dose-dominating radionuclides of the *base case* (Mo-93 and C-14) are not affected by complexing agents. However, the release and dose from Ni-59 increases significantly, dominating the dose after 20000 AD.

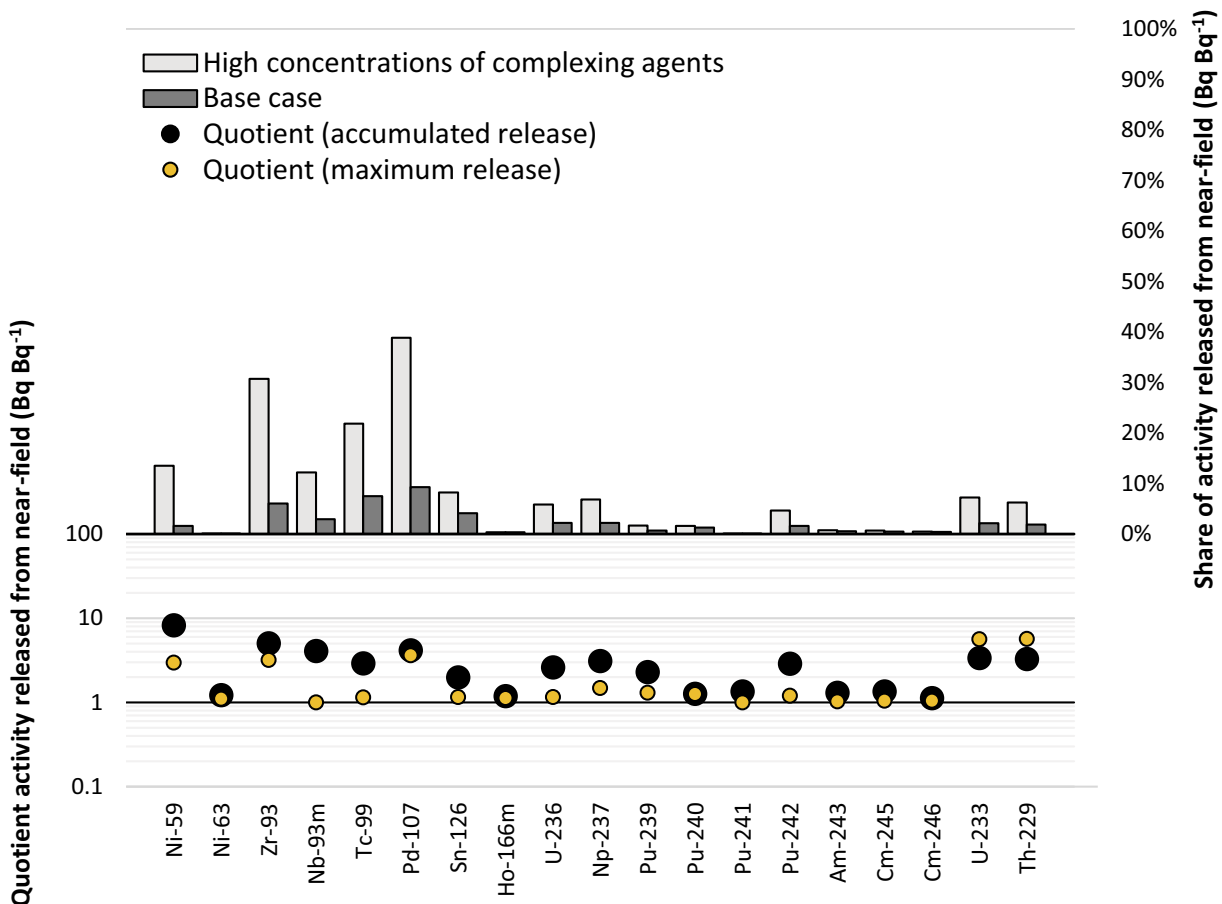


Figure 7-13. Summary of activity releases from the near-field in the high concentrations of complexing agents calculation case. Upper panel: fraction of each radionuclide's initial activity that has been released at the end of the assessment period, for the present case and the base case. Lower panel: quotient between cases for accumulated and maximum release, respectively.

7.4 Alternative concrete evolution calculation case

7.4.1 General description

The *alternative concrete evolution calculation case* is selected to evaluate doses to humans from the *alternative concrete evolution scenario* (**Post-closure safety report**, Section 8.4). The purpose of this calculation case is to assess the effects of uncertainties in the initial state and evolution of the structural concrete and concrete waste packaging. To this end, effects of earlier physical degradation than in the *base case* are evaluated. For the vaults that do not have any credited engineered barriers (1–5 BLA), the handling in the near-field model is identical to the *base case*.

Hydrology and concrete physical properties

In this calculation case, earlier physical degradation of the structural concrete leads to the following differences to the *base case*:

- The hydraulic conductivity of the structural concrete (and thus water flow through the waste) is higher initially and increases earlier than in the *base case*.
- The diffusivities of radionuclides in the structural concrete increases earlier than in the *base case* and the uncertainties in diffusivities are considered to be larger.
- The porosity of the structural concrete increases earlier than in the *base case*.
- Earlier occurrence of cracks due to the earlier concrete degradation.

Cement sorption properties and corrosion-controlled release

Physical and chemical degradation processes are treated separately within this and all other calculation cases, without direct coupling. As in the *base case* (Section 5.3.1), sorption is omitted during advective transport through cracked concrete barriers. Altered chemical degradation of cement is not addressed in this calculation case; the same mineralogical development as in the *base case* is used. The repository sensitivity to chemical-degradation uncertainties is instead illustrated by the sorption-related calculation cases *high concentrations of complexing agents* (Section 7.3), *no sorption in the repository* (Section 8.3), as well as the *oxidising conditions* calculation case (Section 8.6) which affect both sorption and corrosion rates.

Chemical cement degradation also affects the pH development over time which, in turn, affects metal corrosion rates. However, the pH dependence of the steel corrosion rates in 1BRT is pessimistically chosen for the *base case* (Section 5.3.5). The possible enhancement of chemical degradation, due to increased flow via physical degradation, is hereby judged to be smaller or similar to the margin of caution of the assumed pH development.

The handling of complexing agents is cautious here because the outflow of complexing agents is assumed to proceed in the same low rate as in the *base case* based on the water fluxes in intact concrete. Thus, the same chemical conditions as in the *base case* are used in all vaults.

7.4.2 Silo calculations and results

Handling in the silo model

Hydrology

At the start of the simulated period, the structural concrete is assumed to already be in a severely degraded state. However, the transition to a completely degraded state occurs at the same time as in the *base case*, because the concrete structure is protected by the bentonite (**Post-closure safety report**, Chapter 8).

Concrete structures and bentonite

Over time, as the concrete degrades, the diffusion-available porosity of the concrete structure and radionuclide diffusivities increase. The time-dependent hydraulic conductivity and porosity of the cementitious materials in the silo, as well as the effective diffusivity of radionuclides are shown in Table 7-5 and Table 7-6.

The handling of the properties of bentonite is identical to the *base case*.

Table 7-5. Development of silo cementitious material properties: hydraulic conductivity K and porosity ϕ in the alternative concrete evolution calculation case.

Time (AD)	Concrete structure		Concrete lid*	Mould walls	Waste domain**	Grout
	K (m s ⁻¹)	ϕ (-)	K (m s ⁻¹)	ϕ (-)	K (m s ⁻¹)	ϕ (-)
2000–2100	1.0×10^{-5}	0.11	1.0×10^{-5}	0.11	1.0×10^{-6}	0.3
2100–12 000	1.0×10^{-5}	0.14	1.0×10^{-5}	0.11	1.0×10^{-6}	0.3
12 000–22 000	1.0×10^{-5}	0.18	1.0×10^{-5}	0.11	1.0×10^{-6}	0.3
22 000–52 000	1.0×10^{-5}	0.30	1.0×10^{-5}	0.11	1.0×10^{-6}	0.3
52 000–102 000	1.0×10^{-3}	0.30	1.0×10^{-3}	0.11	1.0×10^{-6}	0.3

* Silo lid with gas evacuation channels (vertical direction).

** Interior of the shafts i.e. grout and waste.

Table 7-6. Development of the effective diffusivity D_e of radionuclides in the cementitious materials of the silo, given by log-triangular distributions with best estimate (BE), minimum and maximum values in the concrete structure and as single (deterministic) values in the mould walls and surrounding grout in the alternative concrete evolution calculation case.

Time (AD)	Concrete structure			Concrete moulds	Grout
	D_e BE (m ² s ⁻¹)	D_e Min (m ² s ⁻¹)	D_e Max (m ² s ⁻¹)	D_e (m ² s ⁻¹)	D_e (m ² s ⁻¹)
2000–2100	3.5×10^{-12}	3.5×10^{-12}	1.0×10^{-11}	3.5×10^{-12}	3.5×10^{-10}
2100–3000	5.0×10^{-12}	3.5×10^{-12}	1.0×10^{-11}	2.0×10^{-11}	3.5×10^{-10}
3000–12 000	5.0×10^{-12}	5.0×10^{-12}	5.0×10^{-11}	5.0×10^{-11}	5.0×10^{-10}
12 000–22 000	1.0×10^{-11}	7.0×10^{-12}	1.0×10^{-10}	1.0×10^{-10}	1.0×10^{-9}
22 000–102 000	1.0×10^{-10}	2.0×10^{-11}	3.0×10^{-10}	1.0×10^{-10}	1.0×10^{-9}

Transport through the near-field

Groundwater flow through the silo (Figure 7-14) is determined by the hydraulic conductivity of the bottom sand-bentonite layer rather than the concrete barrier. Thus, the earlier increase in concrete conductivity in the *alternative concrete evolution calculation case* has an insignificant impact on groundwater flow and advective radionuclide transport compared with the *base case*. Despite the low flow, advection is still the dominating transport mechanism in both cases because of the very slow diffusive transport from the bentonite to the geosphere (Q_{eq} , Equation 4-8). However, the earlier increase of the diffusivity due to physical concrete degradation has an impact on the transport and release of strongly sorbing radionuclides, such as Ni-59.

Annual near-field release from the silo

The annual near-field releases of radionuclides from the silo in the *alternative concrete evolution calculation case* and the *base case* are shown in Figure 7-15. The annual release is similar for both cases except for Ni-59. The increased release of this strongly sorbing radionuclide is mainly due to an increase of the diffusivity (the maximum value in the log-triangular distributions) in the concrete in the *alternative concrete evolution calculation case*.

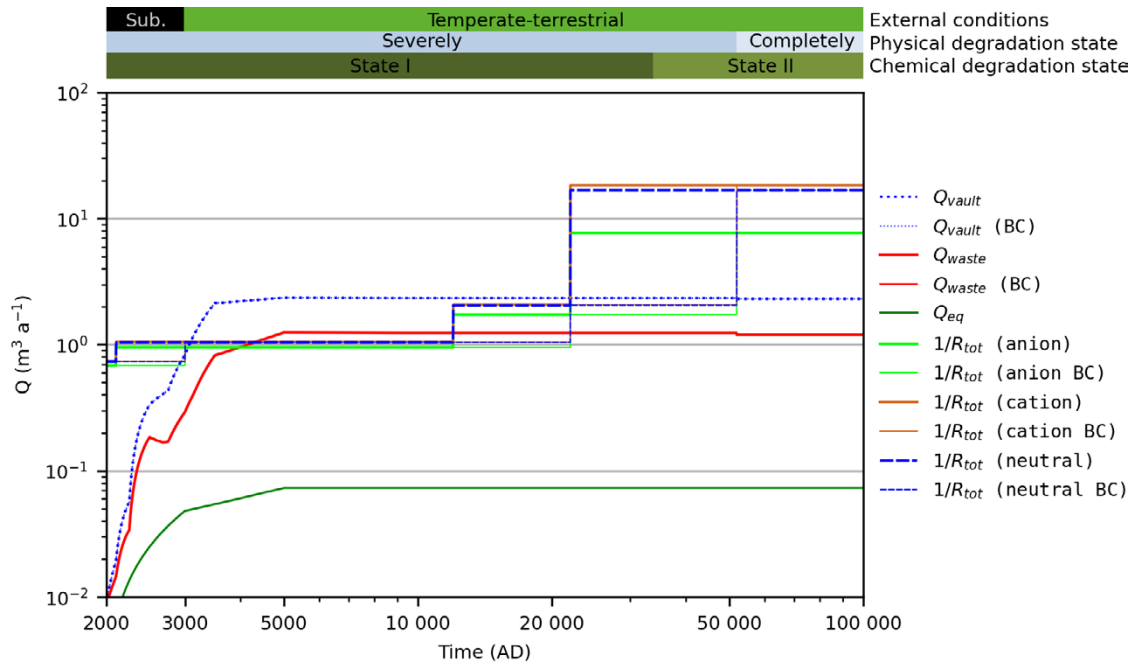


Figure 7-14. Comparison of groundwater flow through the waste Q_{waste} , equivalent flow Q_{eq} and inverse diffusive resistance of the concrete and bentonite silo structures where $R_{tot} = R_{concrete\ side} + R_{bentonite\ sides}$ (see Appendix E for definitions) as a function of time in the alternative concrete evolution calculation case (thick lines) and the base case (BC, thin lines). The effective diffusivity and thus the diffusive resistance are different for cationic, anionic and neutral radionuclide species. Q_{vault} is the flow through the whole silo vault including the top backfill. Coloured horizontal bars (top) as in Figure 5-3.

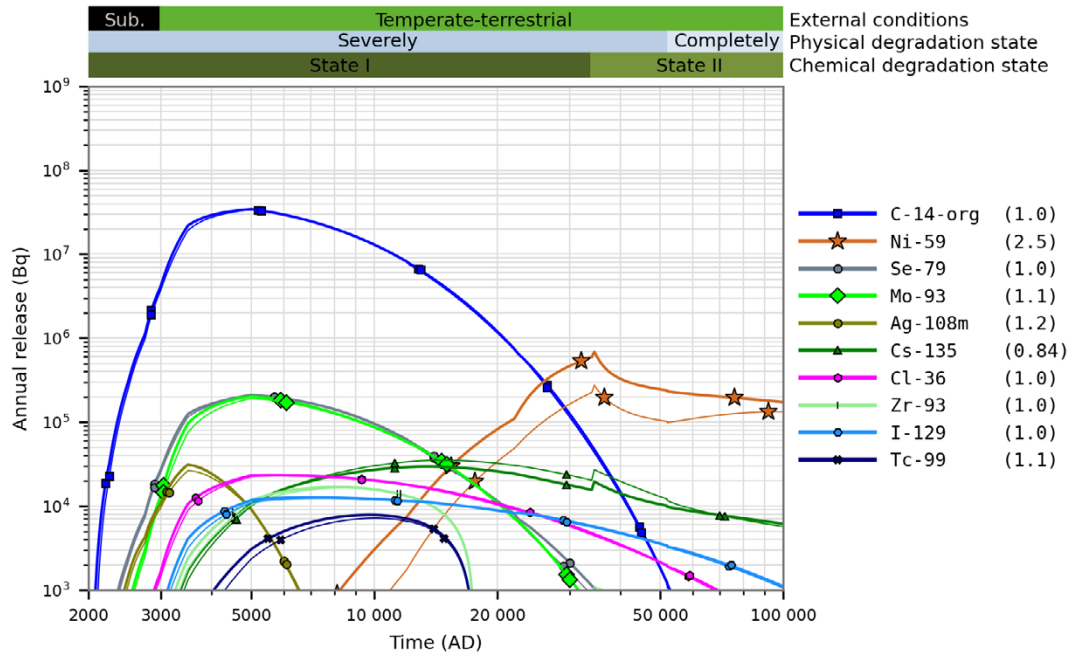


Figure 7-15. Annual activity releases (Bq) from the silo in the alternative concrete evolution calculation case (thick lines) and the base case (thin lines). The ratio between the maximum releases in the present calculation case and the base case are shown in parentheses in the key. Coloured horizontal bars (top) as in Figure 5-3.

7.4.3 1BMA calculations and results

Handling in the 1BMA model

Hydrology

In the near-field groundwater flow model, the different parts of 1BMA are assigned different hydraulic conductivities for different physical degradation states as shown in Figure 5-5. In the *alternative concrete evolution calculation case*, the external (new) parts of the concrete structure are assumed to be in a moderately degraded state ($K = 10^{-7}$ m/s, see Table 5-1) at the start of the simulated period. The transition to a severely degraded state ($K = 10^{-5}$ m/s, see Table 5-1) occurs at 3000 AD (compared to 22 000 AD in the *base case*) and to a completely degraded state at 22 000 AD (compared to 52 000 AD in the *base case*). As in the *base case*, the existing parts of the concrete structure are initially assumed to be in a severely degraded state. The transition to a completely degraded state occurs earlier in the *alternative concrete evolution calculation case* than in the *base case* (3000 AD versus 22 000 AD).

Concrete barriers

Over time, as the concrete degrades, the diffusion-available porosity of the concrete structures and radionuclide diffusivities increase more rapidly than in the *base case*. The time-dependent hydraulic conductivity, porosity and effective diffusivity of the cementitious materials in 1BMA are shown in Table 7-7 and Table 7-8.

Table 7-7. Development of 1BMA cementitious materials properties: concrete hydraulic conductivity K , diffusivity D_e and porosity ϕ used in the alternative concrete evolution calculation case. Diffusivities are given by log-triangular distributions with best estimate (BE), minimum and maximum values in the concrete structure and as single (deterministic) values in the mould walls.

Time (AD)	External (new) concrete structure K (m s ⁻¹)	Existing concrete structure K (m s ⁻¹)	Inner and outer concrete structure				Concrete mould walls	
			ϕ (-)	D_e BE (m ² s ⁻¹)	D_e min (m ² s ⁻¹)	D_e max (m ² s ⁻¹)	ϕ (-)	D_e (m ² s ⁻¹)
2000–2100	1.0×10^{-7}	1.0×10^{-5}	0.14	5.0×10^{-12}	5.0×10^{-12}	1.0×10^{-11}	0.11	3.5×10^{-12}
2100–3000	1.0×10^{-7}	1.0×10^{-5}	0.14	5.0×10^{-12}	5.0×10^{-12}	1.0×10^{-11}	0.14	2.0×10^{-11}
3000–12 000	1.0×10^{-5}	1.0×10^{-3}	0.14	5.0×10^{-12}	5.0×10^{-12}	5.0×10^{-11}	0.14	5.0×10^{-11}
12 000–22 000	1.0×10^{-5}	1.0×10^{-3}	0.18	1.0×10^{-11}	7.0×10^{-12}	1.0×10^{-10}	0.18	1.0×10^{-10}
22 000–102 000	1.0×10^{-3}	1.0×10^{-3}	0.3	2.0×10^{-10}	2.0×10^{-11}	3.0×10^{-10}	0.3	5.0×10^{-10}

Cracks

The side walls (both the inner and outer parts) and lid of all waste compartments in 1BMA are modelled as being cracked after the concrete structure transitions from the moderately degraded to the severely degraded physical degradation state, which occurs at 3000 AD in the *alternative concrete evolution calculation case*.

As in the *base case* the slab is assumed to be cracked directly after closure.

Transport through the near-field

The water flow through the waste domain of 1BMA is higher in the *alternative concrete evolution calculation case* than in the *base case* (as shown in Figure 7-16). This is due to the more rapid concrete degradation e.g. of the outer (new) parts of the concrete structure transition to a severely degraded state ($K = 10^{-5}$ m/s, see Table 5-1) associated with crack formation at 3000 AD. As in the *base case*, diffusion is initially, during submerged conditions, the dominating transport mechanism in 1BMA ($1/R_{\text{barrier}} > Q_{\text{waste}}$ in Figure 7-16). However, advection becomes clearly dominating after 3000 AD, lasting until 22 000 AD when concrete degradation leads to maximum effective diffusivity and porosity values.

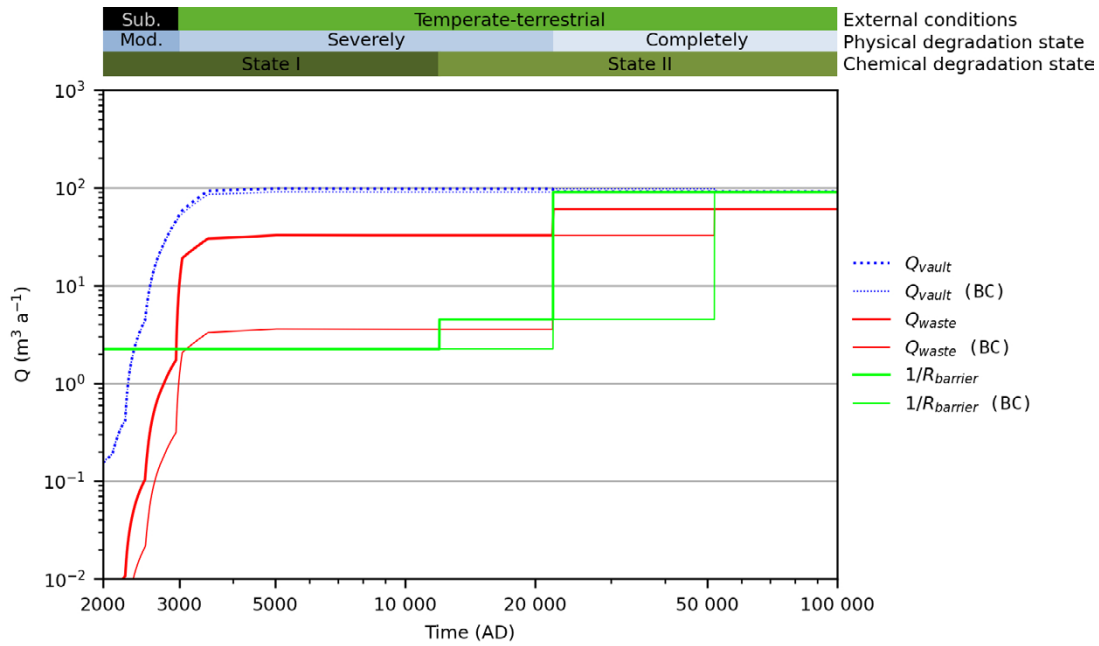


Figure 7-16. Comparison of water flow through the waste Q_{waste} and inverse diffusive resistance of the concrete structure $1/R_{\text{barrier}}$ as a function of time for alternative concrete evolution calculation case (thick lines) and the base case (BC, thin lines). R_{barrier} is defined in Equation E-13. Q_{vault} is the flow through the whole 1BMA vault including the backfill. Coloured horizontal bars (top) as in Figure 5-3.

Annual near-field release from 1BMA

The annual near-field releases of radionuclides from 1BMA in the *alternative concrete evolution calculation case* and the *base case* are shown in Figure 7-17. The higher release peaks of the weakly sorbing radionuclides Mo-93, Cs-135 and C-14-org between 3000 AD and 4000 AD in the present case are mainly caused by increased groundwater flow through the waste of 1BMA. The impact of crack formation on the release of radionuclides is generally limited in 1BMA, but an earlier release of the strongly sorbing radionuclides Ni-59 and C-14-inorg is partially caused by the cracks in the barriers.

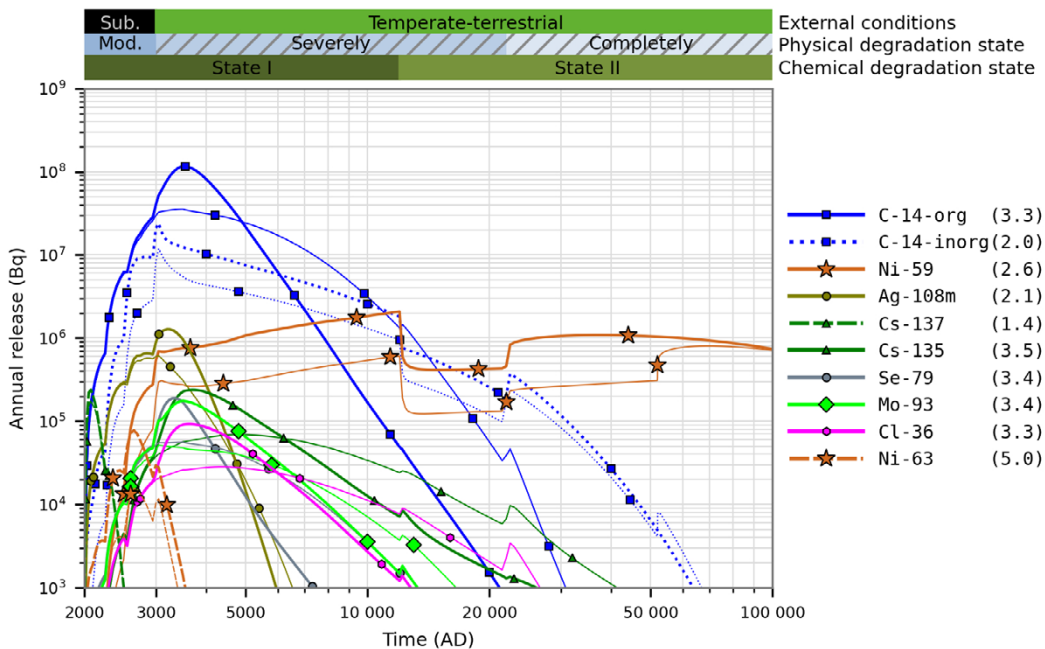


Figure 7-17. Annual activity releases (Bq) from 1BMA in the alternative concrete evolution calculation case (thick lines) and the base case (thin lines). The ratio between the maximum releases in the present calculation case and the base case are shown in parentheses in the key. Coloured horizontal bars (top) as in Figure 5-9.

In 1BMA, the increase in annual release is particularly pronounced at 3000 AD and 22 000 AD in the *alternative concrete evolution calculation case* due to a combination of a diffusivity increase in the concrete structures and waste domain and the increased water flow, both caused by physical concrete degradation.

7.4.4 2BMA calculations and results

Handling in the 2BMA model

Hydrology

In the *alternative concrete evolution calculation case* the concrete structure is assumed to be in a moderately degraded state (see Table 5-1) at the start of the simulated period. The transition to a severely degraded state occurs at 3000 AD (compared to 22 000 AD in the *base case*) and to a completely degraded state at 22 000 AD (compared to 52 000 AD in the *base case*).

Concrete barriers

Over time, as the concrete degrades, the diffusion-available porosity of the concrete structures and radionuclide diffusivities increase more rapidly than in the *base case*. The time-dependent hydraulic conductivity and porosity of the cementitious materials in 2BMA and the effective diffusivity of radionuclides are shown in Table 7-8.

Table 7-8. Development of 2BMA cementitious material properties: concrete hydraulic conductivity K , diffusivity D_e and porosity ϕ in the alternative concrete evolution calculation case. Diffusivities are given by log-triangular distributions with best estimate (BE), minimum, and maximum values, in the structures and by single (deterministic) values in the gas evacuation channels.

Time (AD)	Concrete structure/barrier					Gas evacuation channels
	K (m s ⁻¹)	ϕ (-)	D_e BE (m ² s ⁻¹)	D_e Min (m ² s ⁻¹)	D_e Max (m ² s ⁻¹)	D_e (m ² s ⁻¹)
2000–2100	1.0×10^{-7}	0.11	3.5×10^{-12}	3.5×10^{-12}	5.0×10^{-12}	3.5×10^{-10}
2100–3000	1.0×10^{-7}	0.14	5.0×10^{-12}	3.5×10^{-12}	5.0×10^{-12}	3.5×10^{-10}
3000–12000	1.0×10^{-5}	0.14	5.0×10^{-12}	5.0×10^{-12}	9.0×10^{-12}	5.0×10^{-10}
12000–22000	1.0×10^{-5}	0.18	1.0×10^{-11}	7.0×10^{-12}	1.0×10^{-10}	1.0×10^{-9}
22000–102000	1.0×10^{-3}	0.3	2.0×10^{-10}	2.0×10^{-11}	3.0×10^{-10}	1.0×10^{-9}

Cracks

In the 2BMA model, transport through cracks is explicitly modelled (see Section 5.3.4). The transition to a model with cracks occurs at 3000 AD in the *alternative concrete evolution calculation case*.

Transport through the near-field

The water flow through the waste domain of 2BMA is higher in the *alternative concrete evolution calculation case* than in the *base case* (as shown in Figure 7-18). This is due to the more rapid concrete degradation in the *alternative concrete evolution calculation case*, e.g. the concrete structure transition to a severely degraded state ($K = 10^{-5}$ m/s, see Table 5-1) associated with crack formation at 3000 AD. Initially, during submerged conditions, diffusion is the dominating transport mechanism in the *alternative concrete evolution calculation case* ($1/R_{\text{barrier}} > Q_{\text{waste}}$ in Figure 7-18). After 3000 AD, advection becomes the dominating transport mechanism. After 22 000 AD when concrete degradation leads to maximum effective diffusivity and porosity values, the diffusive transport becomes equally important as the advective transport.

Annual near-field release from 2BMA

The annual near-field release of radionuclides from 2BMA in the *alternative concrete evolution calculation case* and the *base case* is shown in Figure 7-19. The higher release peaks of the weakly sorbing radionuclides Mo-93, Cs-135 and C-14-org shortly after 3000 AD in the *alternative concrete evolution calculation case* is mainly caused by the increased water flow through the waste of 2BMA.

The increased early release of the strongly sorbing radionuclides Ni-59, Ca-41 and C-14-inorg by more than two orders of magnitude after 3000 AD in the present case cannot be explained entirely by the increased flow. A contributing factor is the assumed formation of cracks that impacts the release of strongly sorbing radionuclides because fewer sorption sites in the concrete barrier are available to the radionuclides migrating through the cracks when compared with through intact concrete. However, the impact of crack formation on the release of weakly- or non-sorbing radionuclides is less significant than for sorbing radionuclides.

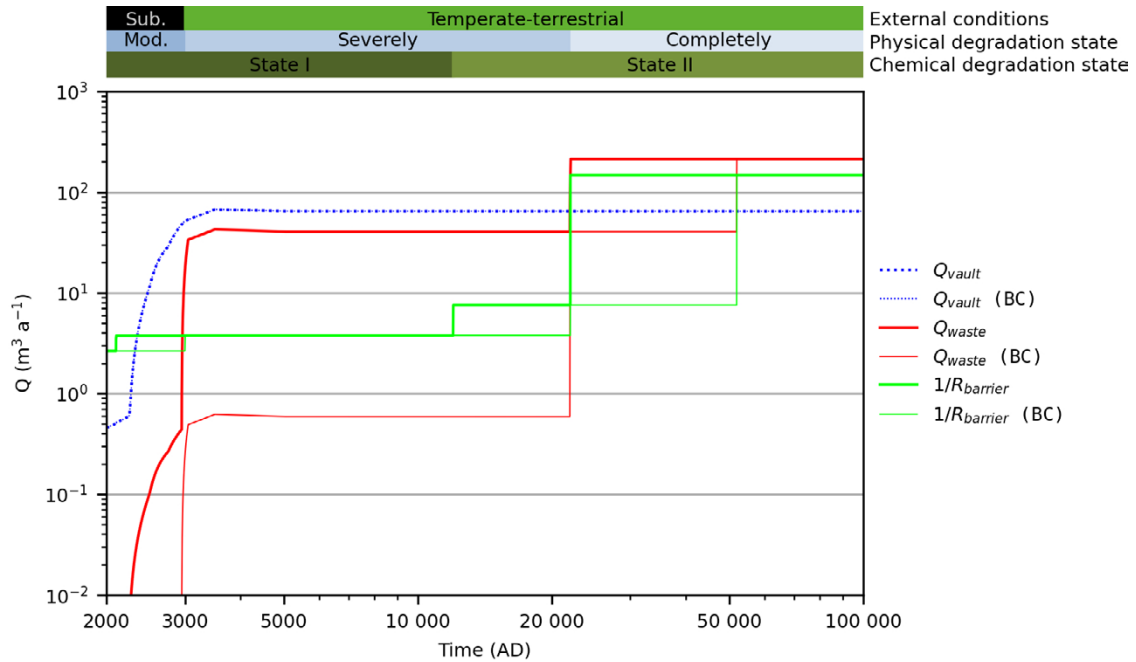


Figure 7-18. Comparison of groundwater flow through the waste Q_{waste} and inverse diffusive transport resistance of the concrete structure $1/R_{\text{barrier}}$ as a function of time for alternative concrete evolution calculation case (thick lines) and the base case (BC, thin lines). R_{barrier} is defined in Equation E-16. Q_{vault} is the flow through the whole 2BMA vault including the backfill. Coloured horizontal bars (top) as in Figure 5-3.

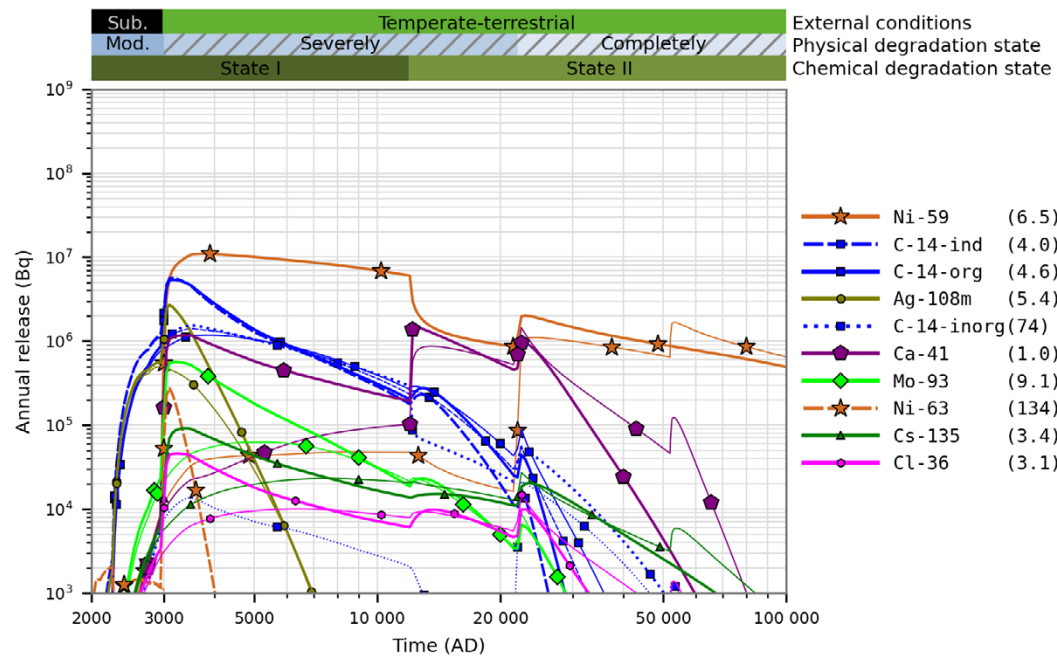


Figure 7-19. Annual activity releases (Bq) from 2BMA in the alternative concrete evolution calculation case (thick lines) and the base case (thin lines). The ratio between the maximum releases in the present calculation case and the base case are shown in parentheses in the key. Coloured horizontal bars (top) as in Figure 5-9.

7.4.5 1BRT calculations and results

Handling in the 1BRT model

Hydrology

In both the *alternative concrete evolution calculation case* and *base case*, the concrete structure is initially assumed to be in a severely degraded state (see Table 5-1). However, in the *alternative concrete evolution calculation case*, the transition to a completely degraded state occurs earlier, at 3000 AD, compared to 52 000 AD in the *base case*.

Concrete barriers

Over time, as the concrete degrades, the diffusion-available porosity of the concrete structures and radionuclide diffusivities increase more rapidly than in the *base case*. The time-dependent hydraulic conductivity and porosity of the cementitious materials in 1BRT, as well as the effective diffusivity of radionuclides are shown in Table 7-9.

Table 7-9. Development of 1BRT cementitious material properties: concrete hydraulic conductivity K , diffusivity D_e , porosity ϕ in the alternative concrete evolution calculation case. Diffusivities are given by log-triangular distributions with best estimate (BE), minimum and maximum values, in the structures. For waste and after 12 000 AD for the structures single (deterministic) diffusivity values are used.

Time (AD)	Concrete structure				Concrete structure and waste domain	Waste domain	
	D_e BE ($\text{m}^2 \text{s}^{-1}$)	D_e min ($\text{m}^2 \text{s}^{-1}$)	D_e max ($\text{m}^2 \text{s}^{-1}$)	ϕ (-)	K^a (m s^{-1})	D_e ($\text{m}^2 \text{s}^{-1}$)	ϕ (-)
2000–3000	5.0×10^{-12}	-	-	0.14	1.0×10^{-4}	3.5×10^{-10}	0.3
3000–12 000	5.0×10^{-12}	-	-	0.14	1.0×10^{-3}	4.0×10^{-10}	0.4
12 000–22 000	1.0×10^{-11}	7.0×10^{-12}	5.0×10^{-11}	0.18	1.0×10^{-3}	5.0×10^{-10}	0.5
22 000–102 000	2.0×10^{-10}	2.0×10^{-11}	3.0×10^{-10}	0.3	1.0×10^{-3}	1.0×10^{-9}	0.5

^a Average hydraulic conductivity of the concrete structure surrounding the waste and its interior.

Cracks

The handling of cracks in the 1BRT model is identical to the *base case* i.e. cracks are included explicitly in the model already at the beginning of the assessment period.

Transport through the near-field

The groundwater flow through the waste domain of 1BRT (Figure 7-20) is slightly higher in the *alternative concrete evolution calculation case* than in the *base case*. This is due to the more rapid concrete degradation and subsequent hydraulic conductivity increase. Initially, diffusion is the dominating transport mechanism in the *alternative concrete evolution calculation case* ($1/R_{\text{barrier}} > Q_{\text{waste}}$ in Figure 7-20). After 3000 AD, advection becomes the dominating transport mechanism until 22 000 AD when concrete degradation leads to maximum porosities and effective diffusivities.

Annual near-field release from 1BRT

The annual near-field release of radionuclides from 1BRT in the *alternative concrete evolution calculation case* and the *base case* are shown in Figure 7-21. The slightly higher release of Ni-59 is mainly caused by the increased groundwater flow through the waste of 1BRT. The release of induced radionuclides from 1BRT is not significantly affected by this calculation case, as the corrosion-controlled release is not affected (Section 7.4.1).

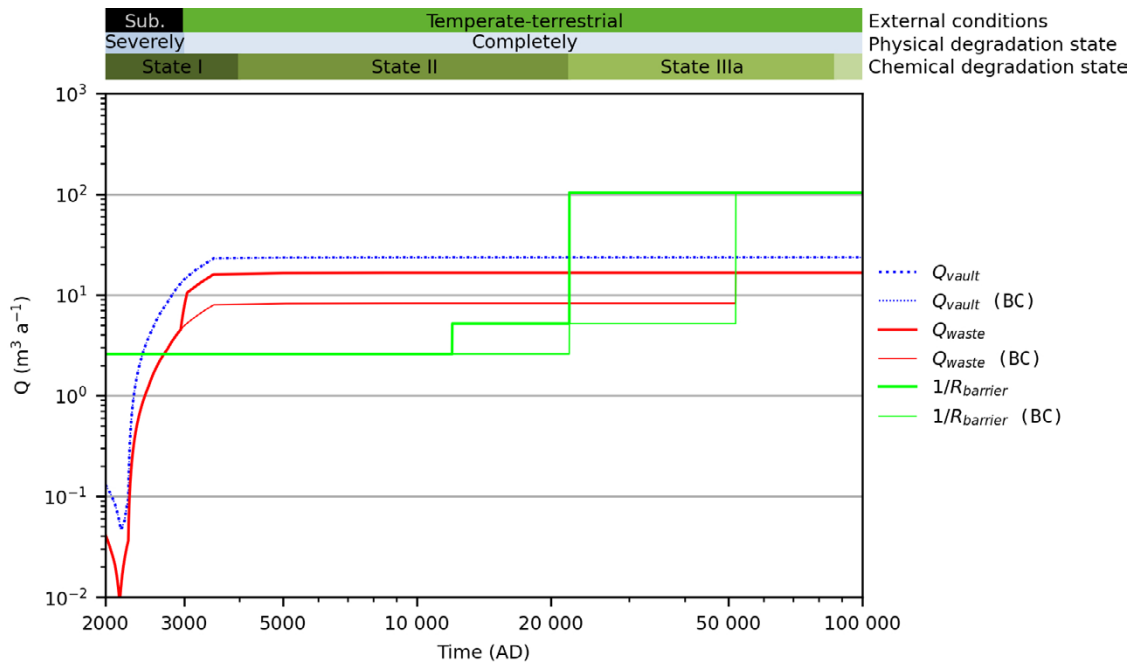


Figure 7-20. Comparison of water flow through the waste Q_{waste} and inverse diffusive transport resistance of the concrete structure $R_{barrier}$ as a function of time in the alternative concrete evolution calculation case (thick lines) compared to the base case (thin lines). $R_{barrier}$ is defined in Equation E-19. Q_{vault} refers to the flow through the whole 1BRT vault including the backfill. Coloured horizontal bars (top) as in Figure 5-3.

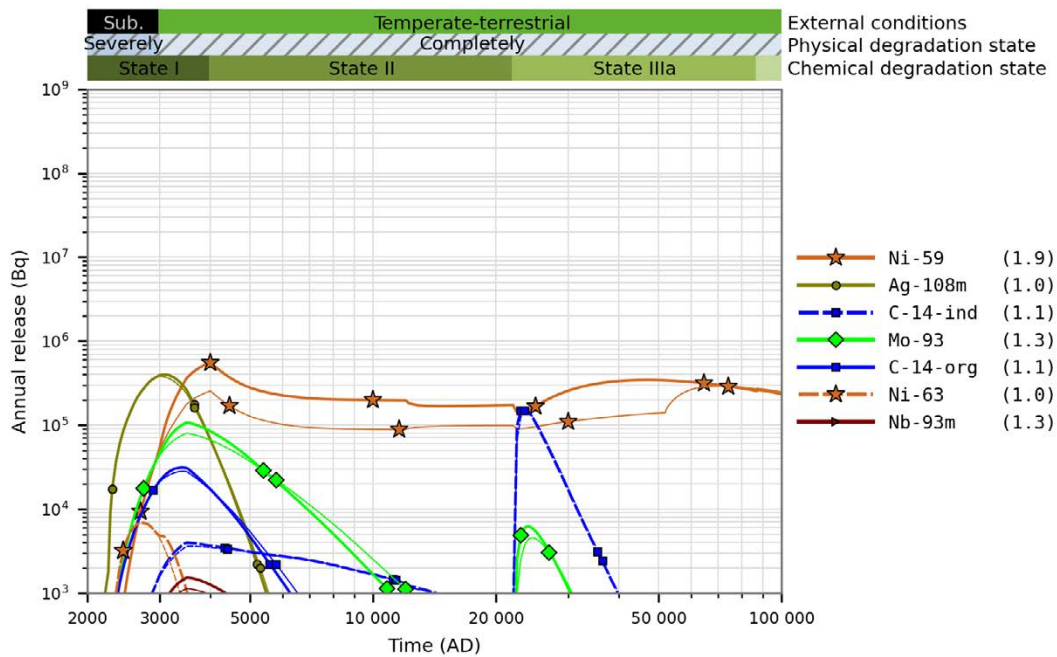


Figure 7-21. Annual activity releases (Bq) from 1BRT in the alternative concrete evolution calculation case (thick lines) and the base case (thin lines). The ratio between the maximum releases in the present calculation case and the base case are shown in parentheses in the key. Coloured horizontal bars (top) as in Figure 5-9.

7.4.6 1–2BTF calculations and results

Handling in the 1-2BTF models

Hydrology

At the start of the simulated period, the concrete barrier is assumed to already be in a severely degraded state (see Table 5-1) and the transition to a completely degraded state occurs earlier than in the *base case*.

Concrete barriers

Over time, as the concrete degrades, the diffusion-available porosity of the concrete structures and radionuclide diffusivities increase more rapidly than in the *base case*. The time-dependent hydraulic conductivity and porosity of the cementitious materials in 1–2BTF, as well as the effective diffusivity of radionuclides are shown in Table 7-10.

Table 7-10. Development of 1–2BTF cementitious materials properties: hydraulic conductivity K , effective diffusivity D_e and porosity ϕ in the alternative concrete evolution calculation case.

Time (AD)	Structural concrete			Concrete tanks		Waste-domain ^a	Grout ^b	
	All	Vault lid, slab		D_e ($m^2 s^{-1}$)	ϕ (-)	K ($m s^{-1}$)	D_e ($m^2 s^{-1}$)	ϕ (-)
K ($m s^{-1}$)	D_e ($m^2 s^{-1}$)	ϕ (-)						
2000–2100	1.0×10^{-5}	3.5×10^{-12}	0.14	3.5×10^{-12}	0.11	6.0×10^{-5}	3.5×10^{-10}	0.2
2100–3000	1.0×10^{-5}	2.0×10^{-11}	0.14	5.0×10^{-11}	0.11	6.0×10^{-5}	3.5×10^{-10}	0.2
3000–12 000	1.0×10^{-3}	1.0×10^{-10}	0.30	2.0×10^{-10}	0.30	1.0×10^{-3}	5.0×10^{-10}	0.5
12 000–102 000	1.0×10^{-3}	5.0×10^{-10}	0.30	8.0×10^{-10}	0.30	1.0×10^{-3}	1.0×10^{-9}	0.5

^a Average hydraulic conductivity of concrete tanks and surrounding grout (Abarca et al. 2020).

^b Grout on the sides of the waste-domain and the grout between the waste packages in the waste-domain.

Transport through the near-field – 1-2BTF

In the *alternative concrete evolution calculation case*, groundwater flow through the waste domains of 1-2BTF increases at 3000 AD (Figure 7-22) and becomes slightly higher than in the *base case*. This is due to the more rapid concrete degradation and subsequent hydraulic conductivity increase at this time. Initially, diffusion is the dominating transport mechanism ($1/R_{lid} > Q_{waste}$ in Figure 7-22). After 3000 AD, advection is the dominating transport mechanism for both cases.

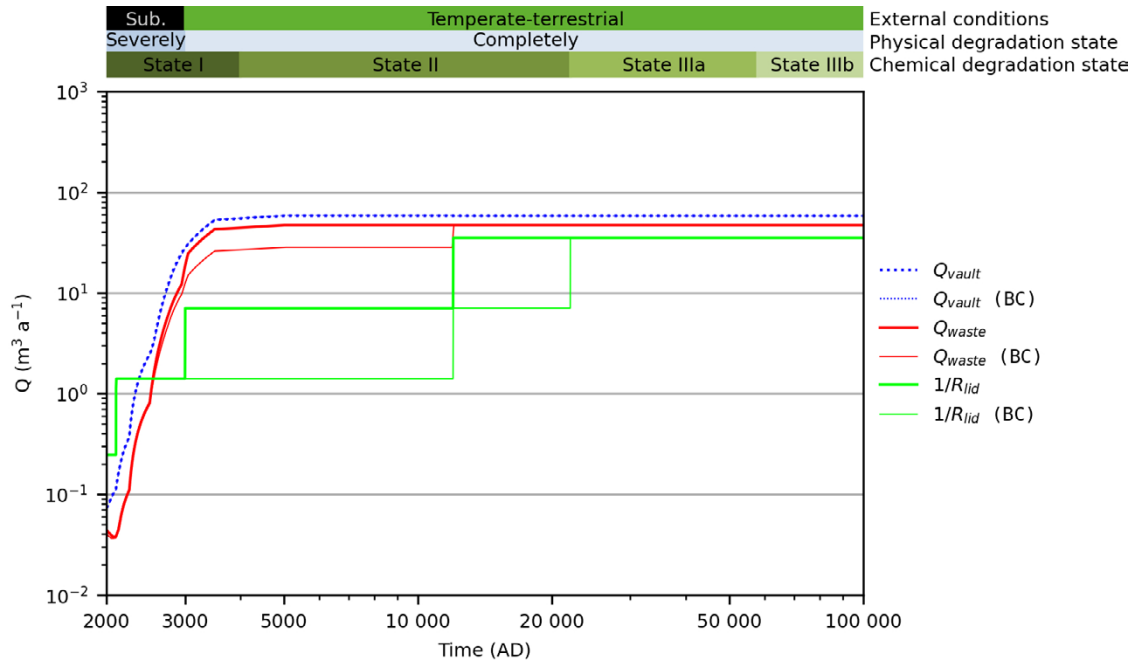


Figure 7-22. Comparison of water flow through the waste Q_{waste} and inverse diffusive resistance of the concrete lid, R_{lid} for 2BTF as a function of time in the alternative concrete evolution calculation case (thick lines) compared to the base case (thin lines). Q_{vault} is the flow through the whole vault including the backfill. Coloured horizontal bars (top) as in Figure 5-3.

Annual near-field release from 1-2BTF

The annual near-field releases of radionuclides from 1BTF and 2BTF in the *alternative concrete evolution calculation case* and the *base case* are shown in Figure 7-23 and Figure 7-24, respectively. The annual release is similar for both cases, although the release maximum is slightly higher in the *alternative concrete evolution calculation case*. The increase is caused by the relatively modest increase of groundwater flow through the waste of 1-2BTF.

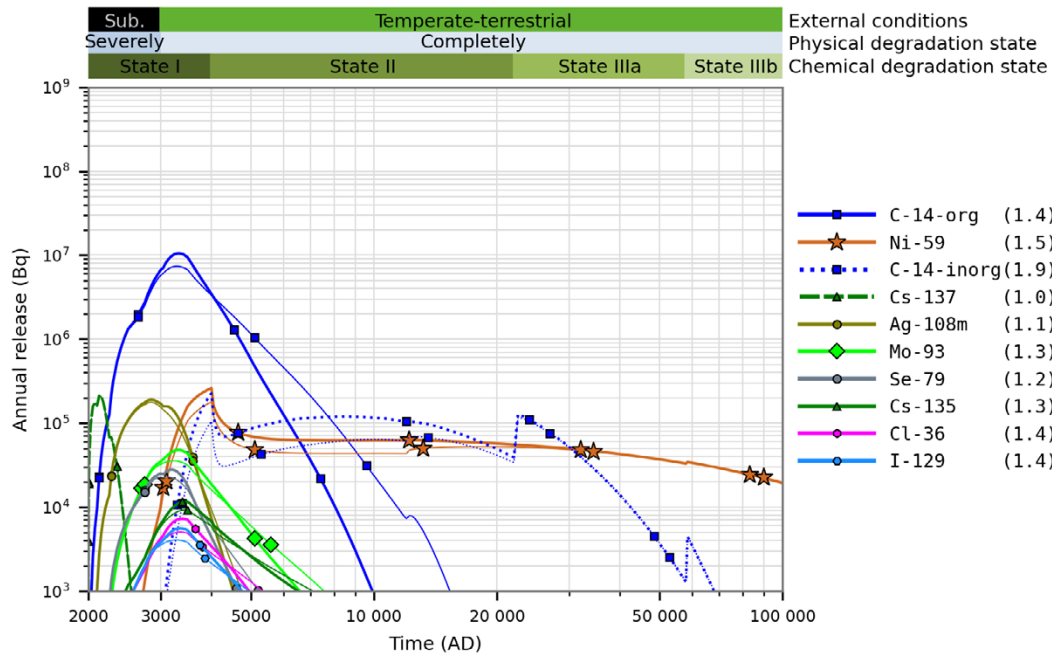


Figure 7-23. Annual activity releases (Bq) from 1BTF in the alternative concrete evolution calculation case (thick lines) and the base case (thin lines). The ratio between the maximum releases in the present calculation case and the base case are shown in parentheses in the key. Coloured horizontal bars (top) as in Figure 5-3.

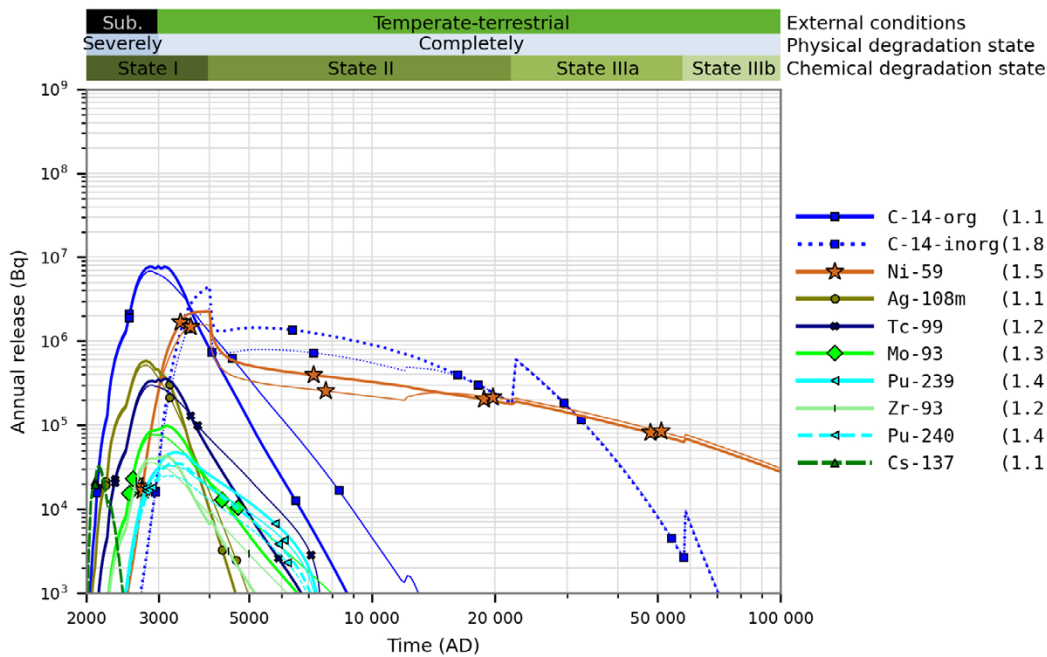


Figure 7-24. Annual activity releases (Bq) from 2BTF in the alternative concrete evolution calculation case (thick lines) and the base case (thin lines). The ratio between the maximum releases in the present calculation case and the base case are shown in parentheses in the key. Coloured horizontal bars (top) as in Figure 5-3.

7.4.7 Releases from the near-field

Figure 7-25 shows total releases from the near-field of SFR in the *alternative concrete evolution calculation case* compared with the *base case*. Early concrete degradation causes a more pronounced peak release around 3000–4000 AD, which is mainly due to increased releases from 1–2BMA, see Figure 7-17 and Figure 7-19. The release of C-14-org and Mo-93 increases only moderately from the silo (Figure 7-15), but the increases from 1–2BMA are large and affect the total releases significantly.

The initial peak releases of the relatively short-lived Cs-137 and Ni-63 as well as the later releases of U-238 are dominated by releases from 1–5 BLA, see Figure 5-28 and Figure 5-29. These releases are unaffected by this calculation case and overshadow the releases of these radionuclides from the vaults with concrete barriers. Thus, no effect is seen on the total releases of these radionuclides in this calculation case.

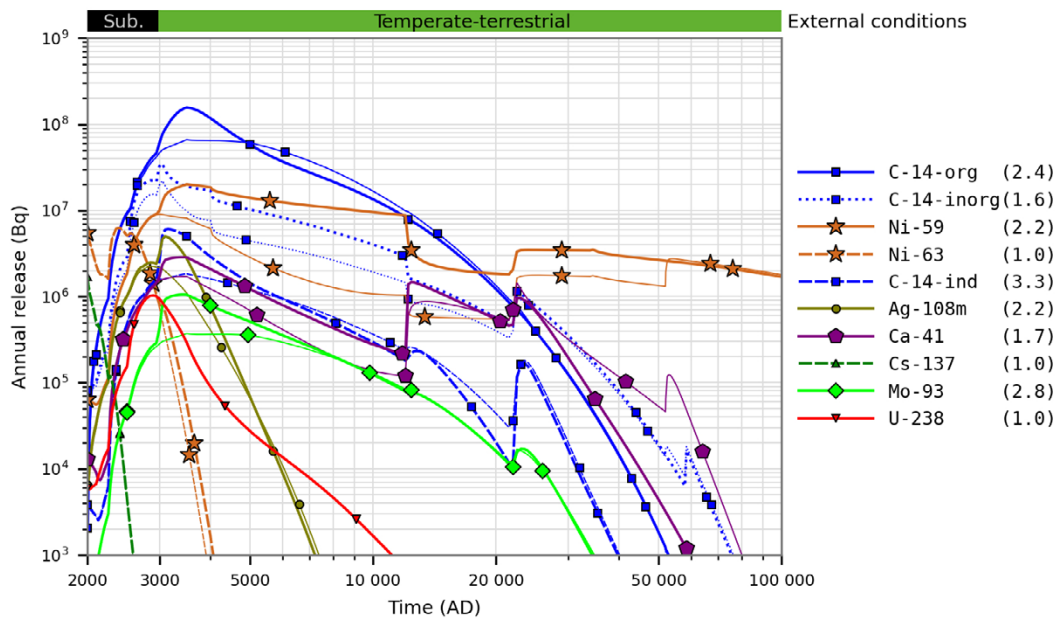


Figure 7-25. Annual activity releases (Bq) from the entire SFR in the alternative concrete evolution calculation case (thick lines) and the base case (thin lines). The ratio between the maximum releases in the present calculation case and the base case are shown in parentheses in the key. Coloured horizontal bar (top) shows the evolution of the external conditions.

7.4.8 Handling in the geosphere model

The handling in the geosphere model is identical to the *base case*.

7.4.9 Handling in the biosphere model

The handling in the biosphere model is identical to the *base case*.

7.4.10 Annual doses

The annual dose from the total release from SFR is presented in Figure 7-26. The dose maximum is higher in the *alternative concrete evolution calculation case* compared with the *base case*. The dose is dominated primarily by Mo-93 and secondarily C-14-org, which have significantly increased dose contributions from 1-2BMA (Figure 7-27 and Figure 7-28) in the present case.

Other radionuclides that are significantly affected in this calculation case include Ni-59 and Ca-41. However, their contributions to dose occur later in the assessment period and therefore do not influence the maximum dose significantly.

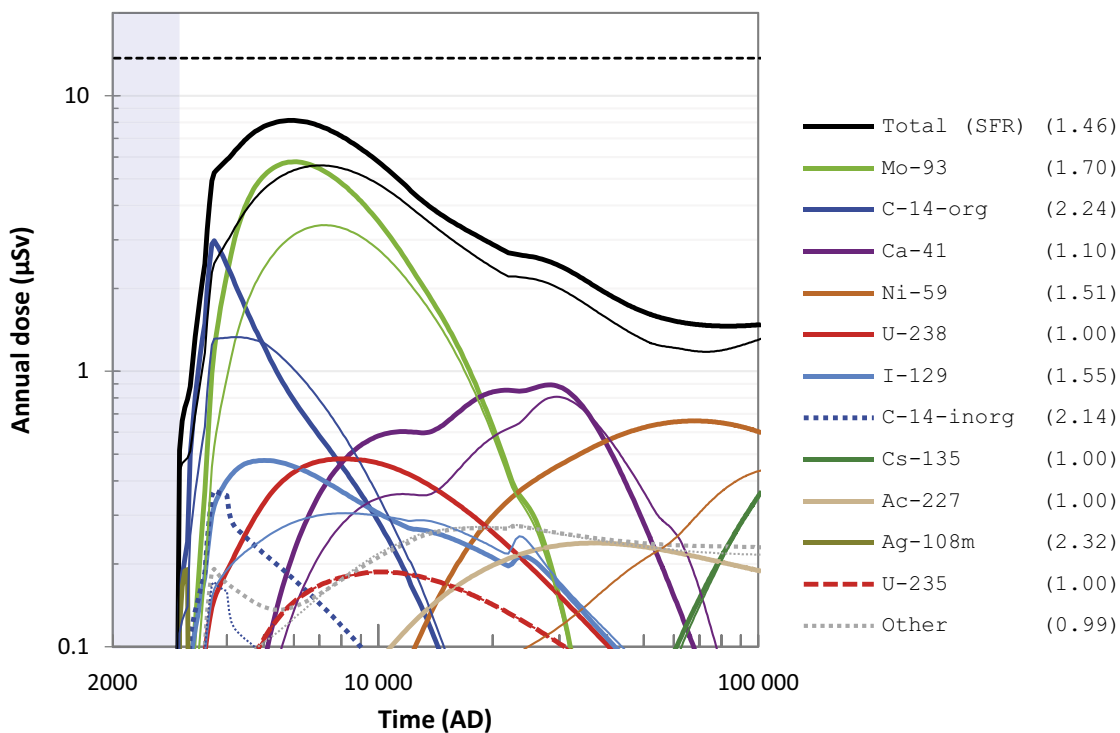


Figure 7-26. Annual dose (μSv) to the most exposed group (black line), including radionuclide specific contributions (coloured lines), for releases from the entire SFR in the alternative concrete evolution calculation case (thick lines) and the base case (thin lines). The combined contribution from radionuclides not shown is indicated by the grey dotted line. The ratio between the maximum doses in the present calculation case and the base case are shown in parentheses in the key. The annual dose corresponding to the regulatory risk criterion ($14 \mu\text{Sv}$) is indicated by the black dashed line and the submerged period is illustrated by the blue shading.

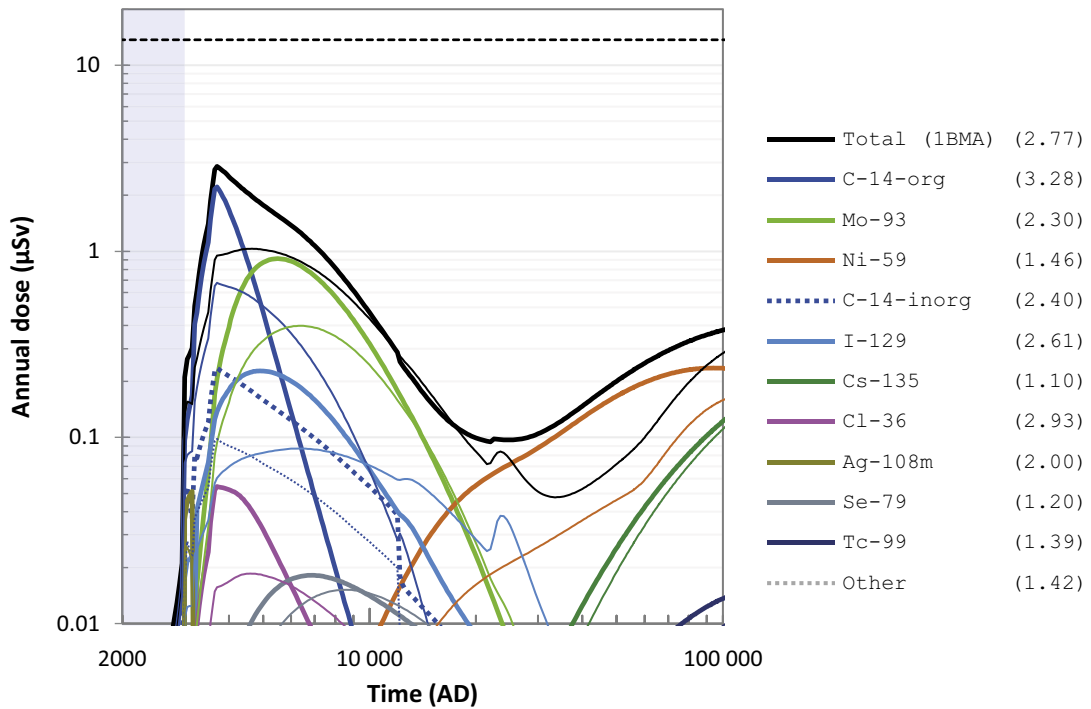


Figure 7-27. Annual dose (μSv) to the most exposed group (black line), including radionuclide specific contributions (coloured lines), for releases from 1BMA in the alternative concrete evolution calculation case (thick lines) and the base case (thin lines). The combined contribution from radionuclides not shown is indicated by the grey dotted line. The ratio between the maximum doses in the present calculation case and the base case are shown in parentheses in the key. The annual dose corresponding to the regulatory risk criterion (14 μSv) is indicated by the black dashed line and the submerged period is illustrated by the blue shading.

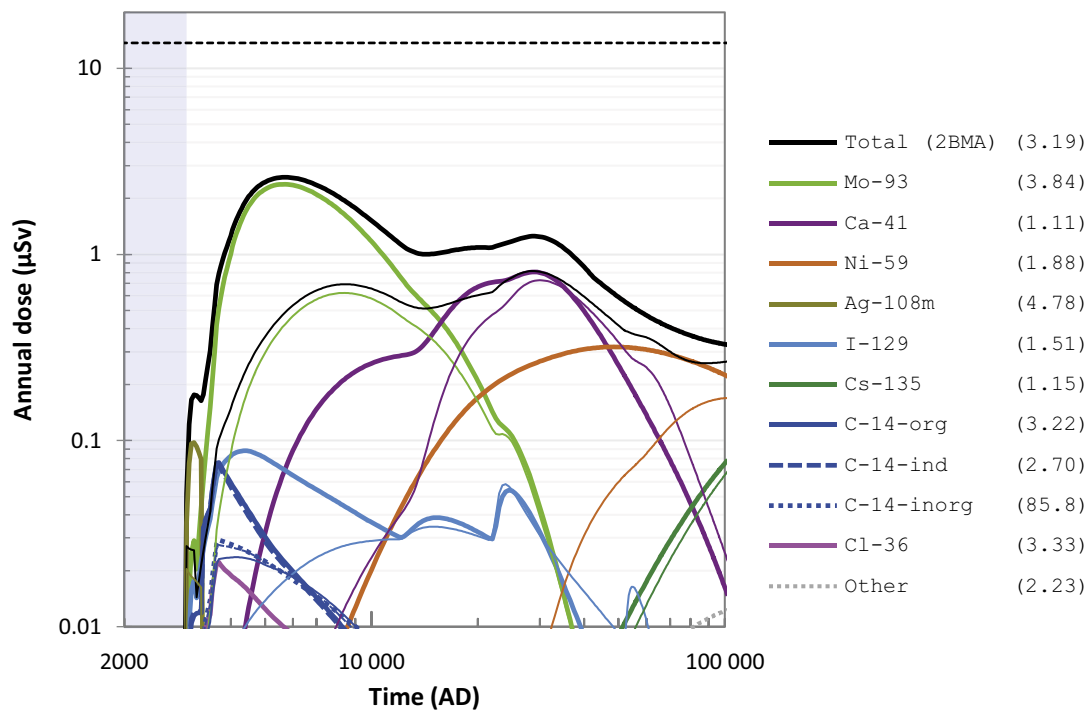


Figure 7-28. Annual dose (μSv) to the most exposed group (black line), including radionuclide specific contributions (coloured lines), for releases from 2BMA in the alternative concrete evolution calculation case (thick lines) and the base case (thin lines). The combined contribution from radionuclides not shown is indicated by the grey dotted line. The ratio between the maximum doses in the present calculation case and the base case are shown in parentheses in the key. The annual dose corresponding to the regulatory risk criterion (14 μSv) is indicated by the black dashed line and the submerged period is illustrated by the blue shading.

7.4.11 Summary and conclusions

In the *alternative concrete evolution calculation case*, it is assumed that the hydraulic conductivity is higher initially and increases earlier than in the *base case*. Additionally, the porosity of concrete barriers, as well as the diffusivity of radionuclides in the concrete, increases earlier and uncertainties in diffusivities are considered larger than in the *base case*.

This leads to significantly increased releases of many radionuclides important for the total maximum dose from SFR. 1–2BMA, where the concrete structures are the main hydraulic barriers, are the most affected vaults in terms of increased contribution to the total dose from SFR. The silo release is moderately affected (Figure 7-15) because the intact bentonite reduces the effect of concrete degradation. 1–2BTF have limited contribution to the total near-field release and dose, thus their impact in this calculation case is limited.

The impact of an alternative concrete evolution scenario on 1BRT is limited since the release is mostly determined by the steel corrosion rates. The 1–5BLA vaults are not affected by the concrete evolution since they do not have any concrete barriers.

The maximum of the total mean annual dose is about 50 % higher in the *alternative concrete evolution calculation case* compared with the *base case*.

Figure 7-29 gives an illustrative summary of the performance of the near-field in this calculation case compared with the *base case*, for the most affected radionuclides (radionuclides whose maximum release increases by more than 50 %). The vertical bars show how much of the initial activity is released from the near-field over the assessment period, i.e. the accumulated release divided by the initial activity, in the present case and in the *base case*. The figure also shows the quotient between the cases for maximum annual release (yellow circles) and the quotient of accumulated release in the present case and the *base case* (black circles). Most significant effects can be seen on maximum (peak) releases while the effect on cumulative (total) releases during the whole assessment period is more moderate.

Radionuclides dominating the release from 1–2BMA are the ones most affected by the alternative concrete evolution scenario since the concrete structures are the main hydraulic barriers in these vaults. Hence, as expected, the radionuclides shown in Figure 7-29, are also the radionuclides that dominates the release from 1–2BMA, see Figure 7-17 and Figure 7-19. The increase of the peak release is greater than the increase of the accumulated release because early concrete degradation causes a more pronounced peak release around 3000–4000 AD, which has a limited effect on the accumulated release.

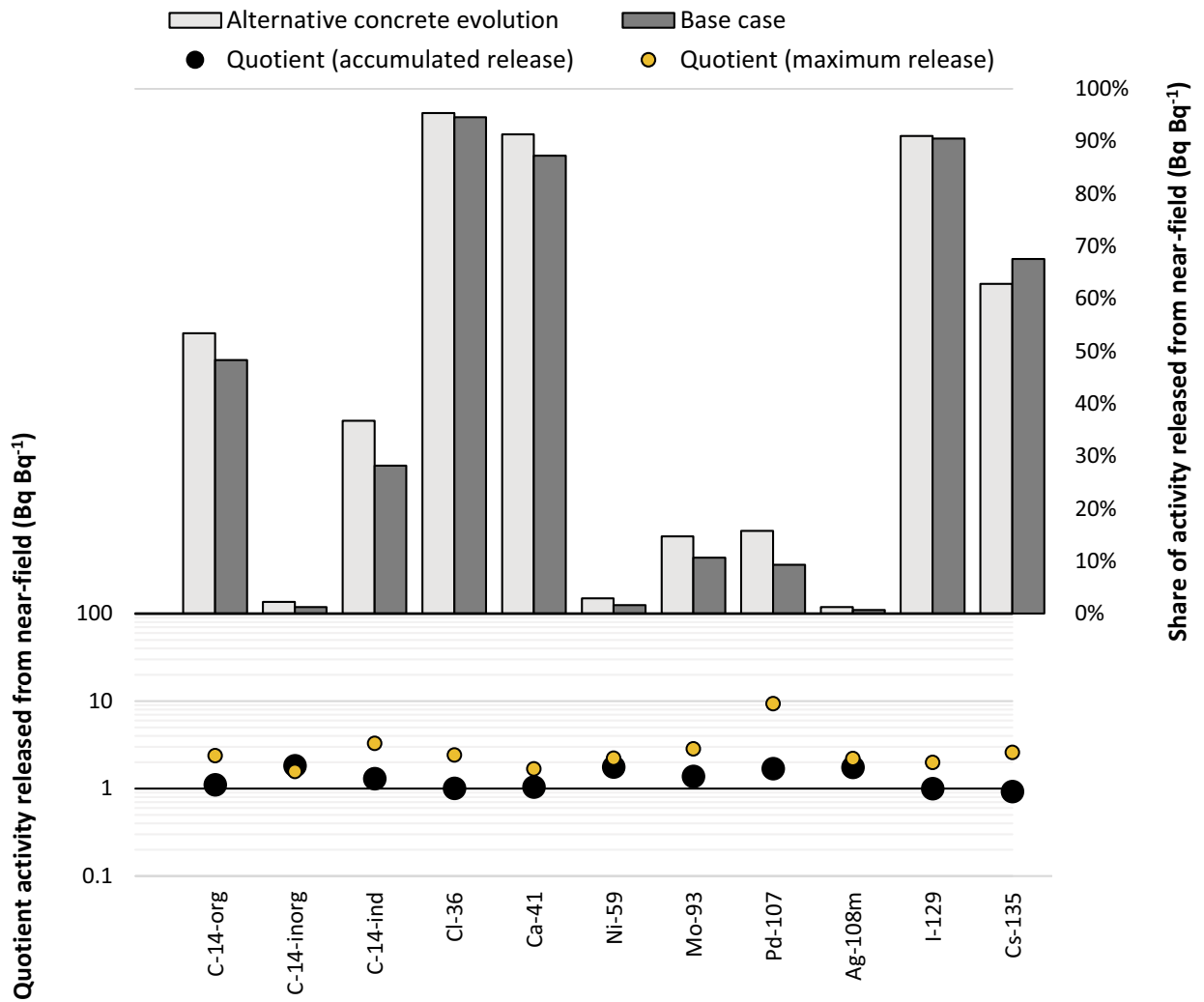


Figure 7-29. Summary of activity releases from the near-field in the alternative concrete evolution calculation case in relation to the base case for most affected radionuclides. Upper panel: percentage of the cumulative release in the two calculation cases relative to the total initial activity in the waste vaults. Lower panel: quotient of the cumulative (black circles) and maximum (yellow circles) releases between the alternative concrete evolution calculation case and the base case.

7.5 Earthquake calculation case

7.5.1 General description

The *earthquake calculation case* is selected to evaluate doses to humans from the *earthquake scenario* (**Post-closure safety report**, Section 8.6). In this scenario, it is assumed that an earthquake causes such adverse effects that several safety functions cannot be upheld (**Post-closure safety report**, Sections 8.2.3, 8.2.6, 8.2.8 and 8.2.9).

This calculation case assumes that an earthquake damages the silo concrete structure and also adversely affects the structural and mechanical properties of the rock. As a detailed quantification of the effects of an earthquake on radionuclide transport is associated with large uncertainties, a highly simplified modelling methodology is used, that intentionally overestimates the radiological consequences of an earthquake. The same methodology was used in the SR-PSU (SKB TR-14-01, Section 8.4.5) and in SAR-08 (SKB R-08-130, Section 8.4.3).

7.5.2 Handling in the transport models

Up until the time of an earthquake event, radionuclide transport occurs in the same way as in the *base case*. After the event, the concrete structure is assumed to become damaged to such an extent that the concrete barriers in the silo are no longer fully functioning. The effects on radionuclide transport of the damaged concrete structure are highly uncertain; with current knowledge it is not possible to rule out that the radionuclide transport pathways out from the silo would change compared with the *base case*. It is reasonable to believe that most of the transport would not be radically altered due to the integrity of the silo bentonite. However, as alternative transport pathways may be created, it is not possible to rule out a reduced transport-interaction with the engineered barriers.

The groundwater flow through the silo following the concrete structural damage was analysed in the safety assessment SAFE (SKB 2001). Since the bentonite constitutes the main hydraulic barrier of the silo, the change of groundwater flow used in this calculation case is relatively small compared with the *base case*, amounting to $1 \text{ m}^3 \text{ a}^{-1}$ (Holmén and Stigsson 2001). However, because of eventual new transport pathways after the concrete structure failure, both sorption and the diffusive resistance in the engineered barriers in the silo is pessimistically disregarded. Consequently, the remaining radionuclide activity is assumed to be located in the full network of pores in the silo, with releases linked to the turnover time of the passing groundwater flow. This is a pessimistic assumption, since radionuclides can be expected to sorb (both onto the cement in the damaged concrete and to the bentonite) and the repository's pore network cannot be expected to be fully interconnected even after an earthquake.

The conditions in the geosphere are assumed to be adversely affected by an earthquake large enough to damage the silo concrete structure, but such effects on the geosphere have not been quantified. Therefore, it is pessimistically assumed that there is no transport retention in the geosphere in this calculation case. Because of this simplification, and since the activity release into the till in the discharge area (from which groundwater from a dug well is extracted) is highly overestimated, exposure from a drilled well downstream the repository is not considered in this calculation case.

Calculations over the entire assessment period are made for single earthquakes, and the calculations are repeated for earthquakes occurring every 100th year from repository closure up until the end of the assessment period. Due to the large number of simulations, fully probabilistic calculations are not deemed feasible considering the available computational capacity. Instead, a combination of a deterministic approach using best-estimate values and a probabilistic approach using random samples based on parameter PDFs is applied in this calculation case.

For most modelled radionuclides, a deterministic approach using best estimates produces a similar dose response as the arithmetic mean across the probabilistic simulations (about 60 % of the radionuclides exhibit a difference in LDFs amounting to less than 10 % when comparing deterministic and probabilistic simulations, see the **Biosphere synthesis report**, Appendix C). However, the radionuclides that contribute most to the dose in the *base case* (Mo-93, C-14, Ni-59, Ca-41, I-129 and the uranium isotopes) typically have, at each time point, an approximately log-normally distributed dose response. Thus, for these radionuclides, the arithmetic means of the probabilistic simulations yield higher doses than the deterministic ones. As the cumulative probability of an earthquake event is very low for the first 10 000 years after closure (less than 1 %, see lower panel of Figure 7-30), radionuclides that contribute most to the dose within this time-span (shorter-lived Mo-93 and C-14) have a very low

likelihood to be affected by an earthquake. Ca-41, which exhibits the greatest deviation between the deterministic and the probabilistic simulations, will not be disposed in the silo. For uranium isotopes, only small amounts will be disposed in the silo compared to the BLA-vaults. The dose consequence of an earthquake on I-129 is expected to be small as I-129 is relatively mobile and thus almost 90 % of its initial inventory in the silo is released within the assessment period, even in the absence of an earthquake (Figure 5-68). Ni-59, however, is a long-lived, non-mobile radionuclide, and more than 70 % of the total activity of Ni-59 in SFR is planned to be disposed in the silo. In the *base case*, the silo retains most of this activity over the whole assessment period (only 0.1 % of the initial activity is assessed to be released, see Section 5.3.8). In summary, the effect of the differences between using a deterministic and probabilistic approach for the radionuclide transport and dose calculations in the *earthquake calculation case* is expected to be small for all radionuclides contributing most to the dose, except for Ni-59. Therefore, deterministic simulations using best-estimates are used for all radionuclides, except for Ni-59, for which fully probabilistic simulations are performed.

7.5.3 Annual doses

The annual dose to the most exposed group from releases from the silo is presented in Figure 7-30 for several calculations. The difference between the calculations is the timing of the earthquake. Timings with an interval of 1 000 years are included in the figure. The reason for including every 1 000 years (as opposed to the calculated interval of 100 years) is to improve the readability of the figure. For all evaluated earthquakes, the highest dose is shown in the figure for each point in time, irrespective of when the earthquake occurs. The calculation with the highest maximum dose (41 μSv), at 24 500 AD, is caused by an earthquake occurring at repository closure. After reaching its maximum, the dose gradually decreases and is approximately halved by the end of the assessment period. The delayed dose maximum with respect to the earthquake event is primarily caused by the time it takes for Ni-59 to break through the bottom till layer in the surface system and thus become available for exposure after draining the mire (**Biosphere synthesis report**, Section 9.3). The maximum dose due to releases from the silo in this calculation case is almost 20 times greater than the 2.4 μSv dose calculated in the *base case*.

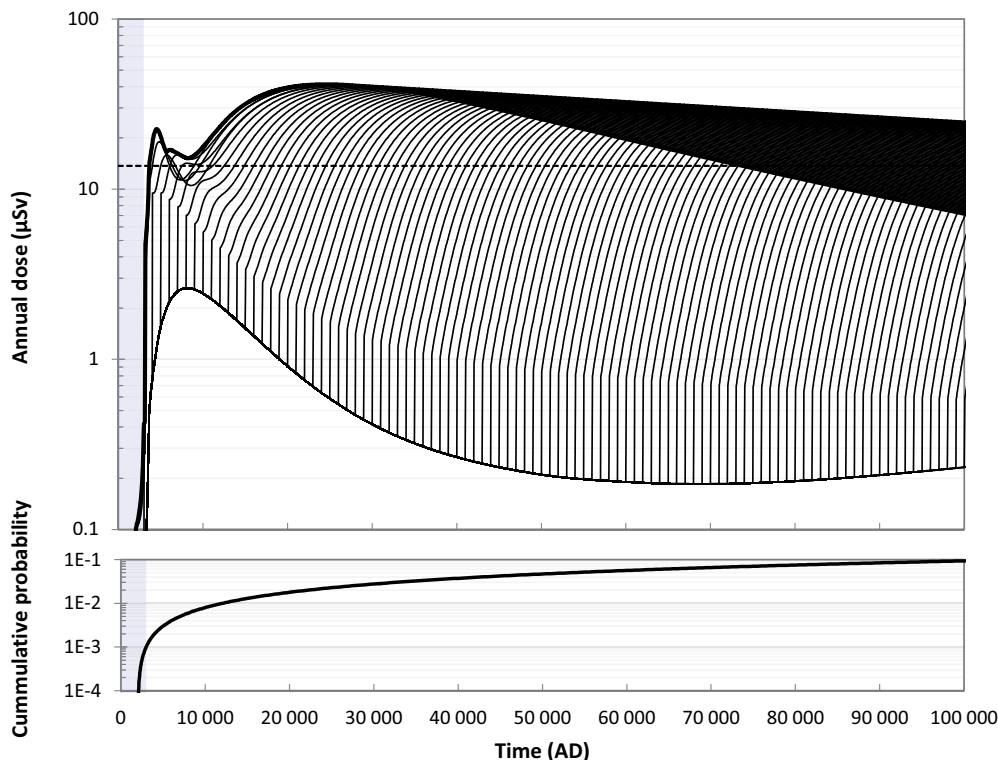


Figure 7-30. Upper panel: annual dose (μSv) to the most exposed group from releases from the silo calculated for earthquake occurring at times separated by intervals of one thousand years (thin lines) and the highest annual dose from all calculations (upper thick line) in the earthquake calculation case. The lower line shows the dose from the silo in the absence of earthquakes during the assessment period. The annual dose corresponding to the regulatory risk criterion (14 μSv) is indicated by the black dashed line. Lower panel: cumulative probability of an earthquake event. The submerged period is illustrated by the blue shading in both panels.

Radionuclide-specific doses contributing to the maximum dose for the DM group (which is the most exposed group from approximately the beginning of the terrestrial period) due to earthquake events are illustrated in Figure 7-31 and compared with the corresponding dose from the silo in the *base case*. During the first 10 000 years after closure, using a deterministic approach underestimates the dose for the most contributing radionuclides compared to using a probabilistic approach. However, as the cumulative probability of an earthquake event in this period is very low (lower panel of Figure 7-30), the magnitude of the calculated risk will be very small. The assessment of risk is discussed in the **Post-closure safety report**, Chapter 10, and will not be further discussed in this report.

After approximately the first 10 000 years after closure, Ni-59 contributes most to the total dose. Most of the Ni-59 activity is retained or has decayed in the silo in the *base case* (99.9 % over the whole assessment period). The elevated doses from Ni-59 after an earthquake are thus caused by a rapid release of the remaining inventory due to the assumed lack of sorption. In addition, since Ni-59 has such a long half-life (101 000 years), the maximum dose will be similar for every earthquake event evaluated in this calculation case. Hence, the slow decrease in maximum dose, as seen in Figure 7-31, is caused mainly by radioactive decay.

Deterministic simulations of Ni-59 would have underestimated the dose consequences by roughly a factor 2, as compared to a probabilistic approach (cf. dashed and solid lines for “Total” and “Ni-59” in Figure 7-31). Additionally, as Ni-59 is also the only radionuclide contributing to the total dose after approximately 10 000 years post-closure in the deterministic approach, it further supports the validity of the chosen modelling approach.

7.5.4 Summary and conclusions

In this calculation case, radiological consequences of an earthquake on post-closure safety are evaluated. Following the methodology adopted for SAR-08 and SR-PSU, this calculation case assumes that an earthquake damages the silo concrete structure. This methodology is highly simplified and is considered to overestimate the radiological consequences of an earthquake. As a result, the maximum dose due to releases from the silo is estimated to be pessimistically high in this calculation case (41 μSv), almost 20 times higher than in the *base case* (2.4 μSv).

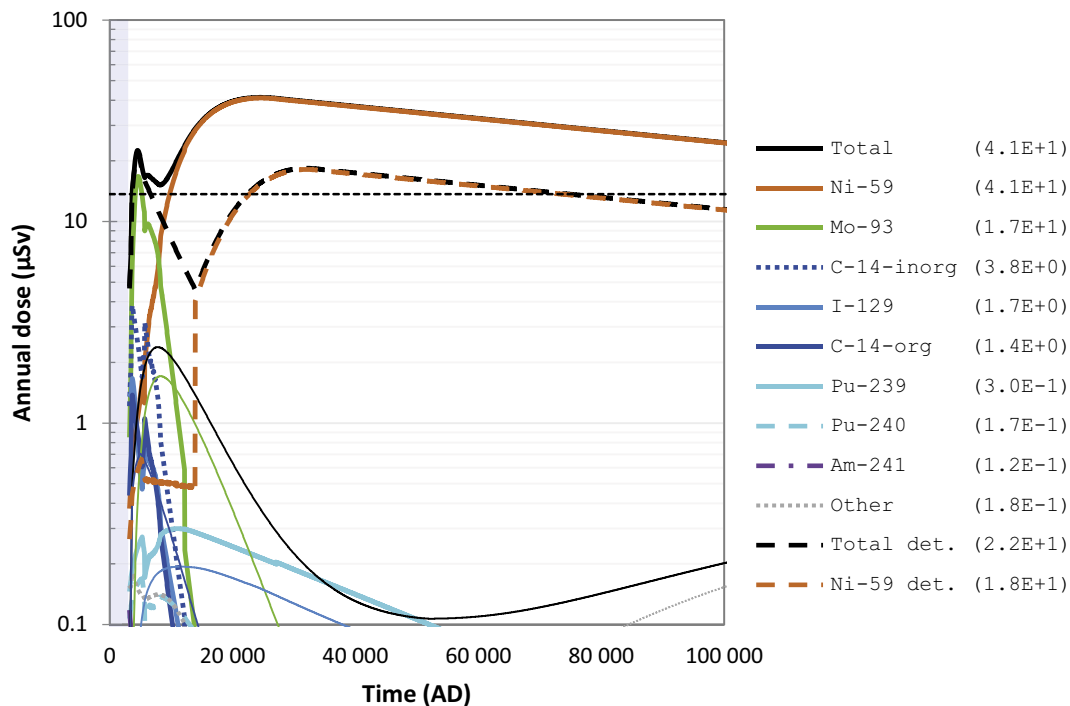


Figure 7-31. Annual dose (μSv) to the DM group from releases from the silo in the earthquake calculation case (maximum due to previous earthquake events, thick lines) and the base case (thin lines). Dashed thick lines show the dose if using a deterministic approach for Ni-59 (Ni-59 det.) as well as for the sum of all radionuclides (Total det.). The annual dose corresponding to the regulatory risk criterion (14 μSv) is indicated by the black dashed line and the submerged period is illustrated by the blue shading.

8 Calculation cases in the residual scenarios

8.1 Introduction

In addition to the main scenario and the less probable scenarios, whose calculation cases are presented in Chapters 5, 6 and 7, residual scenarios are also selected and analysed. Primarily, the residual scenarios aim to illustrate the significance of individual barriers and barrier functions and how they contribute to the protective capability of the repository. Furthermore, the scenarios are selected to contribute to discussion of the robustness of the repository regarding the protection of human health. To this end, the scenarios may include hypothetical assumptions that are associated with a low degree of realism or events with exceptionally low likelihood of occurrence. The residual scenarios comprise sequences of events and conditions that are selected and studied independently of probabilities, and the results are thus not considered in the assessment of risk in the **Post-closure safety report**, Chapter 10.

The general advice to SSM's regulations gives recommendations on how to select the residual scenarios; this is further described in the **Post-closure safety report**, Section 9.2 together with the approach for selecting the scenarios. This chapter presents the calculation cases that are selected to analyse the identified residual scenarios; these are:

- Hypothetical early permafrost scenario (Section 8.2).
- Loss of engineered barrier function scenario (Section 8.3).
- Loss of geosphere barrier function scenario (Section 8.4).
- Alternative radionuclide inventory scenario (Section 8.5).
- Oxidising conditions scenario (Section 8.6).
- Initial concrete cracks scenario (Section 8.7).
- Unrepaired IBMA scenario (Section 8.8).
- Unsealed repository scenario (Section 8.9).

Note that scenarios addressing inadvertent future human actions (FHA) are also classified as residual scenarios. These include actions potentially resulting in changes to the barrier system, affecting, directly or indirectly, the rate of the release of radionuclides from SFR. Radioactive waste being brought to the surface giving rise to exposure to people at the surface is also addressed. Four FHA scenarios are selected: the *drilling into the repository scenario*, the *intrusion well scenario*, the *water management scenario* and the *underground construction scenario*. These are presented in the **FHA report** and are not addressed further here.

Each scenario is evaluated in one or several calculation cases. The resulting releases and doses for the calculation cases are compared with the *base case* with regards to contributions from different waste vaults and radionuclides. The calculation cases in the residual scenarios are analysed with probabilistic calculations in the same way as the calculation cases in the main scenario, with the exception for the *unsealed repository calculation case*. As this calculation case is highly simplified and pessimistic, it is considered appropriate to apply only deterministic calculations.

8.2 Hypothetical early permafrost

8.2.1 General description and external conditions

The *hypothetical early permafrost scenario* is developed to evaluate the significance of individual barriers and barrier functions independently of probabilities under the hypothetical assumption of permafrost development and freezing of engineered barrier structures within the first 50 000 years after closure. To this end, the scenario is based on the early periglacial variant of the main scenario in the SR-PSU. However, owing to its very low likelihood of occurrence (**Climate report**, Section 4.3) and its demonstrated low impact on annual dose in the SR-PSU (SKB TR-14-01, Brandefelt et al. 2016, Näslund et al. 2017a, b), an early period of permafrost development is analysed as a residual scenario rather than in the main scenario in the present safety assessment (see further the **Post-closure safety report**, Section 9.3).

The development of external conditions is described by the hypothetical early permafrost climate case (**Climate report**, Section 5.4.1). The timing and duration of the early periglacial period in this climate case are inferred from the SR-PSU supplementary study of Näslund et al. (2017b). Based on this study, the evolution of climate domains is identical to the *base case* with the exception of a hypothetical periglacial period between 12 000 AD and 17 000 AD (Figure 8-1)²⁶.

The *hypothetical early permafrost scenario* is evaluated in two calculation cases.

In the first calculation case, *no effect on engineered barriers calculation case*, the periglacial climate is assumed to be sufficiently cold to result in freezing of the bedrock, yet warm enough to maintain unfrozen conditions in the engineered barriers. This calculation case is evaluated in two variants, identical to those of the *cold climate calculation case* (Section 6.3), i.e. the *permafrost with talik* variant and the *continuous permafrost* variant.

The second calculation case, *effect on engineered barriers calculation case*, represents a hypothetical situation in which the properties of the engineered barriers are significantly affected by early freezing. This calculation case is also evaluated in two variants. In the *frozen concrete* variant, freezing of the concrete pore water is assumed, resulting in a complete physical degradation of the structural concrete in the repository. The other variant, *bentonite degradation*, assumes that an ice-lens is formed in the silo bentonite, causing damage that lasts throughout the subsequent temperate period.

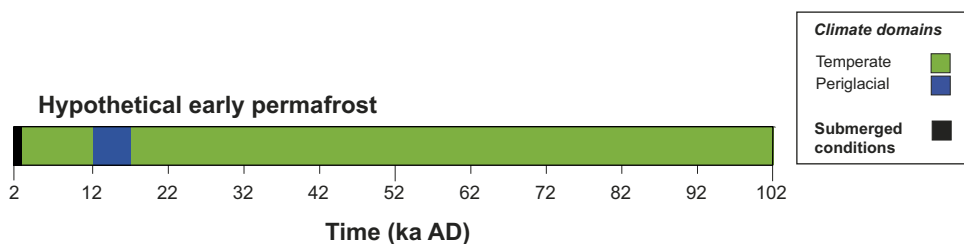


Figure 8-1. Succession of climate domains in the hypothetical early permafrost scenario.

²⁶ The periglacial periods of the last 50 000 years of the assessment period in Näslund et al. (2017b), originally developed for the SR-PSU global warming climate case, are for simplicity omitted in this scenario. Radiological consequences of periglacial periods within the last 50 000 years of the assessment period are analysed in the *cold climate calculation case* (Section 6.3).

8.2.2 Description of the calculation cases

Both calculation cases are identical to the *base case* up until the onset of the periglacial period at 12 000 AD. The handling in the modelling of the periglacial and subsequent temperate period is described in the following for each of the calculation cases.

No effect on the engineered barriers

The handling in all radionuclide transport models during periglacial conditions is identical to the corresponding variants of the *cold climate calculation case* (Section 6.3). The handling during the subsequent temperate period follows that of the *base case*.

Effect on engineered barriers

In both variants, the handling in the geosphere and biosphere is the same as in the *continuous permafrost* variant of the *cold climate calculation case*. The handling in the near-field models is summarised for each variant separately in the following.

Frozen concrete – Following Näslund et al. (2017b), the concrete barriers are assumed to transition to a completely degraded state (i.e. hydraulic conductivity is $K = 10^{-3}$ m/s; see Table 5-1) due to freezing at the onset of the periglacial period (12 000 AD). As the concrete degrades, the diffusion-available porosity of the concrete barrier and radionuclide diffusivities change. The hydraulic conductivity, porosity and diffusivity values are, from this point in time until the end of the assessment period, assumed to be identical to those of the *base case* for the period 52 000–102 000 AD. Chemical degradation of cementitious materials, and thus changes in K_d values, are also adopted from Näslund et al. (2017b), see Table 8-1.

Bentonite degradation – The hydraulic properties of the bentonite around the silo are assumed to deteriorate due to the formation of an ice-lens in the bentonite during the periglacial period, with the consequences of higher groundwater flow in the silo during the subsequent period of temperate climate conditions. A set of water flux parameters has been calculated specifically for the ice-lens case in the detailed modelling of the near-field hydrology (Abarca et al. 2020). In this variant, radionuclide release calculations are performed using these specific water fluxes for the silo. The other vaults are modelled as in the *continuous permafrost* variant of the *cold climate calculation case*.

Table 8-1. Evolution of chemical concrete degradation states in the *continuous permafrost with frozen concrete calculation case*, adopted from Table 4-4 in Näslund et al. (2017b). For the period up until 12 000 AD, the chemical degradation is identical to the *base case*. The different chemical degradation states are described in Section 5.3.1 and the associated K_d -values are given in Tables 7-4 to 7-7 of the Data report.

Time (AD)	12 000–22 000	22 000–27 000	27 000–58 000	58 000–95 000	95 000–102 000
1BMA	II	II	II	II	IIIa
2BMA	II	II	II	II	IIIa
Silo	I	I	II	II	II
1BTF	II	IIIa	IIIa	IIIb	IIIb
2BTF	II	IIIa	IIIa	IIIb	IIIb
1BRT	II	IIIa	IIIa	IIIb	IIIb

8.2.3 Results

Radionuclide releases from the near-field and the geosphere and doses to humans are identical to the *base case* up until 12 000 AD. Similar to the *cold climate calculation case*, doses during periglacial conditions, in both calculation cases, are more than one order of magnitude below the doses in the *base case* at the corresponding time (Figure 8-2). The reason is mainly that hunting and gathering is the only possible exposure pathway during periglacial conditions, and this generally results in lower doses than cultivation and well water usage (Section 6.3.6).

The largest differences between the calculation cases evaluated in this scenario are seen during the post-periglacial temperate period, i.e. after 17 000 AD. Therefore, this period is discussed separately for each calculation case below.

No effect on engineered barriers

When farming is possible again during the subsequent temperate period, drained mire (DM) doses in object 157_2 exceed the doses during the periglacial period by more than one order of magnitude. In the *permafrost with talik* variant, the transport of radionuclides to the talik during the periglacial period results in doses that are somewhat lower than in the *base case* during the subsequent temperate period (Figure 8-2). A similar result was also obtained for the corresponding variant in the *cold climate calculation case* (Section 6.3.6).

In the *continuous permafrost* variant, doses during the post-periglacial temperate period are marginally higher than in the *base case*. This is in contrast to the corresponding variant of the *cold climate calculation case*, for which the doses during the subsequent temperate period were found to be slightly lower than in the *base case* (Section 6.3.6). In both variants, releases of radionuclides from the near-field are interrupted during the periglacial period, resulting in a higher remaining inventory of radionuclides in the waste vaults and, thus, in higher annual releases at the onset of the subsequent temperate period than during the corresponding time in the *base case*. The change in total dose during the subsequent temperate period is then broadly determined by whether or not these higher releases, together with potential ingrowth of decay products, can be compensated for by the lack of accumulation in the biosphere during the periglacial period. While the effect of ingrowth during periglacial conditions generally results in elevated doses from decay products during the subsequent temperate period, this effect is also reportedly small (Section 6.3.6) and qualitatively similar for both variants. The slightly higher doses during the post-periglacial temperate period in this variant than the corresponding variant of the *cold climate calculation case* is instead, at least partially, attributed to the shorter duration of the periglacial period (5 000 years versus 8 000 years), during which accumulation in the biosphere ceases and radionuclides may decay in the near-field and the geosphere. Moreover, the lack of groundwater flow under periglacial conditions results in a higher radionuclide inventory remaining in the near-field that is released during the subsequent temperate period. In the *continuous permafrost* variant of this calculation case, the higher remaining inventory is also combined with degradation of the concrete barriers during the initial 50 000 years, resulting in a further increase of the radionuclide releases. This effect is not present in the *cold climate calculation case* as all concrete barriers have completely degraded before the onset of the first periglacial period (61 000 AD).

Effect on engineered barriers

The effect of concrete degradation on the total dose is evaluated in the *frozen concrete* variant of the *effect on engineered barriers calculation case*. In this variant, the enhanced degradation of the concrete barriers results in elevated doses for the entire post-periglacial temperate period compared with the *no effect on engineered barriers calculation case* and, thus, also the *base case* (Figure 8-2). The highest dose during the post-periglacial temperate period is obtained a few thousand years after the periglacial period, when it is approximately 30 % higher than in the *base case* at the corresponding time. The highest dose during this period, however, is well below the maximum dose at about 7 000 AD (same as in the *base case*; Figure 8-2). The radionuclides that contribute most to the increased dose after the periglacial period in this calculation case are primarily Ca-41 and Ni-59 (Figure 8-3). These radionuclides dominate the dose in the *base case* after 20 000 AD (Figure 5-54) and this is partly a result of concrete degradation in that calculation case (Sections 5.3 and 5.7). The enhanced concrete degradation in the *frozen concrete* variant of this calculation case leads to a higher accumulation of these radionuclides in the biosphere, and thus to higher doses, than in the *base case*.

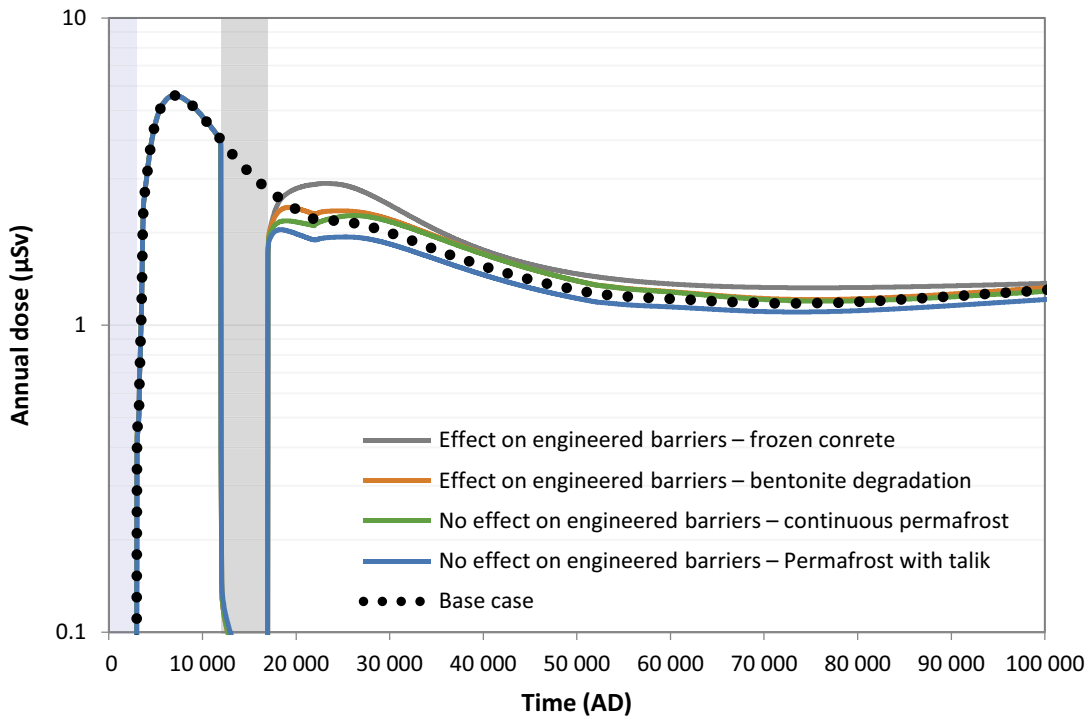


Figure 8-2. Annual dose (μSv) to the most exposed group for the calculation cases in the hypothetical early permafrost scenario (solid lines) and the base case (dotted line). The submerged and the periglacial periods are illustrated by the blue and grey shadings, respectively. The most exposed group is HG during the periglacial period and DM during periods of temperate-terrestrial conditions (see further Section 6.3). Note that the time is presented on a linear scale.

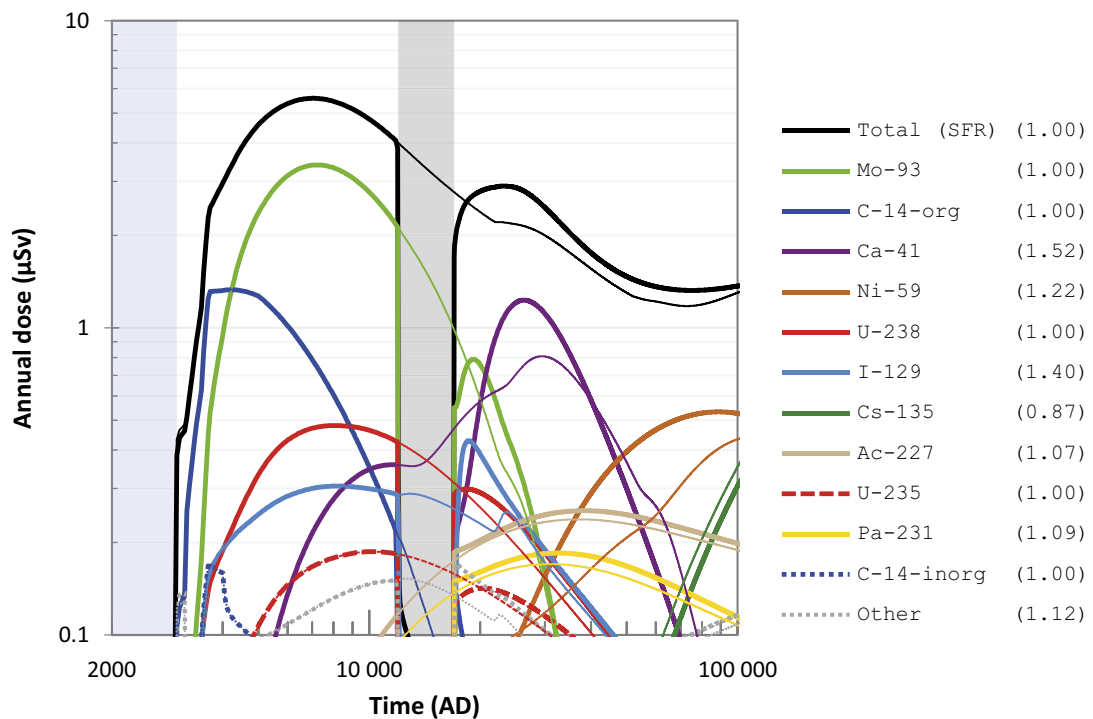


Figure 8-3. Annual dose (μSv) to the most exposed group (black line), including radionuclide specific contributions (coloured lines), in the frozen concrete variant of the effect on engineered barriers calculation case (thick lines) and the base case (thin lines). The combined contribution from radionuclides not shown is indicated by the grey dotted line. The ratio between the maximum doses in the present calculation case and the base case are shown in parentheses in the key. The submerged period is illustrated by the blue shading and the periglacial period by the grey shading.

The effect of a hypothetical ice-lens on the hydraulic properties of the silo bentonite is evaluated in the *bentonite degradation* variant of the *engineered barriers calculation case*. In this variant, doses are slightly higher than in the *base case* due to the increased groundwater flow in the silo. The highest dose during the post-periglacial temperate period is obtained at about 20 000 AD, when it is approximately 10 % higher than during the corresponding time in the *base case*. This increase is mainly due to an increased release of Mo-93. However, the highest dose during the post-periglacial period is still much lower than the maximum dose at around 7000 AD.

8.2.4 Summary and conclusions

In this scenario, radiological consequences of hypothetical periglacial conditions between 12 000 AD and 17 000 AD at Forsmark are evaluated in two calculation cases. The first calculation case, *no effect on engineered barriers*, assumes that the periglacial climate does not result in freezing of the engineered barriers, i.e. it is similar to the *cold climate calculation case* evaluated in Section 6.3. The second calculation case, *effect on engineered barriers calculation case*, assumes that periglacial conditions will result in freezing of the repository concrete structures or in the formation of an ice-lens in the silo bentonite. The calculation cases are developed based on the results from the SR-PSU assessment, including its complementary studies (SKB TR-14-01, Brandefelt et al. 2016, Näslund et al. 2017a, b).

In both calculation cases, doses are identical to the *base case* until the onset of the periglacial period at 12 000 AD, at which point they drop by more than one order of magnitude compared with the preceding temperate period. A large difference in dose between periglacial and temperate conditions was also obtained in the *cold climate calculation case* and is explained mainly by differences in exposure pathways (Section 6.3). During the post-periglacial temperate period, doses again increase to levels comparable to those during the corresponding time in the *base case*. The maximum dose is about 30 % higher during this period compared with the corresponding time in the *base case* and occurs as a consequence of the enhanced concrete degradation considered in the *effect on engineered barriers calculation case*. However, the maximum dose during the post-periglacial temperate period in this calculation case is well below the maximum dose before the periglacial period, thereby confirming the main conclusion from Näslund et al. (2017b).

8.3 Loss of engineered barrier function

8.3.1 General description

The aim of the *loss of engineered barrier function scenario* is to illustrate how the engineered barriers contribute to the protective capability of the repository (**Post-closure safety report**, Section 9.4). To this end, two calculation cases are selected to analyse the importance of sorption and hydraulic barriers in the repository:

- *No sorption in the repository calculation case.*
- *No hydraulic barriers in the repository calculation case.*

The importance of cracks in the repository concrete is evaluated specifically in the *initial concrete cracks calculation case* (Section 8.7).

8.3.2 No sorption in the repository calculation case

The *no sorption in the repository calculation case* is selected to illustrate the importance of sorption in the repository. This is done by setting sorption coefficients for all radionuclides in the near-field materials to zero. This change affects releases from all vaults apart from the BLA-vaults, for which sorption is not credited (Section 2.4.4). Other than setting the K_d values to zero, all other input data used in the near-field models, the geosphere model and the biosphere model are identical with the *base case*.

Annual release from the near-field

As expected, assuming no sorption results in an increased release from the near-field of most radionuclides (Figure 8-4). In general, radionuclides that exhibit strong sorption in the *base case* are most affected. This means that Ni-59 and C-14-inorg dominate the release from SFR in this calculation case (Figure 8-4). The relatively short-lived radionuclide Ni-63, with a half-life of 100 years, has the third largest annual release. In addition, the release of Pu-239 is significantly higher.

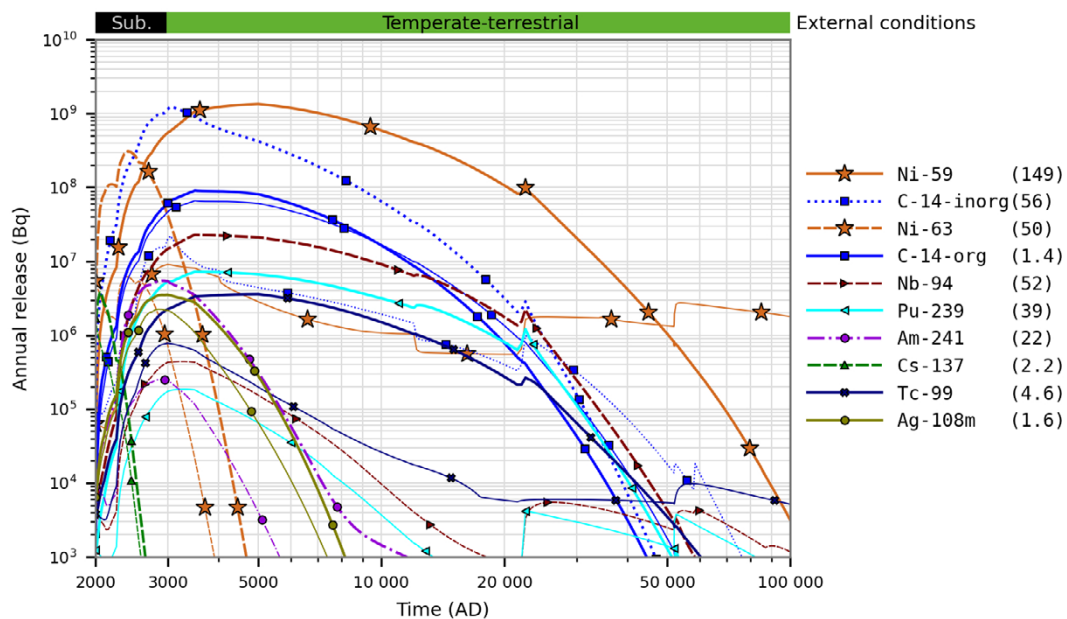


Figure 8-4. Annual activity releases (Bq) from the entire SFR in the no sorption in the repository calculation case (thick lines) and the base case (thin lines). The ratio between the maximum releases in the present calculation case and the base case are shown in parentheses in the key. Coloured horizontal bar (top) shows the evolution of the external conditions.

The releases of Ni-59 and C-14-inorg increase from all waste vaults affected in this calculation case (i.e. all except the BLA vaults). However, the largest increases are found in the silo, 1BMA and 2BMA (Figure 8-5) with these waste vaults contributing most to the increase in the total release of these radionuclides in Figure 8-4.

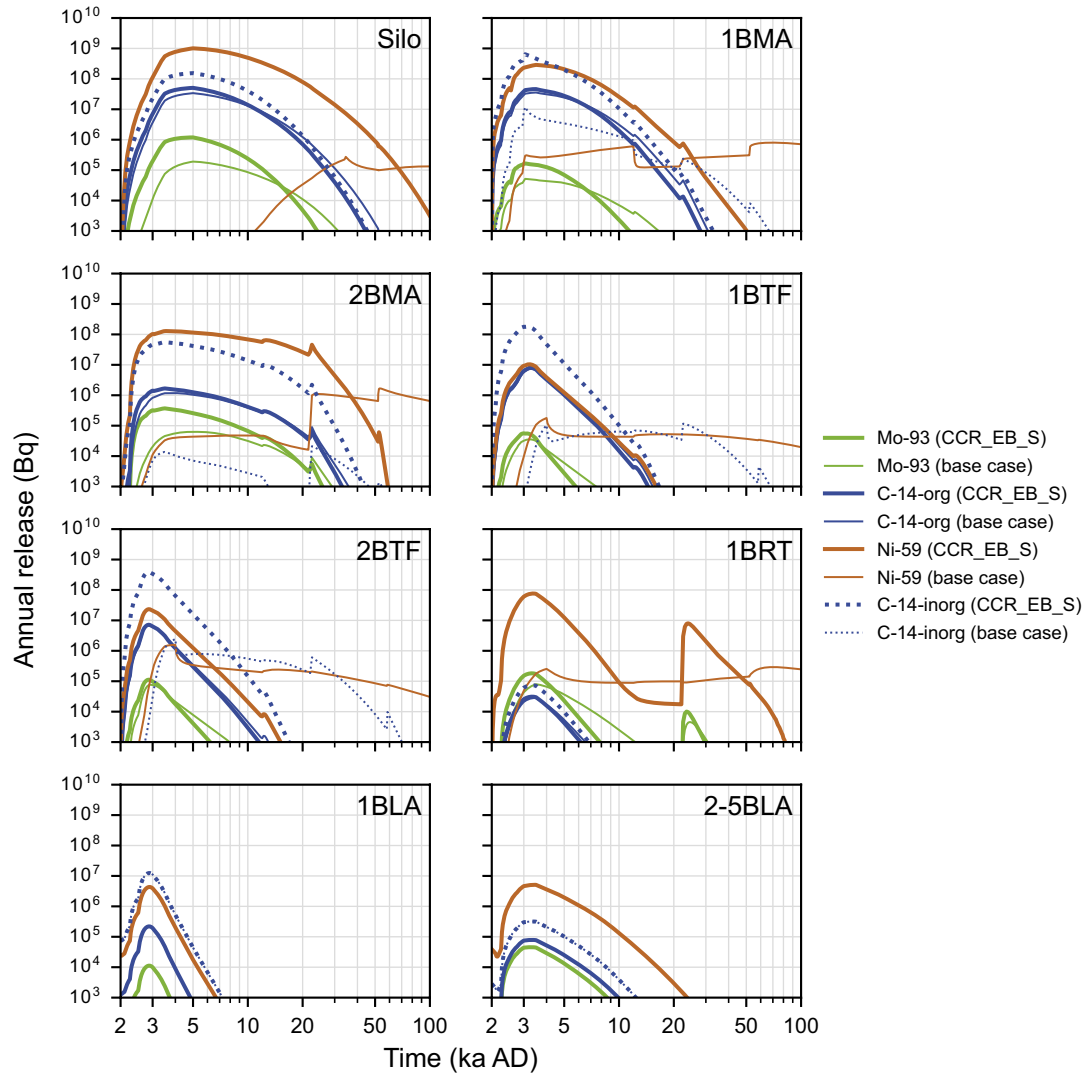


Figure 8-5. Annual activity releases (Bq) from waste vaults in SFR for selected radionuclides in the no sorption in the repository calculation case (thick lines) and the base case (thin lines). Note that for 2-5BLA the sum of the releases from all four vaults is shown in the figure.

Annual dose

Assuming no sorption in the near-field results in a total annual dose that is significantly higher than in the *base case*, with the maximum dose being almost one order of magnitude higher than the maximum dose in the *base case* (Figure 8-6). Mo-93 contributes most to the dose during the first ~10 000 years in the *base case* and it has a significant contribution during this time in this calculation case too.

As a result of the increased releases from the waste vaults of Ni-59 (Figure 8-5), this radionuclide contributes most to the total dose in this calculation case (Figure 8-6). Owing to its long half-life (101 000 years) and long transport times in the biosphere (Section 5.7.2), the dose from Ni-59 increases towards to the end of the assessment period. As a result, the total maximum dose occurs significantly later in this calculation case (~30 000 AD) than in the *base case* (~7 000 AD).

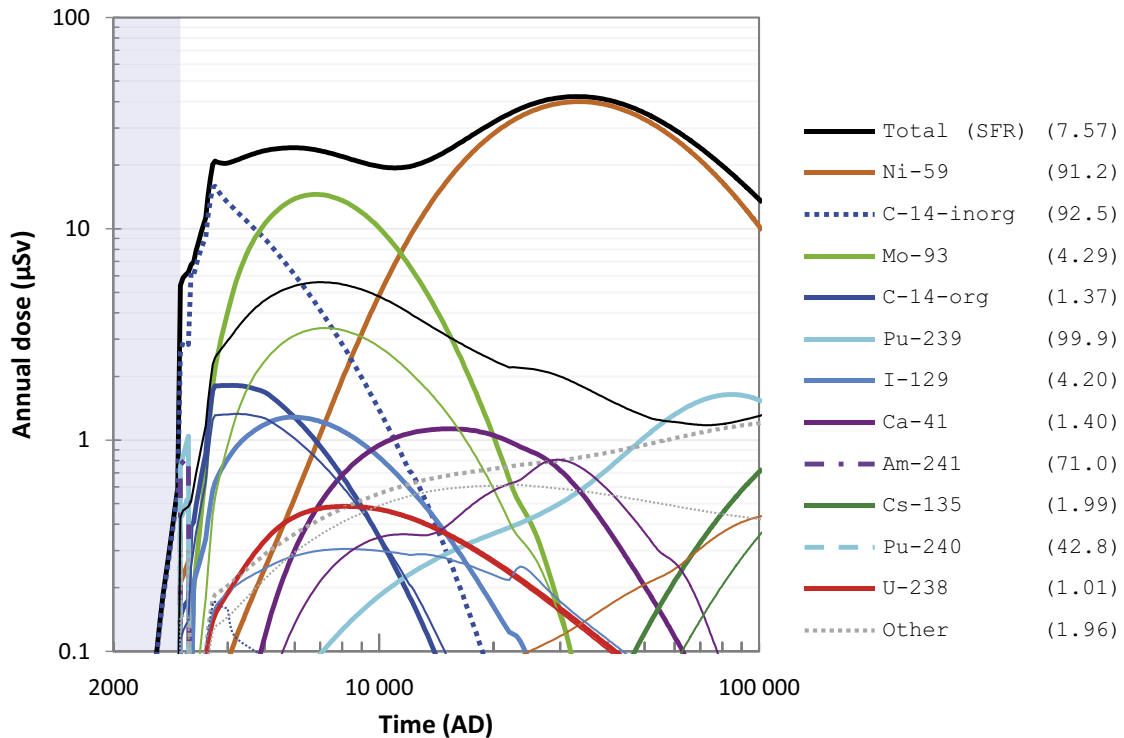


Figure 8-6. Annual dose (μSv) to the most exposed group (black line), including radionuclide specific contributions (coloured lines), in the no sorption in the repository calculation case (thick lines) and the base case (thin lines). The combined contribution from radionuclides not shown is indicated by the grey dotted line. The ratio between the maximum doses in the present calculation case and the base case are shown in parentheses in the key. The submerged period is illustrated by the blue shading.

8.3.3 No hydraulic barriers in the repository

The *no hydraulic barriers in the repository calculation case* is selected to illustrate the importance of the engineered barriers capability for limiting the groundwater flow through the waste. In this calculation case, the near-field water flow from the “no barriers” case in the hydrological calculations (Abarca et al. 2020) is used during the whole assessment period. The groundwater flow is calculated assuming no resistance to flow due to concrete and bentonite barriers in the vault structures. Furthermore, the effect of tunnel closure plugs is neglected. Other conditions, including sorption, are the same as in the *base case*.

Annual release from the near-field

Similar to the *no sorption in the repository calculation case*, release from the repository increases significantly for most radionuclides in this calculation case. The increased release from SFR is primarily dominated by Ni-59, C-14-org and C-14-inorg. However, for sorbing radionuclides, the chemical barrier function still limits the releases to some extent. The hydraulic barrier function is of greater importance for e.g. the silo and 1–2BMA than 1BRT, because the release of radionuclides from 1BRT is largely limited by the steel corrosion rate. Since the BLA vaults have no internal barriers, only the plugs influence this calculation for the BLA vaults and releases from 1–5BLA increase by only about a factor of two. The early releases of Ni-59, Mo-93 and C-14-org from most vaults increase significantly as shown in Figure 8-8. Thus, the radionuclides that contribute most to the maximum dose in the *base case*, i.e. Mo-93 and C-14-org, are more strongly affected in this calculation case than in the *no sorption in the repository calculation case*.

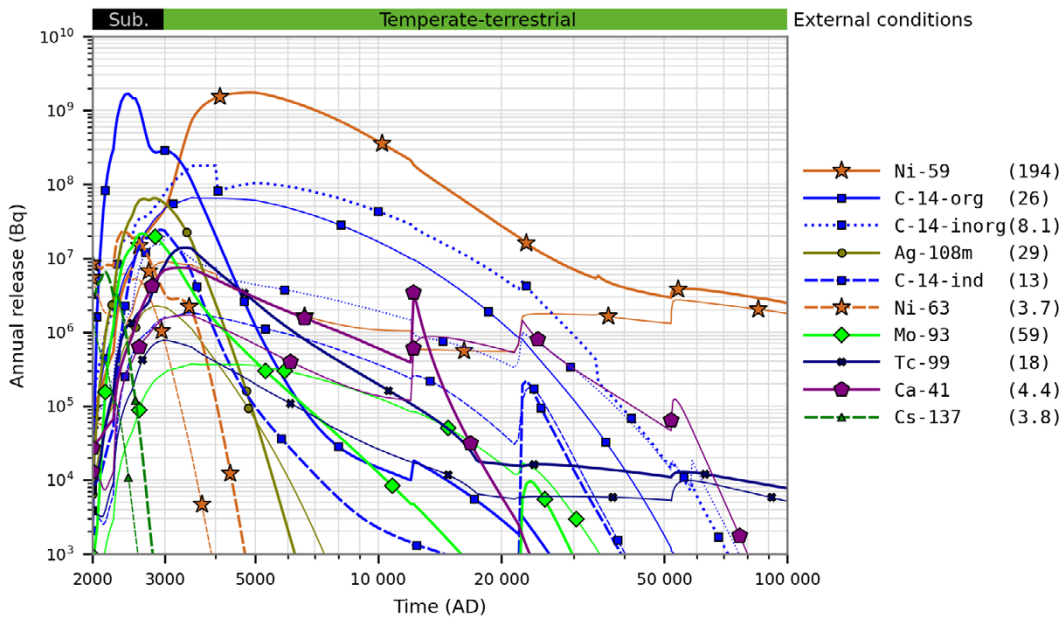


Figure 8-7. Annual activity releases (Bq) from the entire SFR in the *no hydraulic barriers in the repository calculation case* (thick lines) and the *base case* (thin lines). The ratio between the maximum releases in the present calculation case and the base case are shown in parentheses in the key. Coloured horizontal bar (top) shows the evolution of the external conditions.

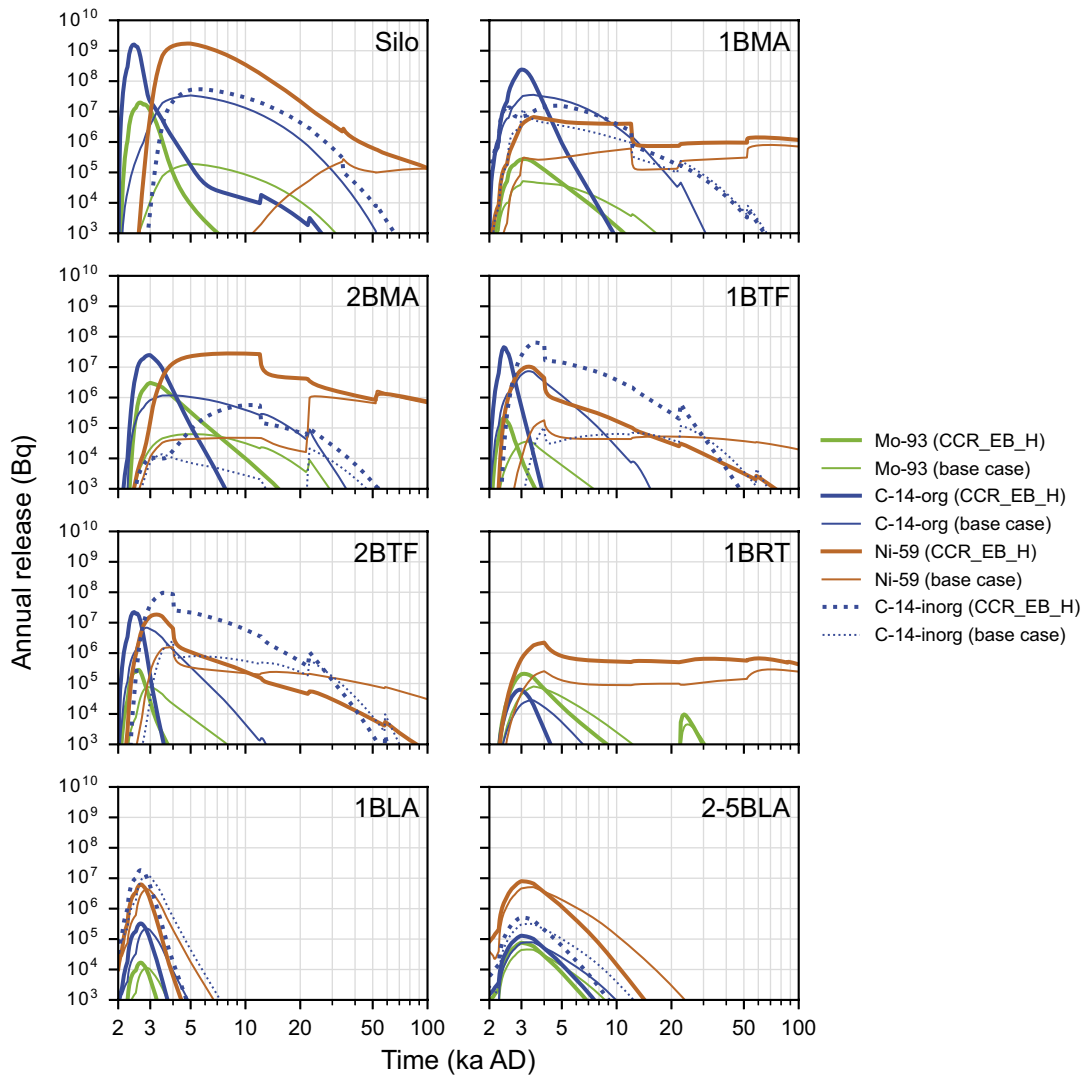


Figure 8-8. Annual activity releases (Bq) from waste vaults in SFR for selected radionuclides in the no hydraulic barriers in the repository calculation case (thick lines) and the base case (thin lines). Note that for 2-5BLA the sum of the releases from all four vaults is shown in the figure.

Annual dose

Assuming no hydraulic barriers in the near-field results in a total annual dose that is more than one order of magnitude higher than the maximum dose in the *base case* (Figure 8-9). As with the *no sorption in the repository calculation case*, there is a significant increase of the dose from Ni-59 in this calculation case too, particularly towards the end of the assessment period. In contrast to the *no sorption in the repository calculation case*, however, Ni-59 contributes less to the total maximum dose in this calculation case. The reason is that the release of Mo-93 from the near-field is significantly higher in this calculation case (Figure 8-8). As a result, Mo-93 contributes most to the maximum dose and it occurs much earlier than in the *no sorption in the repository calculation case* (Figure 8-9).

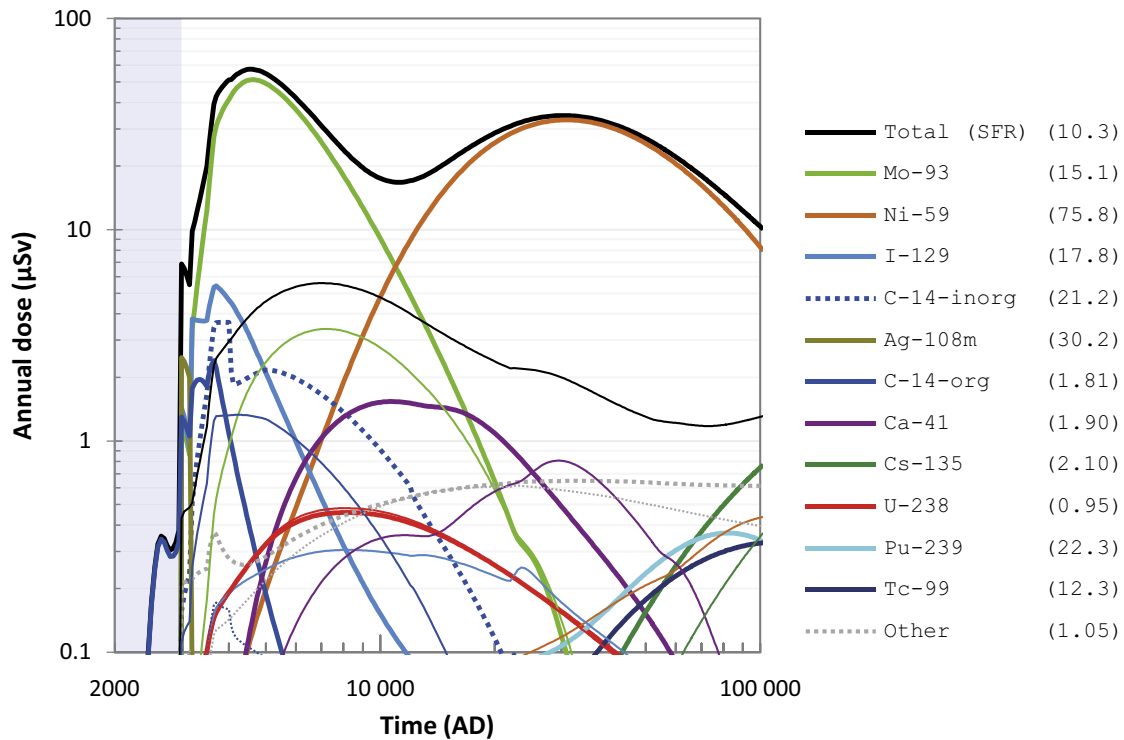


Figure 8-9. Annual dose (μSv) to the most exposed group (black line), including radionuclide specific contributions (coloured lines), in the *no hydraulic barriers in the repository calculation case* (thick lines) and the *base case* (thin lines). The combined contribution from radionuclides not shown is indicated by the grey dotted line. The ratio between the maximum doses in the present calculation case and the base case are shown in parentheses in the key. The submerged period is illustrated by the blue shading.

8.3.4 Summary and conclusions

The *loss of engineered barriers scenario* illustrates the significance of the engineered barriers for the protective capability of the repository. To this end, two calculation cases were evaluated: *no sorption in the repository calculation case* and *no hydraulic barriers in the repository calculation case*.

Both calculation cases result in doses about one order of magnitude higher than the *base case* (Figure 8-10). However, the *no hydraulic barriers in the repository calculation case* gives a significantly higher dose initially, mainly due to a large release of the weakly sorbing radionuclide Mo-93, whereas the *no sorption in the repository calculation case* yields the highest doses later in the assessment period due to an increased release of the strongly sorbing radionuclide Ni-59.

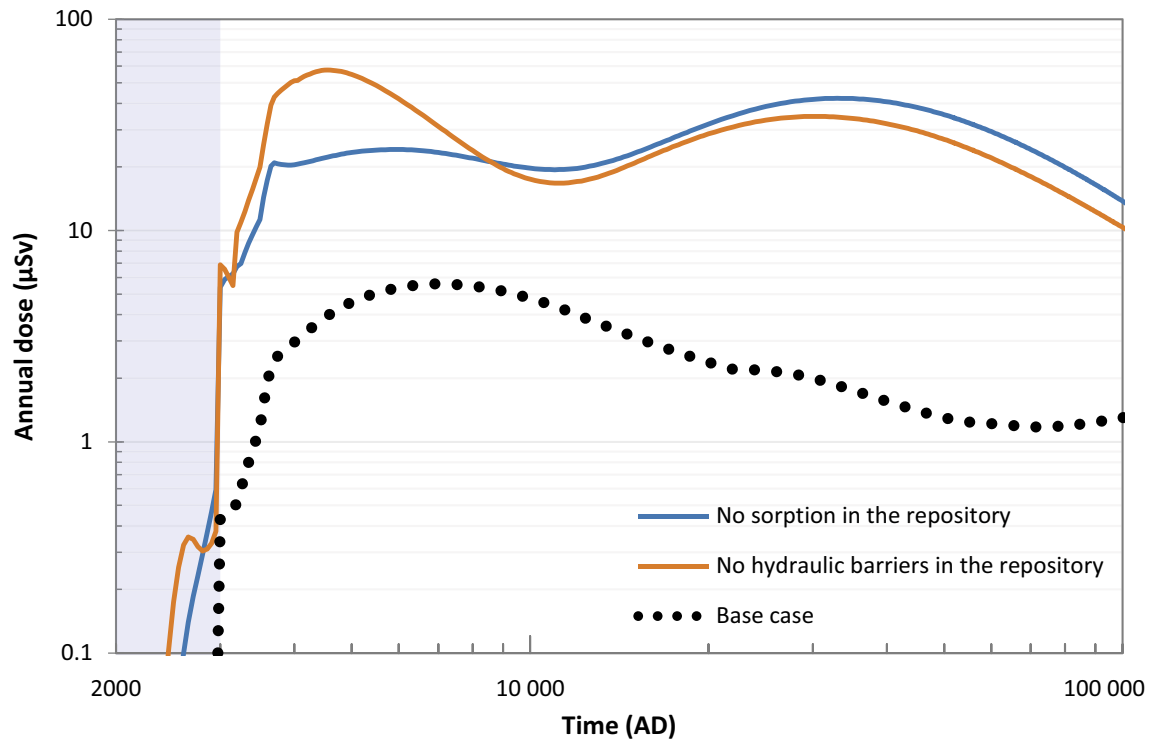


Figure 8-10. Annual dose (μSv) to the most exposed group for the calculation cases the loss of engineered barrier function scenario (solid lines) and the base case (dotted line). The submerged period is illustrated by the blue shading. Note that the timescale is presented on a linear scale.

Figure 8-11 and Figure 8-12 provide summaries of the performance of the near-field in the case of *no sorption in the repository* and *no hydraulic barriers in the repository*, respectively, for those radionuclides substantially affected (release increased more than five times, to a level of at least 1 000 Bq) by these cases. The vertical bars show how much of the initial activity is released from the near-field during the assessment period, i.e. the accumulated release divided by the initial activity, in the present case and in the *base case*.

The quotient of accumulated releases between the calculation cases and the *base case* (black dots) show that Ni-59 is strongly affected in terms of accumulated release, with almost 50 times larger accumulated release in the present cases.

As expected, the non- or weakly sorbing radionuclides e.g. C-14-ind, C-14-org and Se-79 (not shown in Figure 8-11) are unaffected or almost unaffected in the *no sorption in the repository calculation case*, but significantly affected in the *no hydraulic barriers calculation case* (Figure 8-12).

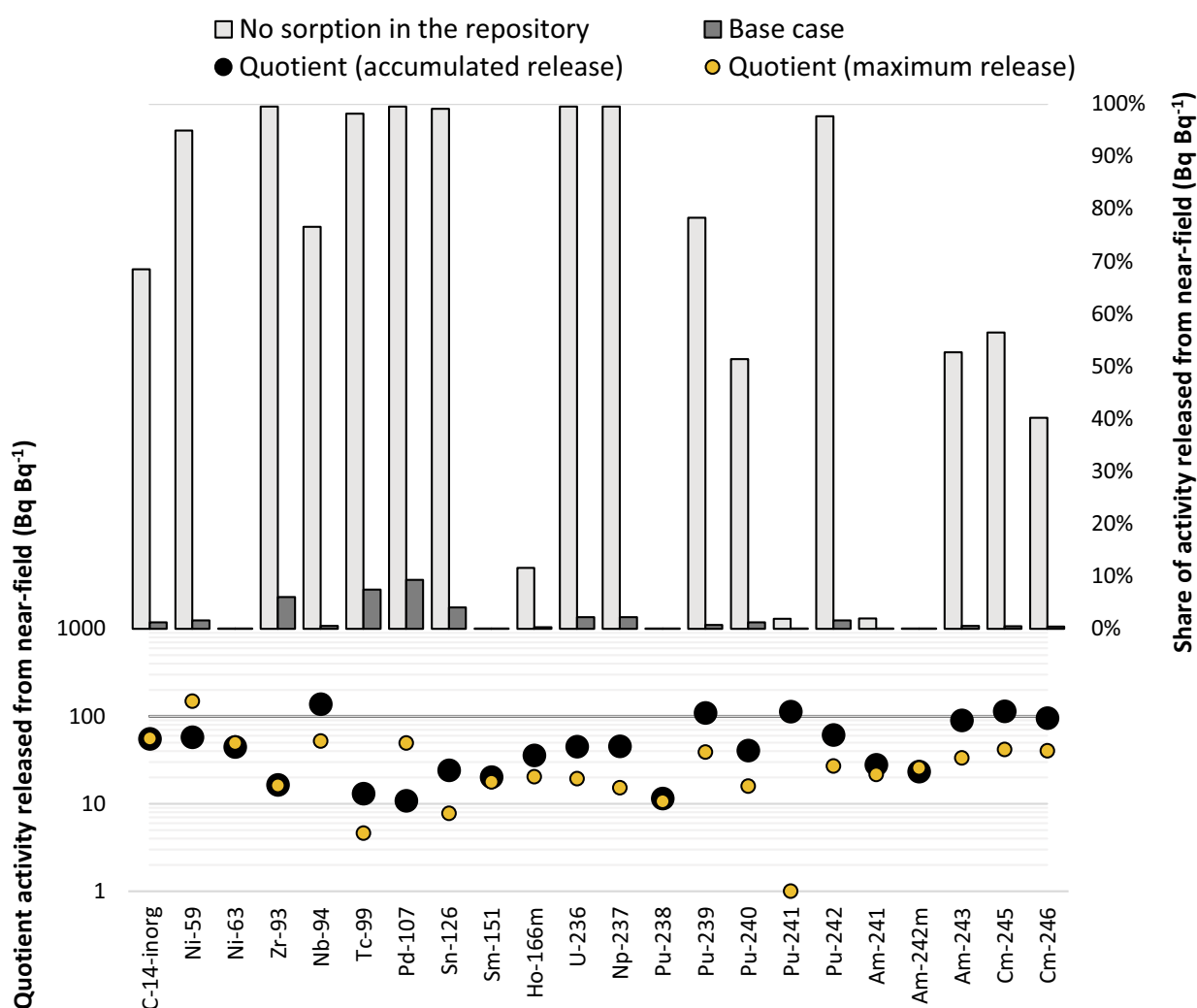


Figure 8-11. Summary of activity releases from the near-field in the *no sorption in the repository* calculation case in comparison with the *base case*. Upper panel: fraction of each radionuclide's initial activity released at the end of the assessment period, for the present case and the *base case*. Lower panel: quotients between cases for accumulated (black dots) and maximum (yellow dots) release, respectively.

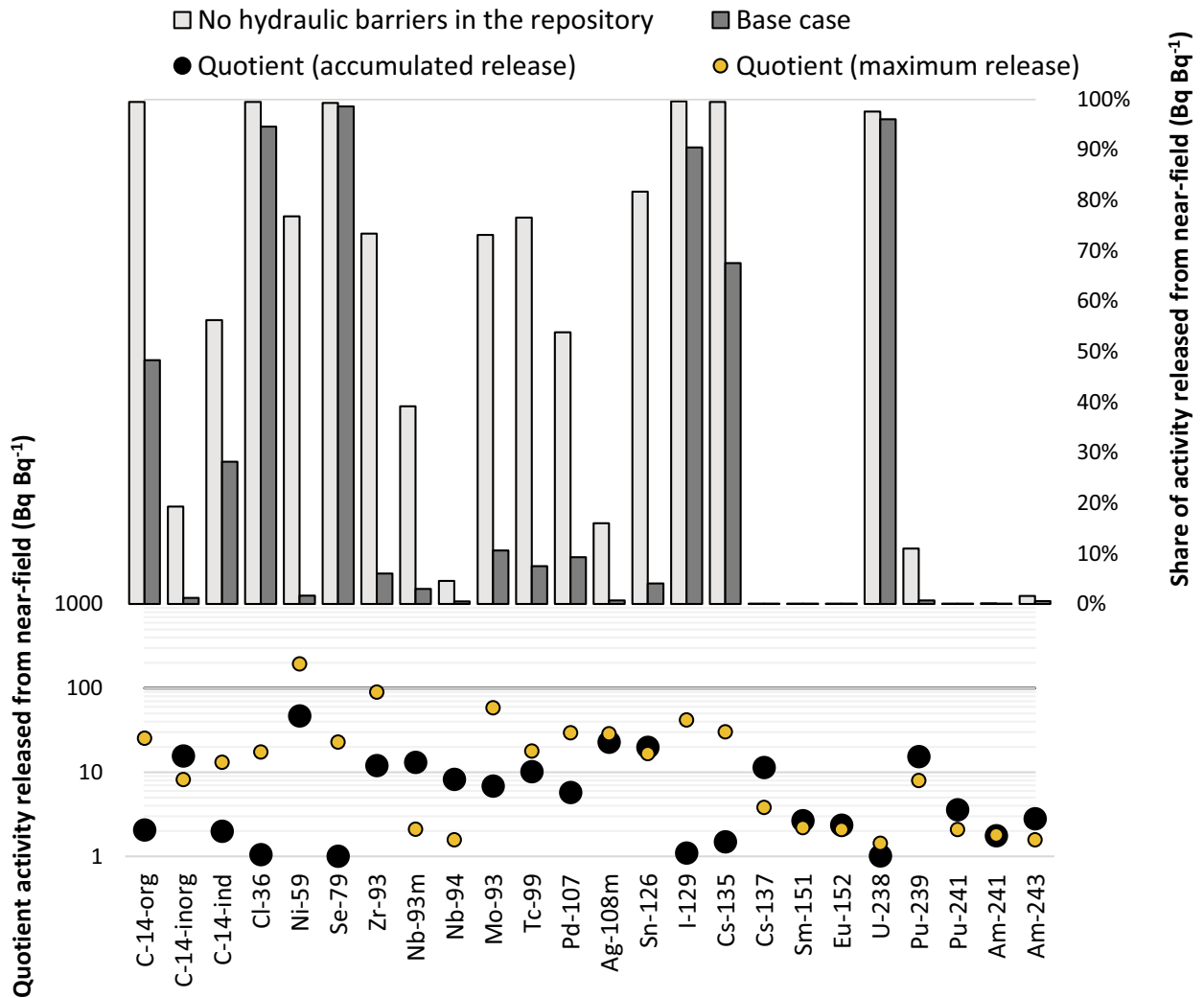


Figure 8-12. Summary of activity releases from the near-field in the no hydraulic barriers in the repository calculation case in comparison with the base case. Upper panel: fraction of each radionuclide's initial activity released at the end of the assessment period, for the present case and the base case. Lower panel: quotients between cases for accumulated (black dots) and maximum (yellow dots) release, respectively.

8.4 Loss of geosphere barrier function

8.4.1 General description

The aim of the *loss of geosphere barrier function scenario* is to illustrate how the geosphere contributes to the protective capability of the repository (**Post-closure safety report**, Section 9.5). To this end, two calculation cases are evaluated to illustrate the importance of sorption in the bedrock matrix and the full effect of the geosphere retention, respectively.

The calculation cases are:

- *No sorption in the geosphere calculation case.*
- *No transport retention in the geosphere calculation case.*

These calculation cases focus only on radionuclide transport through the geosphere and the resulting doses under the assumption of neglecting sorption or retention in the geosphere. The effects of the geosphere barrier on the near-field release, e.g. by creating favourable conditions in terms of a low groundwater flow around (and through) the near-field and favourable chemical conditions (i.e. reducing conditions), are not considered in these calculation cases. Those aspects are instead partly evaluated in the *water management scenario* (Section 4.4 in the **FHA report**) and the *oxidising conditions scenario* (Section 8.6). Besides, changes in groundwater flow are also included in the *timing of shoreline*

regression calculation case (Section 5.8.2), the *warm climate calculation case* (Section 6.2), the *cold climate calculation case* (Section 6.3) and the calculation cases of the *hypothetical permafrost scenario* (Section 8.2). The *glaciation calculation case* (Section 7.2) includes changes in both groundwater flow and geosphere sorption.

8.4.2 Description of the calculation cases

No sorption in the geosphere

The assumption in this calculation case is that there is no sorption in the bedrock matrix, which is implemented by setting all sorption coefficients in the geosphere to zero. Aside from this change, the representation of the geosphere as well as the representations of the near-field and biosphere are identical with the *base case*.

No transport retention in the geosphere

In this calculation case, the retention in the bedrock is disregarded by setting the transport time through the geosphere to zero, i.e. the geosphere release is identical to the near-field release. All other input data in the near-field and the biosphere models are identical with the *base case*, including the geosphere properties that affect the near-field, such as hydrological conditions and redox state.

8.4.3 Results

No sorption in the geosphere

The highest doses are, as in the *base case*, received by the DM group throughout the terrestrial period, apart from the first few hundred years when a GP group with a drilled well gets higher doses (Figure 8-13). In general, total doses to the DM are somewhat higher without sorption in the geosphere than in the *base case* and the maximum total dose is about 75 % greater than in the *base case*. One reason for the relatively limited increase in total dose is that the radionuclides that dominate in the *base case* are almost unaffected by disregarding sorption in the bedrock matrix, as sorption was cautiously set to zero (C-14-org and Ca-41), close to zero (Mo-93) or relatively low (Ni-59) already in the *base case* (Section 5.5). Thus, the limited increase in dose relative to the *base case* could, to some extent, be attributed to cautious choices of sorption coefficients in that calculation case (Section 5.5).

Most radionuclides whose geosphere releases increase in the absence of sorption in the geosphere do not reach levels that influence the total dose. The main reason for the higher total doses without sorption is that the geosphere releases of U-238 and U-235 increase by more than one order of magnitude (Figure 8-14). This results in five to ten times higher doses from those uranium isotopes as well as the decay products of U-235: Pa-231 and Ac-227 (Figure 8-13). The maximum doses of those radionuclides occur earlier than in the *base case*, because of a faster transport through the geosphere in the absence of sorption. Thus, U-238 and U-235 dominate the dose before and Pa-231 and Ac-227 shortly after the total dose maximum, that is dominated by Mo-93 (as in the *base case*).

U-238 and U-235, together with Pu-238, Pu-239 and Am-241, also contribute to the exposure from the drilled well to GP during the initial terrestrial period. The dose due to exposure from a drilled well is higher than in the *base case*, but still lower than the maximum dose to DM.

No transport retention in the geosphere

The total dose and the radionuclides contributing significantly to the total dose in the *no transport retention in the geosphere calculation case* are almost identical to the *no sorption in the geosphere calculation case* (and therefore not shown in a separate figure). The reason is that the retention in the geosphere in the *base case*, apart from sorption, is caused mainly by the advective groundwater travel time through the geosphere and this time is limited. Median advective groundwater travel times through the geosphere are only a few years during terrestrial conditions after 3000 AD (Table 5-14). This time is too short to noticeably influence the release of any radionuclide that contributes to dose.

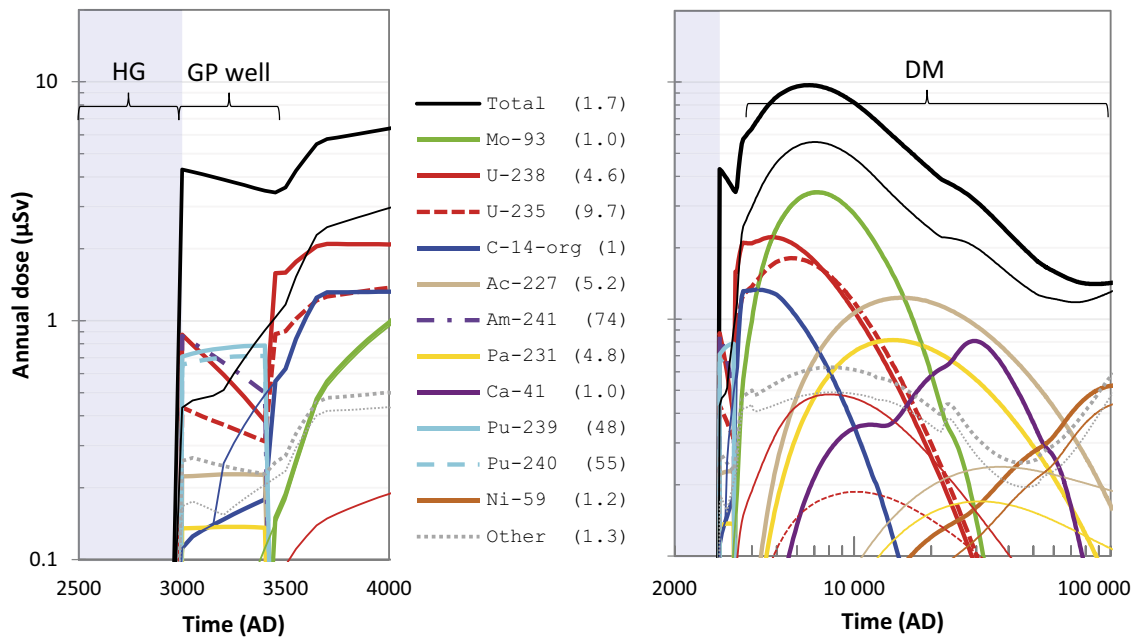


Figure 8-13. Annual dose (μSv) to the most exposed group (black line), including radionuclide specific contributions (coloured lines), in the no sorption in the geosphere calculation case (thick lines) and the base case (thin lines). The combined contribution from radionuclides not shown is indicated by the grey dotted line. The ratio between the maximum doses in the present calculation case and the base case are shown in parentheses in the key. The left panel shows doses between 2500 AD and 4000 AD with a linear scale on the time-axis. The right panel shows doses during the entire assessment period with a log-scale on the time-axis. The most exposed groups during different periods of the simulation are indicated in the upper part of the panels; HG, GP with a drilled well (GP well) and DM. The submerged period is illustrated by the blue shading in both panels.

8.4.4 Summary and conclusions

The *loss of geosphere barrier function scenario* illustrates the significance of the geosphere to the protective capability of the repository. The main conclusion from this scenario is that even if sorption and retention in the geosphere are completely neglected, the maximum annual dose is not that high ($\sim 10 \mu\text{Sv}$) and is lower than the dose corresponding to the risk criterion ($14 \mu\text{Sv}$). Another result is that the geosphere retention assumed in the *base case* has a limited effect on the total doses. Consequently, there is no risk that total doses are substantially underestimated due to overestimated rock-matrix sorption or due to underestimated advective groundwater transport rates through the geosphere.

The role of geosphere retention on specific radionuclides has been illustrated in the *base case* (Sections 5.5.2 and 5.5.3). The results from the *loss of geosphere barrier function scenario* agree with the conclusions in the *base case* (further discussed below) and provide further understanding about what the effects on doses would be if geosphere retention was lower or completely missing.

In the *base case*, four groups of radionuclides based on their properties and behaviour in the geosphere were identified (see Section 5.5.3). The first group is radionuclides with geosphere releases close to identical or slightly lower than near-field releases because of zero or relatively weak sorption in the *base case* in combination with a half-life long enough for decay in the geosphere to be insignificant (blue circles in Figure 8-14). The dose-dominating radionuclides in the *base case*, C-14, Mo-93, Ca-41 and Ni-59, all belong to this group, and they are consequently not substantially affected by excluding geosphere retention (Figure 8-13).

The second group contains sorbing radionuclides with long half-lives, for which retention in the geosphere results in dispersion (orange triangles in Figure 8-14). Dispersion means here that the near-field releases are dispersed over time within the geosphere (more details in Sections 5.5.2 and 5.5.3), so that the maximum geosphere release becomes smaller than the maximum near-field release. The effect is

most pronounced for radionuclides with a distinct near-field release peak and high geosphere retention. This group includes U-238, U-235 and Pu-239, with maximum geosphere releases and maximum doses that increase due to decreased dispersion in absence of geosphere retention.

The third group includes radionuclides with half-lives similar to or shorter than their transport time through the geosphere in the *base case*, so that decay within the geosphere decreases geosphere releases (grey diamonds in Figure 8-14). Without geosphere retention, releases of this group would consequently become greater due to a combination of decreased dispersion and less decay. For some radionuclides in this group (i.e. Pu-240 and Am-241), the greater geosphere releases result in greater doses that contribute to the total dose in the *loss of geosphere barrier function calculation cases*. Despite substantially higher geosphere releases than in the *base case* of some radionuclides within this group, especially in the *no transport retention in the geosphere calculation case* (unfilled diamonds in Figure 8-14), total doses are not affected. This is either because

- the radionuclides are associated with low near-field radiotoxicity releases, which mainly occur during the submerged period (before 3000 AD) when groundwater flow in the regolith is low, dilution in the sea basins is high, and neither exposure through a drilled well or cultivation is possible; or
- retention and decay in the till prevent transport to the regolith layers that can be cultivated.

The last group includes decay products that can be affected by both dispersion and decay, but also by ingrowth from parent radionuclides in the geosphere and in the surface system (yellow squares in Figure 8-14). Therefore, the relationship between near-field releases, geosphere releases and doses is more complex for this group. An example is that despite lower geosphere releases of Ac-227 due to less ingrowth from Pa-231 in the geosphere, in the *loss of geosphere retention barrier function calculation cases* doses from Ac-227 increase relative to the *base case* due to more ingrowth in the regolith layers.

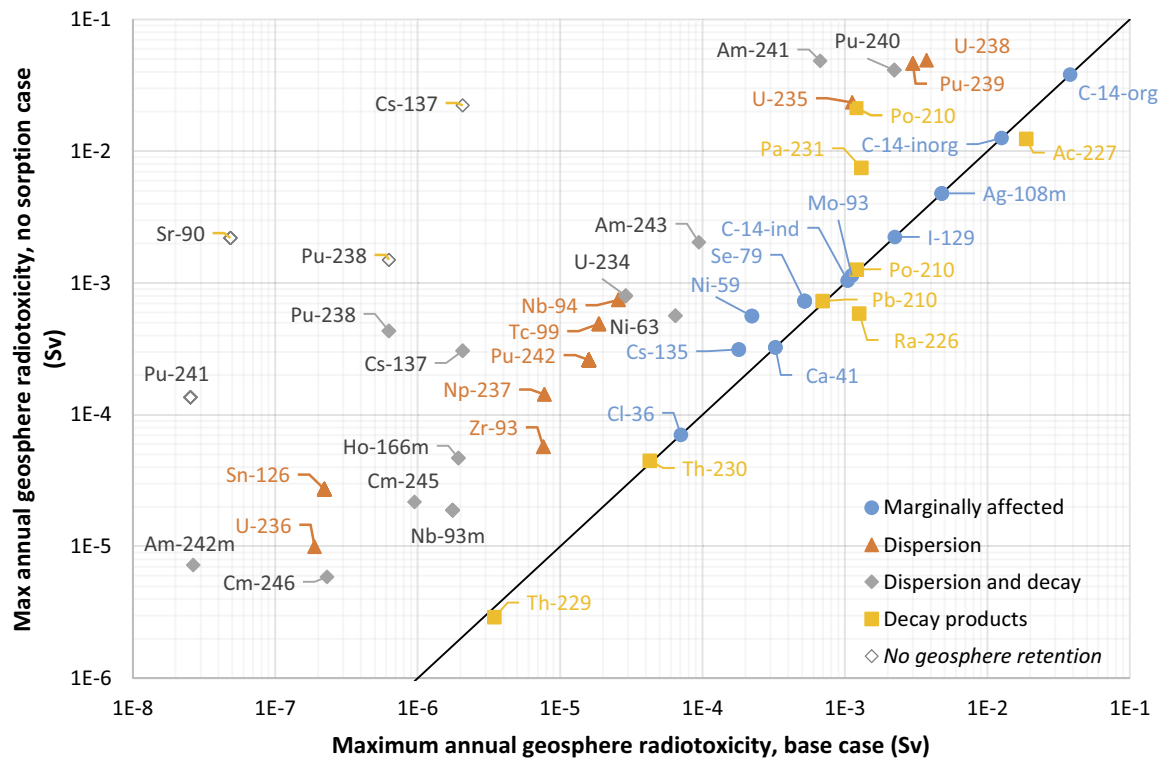


Figure 8-14. Radiotoxicity in the geosphere release in the no sorption calculation case (y-axis) in relation to the base case (x-axis). Radionuclides are broadly classified into four groups based on their base case behaviour in the geosphere (Section 5.5.3): Marginally affected by geosphere retention (blue – Group 1 of Table 5-3), affected by dispersion (orange – Group 2 of Table 5-3), affected by dispersion and decay (grey – Group 3 of Table 5-3), and decay products (yellow – Group 4 of Table 5-3) that might also be affected by ingrowth within the geosphere. Radionuclides with short half-life that have a significantly higher maximum geosphere release in the no geosphere retention case than in the no sorption calculation case are plotted as unfilled circles for comparison. The black line shows where maximum geosphere releases with and without sorption are identical.

8.5 Alternative radionuclide inventory

8.5.1 General description

The *alternative radionuclide inventory scenario* is selected to illustrate the potential effects of radionuclide inventories that deviate from those used in the main scenario. Three alternative radionuclide inventories are estimated, based on the assumptions

- that the operating times of the reactors at the nuclear power plants are prolonged,
- that fuel damage during the remaining operational period increases,
- that the use of molybdenum alloy fuel spacers is extended.

Thus, this scenario is analysed by the following three calculation cases:

- *Extended operation of reactors calculation case.*
- *Increased fuel damage frequency calculation case.*
- *Extended use of molybdenum alloy fuel spacers calculation case.*

It should be noted that the inventories used in these three cases are estimated from potential future conditions at the Swedish nuclear power plants and do not necessarily comply with the current licensing conditions given for SFR.

The main scenario handles modelling and data uncertainties in the inventory by a probabilistic approach. Probabilistic handling of the radionuclide inventory is also applied in the three calculation cases presented in this section. Further details on the probabilistic handling of the radionuclide inventory are presented in Section 3.3.4.

8.5.2 Extended operation of reactors

The calculation case evaluates the effects of prolonged operation of the remaining reactors from 60 to 80 years, which affects only future waste and sites that are still in operation (including Clab) (**Data report**, Chapter 4.5.1). The increase in waste volume that a prolonged operation could give rise to is not considered. This is a cautious assumption as the amount of sorbing materials in the waste is underestimated²⁷. Hence, only the change in radioactivity is evaluated in this alternative inventory. All other properties of the modelling are handled in the same way as in the *base case*, i.e. the extension of the operating time of the reactors is here not assumed to affect the time of repository closure.

Radionuclide inventory

Figure 8-15 shows a comparison of the inventory in SFR in the *extended operation of reactors calculation case*, compared with the *base case* (for affected radionuclides). The figure shows the total radionuclide inventory in SFR. The details of the inventory for different vaults and waste types are presented in the **Data report**, Tables 4-1 and 4-2.

Doses

Figure 8-16 shows the total dose in the *extended operation of reactors calculation case*. The radionuclide-specific doses are higher than in the *base case* with an extended operation of the reactors as is the total dose. However, the increase of the maximum dose is relatively small, amounting to less than 20 % higher than in the *base case* for most radionuclides.

²⁷ This calculation does not consider possible addition of more complexing agents, this is likely an insignificant omission as the dose-dominating radionuclides are not significantly affected by complexing agents (Section 7.3). In addition, the increased volume of waste is not considered in this calculation case.

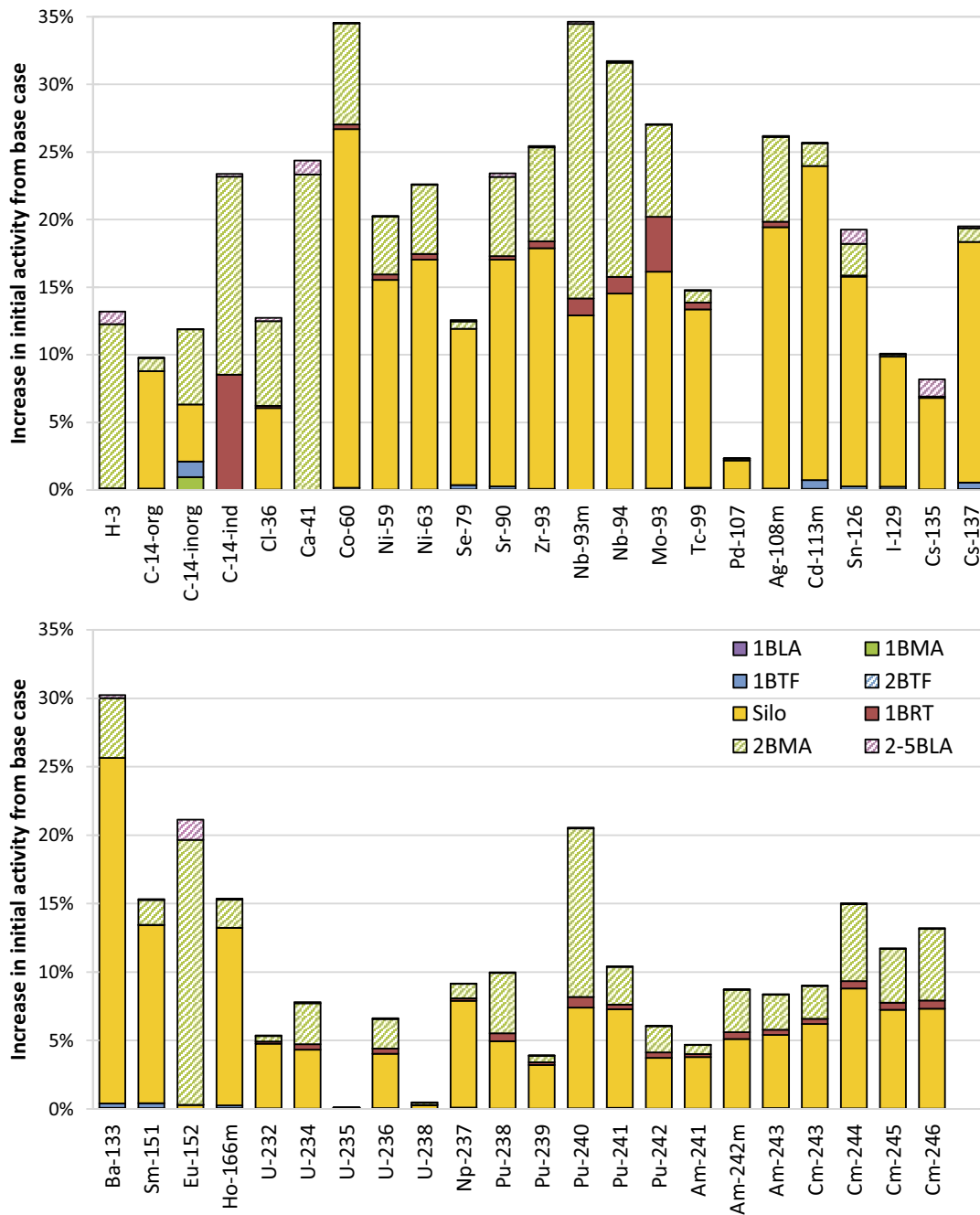


Figure 8-15. Increase of the total initial radionuclide inventory in SFR in the extended operation of reactors calculation case compared with the base case.

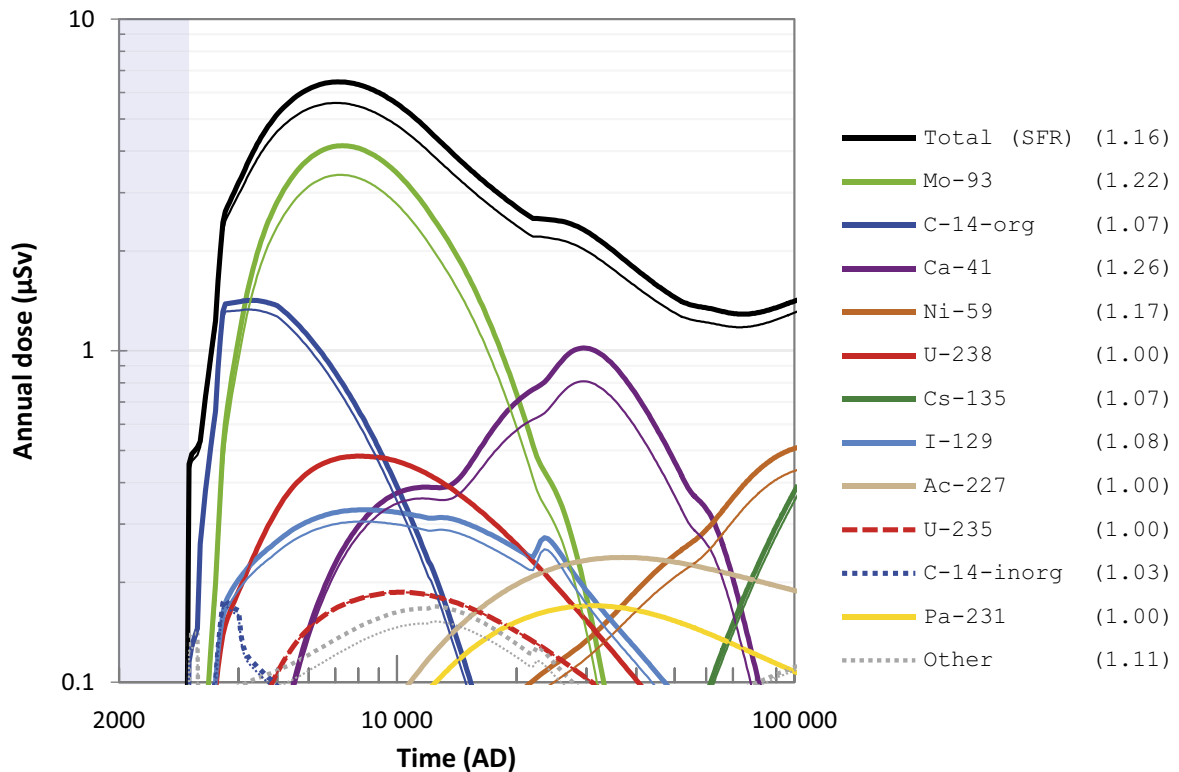


Figure 8-16. Annual dose (μSv) to the most exposed group (black line), including radionuclide specific contributions (coloured lines), in the extended operation of reactors calculation case (thick lines) and the base case (thin lines). The combined contribution from radionuclides not shown is indicated by the grey dotted line. The ratio between the maximum doses in the present calculation case and the base case are shown in parentheses in the key. The submerged period is illustrated by the blue shading.

8.5.3 Increased fuel damage frequency

The calculation case evaluates potential effects of increased fuel damage frequency during the remaining operation of the reactors, which affects only future waste and sites that are still in operation (including Clab). Radionuclides related to fuel and fission in both forecasted operational waste as well as decommissioning waste, most importantly I-129 and Cs-135, are assumed to be affected (**Data report**, Section 4.5.2).

Radionuclide inventory

For this alternative inventory, the activity of radionuclides related to fuel and fission is increased by a factor of 10. The increase in activity is not applied to waste that has already been disposed in SFR. Figure 8-17 shows a comparison of the inventory in SFR between the *increased fuel damage frequency calculation case* and the *base case* (for affected radionuclides). The figure shows the total radionuclide inventory in SFR. The details of the inventory for different vaults and waste types are presented in the **Data report**, Tables 4-3 and 4-4.

Doses

Figure 8-18 shows the total doses in the *increased fuel damage frequency calculation case*. The increased inventory of I-129 contribute most to the increased doses in this calculation case. The total maximum dose is however only about 15 % higher than in the *base case*, even with increased fuel damage frequency.

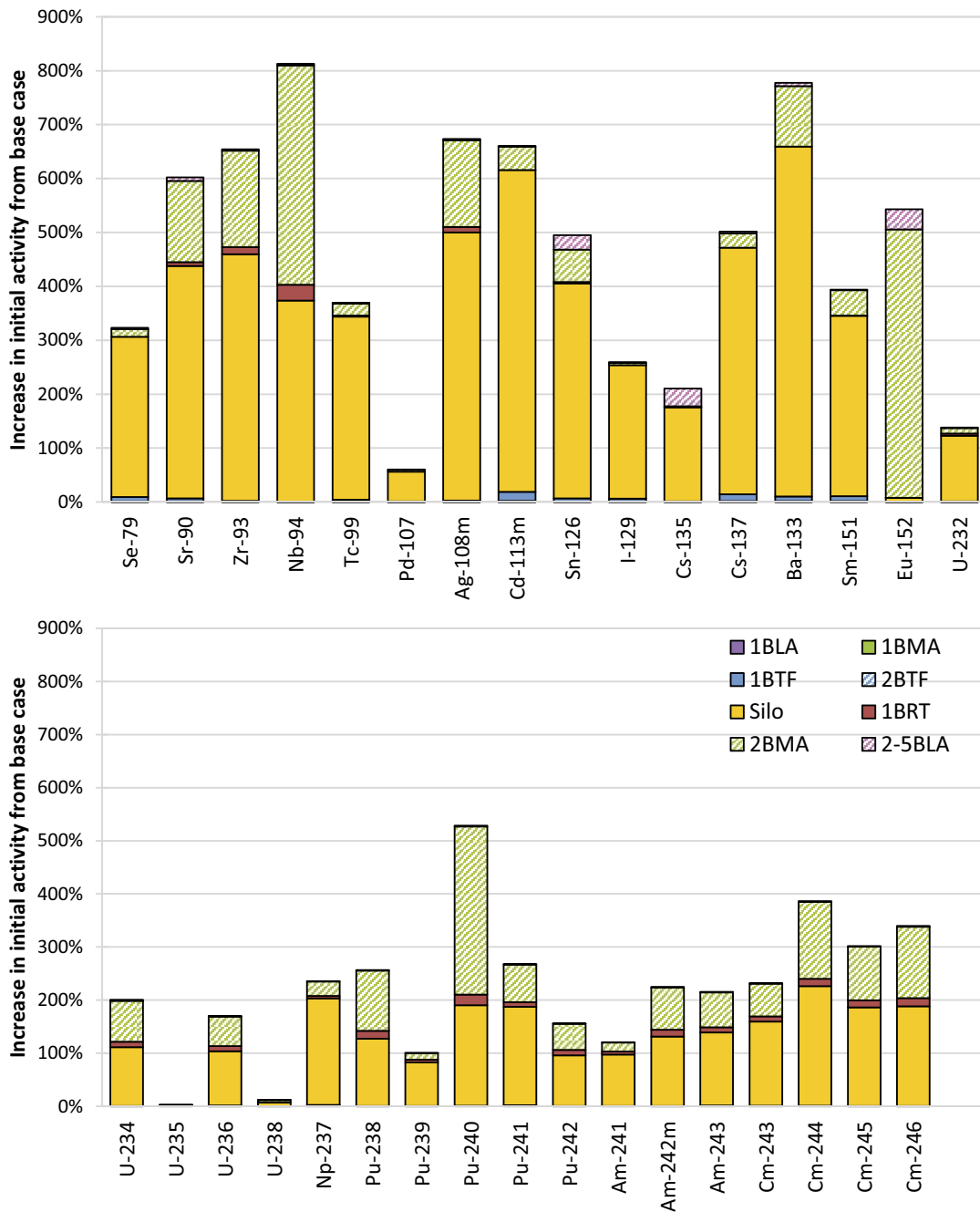


Figure 8-17. Increase of the total radionuclide inventory in SFR in the increased fuel damage frequency calculation case compared with the base case.

8.5.4 Extended use of molybdenum alloy fuel spacers

The calculation case, analysing the effects of extended use of molybdenum alloy fuel spacers, affects only future waste from sites with BWRs still in operation, as well as Clab (**Data report**, Section 4.5.3).

Radionuclide inventory

Figure 8-19 shows a comparison of the Mo-93 inventory in each vault and for the whole SFR between the *extended use of molybdenum alloy fuel spacers calculation case* and the *base case*. The details of the inventory for different vaults and waste types are presented in the **Data report**, Tables 4-5 and 4-6.

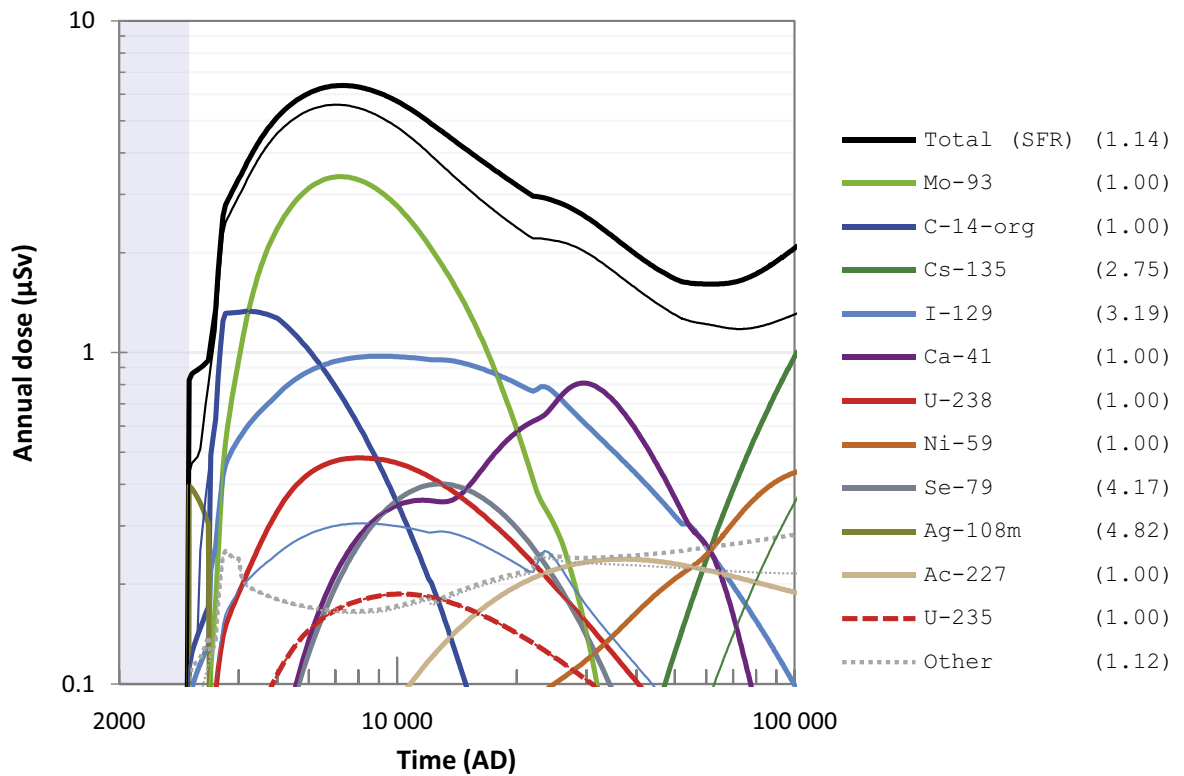


Figure 8-18. Annual dose (μSv) to the most exposed group (black line), including radionuclide specific contributions (coloured lines), in the increased fuel damage frequency calculation case (thick lines) and the base case (thin lines). The combined contribution from radionuclides not shown is indicated by the grey dotted line. The ratio between the maximum doses in the present calculation case and the base case are shown in parentheses in the key. The submerged period is illustrated by the blue shading.

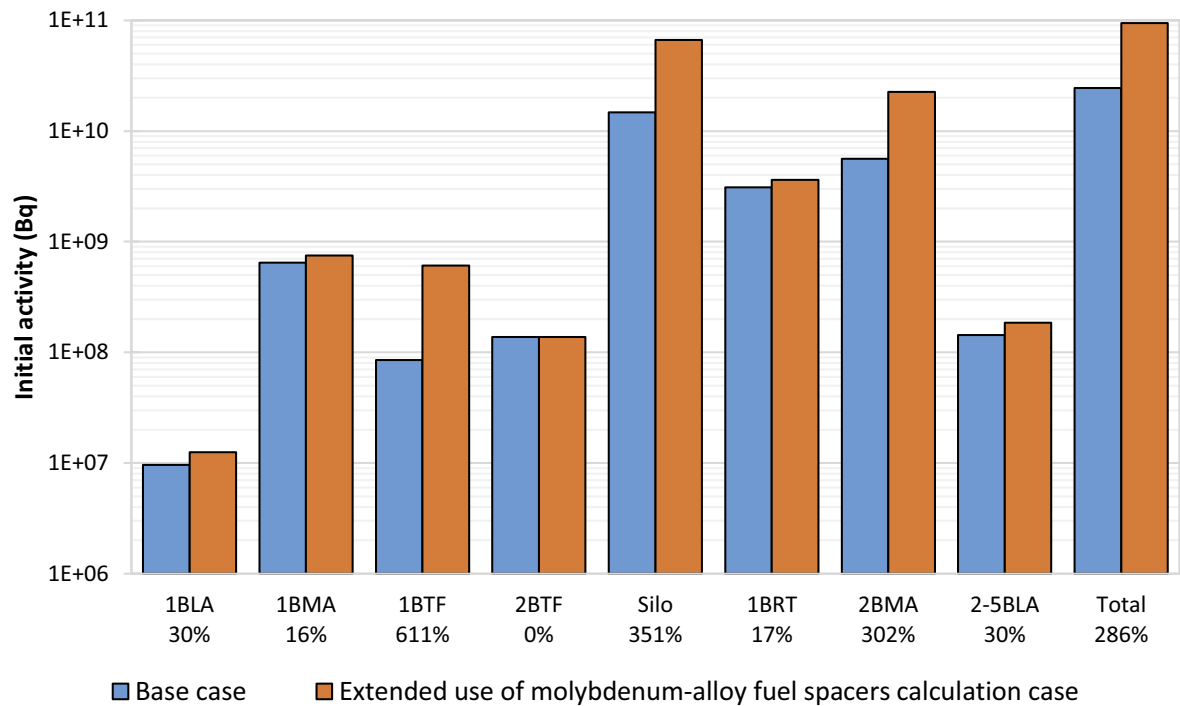


Figure 8-19. Comparison of Mo-93 radionuclide inventory in each vault and the total inventory in SFR in the extended use of molybdenum alloy fuel spacers calculation case (orange bars) and the base case (blue bars). The numbers below the vault labels show the ratios between the inventory in the present case and the base case.

Annual dose

Figure 8-20 shows the total dose from SFR in the *extended use of molybdenum alloy fuel spacers calculation case*. The increase in the inventory leads to a maximum dose from SFR that is almost three times higher than the corresponding dose in the *base case*. Thus, the maximum dose in this calculation case is similar to the dose corresponding to the risk criterium (14 μSv). Apart from the effect on Mo-93, a very small effect can be seen for its decay product Nb-93m (included among “Other” in Figure 8-20), although the effect of this is insignificant for the total dose.

8.5.5 Summary and conclusions

This scenario illustrates the potential effects of radionuclide inventories estimated for a selection of changes in operational conditions at the Swedish nuclear power plants. These conditions are that the operation time of the nuclear power plant reactors are extended by 20 years, that the fuel damage frequency during the remaining operational period increases and that the use of molybdenum alloy fuel spacers is extended. The results show that extended operation time and increased fuel damage only have a minor impact on the resulting maximum dose, about 15 % increase. The inventory of Mo-93 due to extended use of molybdenum alloy fuel spacers has a larger impact on the dose, leading to a maximum dose that is almost three times higher than the maximum dose in the *base case*.

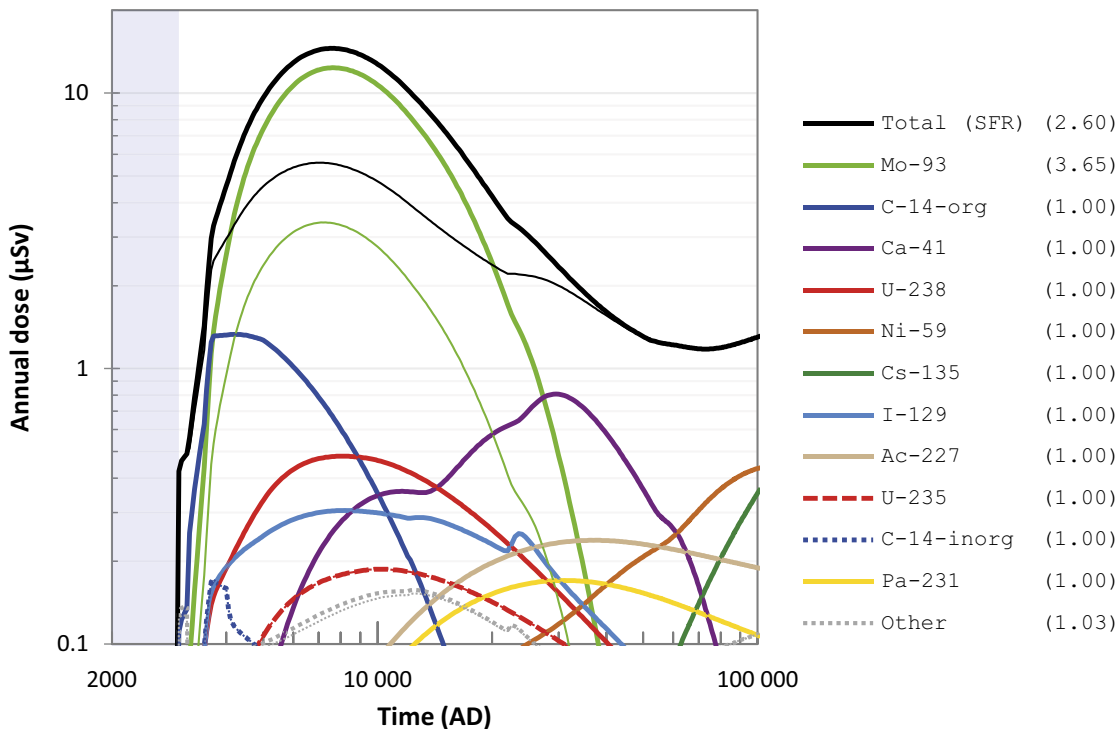


Figure 8-20. Annual dose (μSv) to the most exposed group (black line), including radionuclide specific contributions (coloured lines), in the *extended use of molybdenum alloy fuel spacers calculation case* (thick lines) and the *base case* (thin lines). The combined contribution from radionuclides not shown is indicated by the grey dotted line. The ratio between the maximum doses in the present calculation case and the base case are shown in parentheses in the key. The submerged period is illustrated by the blue shading.

8.6 Oxidising conditions

8.6.1 General description

The aim of the *oxidising conditions scenario* is to illustrate how redox conditions in the repository and the bedrock contribute to the protective capability of the repository. To this end, one calculation case, the *oxidising conditions calculation case*, is selected to evaluate the hypothetical assumption of oxidising conditions throughout the assessment period. The assumption is applied to the near-field and the geosphere, whereas the biosphere is configured as in the *base case*. The same assumptions for the near-field and geosphere chemical conditions are made in the present case as during the oxidising periods (63 900–68 200 AD, 92 800–102 000 AD) in the *glaciation calculation case* (Section 7.2). In the present case, however, such conditions are assumed to prevail from repository closure throughout the entire assessment period.

8.6.2 Description of the calculation case

Handling in the near-field models

The handling in the near-field models is analogous to that during oxidising periods in the *glaciation calculation case* (Section 7.2), where the implementation of oxidising conditions is described in detail. It is summarised here, as follows.

- Redox-sensitive radionuclides Np, Pa, Pu, Se, and Tc change their oxidation state in the present case. As a consequence, their sorption coefficients K_d are correspondingly modified (Table 7-2).
- The SRFs of the same radionuclides are modified to correspond to their higher oxidation states (Table 7-3).

In addition to the points listed above, higher corrosion rates are applied in 1BRT in this calculation case. The long-term corrosion rate of carbon steel for oxidising, alkaline conditions is assumed to range between 1 and 100 $\mu\text{m/a}$, which is three orders of magnitude greater than the 0.001–0.1 $\mu\text{m/a}$ range for reducing, alkaline conditions (**Data report**, Section 5.10) applied at the start of the *base case* (Section 5.3.5). Both the physical and the chemical concrete-degradation evolution are assumed to be identical to those in the base case (Table 5-9). Thus, at 22 000 AD, the pH in 1BRT decreases to 12.0 and after this point corrosion rates for near-neutral, oxidising conditions are pessimistically assumed: 10–400 $\mu\text{m/a}$ (**Data report**, Section 5.10). This is a very high corrosion rate, but it has little impact since most of the steel has already corroded before it is applied.

Handling in the geosphere model

The handling of K_d values is analogous to the periods with oxidising conditions in the *glaciation calculation case* (Section 7.2.5)²⁸.

Handling in the biosphere model

The handling in the biosphere model is identical to the *base case*.

²⁸ This simplification leads to a somewhat illogical handling of Ba, Cs, Ra and Sr as the sorption of these elements is not sensitive to redox-state, but in the *glaciation calculation case* their K_d values are still changed due to chemical properties of glacial waters. Nevertheless, this is of little significance, as these radionuclides do not contribute much to the total dose.

8.6.3 Results

Releases from the near-field

In Figure 8-21 the annual release of radionuclides for the *oxidising conditions calculation case* is shown and compared with the *base case*. Substantial increases can be observed for Mo-93 and C-14-ind, due to the increased corrosion rate in 1BRT. The release of Tc-99 increases slightly due to lower sorption in the near-field.

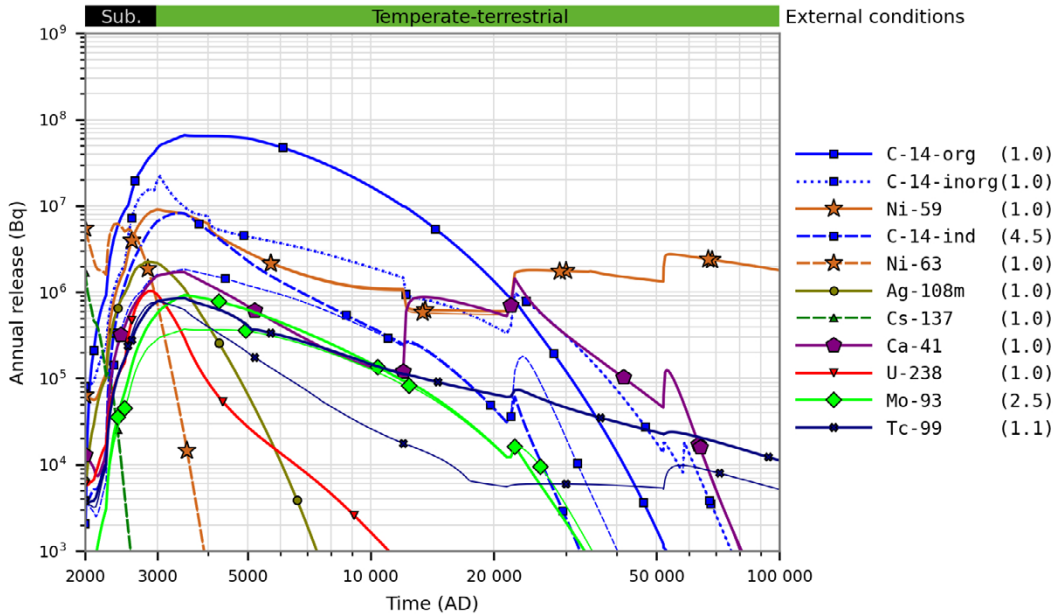


Figure 8-21. Annual activity releases (Bq) from the entire SFR in the oxidising conditions calculation case (thick lines) and the base case (thin lines). The ratio between the maximum releases in the present calculation case and the base case are shown in parentheses in the key. For many radionuclides, the difference between the two cases is too small to be visible on this scale. Coloured horizontal bar (top) shows the evolution of the external conditions.

An alternative presentation of the release results is given in Figure 8-22 for radionuclides with significant releases (maximum release greater than 1 000 Bq) and substantially affected (increase or decrease by at least 10 %) by *oxidising conditions*. The vertical bars show the percentage of the initial activity that is released from the near-field over the assessment period, i.e. the accumulated release divided by the initial activity, in the present case and in the *base case*, respectively. The figure also shows the quotient of accumulated release between the present case and the *base case* (black dots) and the corresponding quotient between cases for maximum annual release (yellow dots).

Se-79 is the radionuclide in Figure 8-22 with the greatest accumulated-release fraction, due to its long half-life and weak sorption. Se-79 is also the only radionuclide with stronger cement sorption during oxidising conditions (Table 7-2), resulting in a smaller release in the present case than in the *base case*. Other redox-sensitive radionuclides sorb more weakly during oxidising conditions and their release fractions are thus larger in the present case, particularly the accumulated release (black dots in Figure 8-22). C-14-ind and Mo-93 are not redox-sensitive but still show increased releases in the present case, particularly their maximum release (yellow dots in Figure 8-22), due to the increased steel corrosion rate in 1BRT.

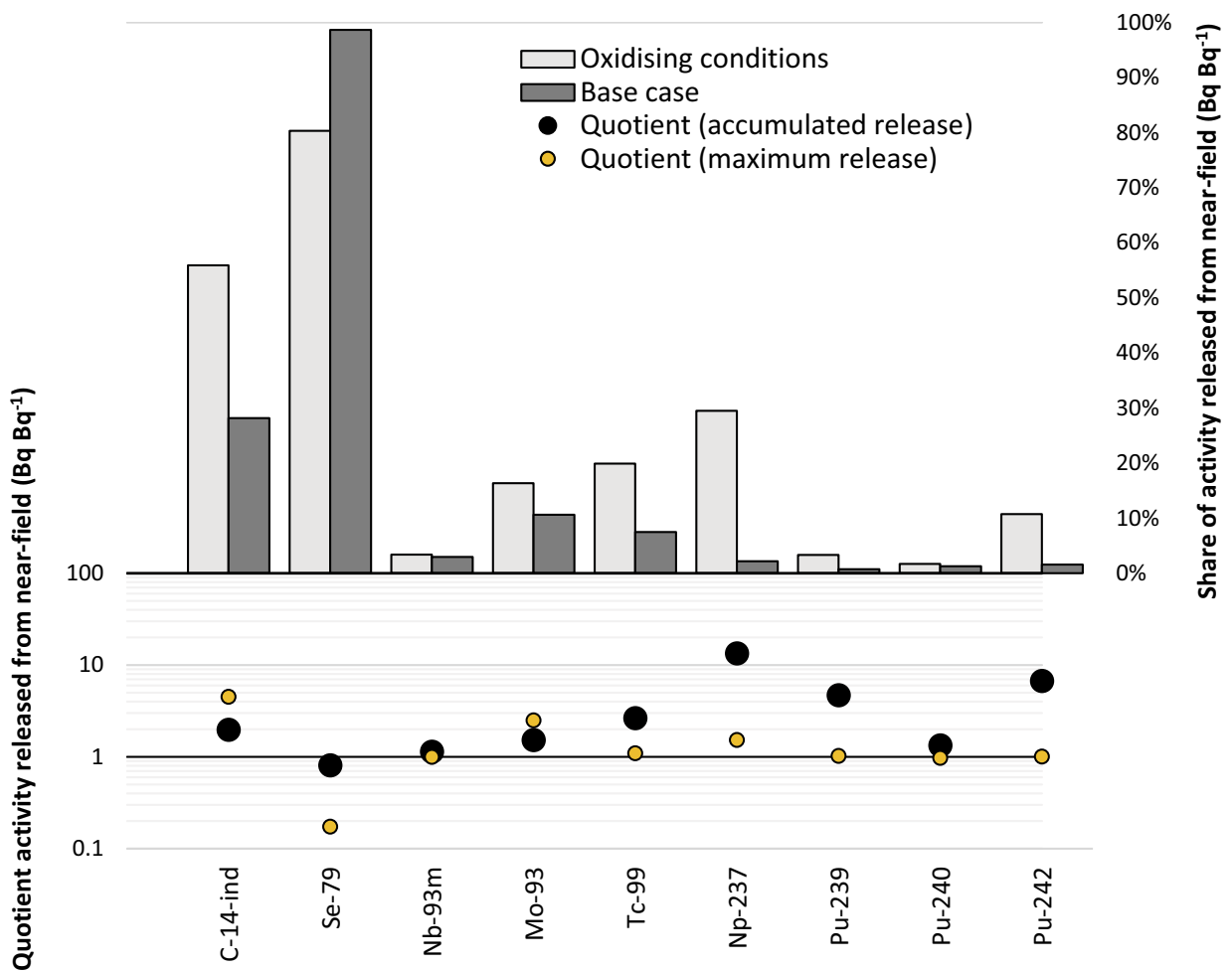


Figure 8-22. Summary of activity releases from the near-field in the oxidising conditions calculation case. Upper panel: fraction of each radionuclide's initial and ingrown activity that has been released at the end of the assessment period, for the present case and the base case. Lower panel: quotient between the two cases of the accumulated (black dots) and maximum (yellow dots) release, respectively.

Releases from the geosphere

Figure 8-23 is the same type of figure as Figure 8-22 but also includes the effects of the transport through the geosphere. The quotients of maximum release (yellow dots) and accumulated release (black dots) in the present case and the *base case* show that the effect of oxidising conditions is larger when considering the geosphere too; a larger number of radionuclides are substantially affected and thus included in Figure 8-23 than in Figure 8-22, and the release quotients are in many cases larger than 10. The release increase is greatest for actinides and Tc-99. Sr-90 and Cs-137, however, have significantly lower releases in the present case than the *base case*, explained by stronger bedrock sorption during oxidising conditions (Table 7-4).

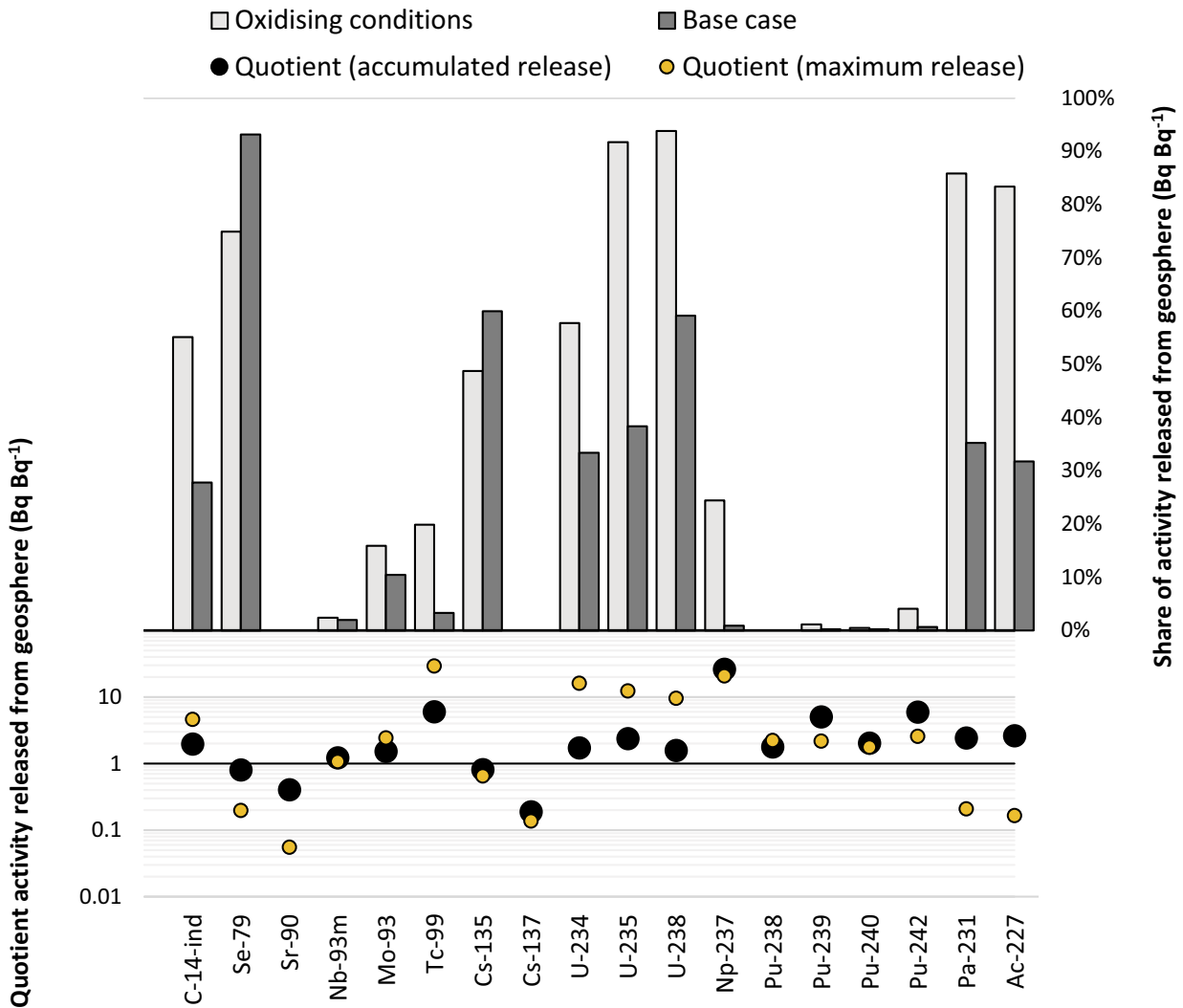


Figure 8-23. Summary of activity releases from the geosphere in the oxidising conditions calculation case. Upper panel: fraction of each radionuclide's initial and ingrown activity that has been released at the end of the assessment period, for the present case and the base case. Lower panel: quotient between the cases of the accumulated (black dots) and maximum (yellow dots) release, respectively. The radionuclides are shown in increasing order of mass (from left to right), except for the rightmost (Pa-231 and Ac-227) which are decay products without initial inventory.

Annual dose

The maximum total annual dose from SFR roughly doubles (exceeding 10 μSv) if oxidising conditions are assumed in the near-field and geosphere (Figure 8-24). This is mainly due to the dose-dominant Mo-93. Significant increases are also observed for U-235 and U-238. These radionuclides mainly originate from the 1–5BLA vaults which are not affected by oxidising conditions in the near-field. Thus, the increased doses from these radionuclides are explained mainly by weaker sorption due to oxidising conditions in the geosphere. In addition, the dose from Tc-99 increases significantly, but from very low levels and only at the end of the assessment period.

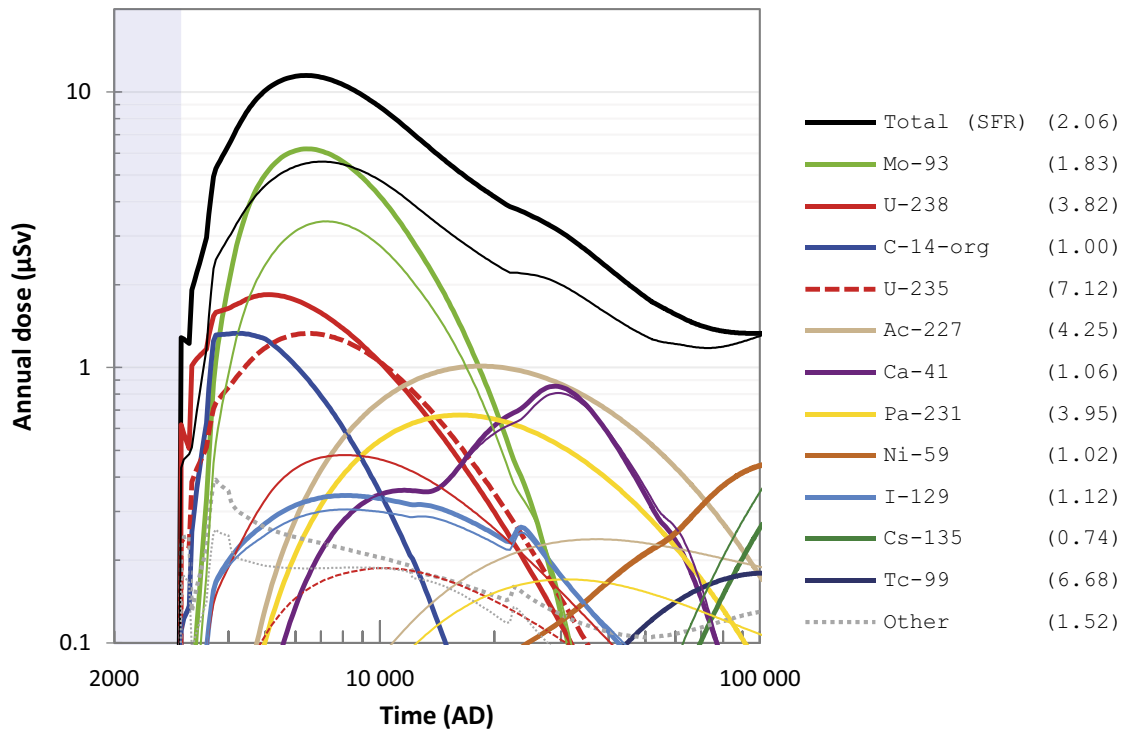


Figure 8-24. Annual dose (μSv) to the most exposed group (black line), including radionuclide specific contributions (coloured lines), in the oxidising conditions calculation case (thick lines) and the base case (thin lines). The combined contribution from radionuclides not shown is indicated by the grey dotted line. The ratio between the maximum doses in the present calculation case and the base case are shown in parentheses in the key. The submerged period is illustrated by the blue shading.

8.6.4 Summary and conclusions

This calculation case is based on the hypothetical assumption of oxidising conditions in the near-field and the geosphere throughout the assessment period. This affects the sorption of some radionuclides and increases the corrosion rate of steel in 1BRT.

Oxidising conditions in the near-field and geosphere would lead to about a doubling of the maximum annual dose, compared with the *base case*. The greatest impact in the near-field comes from Mo-93 with a higher release due to the increased corrosion rates in 1BRT and in the geosphere from the weaker bedrock sorption of uranium.

As a calculation case in a residual scenario, *oxidising conditions calculation case* is excluded from the assessment of risk. However, it may be interesting to note that the resulting maximum annual dose is below the 14 μSv corresponding to the regulatory risk criterion.

8.7 Initial concrete cracks

8.7.1 General description

The aim of the *initial concrete cracks scenario* is to illustrate how the concrete in the engineered barriers contributes to the protective capability of the repository. To this end, one calculation case, the *initial concrete cracks calculation case*, is selected to evaluate the hypothetical assumption of initial cracks in all concrete structures. For consistency, the concrete structures are assumed to have a high hydraulic conductivity ($K = 10^{-5}$ m/s) from the start. The calculations do not affect 1BRT and 1-5BLA as 1BRT has initial cracks also in the *base case* and 1-5BLA have no concrete barriers.

8.7.2 Description of the calculation case

The calculations are done with modified near-field models where cracks (as described in Section 4.2.3) are explicitly included in the concrete structures. The concrete structures are assumed to be in the severely degraded physical degradation state (hydraulic conductivity of 10^{-5} m/s as described in Section 5.3.1) at initial state. For the silo and 1-2BMA, as in the *base case*, the hydraulic conductivity of the main concrete hydraulic barrier increases to 10^{-3} m/s at 52 000 AD. For 1-2BTF, as in the *base case*, the hydraulic conductivity of the main concrete hydraulic barrier increases to 10^{-3} m/s at 12 000 AD. Moreover, as in the *base case*, sorption is omitted during advective transport through the cracked concrete barriers. The geosphere and biosphere models are configured as in the *base case*.

8.7.3 Results

Annual release from the near-field

In Figure 8-25 the annual release of radionuclides for the *initial concrete cracks calculation case* and the *base case* is shown. The inclusion of initial concrete cracks causes more pronounced peak releases around 2500–4000 AD, which is mainly due to increased releases from 1-2BMA (see Figure 8-26 where the releases from individual vaults are shown for select radionuclides). In Figure 8-26 it can be seen that 2BMA is the most significantly affected vault. The releases from the silo and 1-2BTF also increase for radionuclides that sorb strongly to cement, e.g. Ni 59, but their release provides only a minor contribution to the total release. 1BRT and 1-5BLA are not affected by this calculation case but their releases are also included in the figure to show their contribution to the total release.

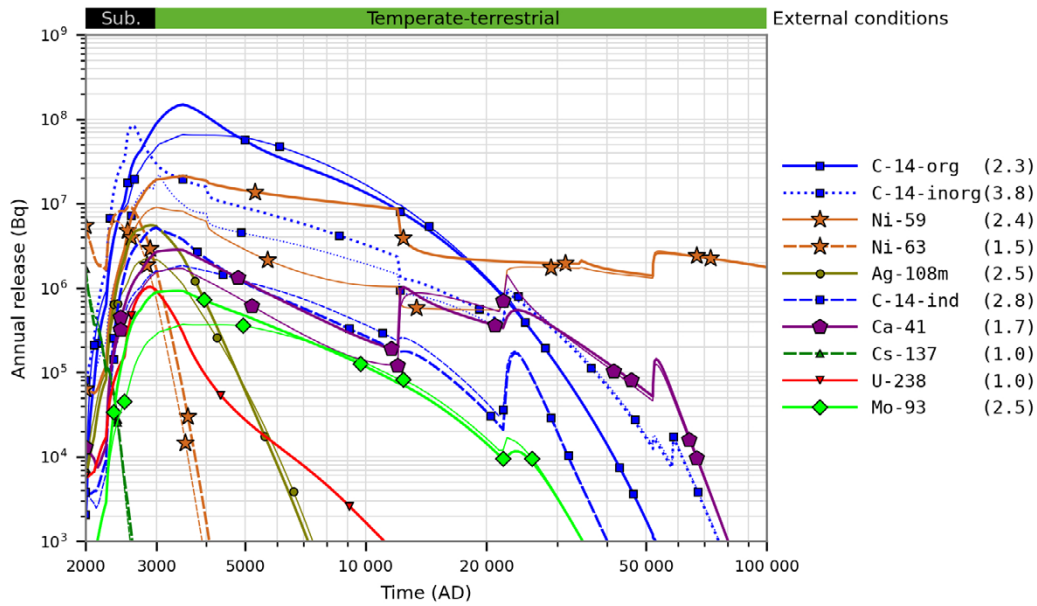


Figure 8-25. Annual activity releases (Bq) from the entire SFR in the initial concrete cracks calculation case (thick lines) and the base case (thin lines). The ratio between the maximum releases in the present calculation case and the base case are shown in parentheses in the key. Coloured horizontal bar (top) shows the evolution of the external conditions.

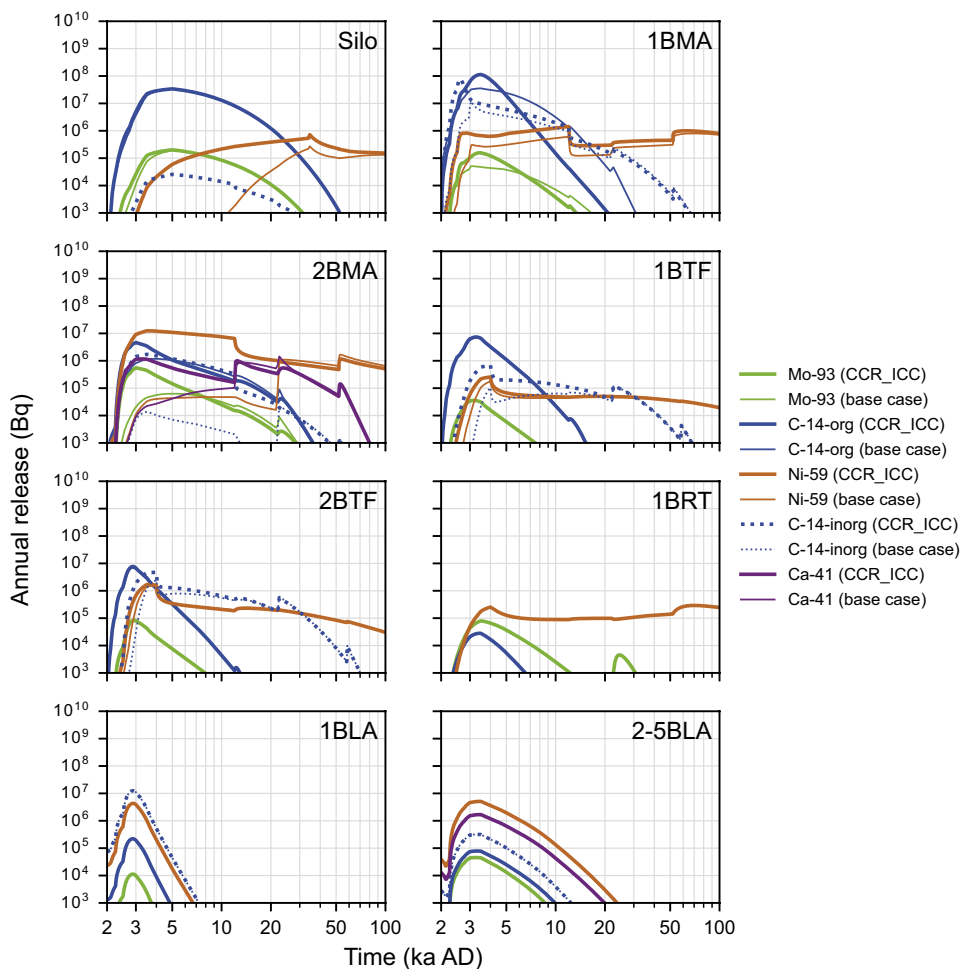


Figure 8-26. Annual activity releases (Bq) from waste vaults in SFR for selected radionuclides in the initial concrete cracks calculation case (thick lines) and the base case (thin lines). Note that for 2-5BLA the sum of the releases from all four vaults is shown in the figure.

Annual doses

The results from the dose calculation (Figure 8-27) show that assuming cracks and a higher initial conductivity in the concrete have a limited effect on total doses from SFR. However, noticeable effects can be seen on dose contributions from Mo-93, C-14 (both organic and inorganic), I-129 and Ni-59.

8.7.4 Summary and conclusions

The *initial concrete cracks calculation case* is based on the hypothetical assumption of initial cracks in all concrete structures. In addition, a higher hydraulic conductivity ($K = 10^{-5}$ m/s) is assumed for the concrete structures from the start in the calculation. This leads to significantly increased releases of many radionuclides important for the total maximum dose from SFR. 1-2BMA, where the concrete structures are the main groundwater hydraulic barriers, are the most affected vaults in terms of increased contribution to the total dose from SFR. The silo release is moderately affected (Figure 8-26), because the intact bentonite reduces the effect of concrete cracks. 1-2BTF have limited contributions to the total dose, so their impact in this calculation case is limited.

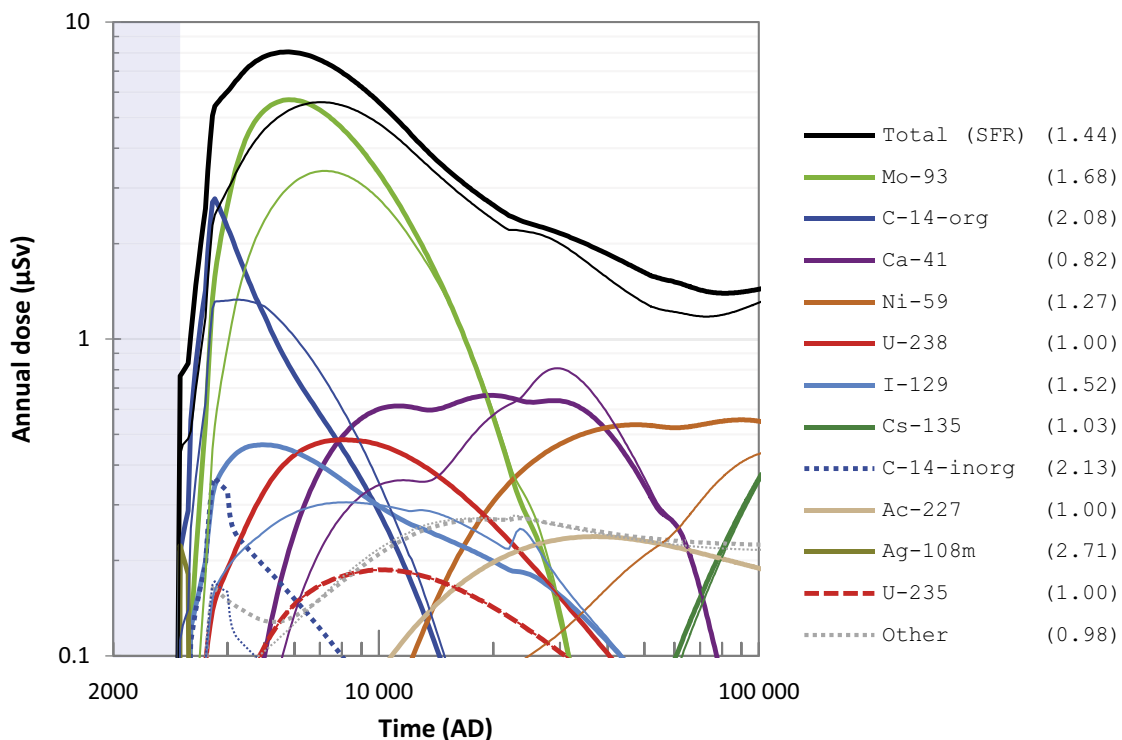


Figure 8-27. Annual dose (μSv) to the most exposed group (black line), including radionuclide specific contributions (coloured lines), in the initial concrete cracks calculation case (thick lines) and the base case (thin lines). The combined contribution from radionuclides not shown is indicated by the grey dotted line. The ratio between the maximum doses in the present calculation case and the base case are shown in parentheses in the key. The submerged period is illustrated by the blue shading.

Figure 8-28 provides an illustrative summary of the performance of the near-field in this calculation case for the most affected radionuclides (i.e. those whose maximum release increases by more than 50 % in the present case compared with the *base case*). The vertical bars show how much of the initial activity is released from the near-field over the assessment period, i.e. the accumulated release divided by the initial activity, in the present case and in the *base case*. The figure also shows the corresponding quotient between cases for maximum annual release (yellow dots) and the quotient of accumulated release between the present case and the *base case* (black dots).

As for the *alternative concrete evolution calculation case*, radionuclides dominating the release from 1–2BMA, shown in Figure 7-17 and Figure 7-19, are also most affected in the *initial concrete cracks calculation case*. The increase of the peak release is greater than the increase of the accumulated release because early concrete degradation (via the presence of cracks) causes a more pronounced peak release around 2500–4000 AD, which has a limited effect on the accumulated release.

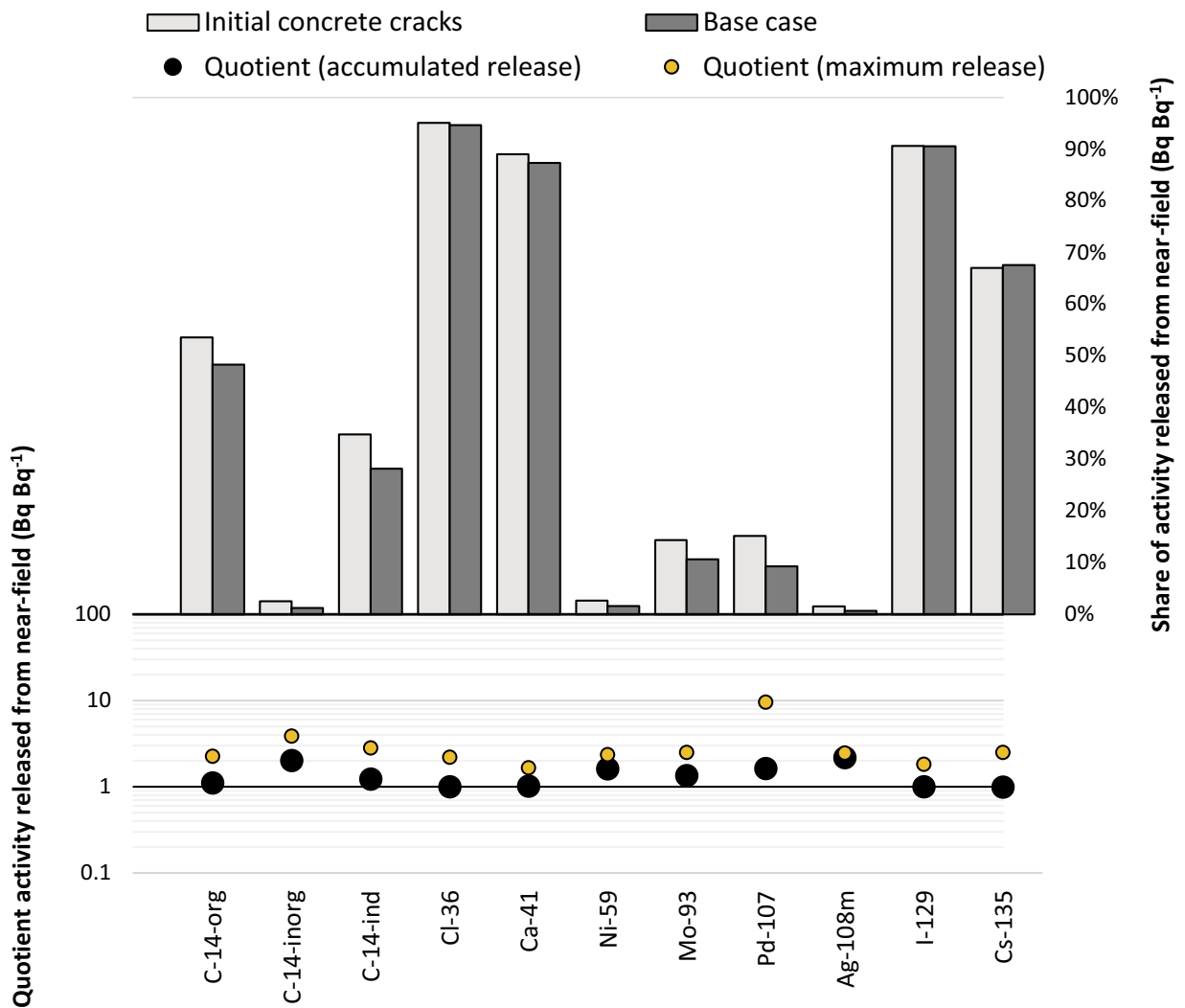


Figure 8-28. Summary of activity releases from the near-field in the initial concrete cracks calculation case in relation to the base case for most affected radionuclides. Upper panel: percentage of the accumulated release in the two calculation cases relative to the total initial activity in the waste vaults. Lower panel: quotients of the accumulated (black dots) and maximum (yellow dots) releases between the present case and the base case.

8.8 Unrepaired 1BMA

8.8.1 General description

The Closure plan for SFR (Mårtensson et al. 2022) outlines extensive repair and strengthening measures that need to be adopted to achieve the desired hydraulic and mechanical properties of 1BMA at closure. The measures include erecting new reinforced outer concrete walls on the outside of the existing ones (**Post-closure safety report**, Section 4.3.2). In accordance with the Closure plan, the new outer concrete walls in 1BMA are included in the calculations of the main scenario (Section 5.3.3).

The aim of the *unrepaired 1BMA scenario* is to illustrate the importance of the planned repair and strengthening measures for post-closure safety. To this end, an alternative initial state of 1BMA where no additional concrete structure has been erected around the existing concrete structure is evaluated in the *unrepaired 1BMA calculation case*. A detailed description of the alternative initial state is given in Section 4.1.2 in Elfving et al. (2018). The purpose of the calculation case is to assess the effects of the planned repair and strengthening measures prior to closure of 1BMA.

This calculation case is set up to as closely as possible resemble the *No repair* case in the updated analysis of the post-closure safety for 1BMA (Elfving et al. 2018). The main assumption made in the *unrepaired 1BMA calculation case* is that the drainage and grouting holes (Elfving et al. 2018) in the existing concrete structure are filled so that they have the same properties as the surrounding concrete itself at closure. It is also assumed that the beams upon which the concrete structure is resting have a high hydraulic conductivity. Apart from changing the initial state of the 1BMA barriers, the handling in the radionuclide transport modelling is identical to the *base case*.

8.8.2 Description of the calculation case

Handling in the near-field

Hydrology

The radionuclide transport models use values of steady-state groundwater flow obtained from near-field (Abarca et al. 2013, 2014) and regional hydrological (Odén et al. 2014) modelling. The steady-state groundwater flow through the repository over time is obtained from simulations accounting for three shoreline positions (2000 AD, 3000 AD and 5000 AD) and four physical concrete degradation states (intact, moderately degraded, severely degraded and completely degraded). Changes in groundwater flow between the time slices are handled by means of linear interpolation in the same way as in the *base case*.

The different parts of 1BMA are assigned hydraulic conductivities corresponding to different physical degradation states as shown in Figure 8-29. The main difference between the *base case* and the *unrepaired 1BMA calculation case* is that, in the latter, no outer concrete structure has been added to the existing 1BMA concrete structure and consequently concrete degradation progresses more rapidly i.e. the hydraulic conductivity increases earlier.

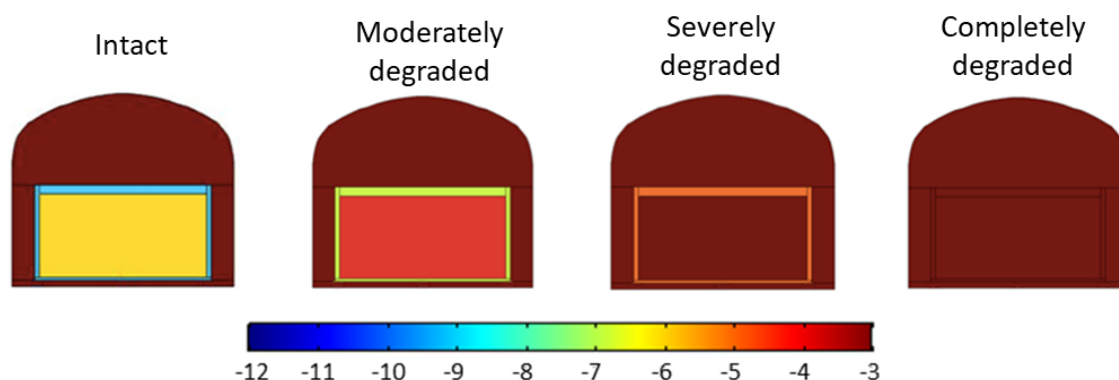


Figure 8-29. Cross sections of the 1BMA vault showing the logarithm of hydraulic conductivity K (m/s) ($\log_{10}(K)$) for different physical degradation states. Adapted from Abarca et al. (2013, 2014).

Cement properties

In addition to the physical–hydrological properties of concrete, the chemical–mineralogical properties change over time too as the cement minerals in the concrete undergo chemical degradation. Chemical degradation is handled identically to the *base case*.

Concrete barriers

In the *unrepaired IBMA calculation case*, the walls and the lid of the IBMA concrete structure are thinner than in the *base case*. The dimensions of the original structure are given in the **Initial state report**, Section 5.5. The concrete structure follows the same evolution as the outer concrete in the *alternative concrete evolution calculation case* (Table 7-7).

Cracks

Cracks are assumed to form in the concrete structure as it transitions from a moderately degraded to a severely degraded state, which occurs at 3000 AD in the *unrepaired IBMA calculation case*. The slab is, as in the *base case*, assumed to be cracked initially.

Transport through the near-field

The IBMA residence time is estimated from Equation 4-13. All factors included in the total effective volume flow rate in IBMA (the denominator in Equation 4-13) are plotted in Figure 8-30. The figure also shows the corresponding quantities for the *base case*.

Groundwater flow through the waste domain of IBMA (Q_{waste}) is higher in the *unrepaired IBMA calculation case* than in the *base case*. This is due to the more rapid concrete degradation and consequent hydraulic conductivity increase (as well as fracture flow considered from 3000 AD). The inverse diffusive transport resistance of the concrete structure ($1/R_{\text{tot}}$) increases earlier compared with the *base case*.

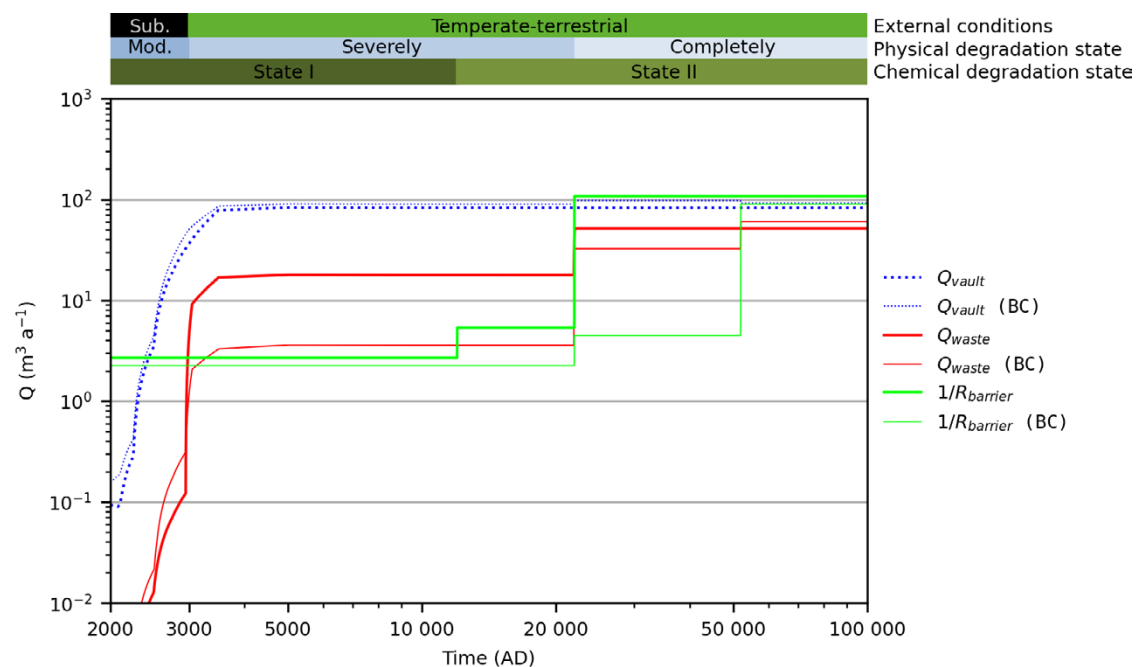


Figure 8-30. Comparison of transport quantities in IBMA as a function of time for the base case (BC) and the unrepaired IBMA calculation case. Groundwater flow through the waste Q_{waste} and inverse diffusive transport resistance of the concrete structure (R_{barrier}) as a function of time. R_{barrier} is defined in Equation 4-5. Q_{vault} is groundwater flow through the whole IBMA vault. Coloured horizontal bars (top) as in Figure 5-3.

At the beginning of the assessment period, groundwater flow through the concrete structure is very low and diffusion is the dominating transport mechanism ($1/R_{tot} > Q_{waste}$). As the shoreline moves past the repository and the concrete degrades, groundwater flow increases, and, at 3000 AD, advective transport becomes the dominating transport mechanism ($1/R_{tot} < Q_{waste}$). As the concrete structure reaches its completely degraded state at 22 000 AD and the effective diffusivity of radionuclides in the concrete structure increases, diffusion becomes equally as important as advection. Flow through the vault Q_{vault} is also plotted in Figure 8-30.

Handling in the biosphere and geosphere models

The handling in the biosphere and geosphere models is identical to the *base case*.

8.8.3 Results

Annual release from the near-field

The annual release of radionuclides from 1BMA in the *unrepaired 1BMA calculation case* and the *base case* is shown in Figure 8-31. The higher release peaks of the weakly adsorbing radionuclides Mo-93, Cs-135 and non-sorbing radionuclide C-14-org at 3000 AD in the *unrepaired 1BMA calculation case* are mainly caused by increased groundwater flow through the waste of 1BMA. The increased groundwater flow also causes an increased release of the strongly sorbing radionuclides Ni-59 and C-14-inorg. The increase of the annual release of the strongly sorbing radionuclides Ni-59 and C-14-inorg at 22 000 AD is for the *unrepaired 1BMA calculation case* caused by the increased effective diffusivity in the concrete structure whereas, for the *base case*, the corresponding increase is caused by increased groundwater flow through the waste. The earlier formation of cracks in the concrete barriers in the *unrepaired 1BMA calculation case* effectively means fewer available sorption sites, which increases the annual release of Ni-59.

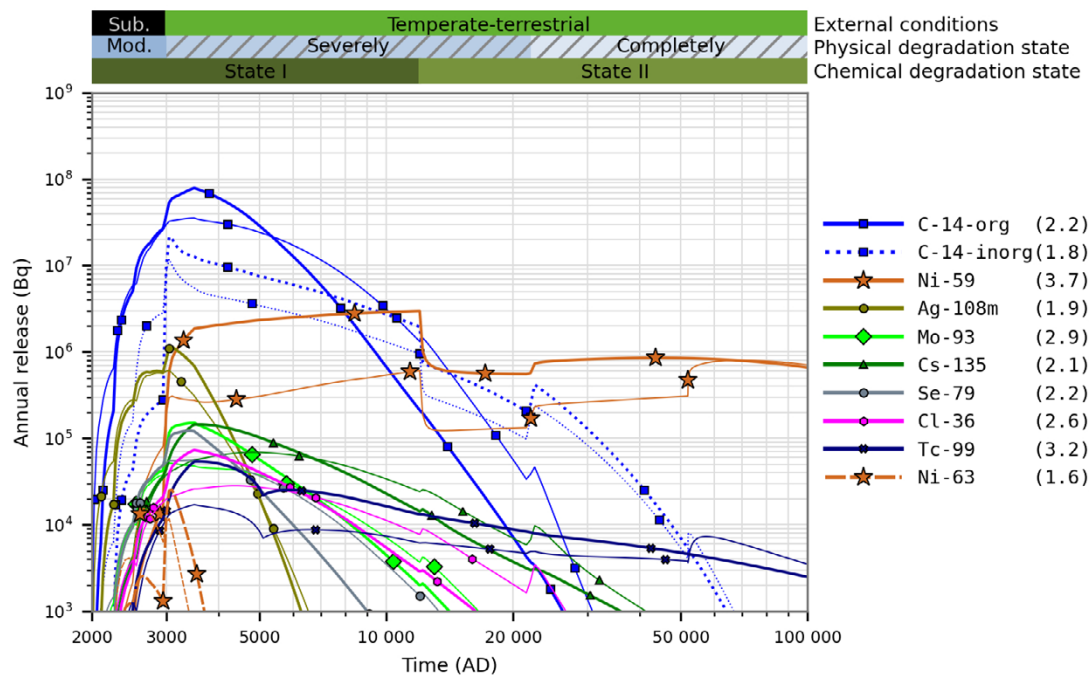


Figure 8-31. Annual activity releases (Bq) from 1BMA in the *unrepaired 1BMA calculation case* (thick lines) and the *base case* (thin lines). The ratio between the maximum releases in the present calculation case and the *base case* are shown in parentheses in the key. Coloured horizontal bars (top) as in Figure 5-9.

Annual doses

The annual doses to humans from 1BMA in the *unrepaired 1BMA calculation case* and the *base case* are shown in Figure 8-32. Exposures starting shortly after the submerged period and continuing for approximately 5 000 years result in the highest doses from 1BMA, with about a factor two higher dose compared with the *base case*. During this period, the dose response from C-14-org, Mo-93 and I-129 is a direct consequence of increased groundwater flow through the waste of 1BMA as explained above. The effect on the total dose of the fast breakthrough of Ni-59 (visible already at 20 000 AD; see Figure 8-30) is a result of the increased release from 1BMA due to increased groundwater flow and earlier formation of cracks.

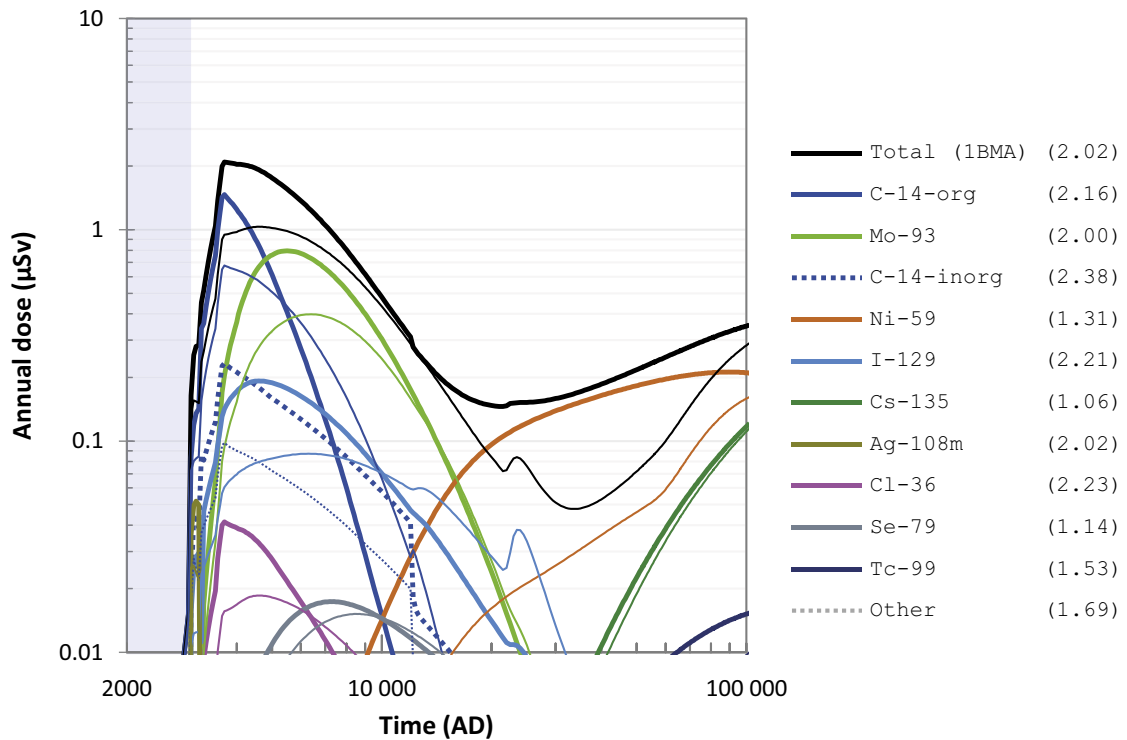


Figure 8-32. Annual dose (μSv) to the most exposed group (black line), including radionuclide specific contributions (coloured lines), from releases from 1BMA in the unrepaired 1BMA calculation case (thick lines) and the base case (thin lines). The combined contribution from radionuclides not shown is indicated by the grey dotted line. The ratio between the maximum doses in the present calculation case and the base case are shown in parentheses in the key. The submerged period is illustrated by the blue shading.

The corresponding figure of the annual dose to humans from the entire SFR is shown in Figure 8-33. The same trends as the matching figure for IBMA are seen, although the trends are weaker since the releases and doses from the other vaults are the same as for the *base case*. Specifically, the maximum total dose from SFR is about 5 % higher than in the *base case*. Furthermore, the dose curve exhibits a steeper and earlier rise in this calculation case due to the elevated releases from IBMA. In the approximate period between 20 000 AD and 90 000 AD, the total dose is slightly elevated due to the fast breakthrough of Ni-59.

8.8.4 Summary and conclusions

This scenario illustrates the significance of the planned repair and strengthening measures of IBMA for the protective capability of the repository. Neglecting the hydraulic properties of the new outer concrete structure in IBMA results in a 5 % increase in the maximum dose from SFR compared with the main scenario. This minor difference in dose suggests that the planned repair and strengthening measures of IBMA are not of critical importance for post-closure safety.

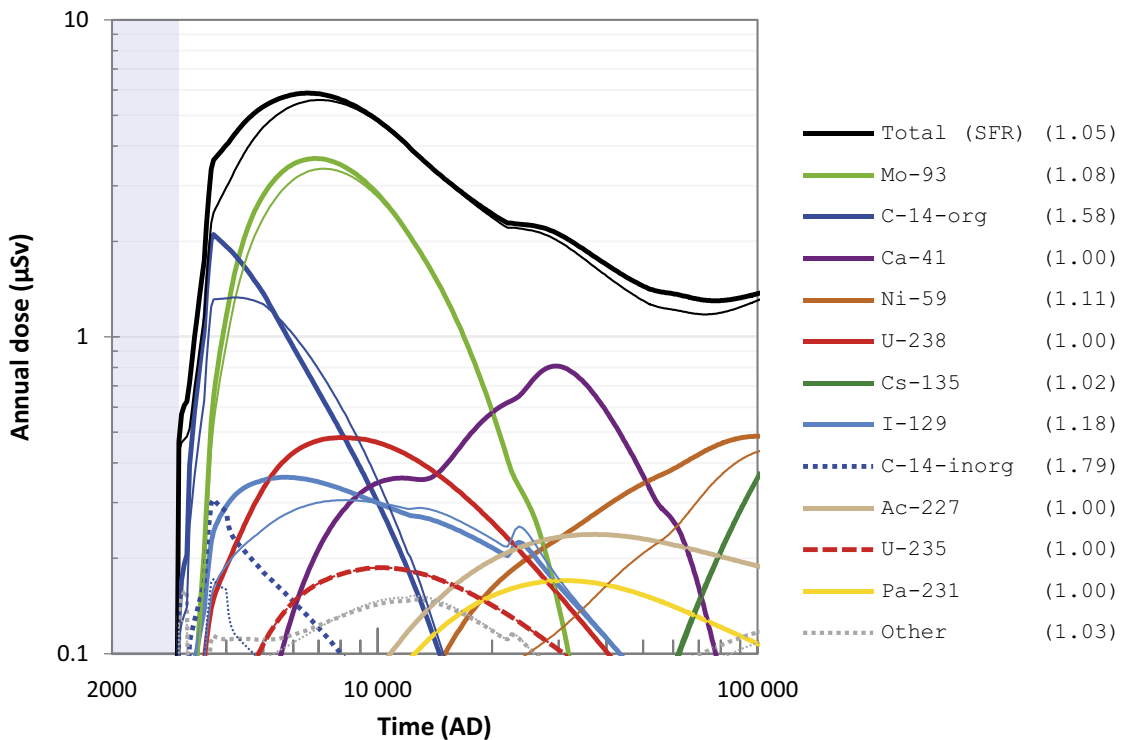


Figure 8-33. Annual dose (μSv) to the most exposed group (black line), including radionuclide specific contributions (coloured lines), for releases from the entire SFR in the unrepaired IBMA calculation case (thick lines) and the base case (thin lines). The combined contribution from radionuclides not shown is indicated by the grey dotted line. The ratio between the maximum doses in the present calculation case and the base case are shown in parentheses in the key. The submerged period is illustrated by the blue shading.

8.9 Unsealed repository

8.9.1 General description

The *unsealed repository scenario* is evaluated since, according to the regulations (SSMFS 2008:21), it is required to define and analyse a scenario that illustrates the consequences of an unsealed repository that is not monitored (**Post-closure safety report**, Section 9.10). The scenario is evaluated in one calculation case: the *unsealed repository calculation case*.

8.9.2 Description of the calculation case

In this calculation case, it is assumed that, following completion of waste disposal, the repository is for some reason neither closed nor monitored. As this calculation case is highly simplified and pessimistic, it is considered appropriate to apply only deterministic calculations. It is assumed that no transport out of the repository takes place and the radionuclide concentration in the whole tunnel system equilibrates within a very short time. The whole system is handled as a mixed tank with the exception of the silo, for which the release is limited. The concrete and bentonite barriers in the top of the silo may not be completed. However, as the silo is grouted progressively during operations, it is considered unrealistic to assume an instant release from the silo. Thus, the diffusive resistance of the grout in the silo is taken into account in the calculation of the release from the silo to the other parts of the tunnel system.

In this calculation case, the repository will become filled with water within a few years. However, since the groundwater that is pumped out of the repository today is relatively saline, it is not likely that the water volume that fills the repository will be used as a water supply as long as the repository is situated near the sea. However, it is not unreasonable to assume that the influx of meteoric water and limited mixing due to the difference in salinity and temperature could lead to the formation of a freshwater pool near the tunnel opening. Viewed over an extended period, freshwater could seep down into the repository and replace the present saline water with potable water. Hence, exposure to humans in this calculation case is assumed to occur due to utilising water from the tunnel entrance as drinking water; this is the only considered exposure pathway in this calculation case.

As in the considerations of FHA (**FHA report**), this calculation case addresses only inadvertent actions, meaning that the people pumping the water out of the repository have no knowledge of the potential radiological hazard. It is assumed that inadvertent FHAs are only possible after the memory of the repository is lost, i.e. the existence and location of, and/or the nature of, the repository is forgotten. Memory is assumed to be preserved for at least 300 years after closure in the FHA scenarios. However, that is under the presumptions that present-day social conditions and technical capabilities will prevail and that the repository is closed as planned. The premise for the *unsealed repository scenario* is that the repository is neither closed nor monitored. For this to occur, it may be reasonable to assume that social conditions have drastically changed. This implies that the memory might not be preserved for a minimum of 300 years. In this calculation case, it is assumed that memory may be lost earlier, already after 100 years. Thus, doses are calculated from 100 years and onward after the repository has been abandoned²⁹.

8.9.3 Results

Table 8-2 presents the resulting dose maximum which, as expected, occurs at the start of the calculations. This is due to relatively short-lived radionuclides with high initial radiotoxicity (e.g. Cs-137, Ni-63, Sr-90 and Ag-108m, Figure 8-34) which contribute most to the initial doses. It may be considered too pessimistic to assume only 100 years for the period during which the memory of the repository is preserved and more suitable to use the same 300-year assumption as in the FHA scenarios (**FHA report**). Table 8-2 presents the resulting dose maxima for both assumptions for comparison. As can be seen, the dose decreases considerably from 100 years to 300 years after closure, mainly due to decay of Cs-137.

²⁹ The repository is assumed to be abandoned at the planned time of closure.

Table 8-2. Annual doses from ingestion of water from the tunnel entrance 100 and 300 years after abandoning the repository.

Time of exposure (years after the repository was abandoned)	Annual dose (mSv)	Most contributing radionuclides
100	14.3	Cs-137 (90 %), Ni-63 (6.0 %), Sr-90 (1.8 %)
300	0.59	Ni-63 (36 %), Cs-137 (22 %), Ag-108 (22 %)

At later times, ingrowth radionuclides such as Po-210 start to dominate the doses (Figure 8-34). However, it should be noted that, as the calculation disregards transport of radionuclides away from the repository, this is to be considered a very pessimistic result.

8.9.4 Summary and conclusions

In conclusion, the maximum dose due to exposure of radionuclides in drinking water from an unsealed repository is several orders of magnitude higher than in the main scenario. These results clearly demonstrate the importance of adequately closing and sealing the repository.

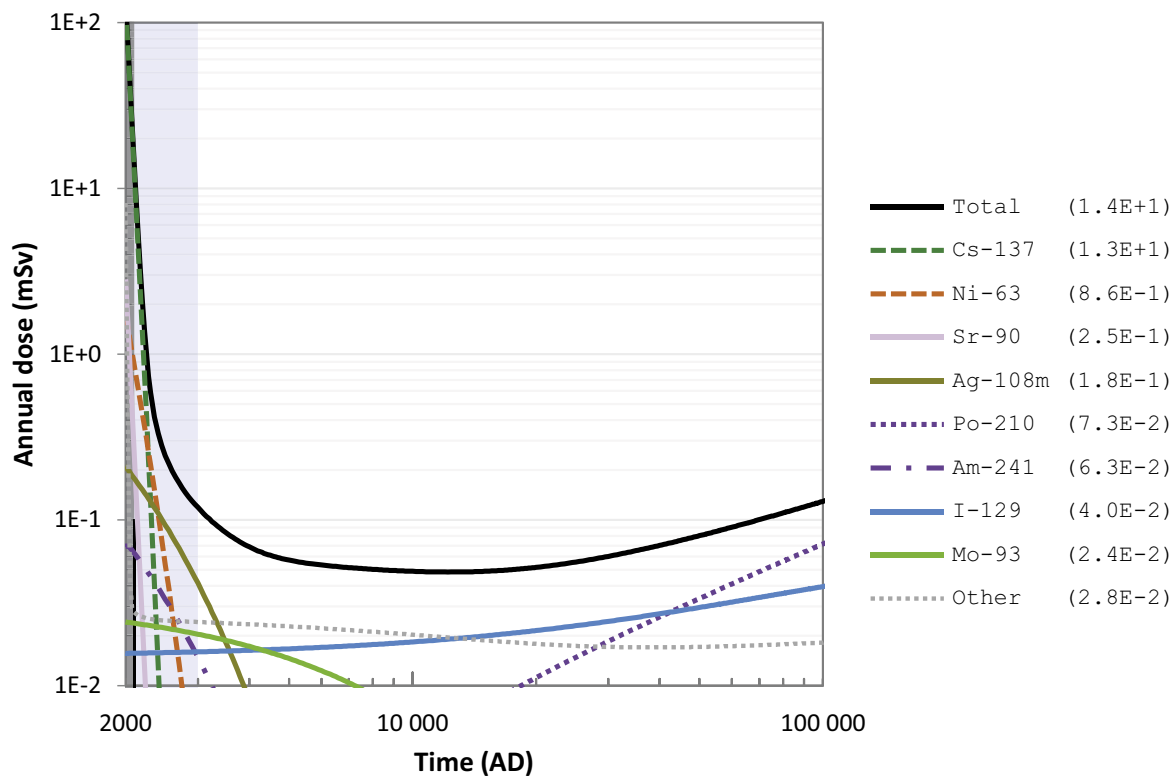


Figure 8-34. Annual dose (mSv) to the exposed group (black line), including radionuclide specific contributions (coloured lines), in the unsealed repository calculation case. The combined contribution from radionuclides not shown is indicated by the grey dotted line. The total and radionuclide-specific annual dose maxima (mSv) are shown in parentheses in the key. Note that the first 100 years (greyed out in the figure) are not included in the present calculation case. The submerged period is illustrated by the blue shading.

9 Collective doses

9.1 Introduction

In addition to individual radiological risk, the regulations require collective dose to be calculated. The regulations (SSMFS 2008:37) specify that: “The collective dose, as a result of the expected outflow of radioactive substances over a period of 1 000 years after closure of a repository for spent nuclear fuel or nuclear waste shall be estimated as the sum, over 10 000 years, of the annual collective dose”. This chapter first describes the approach used to estimate collective doses (Section 9.2) and then presents the results from the calculation cases (Section 9.3).

Collective doses in the PSAR are treated as an assessment endpoint that, in principle, can be derived for any calculation case. The approach is to calculate collective doses for the calculation cases in the main scenario and in the less probable scenarios, that is for the cases for which resulting annual doses are propagated to the assessment of radiological risk (**Post-closure safety report**, Chapter 10).

Calculation cases with releases during the first 1 000 years that are either zero or identical to the *base case* are excluded. In addition, the *earthquake calculation case* is excluded, even though it is identified to analyse a less probable scenario. The reasoning for this is that the annual probability of an earthquake severe enough to damage the barriers is selected to be 10^{-6} (**Post-closure safety report**, Chapter 8). Hence, the cumulative probability for at least one earthquake to occur is significant considering the entire assessment period but is two orders of magnitudes lower if it is postulated that the earthquake occurs during the first 1 000 years.

The cases for which collective doses are calculated are the *base case*, the *warm climate calculation case* (*high summer precipitation variant*), the *alternative concrete evolution calculation case* and the *high concentrations of complexing agents calculation case*.

9.2 Estimating collective doses

Collective doses are estimated for two populations: the global population exposed to C-14 releases, and the Baltic population affected by the release of radionuclides to the Baltic Sea via subsequent exposure due to ingestion of fish.

9.2.1 Collective dose to the global population

C-14 is a key contributor to the collective dose from global dispersion of long-lived radionuclides discharged from nuclear energy production. UNSCEAR (United Nations Scientific Committee on the Effects of Atomic Radiation) recommends using the factor 109 000 man Sv/PBq for the collective dose commitment per unit discharge to atmosphere (UNSCEAR 2017, Annex A, page 71), which is the same as was previously recommended in UNSCEAR (2000). Furthermore, collective doses from unit discharge to the surface waters of oceans can be considered to be about the same as those from unit discharges to the atmosphere. The conversion factor is mainly based on the work by Titley et al. (1995) and is the complete collective dose (defined as the sum over 50 000 years). It has been calculated under the assumptions that the future world population stabilises at 10 billion and that the global inventory of stable carbon in the atmosphere does not increase from its present value. To estimate the collective dose as the sum over 10 000 years, the conversion factor is multiplied by 0.75; this factor is based on estimates that 75 % of the complete dose commitment from a single release is delivered within 10 000 years (UNSCEAR 2000, Annex A, p 53).

9.2.2 Collective dose to the regional population

The Baltic Sea region is represented by a single compartment, with a volume of $2.1 \times 10^{13} \text{ m}^3$. The only radionuclide transport processes considered are the water retention time of the Baltic Sea (30 years; Stigebrandt and Gustafsson 2003) and radioactive decay and in-growth. The exposed population considered is people in the Baltic region, who are assumed to consume the total amount of fish captured by commercial fishing, about $8.5 \times 10^7 \text{ kgC a}^{-1}$ (Elmgren 1989, Table 4) The collective effective dose is calculated for releases to the sea during the first 1 000 years after closure, as recommended in the regulations.

9.3 Results

The resulting collective doses, summed over 10 000 years, to the global and the regional populations are summarised in Table 9-1.

The collective dose for the global population due to C-14 releases ranges from 1.6 to 2.0 man Sv, except for the *warm climate calculation case* which yields considerably lower doses. This is due to the differences in the applied temporal evolution of the groundwater flow in the near-field and geosphere. The same groundwater flow is applied in the *base case*, the *alternative concrete evolution calculation case* and the *high concentrations of complexing agents calculation case*. The same shoreline regression is also used in the *warm climate calculation case*, but shifted 3 500 years forward in time (Section 6.2.3). This results in considerably lower groundwater flow in the first 1 000 years and, hence, geosphere releases in the *warm climate calculation case* compared with the three other cases.

The collective doses for the regional population around the Baltic Sea range from 0.12 to 0.14 man Sv, with the exception of the *warm climate calculation case* which, for the same reason as for the global collective doses, yields a considerably lower dose. C-14 dominates the regional collective doses in all four calculation cases and generally with Ag-108m as the second most contributing radionuclide.

As comparison, the total worldwide collective dose to the public arising from electricity generation by nuclear power is estimated to 7 600 man Sv (UNSCEAR 2017, Table 17). To the total dose, the global collective dose from mining and milling, power plant operation and reprocessing (integrated to 10 000 years) contributes with 7 470 man Sv, and the local and regional collective dose (integrated over 100 years) contributes with 130 man Sv.

Table 9-1. Global and regional collective doses from C-14 and contributions to the regional doses from most contributing radionuclides.

Calculation case	Collective dose (man Sv)		Contributions to the regional collective dose (%)	
	Global	Regional	C-14	Ag-108m
Base case	1.6	0.12	96.0	3.8
Warm climate	0.0016	0.00012	96.3	-
Alternative concrete evolution	2.0	0.14	96.4	3.4
High concentration of complexing agents	1.6	0.12	96.0	3.8

10 Summary and conclusions

10.1 Introduction

This report presents the results from radionuclide transport and dose calculations performed for the PSAR for SFR. The models used for the radionuclide transport and dose calculations are similar to those used in the SR-PSU, the previous safety assessment for SFR. However, they have been modified to reflect the revised description of the existing and planned extension of SFR, as described in the **Post-closure safety report**, Section 4.4. In addition, in response to SSM's review of the SR-PSU, and due to new knowledge acquired since that assessment, several input datasets have been updated for the PSAR (Section 1.3.2). Some of these updates have also resulted in noticeable differences in the modelling results compared with those obtained in the SR-PSU, as described in Appendix C.

In this report, radionuclide transport and dose are calculated for 20 calculation cases evaluating the main scenario, less probable scenarios and residual scenarios (Chapters 5 to 8). In addition, two calculation cases supporting the assumptions in the main scenario are included to provide a sensitivity analysis of specific uncertainties in the future evolution of the repository and its environs. All calculation cases analysed in this report are listed in Table 10-1. The calculations were carried out for an assessment period of 100 000 years. Demonstration of compliance with regulatory requirements is presented in the **Post-closure safety report**, whereas this report presents the annual dose for each calculation case. For each calculation case, the results consist of annual effective dose to a representative individual of the most exposed group for the defined calculation cases, denoted annual dose or dose for short.

Calculations were also performed to assess collective doses. Collective dose was calculated for two populations: 1) a global population which is exposed to C-14 in the atmosphere and 2) a regional population in the vicinity of the Baltic Sea exposed by ingestion of fish.

This chapter is organised as follows. A summary of the calculation cases analysed in this report, including the most important results, is given in Section 10.2. This is followed by a discussion about the management of uncertainties in Section 10.3 based on the uncertainty classifications in Section 2.5. Finally, in Section 10.4, conclusions from the results of the calculations are drawn.

Table 10-1. Calculation cases analysed in this report.

Scenario		Calculation case	Short cc-name
Main scenario		Present-day climate (<i>base case</i>)*	BC
		Warm climate*	WC
		Cold climate	CC
		Timing of shoreline regression	SR
		Delayed release from repository	DR
Less probable scenarios	Glaciation	Glaciation	GC
	High concentrations of complexing agents	High concentrations of complexing agents*	CA
	Alternative concrete evolution	Alternative concrete evolution*	ACE
	Earthquake	Earthquake	EQ
Residual scenarios	Hypothetical early permafrost	No effect on engineered barriers	HEP NE
		Effect on engineered barriers	HEP
	Loss of engineered barrier function	No sorption in the repository	EB S
		No hydraulic barriers in the repository	EB H
	Loss of geosphere barrier function	No sorption in the geosphere	GB S
		No transport retention in the geosphere	GB TR
	Alternative radionuclide inventory	Extended operation of reactors	AI EO
		Increased fuel damage frequency	AI FD
		Extended use of molybdenum-alloy fuel spacers	AI Mo
	Oxidising conditions	Oxidising conditions	Ox
	Initial concrete cracks	Initial concrete cracks	ICC
Unrepaired 1BMA	Unrepaired 1BMA	U1BMA	
Unsealed repository	Unsealed repository	UR	

Included in the risk assessment.

* Included in the calculations of collective dose.

10.2 Summary of calculation cases

This section contains a summary of the calculation cases analysed in this report. To facilitate the discussion, Figure 10-1 shows the statistical distribution of the maximum annual dose over the assessment period from each of these calculation cases. The statistical distribution is shown as the mean and 5–95th percentile range from the probabilistic calculations³⁰. Further, for each of the calculation cases, Figure 10-2 shows the relative contributions to the maximum dose from different radionuclides.

³⁰ The unsealed *repository calculation case* (UR) is the only calculation case that is evaluated without any probabilistic handling of the input data. As a result, this calculation case is presented without any 5–95th percentile range in Figure 10-1.

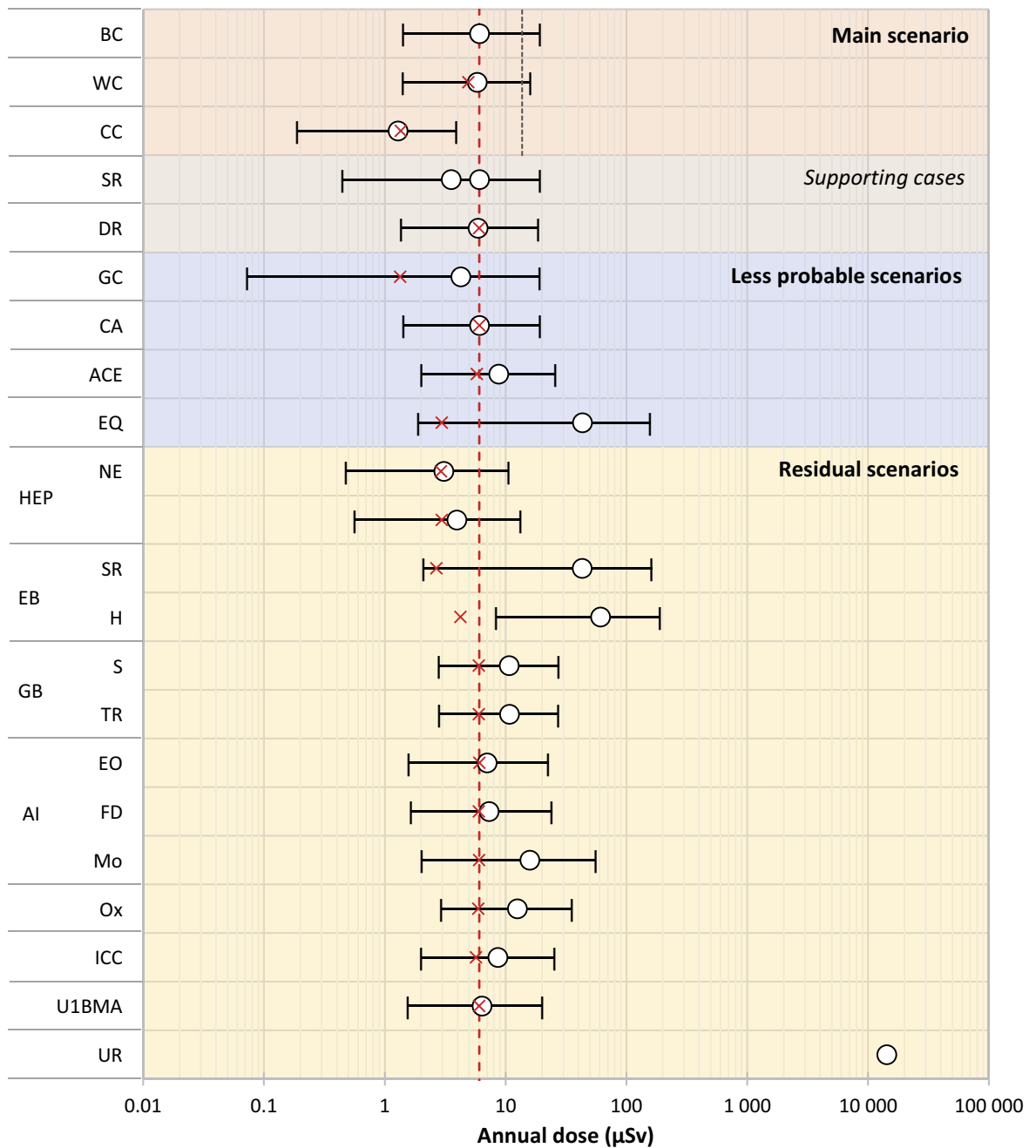


Figure 10-1. Maximum annual doses (μSv) over the assessment period from the calculation cases analysed in this report (short cc-names in Table 10-1), expressed as the mean (white circles) and 5–95th percentiles (bars) across the probabilistic simulations. The maximum mean dose in the base case is indicated by the red dashed line, and the dose corresponding to the regulatory risk criterion ($14 \mu\text{Sv}$) is indicated by the vertical black dashed line in the main scenario-area. The mean dose for the base case at the year of the maximum dose in the calculation cases is also indicated (red crosses). For calculation cases evaluated with different variants, only the variant resulting in the highest maximum dose is shown. For the cold climate calculation case (CC), glaciation calculation case (GC) and the calculation cases in the hypothetical early permafrost scenario (HEP), the maximum dose is the same as in the base case; here the maximum dose after the onset of the first periglacial period is shown. For the timing of shoreline regression calculation case (SR) the two bounding calculations are illustrated, corresponding to a shoreline-regression delay of 0 years (same as base case) and 20 000 years.

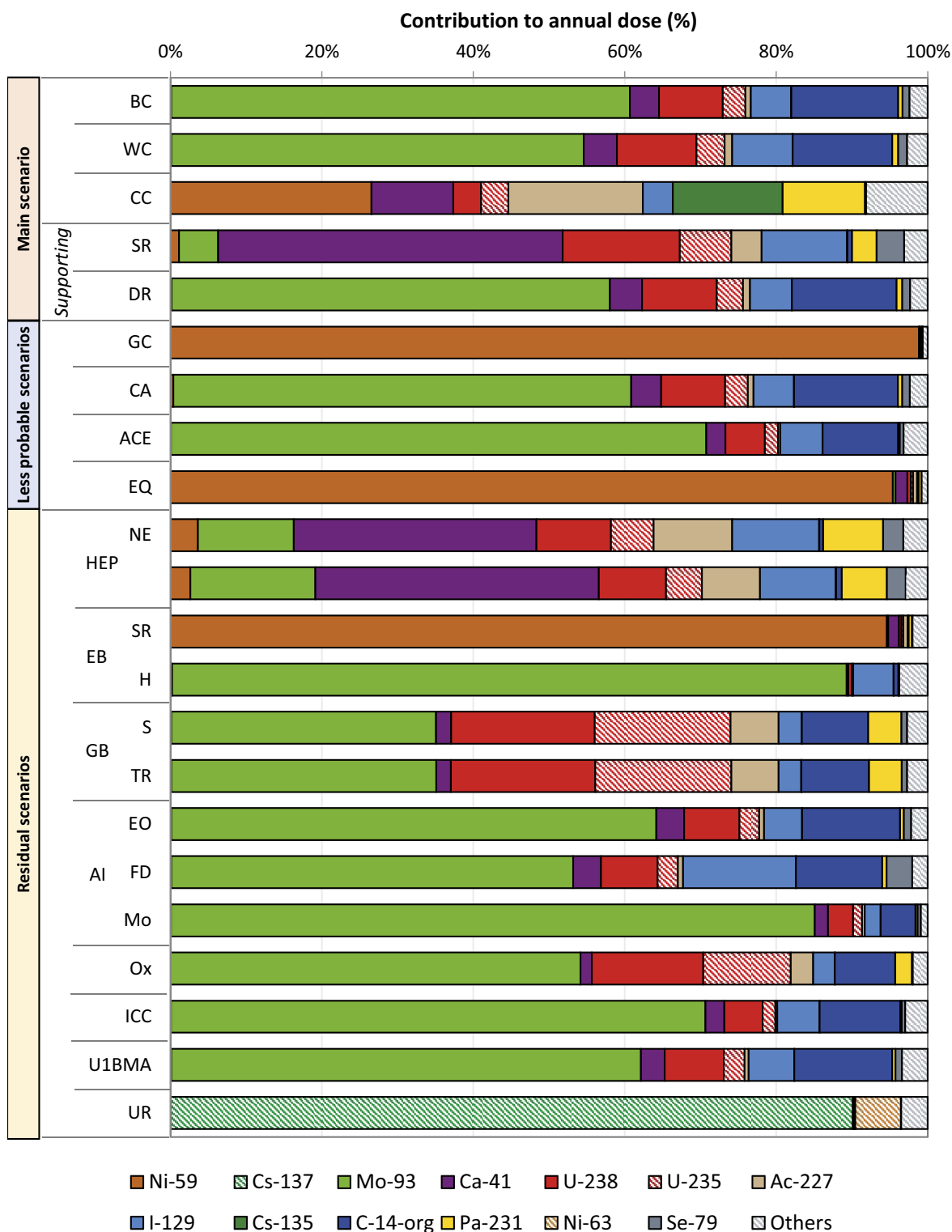


Figure 10-2. Radionuclide contributions to the probabilistic mean of the maximum annual dose over the assessment period (i.e. the dose corresponding to the white circles in Figure 10-1) for the calculation cases analysed in this report (short cc-names in Table 10-1). For calculation cases evaluated with different variants, only the variant resulting in the highest maximum doses is shown. For the cold climate calculation case (CC), glaciation calculation case (GC) and the calculation cases in the hypothetical early permafrost scenario (HEP), the maximum dose is the same as in the base case; here the maximum dose after the onset of the first periglacial period is shown. For timing of shoreline regression calculation case (SR), the radionuclide contribution for the calculation with the most extended shoreline-regression delay (20 000 years) is shown.

10.2.1 Main scenario

The main scenario (**Post-closure safety report**, Chapter 7) takes the most probable changes within the repository and its environs into account. Calculation cases in the main scenario include the *present-day climate calculation case*, selected as the *base case* for the present safety assessment, the *warm climate calculation case* and the *cold climate calculation case*. The calculation cases are summarised below.

Base case (BC)

The *base case* (Chapter 5) is defined based on the *present-day climate variant* of the reference evolution (**Post-closure safety report**, Sections 6.2 and 6.3), representing present-day conditions in the repository environs including the effect of shoreline displacement following the last glacial. In this *base case*, the maximum dose, 5.6 μSv , is reached around 7000 AD. Four radionuclides are found to be most important for the dose throughout the assessment period (Section 5.7): C-14-org and Mo-93 contribute most to the maximum dose (Figure 10-2), Ca-41 contributes most in the middle of the assessment period and Ni-59 contributes most towards the end of the assessment period.

The *base case* is included in the calculation of collective doses. The dose to the global population yields about 1.6 man Sv and the regional dose to the Baltic Sea population yields about 0.12 man Sv, with a 96 % contribution from C-14.

Warm climate calculation case (WC)

The *warm climate calculation case* (Section 6.2) is defined based on the *warm climate variant* of the reference evolution (**Post-closure safety report**, Sections 6.2 and 6.4), representing warmer-than-present conditions including the effect of a global sea-level rise resulting in a delayed shoreline regression in the area above the repository.

The maximum dose in the *warm climate calculation case* is slightly lower than the maximum dose in *base case* (Figure 10-1). The main reason is the delayed shoreline regression which results in a lower contribution of Mo-93 (due to radioactive decay) to the total dose (Figure 10-2). However, the dose in the *warm climate calculation case* is higher than in the *base case* after 20 000 AD (Figure 6-4).

The *warm climate calculation case* is included in the calculation of collective doses. The dose to the global population yields about 0.0016 man Sv and the dose to the Baltic Sea population yields about 0.00012 man Sv, with a 96 % contribution from C-14. The much lower collective doses compared with the *base case* is explained by the extended submerged period, which results in considerably lower groundwater flow rates during the first 1 000 years after closure than in the *base case*.

Cold climate calculation case (CC)

The *cold climate calculation case* (Section 6.3) is defined based on the *cold climate variant* of the reference evolution (**Post-closure safety report**, Sections 6.2 and 6.5), representing a development towards colder conditions, including the effect of periglacial conditions, during the last 50 000 years of the assessment period. The maximum dose in the *cold climate calculation case* is identical to the maximum dose in the *base case*, as it occurs before the onset of periglacial conditions. During the periglacial periods the dose is significantly lower than in the *base case*. During the post-periglacial temperate period, the dose is similar to the *base case* (Figure 10-1).

As all modelling assumptions in the *cold climate calculation case* are the same as in the *base case* during the first 1 000 years post-closure, collective doses are not evaluated for this calculation case.

10.2.2 Supporting calculation cases

The calculation cases of the main scenario are complemented with a set of supporting calculation cases, selected to provide a sensitivity analysis of specific uncertainties in external conditions and internal processes that important for radionuclide transport through the repository system. They are not propagated to the radiological risk assessment but serve to support the selection of assumptions for the *base case* and improve the confidence in the results of the main scenario. Calculated doses for

the supporting calculation cases are shown in Figure 10-1 (beige field) and the radionuclide contributions to the maximum dose in each calculation case are summarised in Figure 10-2. Two supporting calculation cases are included in this report (Table 10-1), summarised below.

Timing of shoreline regression calculation case (SR)

The *timing of shoreline regression calculation case* (Section 5.8.2) evaluates radiological consequences of a delayed shoreline regression compared with the *base case*. It includes five calculations with increasing delays of the shoreline regression until a maximum of 20 000 years. The maximum dose for all calculations with increased shoreline-regression delays is lower than the maximum dose in the *base case* (Figure 10-1) due to increased radioactive decay of the two radionuclides contributing most to the maximum dose (Mo-93 and C-14-org). This indicates that the assumption regarding the timing of the shoreline regression in the *base case* is pessimistic. The timing of the maximum dose increases gradually with the delay of shoreline regression. As Mo-93 and C-14-org are significantly affected by radioactive decay in these time perspectives, the contribution of Ca-41 to the maximum dose increases when shoreline regression is delayed such that it becomes the radionuclide contributing most to the maximum dose for shoreline-regression delays greater than 10 000 years (Figure 10-2).

Delayed release from repository calculation case (DR)

This *delayed release from repository calculation case* (Section 5.8.3) is developed to evaluate radiological consequences of simplifying assumptions whereby several processes are omitted in the near-field modelling. The overall consequence of these simplifications is an earlier release from the near-field compared to if more realistic parameterisations were to be used. Thus, the simplifications could possibly result in an exaggerated release during the submerged period in the *base case*, when doses are significantly lower than during the subsequent period when land has emerged. A delay period of 1 000 years for the release is therefore chosen based on the length of the submerged period above the repository. The *delayed release calculation case* gives higher doses than the *base case* during the first few centuries after 3000 AD, but marginally lower or equal doses thereafter, including during the period of maximum dose around 7000 AD (Figure 10-1). Thus, the simplistic representation in the *base case*, where several release-delaying processes are omitted, is considered to be adequate.

10.2.3 Less probable scenarios

Less probable scenarios are included in the risk assessment (**Post-closure safety report**, Chapter 10). This means that the lower probability of occurrence of these scenarios is considered when the total risk is calculated. Calculated doses for the calculation cases in the less probable scenarios are shown in the middle (blue) field in Table 10-1 and Figure 10-1, and the radionuclide contributions to the maximum dose in each calculation case are summarised in Figure 10-2. The calculation cases are summarised below.

Glaciation calculation case (GC)

The *glaciation calculation case* (Section 7.2) evaluates radiological consequences of a glaciation above SFR within the assessment period. The underlying assumption is the same as in the *cold climate calculation case*. However, in this calculation case, it is assumed that a development towards colder climate conditions result in the development of ice sheets above the repository within the latter half of the assessment period.

At the time of the first ice-sheet advance over the area, the concrete barriers in the waste vaults are completely degraded, as in the *base case*. A glaciation in the area above the repository is considered to also result in a reduced performance of the bentonite, an altered sorption capacity for some radionuclides due to the intrusion of oxygen-rich glacial meltwater, and elevated groundwater flow in the near-field and the geosphere in response to the ice-sheet retreat from the area. The maximum dose in the *glaciation calculation case* (Figure 10-1) occurs before the first glacial period and is thus identical to the *base case*. However, during the temperate period following the first glacial period, the dose is significantly higher than during the same period in the *base case*, mainly due to a significant release of Ni-59 (Figure 10-2).

As all models and input data in the *glaciation calculation case* are the same as in the *base case* during the first 1 000 years post-closure, collective doses are not evaluated for this calculation case.

High concentrations of complexing agents calculation case (CA)

The *high concentrations of complexing agents calculation case* (Section 7.3) evaluates radiological consequences of uncertainties related to complexing agents and their potential impact on sorption in the engineered barriers, waste form and packaging. The effect of these uncertainties is implemented in terms of an assumed additional tenfold reduction in sorption for species affected by complexing agents, including nickel.

In terms of maximum dose (Figure 10-1), the presence of additional complexing agents is shown to have a minor effect, since the dose-dominating radionuclides of the *base case* (Mo-93 and C-14-org) are not affected by complexing agents. However, the dose from Ni-59 increases significantly, dominating the dose after 20 000 AD (Figure 7-12).

The *high concentrations of complexing agents calculation case* is included in the calculation of collective doses. The doses to the global and regional populations are virtually the same as in the *base case*.

Alternative concrete evolution calculation case (ACE)

The *alternative concrete evolution calculation case* (Section 7.4) evaluates radiological consequences of uncertainties in the initial state and evolution of the structural concrete and waste packaging. To this end, it is assumed that the hydraulic conductivity and porosity of the concrete barriers, as well as the diffusivity of radionuclides in the concrete, are initially higher and increase earlier than in the *base case*. In this calculation case, the maximum dose increases by about 50 % compared with the *base case* (Figure 10-1), due to significant increases in the releases of primarily Mo-93 and C-14-org (Figure 10-2). The increase is mainly due to elevated releases from the two BMA-vaults.

The *alternative concrete evolution calculation case* is included in the calculation of collective doses. The dose to the global population yields about 2.0 man Sv (1.6 man Sv in the *base case*) and the dose to the Baltic Sea population yields about 0.14 man Sv (0.12 man Sv in the *base case*), with a 96 % contribution from C-14-org.

Earthquake calculation case (EQ)

The *earthquake calculation case* (Section 7.5) evaluates radiological consequences of an earthquake. Following the methodology adopted for SAR-08 and SR-PSU, this calculation case assumes that an earthquake damages the silo concrete structure. This methodology is highly simplified and overestimates the radiological consequences of an earthquake. As a result, the maximum dose due to releases from the silo is estimated to be pessimistically high in this calculation case (41 μ Sv), almost 20 times higher than in the *base case* (2.4 μ Sv; Figure 10-2). Ni-59 contributes most to the elevated doses in this calculation case (Figure 10-2).

As the probability of an earthquake event that damages the silo during the first 1 000 years post-closure is very low, separate collective doses are not evaluated for this calculation case (**Post-closure safety report**, Chapter 10).

10.2.4 Residual scenarios

Calculation cases in the residual scenarios are excluded from the risk assessment (**Post-closure report**, Chapter 9). These calculation cases often include hypothetical assumptions that are associated with a low degree of realism or events with exceptionally low likelihood of occurrence. The objective of these calculation cases is primarily to illustrate the significance of individual barriers and barrier functions and how they contribute to the protective capability of the repository.

The calculation cases for residual scenarios are shown in the bottom (yellow) field in Table 10-1 and Figure 10-1, and the radionuclide contributions to the maximum dose in each calculation case are summarised in Figure 10-2. The calculation cases are summarised below.

Calculation cases in the hypothetical early permafrost scenario (HEP NE, HEP)

Two calculation cases are selected to evaluate the *hypothetical early permafrost scenario* (Section 8.2), *no effect on engineered barriers calculation case* and *effect on engineered barriers calculation case*. In the latter it is assumed that the engineered barriers are degraded due to freezing during an early periglacial period. The highest dose during the post-periglacial period occurs for the calculation with degradation of concrete shown in Figure 10-1. In this post-periglacial temperate period, the dose in this calculation is about 30 % higher than during the corresponding time in the *base case*. However, the dose during this time is lower than the maximum dose that occurs prior to the onset of the periglacial period.

Calculation cases in the loss of engineered barrier function scenario (EB S, EB H)

Two calculation cases are selected to evaluate the *loss of engineered barrier function scenario* (Section 8.3), the *no sorption in the repository calculation case* and the *no hydraulic barriers in the repository calculation case*. Both calculation cases result in dose maxima about a factor of ten higher than in the *base case* (Figure 10-1). The *no sorption in the repository calculation case* further yields a shift of the dose maximum to around 30 000 AD, mainly due to release of Ni-59 (Figure 10-2). The *no hydraulic barriers in the repository calculation case* yields a shift of the maximum dose to around 3500 AD, mainly due to an increased release of Mo-93 (Figure 10-2).

Calculation cases in the loss of geosphere barrier function scenario (GB S, GB TR)

Two calculation cases are selected to evaluate the *loss of geosphere barrier function scenario* (Section 8.4), the *no sorption in the geosphere calculation case* and the *no transport retention in the geosphere calculation case*. Both calculation cases result in a maximum dose about a factor of two higher than in the *base case*. The increases in dose are mainly due to the lack of retention of the releases of U-235 and U-238 originating from the waste in 1-5BLA.

Calculation cases in the alternative radionuclide inventory scenario (AI EO, AI FD, AI Mo)

Three calculation cases are selected to evaluate the *alternative radionuclide inventory scenario* (Section 8.5); *extended operation of reactors calculation case*, *increased fuel damage frequency calculation case* and the *extended use of molybdenum-alloy fuel spacers calculation case*. The largest effect on maximum dose can be seen in the *extended use of molybdenum-alloy fuel spacers calculation case* for which the maximum dose increases by almost a factor of 3 compared with the *base case* (Figure 10-1).

Oxidising conditions calculation case (Ox)

This calculation case (Section 8.6) considers oxidising conditions for the entire assessment period as compared to the reducing conditions in the *base case*. This affects sorption in the near-field and the geosphere as well as corrosion rates for the steel from reactor pressure vessels in 1BRT. The maximum dose for the calculation case is about a factor of two higher than in the *base case* (Figure 10-1). The increase is mainly explained by early release of induced Mo-93 from 1BRT due to the increased corrosion rate.

Initial concrete cracks calculation case (ICC)

This calculation case (Section 8.7) considers initial cracks in all concrete structures. In addition, the concrete structures are more degraded initially than in the *base case*. The dose maximum (Figure 10-1) is increased by about 50 % compared with the *base case*, due mainly to increase in the releases of Mo-93 and C-14-org (Figure 10-2).

Unrepaired 1BMA calculation case (U1BMA)

This calculation case (Section 8.8) is selected to evaluate an alternative initial state of 1BMA where no additional concrete structure is cast around the existing concrete structure. The purpose of the calculation case is to assess the effects of the planned repair and strengthening measures prior to closure of

1BMA. This calculation case yields a dose contribution from 1BMA which is about a factor two higher than the 1BMA-contribution in the *base case*, mainly due to increased release of C-14-org, Mo-93 and I-129. The total dose from SFR, however, increases only about 5 % (Figure 10-1) compared with the *base case*.

Unsealed repository calculation case (UR)

This calculation case (Section 8.9) assumes that, following completion of waste disposal, the repository is for some reason neither closed nor monitored. The radionuclide concentrations at the entrance of an access tunnel are considered in estimation of dose from drinking water. The resulting estimated maximum dose at 100 years after abandonment is 14.3 mSv (Figure 10-1), dominated by exposure from Cs-137 (Figure 10-2). The dose decreases rapidly as the time of first use of water from the abandoned repository increases.

10.3 Management of uncertainties

Management of uncertainties is an integral part of the overall safety assessment including the radionuclide transport and dose calculations (**Post-closure safety report**, Section 2.5). Uncertainties are classified as system, data, scenario or modelling uncertainties (Section 2.5). While system uncertainty concerns comprehensiveness issues and so is generally dealt with in the FEP analysis (**FEP report and Biosphere synthesis report**, Chapter 6), the other uncertainties (data, scenario and modelling) are considered in the radionuclide transport calculations. The *base case* constitutes the starting point for the analysis of uncertainties in the radionuclide transport and dose calculations in this report. An important aspect of the management of uncertainties in the *base case* is to evaluate how individual parameters contribute to the dose from the most important radionuclides. This is documented in Appendix D.

Data uncertainties, i.e. uncertainties in input parameters, are mostly handled by using a probabilistic approach, whereby stochastic values of the parameters are drawn from probability density functions (PDFs). A comprehensive analysis of the data uncertainty in the *base case* is given in the **Biosphere synthesis report**, Section 9.4. In that analysis, it was concluded that a probabilistic handling of uncertain parameters does not lead to an underestimation of the dose. The reason is that deterministic simulations, using best estimates for each input parameter, yield a systematically lower dose than the average dose from probabilistic calculations. Except for the *unsealed repository calculation case*, all calculation cases in this report include a probabilistic representation of parameters to the extent appropriate to quantifying the significance of data uncertainties. The impact of these uncertainties on the maximum annual dose over the assessment period for these calculation cases as well as the *base case* is summarised in Figure 10-1. For most of the calculation cases, the 5 – 95th percentile range across the probabilistic dose calculations has a similar magnitude as in the *base case*, i.e. extending approximately one order of magnitude. The calculation cases that exhibit a wider 5–95th percentile range and thus a greater data uncertainty than in the *base case*, are primarily those that have significant dose consequences later in the assessment period (e.g. the *glaciation calculation case* and *earthquake calculation case*; GC and EQ in Figure 10-1, respectively). This pattern in the simulations primarily reflects the differences in uncertainties associated with individual radionuclides that contribute to the dose. That is, the uncertainties in the dose from radionuclides that contribute early (e.g. C-14 and Mo-93), are relatively small compared with the uncertainties in the dose from radionuclides that contribute later in the simulations (e.g. Ca-41 and Ni-59), see further the **Biosphere synthesis report**, Sections 9.4 and 11.2.

As described in Section 2.5.4, the probabilistic approach is not considered feasible for input parameters that are already handled cautiously or pessimistically in the modelling, or for parameters that are subject to considerable modelling or scenario uncertainty. Instead, the impact on the dose of scenario and modelling uncertainties is generally covered by the individual calculation cases in the main scenario, including the supporting calculations, and less probable scenarios. These calculation cases cover alternative evolutions and events that might affect the capability to protect human health and the environment. While some of the calculation cases have been identified from specific scenario uncertainties, such as the uncertainty in post-closure evolution of the climate and degradation of concrete barriers, others have been selected to evaluate modelling uncertainties, such as uncertainties related to the timing of releases

from the waste. One calculation case, *high concentrations of complexing agents*, evaluates both scenario and modelling uncertainties. The objective of calculation cases evaluating residual scenarios is to illustrate the significance of individual barriers and barrier functions and their capability to protect the repository, rather than evaluating plausible scenario or modelling uncertainties.

The full extent of scenario and modelling uncertainties cannot be estimated accurately based on the radionuclide transport calculations as several parameters are cautiously or pessimistically assigned in all calculation cases, including the *base case*. However, the impact of these uncertainties on the dose can be crudely highlighted by comparing the probabilistic mean of the maximum dose for the calculation cases in the main scenario and less probable scenarios to the corresponding dose in the *base case* (difference between the white circles and the red crosses in Figure 10-1). These uncertainties may have a significant impact on the dose at specific times of the assessment period, resulting in higher dose than during the corresponding time in the *base case* (e.g. the *warm climate calculation case* and *glaciation calculation case*; WC and GC in Figure 10-1, respectively). However, for most of the calculation cases, these uncertainties do not result in a dose that is higher than the maximum dose in the *base case* (cf. white circles and red dashed line in Figure 10-1). Only for the *alternative concrete evolution* and *earthquake calculation cases* are the maximum doses higher than that of the *base case*.

An example of how one type of modelling and scenario uncertainty may influence the temporal evolution of dose is shown in Figure 10-3, which illustrates the dose, including data uncertainties, in the *base case* compared with the evolution of the mean dose from the *alternative concrete evolution calculation case* and the *high concentration of complexing agents calculation case*. While the mean dose in the *alternative concrete evolution calculation case* is systematically higher than in the *base case* for the entire assessment period, the mean dose in the *high concentration of complexing agents calculation case* is only significantly higher than in the *base case* towards the end of the assessment period. Further, as the mean doses of these calculation cases are bracketed within the 5–95th percentile range of the probabilistic *base case* calculations for most of the assessment period, the evaluated uncertainties in these calculation cases have a relatively modest impact on the dose for most of the assessment period compared with the uncertainties accounted for in the probabilistic handling of input parameters.

Further discussion about the management of uncertainties in calculations are given in the **Post-closure safety report**, Chapter 11 and the **Biosphere synthesis report**, Chapter 13.

10.4 Conclusions

In the calculation cases adopted for analysing the main scenario, the maximum annual dose throughout the assessment period is less than 6 μSv , i.e. well below the dose corresponding to the regulatory risk criterion that is approximately 14 μSv . For calculation cases evaluating less probable scenarios, which have a lower probability than the calculation cases in the main scenario, the maximum doses are within the range 5–50 μSv . The resulting doses presented in this report are further propagated to the evaluation of regulatory compliance against requirements related to the protection of human health and the environment (**Post-closure safety report**, Chapter 10). The significance of the protective capability of specific barriers and barrier functions is illustrated by calculation cases evaluating residual scenarios. Taken together, the results from these calculation cases show that specific barriers and barrier functions serve to reduce the maximum annual dose by up to one order of magnitude.

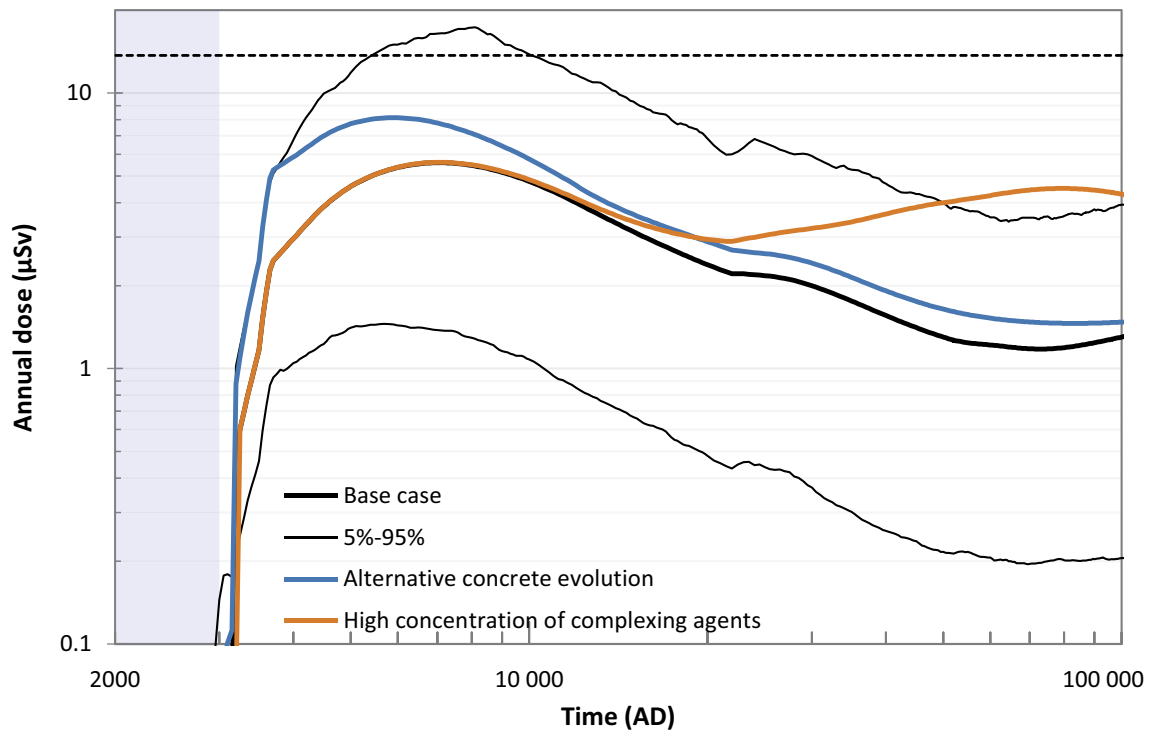


Figure 10-3. Annual dose (μSv) to the most exposed group from releases from the entire SFR in the base case (black line) and two calculation cases in the less probable scenarios (coloured lines). The 5th and 95th percentiles of the annual dose in the base case are shown with thin black lines. The annual dose corresponding to the regulatory risk criterion ($14 \mu\text{Sv}$) is indicated by the black dashed line and the submerged period is illustrated by the blue shading.

References

SKB's (Svensk Kärnbränslehantering AB) publications can be found at www.skb.com/publications. SKBdoc documents will be submitted upon request to document@skb.se.

References with abbreviated names

Post-closure safety report, 2023. Post-closure safety for SFR, the final repository for short-lived radioactive waste at Forsmark. Main report, PSAR version. SKB TR-23-01, Svensk Kärnbränslehantering AB.

Barrier process report, 2023. Post-closure safety for SFR, the final repository for short-lived radioactive waste at Forsmark. Engineered barrier process report, PSAR version. SKB TR-23-04, Svensk Kärnbränslehantering AB.

Biosphere synthesis report, 2023. Post-closure safety for SFR, the final repository for short-lived radioactive waste at Forsmark. Biosphere synthesis report, PSAR version. SKB TR-23-06, Svensk Kärnbränslehantering AB.

Climate report, 2023. Post-closure safety for SFR, the final repository for short-lived radioactive waste at Forsmark. Climate and climate-related issues, PSAR version. SKB TR-23-05, Svensk Kärnbränslehantering AB.

Data report, 2023. Post-closure safety for SFR, the final repository for short-lived radioactive waste at Forsmark. Data report, PSAR version. SKB TR-23-10, Svensk Kärnbränslehantering AB.

FEP report, 2014. FEP report for the safety assessment SR-PSU. SKB TR-14-07, Svensk Kärnbränslehantering AB.

FHA report, 2023. Post-closure safety for SFR, the final repository for short-lived radioactive waste at Forsmark. Handling of future human actions, PSAR version. SKB TR-23-08, Svensk Kärnbränslehantering AB.

Geosphere process report, 2014. Geosphere process report for the safety assessment SR-PSU. SKB TR-14-05, Svensk Kärnbränslehantering AB.

Initial state report, 2023. Post-closure safety for SFR, the final repository for short-lived radioactive waste at Forsmark. Initial state of the repository, PSAR version. SKB TR-23-02, Svensk Kärnbränslehantering AB.

Model tools report, 2023. Post-closure safety for SFR, the final repository for short-lived radioactive waste at Forsmark. Model tools summary report, PSAR version. SKB TR-23-11, Svensk Kärnbränslehantering AB.

Waste process report, 2023. Post-closure safety for SFR, the final repository for short-lived radioactive waste at Forsmark. Waste form and packaging process report, PSAR version. SKB TR-23-03, Svensk Kärnbränslehantering AB.

Regular references

Abarca E, Idiart A, de Vries L M, Silva O, Molinero J, von Schenck H, 2013. Flow modelling on the repository scale for the safety assessment SR-PSU. SKB TR-13-08, Svensk Kärnbränslehantering AB.

Abarca E, Silva O, Idiart A, Nardi A, Font J, Molinero J, 2014. Flow and transport modelling on the vault scale. Supporting calculations for the safety assessment SR-PSU. SKB R-14-14, Svensk Kärnbränslehantering AB.

Abarca E, Sampietro D, Sanglas J, Molinero J, 2020. Modelling of the near-field hydrogeology. Report for the safety assessment SR-PSU (PSAR). SKB R-19-20, Svensk Kärnbränslehantering AB.

Almkvist L, Gordon A, 2007. Low and intermediate level waste in SFR 1. Reference waste inventory 2007. SKB R-07-17, Svensk Kärnbränslehantering AB.

Auqué L F, Gimeno M J, Acero P, Gómez J B, 2013. Compositions of groundwater for SFR and its extension, during different climate cases, SR-PSU. SKB R-13-16, Svensk Kärnbränslehantering AB.

- Avila R, Bergström U, 2006.** Methodology for calculation of doses to man and implementation in Pandora. SKB R-06-68, Svensk Kärnbränslehantering AB.
- Avila R, Ekström P-A, Åstrand P-G, 2010.** Landscape dose conversion factors used in the safety assessment SR-Site. SKB TR-10-06, Svensk Kärnbränslehantering AB.
- Bellamy M B, Dewji S A, Leggett R W, Hiller M, Veinot K, Manger P, Eckerman K F, Ryman J C, Easterly C E, Hertel N E, Stewart D J, 2019.** External exposure to radionuclides in air, water, and soil. Federal Guidance Report No. 15 (No. EPA-402/R19/002), U.S. Environmental Protection Agency, Washington, DC.
- Bergman R, Bergström U, Evans S, 1977.** Ecologic transport and radiation doses from groundwater-borne radioactive substances. KBS TR 40, Svensk Kärnbränsleförsörjning AB.
- Bergman R, Bergström U, Evans S, 1979.** Dose and dose commitment from groundwater-borne radioactive elements in the final storage of spent nuclear fuel. KBS TR 100, Svensk Kärnbränsleförsörjning AB.
- Bergström U, 1983.** Dose and dose commitment calculations from groundwater borne radioactive elements released from a repository for spent nuclear fuel. SKBF/KBS TR 83-49, Svensk Kärnbränsleförsörjning AB.
- Bosson E, Sassner M, Sabel U, Gustafsson L-G, 2010.** Modelling of present and future hydrology and solute transport at Forsmark. SR-Site Biosphere. SKB R-10-02, Svensk Kärnbränslehantering AB.
- Bosson E, Selroos J-O, Stigsson M, Gustafsson L-G, Destouni G, 2013.** Exchange and pathways of deep and shallow groundwater in different climate and permafrost conditions using the Forsmark site, Sweden, as an example catchment. *Hydrogeology Journal* 21, 225–237.
- Brandefelt J, Näslund J-O, Andersson E, 2016.** Kompletterande information om hantering av klimatscenerierna i ansökan om utbyggnad av SFR. SKBdoc 1541317 ver 1.0, Svensk Kärnbränslehantering AB. (In Swedish.)
- Bruno J, González-Siso M R, Duro L, Gaona X, Altmaier M, 2018.** Key master variables affecting the mobility of Ni, Pu, Tc and U in the near field of the SFR repository. Main experimental findings and PA implications of the PhD thesis. SKB TR-18-01, Svensk Kärnbränslehantering AB.
- Brydsten L, Strömgren M, 2010.** A coupled regolith-lake development model applied to the Forsmark site. SKB TR-10-56, Svensk Kärnbränslehantering AB.
- Brydsten L, Strömgren M, 2013.** Landscape development in the Forsmark area from the past into the future (8500 BC – 40 000 AD). SKB R-13-27, Svensk Kärnbränslehantering AB.
- Börgesson L, Åkesson M, Kristensson O, Malmberg D, Birgersson M, Hernelind J, 2015.** Modelling of critical H-M processes in the engineered barriers of SFR. SKB TR-14-27, Svensk Kärnbränslehantering AB.
- COMSOL, 2017.** COMSOL Multiphysics® v. 5.3. Stockholm: COMSOL AB.
- Cohen-Corticchiato D, Zwinger T, 2021.** Modeling permafrost evolution at Olkiluoto for the next 120 000 years. Posiva Working Report 2021-14, Posiva Oy, Finland.
- Crawford J, 2013.** Quantification of rock matrix K_d data and uncertainties for SR-PSU. SKB R-13-38, Svensk Kärnbränslehantering AB.
- Crawford J, 2017.** Organic complexation in the geosphere for SR PSU. SKBdoc 1577134 ver 1.0, Svensk Kärnbränslehantering AB.
- Crawford J, 2018.** Technical Note – K_d values for oxyanions in SR-PSU. Updated K_d recommendations for Mo-93 and Se-79. Kemakta Konsult AB. SKBdoc 1689868 ver 1.0, Svensk Kärnbränslehantering AB.
- Ekström P-A, Källström K, Åstrand P-G, 2017.** Försiktiga antaganden i analysen av säkerhet efter förslutning SR-PSU. SKBdoc 1579024 ver 1.0, Svensk Kärnbränslehantering AB.
- Elert M, Gylling B, Lindgren M, 2004.** Assessment model validity document FARF31. SKB R-04-51, Svensk Kärnbränslehantering AB.

- Elfving M, von Schenck H, Åstrand P-G, 2018.** Uppdaterad analys av strålsäkerheten efter förslutning för 1BMA i SFR1. SKBdoc 1686798 ver 1.0, Svensk Kärnbränslehantering AB. (In Swedish.)
- Elmgren R, 1989.** Man's impact on the ecosystem of the Baltic Sea: Energy flows today and at the turn of the century. *Ambio* 18, 326–332.
- Gosling S, Müller Schmied H, Betts R, Chang J, Ciais P, Dankers R, Döll P, Eisner S, Flörke M, Gerten D, Grillakis M, Hanasaki N, Hagemann S, Huang M, Huang Z, Jerez S, Kim H, Koutroulis A, Leng G, Liu X, Masaki Y, Montavez P, Morfopoulos C, Oki T, Papadimitriou L, Pokhrel Y, Portmann F T, Orth R, Ostberg S, Satoh Y, Seneviratne S, Sommer P, Stacke T, Tang Q, Tsanis I, Wada Y, Zhou T, Büchner M, Schewe J, Zhao F, 2019.** ISIMIP2a Simulation Data from Water (global) Sector (V. 1.1). GFZ Data Services. Available at: <https://doi.org/10.5880/PIK.2019.003>
- Grolander S, 2013.** Biosphere parameters used in radionuclide transport modelling and dose calculations in SR-PSU. SKB R-13-18, Svensk Kärnbränslehantering AB.
- Hartikainen J, Kouhia R, Wallroth T, 2010.** Permafrost simulations at Forsmark using a numerical 2D thermo-hydro-chemical model. SKB TR-09-17, Svensk Kärnbränslehantering AB.
- Holmén J G, Stigsson M, 2001.** Modelling of future hydrogeological conditions at SFR. SKB R-01-02, Svensk Kärnbränslehantering AB.
- Hummel R, Claassen E A, Wolfinger R D, 2021.** JMP for mixed models. SAS Institute.
- Höglund L O, 2014.** The impact of concrete degradation on the BMA barrier functions. SKB R-13-40, Svensk Kärnbränslehantering AB.
- IAEA, 2012.** The safety case and safety assessment for the disposal of radioactive waste. Vienna: International Atomic Energy Agency. (IAEA Safety Standards Series SSG-23)
- ICRP, 1991.** 1990 Recommendations of the International Commission on Radiological Protection. Oxford: Pergamon Press. (ICRP Publication 60; Annals of the ICRP 21 (1–3))
- ICRP, 2000.** Radiation protection recommendations as applied to the disposal of long-lived solid radioactive waste. Oxford: Pergamon. (ICRP Publication 81; Annals of the ICRP 28 (4))
- ICRP, 2008.** Nuclear decay data for dosimetric calculations. Amsterdam: Elsevier. (ICRP Publication 107; Annals of the ICRP 38 (3))
- ICRP, 2012.** Compendium of dose coefficients based on ICRP Publication 60. Amsterdam: Elsevier. (ICRP Publication 119; Annals of the ICRP 41(Suppl.))
- Johansson M, Christensen T R, Åkerman J, Callaghan T V, 2006.** What determines the current presence or absence of permafrost in the Torneträsk region, a sub-Arctic landscape in Northern Sweden? *Ambio* 35, 190–197.
- Keith-Roach M, Lindgren M, Källström K, 2021.** Assessment of complexing agent concentrations for the post-closure safety assessment in PSAR SFR. SKB R-20-04, Svensk Kärnbränslehantering AB.
- Leggett R W, 2004.** A biokinetic model for carbon dioxide and bicarbonate. *Radiation Protection Dosimetry* 108, 203–213.
- Lindgren M, Pettersson M, Karlsson S, Moreno L, 2001.** Project SAFE. Radionuclide release and dose from the SFR repository. SKB R-01-18, Svensk Kärnbränslehantering AB.
- Lord N S, Lunt D, Thorne M, 2019.** Modelling changes in climate over the next 1 million years. SKB TR-19-09, Svensk Kärnbränslehantering AB.
- Löfgren M, 2014.** Recommendation of rock matrix effective diffusivities for SR-PSU. Based on formation factor logging in situ by electrical methods in KFR102B and KFR105. SKB R-13-39, Svensk Kärnbränslehantering AB.
- Mårtensson P, Luterkort D, Nyblad B, Wimelius H, Pettersson A, Aghili B, Andolfsson T, 2022.** SFR Förslutningsplan. SKBdoc 1358612 ver 3.0, Svensk Kärnbränslehantering AB. (In Swedish.)
- NEA, 2012.** Methods for safety assessment of geological disposal facilities for radioactive wastes: outcomes of the NEA MeSA Initiative. Paris: OECD/NEA.

- Neretnieks I, Moreno L, 2013.** Flow and transport in fractures in concrete walls in BMA – Problem formulation and scoping calculations. SKB R-13-51, Svensk Kärnbränslehantering AB.
- Neretnieks I, Arve S, Moreno L, Rasmuson A, Zhu M, 1987.** Degradation of concrete and transport of radionuclides from SFR-repository for low- and intermediate-level nuclear waste. SKB SFR 87-11, Svensk Kärnbränslehantering AB.
- Norman S, Kjellbert N, 1990.** FARF31 – A far field radionuclide migration code for use with the PROPER package. SKB TR 90-01, Svensk Kärnbränslehantering AB.
- Näslund J-O, Mårtensson P, Andersson E, 2017a.** Svar till SSM på begäran om komplettering av ansökan om utökad verksamhet vid SFR – effekter av tidig permafrostpåverkan. SKBdoc 1564242 ver 1.0, Svensk Kärnbränslehantering AB. (In Swedish.)
- Näslund J-O, Mårtensson P, Lindgren M, Åstrand P-G, 2017b.** Information om klimat och effekter på SFR till följd av frysning av betong. SKBdoc 1572377 ver 1.0, Svensk Kärnbränslehantering AB. (In Swedish.)
- Odén M, Follin S, Öhman J, Vidstrand P, 2014.** SR-PSU Bedrock hydrogeology. Groundwater flow modelling methodology, setup and results. SKB R-13-25, Svensk Kärnbränslehantering AB.
- Rasmuson A, Neretnieks I, 1981.** Migration of radionuclides in fissured rock: the influence of micropore diffusion and longitudinal dispersion. *Journal of Geophysical Research: Solid Earth* 86, 3749–3758.
- Saetre P, Nordén S, Keesmann S, Ekström P-A, 2013.** The biosphere model for radionuclide transport and dose assessment in SR-PSU. SKB R-13-46, Svensk Kärnbränslehantering AB.
- Schroeder L D, Sjoquist D L, Stephan P E, 1986.** Understanding regression analysis: an introductory guide. Beverly Hills, CA: Sage.
- SenGupta A K, 2017.** Ion exchange in environmental processes: fundamentals, applications and sustainable technology. Hoboken, NJ: Wiley.
- SFS 1984:3.** Lag om kärnteknisk verksamhet (Nuclear Activities Act). Stockholm: Ministry of the Environment. (In Swedish.)
- SFS 1998:808.** Miljöbalk (Environmental Code). Stockholm: Ministry of the Environment. (In Swedish.)
- SKB, 2001.** SFR 1. Slutförvar för radioaktivt driftavfall. Slutlig säkerhetsrapport, version 1.0. Svensk Kärnbränslehantering AB. (In Swedish.)
- SKB R-01-14.** SKB 2001. Project SAFE. Compilation of data for radionuclide transport analysis. Svensk Kärnbränslehantering AB.
- SKB R-08-130.** SKB 2008. Safety analysis SFR 1. Long-term safety. Svensk Kärnbränslehantering AB.
- SKB R-13-37.** SKB 2013. Låg- och medelaktivt avfall i SFR. Referensinventarium för avfall 2013. Svensk Kärnbränslehantering AB. (In Swedish.)
- SKB R-13-43.** SKB 2013. Components, features, processes and interactions in the biosphere. Svensk Kärnbränslehantering AB.
- SKB R-14-02.** SKB 2015. Handling of biosphere FEPs and recommendations for model development in SR-PSU. Svensk Kärnbränslehantering AB.
- SKB R-18-07.** SKB 2019. Låg- och medelaktivt avfall i SFR. Referensinventarium för avfall 2016. Svensk Kärnbränslehantering AB. (In Swedish.)
- SKB TR-10-49.** SKB 2010. Climate and climate-related issues for the safety assessment SR-Site. Svensk Kärnbränslehantering AB.
- SKB TR-10-50.** SKB 2010. Radionuclide transport report for the safety assessment SR-Site. Svensk Kärnbränslehantering AB.
- SKB TR-10-51.** SKB 2010. Model summary report for the safety assessment SR-Site. Svensk Kärnbränslehantering AB.

- SKB TR-10-52.** SKB 2010. Data report for the safety assessment SR-Site. Svensk Kärnbränslehantering AB.
- SKB TR-13-05.** SKB 2014. Climate and climate-related issues for the safety assessment SR-PSU. Svensk Kärnbränslehantering AB.
- SKB TR-14-01.** SKB 2015. Safety analysis for SFR. Long-term safety. Main report for the safety assessment SR-PSU. Revised edition. Svensk Kärnbränslehantering AB.
- SKB TR-14-06.** SKB 2014. Biosphere synthesis report for the safety assessment SR-PSU. Svensk Kärnbränslehantering AB.
- SKB TR-14-09.** SKB 2015. Radionuclide transport and dose calculations for the safety assessment SR-PSU. Revised edition. Svensk Kärnbränslehantering AB.
- SKB TR-19-01.** SKB 2019. Post-closure safety for a proposed repository concept for SFL. Main report for the safety evaluation SE-SFL. Svensk Kärnbränslehantering AB.
- SKB TR-19-05.** SKB 2019. Biosphere synthesis for the safety evaluation SE-SFL. Svensk Kärnbränslehantering AB.
- SKB TR-19-06.** SKB 2019. Radionuclide transport and dose calculations for the safety evaluation SE-SFL. Svensk Kärnbränslehantering AB.
- SSM, 2017.** SSM's external experts' review of SKB's safety assessment SR-PSU – dose assessment, K_d -values, and safety analysis methodology. Report 2017:33, Swedish Radiation Safety Authority.
- SSM, 2018.** Strålsäkerhet efter slutförvarets förslutning. Beredning inför regeringens prövning Slutförvaring av använt kärnbränsle. Rapport 2018:07, Swedish Radiation Safety Authority. (In Swedish.)
- SSMFS 2008:21.** Strålsäkerhetsmyndighetens föreskrifter och allmänna råd om säkerhet vid slutförvaring av kärnämne och kärnavfall (Regulations concerning safety in connection with the disposal of nuclear material and nuclear waste). Stockholm: Swedish Radiation Safety Authority. (In Swedish.)
- SSMFS 2008:37.** Strålsäkerhetsmyndighetens föreskrifter och allmänna råd om skydd av människors hälsa och miljön vid slutligt omhändertagande av använt kärnbränsle och kärnavfall (Regulations on the protection of human health and the environment in connection with the final management of spent nuclear fuel and nuclear waste). Stockholm: Swedish Radiation Safety Authority. (In Swedish.)
- Stigebrandt A, Gustafsson B G, 2003.** Response of the Baltic Sea to climate change – theory and observations. *Journal of Sea Research* 49, 243–256.
- Tang D H, Frind E O, Sudicky E A, 1981.** Containment transport in fractured porous media: analytical solution for a single fracture. *Water Resources Research* 17, 555–564.
- Thomson G, Miller A, Smith G, Jackson D, 2008.** Radionuclide release calculations for SAR-08. SKB R-08-14, Svensk Kärnbränslehantering AB.
- Titley J G, Cabianca T, Lawson G, 1995.** Improved global dispersion models for iodine-129 and carbon-14. European Commission, EUR 15880 EN.
- UNSCEAR, 2000.** Sources and effects of ionizing radiation. Volume I: Sources. UNSCEAR 2000 report to the General Assembly, with scientific annexes. United Nations Scientific Committee on the Effects of Atomic Radiation.
- UNSCEAR, 2017.** Sources, effects and risks of ionizing radiation. UNSCEAR 2016 Report to the General Assembly, Scientific annexes A, B, C and D. United Nations Scientific Committee on the Effects of Atomic Radiation.
- van Loon L R, Glaus M A, Stallone S, Laube A, 1997.** Sorption of isosaccharinic acid, a cellulose degradation product, on cement. *Environmental Science & Technology* 31, 1243–1245.
- Vidstrand P, Follin S, Selroos J-O, Näslund J-O, Rhén I, 2013.** Modeling of groundwater flow at depth in crystalline rock beneath a moving ice-sheet margin, exemplified by the Fennoscandian Shield, Sweden. *Hydrogeology Journal* 21, 239–255.
- Vidstrand P, Follin S, Öhman J, 2014a.** SR-PSU Hydrogeological modelling. TD13 – Periglacial climate conditions. SKB P-14-06, Svensk Kärnbränslehantering AB.

Vidstrand P, Follin S, Selroos J-O, Näslund J-O, 2014b. Groundwater flow modeling of periods with periglacial and glacial climate conditions for the safety assessment of the proposed high-level nuclear waste repository site at Forsmark, Sweden. *Hydrogeology Journal* 22, 1251–1267.

Walke R, Limer L, Shaw G, 2017. In-depth review of key issues regarding biosphere models for specific radionuclides in SR-PSU. In SSM's external experts' review of SKB's safety assessment SR-PSU – dose assessment, K_d -values and safety analysis methodology. Main review phase. Report 2017:33, Swedish Radiation Safety Authority, Part 2.

Werner K, Sassner M, Johansson E, 2013. Hydrology and near-surface hydrogeology at Forsmark – synthesis for the SR-PSU project. SR-PSU Biosphere. SKB R-13-19, Svensk Kärnbränslehantering AB.

Åstrand P-G, Rasmusson M, Wessely O, 2022. Near-field radionuclide transport models for the post-closure safety assessment in PSAR SFR. SKB R-21-02, Svensk Kärnbränslehantering AB.

Öhman J, Odén M, 2018. SR-PSU (PSAR) Bedrock hydrogeology. TD18 – Temperate climate conditions. SKB P-18-02, Svensk Kärnbränslehantering AB.

Öhman J, Vidstrand P, 2014. SR-PSU Bedrock hydrogeology. TD12 – Water-supply wells in rock. SKB P-14-05, Svensk Kärnbränslehantering AB.

Öhman J, Bockgård N, Follin S, 2012. Bedrock hydrogeology. Site investigation SFR. SKB R-11-03, Svensk Kärnbränslehantering AB.

Öhman J, Follin S, Odén M, 2014. SR-PSU Hydrogeological modelling. TD11 – Temperate climate conditions. SKB P-14-04, Svensk Kärnbränslehantering AB.

Input data and quality assurance

The main sources of data for the radionuclide transport calculations in the near-field and geosphere are the **Data report** and the **Initial state report**. The usage and handling of data for the biosphere is described in Chapter 8 in the **Biosphere synthesis report**. This appendix presents a short description of the usage and quality assurance of the model data. Some additional data (not described elsewhere) for the near-field and geosphere models are also presented here. This appendix also contains dose coefficients used to calculate radiotoxicity of inventory and releases and for calculation of doses to humans.

A1 Handling of data

The data used in the radionuclide transport modelling are stored together with relevant metadata (authorship, date of change, revision number and references) in Excel spreadsheets to facilitate input, review and quality management by modellers as well as the data suppliers (subject experts). These Excel spreadsheets are automatically read by the modelling software.

To ensure that the data in supporting documents are interpreted and handled correctly, the subject experts review the Excel spreadsheets before the final calculations. Intermediate and final versions of the Excel spreadsheets are stored in a revision control system with a central server-based data repository using the software Subversion (SVN; <https://subversion.apache.org/>).

Each dataset has a specified delivery file on SVN where data are stored. In SVN, files are version controlled which increases the traceability of data. Documentation and background material used in the parameterisation process can be stored in SVN together with the delivery files. This handling simplifies data access and quality management, including tracing of data. Further details on the delivery file are given in Appendix A in Åstrand et al. (2022).

The modeller has the responsibility for the model development and specifies the parameters, the descriptions and units. The modeller helps to create the structure of the delivery files so that the use of dependencies, categories and parameter names and units will be compatible with the model implemented in the modelling software.

Normally a subject expert is responsible for and delivers data according to the specifications given by the modeller. The data delivery comprises three elements.

1. Parameter data in the specified delivery files.
2. Text describing the data, how the data have been derived and source references.
3. References and background files where calculations have been carried out (where applicable).

A second (independent) subject expert reviews the data set. The reviewer documents the review in the delivery file both through a general review statement and by commenting on each parameter in a dedicated column of the delivery file. An exception to this is the handling of some simple data, for which QA requires no subject expertise.

For large datasets, text files with data are preferred (instead of Excel). This is typical for data that are delivered from calculations or programs which already are quality assured. However, these data are also stored on SVN, for traceability. Some other smaller datasets are also stored in text files. This is done to avoid “hard coding” such data in the calculation codes.

After a radionuclide transport model has been run for a calculation case, the result is saved to SVN together with the model that was prepared with data for that calculation case.

A2 Near-field data

This section contains some data, not described elsewhere, used in the near-field calculations.

Vault flow scale-factors, U-Factors

The vault flows calculated in the near-field hydrological model are based on boundary values given by the regional hydrogeological model (Öhman and Odén 2018). However, the set of near-field hydrological calculations (Abarca et al. 2020) is only performed with boundary values for one representative bedrock case (case 1) in Öhman and Odén (2018). To obtain best-estimate values for vault flow representative of the full set of bedrock cases, scale-factors are applied to the vault flows calculated in the near-field hydrological model. This is done by applying scale-factors based on the geometric mean of the groundwater flow in three representative bedrock cases (cases 1, 11, and 15 in Öhman and Odén 2018) further discussed in Section A.4. This is analogous to how best estimates for flow-related parameters in the geosphere model are derived, as described in Section 5.5. The scale-factors used in the deterministic calculations are shown in Table A-1. In the probabilistic calculation the vault flow is varied according to probabilistic distributions as described in Section A.4.

Table A-1. Scale-factors (-) applied to the vault flow in the deterministic calculations.

Time	Silo	1BMA	2BMA	1BRT	1BTF	2BTF	1BLA	2BLA
2000 AD	1.53	2.04	1.16	0.95	1.72	1.34	1.0	0.98
2100 AD	1.58	1.77	1.24	0.95	1.43	1.12	0.87	1.0
2250 AD	1.20	1.37	1.51	1.01	1.19	0.91	0.7	0.89
2500 AD	0.90	1.27	2.20	1.08	1.16	0.81	0.62	0.95
2750 AD	0.72	1.19	1.72	0.99	1.42	1.10	0.73	0.96
3000 AD	0.68	1.23	1.53	0.96	1.24	1.12	0.73	0.98
3500 AD	0.69	1.27	1.65	0.94	1.17	1.09	0.72	0.94
5000 AD	0.71	1.27	1.63	0.92	1.14	1.08	0.72	0.92
9000 AD	0.71	1.27	1.63	0.91	1.14	1.07	0.71	0.92

Additional hydrological calculations

Hydrological calculations have been performed to obtain water flow rates inside the vaults (Abarca et al. 2013, 2014, 2020). Near-field water flow is calculated using repository-scale models implemented in COMSOL Multiphysics (COMSOL 2017). One of the endpoints of the detailed near-field hydrological modelling is the water flow through a large number of surfaces of control volumes (see Section 4.2.1) in the near-field. These flow fields are delivered in text files and then converted to the Excel spreadsheet format used by the radionuclide transport models for the near-field.

Most of the water flow rates used in the radionuclide transport calculations in the PSAR are obtained from the models presented in Abarca et al. (2020). The exceptions are the flow rates used in the *Unrepaired 1BMA calculation case* and the early flow rates for the severely degraded state used in the *Alternative concrete evolution calculation case*.

Unrepaired 1BMA calculation case

For the *Unrepaired 1BMA calculation case* water flow is obtained from the model presented in Abarca et al. (2014). In the model by Abarca et al. (2014) the water flow rates through the surfaces of two small waste compartments (compartment number 14 and 15 in Figure 7-4 in Abarca et al. 2020) are integrated separately. Since the PSAR radionuclide transport model handles these two small waste compartments as a single entity, the flow through the merged surfaces was summed.

Alternative concrete evolution case

In the *Alternative concrete evolution case*, the concrete is assumed to become completely degraded at a much earlier point in time compared with the *base case*.

In Abarca et al. (2020), no results for severely degraded states at the early time points were presented. Hence, the models were re-run with complementary calculations of flow through the waste for additional time points here, see Figure A-1. The results from these calculations were incorporated in the data files for Ecolego and are stored on SVN as described in Appendix A in Åstrand et al. (2022).

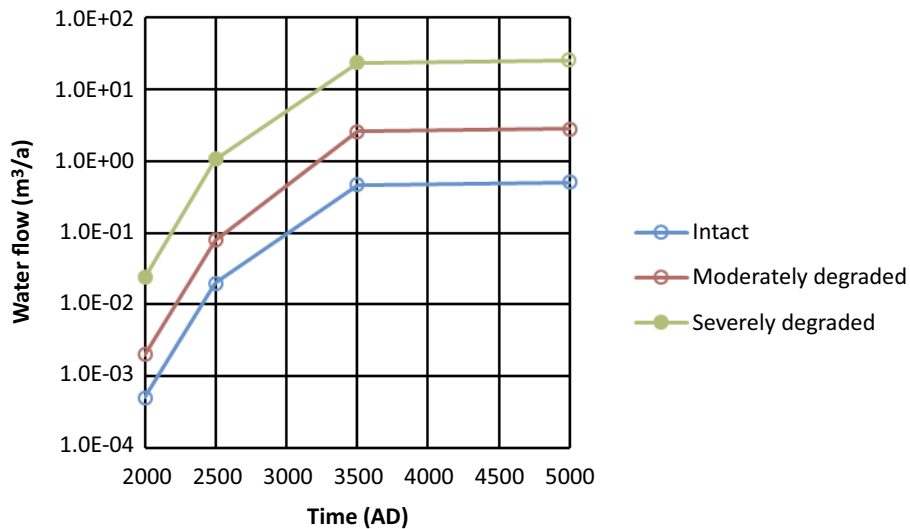


Figure A-1. Water flow through the waste in 1BMA for different concrete physical degradation states as a function of time. Empty circles are values reported in Abarca et al. (2020) and filled circles are values from the additional calculations only presented here.

Cement content in waste packages

The average cement fraction in cement-solidified waste (0.6 kg kg^{-1}) and concrete-embedded waste (0.1 kg kg^{-1}) is estimated based on an average of the data for real waste-package types given in Table C-4 in SKB (R-18-07). This is done as the waste packages are represented in a simplified way in the model by a small number of “model waste packages”. The relation between model waste packages and real waste packages is further discussed in Chapter 5 in Åstrand et al. (2022).

A3 Geosphere data

This section contains some data, not described elsewhere, used in the geosphere calculations.

Maximum matrix penetration depth

The maximum penetration depth L_D (m) signifies the thickness of the rock matrix around a flow path that can be utilised for matrix diffusion. If the connectivity of the microporous system is limited, the connectivity sets the maximum penetration depth of a contaminant. If there is unlimited connectivity of the microporous system, half the spacing between flow paths sets the maximum penetration depth. As indicated by in situ measurements at the SFR site (Löfgren 2014) and as discussed in the **Geosphere process report** and SKB (TR-10-52, Section 6.8), the microporosity of the Forsmark and SFR host rock matrix has an unlimited connectivity (at scales relevant for the safety assessment).

Therefore, the maximum penetration depth is set as half the spacing between neighbouring flow paths. A measure of this is the modelled intensity (frequency) of observed flow-bearing fractures, measured by the Posiva flow log (PFL) in the site investigations. This measurement is called $P_{32,PFL}$ ($\text{m}^2 \text{m}^{-3}$), and it is modelled as part of the hydrogeological DFN for hydraulic rock domains.

The modelled intensity of observed flow anomalies from the Posiva flow logging, $P_{32,PFL}$, is given for different fracture sets and domains in Öhman et al. (2012).

The suggested data, applying for all solutes, is:

- Maximum penetration depth $L_D = 0.9 \text{ m}$,

with the following justification.

It is reasonable to generally assume that, locally, an individual flow path that transports radionuclides will follow fracture sets of a similar direction. For the rock volume between the elevations 0 to -200 m , the two fracture sets having the largest intensities are Gd (gently dipping) and Hz (horizontal).

In Figure G-9 (Öhman et al. 2012) the overall intensity of $P_{32,PFL}$ values are plotted as a function of transmissivity for different depths. By combining the data for 0–200 m (data used for a, b Figure G-9 in Öhman et al. 2012) the $P_{32,PFL}$ values for these fracture sets ($T_{lim} = 1 \times 10^{-9} \text{ m}^2 \text{ s}^{-1}$) are 0.32 m^{-1} for Gd and 0.21 m^{-1} for Hz. The summed intensity for these two fracture sets becomes 0.53 m^{-1} . Converted to spacing between two flow paths, this results in 1.89 m. Half of this spacing, corresponding to the maximum penetration depth, becomes 0.94 m.

As a comparison, the average spacing between the PFL-anomalies calculated from the number of anomalies and the length of the borehole measurement for two different boreholes is presented in Table A-2 below.

Based on this, a value of 0.9 m for the maximum penetration depth is cautiously chosen.

Table A-2. Average spacing between the PFL-anomalies calculated from the number of anomalies and the length of the borehole measurement for KFR105 and KFR102B (Data from Löfgren 2014, Sections 4.2.3 and 4.2.6).

	Number of PFL-anomalies	Length of bore hole (m)	Spacing (m)	Half spacing (m)
KFR105	150	302	2.01	1.01
KFR102B	89	160	1.80	0.90
Sum	239	462		
Weighted average			1.93	0.97

Particle trajectories

Flow-related migration parameters are important input data in calculations of the radionuclide transport in the geosphere. As described in Section 5.5.1, so-called “effective trajectories” are applied to the geosphere radionuclide transport calculations in the PSAR. Instead of considering all particle trajectories for each bedrock case (Öhman and Odén 2018), the effective trajectories are computed as the median values of the individual underlying flow-related properties (advective travel time, t_w , a , and the flow-related transport resistance, F , a m^{-1}) for each waste vault and time-slice. Between the time-slices, it is assumed that the variation in parameters reflects a continuous change due to isostatic rebound and, hence, a linear interpolation is used. In Öhman and Odén (2018), the particle trajectories were simulated in a steady-state flow field for all considered time-slices. As such, the particle trajectories for the different time slices in their simulations are completely uncorrelated with each other. The introduction of effective trajectories provides a simplified, yet systematic, framework to overcome this drawback as the change between time-slices becomes straightforward. Further, it makes the calculations more efficient, thereby reducing the computational costs for calculating radionuclide transport through the geosphere. This simplification, however, also entails that the dispersion that is described by the full set of the calculated particle trajectories is potentially underestimated. The objective of the following text is to illustrate that the approach of using effective trajectories is satisfactory for the geosphere transport calculations for a typical parameterisation.

The illustration is based on a comparative deterministic analysis for six selected dose-relevant radionuclides with different transport characteristics between a calculation where the potential geosphere releases from all particle trajectories in the reference bedrock case (BASE_CASE1_DFN_R85_EXT1, see Öhman and Odén 2018) are considered and a calculation with effective trajectories. In the transport calculation with all particle trajectories, the magnitudes of the Darcy flux at the interface between the near-field and geosphere from Öhman and Odén (2018) calculations, are used to sort and pair trajectories over time.

For all selected radionuclides, the average geosphere release from all waste vaults in the calculation with effective trajectories is in close agreement with the corresponding release from the calculation with all particle trajectories (see Figure A-2). For non- or low-sorbing radionuclides (Mo-93, C-14, Ca-41 and I-129) the geosphere release is virtually identical between the two calculations. For more strongly sorbing radionuclides, such as Ni-59 and U-238, there is a marked difference between the two calculations. Due to the reduced dispersion when using effective trajectories, there is a small but noticeable delay in the initial release of U-238 and in the later release of Ni-59. Further, it is clear that there is a spread in the release curves of individual fractures for sorbing radionuclides (illustrated by the 5–95 % percentile range in Figure A-2) giving potential for dispersion. However, the maximum annual geosphere releases using the effective trajectories is only slightly underestimated for Ni-59 (by ~ 5 %) and overestimated by up to 3 % for the other radionuclides when compared with the calculation for the average of all particle trajectories. Note that the reason for the spread being lower where interpolation occurs is because the variation of a weighted average of two not fully correlated stochastic variables is less than the average of the variation of the individual variables.

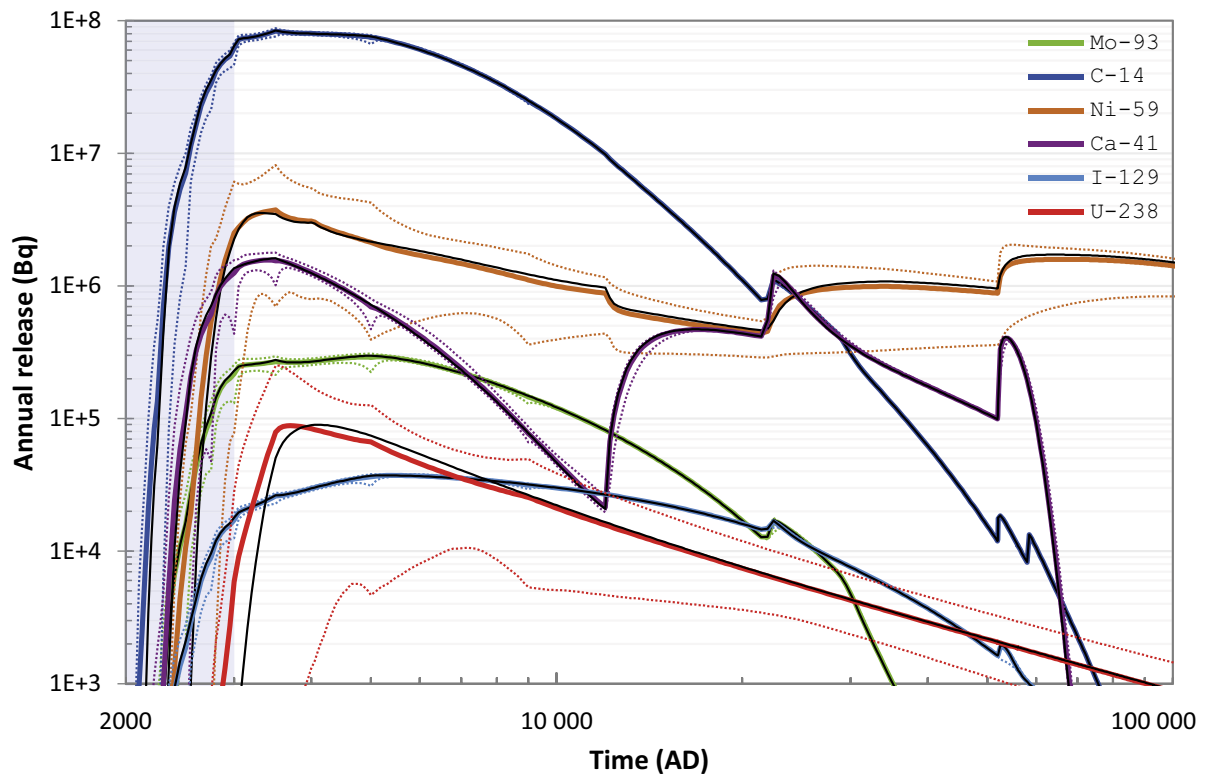


Figure A-2. Total deterministic geosphere releases from SFR for six dose-relevant radionuclides, averaged over all particle trajectories (thick coloured lines), including their 5–95 percentiles (dotted coloured lines), compared with effective trajectories as in the base case (thin black lines).

A4 Uncertainties in flow-related migration properties due to fractured bedrock

When properties of flow trajectories such as travel time (t_w) and transport resistance (F) are examined, their variation is not independent in time and space. For example, a bedrock case with high groundwater flow at 2500 AD also tends to have high flow rates at later shoreline positions, and groundwater flow in neighbouring vaults (e.g. in SFR1) varies in a similar way (see, for example, Section 5.5.1 and Odén et al. 2014, Tables 6-2 and 6-3). Moreover, cases with a short travel time (t_w) tend to have a low transport resistance (F) and a high vault cross flow (Q ; see Section 5.5.1). These dependencies make intuitive sense since the structure of the bedrock is constant over time and flow paths from neighbouring vaults are partly overlapping. Moreover, the strong link between t_w and F is intrinsic in the definitions of the parameters (as they are directly linked through the aperture of the fractures). Taken together, this means that it is reasonable to handle the uncertainties of flow-related migration properties jointly, accounting for spatial and temporal dependencies.

Thus, in PSAR the uncertainties of t_w , F and Q are jointly derived from variation between three bedrock fracture cases that are considered representative, covering the range of uncertainty in bedrock parametrisation (Öhman and Odén 2018). From an earlier comparative analysis of 17 bedrock cases (Odén et al. 2014) it is observed that the flow in the silo is not correlated to that of other vaults in SFR1 (Table A-3). Thus, the uncertainty of flow-related properties caused by variation in bedrock cases is assumed to be approximately independent in SFR1, the silo and SFR3, respectively. This assumption is also reasonable given the physical distance between these repository units. This means that a bedrock case that is associated with high groundwater flow in SFR1, is expected to yield a relatively high Q , and relatively low t_w and F values in all SFR1 waste vaults, but not necessarily in the silo or in SFR3.

Table A-3. Average vault cross flow (Q) for times 2500 to 9000 AD for 17 bedrock cases . Flow was ranked (and expressed on a scale from 0 to 1) prior to averaging. Based on a statistical ranking analysis of the 17 cases, three bedrock cases were selected as representative for covering the range in cross flow for all cases (Öhman et al. 2014). These are outlined in grey shading in the left column. The data have been colour coded from low flow (dark blue) to high flow (bright yellow). Lower panel compares mean flow and standard deviation for all 17 bedrock cases with the corresponding values based on the three representative cases. Data from Table 6-3 in Öhman et al. (2014).

BC	1BTF	2BTF	1BLA	1BMA	Silo	1BRT	2BLA	3BLA	4BLA	5BLA	2BMA
1	0.22	0.61	0.72	0.31	0.77	0.48	0.63	0.69	0.42	0.18	0.15
2	0.12	0.41	0.45	0.11	0.78	0.03	0.26	0.18	0.34	0.44	0.04
3	0.28	0.64	0.76	0.32	0.82	0.42	0.56	0.65	0.37	0.15	0.09
4	0.38	0.12	0.12	0.7	0.36	0.74	0.28	0.54	0.95	0.97	0.7
5	0.89	0.49	0.5	0.45	0.31	0.62	0.76	0.84	0.85	0.69	0.5
6	0.55	0.34	0.36	0.15	0.31	0.24	0.37	0.31	0.36	0.21	0.23
7	0.92	0.66	0.58	0.52	0.83	0.32	0.5	0.78	0.14	0.17	0.3
8	0.77	0.39	0.52	0.51	0.5	0.97	0.97	0.82	0.44	0.64	0.88
9	0.71	0.28	0.21	0.26	0.61	0.91	0.91	0.49	0.41	0.81	0.81
10	0.9	0.96	0.95	0.81	0.92	0.46	0.79	0.52	0.57	0.03	0.28
11	0.52	0.92	0.92	0.91	0.14	0.85	0.82	0.95	0.85	0.62	0.96
12	0.68	0.77	0.66	0.81	0.34	0.26	0.22	0.69	0.82	0.71	0.89
13	0.09	0.05	0.05	0.63	0.41	0.69	0.09	0.06	0.58	0.85	0.61
14	0.58	0.26	0.37	0.25	0.44	0.66	0.62	0.35	0.11	0.35	0.45
15	0.45	0.14	0.12	0.04	0.61	0.09	0.19	0.08	0.04	0.5	0.37
16	0.38	0.81	0.86	0.74	0.16	0.54	0.5	0.39	0.51	0.36	0.55
17	0.05	0.65	0.32	0.97	0.21	0.22	0.03	0.16	0.75	0.83	0.71
Mean	0.50	0.50	0.50	0.50	0.50	0.50	0.50	0.50	0.50	0.50	0.50
(1,11,15)	0.40	0.56	0.59	0.42	0.51	0.47	0.55	0.57	0.44	0.43	0.49
Std dev	0.29	0.28	0.29	0.29	0.25	0.28	0.29	0.28	0.27	0.29	0.29
(1,11,15)	0.16	0.39	0.42	0.45	0.33	0.38	0.32	0.45	0.41	0.23	0.42

Öhman et al. (2014) selected three bedrock cases as being representative for covering the range of uncertainty in bedrock parametrisation, namely: 15 (low flow), 1 (*base case*) and 11 (high flow). A numeric comparison of normalised vault cross flow shows that the three representative cases in general seems to capture the mean flux of all 17 examined cases reasonably well. That is, the mean value of the three cases is somewhat lower (2–20 %) for six vaults and somewhat higher (1–20 %) for five vaults. However, the spread between the three cases, as characterised by the standard deviation, is systematically higher (~30 %) for the three representative cases. This suggests that estimates based on the three representative cases will yield a higher variability than if a full set of 17 bedrock cases are used. This implied that the three characteristic bedrock cases can be used for unbiased estimates of flow and that the associated variation does not underestimate the uncertainty in the bedrock parametrisation.

To describe the patterns of variation and co-variation of the flow-related properties, the three representative bedrock cases are analysed with a mixed linear model (Hummel et al. 2021). As the general pattern of flow trajectories change when the shoreline regresses over the repository and as the early geosphere release is limited (Section 5.5.2), the analysis is restricted to the time after 2500 AD. This restriction is also supported by previously reported patterns of vault cross flow (Table 6-2 in Öhman et al. 2014). The model is fitted separately to data from SFR1 (n = 216), silo (n = 54) and SFR3 (n = 324) and, in this context, they are referred to as three repository units. The number of observations corresponds to the product of number of vaults (4, 1 or 6), time points (6), bedrock cases (3) and flow properties (3).

In the mixed linear model, the observational unit (a) for the analysis is the value of each property for each combination of vault, time and bedrock case and all three properties are analysed jointly in the same model. For t_w and F , the values used in the analysis are the effective properties (i.e. the median of all trajectories), whereas there is only one Q value for each combination of vault, time and bedrock case (Öhman and Odén 2018). In the model time [2500, 2750, 3000, 3500, 5000, 9000], vault [e.g. 1BLA, 1BMA, 1BTF, 2BTF] and property class [Q , t_w , F] and their interactions, are treated as categorical fixed effects³¹:

$$y = \text{vault} + \text{time} + \text{vault} \times \text{time} + \text{prop} + \text{vault} \times \text{prop} + \text{time} \times \text{prop} \\ + \text{vault} \times \text{time} \times \text{prop}$$

This part of the model accounts for the mean of each property per vault and time (as shown for t_w in Table 5-14). Bedrock cases [1, 11 and 15] and the interaction between bedrock case and property, are used to estimate variance components, and are thus treated as random effects in the model. The two random factors capture dependencies across vaults, times and properties caused by variation in the bedrock case (see below).

The analysis is performed on logarithmic transformed data, which yields approximately normally distributed residuals (Figure 5-44). Prior to the analysis, each property, is normalised for each repository unit, by division with its standard deviation (see below). Q was then multiplied by -1 to capture its negative relationship to the other two properties.

The total random variation of flow-related properties, caused by the representative bedrock case, was largest for SFR1 and smallest for SFR3, with the silo in between (left panel Figure A-3). There were some differences in this pattern between the properties. Thus, in SFR1 the variation of t_w was smaller than that of the other two properties and, in SFR3, the variation of Q was notably larger than for F and t_w . The difference in total variation between properties and the three repository units were removed (by division with the standard deviation, s_i) prior to partitioning of the variation with the mixed model.

The mixed models fitted the data very well ($r^2 > 0.99$), suggesting that the main components with respect to systematic and random variation of flow-related properties were captured. Moreover, the majority of the variation could be attributed to the systematic effects described by the fixed factors (i.e. variation due to time, vault and property).

³¹ For the analysis of the silo there is only one vault and thus the fixed factor vault and its interactions are not included as fixed factors in the model.

The two random factors (bedrock case and bedrock case \times property class) correspond to two separate variance-components and the residual variation from the model fit yields a third variance-component. Thus for each repository unit (SFR1, silo and SFR3), the total variation of the normalised data was partitioned into; a component describing how the random bedrock case affects all three properties in all vaults at the examined times ($\sigma_{BC,shared}^2$), a component describing how the bedrock case affects each property individually, in all vaults and at all times ($\sigma_{BC,ind}^2$), and a residual variance component describing how a flow-related property varies randomly when the effects of property class, vault, time and bedrock case have been taken into account (σ_{res}^2).

In SFR1 approximately half of the random variation caused by bedrock cases can be attributed to the fact that the three properties varied jointly in all vaults at all times ($\sigma_{BC,shared}^2$, right panel Figure A-3). Similarly, more than half of the random variation in flow properties in the silo can be attributed to variation that is shared across all times. However, the link between the flow properties is not as strong as in SFR1 and the coordinate response in one flow property is partly independent from the response in the other two properties ($\sigma_{BC,shared}^2 \sim \sigma_{BC,ind}^2$). In SFR3, less random variation is coordinated between vaults and time ($\sigma_{BC,shared}^2 + \sigma_{BC,ind}^2 \sim 30\%$) and, as in the silo, a noticeable part of the coordinated variation is independent for the three flow properties. It can be noted that the sum of the variance-components exceeds one (right panel in Figure A-3). This is because estimated mixed-effects variance in theory and in practice is larger than the estimated fixed-effects variance and the derived variance-components thus give more cautious estimates of the underlying variation.

To mimic the above structure, the variation can be represented by drawing random error terms (e) from normal distributions in Monte-Carlo simulations. For a specified repository unit (SFR1, silo or SFR3), these can then be summed as follows:

$$\begin{aligned} e_{total_Q} &= -e_{BC,shared} + e_{BC,ind,Q} + e_{res,Q,jk} \\ e_{total_F} &= e_{BC,shared} + e_{BC,ind,F} + e_{res,F,jk} \\ e_{total_{tw}} &= e_{BC,shared} + e_{BC,ind,tw} + e_{res,tw,jk} \end{aligned}$$

Where $e_{BC,shared}$ is $N(0, \sigma_{BC,shared}^2)$ distributed, $e_{BC,ind}$ is $N(0, \sigma_{BC,ind}^2)$ distributed and $e_{res,Q,jk}$ is $N(0, \sigma_{res}^2)$ distributed. Note that the error terms can be either negative or positive, and that for each Monte-Carlo realisation one shared bedrock case error term ($e_{BC,shared}$) is drawn and applied to all properties, all vaults and all time. Then three independent bedrock case terms ($e_{BC,ind}$) are drawn and applied to all vaults and times for each property separately. Finally, one residual error term per property, vault, and time point is drawn. The negative sign associated with Q is only needed for the shared error component and implies that this error term affects Q and the other two components (F and t_w) in different directions.

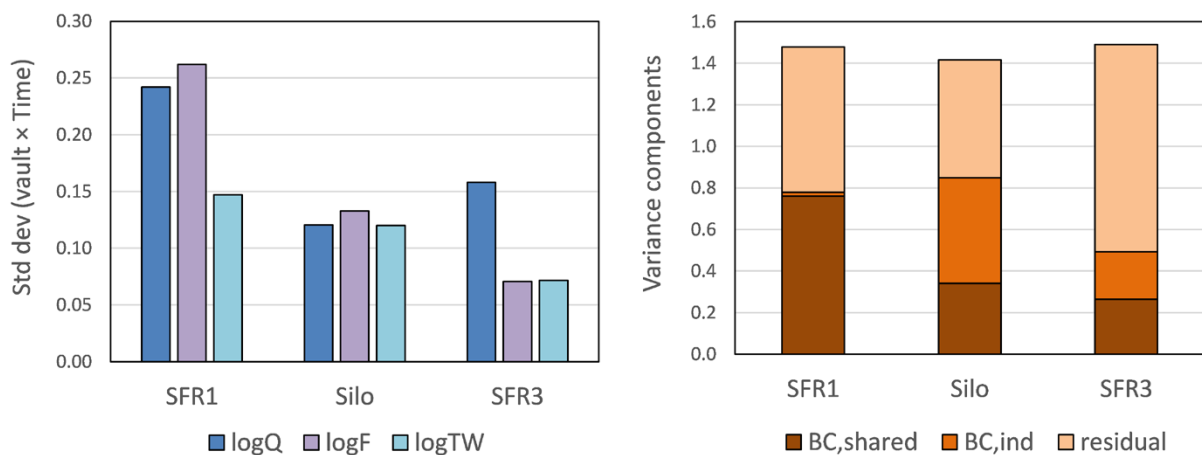


Figure A-3. Random variation in flow properties driven by representative bedrock cases. Left) Total variation for each property around best estimates (geometric mean) for each waste vault and time (at 2500 AD or later) expressed as the standard deviation on a logarithmic scale. Right) Components of random variation ($\sigma_{BC,shared}^2$, $\sigma_{BC,ind}^2$, σ_{res}^2) for normalised flow properties (see text for details).

These total error terms (e_{total}) then need to be scaled back with the corresponding standard deviation (left panel in Figure A-3). Additivity on a logarithmic scale is equivalent to multiplicativity in the linear scale. This means that the error term can be expressed as a scale factor (Sf) which is multiplied with the best estimate for each property, vault and time, respectively. For SFR1 this can be expressed as:

$$Sf_{ijk} = 10^{S_i e_{total,ijk}} \quad ; \quad i = Q, t_w, F ; \quad j = 1BMA, 1BTF, 2BTF, 1BLA ; \quad k = 2500, \dots, 9000$$

In summary, a new system to account for uncertainties in bedrock properties has been introduced in the PSAR. The selected method mimics the variation structure for Q , F and t_w in three representative bedrock cases, that together span relevant uncertainties in flow related properties. Parameter values for flow characteristics that are correlated across time, repository unit and property type are then generated by multiplying best estimates with scaling factors generated in Monte Carlo simulations.

A5 Dose coefficients

In the calculations of potential doses to humans, radionuclide-specific dose coefficients are used for converting the activity levels (Bq) of ingested or inhaled radionuclides as well as the activity concentrations in environmental media (Bq m⁻³) to dose to humans (Sv). Humans can be exposed to radionuclides both externally and internally. External exposure comes from radiation emitted by radionuclides in surrounding environmental media such as air, water and soils, whilst internal exposure is always preceded by incorporation of radionuclides into the human body. Relevant pathways for internal exposure are mainly by inhalation of contaminated air, or ingestion of contaminated water and food (Avila and Bergström 2006). Other exposure pathways are discussed and dismissed as being of little significance for the post-closure safety of a geological disposal facility at the Forsmark site in SKB (R-14-02).

Assessing the risk to a representative individual of the most exposed group is the motivation for the dose calculations and, for doing this, three different kinds of radionuclide-specific dose coefficients considering the above-mentioned main exposure routes are used:

- dose coefficients for external exposure from radionuclides in the ground (soil; Sv Bq⁻¹ h⁻¹ m³),
- dose coefficients for ingestion (Sv Bq⁻¹),
- dose coefficients for inhalation (Sv Bq⁻¹).

Doses obtained with these coefficients are the committed effective doses to members of the public that are classified as adults. Any radioactive contamination of the biosphere due to releases from a geological disposal facility could be assumed to remain relatively constant over time periods spanning considerably longer than the human life span. Therefore, ICRP (ICRP 2000) states that it is reasonable to calculate the annual dose averaged over the lifetime of the individuals, which means that it is not necessary to calculate dose to different age groups; this average can be adequately represented by the annual effective dose to an adult. External dose coefficients defined in Bellamy et al. (2019) and internal dose coefficients defined in ICRP (2012) are used in this safety assessment.

Previous safety assessments of planned geologic repositories in Sweden (Bergman et al. 1977, 1979, Bergström 1983) have shown that the only external exposure contributing significantly to the total dose is that from contaminated ground, this is also shown and discussed in SKB (R-14-02). Thus, the external exposure from air and water is negligible for all radionuclides of relevance, whereas for some radionuclides with high gamma-energy emissions and low bioavailability, such as Nb-94, the external exposure to radionuclides accumulated in the ground may give an important contribution to the total dose. Hence, exposure from radionuclides accumulated in the ground is included in the PSAR.

The dose calculations for most radionuclides are straightforward; the activity concentrations in environmental media are multiplied by the corresponding dose-coefficients. However, for some radionuclides, decay products building up in the environmental media must be considered too. Thus, it is appropriate to consider exposure from both the radionuclide and the decay products when assessing dose. The contribution of radioactive decay products is handled by assuming secular equilibrium³² and including the contribution of the decay products in the dose coefficient of the parent radionuclide.

³² A decay product is said to be in secular equilibrium when the ratio of its activity to that of the parent no longer changes with time.

The reason for adopting this assumption is that the decay products in these chains have much shorter half-lives (many orders of magnitude) than those radionuclides explicitly modelled (parents). In the situation of secular equilibrium, the decay rate of the parent radionuclide, and hence the production rate of the decay products, is approximately constant, because the half-life of the parent radionuclide is very long compared to the timescale being considered. The quantity of the decay product builds up until the number of atoms decaying per unit time becomes equal to the number being produced per unit time; the quantity of decay product then reaches a constant, equilibrium value. Assuming that the initial concentration of the decay product is zero, full equilibrium usually takes several half-lives of the decay product to establish. Thus, the equilibrium value for the activity in a decay product is the same as the activity of parent radionuclide, adjusted by the branching ratio.

As an example, assume a unit activity of radionuclide Cs-137. The half-life is 30 years and in 94.4 % of its transformations, the radioactive decay product Ba-137m is formed. Ba-137m has a half-life of 2.552 minutes and forms no radioactive decay products. Figure A-4 illustrates the dynamic change of activity of Cs-137 and Ba-137m, assuming an initial unit activity of Cs-137. It shows that after about 20 minutes (~7 half-lives of Ba-137m), secular equilibrium has been established between Cs-137 and Ba-137m. Thus, when modelling Cs-137 there is no need to explicitly model Ba-137m. Instead, it is assumed that wherever there is any activity of Cs-137 there are the same activities corrected by 94.4 % (the branching ratio) of Ba-137m. Accordingly, the dose coefficients for Cs-137 include the contribution of radiation from Ba-137m and thus Ba-137m is not modelled explicitly in the transport model.

In other cases, the contribution of decay products is small and can therefore be neglected in the dose calculations. As an example, Gd-152 is very long-lived (half-life of 1.08×10^{14} years) and is the decay product of the short-lived radionuclide Eu-152 (half-life of approximately 13 years). Consequently, not much Gd-152 will be built up before Eu-152 has decayed. Figure A-5 illustrates the amount of Gd-152 (and also Sm-147, half-life of 1.06×10^{11} years) that will build up from a unit initial activity of Eu-152 (and Pm-147, half-life of 2.6 years). Only 3.4×10^{-14} of the initial Eu-152 activity (and 2.5×10^{-11} of the initial Pm-147 activity) will build up as Gd-152 (and Sm-147). Further, the inhalation dose coefficient is only about 450 times and the ingestion coefficient is only about 30 times larger for Gd-152 than for Eu-152 (corresponding values for Sm-147 and Pm-147 are 1920 and 188) (see Table A-4). Therefore, as the potential dose contribution would be negligible, there is no need to take the dose contribution into account in the dose coefficients of the parent radionuclide or to explicitly model the long-lived radionuclides Gd-152 (and Sm-147) based on any activity of the parent radionuclide.

The dose coefficient for external exposure used in the assessment is defined as the dose rate to which an individual is exposed from a unit volumetric concentration in soil or from a unit surface concentration of the radionuclide. The values used for external exposure from a volumetric source are based on homogeneous distribution of the radionuclides in a soil layer of infinite depth and infinite lateral extent (Bellamy et al. 2019). The values were derived from calculations for a typical silt soil with a density of 1600 kg m^{-3} , 20 % air and 30 % water content reported in Bellamy et al. (2019) considering the latest values of tissue weighting factors recommended by ICRP (2012). The very low water content, presumably based on an arid area, is cautious because the dose rates are expressed on a volumetric basis and would be decreased at higher densities corresponding to larger percentage water contents. In modelling of external exposure, the external coefficients could be converted to consider the actual density of the modelled soil (Bellamy et al. 2019), but this has not been considered in the PSAR. This would not make a large difference for mineral soils. The effect would be larger for peat soils because of their low bulk density, but this would partly be compensated by the higher water content. Overall, for an example density of 1000 kg m^{-3} , the dose rates would increase by about 60 %.

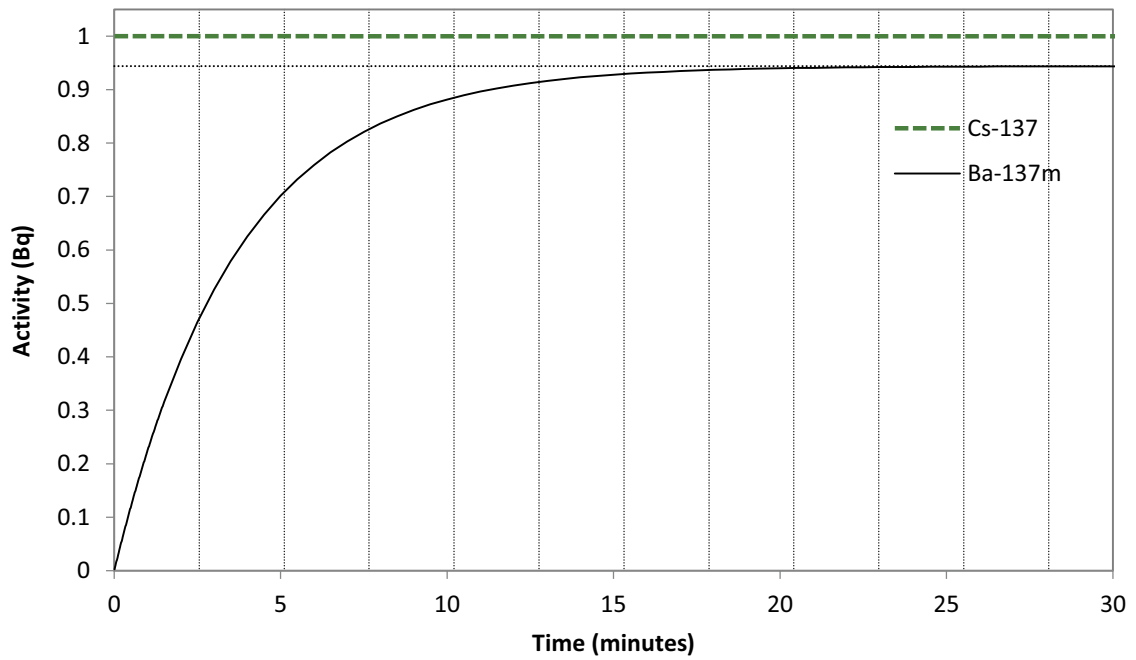


Figure A-4. Dynamic change of activity of Cs-137 and Ba-137m assuming an initial unit activity of Cs-137 and no initial activity of Ba-137m. Vertical dotted lines correspond to one half-life of Ba-137m (~2.5 minutes). Horizontal dotted line corresponds to the branching ratio Cs-137 → Ba-137m (94.4 %).

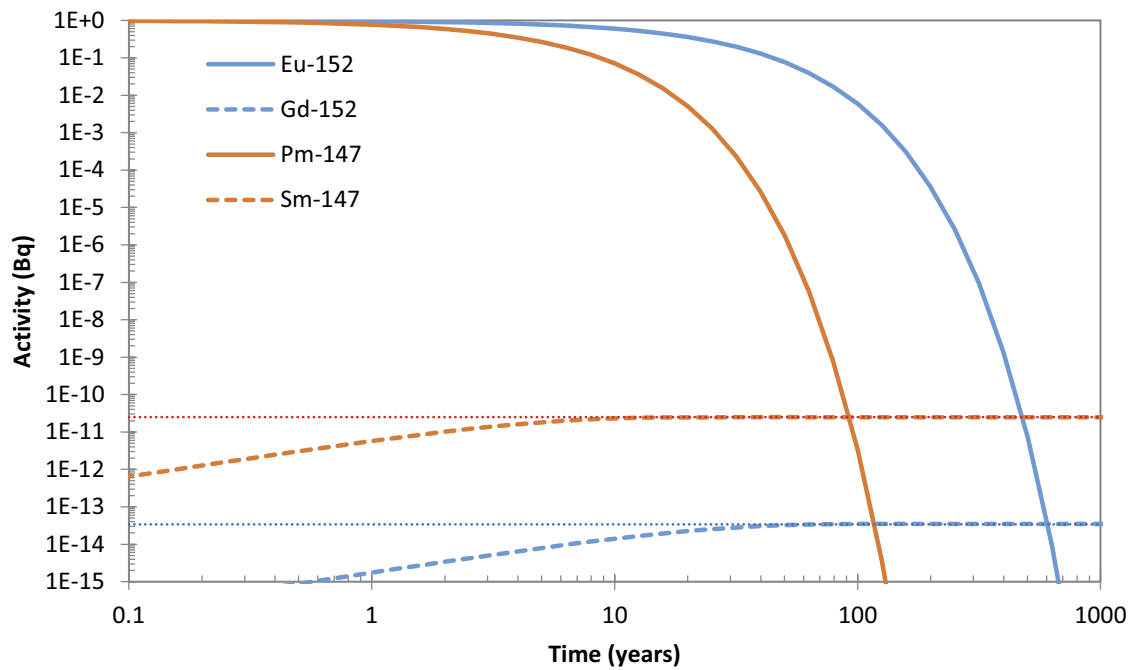


Figure A-5. Dynamic change of activity of Eu-152, Gd-152, Pm-147 and Sm-147 assuming an initial unit activity of Eu-152 and Pm-147 and no initial activity of Gd-152 and Sm-147. Horizontal dotted lines correspond to the activity levels that Gd-152 (3.4×10^{-14} Bq) and Sm-147 (2.5×10^{-11} Bq) will reach before Eu-152 and Pm-147 have decayed.

The internal dose coefficients presented in ICRP (ICRP 2012) consider the dose due to ingrowth of radioactive decay products within the body, following an intake of unit activity of the parent radionuclide. The dose coefficient for internal exposure is defined as the committed effective dose to an individual from a unit intake of the radionuclide orally (ingested food/water or inhaled air).

As noted above, for intake of radionuclides, the dose coefficients consider the radioactive decay products that are formed within the body (ICRP 2012). The extra contribution to dose from intake of short-lived decay products present in the environment is very small, sometimes extremely small. However, for completeness, it is pessimistically included in the final dose coefficients used in the assessment in the same way as for external exposure.

The dose coefficients for ingestion are independent of the ingestion pathway, i.e. via food or water. The only exception is C-14, for which different dose coefficients are used for ingestion via food and via water, because carbon is present in different chemical forms in water and food and C-14 in food is more bioavailable (Leggett 2004). The coefficient for food is about 10 times higher than that for water.

The inhalation dose coefficients are specified for different absorption rates from the respiratory tract: fast (F), moderate (M) and slow (S). Slow adsorption rates cause the highest exposure for most radionuclides, but there are exceptions; for example, for isotopes of the actinides Np, Pu, Am and Cm the highest exposure is observed for fast absorption rates. The highest value for each isotope across different classes of absorption rates is pessimistically chosen. The selected value for C-14 is in the form of carbon dioxide (CO₂).

In Table A-4 the dose coefficients due to exposure from each of the radionuclides that is explicitly modelled are listed along with dose coefficients for short-lived decay products of these radionuclides. The dose coefficients are used to calculate the dose coefficients presented in Table A-5 which includes both the contribution of the parent radionuclide and those of the short-lived decay products. The dose coefficients listed in Table A-5 are used in the dose calculations.

Table A-4. List of all radionuclides with initial inventory to be disposed in SFR (SKB R-18-07), and all decay products together with their half-lives and decay modes (ICRP 2008), dose coefficients for ingestion and inhalation and selected type for inhalation (ICRP 2012) and external exposure (Bellamy et al. 2019).

Radionuclide	Half-life		Decay modes ¹	Dose coefficients		Type ² (Sv)	External (h ⁻¹ Bq ⁻¹ m ³)	Radionuclide	Half-life		Decay modes ¹	Dose coefficients		Type (Sv)	External (h ⁻¹ Bq ⁻¹ m ³)
				Ingestion (Sv Bq ⁻¹)	Inhalation (Sv Bq ⁻¹)							Ingestion (Sv Bq ⁻¹)	Inhalation (Sv Bq ⁻¹)		
H-3	12.32	a	β-	1.8E-11	2.6E-10	S	1.2E-19	Po-213	4.2	μs	α				4.1E-18
Be-10	1.51 × 10 ⁶	a	β-	1.1E-09	3.5E-08	S	1.3E-15	Bi-214	1194	s	β-,α	1.1E-10	1.4E-08	M	1.8E-13
C-14	5700	a	β-	5.8E-10	6.2E-12	CO ₂	1.1E-16	Pb-214	1608	s	β-	1.4E-10	1.5E-08	S	2.5E-14
Cl-36	3.01 × 10 ⁵	a	β-,EC,β+	9.3E-10	7.3E-09	M	1.5E-15	Po-214	164.3	μs	α				9.2E-18
Ca-41	1.02 × 10 ⁵	a	EC	1.9E-10	1.8E-10	S	0.0E+00	Bi-215	456	s	β-				3.1E-14
Fe-55	2.74	a	EC	3.3E-10	7.7E-10	F	1.2E-23	Po-215	1.78	ms	α				1.8E-17
Ni-59	1.01 × 10 ⁵	a	EC,β+	6.3E-11	4.4E-10	S	1.6E-18	Po-216	0.145	s	α				1.7E-18
Co-60	5.27	a	β-	3.4E-09	3.1E-08	S	3.0E-13	At-217	0.032	s	α				2.3E-17
Ni-63	100.1	a	β-	1.5E-10	1.3E-09	S	1.5E-17	At-218	1.5	s	α,β-				1.0E-17
Se-79	2.95 × 10 ⁵	a	β-	2.9E-09	6.8E-09	S	1.3E-16	Po-218	186	s	α,β-				4.4E-20
Sr-90	28.79	a	β-	2.8E-08	1.6E-07	S	9.5E-16	Rn-218	0.035	s	α				8.1E-17
Y-90	64.1	h	β-	2.7E-09	1.5E-09	S	8.1E-15	At-219	56	s	α				0.0E+00
Mo-93	4000	a	EC	3.1E-09	2.3E-09	S	6.1E-18	Rn-219	3.96	s	α				5.7E-15
Zr-93	1.53 × 10 ⁶	a	β-	1.1E-09	2.5E-08	F	1.7E-17	Rn-220	55.6	s	α				6.6E-17
Nb-93m	16.13	a	IT	1.2E-10	1.8E-09	S	1.1E-18	Fr-221	294	s	α				2.6E-15
Nb-94	2.03 × 10 ⁴	a	β-	1.7E-09	4.9E-08	S	1.7E-13	Rn-222	3.82	d	α				4.1E-17
Tc-99	2.11 × 10 ⁵	a	β-	6.4E-10	1.3E-08	S	3.6E-16	Fr-223	1320	s	β-,α	2.4E-09	8.9E-10	F	5.5E-15
Pd-107	6.5 × 10 ⁶	a	β-	3.7E-11	5.9E-10	S	2.5E-18	Ra-223	11.4	d	α	1.0E-07	8.7E-06	S	1.1E-14
Ag-108	142.2	s	β-,EC,β+				6.5E-15	Ra-224	3.66	d	α	6.5E-08	3.4E-06	S	9.5E-16
Ag-108m	418	a	EC,IT	2.3E-09	3.7E-08	S	1.7E-13	Ac-225	10	d	α	2.4E-08	8.5E-06	S	1.0E-15
Cd-113	7.70 × 10 ¹⁵	a	β-	2.5E-08	1.2E-07	F	3.3E-16	Ra-225	14.9	d	β-	9.9E-08	7.7E-06	S	4.9E-16
Cd-113m	14.1	a	β-,IT	2.3E-08	1.1E-07	F	8.9E-16	Ra-226	1600	a	α	2.8E-07	9.5E-06	S	6.2E-16
In-115	4.41 × 10 ¹⁴	a	β-	3.2E-08	3.9E-07	F	6.7E-16	Ac-227	21.8	a	β-,α	1.1E-06	5.5E-04	F	8.4E-18
Sb-125	2.76	a	β-	1.1E-09	1.2E-08	S	4.4E-14	Th-227	18.7	d	α	8.8E-09	1.0E-05	S	1.1E-14
Te-125m	57.4	d	IT	8.7E-10	4.2E-09	S	1.8E-16	Ac-228	6.15	h	β-	4.3E-10	2.5E-08	F	9.9E-14
Sb-126	12.35	d	β-	2.4E-09	3.2E-09	S	3.0E-13	Ra-228	5.75	a	β-	6.9E-07	1.6E-05	S	2.6E-18
Sn-126	2.3 × 10 ⁵	a	β-	4.7E-09	2.8E-08	M	2.9E-15	Th-228	1.91	a	α	7.2E-08	4.0E-05	S	1.4E-16
Sb-126m	1149	s	β-,IT	3.6E-11	2.0E-11	S	1.7E-13	Th-229	7340	a	α	4.9E-07	2.4E-04	F	5.7E-15
I-129	1.57 × 10 ⁷	a	β-	1.1E-07	3.6E-08	F	2.8E-16	Th-230	7.54 × 10 ⁴	a	α	2.1E-07	1.0E-04	F	2.2E-17
Ba-133	10.52	a	EC	1.5E-09	1.0E-08	S	3.5E-14	Pa-231	3.28 × 10 ⁴	a	α	7.1E-07	1.4E-04	M	3.1E-15
Cs-134	2.06	a	β-,EC	1.9E-08	2.0E-08	S	1.7E-13	Th-231	25.5	h	β-	3.4E-10	3.3E-10	S	9.0E-16

Table A-4. Continued.

Radionuclide	Half-life		Decay modes ¹	Dose coefficients		Type ²	External (h ⁻¹ Bq ⁻¹ m ³)	Radionuclide	Half-life		Decay modes ¹	Dose coefficients		Type	External (h ⁻¹ Bq ⁻¹ m ³)
				Ingestion (Sv Bq ⁻¹)	Inhalation (Sv Bq ⁻¹)							Ingestion (Sv Bq ⁻¹)	Inhalation (Sv Bq ⁻¹)		
Cs-135	2.3 × 10 ⁶	a	β-	2.0E-09	8.6E-09	S	3.0E-16	Th-232	1.41 × 10 ¹⁰	a	α	2.3E-07	1.1E-04	F	9.9E-18
Cs-137	30.2	a	β-	1.3E-08	3.9E-08	S	9.3E-16	U-232	68.9	a	α	3.3E-07	3.7E-05	S	1.4E-17
Ba-137m	153	s	IT				6.4E-14	Pa-233	27.0	d	β-	8.7E-10	3.9E-09	S	2.0E-14
Nd-144	2.29 × 10 ¹⁵	a	α				0.0E+00	U-233	1.59 × 10 ⁵	a	α	5.1E-08	9.6E-06	S	1.8E-17
Pm-147	2.62	a	β-	2.6E-10	5.0E-09	M	1.7E-16	Pa-234	6.7	h	β-	5.1E-10	4.0E-10	S	1.6E-13
Sm-147	1.06 × 10 ¹¹	a	α	4.9E-08	9.6E-06	M	0.0E+00	Th-234	24.1	d	β-	3.4E-09	7.7E-09	S	5.8E-16
Sm-148	7.00 × 10 ¹⁵	a	α				0.0E+00	U-234	2.46 × 10 ⁵	a	α	4.9E-08	9.4E-06	S	6.8E-18
Sm-151	90	a	β-	9.8E-11	4.0E-09	M	2.0E-17	Pa-234m	70.2	s	β-,IT				8.6E-15
Eu-152	13.5	a	EC,β+,β-	1.4E-09	4.2E-08	M	1.3E-13	U-235	7.04 × 10 ⁸	a	α	4.7E-08	8.5E-06	S	1.4E-14
Gd-152	1.08 × 10 ¹⁴	a	α	4.1E-08	1.9E-05	F	0.0E+00	U-235m	1560	s	IT				0.0E+00
Eu-154	8.59	a	β-,EC	2.0E-09	5.3E-08	M	1.4E-13	U-236	2.34 × 10 ⁷	a	α	4.7E-08	8.7E-06	S	3.4E-18
Eu-155	4.76	a	β-	3.2E-10	6.9E-09	M	3.4E-15	Np-237	2.14 × 10 ⁶	a	α	1.1E-07	5.0E-05	F	1.3E-15
Ho-166m	1200	a	β-	2.0E-09	1.2E-07	M	1.7E-13	U-237	6.75	d	β-	7.6E-10	1.9E-09	S	9.6E-15
Hg-206	489	s	β-				1.4E-14	Np-238	2.12	d	β-	9.1E-10	3.5E-09	F	6.8E-14
Tl-206	252	s	β-				3.9E-15	Pu-238	87.7	a	α,SF	2.3E-07	1.1E-04	F	1.9E-18
Tl-207	286.2	s	β-				3.7E-15	U-238	4.47 × 10 ⁹	a	α,SF	4.5E-08	8.0E-06	S	3.3E-18
Tl-208	183	s	β-				4.2E-13	Np-239	2.36	d	β-	8.0E-10	1.0E-09	S	1.4E-14
Pb-209	3.25	h	β-	5.7E-11	6.1E-11	S	9.8E-16	Pu-239	2.41 × 10 ⁴	a	α	2.5E-07	1.2E-04	F	5.3E-18
Tl-209	129.6	s	β-				2.5E-13	Pu-240	6564	a	α,SF	2.5E-07	1.2E-04	F	2.0E-18
Bi-210	5.01	d	β-,α	1.3E-09	9.3E-08	M	2.5E-15	Am-241	432	a	α	2.0E-07	9.6E-05	F	7.9E-16
Pb-210	22.2	a	β-,α	6.9E-07	5.6E-06	S	4.5E-17	Pu-241	14.35	a	β-,α	4.8E-09	2.3E-06	F	2.7E-19
Po-210	138	d	α	1.2E-06	4.3E-06	S	1.1E-18	Am-242	16.02	h	β-,EC	3.0E-10	2.0E-08	S	1.7E-15
Tl-210	78	s	β-				3.3E-13	Cm-242	162.8	d	α,SF	1.2E-08	5.9E-06	S	2.1E-18
Bi-211	128.4	s	α,β-				4.6E-15	Pu-242	3.75 × 10 ⁵	a	α,SF	2.4E-07	1.1E-04	F	1.1E-17
Pb-211	2166	s	β-	1.8E-10	1.2E-08	S	9.9E-15	Am-242m	141	a	IT,α	1.9E-07	9.2E-05	F	2.0E-17
Po-211	0.52	s	α				9.0E-16	Am-243	7370	a	α	2.0E-07	9.6E-05	F	2.7E-15
Bi-212	3636	s	β-,α	2.6E-10	3.1E-08	M	1.6E-14	Cm-243	29.1	a	α,EC	1.5E-07	6.9E-05	F	1.0E-14
Pb-212	10.6	h	β-	6.0E-09	1.9E-07	S	1.3E-14	Cm-244	18.1	a	α,SF	1.2E-07	5.7E-05	F	3.6E-18
Po-212	0.299	μs	α				0.0E+00	Cm-245	8500	a	α,SF	2.1E-07	9.9E-05	F	7.0E-15
Bi-213	2736	s	β-,α	2.0E-10	3.0E-08	M	1.6E-14	Cm-246	4760	a	α,SF	2.1E-07	9.8E-05	F	4.5E-16

¹ Decay modes: β- for beta minus decay, β+ for beta plus decay, EC for electron capture, α for alpha decay, IT for isometric transition and SF for spontaneous fission.

² The solubility of particulate materials deposited in the respiratory tract is specified in terms of lung clearance types, with Types F, M, and S referring to fast, moderate, and slow rates of absorption into blood, respectively. For C-14, carbon dioxide (CO₂) is selected.

Table A-5. List of all radionuclides selected to be explicitly modelled in radionuclide transport calculations. Radionuclides in *italic* are not included in the initial inventory but are added due to potential exposure due to ingrowth of decay products. Each radionuclide is accompanied by three derived dose coefficients for ingestion, inhalation and external exposure, respectively. The last column lists the activity ratio in percent for the decay products included in the derived dose coefficients assuming secular equilibrium.

Radionuclide	Ingestion (Sv Bq ⁻¹)	Inhalation (Sv Bq ⁻¹)	External (Sv Bq ⁻¹ h ⁻¹ m ³)	Decay product radionuclides included in derived dose coefficient with corresponding activity ratio in percent
H-3	1.8E-11	2.6E-10	1.2E-19	
C-14	5.8E-10	6.2E-12	1.1E-16	
C-14	2.9E-11			
Cl-36	9.3E-10	7.3E-09	1.5E-15	
Ca-41	1.9E-10	1.8E-10	0.0E+00	
Co-60	3.4E-09	3.1E-08	3.0E-13	
Ni-59	6.3E-11	4.4E-10	1.6E-18	
Ni-63	1.5E-10	1.3E-09	1.5E-17	
Se-79	2.9E-09	6.8E-09	1.3E-16	
Sr-90	3.1E-08	1.6E-07	9.1E-15	Y-90 (100 %)
Zr-93	1.1E-09	2.5E-08	1.7E-17	
Nb-93m	1.2E-10	1.8E-09	1.1E-18	
Nb-94	1.7E-09	4.9E-08	1.7E-13	
Mo-93	3.1E-09	2.3E-09	6.1E-18	
Tc-99	6.4E-10	1.3E-08	3.6E-16	
Pd-107	3.7E-11	5.9E-10	2.5E-18	
Ag-108m	2.3E-09	3.7E-08	1.7E-13	Ag-108 (8.7 %)
Cd-113m	2.3E-08	1.1E-07	8.9E-16	
Sn-126	5.1E-09	2.8E-08	2.2E-13	Sb-126m (100 %), Sb-126 (14 %)
I-129	1.1E-07	3.6E-08	2.8E-16	
Cs-135	2.0E-09	8.6E-09	3.0E-16	
Cs-137	1.3E-08	3.9E-08	6.2E-14	Ba-137m (94.4 %)
Ba-133	1.5E-09	1.0E-08	3.5E-14	
Sm-151	9.8E-11	4.0E-09	2.0E-17	
Eu-152	1.4E-09	4.2E-08	1.3E-13	
Ho-166m	2.0E-09	1.2E-07	1.7E-13	
U-232	4.7E-07	8.1E-05	1.8E-13	Th-228, Ra-224, Rn-220, Po-216, Pb-212, Bi-212 (100 %), Po-212 (64.06 %), Tl-208 (35.94 %)
U-234	4.9E-08	9.4E-06	6.8E-18	
U-235	4.7E-08	8.5E-06	1.5E-14	Th-231 (100 %)
U-236	4.7E-08	8.7E-06	3.4E-18	
U-238	4.8E-08	8.0E-06	9.4E-15	Th-234, Pa-234m (100 %), Pa-234 (0.16 %)
Np-237	1.1E-07	5.0E-05	2.1E-14	Pa-233 (100 %)
Pu-238	2.3E-07	1.1E-04	1.9E-18	
Pu-239	2.5E-07	1.2E-04	5.3E-18	U-235m (99.94 %)
Pu-240	2.5E-07	1.2E-04	2.0E-18	
Pu-241	4.8E-09	2.3E-06	5.0E-19	U-237 (~0 %)
Pu-242	2.4E-07	1.1E-04	1.1E-17	
Am-241	2.0E-07	9.6E-05	7.9E-16	
Am-242m	2.0E-07	9.7E-05	2.0E-15	Am-242 (99.55 %), Cm-242 (82.33 %), Np-238 (0.45 %)
Am-243	2.0E-07	9.6E-05	1.7E-14	Np-239 (100 %)
Cm-243	1.5E-07	6.9E-05	1.0E-14	
Cm-244	1.2E-07	5.7E-05	3.6E-18	
Cm-245	2.1E-07	9.9E-05	7.0E-15	
Cm-246	2.1E-07	9.8E-05	4.5E-16	

Table A-5. Continued.

Radionuclide	Ingestion (Sv Bq ⁻¹)	Inhalation (Sv Bq ⁻¹)	External (Sv Bq ⁻¹ h ⁻¹ m ³)	Decay product radionuclides included in derived dose coefficient with corresponding activity ratio in percent
<i>U-233</i>	5.1E-08	9.6E-06	1.8E-17	
<i>Th-229</i>	6.1E-07	2.6E-04	3.2E-14	Ra-225, Ac-225, Fr-221, At-217 (100 %), Bi-213, Pb-209 (99.99 %), Po-213 (97.90 %), Tl-209 (2.09 %)
<i>Th-230</i>	2.1E-07	1.0E-04	2.2E-17	
<i>Ra-226</i>	2.8E-07	9.5E-06	2.1E-13	Rn-222, Po-218, Bi-214 (100 %), Pb-214, Po-214 (99.98 %), Tl-210, At-218 (0.02 %), Rn-218 (~0 %)
<i>Pb-210</i>	6.9E-07	5.7E-06	2.5E-15	Bi-210 (100 %), Tl-206, Hg-206 (~0 %)
<i>Po-210</i>	1.2E-06	4.3E-06	1.1E-18	
<i>Pa-231</i>	7.1E-07	1.4E-04	3.1E-15	
<i>Ac-227</i>	1.2E-06	5.7E-04	4.6E-14	Th-227 (98.62 %), Ra-223, Rn-219, Po-215, Pb-211, Bi-211 (100 %), Tl-207 (99.72 %), Po-211 (0.28 %), Fr-223 (1.38 %), At-219, Bi-215 (~0 %)

[†] Dose coefficient used for ingestion of water (Leggett 2004).

Modelling of radionuclide transport through cracks in the concrete structures

B1 Introduction

This appendix discusses the approach for modelling transport through concrete barriers. As concrete degrades, cracks may form (**Post-closure safety report**, Section 6.3.9) and the purpose of this appendix is to justify the way cracks are represented in the radionuclide transport modelling.

B2 Concrete degradation and transport modelling

Concrete degradation and hydrological modelling

Concrete degradation is considered in the near-field hydrological models (Abarca et al. 2013, 2014, 2020). In the near-field hydrological models the various parts of the concrete structures are assigned homogeneous properties. The intact concrete structures are assigned a low hydraulic conductivity that takes into account the presence of microcracks (Höglund 2014, Section 6.3). Additional cracks might form, and existing cracks may get clogged or become wider due to different processes affecting the properties of the concrete barriers (**Post-closure safety report**, Section 6.3.9) and this could drastically change the hydraulic properties of the concrete. In the near-field hydrological models, this is handled by defining a set of concrete degradation states, intact, moderately degraded, severely degraded and completely degraded for which the hydraulic conductivity successively increases. In general, for intact or moderately degraded concrete, the groundwater flow is relatively slow and is considered to be distributed over many small cracks. However, for a severely or completely degraded concrete, the magnitude of the groundwater flow is larger and could become localised to a few major cracks.

Concrete degradation and radionuclide transport modelling

Diffusion plus advection and dispersion are the main transport processes included in the radionuclide transport modelling and both these processes are influenced by the concrete degradation. In particular, the formation of cracks will have an impact on the advective transport. A large crack becomes a preferential flow path that diverts the advective flow through the concrete barrier to the crack making some of the sorption sites inside the concrete barrier out of range for radionuclides dissolved in the water flowing through the cracks. Advective radionuclide transport through concrete barriers is included in the near-field radionuclide modelling in two ways, either by considering advection in a homogenous porous medium or a cracked medium. A criterion for when either of the two approaches should be applied can be defined based on a comparison of three different models:

1. The *reference model*.
2. The *homogeneous model*.
3. The *crack model*.

The *reference model* is introduced and used only in this appendix. The reference model describes transport through cracks with a dual porosity approach, i.e. with purely advective transport in the crack and diffusion and sorption in the matrix (Neretnieks and Moreno 2013). The reference model is considered to give a more correct representation of advection in a cracked medium than the other two models. The reference model is, in this work, only used for comparison with the homogeneous model. The purpose of the comparison is to find a range of water flow rates (governed mainly by the frequency and aperture of cracks) where the homogeneous model can be expected to give a cautious result compared with the reference model. Within this range the homogeneous model is later used in the near-field radionuclide modelling. If this condition does not apply, a more pessimistic approach where the crack model is applied in the modelling, can be more appropriate.

The *homogeneous model* is a compartment model as described in Chapter 4 where all compartments are connected by advective transfer coefficients. The model represents the concrete barriers as homogeneous porous media. In the homogeneous model discussed in this appendix, a single compartment is used to represent the concrete barrier. However, in the radionuclide transport modelling the concrete barriers are represented by using several sub-compartments (Åstrand et al. 2022, Section 2.1).

The *crack model* represents the advective transport of radionuclides through a barrier using an advective transfer directly from the waste domain to the crushed rock backfill without taking any sorption in the concrete barrier into account. However, in the crack model, diffusive transfer through the concrete structure is retained, hence the sorption sites are still available for the radionuclides that diffuse into the concrete structure.

B3 Mean transit time

The mean transit time is a way of quantifying the time it takes for a radionuclide to migrate through a barrier. A comparison between the concrete barrier mean transit times calculated using the reference model and the homogeneous model, can be made to estimate the range of water flow rates for which the homogeneous model gives a cautious estimate of the mean transit time. In this section the mean transit time calculations of the concrete caissons in 2BMA is analysed in some detail. Based on this analysis the applicability of a homogeneous or cracked media modelling approach for the caissons is discussed. The 2BMA section is followed by sections where, for each vault with concrete barriers, the adopted representation of cracks in the radionuclide transport modelling is discussed.

Conceptual representation of a concrete barrier and definition of mean transit time

The mean transit times of radionuclides are estimated for the conceptual representation of the concrete barrier shown in Figure B-1. The radionuclides are initially only present on the left, or inlet, side of the concrete barrier, denoted waste domain in Figure B-1. In the waste domain, the concentration of a radionuclide in the pore-water is kept constant. Initially, the radionuclide concentration is zero in the pore-water within the concrete and in the backfill on the outlet side. The concentration of radionuclides both in concrete pore-water and the water flowing in the crack at the outlet side, will gradually increase and eventually reach a steady-state concentration. Both the reference model and the homogeneous model can be used to estimate the time it takes to reach half the steady-state concentration at the outlet, here denoted mean transit time, for further details see SKB (TR-14-09 Appendix D). In the following sections the calculations are made without taking decay into account i.e. assuming the half-life of the radionuclide to be long compared with the travel times through the system.

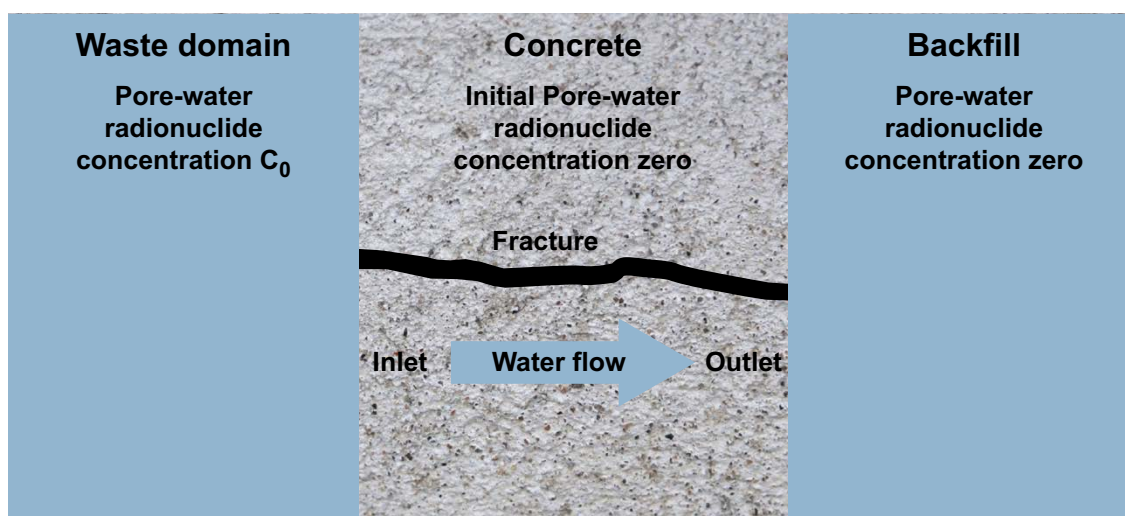


Figure B-1. Conceptual representation of the modelled system.

Cracks and radionuclide transport in 2BMA

In 2BMA, the waste is disposed in concrete caissons with a base of 18.12×18.12 m and a height of 9 m. The thickness of the caisson walls is 0.68 m. The sections below show how the mean transit time of the caissons can be calculated using the three different models

The reference model

For the reference model the mean transit time is given by (SKB TR-14-09, Equation D-9):

$$t_{half}^{ref} = \left(\frac{FWS \cdot MPG}{Q \cdot 0.5} \right)^2 \quad \text{Equation B-1}$$

where:

Q = water flow ($\text{m}^3 \text{a}^{-1}$),

FWS = the flow-wetted surface area of the cracks. For a 2BMA caisson with n cracks in the concrete wall $FWS^{33} = n \times 2 \times 0.68 \times 9$ (m^2),

MPG = materials property group that accounts for the access to the pore volume and inner surfaces of the concrete on which the sorbing radionuclide can attach ($\text{m/a}^{1/2}$).

MPG is defined as:

$$MPG = \phi \sqrt{D_e \left(1 + \frac{K_d(1 - \phi)\rho}{\phi} \right)} \quad \text{Equation B-2}$$

where³⁴:

ϕ = porosity of the concrete wall = 0.11 (-),

ρ = particle density of the concrete wall = 2700 (kg m^{-3}),

D_e = effective diffusivity of the concrete wall = 1.1×10^{-4} ($\text{m}^2 \text{a}^{-1}$),

K_d = radionuclide sorption coefficient ($\text{m}^3 \text{kg}^{-1}$).

The homogeneous model

For the homogeneous model, the mean transit time is approximately given by (SKB TR-14-09, Equation D-10):

$$t_{half}^{hom} = \frac{Capacity}{Q + \frac{4AD_e}{L}} \times \ln(2) \quad \text{Equation B-3}$$

where³⁵:

L = thickness of the concrete wall = 0.68 (m),

A = cross sectional area of the concrete wall = 9×18.12 (m^2),

$Capacity$ = capacity of the compartment (m^3).

Capacity is defined as:

$$Capacity = Volume(\phi + K_d(1 - \phi)\rho) \quad \text{Equation B-4}$$

where:

$Volume$ = volume of the concrete wall = $0.68 \times 9 \times 18.12$ (m^3).

³³ Dimensions apply to the concrete wall in a caisson in 2BMA (**Initial state report**).

³⁴ Numeric values apply to the concrete wall in a caisson in 2BMA (**Data report**).

³⁵ Dimensions apply to the concrete wall in a caisson in 2BMA (**Initial state report**).

The crack model

In the crack model, the outflowing concentration will be identical to the inflow concentration because the model considers an instant advective transfer directly from the waste domain out to the gravel backfill, i.e. the mean transit time is zero.

Mean transit time as a function of water flow

The mean transit times, t_{half}^{ref} estimated by the reference model and homogeneous model for a non-sorbing radionuclide ($K_d = 0 \text{ m}^3/\text{kg}$) are compared in Figure B-2. For the reference model the mean transit time depends on the number of cracks in the concrete wall since the total flow-wetted surface is the sum of the flow-wetted surfaces in all cracks. In Figure B-2 the mean transit time is calculated for 2, 18 and 180 cracks corresponding to a spacing between cracks of 10, 1 and 0.1 m respectively. A similar comparison for a sorbing radionuclide was made in SKB (TR-14-09, Appendix B). The impact of sorption will not change the conclusions made in this appendix.

As shown in Figure B-2, the mean transit time for both the homogeneous model and the reference model is dependent on the magnitude of water flow through the concrete structure (mostly focused to the largest cracks). For high flow rates, the homogeneous model tends to give the longest estimate of mean transit time, i.e. it overestimates the mean transit time compared with the more accurate reference model. Figure B-2 also shows that the reference model estimate of the mean transit time is strongly dependent on the configuration of the cracks i.e. the number of cracks or spacing between cracks in the concrete structure. If the concrete structure is penetrated by many small cracks instead of a few large cracks, the reference model tends to give a longer mean transit time estimate compared with the homogeneous model. As justified in the next section, if the water flow through a concrete structure is distributed over many small cracks, the concrete can be represented as a homogeneous medium. As concrete degrades, new cracks might form and it cannot be excluded that the water flow becomes focused to only a few large cracks. That means that, as the concrete degrades, the number of penetrating cracks is considered to decrease since the water flow could be focused to a smaller number of newly formed large cracks.

Applicability of the different model approaches

If the mean transit time estimated by the homogeneous model is shorter than the mean transit time estimated using the reference model for a certain water flow rate it is justified to not explicitly represent the radionuclide transport through the crack, i.e. the homogeneous model approach without cracks can be applied in the radionuclide transport modelling. In Figure B-2, it can be seen that, for a moderately degraded caisson where the water flow is distributed over more than 18 cracks (1 m spacing between cracks), the homogeneous model can be applied.

Alternatively, if the mean transit time estimated by the homogeneous model is longer than the mean transit time estimated using the reference model, a pessimistic approach can be considered where the cracks are regarded as preferential flow paths for dissolved radionuclides which channel radionuclide advection through the concrete. This can be done by applying the crack model where the cracks are represented by advective transfer directly from the waste domain to the crushed rock backfill without taking any sorption in the concrete structure into account. In the crack model, diffusive transfer through the concrete structure is retained, hence the sorption sites are still available for the radionuclides that diffuse into the concrete structure.

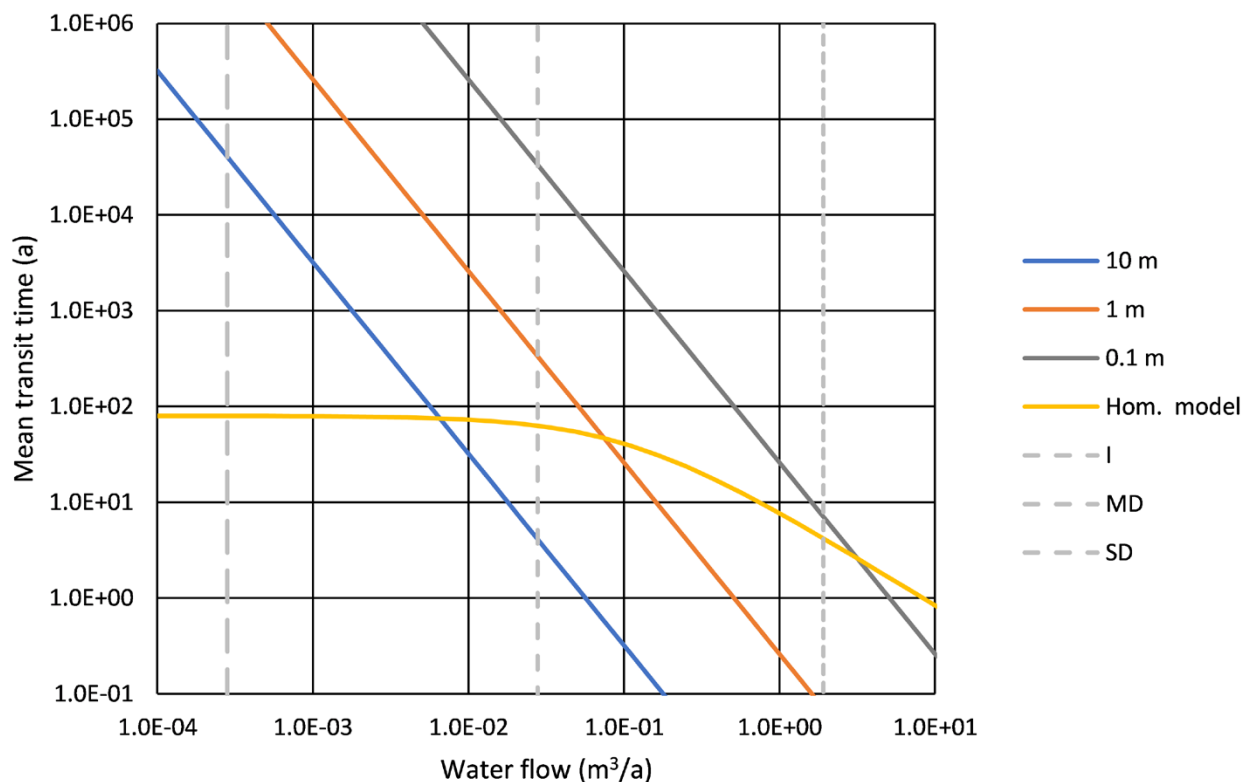


Figure B-2. Mean transit time, i.e., time to reach half steady-state concentration at the concrete wall outlet as a function of water flow rate in the concrete wall. The results of the homogeneous model (yellow curve) and the reference model for different spacing between cracks (blue curve – 10 m, orange curve – 1 m and grey curve – 0.1 m). The grey dotted lines indicate predicted water flow rates through a caisson at 5000 AD for different physical degradation states, intact (I), moderately degraded (MD) and severely degraded (SD) (Abarca et al. 2020).

Cracks and radionuclide transport in 1BMA

As discussed for 2BMA, whether in the radionuclide transport modelling it is appropriate to represent the cracks through a concrete structure with the crack model or not depends on the configuration of the cracks and the water flow rate. In 1BMA most of the water flowing through the waste will exit through the slab (Abarca et al. 2020). Since cracks have already been found in the slab of 1BMA, flow through the slab is considered to be concentrated in a few cracks (**Initial state report**). If the reference model were applied to calculate the mean transit time of the concrete slab, the obtained mean transit time would be relatively short compared with the homogeneous model. The homogeneous model, will, for this case, overestimate the mean transit time since the water flow is concentrated in a few cracks, i.e., it is in the radionuclide transport modelling appropriate to explicitly represent the cracks in the slab using the crack model. In 1BMA, a new reinforced concrete wall will be erected on the outside of the existing ones compensating for the cracking that has been observed in the existing structure. This will limit groundwater flow through the walls and no major cracking is expected until the walls become severely degraded. Hence, no explicit representation of cracks in the walls of 1BMA is required in the radionuclide transport model until the walls becomes severely degraded. The same holds for the lid of 1BMA.

Cracks and radionuclide transport in 1BRT

The concrete structure in 1BRT is not considered to constitute a hydraulic barrier and is assumed to initially be in the severely degraded physical degradation state. The crack model is cautiously applied already from the start (2000 AD) in the *base case*.

Cracks and radionuclide transport in 1–2BTF

The main concrete barrier in 1–2BTF is the concrete tanks. No major cracks are expected in the tanks at closure. The tanks are considered to degrade with time but, even for severely and completely degraded tanks, the preferential water flow paths are considered to be in the space between the tanks. Thus, even though some cracks are expected to form in the concrete tanks and the concrete structures surrounding the tanks in 1–2BTF, the crack model is not applied in the *base case*. However, in the *initial concrete cracks calculation case* it is assumed that all tank concrete structures in 1–2BTF have cracks and the crack model is applied from the start (2000 AD). The resulting increase of the annual near-field release from 1–2BTF is presented in Section 8.6.

Cracks and radionuclide transport in the silo

Water flow through the concrete structure in the silo is low and no major cracks are expected to form. In the *base case* the crack model is not applied in the radionuclide transport modelling. In the *initial concrete cracks calculation case* it is assumed that the concrete structure has cracks and the crack model is applied from the start (2000 AD). The resulting increase of the annual near-field release from the silo is presented in Section 8.6.

B4 Conclusions

For intact or moderately degraded concrete, where the groundwater flow is relatively slow and considered to be distributed over many small cracks, the homogeneous model approach can be applied. However, for a severely or completely degraded concrete, the magnitude of the groundwater flow is greater and considered to be localised to a few major cracks to such an extent that it reduces the mean transit time. Thus, for a severely or completely degraded concrete structure, a cracked medium modelling approach can be more appropriate.

Comparison with SR-PSU

C1 Introduction

This appendix discusses the changes in dose results due to the main updates and differences in the near-field, geosphere and biosphere modelling in the PSAR compared to the SR-PSU. Further details about the updates performed in the near-field modelling can be found in Åstrand et al. (2022). A more in-depth comparison focused on the updates in the modelling related to the surface systems is found in Appendix C in the **Biosphere synthesis report**. A detailed review of the updates and their consequences for the geosphere transport modelling is presented in the last section of this appendix.

The comparison of doses is carried out with the whole calculation chain (near-field, geosphere and biosphere) for the *base cases* in the two analyses (the PSAR and the SR-PSU).

A comparison is also carried out for the near-field and geosphere models. The near-field calculation compares the so-called timing of releases calculation case in the SR-PSU to the *base case* in the PSAR to enable comparison also during the first 1 000 years.

The geosphere calculation is carried out with the same near-field release (the PSAR release) in both calculations. This is done to isolate and illustrate specific differences in the geosphere models.

C2 Main changes affecting the dose results

Updates to the radionuclide transport and dose calculations in the PSAR compared with the SR-PSU (SKB TR-14-09) involve both changes in input data and the models. These changes have been made to incorporate modifications of the repository design as well as new information from recent and ongoing research and development (**Post-closure safety report**, Section 1.5.2).

Most changes have a minor effect on the calculated doses. However, some notable changes are listed below:

- In the SR-PSU, a delay of the start of releases was used to avoid underestimating releases during the later terrestrial period.
- The point in time when draining the mire is first possible is approximately 1 300 years earlier than when cultivation of a drained mire was first considered in the SR-PSU.
- In the SR-PSU, permafrost was included in the *base case* leading to periods with frozen ground and no releases while, in the PSAR, temperate climate conditions are considered throughout the whole assessment period.
- Several transport parameters in the near-field have also been updated, as discussed below.

The releases from the near-field models are affected by several factors, mainly the initial inventory (a comparison of the initial radionuclide inventory for all radionuclides in the PSAR and the SR-PSU is shown in Chapter 3, Table 3-3), radionuclide sorption coefficients (especially for cementitious materials), groundwater flow, timing of concrete degradation, updated model discretisation and handling of cracks in the concrete. Changes of some of the key near-field parameters updated in the PSAR are shown in Table C-1. The shift in chemical degradation state of the cementitious materials has been set to a later time point in the PSAR (12 000 AD in the PSAR compared to 7 000 AD in the SR-PSU).

Table C-1. Key near-field parameters updated in the PSAR. Values are ratios PSAR/SR-PSU.

Radionuclide	Total initial inventory (-)	K_d (first concrete degradation state) (-)	K_d (second concrete degradation state)(-)
C-14-org	0.85	- ^a	- ^a
Ni-59	1.12	8.9	8.3
Ca-41	1.23	1.0	1.0
U-238	0.95	0.07 ^b	0.7 ^b
Mo-93	0.84	1.0	1.0
I-129	0.59	1.0	1.0

a) C-14-org was considered non-sorbing in the SR-PSU but has a low K_d ($1 \times 10^{-5} \text{ m}^3 \text{ kg}^{-1}$) in the PSAR.
 b) U-238 is mainly present in 1-5BLA where no sorption is considered.

C3 Dose in base cases

Figure C-1 shows a comparison of the total and radionuclide specific doses as calculated in the *base case* in the PSAR (thick lines) compared to doses as calculated in the *global warming calculation case* (“*base case*”) in the SR-PSU (thin lines). The total dose and individual doses for the most significant radionuclides are similar in the two calculations. However, the general trend is lower doses in the PSAR, in particular for Ni-59.

The changes can be explained by updates of assumptions, updates in the models and parameter values as described in this appendix.

The *global warming calculation case* in the SR-PSU was the case that was used as a basis from which other calculations were derived and compared to in a similar way as the *base case* in the PSAR. However, there are some fundamental differences in the modelling assumptions of the two cases that explain the largest differences seen in Figure C-1.

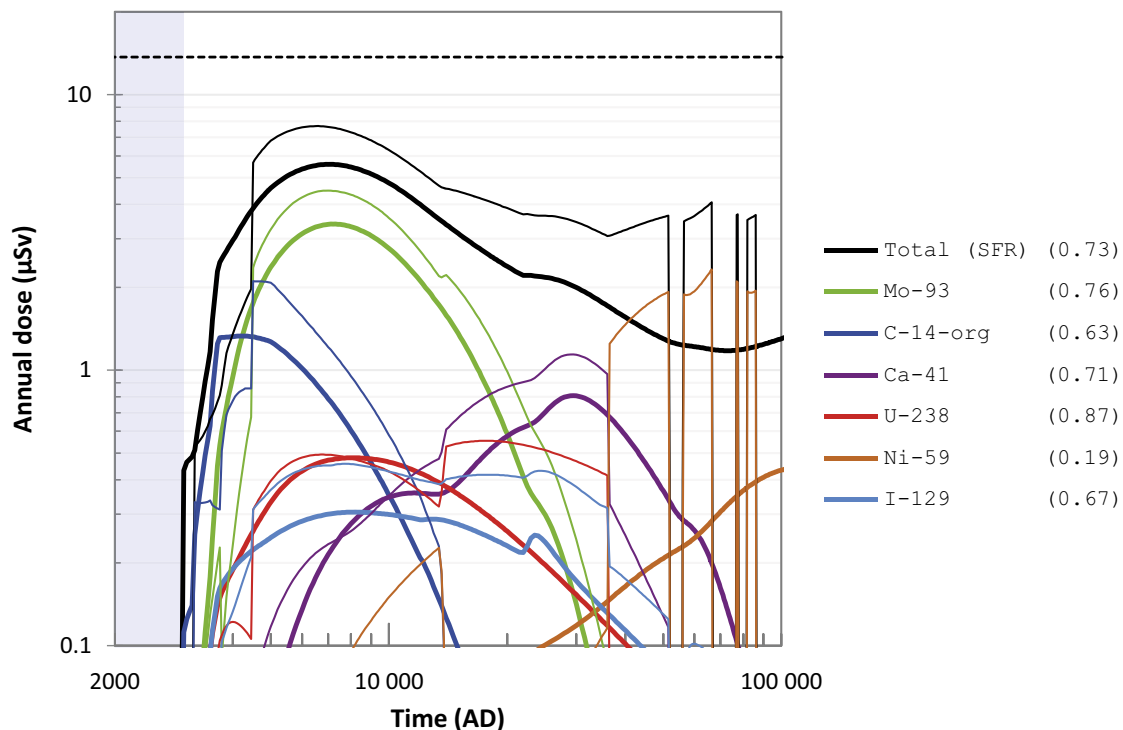


Figure C-1. Annual dose (μSv) to the most exposed group (black line), including radionuclide specific contributions from key radionuclides (coloured lines), in the base case in the PSAR (thick lines) and the global warming calculation case (effectively the base case) in the SR-PSU (thin lines). The ratio between the maximum doses in the calculations in the PSAR and the SR-PSU are shown in parentheses in the key. The annual dose corresponding to the regulatory risk criterion ($14 \mu\text{Sv}$) is indicated by the black dashed line and the submerged period is illustrated by the blue shading.

During the first 1 000 years post-closure, an assumption of no release from the waste vaults was considered in the SR-PSU similar to the supporting calculation case *delayed release from repository* in the PSAR. The *base case* in the PSAR considers releases from the waste vaults directly post-closure (similar to the so-called timing of the release calculation case, in the SR-PSU). As doses are very low during the initial period of submerged conditions, this difference is not visible (in Figure C-1) during this period. However, releases and doses during the terrestrial period are somewhat more dispersed and occurs slightly earlier in the PSAR compared to the SR-PSU.

In the SR-PSU, four periods of periglacial climate were considered in the second half of the assessment period producing significant drops in dose (see thin lines in Figure C-1) as releases are halted and exposure pathways are reduced in the permafrost environment. In the *base case* in the PSAR, present day climate conditions are assumed to prevail during the full assessment period.

In the PSAR, cultivation of a drained mire is evaluated from the time when the highest point in the biosphere object is 1 m above sea level (~3200 AD). In the transitional period, saltwater intrusion is not considered to limit cultivation on the emerged areas. The point in time when draining the mire is first possible is approximately 1 300 years earlier than when cultivation of a drained mire was first considered in the SR-PSU. Therefore, an earlier, and more gradual dose curve due to DM-farmers is seen in the PSAR compared to the SR-PSU.

In the PSAR, a stream is considered to connect the discharge object with the downstream object. In the SR-PSU, surface water was assumed to disperse as overland water to the terrestrial part on the downstream object, elevating dose from radionuclides that accumulate in peat (Ca-41, U-238, U-235 and its decay products). The effect of downstream accumulation is seen in the dose results for the SR-PSU between approximately 15 000-35 000 AD (thin lines in Figure C-1) when DM farmers in the downstream object are the most exposed group.

C4 Comparison for near-field transport calculations

Figure C-2 shows a comparison of radionuclide releases from the near-field as calculated in the PSAR compared to releases calculated in the SR-PSU. With the exception of Ni-59, the calculated total near-field maximum releases in the PSAR agree reasonably well (within a factor of 2) with those in the SR-PSU for radionuclides with large contributions to dose, as can be seen in Figure C-2. The larger difference for Ni-59 can be explained by an almost tenfold higher K_d for nickel used in the PSAR (Table C-1). Note that Figure C-2 shows the releases from the *timing of the release calculation case* in the SR-PSU and the *base case* from the PSAR, as the releases are assumed to start immediately after closure in these two calculation cases. Furthermore, Figure C-2 is based on the detailed comparison presented in Åstrand et al. (2022) where only deterministic calculations are used and hence the figure presents deterministic results.

The main differences seen in Figure C-2 are discussed below.

Higher groundwater flows earlier in the simulation were used in the SR-PSU (due to interpolation between the low water flow at 2000 AD and significantly higher water flows at 3000 AD). An additional time-slice is included in the near-field hydrological calculations in the PSAR (2000 AD, 2500 AD, 3500 AD and 5000 AD) compared to the SR-PSU (2000 AD, 3000 AD and 5000 AD), resulting in a less steep increase in early groundwater flow during shoreline regression for the PSAR. This effect is also enhanced by the extra interpolation points, based on the vault flow from the hydrogeological calculations included in the PSAR (described in Section 5.5). The effect of the updated handling of groundwater flow can be seen as a later onset of the releases of all radionuclides.

The maximum release of Mo-93 is slightly lower in the PSAR compared to the SR-PSU, and this can be explained by the lower initial inventory (a factor 0.84 compared to the SR-PSU) combined with lower water flow rates in the silo (a factor 0.7 compared to the SR-PSU). However, changes in the silo model counteract this to some extent and the resulting maximum release of Mo-93 is 0.63 times the release as calculated in the SR-PSU. A significantly simplified discretisation of the silo model was made to avoid overly detailed implementation of features that are of minor importance to the overall performance of the repository. The simplified silo model is far less computationally demanding and is also far easier to verify and review.

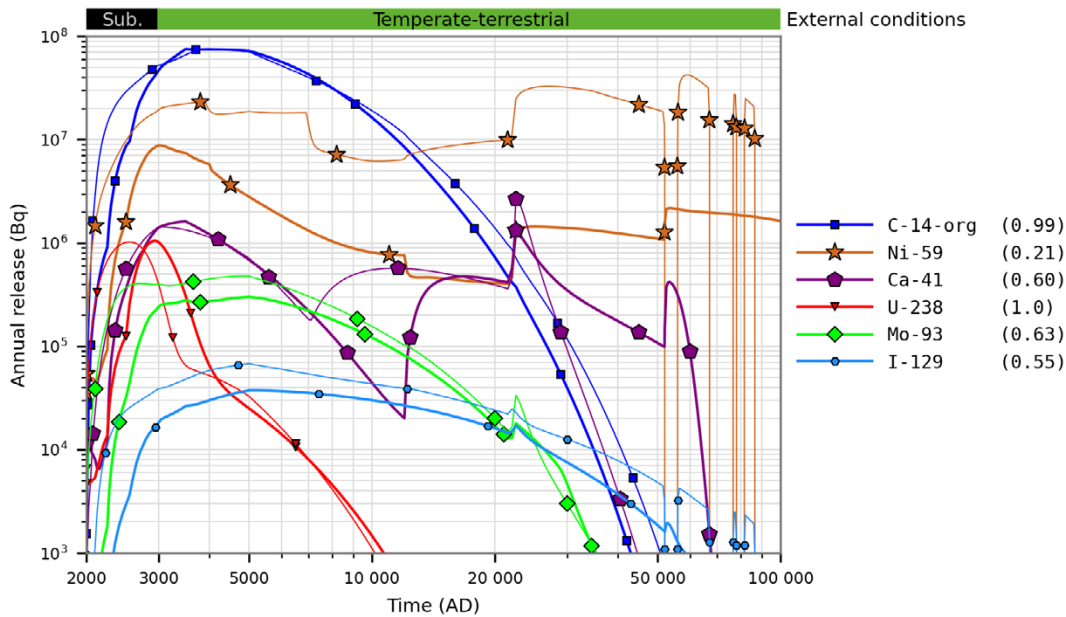


Figure C-2. Annual activity releases (Bq) from the entire SFR in the base case in the PSAR (thick lines) and the timing of the release calculation case in the SR-PSU (thin lines). The ratio between the maximum releases in the calculations in the PSAR and the SR-PSU are shown in parentheses in the key. The coloured bar at the top refers to the PSAR calculation, in the SR-PSU calculation periglacial conditions were considered toward the end of the assessment period.

The maximum release of C-14-org is relatively similar in the two calculations. As the considered K_d for C-14-org in the PSAR is very small, the introduction of sorption for organic C-14 has a negligible effect on the near-field releases. The main effect on C-14-org release is by the updated handling of early water flow rates which gives lower releases during the submerged period.

The overall lower release of Ni-59 can be explained by the higher K_d used in the PSAR. Initially this effect is limited due to the fraction of the early release of Ni-59 from 1-5BLA, which are not affected by sorption. The characteristic decrease in release of Ni-59 (at 7000 AD) in the SR-PSU has been shifted to 12000 AD in the PSAR due to the shift in chemical degradation state of the cementitious materials that has been set to this later time point in the PSAR.

Similarly, the characteristic increase in release of Ca-41 (at 7000 AD) in the SR-PSU has been shifted to 12000 AD in the PSAR. It should be noted that the release of Ca-41 is totally dominated by 2-5BLA in the time interval up to 7000 AD, whereas the decrease in K_d in 2BMA leads to dominating releases from 2BMA for the rest of the assessment. Further, the discretisation of the 2BMA model has been updated to represent radionuclide transport in three dimensions in the PSAR, while the 2BMA model used in the SR-PSU had a simplified representation with transport out of the caissons represented with a one-dimensional model. The more detailed representation of 2BMA results in delayed release which is especially visible as a higher release at later time points (notable for Ca-41), as storage capacity beside the flow path is considered, more inventory remains at later time points and the peak release of Ca-41 is lower.

The release of U-238 is dominated by release from 1BLA and thus not affected by the lower K_d for uranium as sorption is not considered in 1BLA. Therefore, the main effect on U-238 releases is (as for C-14-org) explained by the updated handling of early water flow rates.

For I-129 the decrease in initial inventory accounts for the main decrease in the near-field releases. However, clearly the effect on early submerged releases due the updated handling of early water flow rates, as for the other radionuclides, is seen.

The releases from the geosphere are studied separately in the next section. To isolate the effects on geosphere releases these calculations have been performed with the same source term (near-field releases from the PSAR).

C5 Detailed comparison for geosphere transport calculations

Introduction

As mentioned earlier in this appendix, a detailed comparison of the near-field modelling can be found in Åstrand et al. (2022) and a more detailed comparison for the biosphere can be found in Appendix C in the **Biosphere synthesis report**. However, comparison of the geosphere modelling is only discussed in this appendix and thus a more detailed discussion of changes applied in the geosphere modelling is presented here.

In the SR-PSU, the geosphere transport model was implemented in Ecolego and calculated sequentially together with each near-field model. In the PSAR, the geosphere transport is implemented and calculated separately from the near-field models. For this purpose, the dual porosity radionuclide transport code FARFCOMP, developed within the framework of the SE-SFL (SKB TR-19-01) is used. The change of numerical codes, as well as the separation of the geosphere transport model from the near-field models, helped to reduce the total model size and computation time and thus enabled an increased number of iterations to be carried out in the Monte-Carlo simulations. Therefore, in the PSAR, the number of simulations performed in the probabilistic simulation, both with the near-field models and the geosphere model, have increased by an order of magnitude to 1 000 iterations compared to the 100 iterations as applied in the SR-PSU. The updated code and approach for the geosphere modelling, however, do not have any significant effect on the results, as illustrated in the comparative analysis presented in this section.

Updates in the geosphere modelling since SR-PSU

For the flow-related transport parameters (travel times and the flow-related transport resistance), data from the most recent simulations in (Öhman and Odén 2018) are used for the PSAR calculations instead of the data that were used in the SR-PSU (Odén et al. 2014). In the SR-PSU a large number of particle trajectories for each waste vault (100 000) were used for six time-slices covering the transition from present-day submerged to fully terrestrial conditions above the repository. In the PSAR, an order of magnitude lower number of particle trajectories was produced for each simulation but with an increased number of time-slices during the submerged period (three additional time-slices). These additional time-slices capture changes in the hydraulic gradient in higher detail as the shoreline passes over the repository. The same three bedrock cases were selected as representative bedrock cases (reference case, 1, and bounding cases, 11 and 15, see Section 5.5.1) in the *base case* of both the SR-PSU (i.e. the *global warming calculation case*) and the PSAR. However, whilst only the reference bedrock case propagated to the base model in the transport calculations in the SR-PSU, the geometric mean of all three representative cases is used as input to the transport calculations in the PSAR.

Of the 100 000 calculated particle trajectories in the SR-PSU, only 100 particle trajectory pairs were randomly selected from the reference bedrock case for each time-slice and waste vault, to be used individually (i.e. one per iteration) in the probabilistic geosphere transport calculation. In the PSAR, “effective” trajectory pairs, defined as the median value of all particle trajectories for the travel time and the transport resistance (Section 5.5.1), are considered more representative, especially as general flow-related transport parameters are interpolated over time (see also Appendix A3). Additionally, in the PSAR, the three representative bedrock cases are used to assess the uncertainty of the stochastic fracture network, producing correlated scaling factors for water flow through waste vaults and the particle trajectories. In the SR-PSU the uncertainty in the bedrock cases was considered using the upper bounding bedrock case in the less probable calculation scenario *high flow in the bedrock calculation case* and thus not included in the *base case*.

In the probabilistic calculations performed in the SR-PSU, the effective diffusion coefficient of the rock matrix was randomly sampled for each species independently. In the PSAR, all species use the same sampled data set. This update only affects combinations of radionuclides, e.g. transport of decay products, and the collective radiotoxicity or dose from all radionuclides.

The Peclet number (Pe) defines the magnitude of longitudinal dispersion. In the SR-PSU, this parameter was defined between 2 and 50 using a triangular probability distribution with a mode of 10. Following the methodology in SAR-08, SR-Site and the safety evaluation SE-SFL (SKB TR-19-01), a constant Peclet number of 10 is selected in the PSAR. This change corresponds to a decrease of the average Peclet number in the PSAR from almost 21 in the SR-PSU and thus results in a higher average

longitudinal dispersion in the PSAR. The choice of a lower average Peclet number in the PSAR is to some extent motivated by the use of effective trajectories (see Section 5.5.1 and Appendix A). As a result of using a smaller number of particle trajectories, the modelled macro dispersion will be reduced, and thus using a lower Peclet number in the PSAR compensates, at least partially, for the lower dispersion that stems from using effective trajectories. These changes are not expected to have any significant impact on the resulting geosphere releases as the longitudinal dispersion is of limited importance compared to the macro dispersion (SKB TR-19-06).

The maximum penetration depth into the rock matrix (i.e. the average distance between conducting fractures) is reduced from 1.4 m in the SR-PSU to 0.9 m in the PSAR (Appendix A3). A reduced penetration depth could potentially decrease transport times, however, as the maximum depth is still relatively large, the effect is expected to be negligible.

The radionuclides Mo-93 and Se-79, for which the sorption coefficients were set to zero in the SR-PSU, have been assigned non-zero probability distributions in the PSAR as reported in the **Data report** based on Crawford (2018). The updated sorption coefficient for Mo-93 is however very small, and thus no significant effects on the geosphere release are expected to be introduced by this change (~ 1 % reduction, see Figure 5-47). For Se-79, due to increased dispersion, the introduced K_d -value is expected to lower the maximum geosphere release by approximately 50 % (10 %–90 %, see Figure 5-47).

Evaluation of differences in modelling approach

Method

In the following, the modelling approach for evaluating differences in the geosphere treatment between the PSAR and the SR-PSU is described. Calculations for the PSAR and recalculations for the SR-PSU were performed using FARFCOMP with near-field releases from the (PSAR) *base case*. Input data and modelling concept for the calculations are taken from the *global warming calculation case* in the SR-PSU and from the *base case* in the PSAR. To enable a more straightforward comparison between the *base cases*, the periods of periglacial climate domain in the *global warming calculation case*, which was defined as *base case* in the SR-PSU, are replaced with temperate climate domain. Further, following the methodology in the PSAR, Rn-222 is added as an explicitly modelled radionuclide (though not presented) and Po-210 is ignored in the SR-PSU recalculations also. Since the number of the Monte-Carlo iterations in the SR-PSU were ten times fewer compared to the PSAR, each data set in the recalculation for the SR-PSU is iterated 10 times. The resulting 1 000 iterations are then combined with the corresponding near-field release data sets.

An additional calculation using flow-related transport parameters (travel times and the flow-related transport resistance) from the SR-PSU and non-flow-related transport parameters (K_d , D_e , Pe and maximum matrix penetration depth) from the PSAR is also conducted to isolate and further identify the underlying cause of differences in geosphere transport between the two safety assessments.

Results

Figure C-3 shows the total geosphere release of the radionuclides with the highest activity releases from the two calculations. For non- and very weakly sorbing radionuclides with high geosphere activity releases (e.g. C-14, Ag-108m, Ca-41, Cl-36 and Mo-93), the PSAR updates only have a negligible effect (up to a couple of percent) on the total release.

For radionuclides ¹ (e.g. Ni-59, Ni-63, Se-79, Cs-135 and U-238) with rock matrix sorption coefficients greater than $10^{-4} \text{ m}^3 \text{ kg}^{-1}$, a visible difference can however be noted. As median transport parameters are used in the PSAR instead of randomly chosen singular particle trajectories as in the SR-PSU, an expected result would be a delayed response to time-dependent changes in the PSAR compared to the SR-PSU. The reason for this would be that some SR-PSU iterations use trajectories corresponding to fractures with shorter travel times, producing more immediate responses to changes in the near-field releases than in the PSAR. This trend is observed for Se-79 which has a delayed response curve in the PSAR compared to the SR-PSU and a maximum annual release that is approximately 27 % lower. However, the main reason for the difference in Se-79 is attributed to the introduced non-zero sorption

coefficient in the PSAR. As the sample set applied in the SR-PSU-calculations was small (only 100 out of 100 000 data points) the sampled trajectory data could be biased. An example of this is the sampled travel time for trajectories released from IBLA that is approximately 50 % longer than they should be at the same time-slices during the submerged period and 10 %–30 % shorter after this period. Thus, the first release peak of Ni-59 and the releases of Ni-63 and U-238 seen in Figure C-3 (all due to releases from IBLA) show the opposite behaviour than would be expected.

The total radiotoxicity fluxes out from the geosphere (Figure C-4) illustrate the set of radionuclides that are the most hazardous to ingest directly. In general, similar to the geosphere release (Figure C-3), differences in the radiotoxicity flux between the PSAR and the SR-PSU can be partially explained by the sorption coefficients; low or zero sorption coefficients produce only small changes in the radiotoxicity fluxes, whereas higher coefficients result in larger differences. For radionuclides produced during transport in the geosphere, a somewhat different response can also be noted. Most activity of Pa-231 and Ac-227 is found within the geosphere as a result of U-235 decay. As the transport of U-235 is affected by the updates since SR-PSU, its decay products will also be affected in a similar way. The effect is further amplified as both Pa-231 and Ac-227 sorb onto the rock matrix. For these radionuclides, an increased delay in the transport is therefore noted in the PSAR compared to the SR-PSU. As a result, the total radiotoxicity flux in the PSAR is lower than in the SR-PSU during the first thousands of years, after which it gradually increases. After around 10 000 AD, the radiotoxicity flux exceeds the corresponding flux from the SR-PSU, mainly due to slower transport of U-235 through the geosphere which serves to increase the production of decay products. However, as U-235 is mainly released from IBLA, the changes are considered to mainly be based on the removal of the bias in the drawn trajectory samples.

In Figure C-3 and C-4, it can be noted that, in particular, U-238, U-235, Pa-231, Ac-227, Ra-226, Pu-239, Pu-240 and Se-79 have been notably affected by updates from the SR-PSU. Figure C-5 illustrates the behaviour of these radionuclides when using flow-related parameters from the SR-PSU, while keeping all other parameters as in the PSAR *base case*.

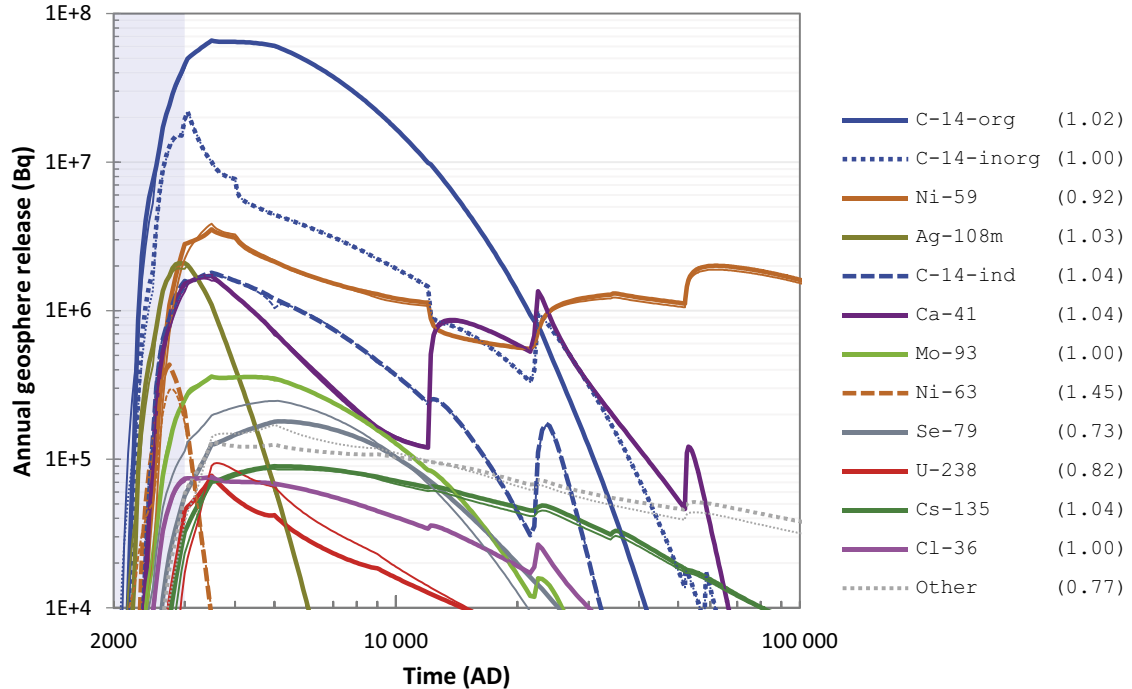


Figure C-3. Annual activity releases (Bq) from the geosphere originating from the entire SFR in the base case in the PSAR (thick lines) and with input data and concepts from the SR-PSU (thin lines). The ratio between the maximum releases in the calculations in the PSAR and the SR-PSU are shown in parentheses in the key. The submerged period is illustrated by the blue shading.

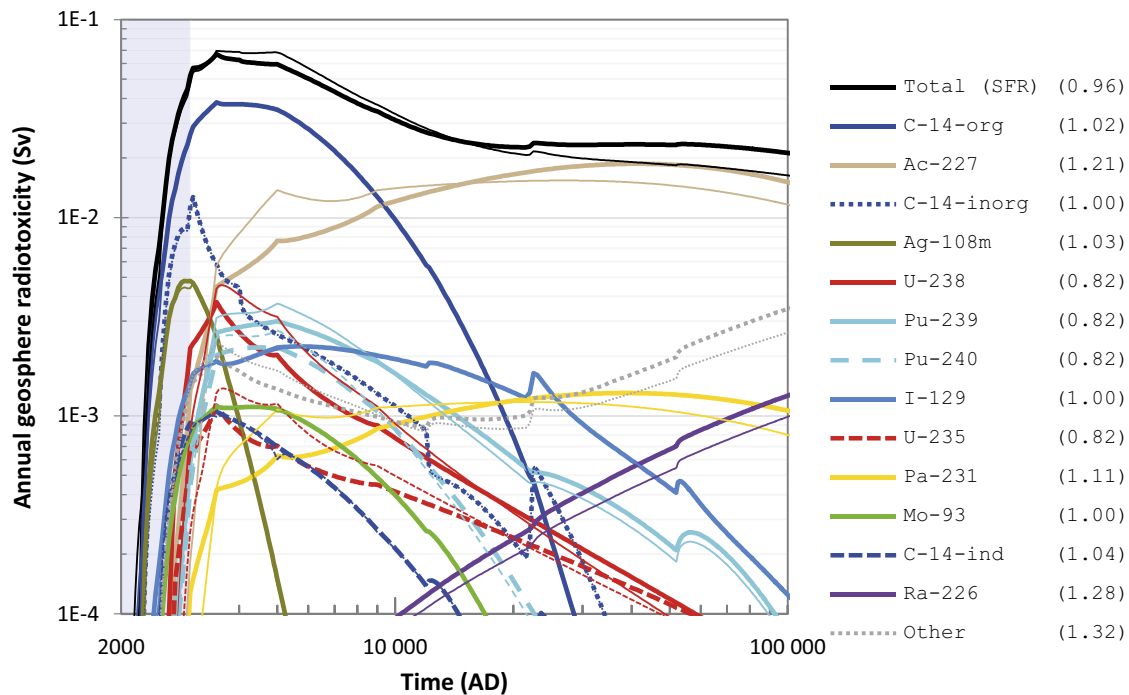


Figure C-4. Annual radiotoxicity (Bq) from the geosphere originating from the entire SFR in the base case in the PSAR (thick lines) and with input data and concepts from the SR-PSU (thin lines). The ratio between the maximum radiotoxicity in the calculations in the PSAR and the SR-PSU are shown in parentheses in the key. The submerged period is illustrated by the blue shading.

As previously noted, the uranium isotopes (U-238 and U-235) that end up as releases to the surface systems are primarily released from 1BLA in SFR1 with some smaller contributions from the other BLA-vaults in SFR3. It is clear that the change in the flow-related parameters explains virtually the entire difference between the SR-PSU and the PSAR (yellow and dotted black lines overlap in Figure C-5), and thus, the effect is mainly due to the bias in flow-related parameters in the fractures from 1BLA.

For the decay products of U-235 (Pa-231 and Ac-227), the breakthrough curves in the PSAR are very different compared to the SR-PSU due to different production rates of these radionuclides during transport through the geosphere. Retention of uranium releases in the geosphere from SFR1 is much lower than for releases from SFR3. Therefore, after the first release peak mainly originating from activity released from SFR1, the releases of decay products thereafter are mainly due to production from slowly moving U-235 released from SFR3. Most of the change, especially during the period for which releases from 1BLA dominate, is caused by updates in the flow-related parameters. However, as production and release of decay products from parents trapped in the rock matrix becomes dominant, the uncorrelated diffusivity applied in the SR-PSU gives an increased release term compared with the fully correlated data-set used in the PSAR, especially for short-lived Ac-227. For Ra-226, which originates from U-238, the change is fully attributed to the update in flow-related parameters.

Releases of Pu-239 and Pu-240 are mainly from 2BTF and the BLA-vaults in SFR3. As indicated in Figure C-5, the updates of the flow-related transport parameters can explain most of the difference between the PSAR and the SR-PSU.

In the SR-PSU, no sorption in the rock matrix was assigned for Se-79, and thus the geosphere release was very similar to the near-field source term. The introduced sorption term in the PSAR explains most of the difference between the calculations.

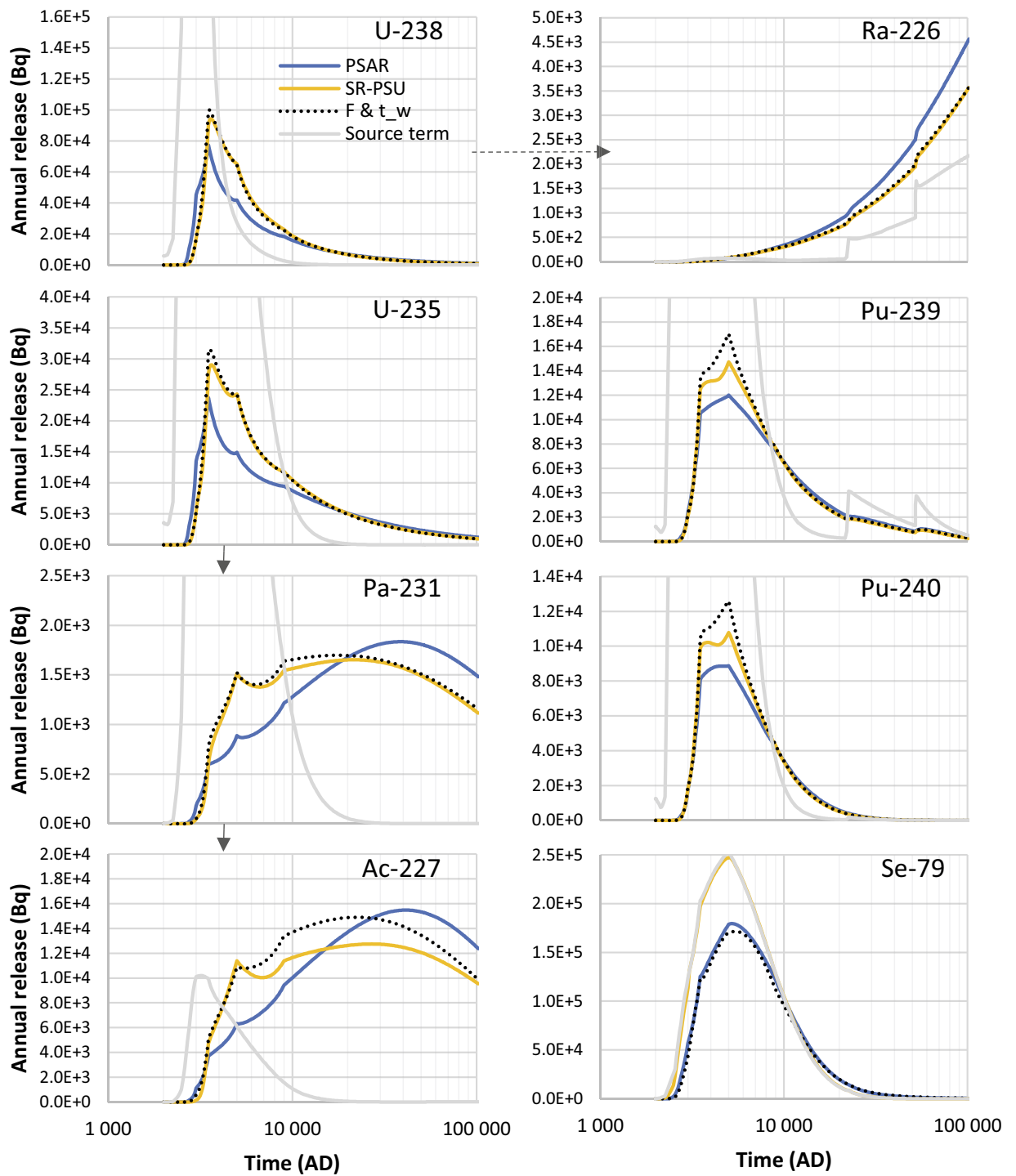


Figure C-5. Geosphere releases from SFR in the base case with input data and concepts from the SR-PSU (yellow lines), in the base case in the PSAR (blue lines) and for the PSAR releases with flow-related parameters (F & t_w) as in the SR-PSU (dotted black lines). Near-field source terms are shown with grey lines. Arrows indicate parent-decay product relationship between radionuclides.

Figure C-6 shows the maximum radiotoxicity flux from the geosphere in the SR-PSU and the PSAR within the assessment period for radionuclides with an annual radiotoxicity exceeding 1 μSv . In general, most of the radionuclides are located close to the 1:1-line, indicating limited changes of the maximum radiotoxicity fluxes in the PSAR compared to the SR-PSU. The difference between the PSAR and the SR-PSU is less than 50 % for all radionuclides.

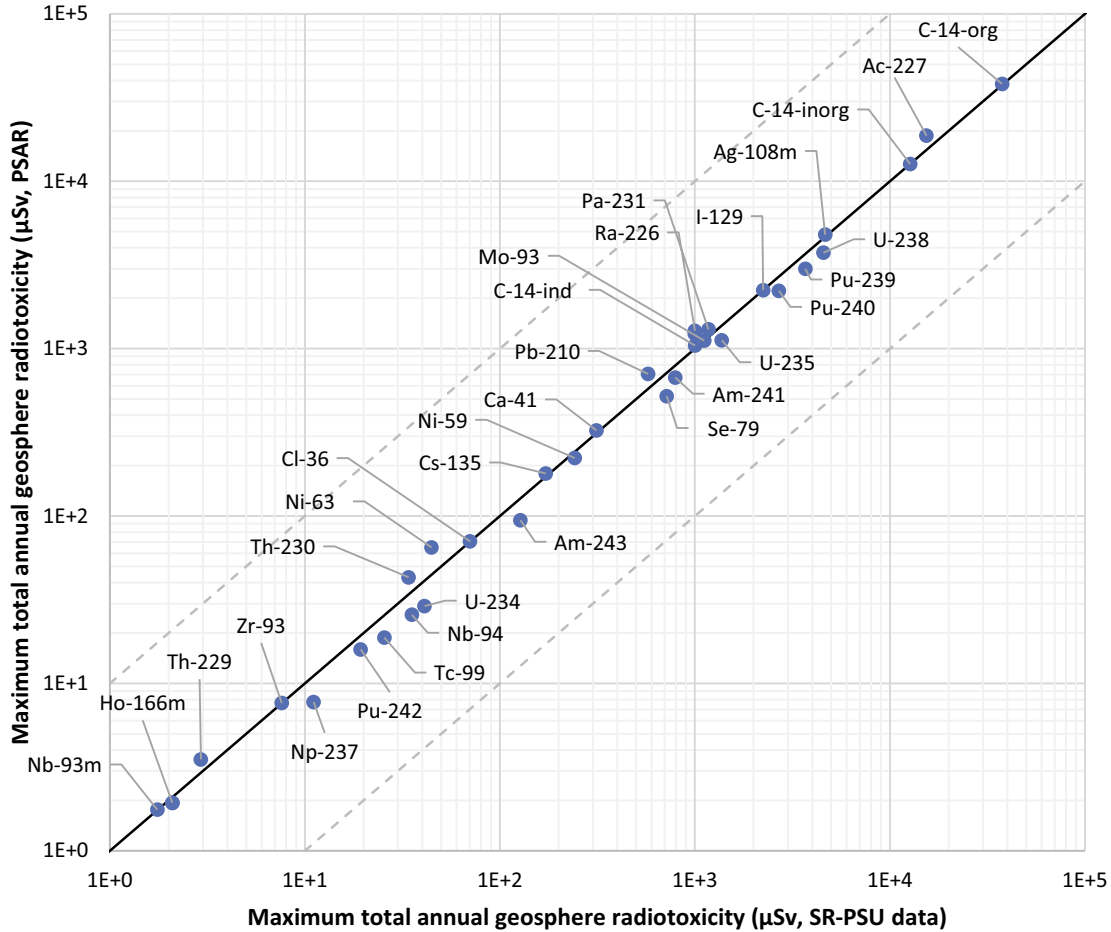


Figure C-6. Maximum geosphere radiotoxicity release from SFR in the base case with input data and concepts from the SR-PSU compared with the maximum geosphere radiotoxicity from SFR in the base case in the PSAR.

The updates introduced in the geosphere transport calculations in the PSAR compared to the SR-PSU do not affect the final total dose in a significant way (see Figure C-7). Using the SR-PSU modelling approach and input data for the geosphere result in a 5 % increase of maximum total dose compared to the *base case*. The increase is attributed to faster geosphere transport and consequently a higher dose from uranium isotopes (mainly U-238) released from IBLA. However, as the dose maximum is dominated by Mo-93, which is only very marginally affected by the geosphere transport in both safety assessments, the increased effect of the total dose from U-238 is small. A 9 % increase of the maximum dose from Ni-59 at the end of the assessment period is also noted for the *base case* in the PSAR compared to the SR-PSU modelling approach.

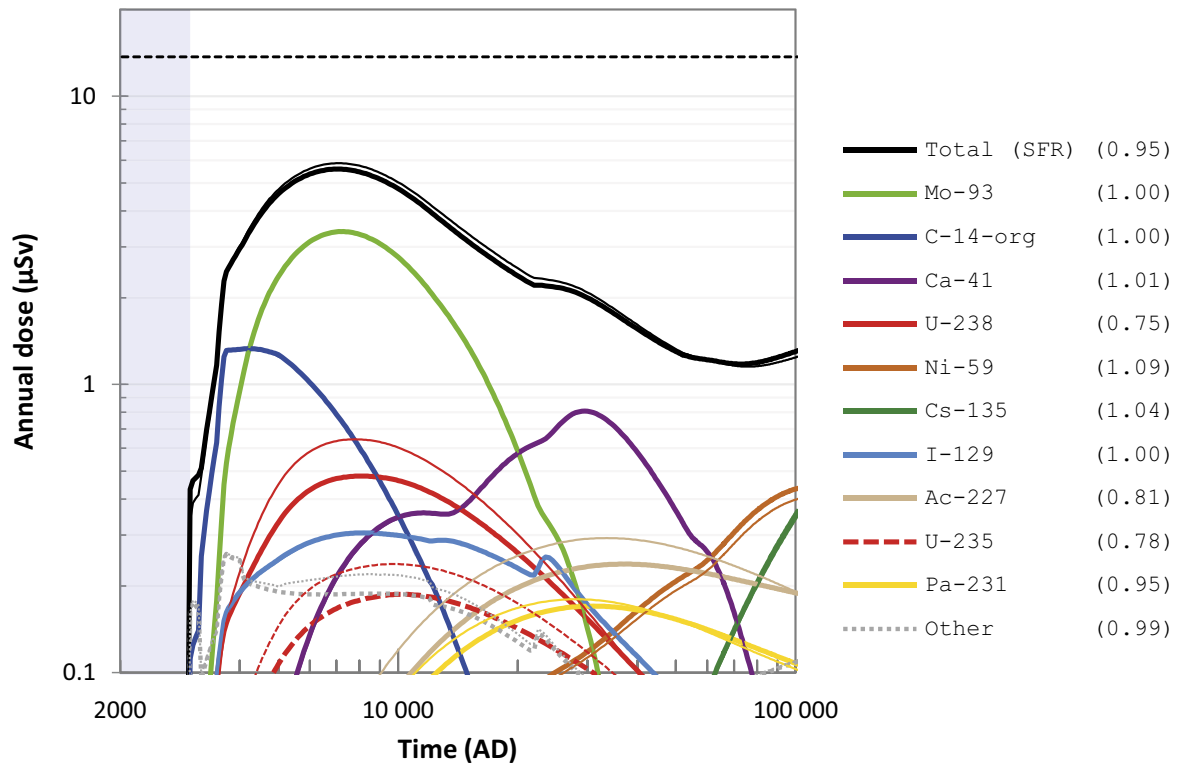


Figure C-7. Annual dose (μSv) to the most exposed group (black line), including radionuclide specific contributions (coloured lines), in the base case (thick lines), and with input data and concepts from the SR-PSU (thin lines). The ratio between the maximum dose in the calculations in the PSAR and the SR-PSU are shown in parentheses in the key. The annual dose corresponding to the regulatory risk criterion ($14 \mu\text{Sv}$) is indicated by the black dashed line and the submerged period is illustrated by the blue shading.

Sensitivity analysis

This appendix presents results for a sensitivity analysis of four selected radionuclides relevant for dose over the 100 000 years long assessment period in the *base case*. The aim of the analysis is to identify parameter uncertainties in the near-field and the geosphere models with a strong influence on the variation in dose from individual radionuclides to potential future human inhabitants. An extensive sensitivity analysis of biosphere parameters, using average geosphere releases of the same four radionuclides originating from all waste vaults, is presented in Section 11.2 in the **Biosphere synthesis report**.

Several hundred parameters are varied according to pre-specified probability density functions (PDFs) in the radionuclide transport and dose calculations (**Data report** and **Biosphere synthesis report**). Due to the numerous parameters, and endpoints that vary dynamically in time, this sensitivity analysis is mainly focused on specific endpoints fixed in time and parameters that have a correlation above a threshold (positive or negative correlation of at least 0.5 %) with those specific endpoints. Thus, for each of the four radionuclides, parameters with a strong influence on the geosphere release and/or the calculated dose to the most exposed group (DM farmers) at a specific point in time are considered. The metric used in the sensitivity analysis is the standardised regression coefficients of first-order effects (SRC; Schroeder et al. 1986). This coefficient indicates both the direction of the effects of a parameter on the endpoint and its importance (if squared, in terms of explained variation). The identified parameters thus tend to have both a clear influence on end results (typically a proportional effect) and a PDF spanning a large variation. For each radionuclide, the most influential parameters (in terms of explained variation) are presented in a tornado diagram (with respect to maximum or cumulative release) and the amount of explained variation is displayed as a function of time (with respect to dose). As most of the underlying relationships are expected to be multiplicative, the sensitivity analysis is carried out on logarithmic scales. The effect of variation in retention parameters, e.g. K_d (sorption) for cement, influences both the timing of peak release and the level of the peak. This means that the results have to be interpreted with care, as the analyses are performed at fixed points in time.

D1 Mo-93

Mo-93 is a radionuclide with a half-life of 4 000 years. The mobility of Mo-93 in both the near-field and geosphere is assumed to be relatively high, hence the significant releases are during the first part of the assessment period (within 10–15 thousand years after closure). The main sources of Mo-93 release are the silo, 1BLA, 1BRT, 2BMA, 2BTF and 1BMA. However, more than 80 % of the initial activity resides in the silo and 2BMA. Almost 60 % of Mo-93 is disposed in the silo and its release from this waste vault contributes to approximately half of the maximum release of and dose from Mo-93.

The maximum releases from the waste vaults occur at the end of the submerged period (1 000 years post-closure for 2BTF, 1BMA and 1–5BLA-vaults), some hundred years later (1BRT and 1BTF) and approximately 2 000 years later (i.e. 3 000 years post-closure; silo and 2BMA; see Section 5.3). The maximum dose from Mo-93 (from all waste vaults) occurs at 7200 AD. The delay of approximately 2 000 years between the maximum releases from the waste vaults and the maximum dose is due to retardation and dispersion in the lowest regolith layer (till) in the surface system.

As the sorption coefficient in the bedrock matrix for molybdenum is very small, no parameters in the geosphere model show a significant effect on the maximum release to the surface systems. Thus, the main parameter uncertainties driving the variation in the maximum release resides in the near-field models. The identified parameter uncertainties in the near-field affecting the maximum release of Mo-93 are the initial activity, the vault flow and mainly the sorption coefficient in the first degradation state for cement (DS1). Thus, for the two most important waste vaults for Mo-93 (silo and 2BMA), the uncertainty in the magnitude of sorption onto cement ($K_{dDS1.Cement}$) explains most (~90 %) of the variation in the maximum release (the parameter value is negatively correlated with the release rate). The uncertainty of the vault flow (U-factor) explains a small part of additional variation (correlating positively with the release rate, see Figure D-1).

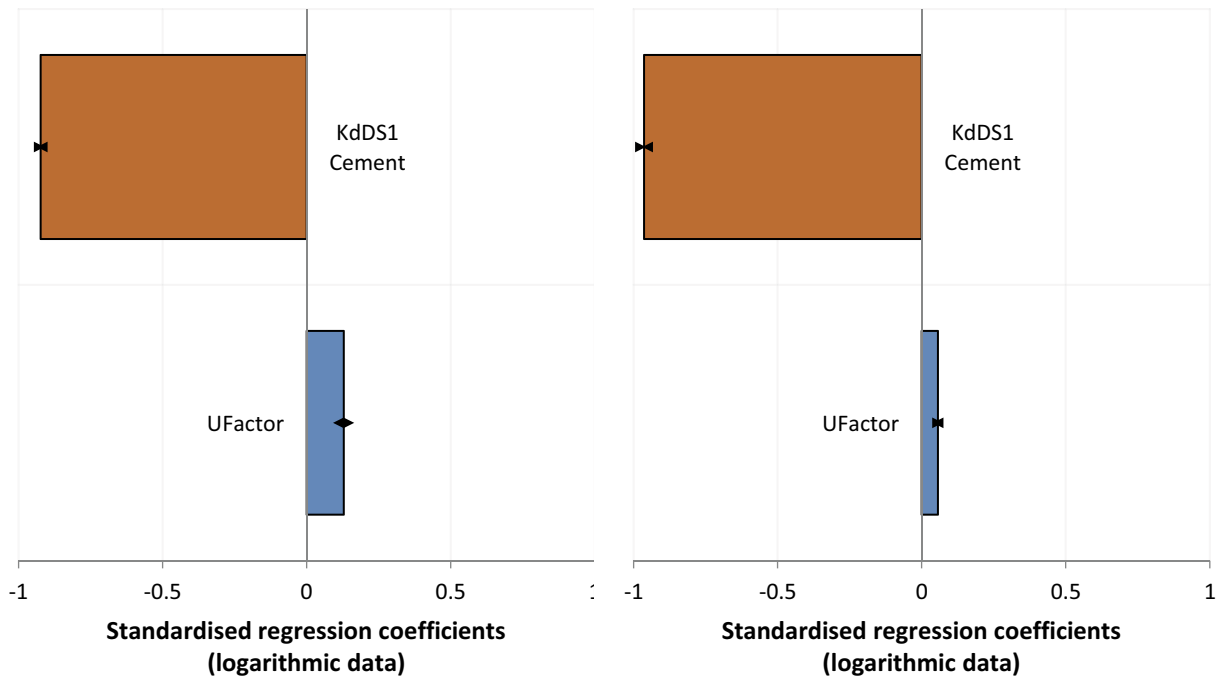


Figure D-1. Parameter sensitivity to the maximum annual release of Mo-93 from the silo (left) and 2BMA (right). Negative and positive correlation with the maximum annual release is highlighted with red and blue colour respectively. Arrows indicate a measure of accuracy (90 % confidence interval). The regression model explains approximately 90 % of the geosphere release variation. $K_{dDS1.Cement}$ – sorption onto cement, UFactor – uncertainty in vault flow.

A sensitivity analysis of the Mo-93 doses due to releases from the silo, over all parts of the transport and dose models (near-field, geosphere and biosphere) shows that sorption in the near-field is the most important factor in the uncertainty in the maximum dose (it accounts for 50 % of the explained dose variation at 8000 AD; Figure D-2). This is also true for the release from 2BMA (data not shown in figure). The biosphere parameters together explain an additional 30 % of variation of the maximum dose. The two main drivers of uncertainty in the biosphere are plant uptake ($cR_{agri,cereal}$) and sorption in clay-gyttja (kD_{regoPG}) and both parameters are positively correlated with the dose. At the beginning of the assessment period, the dose is negatively correlated to the sorption in till ($kD_{regoLow}$), but this effect decreases with time. A detailed discussion of the sensitivity to biosphere parameters is presented in the **Biosphere synthesis report**, Section 11.2.

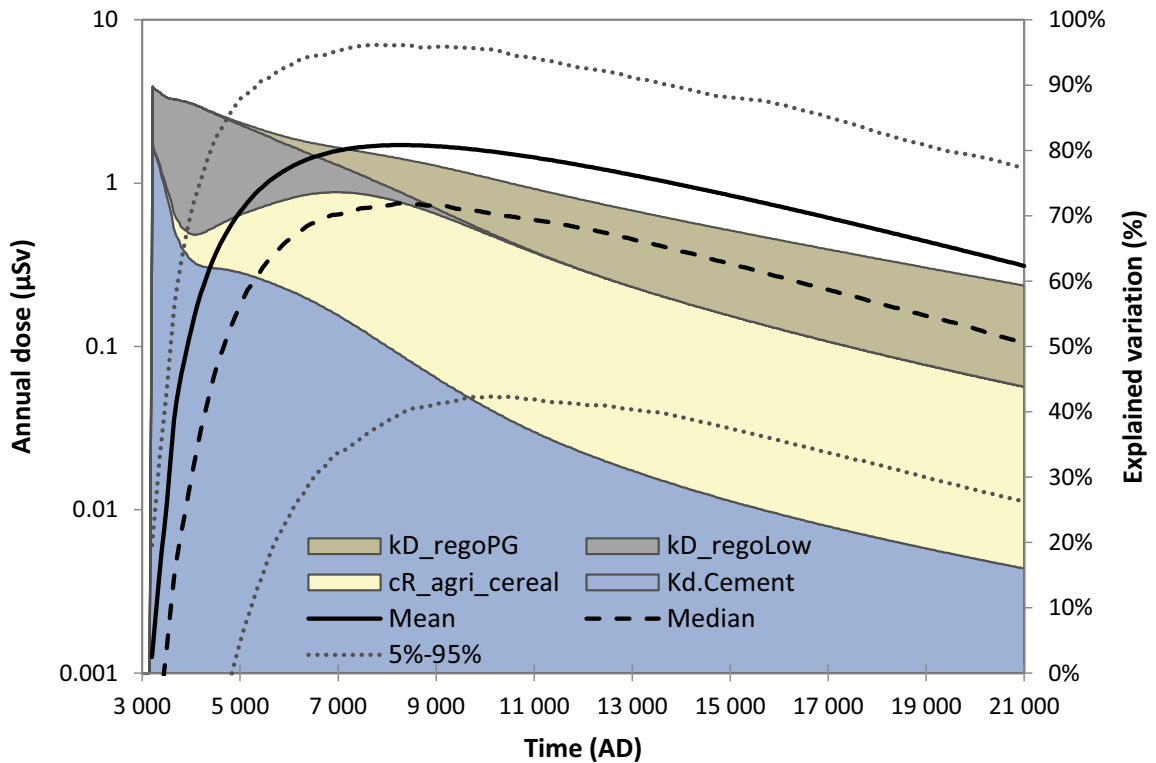


Figure D-2. Uncertainty statistics (black lines, left y-axis) and parameter sensitivity (coloured fields, right y-axis) for annual dose to DM farmers (μSv) due to releases of Mo-93 from the silo. Only parameters contributing more than 5 % at any point in time are shown. At the time of the maximum annual dose (8000 AD), the four displayed parameters explain almost 80 % of the dose variation. kD_{regoPG} – sorption in clay-gyttja, $cR_{agri,cereal}$ – plant uptake, $kD_{regoLow}$ – sorption in till, $Kd.Cement$ – sorption onto cement.

D2 Organic C-14

The half-life of C-14 is 5700 years. In organic form, carbon is considered mobile in the near-field and very mobile in the geosphere (and in the surface systems), hence the significant releases in the first part of the assessment period. C-14-org is assumed to be in the form of low molecular weight compounds and thus is expected to be transformed to CO₂ in the biosphere. The sources of the release of C-14-org are mainly the silo (70 %) and 1BMA (25 %). The maximum of the average dose from exposure of C-14-org occurs at the time when the terrestrial discharge area becomes large enough to fully support a community of DM farmers (at approximately 3700 AD). The dose is then reasonably stable for approximately 2000 years.

As C-14-org is considered very mobile in the geosphere and the surface systems, no parameter uncertainty involved in the transport of carbon in these systems explains any variation. The only parameter uncertainties driving the variation in the release reside (as for Mo-93) in the near-field models. Identified parameters in the near-field affecting the maximum release of C-14-org from the two main waste vaults (silo and 1BMA) are the same as for Mo-93; the initial activity, the uncertainty in the water flow in the vault and the sorption coefficient for the first degradation state for cement. Compared to Mo-93, the uncertainty in the initial activity of C-14-org is relatively large and explains much of the uncertainty in the total release from SFR (data not shown). The maximum release from the silo occurs 2000 years later than the maximum release from 1BMA illustrating the retention capacity of the barriers in the silo. For both waste vaults, the uncertainty in the initial activity explains most of the maximum release variation (55 % and 40 % for the silo and 1BMA respectively). The delay in transport due to sorption in the concrete barriers explains 20 % of the release variation in the silo and 9 % in 1BMA. The variation of water flow in the vault (UFactor) is (as is the initial activity) positively correlated with the maximum release and explains 7 % and 13 % of the variation for the silo and 1BMA respectively. However, the uncertainty in the effect of the vault flow for 1BMA is relatively large (see confidence interval in Figure D-3). It can also be noted that 500 years prior to the release maximum for 1BMA (at the end of the submerged period, 3000 AD), the U-factor explains almost 40 % of the release variation (data not shown in figure).

An analysis of the sensitivity of the dose from C-14-org over all parts of the model chain (near-field, geosphere and biosphere) shows that near-field parameters account for up to 50 % of the variation in maximum dose. This pattern holds for releases from both the silo (Figure D-4) and 1BMA (data not shown). Variation in biosphere parameters explains an additional 30 % of the dose variation. The three main drivers of uncertainty in the biosphere are: groundwater uptake ($q_{\text{sat,unsat,agri}}$), soil respiration ($\text{SoilResp}_{\text{gytja}}$) and the uptake of carbon by roots ($f_{\text{rootUptake}}$), and the effects of biosphere parameters are almost fully multiplicative. A detailed discussion of the sensitivity to biosphere parameters is presented in the **Biosphere synthesis report**, Section 11.2.

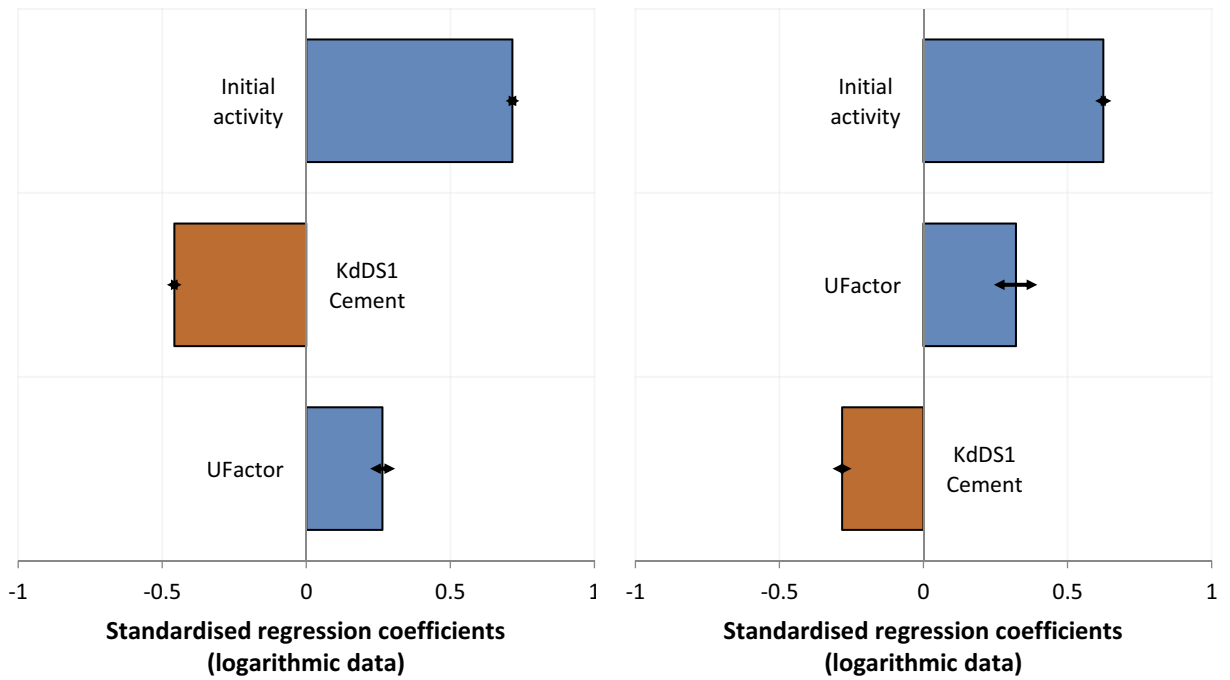


Figure D-3. Parameter sensitivity to the maximum annual release of C-14-org from the silo (left) and 1BMA (right). Negative and positive correlation with the maximum annual release is highlighted with red and blue colour respectively. Arrows indicate a measure of accuracy (90 % confidence interval). The regression model explains approximately 90 % of the geosphere release variation. *KdDS1.Cement* – sorption onto cement, *UFactor* – uncertainty in vault flow.

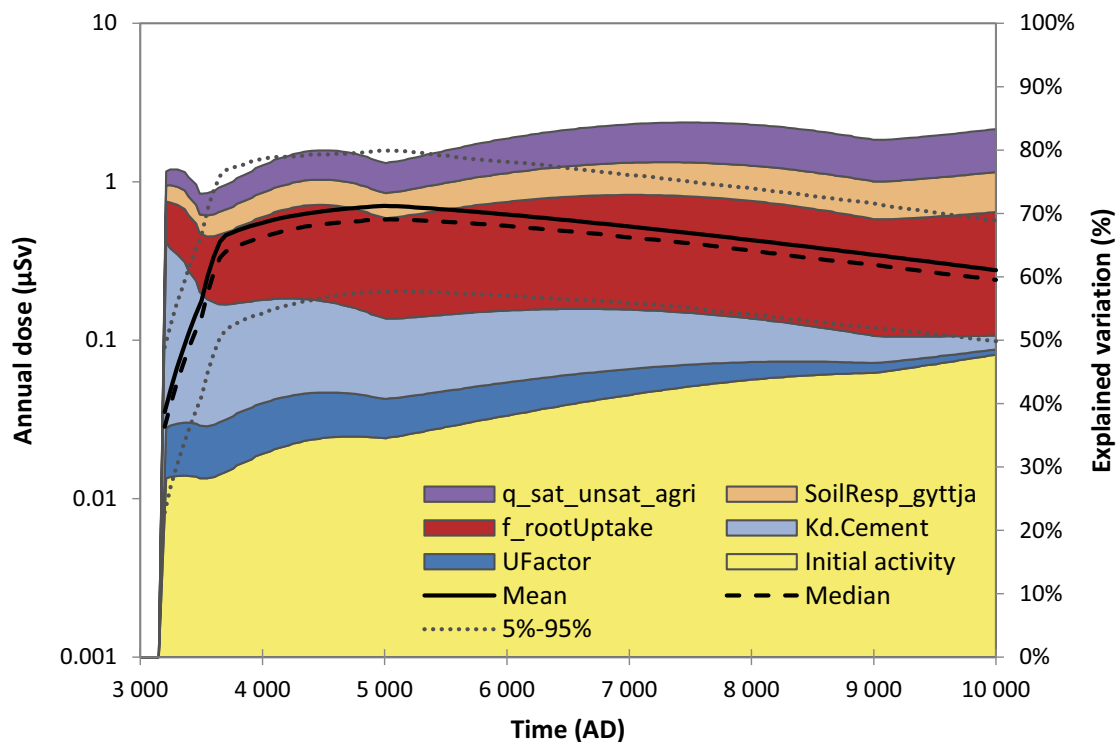


Figure D-4. Uncertainty statistics (black lines, left y-axis) and parameter sensitivity (coloured fields, right y-axis) for annual dose to DM farmers (μSv) due to releases of C-14-org from the silo. Only parameters contributing more than 5 % at any point in time are shown. The six displayed parameters explain almost 80 % of the dose variation at the time for the maximum annual dose. $q_{\text{sat,unsat,agri}}$ – groundwater uptake, $\text{SoilResp}_{\text{gyttja}}$ – soil respiration, $f_{\text{rootUptake}}$ – uptake of carbon by roots, *Kd.Cement* – sorption onto cement, *UFactor* – uncertainty in vault flow.

D3 Ca-41

Ca-41 is a radionuclide with a half-life of 102 000 years. Ca-41 is present in waste planned to be disposed in SFR3, mainly in 2BMA (more than 80 % of the activity) but also in the four BLA-vaults (~5 % each). Calcium is a relatively immobile element as long as concrete barriers are intact and the first chemical degradation state prevails. However, as no sorption is pessimistically considered in the 1–5BLA-vaults and the second chemical degradation state is considered already after 10 000 years post-closure in the 2BMA-vault (Section 5.3.4), much of Ca-41 will be released from SFR3 within the assessment period. In the geosphere, Ca-41 is assumed to be highly mobile, and consequently retention is marginal. However, in the lower regolith layers of the surface systems (till and glacial clay) Ca-41 is highly immobile and a substantial fraction of the cumulative release of Ca-41 is retained in the biosphere, irrespective of the timing of the release. At the time for the maximum dose from Ca-41, just over 20 % and 40 % of the remaining activity is retained in near-field or the geosphere and the regolith layers respectively (which, accounting for radioactive decay, corresponds to approximately 30 % of the initially disposed Ca-41 activity retained in the regolith, Figure 5-64). Thus, the cumulative release of Ca-41 from the geosphere is of more relevance for the maximum dose than the annual geosphere release maximum.

As no sorption is considered in the BLA-vaults, the activity from these vaults is released within some thousand years post-closure. However, the bulk of the activity of Ca-41 (initially stored in 2BMA) starts to be released 10 000 years post-closure when the sorption coefficient in cement decreases by more than an order of magnitude. The timing of the release from 2BMA varies considerably between simulations and the time when half of the Ca-41 has been released ranges between 15 and 30 thousand years AD (Figure D-5, left panel). The most frequent time for a cumulative geosphere release of 50 % occurs approximately at 22 000 AD, which coincides with the time of concrete structure degradation (resulting in an increase of two orders of magnitude in hydraulic conductivity). This results in a maximum release averaged over all simulations. At this time, sorption to cement is the main driver of uncertainty in the cumulative geosphere release. Sorption affects the dynamics of the release directly and high sorption results in less release. As most of the Ca-41 from the 2BMA-vault is released during the second chemical degradation state, it is the corresponding K_{d2} -value that is most important for the cumulative near-field release ($K_{dDS2.Cement}$ in Figure D-5, right panel).

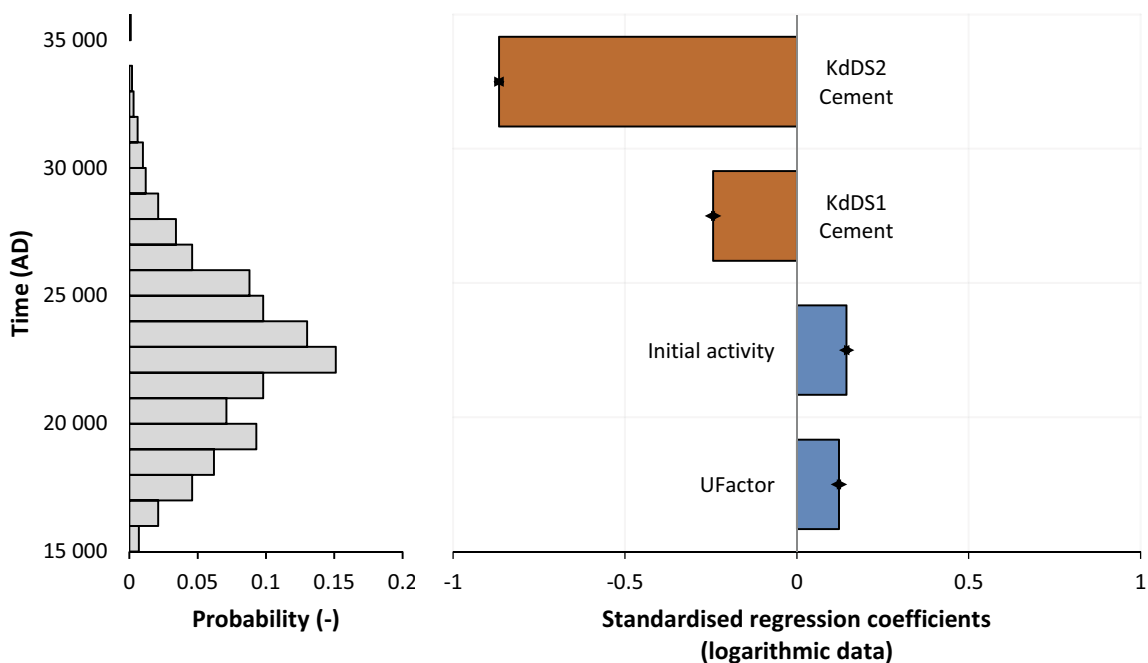


Figure D-5. Histogram of the time when 50 % of the geosphere release of Ca-41 from 2BMA has been reached (left panel). Parameter sensitivity of the cumulative geosphere release of Ca-41 from 2BMA at its annual release maximum (approximately at 22 000 AD) (right panel). Negative and positive correlation with the maximum annual release is highlighted with red and blue colour respectively. Arrows indicate a measure of accuracy (90 % confidence interval). The regression model explains approximately 80 % of the cumulative geosphere release variation. $K_{dDS1.Cement}$ and $K_{dDS2.Cement}$ – sorption onto cement (first and second degradation state respectively), UFactor – uncertainty in vault flow.

The time of the dose maximum from Ca-41 is delayed by the transport through the lower regolith of the surface system. Thus, the time for the maximum dose from Ca-41 occurs around 30 000 AD. At this time, much of the Ca-41 activity has been released from the waste vaults in most of the simulations, and consequently the uncertainty in the cumulative geosphere release has decreased, as compared to the time of the maximum cumulative geosphere release. This is indicated by the span of the 90 % confidence interval (CI90) which decreases with time (Figure D-6). However, the uncertainty of the annual dose is two orders of magnitude larger than that of the cumulative geosphere release at the time for the dose maximum; the CI90 spans a factor of 250 and 2, respectively. Thus, the uncertainty in the cumulative geosphere release has a very limited effect on the uncertainty in the maximum annual dose. Additionally, as Ca-41 is highly mobile in the geosphere, the effect of uncertainties in the geosphere on the annual dose is negligible compared to parameter uncertainties in the near-field (data not shown). Thus, it is primarily parameter uncertainties in the biosphere that drive the maximum dose variation.

If the cumulative geosphere release of Ca-41 and surface parameters are analysed together, biosphere parameters account for more than 60 % of the variation in maximum dose (Figure D-6). The effect from variation in the cumulative geosphere release (from all SFR waste vaults) is notable before and at the release maximum, but accounts for only 1 % of the dose variation at the time of maximum dose. Multiple biosphere parameters affect the dose variation. These parameters reflect sorption (K_d) in regolith layers, plant uptake (CR), and the transfer of Ca-41 from fodder to meat and milk (TC). The effects of biosphere parameters on the uncertainty in the dose from Ca-41 is discussed in the **Biosphere synthesis report**, Section 9.4, including a detailed discussion of the parameter sensitivity (**Biosphere synthesis report**, Section 11.2).

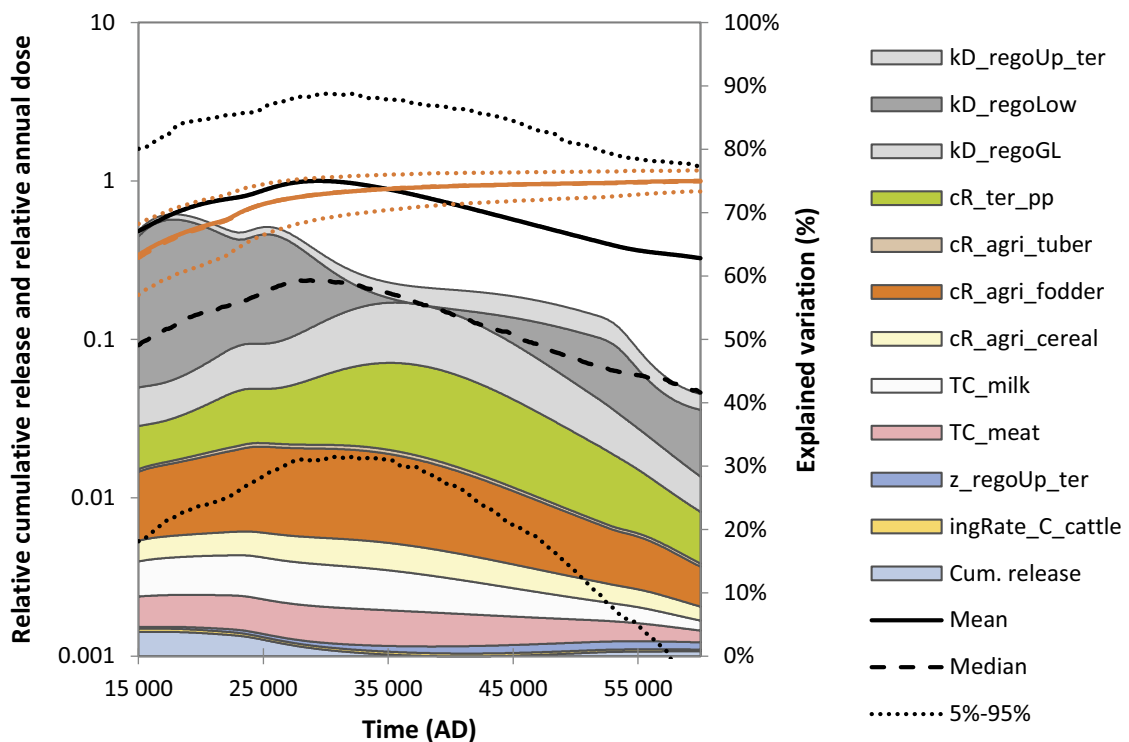


Figure D-6. Uncertainty statistics for cumulative geosphere release of Ca-41 from the entire SFR (orange lines) and for the resulting dose to the DM group (black lines) (left axis). Note that the cumulative geosphere release and the dose have been normalised by the mean so that the highest values correspond to 1. The sensitivity (percent explained variation) of the annual dose to biosphere parameters and the cumulative geosphere release is indicated by coloured fields (right axis). Only parameters contributing with more than 0.5 % at any point in time are shown. $kD_{regUp,ter}$ – sorption in upper peat, kD_{regLow} – sorption in till, kD_{regGL} – sorption in glacial-clay, $cR_{ter,pp}$ – plant uptake (mire primary producers), $cR_{agri,tuber/fodder/cereal}$ – plant uptake (crops), $TC_{milk/eat}$ – transfer from fodder to meat and milk, $z_{regUp,ter}$ – thickness of upper peat, $ingRate_{C,cattle}$ – cattle carbon ingestion rate, Cum. release – cumulative geosphere release.

D4 Ni-59

Ni-59 is a radionuclide with a half-life of 101 000 years. It is mainly present in waste stored in the silo (74 %) and the 1–2BMA vaults (10 and 14 %, respectively). Nickel is highly immobile for all concrete conditions that prevail in the silo during the whole assessment period. The conditions in the 2BMA vault are favourable during the first 20 thousand years but, as the concrete structure physically starts to degrade, releases increase due to increased water flow and increased diffusivity (Section 5.3). The maximum annual dose occurs at the end of the assessment period (Figure D-8). At that time, releases from the two BMA vaults contribute almost 80 % of the dose, whilst the silo only contribute with around 5 %. The remaining dose (15 %) is due to releases from the other vaults. Nickel is highly immobile in the lower regolith layers of the surface systems (till and glacial clay). Less than 30 % of all Ni-59 that is released to the biosphere reaches the stream at the surface and is exported from the system within the assessment period. Thus, the cumulative release of Ni-59 is much more relevant for the maximum dose than the annual release maximum, which occurs during the first thousand years of the assessment (due to fast releases in low quantities from the 1–5BLA-vaults).

The degradation of engineered barriers occurs later in 2BMA than in 1BMA. Still both waste vaults release similar fractions of their initial activity over the full assessment period, corresponding to ~5 % of the disposed activity (see Figure 5-35). The properties of the bedrock differ between the two vaults and this clearly affects the influence of parameter uncertainties. For 1BMA the uncertainty in vault flow (UFactor, 20 %) and the sorption onto cement in the second degradation state (KdDS2.Cement, 40 %) together explain 60 % of the variation of the cumulative geosphere release (Figure D-7, left panel). However, geosphere parameters have negligible influence on the variation for 1BMA. For 2BMA, sorption and diffusivity in the bedrock matrix (KdMatrix and DeMatrix) are as important as the near-field parameters (both sets explaining ~30 %; Figure D-7, right panel). The difference in response to parameter uncertainty is the combined effect of lower water flow, longer travel times and fractures of smaller average aperture for the 2BMA vault (see Table 5-14 and 5-15 in Section 5.5). That is, the travel time from the vault is roughly 6 times longer and the average fracture is roughly half as wide, for 2BMA pathways as compared to pathways from 1BMA. These differences lead to increased retention due to sorption in the bedrock matrix which in turn increases the importance of radioactive decay for modulating activity released to the surface.

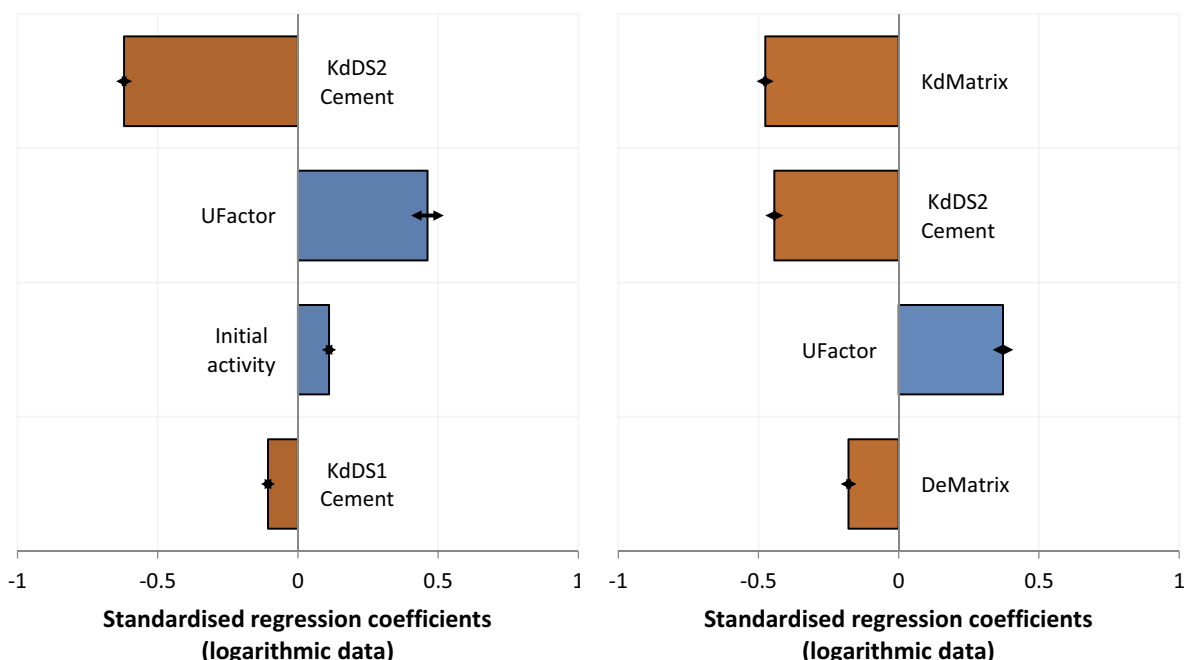


Figure D-7. Parameter sensitivity to the cumulative geosphere release of Ni-59 from 1BMA (left) and 2BMA (right) at the end of the assessment period (100 000 years post-closure). Negative and positive correlation with the maximum annual release is highlighted with red and blue colour respectively. Arrows indicate a measure of accuracy (90 % confidence interval). The regression models explain approximately 60 % of the variation in cumulative geosphere release for both 1 and 2BMA vaults. KdDS1.Cement and KdDS2.Cement – sorption onto cement (first and second degradation state respectively), UFactor – uncertainty in vault flow, KdMatrix – sorption in the bedrock matrix, DeMatrix – diffusivity in the bedrock matrix.

It can be noted that the uncertainty in the annual dose is more than an order of magnitude larger than that of the cumulative geosphere release at the end of the assessment; the CI90 spans a factor of 70 and 5, respectively. Thus, the uncertainty in the cumulative geosphere release has a limited effect on the uncertainty in the maximum annual dose. This indicates that uncertainties in biosphere parameters are the main source for variation in the maximum dose. If the cumulative geosphere release of Ni-59 and biosphere parameters are combined in a sensitivity analysis, biosphere parameters account for almost 70 % of the variation in maximum dose (Figure D-8). The corresponding number is 15 % for the cumulative geosphere release (Figure D-8). Multiple biosphere parameters affect the dose variation. These parameters reflect sorption (K_d) in the two lowermost regolith layers, crop uptake (CR) and the transfer of Ni-59 from fodder to meat (TC). A detailed discussion of the sensitivity to biosphere parameters is presented in the **Biosphere synthesis report**, Section 11.2.

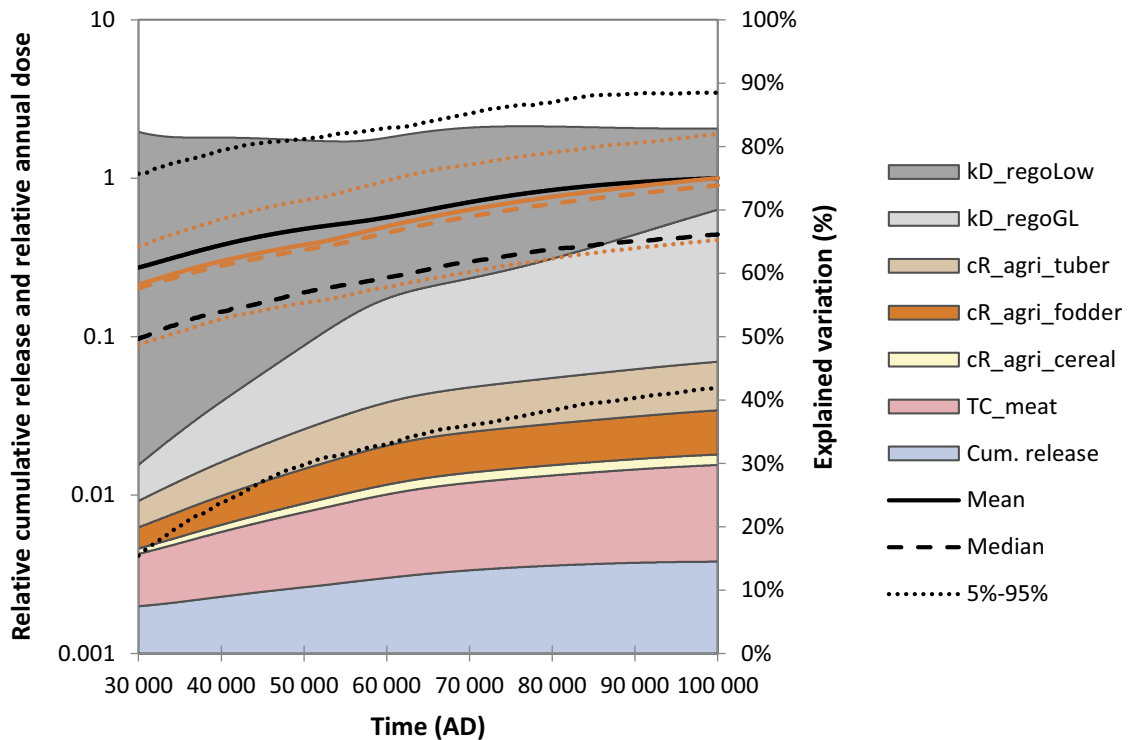


Figure D-8. Uncertainty statistics for cumulative geosphere release of Ni-59 from SFR (orange lines, left axis) and for the resulting dose to DM group (black lines, left axis). Note that the cumulative geosphere release and the dose have been normalised by the mean so that the highest values correspond to 1. The sensitivity (percent explained variation) of the annual dose to biosphere parameters and the cumulative geosphere release is indicated by coloured fields (right axis). Only parameters contributing more than 0.5 % at any point in time are shown. $kD_{regolow}$ – sorption in till, kD_{regogL} – sorption in glacial-clay, $cR_{agri,tuber/fodder/cereal}$ – plant uptake, TC_{meat} – transfer from fodder to meat, Cum. release – cumulative geosphere release.

Analytical expressions for the near-field

This appendix contains a description of simplified analytical estimates of the residence time based on diffusion, flow and vault capacity. The aim of the analytical description is to give a pre-modelling scoping calculation and to illustrate how time-dependent barrier properties, such as effective diffusivity, impact the transport and performance of the different vaults.

The appendix consists of

- Description of analytical expressions for estimating the residence time and release rate based on capacity and flow.
- Vault specific expressions of flow, capacity and residence time.
- Vault specific illustrations of release rate versus half-life of radionuclides.

E1 Analytical expressions

Residence time

The residence time, T_{res} (a), of a radionuclide in a vault is a quantity that gives an estimate of the time until most of its activity has been released from the vault. A long residence time ensures that the annual release is only a small fraction of the initial inventory, such that the release is diluted over time. It is commonly defined as the total inventory A_{vault} (Bq) in the vault divided by the annual release N_{vault} ($Bq\ a^{-1}$) obtained from transport modelling, assuming no decay, using a steady-state solution of the radionuclide transport model for the vault:

$$T_{res}^{transp} = \frac{A_{vault}}{N_{vault}} \quad \text{Equation E-1}$$

An alternative estimate of the residence time, which is not based on explicit transport modelling (but still on hydrogeological modelling), based on vault capacity, Cap_{vault} (m^3) and total effective volume flow rate, Q_{tot} ($m^3\ a^{-1}$), is given by:

$$T_{res}^{cap} = \frac{Cap_{vault}}{Q_{tot}} \quad \text{Equation E-2}$$

Vault capacity

The total capacity of a vault, Cap_{vault} , is given by the summed capacities of the different parts of the vault which can be determined using Equation 4-2. However, since only a fraction of the water flowing through the macadam/crushed rock backfill also flows through the waste, the capacity of the backfill is omitted when summing capacities.

Total effective volume flow

The total effective volume flow rate is the sum of the diffusive and advective volumetric flow rate through the barriers. The diffusive flow rate is calculated from the diffusive transport resistance of the barrier ($1/R_{barrier}$), resulting in an expression for Q_{tot} :

$$Q_{tot} = Q_{diffusive} + Q_{advective} = \frac{1}{R_{barrier}} + Q_{waste} \quad \text{Equation E-3}$$

The advective water flow rate through the barriers $Q_{advective}$ ($m^3\ a^{-1}$) is approximated by the flow through the waste, Q_{waste} , based on hydrogeological simulations.

The diffusive flow rate, $Q_{diffusive}$, is calculated from the transport resistance of a vault by considering the vault subdivided into different paths through different parts. The division is made so that the geometry of each part is simple enough to enable its diffusive resistance to be calculated. The total resistance is calculated by summing the resistances of the respective paths. This procedure can often be simplified by identifying the parts which constitute the most important routes for the radionuclides.

In order to calculate the diffusive resistance of the whole barrier system, the barrier system is subdivided into different paths, e.g. through the slab, lid and walls, through which the diffusion progresses in parallel.

$$\frac{1}{R_{\text{barrier}}} = \sum_j \frac{1}{R_j} \quad \text{Equation E-4}$$

where:

R_{barrier} = Total diffusive resistance of the vault (a m^{-3}),

R_j = Diffusive resistance of path j of the vault (a m^{-3}),

The transport of radionuclides for a specific path is handled as a multi-step process where the radionuclides diffuse sequentially through different parts, e.g. the waste package, inner barrier and outer barrier, through which the diffusion progresses in series.

$$R_j = \sum_i R_i \quad \text{Equation E-5}$$

Where the diffusive transport resistance of each part, R_i , is dependent on its geometry and diffusivity properties, see Equation 4-5.

Flow to the host rock

Vaults with backfill normally have a waterflow of such a magnitude that the advective transport dominates and radionuclides that reach the backfill are transported by the groundwater flowing through the backfill into the host rock. For vaults with an outer barrier in direct contact with the surrounding rock, e.g. the bentonite in the silo, the water flow rate through the rock affects the diffusive transport resistance at the rock–bentonite interface. This is handled by including the diffusive transport resistance given by $1/Q_{\text{eq}}$ in the calculation of the barrier resistance. The equivalent flow, Q_{eq} , depends on the water flow through the rock adjacent to the barrier, see Section 4.2.4.

For example, for the silo the diffusive transport resistance of the concrete side walls, the bentonite outside the side walls and at the rock–bentonite interface is given by:

$$R_{\text{silo side}} = R_{\text{concrete side}} + R_{\text{bentonite side}} + 1/Q_{\text{eq}} \quad \text{Equation E-6}$$

where:

$R_{\text{silo side}}$ = Diffusive resistance of the silo side walls in the radial direction of (a m^{-3}),

$R_{\text{concrete side}}$ = Diffusive resistance of the concrete silo side walls (a m^{-3}),

$R_{\text{bentonite side}}$ = Diffusive resistance of the bentonite outside the concrete silo side walls (a m^{-3})

This equation shows that if the water flow through the rock adjacent to the barrier is sufficiently small, the Q_{eq} will limit the diffusive transport.

Release rate

The release rate of a radionuclide from a vault can be estimated by dividing the radionuclide's inventory, A^i , by its residence time (analogous to Equation 4-12):

$$N_{\text{vault}}^i \approx \frac{A^i}{T_{\text{res}}^i} \quad \text{Equation E-7}$$

An additional simplification is made here by setting the radionuclide inventory on the right side of Equation E-7 to be equal to the initial inventory. This estimate of release does not take decay into account. Moreover, the residence time varies over the assessment period. However, by choosing a residence time representative of the time period where most of the radionuclide is expected to be released, Equation E-7 gives a rough estimate of the maximum release rate. In section E.3 the resulting values of release rate versus half-life are plotted.

In the section below, simplified analytical expressions are given for each vault. The expressions are used in Section 5.3 to illustrate how time-dependent barrier properties, such as effective diffusivity, impact the performance of the different vaults. The results are presented in Section 5.3.

E2 Vault specific expressions for residence time and release rate

Below are the vault specific expressions for the capacity, transport resistance and the resulting residence time provided for each vault. The advective flow rate for each of the vaults is approximated by the flow rate through the waste given in Abarca et al. (2020) unless otherwise specified. The total effective flow can subsequently be calculated from Equation E-3, the residence time from Equation E-2 and the release rate from Equation E-7.

For each vault a brief description is provided below. More details on the layout and functioning of each vault can be found in Section 3.1 which contains a summary of the information provided in the **Initial state report**.

The silo

The silo contains most of the activity in SFR and therefore has engineered barriers with the highest retention capabilities. The transport of radionuclides from the waste packages to the host rock around the silo is a multi-step process. The first step is the migration from the interior of the packages through the package walls to the surrounding grout in the shafts. The second step is the migration from the grout pore water through the concrete structure to the bentonite on the side or the sand-bentonite on top or at the bottom.

Flow and transport resistance

The diffusive resistance of the silo is given by the sum of the resistances of the waste packages R_{waste} and the silo structure R_{silo} . The resistance of the waste packages is small in general compared with the resistance of the surrounding barriers and is neglected.

$$R_{barrier} = R_{waste} + R_{silo} \approx R_{silo} \quad \text{Equation E-8}$$

An additional simplification made is neglecting the diffusive transport through the silo top and bottom and only considering the diffusive transport through the silo side walls, $R_{silo\ side}$. Advective transport, however, is not neglected through the top and bottom.

$$\frac{1}{R_{silo}} = \frac{1}{R_{silo\ top}} + \frac{1}{R_{silo\ bottom}} + \frac{1}{R_{silo\ side}} \approx \frac{1}{R_{silo\ side}} \quad \text{Equation E-9}$$

The radionuclides will travel sequentially through the concrete cylinder to the bentonite, and thereafter leave the vault by migrating into rock fractures either by advection or diffusion. The combined diffusive resistance in the silo side walls is given by:

$$R_{barrier} \approx R_{silo} \approx R_{silo\ side} = R_{concrete\ side} + R_{bentonite\ side} + \frac{1}{Q_{eq}} \quad \text{Equation E-10}$$

Vault Capacity

All sorption sites in the waste, the concrete structure and the bentonite are considered to be available. The vault capacity (Cap) of the silo is calculated by:

$$Cap_{vault} = Cap_{waste} + Cap_{concrete\ structures} + Cap_{bentonite} \quad \text{Equation E-11}$$

Residence time

With the assumptions made above, the residence time for the silo can be calculated from:

$$T_{\text{res}}^{\text{Cap}} = \frac{\text{Cap}_{\text{waste}} + \text{Cap}_{\text{concrete structure}} + \text{Cap}_{\text{bentonite}}}{1} \frac{1}{R_{\text{concrete side}} + R_{\text{bentonite side}} + \frac{1}{Q_{\text{eq}}}} + Q_{\text{waste}} \quad \text{Equation E-12}$$

1BMA

The existing 1BMA waste vault for intermediate-level waste consists of a concrete structure with 15 waste compartments (13 large and 2 small) separated by concrete walls. The transport of radionuclides from the waste packages to the backfill surrounding the concrete structure is modelled as a two-step process. The first step is the migration from the interior of the packages to the surrounding water inside the waste compartments. The second step is the migration through the concrete structure, either to the surrounding backfill or to a neighbouring waste compartment. Radionuclides that reach the backfill are transported by the water flowing through the backfill into the host rock.

Flow and transport resistance

The *base case* assumes that the 1BMA structural concrete barriers have been repaired after their original construction, corresponding to the “partial reinforcement case” in Elfving et al. (2018). As such, the structure is assumed to consist of two parts, the inner part with the original concrete and the outer part with the new concrete from the repairs.

In 1BMA, as in the silo, the diffusive resistance of the waste packages is assumed to be small compared with the resistance of the surrounding concrete structure and the total resistance is estimated from the resistance of the slab, lid and walls of the concrete structure.

$$\frac{1}{R_{\text{barrier}}} \approx \frac{1}{R_{\text{slab}}} + \frac{1}{R_{\text{inner lid}} + R_{\text{outer lid}}} + \frac{1}{R_{\text{inner walls}} + R_{\text{outer walls}}} \quad \text{Equation E-13}$$

Vault capacity

For 1BMA, sorption sites in both waste and concrete structure are considered to be available,

$$\text{Cap}_{\text{vault}} = \text{Cap}_{\text{waste}} + \text{Cap}_{\text{concrete structures}} \quad \text{Equation E-14}$$

Residence time

With the assumptions made above, the residence time for 1BMA can be calculated from:

$$T_{\text{res}}^{\text{Cap}} = \frac{\text{Cap}_{\text{waste}} + \text{Cap}_{\text{concrete structure}}}{\frac{1}{R_{\text{slab}}} + \frac{1}{R_{\text{inner lid}} + R_{\text{outer lid}}} + \frac{1}{R_{\text{inner walls}} + R_{\text{outer walls}}}} + Q_{\text{waste}} \quad \text{Equation E-15}$$

2BMA

In 2BMA, the radioactive waste is stored in 13 free-standing concrete caissons. The transport of radionuclides from the waste to the backfill surrounding the concrete caissons is modelled as a two-step process, characterised by (1) migration through the packaging to the surrounding water inside the caissons, followed by (2) migration through the concrete caissons to the surrounding backfill. As the radionuclides reach the backfill they are transported by the groundwater flowing into the host rock.

Flow and transport resistance

In 2BMA, as in the silo, the diffusive resistance of the waste packages is small compared with the resistance of the surrounding concrete caisson and the total resistance is estimated from the resistance of the caisson slab, lid and walls of the 13 caissons. In addition to the caisson slab, lid and wall the radionuclides can also diffuse through gas evacuation channels having diffusive resistance R_{gec} .

$$\frac{1}{R_{\text{barrier}}} \approx 13 \left(\frac{1}{R_{\text{slab}}} + \frac{1}{R_{\text{lid}}} + \frac{6}{R_{\text{gec}}} + \frac{1}{R_{\text{walls}}} \right) \quad \text{Equation E-16}$$

The water flow through the waste-domain is given in Abarca et al. (2020) but note that the total flow through the waste domain is the sum of the flow through the 13 caissons.

Vault capacity

For 2BMA, sorption sites in both waste and concrete structures are considered to be available:

$$Cap_{\text{vault}} = Cap_{\text{waste}} + Cap_{\text{concrete structures}} \quad \text{Equation E-17}$$

Residence time

With the assumptions made above, the residence time for 2BMA can be calculated from:

$$T_{\text{res}}^{\text{Cap}} = \frac{Cap_{\text{waste}} + Cap_{\text{concrete structures}}}{13 \left(\frac{1}{R_{\text{slab}}} + \frac{1}{R_{\text{lid}}} + \frac{6}{R_{\text{gec}}} + \frac{1}{R_{\text{walls}}} \right) + Q_{\text{waste}}} \quad \text{Equation E-18}$$

1BRT

The waste vault for RPVs will contain mainly steel arising from the decommissioning of boiling water reactors. The pressure vessels will be cut into segments, placed in moulds and stabilised with grout. The waste packages will be placed in a concrete structure and surrounded by grout.

The transport of radionuclides from the irradiation-activated steel waste to the backfill surrounding the concrete structure can be considered as a two-step process. The first step is the corrosion-controlled release of radionuclides from the vessel steel to the embedment material (grout) within the waste packages (moulds) and the grout surrounding the waste packages. The transport resistance of the waste package itself and of the grout are neglected. The second step is the migration of radionuclides through the concrete structure to the surrounding backfill. For the fraction of the inventory that is instantaneously released from the waste, only the second step is relevant. As the radionuclides reach the backfill, they will be transported further by the groundwater flowing into the host rock.

Diffusive flow and transport resistance

For 1BRT the diffusive resistance of the waste packages is neglected and the embedment material (grout) inside the package and grout surrounding the waste packages (backfill) is represented as a single grout compartment. The assumption that the diffusive resistance of the waste packaging can be neglected is justified if the diffusive resistance of the package is small compared with the resistance of the surrounding concrete structure. The grout is viewed as a stirred tank with no resistance. The total resistance is approximated by the resistance of the slab, lid and walls of the concrete structure.

$$\frac{1}{R_{\text{barrier}}} \approx \left(\frac{1}{R_{\text{slab}}} + \frac{1}{R_{\text{lid}}} + \frac{1}{R_{\text{walls}}} \right) \quad \text{Equation E-19}$$

Vault capacity

For 1BRT sorption sites in both waste and concrete structure are considered:

$$Cap_{\text{vault}} = Cap_{\text{waste}} + Cap_{\text{concrete structure}} \quad \text{Equation E-20}$$

Residence time

With the assumptions made above, the residence time for 1BRT can be calculated from:

$$T_{\text{res}}^{\text{Cap}} = \frac{Cap_{\text{waste}} + Cap_{\text{concrete structure}}}{\frac{1}{R_{\text{slab}}} + \frac{1}{R_{\text{lid}}} + \frac{1}{R_{\text{walls}}} + Q_{\text{waste}}} \quad \text{Equation E-21}$$

In addition to the residence time, the sustained release from 1BRT is also dependent on the corrosion time of the steel from the RPVs, see further details in Section 5.3.

1-2BTF

Both 1BTF and 2BTF contain concrete tanks with dewatered ion exchange resins stacked on top of each other on a concrete slab. 1BTF also contains waste drums with ash, with supporting walls consisting of concrete tanks and concrete moulds. 2BTF contains 750 concrete tanks. The spaces between the waste packages, rock walls and the slab are grouted with concrete. A lid of concrete is placed on top of the waste. The remaining empty space is backfilled with gravel.

The transport of radionuclides from the waste packages to the surrounding rock can be considered a two-step process. The first step is the migration from the interior of the packages to surrounding grout. The second step is the migration from the grout through the concrete lid or concrete slab. A simplification made in the estimate of the residence time in 1-2BTF is to neglect the diffusive transport through grout on the sides (the concrete between the tanks and the rock walls). As the radionuclides reach the backfill at the top or bottom of the vault, they will be transported by the groundwater flowing through the backfill into the host rock.

Diffusive flow and transport resistance

The total diffusive resistance, R_{barrier} , of 1-2BTF is given by the sum of the resistances of the waste packaging and the concrete structures (lid and slab). The grout is viewed as a stirred tank with no resistance.

The 750 concrete tanks in 2BTF exhibit the largest volume:area ratio of all types of waste packaging in SFR which implies a relatively large diffusive resistance. The combined diffusive resistance of the 750 tanks in 2BTF is given by:

$$\frac{1}{R_{\text{tanks}}} = 750 \left(\frac{1}{R_{\text{tank floor}}} + \frac{1}{R_{\text{tank lid}}} + \frac{1}{R_{\text{tank walls}}} \right) \quad \text{Equation E-22}$$

In the second step the radionuclides can diffuse both through the concrete lid and slab. For simplicity when estimating the residence time in 2BTF, the small diffusive transport through the slab is neglected and the total diffusive resistance is approximated by:

$$R_{\text{barrier}} = R_{\text{tanks}} + \frac{1}{\frac{1}{R_{\text{lid}}} + \frac{1}{R_{\text{slab}}}} \approx R_{\text{tanks}} + R_{\text{lid}} \quad \text{Equation E-23}$$

In 1BTF, the waste is more diverse than in 2BTF and a general description of the diffusive resistance through the waste packaging cannot be derived for all the different variations. It is assumed that the resistance of the waste packaging, R_{waste} , is, in general, small compared with the resistance of the surrounding structures and that the total resistance is dominated by the lid.

$$R_{\text{barrier}} \approx R_{\text{lid}} \quad \text{Equation E-24}$$

Vault capacity

For both 1BTF and 2BTF the sorption in the waste packaging, grout and concrete structures is considered and the capacity is calculated from

$$Cap_{\text{vault}} = Cap_{\text{waste}} + Cap_{\text{grout}} + Cap_{\text{concrete structure}} \quad \text{Equation E-25}$$

Residence time

With the assumptions made above, the residence time for 1BTF can be calculated from:

$$T_{\text{res}}^{\text{Cap}} = \frac{Cap_{\text{waste}} + Cap_{\text{grout}} + Cap_{\text{concrete structure}}}{\frac{1}{R_{\text{lid}}} + Q_{\text{waste}}} \quad \text{Equation E-26}$$

And for 2BTF from:

$$T_{\text{res}}^{\text{Cap}} = \frac{Cap_{\text{waste}} + Cap_{\text{grout}} + Cap_{\text{concrete structure}}}{\frac{1}{R_{\text{tanks}} + R_{\text{lid}}} + Q_{\text{waste}}} \quad \text{Equation E-27}$$

1–5 BLA

The five vaults 1–5BLA are of similar design with a concrete slab cast on top of a drained foundation within the vault. The waste packages are standard ISO-containers. At closure the vaults are planned to be left unfilled.

Since no dedicated engineered barriers are present in 1–5BLA, the radionuclides are considered to be available for transport with the groundwater flow out to the geosphere as soon as they are dissolved in the vault groundwater. Since the ISO containers are not credited with any barrier function, this process is expected to be very fast relative to the other vaults. Thus, the transport models cautiously consider all radionuclides to be instantaneously dissolved in the water surrounding the waste.

Flow and transport resistance

The vaults of 1–5 BLA are unfilled and the transport resistance of the waste and the ISO containers is neglected. The total effective flow thus corresponds the advective flow through the waste, Q_{waste} .

Vault capacity

For 1–5 BLA sorption of radionuclides onto waste and waste package material is not considered and the capacity of a vault is given by the total pore and void volume of the vault, see Equation 4-2.

Residence time

With the assumptions made above, the residence time for 1–5 BLA can be calculated from:

$$T_{\text{res}}^{\text{Cap}} = \frac{Cap_{\text{vault}}}{Q_{\text{waste}}} \quad \text{Equation E-28}$$

E3 Estimated release rate versus half-life

This section contains vault-specific plots presenting the half-life of the radionuclides versus an estimated release rate. The estimated release rate is calculated using Equation E-7 using the initial inventory of the vault without consideration to radionuclide decay in the vault. The residence time varies as a function of time, see figures in Section 5.3. In the plots, a residence time representative of a longer period (at the start of a plateau in the figures in Section 5.3) is chosen.

Radionuclides closest to the upper right part of the plot with a long half-life and a large inventory – residence-time quotient are expected to dominate the release from the vault.

The silo

The estimated release rate versus half-life can be seen in Figure E-1. The residence time for the silo is taken from 5000 AD, at which point in time the residence-time plateaus and remains constant for a relatively long time afterwards (Section 5.3). Even though the residence-time plateaus at 5000 AD, the maximum release of some radionuclides, e.g. Ni-59, can be at a much later time point.

1BMA

In Figure E-2 the half-life versus the initial inventory divided by the residence time at 3600 AD is plotted, where 3600 AD is chosen because it marks the start of a residence-time plateau.

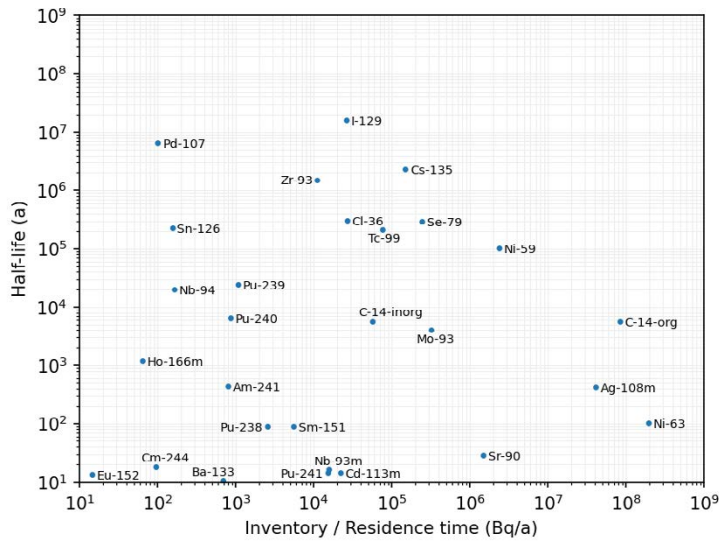


Figure E-1. Half-life versus inventory – residence-time quotient for the silo. The inventory is the inventory at closure and the residence time is calculated at 5000 AD.

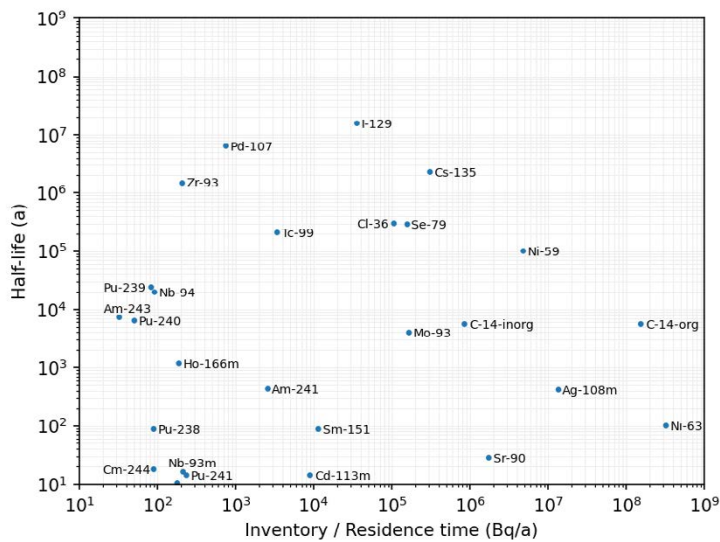


Figure E-2. Half-life versus inventory – residence-time quotient for 1BMA. The inventory is the inventory at closure and the residence time is calculated at 3600 AD.

2BMA

In Figure E-3, half-life versus the estimate of the release rate at 3600 AD is plotted. The time 3600 AD is chosen since the residence-time plateaus at this time, remaining constant for a relatively long time afterwards.

1BRT

An estimate of the release rate of the radionuclides from 1BRT to the surrounding rock which is instantaneously available for transport is obtained by dividing the inventory of instantaneously available radionuclides by their residence times, see Equation E-7. The release rate of induced activity is estimated by the ratio of the inventory to the corrosion time. Total release is estimated by the sum of the two contributions; this approach, however, does not take radioactive decay into account. In Figure E-4 the half-life versus the estimated release rate at 4000 AD is plotted. This point in time (4000 AD) is chosen since the residence time and corrosion rate reach a plateau. As for the other vaults, it is expected that radionuclides closest to the upper right part of the plot will dominate the release.

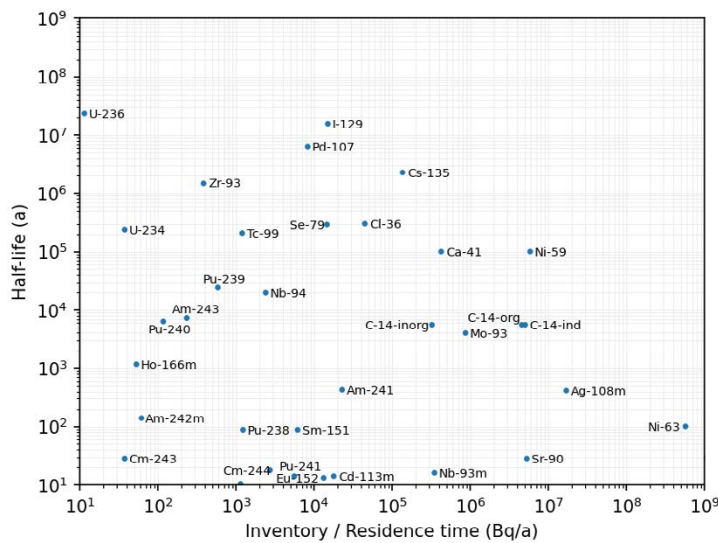


Figure E-3. Half-life versus inventory – residence-time quotient for 2BMA. The inventory is the inventory at closure and the residence time is calculated at 3600 AD.

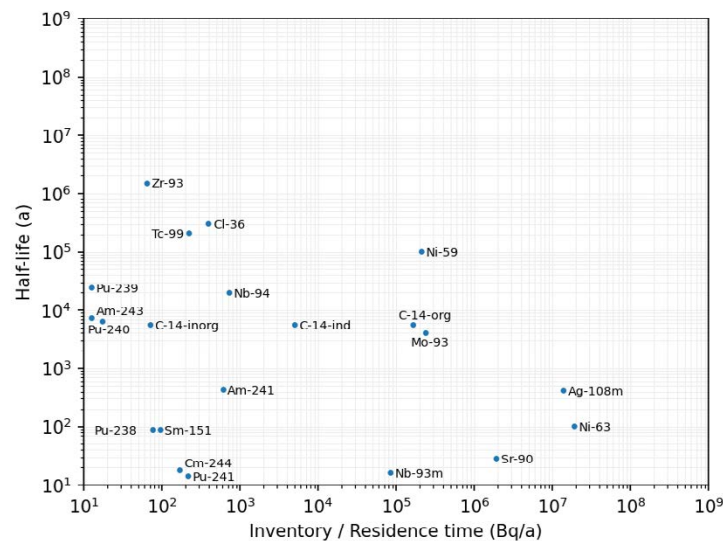


Figure E-4. Half-life versus inventory – residence-time quotient for 1BRT. The inventory is the inventory at closure and the residence time is calculated at 4000 AD.

1-2BTF

In Figure E-5 and E-6 the half-life versus the initial inventory divided by the residence time at 3600 AD is plotted for 1BTF and 2BTF, respectively. As for the other vaults, it is expected that radionuclides closest to the upper right part of the plot will dominate the release.

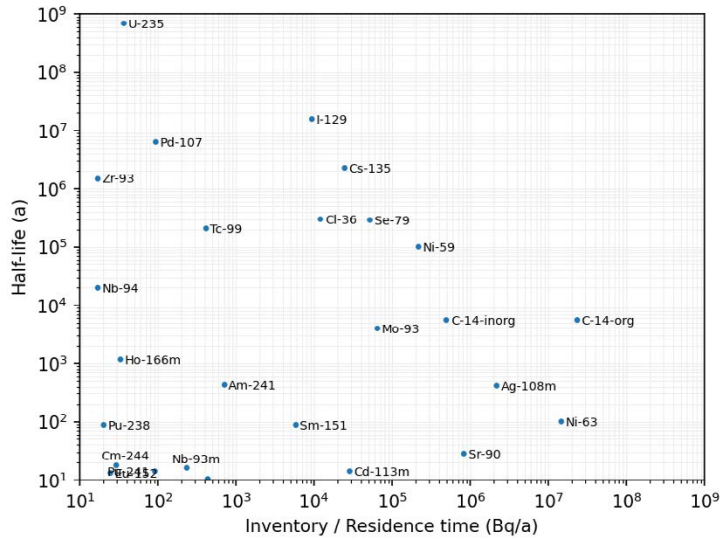


Figure E-5. Half-life versus inventory – residence-time quotient for 1BTF. The inventory is the inventory at closure and the residence time is calculated at 3600 AD.

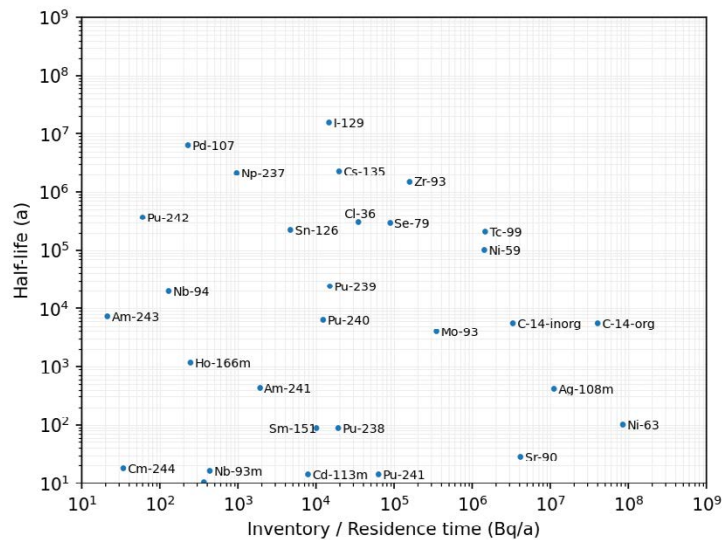


Figure E-6. Half-life versus inventory – residence-time quotient for 2BTF. The inventory is the inventory at closure and the residence time is calculated at 3600 AD.

1-5BLA

In Figures E-7 and E-8, the half-life versus the initial inventory divided by the residence time at 3600 AD is plotted for 1BLA and 2-5BLA, respectively. The time 3600 AD is chosen because the residence time remains constant afterwards. It should be noted that the release from 1BLA is quite early and that the maximum release occurs at ~3000 AD. The analytical estimate of the residence time is, however, higher prior to 3600 AD which means that the release rate would be lower than presented in the figure below.

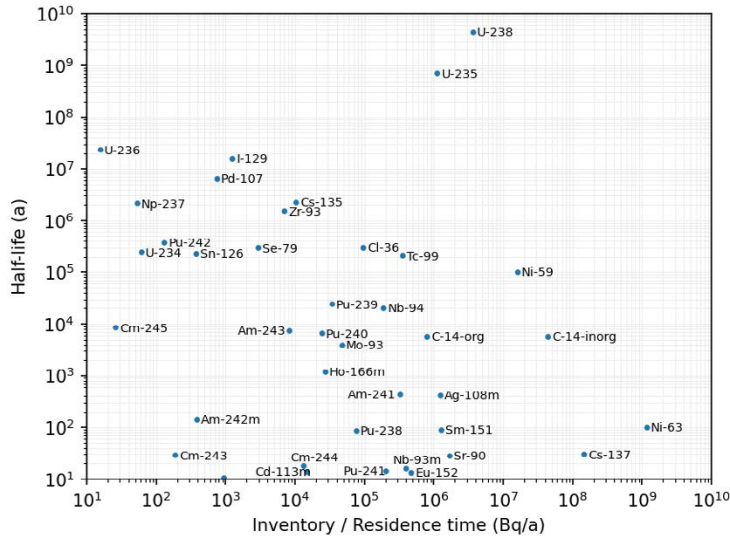


Figure E-7. Half-life versus inventory – residence-time quotient for 1BLA. The inventory is the inventory at closure and the residence time is calculated at 3600 AD.

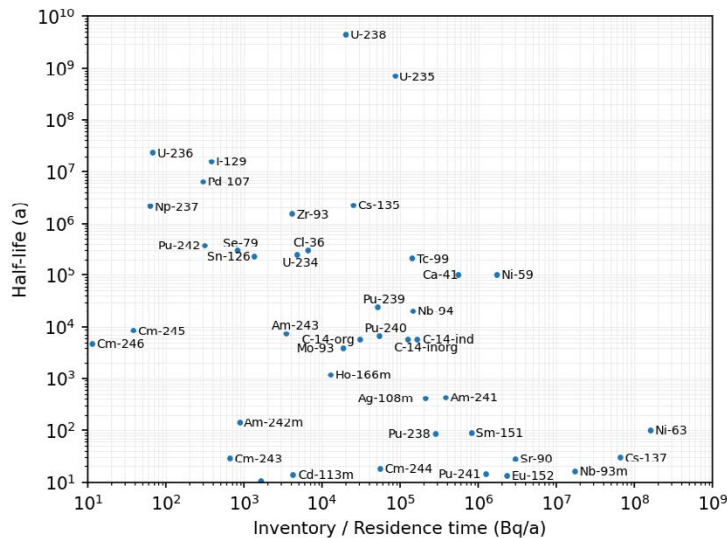


Figure E-8. Half-life versus inventory – residence-time quotient for 2-5BLA. The inventory is the inventory at closure and the residence time is calculated at 3600 AD.

SKB is responsible for managing spent nuclear fuel and radioactive waste produced by the Swedish nuclear power plants such that man and the environment are protected in the near and distant future.

skb.se